Chameleon Security Inks

Artemijs Krimovs

Durham University

Department of Chemistry

Chameleon Security Inks

A thesis submitted for the degree of
Doctor of Philosophy

Artemijs Krimovs

Supervisor: Prof Robert Pal

2026

Declaration

The work described herein was undertaken at the Department of Chemistry, Durham University between October 2022 and December 2025. All work is my own, except where specifically stated otherwise. No part has previously been submitted for a degree at this or any other university.

Statement of Copyright

Abstract

A novel arylalkynylpyridine-sensitised nine-coordinate *quasi*-C_3 symmetric all carboxylate donor europium(III) complex **EuL^1** possessing circularly polarised luminescence (CPL) with exceptionally high CPL brightness (*CPB*) in both ΔJ = 1 and ΔJ = 2 transitions was prepared and tested in solid-state polymethylmethacrylate (PMMA) spin-coated thin films. The structural design was based on the previously reported parent **EuL^0** which contained phenylphosphinate donor groups instead of their carboxylate equivalents in **EuL^1**. This structural modification resulted in 58% brightness increase (34650 mol^{-1} dm^3 cm^{-1}) and eliminated the dependence of the emission properties on the applied solvent. The use of arylalkynylpyridine facilitated sensitisation *via* a low-energy internal charge transfer state, resulting in optimal excitation with commercially available 365 nm LEDs. The Laporte forbidden $^5D_0 \rightarrow {}^7F_J$ transitions gave rise to ~1 millisecond emission lifetime, allowing time-gated methods when used in combination with short-lived (nanoseconds) organic fluorophores. **EuL^1** produced the highest ever reported branching factor-corrected *CPB* (*CPB$_i$*) values of 984 mol^{-1} dm^3 cm^{-1} and 590 mol^{-1} dm^3 cm^{-1} for the ΔJ = 2 (at 607 nm) using the branching factor for the whole and single-sign only regions respectively. The *CPB$_i$* of 307 mol^{-1} dm^3 cm^{-1} for the ΔJ = 1 (at 596 nm) was the third best across all europium(III) complexes and the highest reported for isostructural materials.

The authentication of the CPL security layer of **EuL^1** in PMMA thin films was performed using CPL photography (CPLP) and enantioselective differential chiral contrast (EDCC) imaging for both ΔJ = 1 and ΔJ = 2 transitions simultaneously using band pass optical filters. The effect of film substrate light reflections on the recorded chiral contrast was studied and quantified using the newly introduced CPLP dissymmetry factor (g_{CPLP}), which was found to be equivalent to the average dissymmetry factor obtained using a standard CPL spectrometer. The developed reproducible method of thin film preparation *via* spin-coating resulted in identical g_{CPLP} values for the consecutively spin-coated films, suggesting high reproducibility of the CPL security feature in combination with reliability of the authentication method.

A set of novel **EuL^1**-based materials compatible with the complex-stage functionalisation *via* 'click-chemistry' cycloaddition and nucleophilic substitution reactions was developed for the applications where a covalently linkable material with strong CPL-activity is desired. A proof-of-concept study demonstrated **EuL^3** functionalisation with propargyl glucose units which improved the live-cell uptake for a better bioimaging performance. All novel materials were photophysically characterised and explored in terms of their CPL properties which revealed that structural modifications away from the europium(III) coordination site did not affect the CPL intensity, g_{lum} or spectral shape, even when the total complex symmetry was lowered in **EuL^4** with unsymmetric macrocyclic ligand containing structurally different chromophores.

Acknowledgements

This thesis would not be possible without the support of the following people who I would like to thank:

My supervisor, Prof. Rober Pal, for providing me with the opportunity to work on this project and his continuous support and guidance.

All past and present RP and PB group members including Dr Thomas Bradford, Dr Lewis MacKenzie and Dr Samuel Penty. In particular, I would like to thank Dr. Dominic Black for insightful discussions and help with photophysical instrumentation, Dr. Davide de Rosa for helping me settle in the lab, Paolo Mastroeni for help with live cells and Connor Armstrong for good laugh and good tunes in the lab.

I would also like to thank other members of the Chemistry Department for their contribution: my progress review team Prof. Andrew Beeby and Dr. Russel Taylor, Dr. Aileen Congreve for invaluable help with chiral HPLC, Peter Stokes and Dr. David Parker for mass spectrometry, Dr. Juan Aguilar and Dr. Eric Hughes for NMR spectroscopy, Kelvin Appleby and Brian Denton for their help with the LED module for the camera, Josie Binks and Selene Munos-Vargas for their help with AFM, Marcos Perez-Pucheta for help with spin-coating, Anthony Humphries, Gary Southern and Gary Oswald for maintaining the supply of all lab necessities, Paul Hoffman for helping to maintain our labs in working order and, of course, all lab attendants, for daily supply of Musgrave Coffee which sometimes was the last thing that kept me going.

Thank you, Daicel, who kindly screened one of the samples against all available chiral HPLC columns to develop the separation method.

I also would like to thank DTP - EPSRC for funding this project.

Finally, big thanks to all my family, including my parents, Anna and her family for supporting me through all the highs and lows of this journey.

List of abbre*via*tions

1PE	single photon excitation
2PE	two-photon excitation
AC	absorbance chromatogram
AFM	atomic force microscopy
BET	back energy transfer
Boc	tert-butyloxycarbonyl
BODIPY	boron-dipyrromethene
BPF	band pass filter
CCD	charge-coupled device
CD	circular dichroism
CF	crystal field
CMOS	complementary metal-oxide-semiconductor
CP	circularly polarised
CPB	circularly polarised luminescence brightness
CPL	circularly polarised luminescence
CPLP	circularly polarised luminescence photography
CST	chameleon security tag
cyclen	1,4,7,10-tetraazacyclododecane
DCM	dichloromethane
DFT	density functional theory
DIPEA	*N,N*-diisopropylamine
DMSO	dimethyl sulfoxide
DNA	deoxyribonucleic acid
dpa	dipicolinic acid
dppf	diphenyl phosphino ferrocene
ED	electric dipole
EDCC	enantioselective differential chiral contrast
ESI	electrospray ionisation

ET	energy transfer
Flrscn	fluorescein
Fmoc	fluorenylmethyloxycarbonyl
FOV	field of view
hfbc	3heptafluoro-butylryl-(+)-camphorato
HOMO	highest occupied molecular orbital
HPLC	high performance liquid chromatography
IC	internal conversion
ICT	internal charge transfer
IED	induced electric dipole
ISC	intersystem crossing
LCMS	liquid chromatography-mass spectrometry
L-CP	left-handed circularly polarised
L-CPL	left-handed circularly polarised luminescence
LED	light emitting diode
LIA	lock in amplifier
LP	linear polariser
LPF	long pass filter
LPL	linearly polarised light
LSCM	laser scanning confocal microscopy
LUMO	lowest unoccupied molecular orbital
MD	magnetic dipole
MO	molecular orbital
MS	mass spectrum
NA	numerical aperture
Nd:YAG	neodymium-doped yttrium aluminium garnet
NIR	near-infrared
NMP	*N*-methyl-2-pyrrolidone
NRR	non-radiative relaxation
PD	photodiode

pda	pyridyl-diamide
PE	photoexcitation
PEG	polyethylene glycol
PEM	photo-elastic modulator
PET	polyethylene terephthalate
PL	photoluminescence
PMMA	polymethylmethacrylate
PMT	photomultiplier tube
PVA	polyvinyl acetate
PVP	polyvinylpyrrolidone
QToF	quadrupole time-of-flight
QWP	quarter waveplate
R-CP	right-handed circularly polarised
R-CPL	right-handed circularly polarised luminescence
RhB	rhodamine B
ROI	region of interest
rpm	rotations per minute
RR	radiative relaxation
rt	room temperature
SM	scanning monochromator
sRGB	standard red-green-blue
TACN	1,4,7-triazacyclononane
TEA	triethylamine
TFA	trifluoroacetic acid
TIPS	triisopropylsilane
TLC	thin layer chromatography
UPLC	ultra-performance liquid chromatography
UV	ultraviolet

Table of Contents

CHAPTER I. Introduction to luminescence of trivalent lanthanides and their applications

I.1. Introduction to photoluminescence and vibronic transitions

Luminescence is a process of energy release from electronically excited species in a form of electromagnetic radiation that corresponds to ultraviolet (UV), visible or near infrared (NIR) light. Unlike other types of luminescence such as chemiluminescence, which is facilitated by a chemical reaction, photoluminescence (PL) occurs after absorption of a photon of light by a species in its ground electronic state. Photon absorption promotes the system into an excited electronic state that is higher in energy compared to the ground state, which known as photoexcitation (PE).

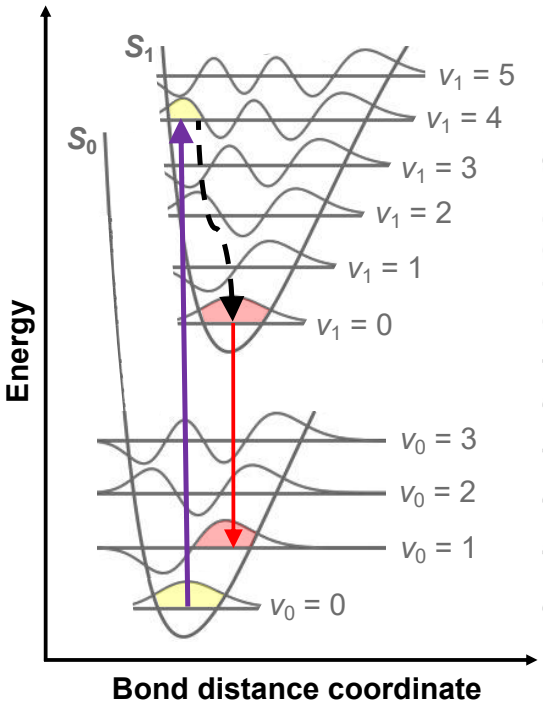

Figure 1.1: Bond distance coordinate-misaligned potential energy wells demonstrating vibrational levels and their wavefunctions of two electronic states, where transitions (PE – purple, PL – red), separated by vibrational relaxation (dashed) occur between states with the in-phase wavefunctions.

In most cases, transitions caused by PE are vibronic in nature. This means they result in a change of the system in terms of both electronic and vibrational states. Vibronic transitions are more common for organic fluorophores and transition metal complexes and less common for lanthanide complexes due to the nature of the orbitals involved. Structures of organic fluorophores can usually be characterised by high degrees of conjugation facilitated by extended networks of p-orbitals that host delocalised electron clouds. Variation in relative phases of these p-orbitals gives rice to molecular orbitals (MOs) of different energies that are involved in PE and PL processes. Similarly, transition metal complexes contain MOs that are combinations of atomic and MOs of the metal and the ligands respectively. Overall, PE of such systems promotes electrons from lower energy bonding MOs to higher energy non-bonding or anti-bonding MOs which weakens the bonds between atoms in organic fluorophores and metal to ligand bonds in transition metal complexes. This leads to an increase in the average bond distance in the electronic excited state, compared to the ground state (Figure 1.1). PE usually promotes the system from the lowest vibrational state of the ground electronic state, which is the most populated at room temperature (rt), into a higher vibrational state of the excited electronic state. According to Franck-Condon principle, during the PE, atomic nuclei can be considered static, since the time

scale of electronic transitions (~10^{-15} s) is much shorter compared to atomic vibrations (~10^{-13} s). Therefore, the probability of the transitions between specific vibrational states of two different electronic states depends on the relative phase of their vibrational wavefunctions at a fixed bond distance coordinate which can be expressed using the Franck-Condon factors. The same principle applies to PL that, according to Kasha's rule, normally involves a transition between the lowest vibrational level of electronic excited state and some higher vibrational levels of electronic ground state.[1] This justifies why absorption and emission spectra of fluorophores and transition metal complexes that undergo vibronic transitions are often mirror images. Due to significant bond vibrations even at rt, the relative energies of the MOs varies, which is attributed to changes in spatial orbital overlap. This results in Gaussian or Lorentzian shaped curves on absorption and emission spectra that often overlap, reducing the informativeness of spectra due to indistinguishability of lower intensity peaks. This is often tackled by spectroscopy performed at very low temperatures (~70 K) to minimise bond vibrations to obtain narrower bands that provide a better insight into electronic structure. On the contrary, emission of trivalent lanthanides appears as inherently narrow bands on emission spectra even at ambient temperature due to a different nature of the orbitals involved (Section I.5.).

I.2. Radiative and non-radiative relaxation

PE of a system is normally followed by its relaxation back to the ground electronic state. This is facilitated by multiple processes that are divided into two categories – radiative relaxation (RR) and non-radiative relaxation (NRR) that can be visualised using a Jablonski diagram (Figure 1.2).[2] In the diagram, S_0, S_1 and S_2 are the ground, first and second singlet excited states, while T_1 is triplet excited state. Photon absorption leads to PE of the system from S_0 to S_1 or S_2 depending on the λ of the excitation light. Due to the vibrionic nature of such transitions, PE leads to population of higher vibrational levels of electronic excited states. This facilitates vibrational relaxation of the system back to its ground vibrational state of an electronic excited state *via* non-radiative energy transfer (ET) to other kinetic modes of the same system or other systems, for example, solvent molecules. Another form of NRR is internal conversion (IC) which can facilitate transition between the S_2 and S_1. Once a higher vibrational state of S_1 is populated, vibrational relaxation will further relax the system to the ground vibrational state of S_1. At this point the system can relax further *via* either fluorescence (RR) or intersystem

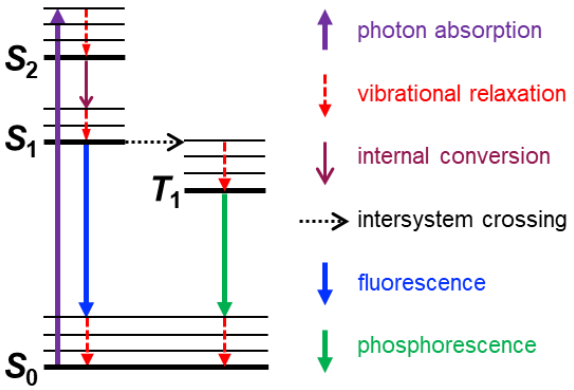

Figure 1.2: Jablonski diagram.

crossing (ISC), which is a NRR process. It is facilitated by an inversion of electron spin to give T_1, which is lower in energy than S_1 due to a higher spin multiplicity. Population of T_1 affords further relaxation in a form of phosphorescence, a long-lived spin-forbidden type of RR. In contrast, fluorescence is spin-allowed and therefore shorter lived. Both types of luminescence usually occur from the lowest vibrational levels of S_1 or T_1 to higher vibrational levels of S_0, according to Franck-Condon principle.

Overall, the relative amount of energy released *via* RR and NRR determines relative position of absorption and emission spectra. Emission spectrum is usually found at a longer λ compared to absorption spectrum, which is known as Stokes shift. Stokes shift is observed in most systems since there is always a fraction of the energy that is released *via* NRR.

I.3. General descriptors of luminescent properties

There is a set of variables that are used to describe photophysical characteristics. The fundamental equation (Equation 1) relates the energy of a photon and the λ through the Planck's constant (h = 6.62607015×10^{-34} J s) and the speed of light (c = 299 792 458 m s^{-1}).

$$E = \frac{hc}{\lambda} \quad [1]$$

Another important quantity, molar absorption coefficient (ε), describes how well the system absorbs light of a particular λ. It has the units of mol^{-1} dm^3 cm^{-1} (M^{-1} cm^{-1}) and is an inherent property of a material. ε can be experimentally determined using Beer-Lambert law that implies proportional relationship (Equation 2) between absorbance (A) and concentration (C) of luminescent species in solution, where L is the optical path length of light through the sample, usually equal to 1.0000 cm for a standard cuvette. The law holds well at low concentrations and tends to break down at higher concentrations. A can be also expressed as common logarithm of the ratio between the intensities of the incident (I_0) and transmitted (I) light through the sample, which also correlates with the principle of absorption spectrum acquisition.

$$A = \varepsilon CL = \log_{10}\left(\frac{I_0}{I}\right) \quad [2]$$

Another significant quantity, photoluminescent quantum yield (Φ), describes how much of the energy of the absorbed light is released by the means of PL. It can be simply expressed as the ratio between the number of photons absorbed and emitted. Φ can also be expressed using the rates of RR (k_{RR}) and NRR (k_{NRR}) as follows (Equation 3).

$$\Phi = \frac{k_{RR}}{k_{RR} + k_{NRR}} \quad [3]$$

It is challenging to determine Φ using relaxation rates. While k_{RR} can be determined using emission lifetime (τ), k_{NRR} would require quantification of all occurring NRR processes. Therefore, there are two sensible ways of experimental determination of Φ. The first method is often referred as absolute, since the relative amount of absorbed and emitted photons can be precisely determined using an integrating sphere. The other method is known as relative, where Φ can be calculated (Equation 4) with respect to a reference compound with a known quantum yield (Φ_R), where *OD* is optical densities and *n* is refractive index.

$$\Phi = \Phi_R \times \frac{I}{I_R}\frac{OD_R}{OD}\frac{n^2}{n_R^2} = \Phi_R \times \frac{I}{I_R}\frac{A_R}{A} \quad [4]$$

If the sample and the reference are both measured in the same solvent, then the ratio of *n* is cancelled out from the equation. The ratio of *OD* can be replaced with the ratio of the measured *A*, allowing for experimental determination of Φ.

Another useful parameter describes the τ of PL which is crucial for time-gated methods exploited in this project. When a luminescent material absorbs light, it undergoes PE that produces a certain initial number of electronically excited species (N_0). This is immediately followed by relaxation of the system that reduces N_0 by the means of RR and NRR. Therefore, the time-dependent decay of the excited state population ($dN(t)/dt$) can be expressed using k_{RR} and k_{NRR} where *N* is the number of electronically excited species at a certain time (*t*) following PE (Equation 5).

$$\frac{dN(t)}{dt} = (k_{RR} + k_{NRR})N(t) \quad [5]$$

Since PL results in the same emission probability for each excited species, *N* follows an exponential decay, where τ is emission lifetime (Equation 6). Since population of the excited state is proportional to the recorded emission intensity, the equation can be re-written and used for experimental determination of τ.

$$N(t) = N_0 exp\left(\frac{-t}{\tau}\right) \qquad I(t) = I_0 exp\left(\frac{-t}{\tau}\right) \quad [6]$$

Finally, PL brightness (*B*) is used to estimate overall PL performance. It is simply a product of ε and Φ (Equation 7) which implies that materials that possess high value of *B* must effectively absorb light and then release this energy mostly through PL.

$$B = \varepsilon\Phi \quad [7]$$

I.4. Electronic states of trivalent lanthanides

In order to describe the transitions between the electronic states that are associated with PE and PL, it is convenient to use Russell-Saunders atomic term symbols. Free-ion term symbol is written in a form of $^{(2S+1)}L_J$, where S is the total electron spin angular momentum, L is the total orbital angular momentum, which can take integer values 0, 1, 2, 3, 4... corresponding to *S, P, D, F, G...* in the place of L respectively, $2S+1$ is spin multiplicity, and J is total angular momentum that is a product of spin-orbit coupling ($J = S + L$). Due to a relatively weak effect of crystal field (CF) on lanthanides, their electronic states are better described using free ion term symbols. In contrast, in the case of transition metal complexes the free ion term symbols are further split into *A*, *E* and *T* terms depending on the point group symmetry of the metal site.

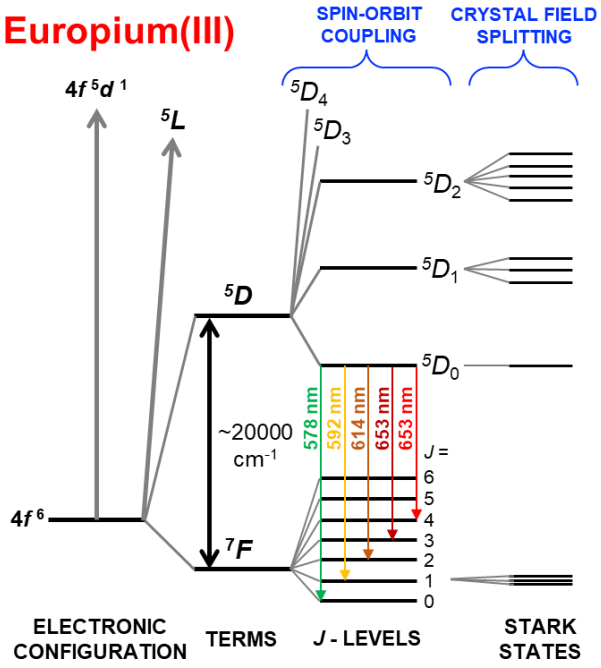

Figure 1.3: Splititng of the elctronic energy levels in Eu^{3+} and approximate $^5D_0 \rightarrow {}^4F_J$ transition energies (reproduced from Bünzli (1987) and Kumar (2010)).[3,4]

In this work, the electronic states of trivalent europium, europium(III), and associated transitions were investigated. Europium(III) has electronic configuration [Xe] $4f^6$, the degeneracy of which is perturbed (Figure 1.3) by such effects as electron repulsion (electrostatic interaction between the electrons in the 4*f* shell), spin-orbit coupling (interaction between the electron spin and its angular momentum) and CF (interaction between the electrons in 4*f* orbitals and orbitals of the ligands).

The electronic ground state of europium(III) is characterised by 6 spin-parallel electrons occupying 4*f* orbitals. This produces maximal values of $L = 3$, $S = 3$ and $2S+1 = 7$ which corresponds to ^7F term symbol. In heavy elements such as lanthanides, the effect of spin-orbit coupling is more significant than that of the CF. Vectoral addition of L and S results in ^7F splitting into 7 possible J states ($^7F_0$, $^7F_1$, $^7F_2$, $^7F_3$, $^7F_4$, $^7F_5$ and $^7F_6$). According to the Hund's Rule, $^7F_0$ is the lowest in energy since it has the lowest value of J ($4f^6$ is less than half full), which makes it the ground electronic state. A relatively weak effect of CF further splits each J state into $2J+1$ Stark states that are just ~10^2 cm^{-1} apart compared to larger ~10^3 cm^{-1} separating sequential J states.[3]

The term symbol of the first electronic excited state, ^5D, is derived in the same way with 5 possible J states ($^5D_0$, $^5D_1$, $^5D_2$, $^5D_3$ and $^5D_4$). The energy difference between ^5D and ^7F is on the order of ~10^4 cm^{-1} which makes it thermally inaccessible (k_BT ~ 200 cm^{-1} at rt). The energy gap between ^5D and the J states of ^7F is on the same order of magnitude with the red region of visible light (620 – 750 nm or 16000 – 13000 cm^{-1}), resulting in a characteristic red glow of europium(III) containing materials when photoexcited.

I.5. Introduction to selection rules affecting europium(III) *f-f* transitions

Light is an electromagnetic wave that comprises both magnetic and electric oscillating magnetic fields. Therefore, effective interaction of a chromophore with light results in electric dipole (ED) and magnetic dipole (MD) transition dipole moments. ED transition can be considered a linear movement of charge which is an odd transformation with respect to an inversion centre (if species contain an inversion centre, each structural unit when translated along the line passing through an inversion centre will coincide exactly with the same structural unit at an equidistant position from the inversion centre). MD transition can be interpreted as rotational displacement of charge, and the sense of such rotation is not inverted with respect to an inversion centre. Therefore, ED and MD transitions are odd and even parity respectively. All ED *f-f* transitions in free-ion form of lanthanides are formally forbidden by the orbital selection rule, known as Laporte rule which applies to centrosymmetric systems with an inversion centre. It allows only those transitions that occur between orbitals of different parity, which describes if an orbital is symmetric or anti-symmetric with respect to inversion. In other words, transitions between the orbitals of the same symmetry are Laporte-forbidden, for example $s\leftrightarrow s$, $p\leftrightarrow p$, $d\leftrightarrow d$ and $f\leftrightarrow f$ transitions, since they have the same L. Laporte-forbidden transitions are associated with low molar extinction coefficients (<1 dm^3 mol^{-1} cm^{-1}) that result in very low absorption of light. Laporte rule in centrosymmetric lanthanide complexes is 'relaxed' due to mixing between orbitals of different parity. This can either occur through permanent mixing between the orbitals of a lanthanide metal centre and the ligands, known as CF, or through asymmetric molecular vibrations that instantaneously reduce the symmetry, known as vibronic coupling. Therefore, ED $f\leftrightarrow f$ transitions in centrosymmetric lanthanide complexes are partially Laporte-allowed and therefore are called induced electric dipole (IED) transitions.

MD transitions are Laporte-allowed transitions that are essentially independent on the environment. They are inherently weaker than ED transitions, since their magnitude depends on the curvature of the charge displacement path which is marginal in a relatively small volume of a lanthanide(III) ion. Normally, this makes MD transitions hardly observable experimentally, which, however, is not the case for lanthanides where all *f-f* transitions are Laporte-forbidden

and lower intensity IED transitions are observed instead. As a result, the MD transitions, for instance, $^5D_0 \rightarrow {}^7F_1$ in europium(III), can be experimentally observed alongside the IED transitions, since their intensity is on a similar order of magnitude.[3–5]

In addition to Laporte selection rule, spin selection rule allows transitions between electronic states that have the same value of *S*. As discussed earlier, ISC relaxes the system from S_1 to T_1 which can be further relaxed to the S_0 *via* phosphorescence. Both ISC and phosphorescence are spin-forbidden since they require and inversion of electron spin. This explains why spin-forbidden phosphorescence has a slower rate and therefore longer τ (10^{-3} to 10^{1} seconds (s)) compared to spin-allowed fluorescence (10^{-9} s).

As a result, the intensity of absorption and emission depends on the probability of the electronic transitions involved, which can be estimated using Laporte and spin selection rules. The selection rules can be then expressed using the changes in *L*, *S* and *J* quantum numbers that describe the states involved (Table 1.1). In the case of moderately heavy lanthanides, *L* and *S* do not provide a good representation due to a significant spin-orbit coupling. As a result, spin and Laporte selection rules are partially relaxed, while total angular momentum selection rules provide the most accurate approximation of the probability of *f-f* transitions.

Table 1.1: Selection rules for intraconfigurational *f-f* transitions (adapted from Binnemans (2015)).[3]

IED transitions	MD transitions
$\Delta S = 0$	$\Delta S = 0$
$\lvert\Delta L\rvert \leq 6$	$\Delta L = 0$
$\lvert\Delta J\rvert \leq 6$ and $\lvert\Delta J\rvert = 2, 4, 6$ if $J = 0$ or if $J' = 0$ (for example, $^5D_0$ of Eu^{3+})	$\Delta J = 0$ (except for $0 \leftrightarrow 0$), ± 1

I.6. The effect of crystal field on emission spectral shape of lanthanides

The effect of the CF is significantly stronger in transition metal complexes compared to lanthanide complexes. 3*d* orbitals of transition metals strongly interact with the orbitals of the ligands, while 4*f* orbitals of trivalent lanthanides are much more 'core' like due to substantial shielding from the CF by electrons in 5*s* and 5*p* orbitals.[6] This gives rise to a characteristic emission spectral profile of lanthanides containing relatively sharp bands at fixed λ positions (Figure 1.4.A) arising from $f \leftrightarrow f$ transitions of intra-atomic nature, as opposed to transitions between MOs in metal complexes that produce wide emission bands due to strong sensitivity towards metal-ligand bond vibrations.

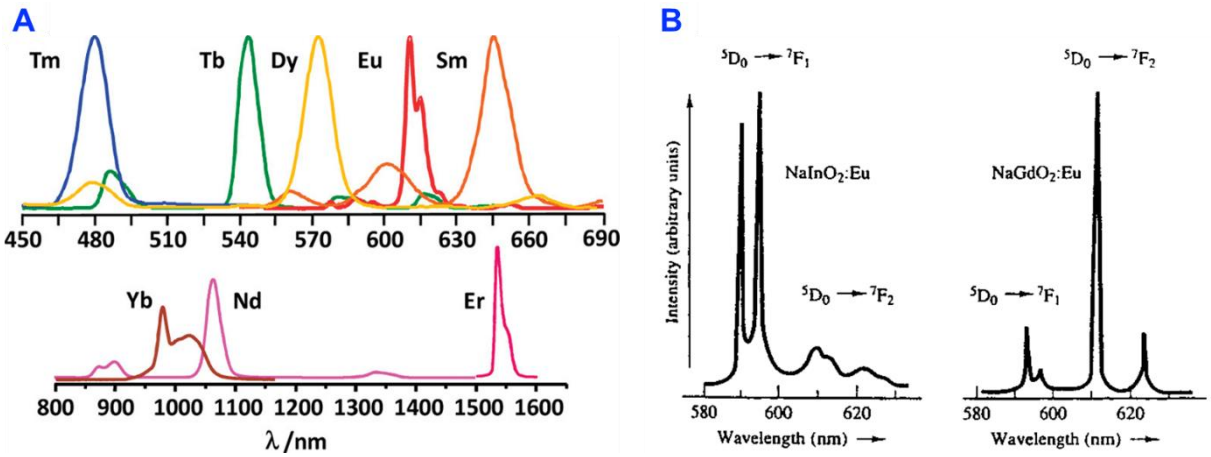

Figure 1.4. **A**: Low-resolution emission spectra of some lanthanide (III) tris(β-diketonates) (adapted from Bünzli (2010)).[7] **B**: Emission spectra of europium(III) doped $NaInO_2$ and $NaGdO_2$ (adapted from Cotton (2006)).[7]

CF effect in lanthanide metal complexes is relatively weak but not negligible. As a result, transitions to each individual ^7F_J state appears as multiple bands corresponding to the CF splitting of that state. As a result, the emission spectral shape and relative intensity of individual bands are strongly dependent on the symmetry of the europium(III) site provided by the ligand coordination. For example, the appearance of $\Delta J = 0$ ($^5D_0 \rightarrow {}^7F_0$) as multiple transitions would indicate a presence of multiple europium(III) sites since both $^5D_0$ and $^7F_0$ are always singly degenerate. Additionally, $\Delta J = 0$ transition is only observed for relatively low-symmetry environments of europium(III). On the contrary, MD $\Delta J = 1$ ($^5D_0 \rightarrow {}^7F_1$) transition is insensitive to the environment and always produces observable intensity, while relatively weak band splitting due to CF can be observed at sufficient spectral resolution. IED $\Delta J = 2$ ($^5D_0 \rightarrow {}^7F_2$) transition is known as 'hypersensitive' towards the environment. The intensity of this transition varies from very strong to very weak for the europium(III) environments with low and high symmetries respectively. For complexes with an inversion centre, $\Delta J = 2$ transition appears very weak (Table 1.2). For example, emission spectra of europium(III) doped $NaInO_2$ and $NaGdO_2$ solid-state oxides demonstrate significantly different features that depend on the symmetry of europium(III) site. While $\Delta J = 2$ emission band has marginal intensity of the emission spectrum of the centrosymmetric $NaInO_2$:Eu, it appears very intense for $NaGdO_2$ that lacks an inversion centre (Figure 1.4.B). Although lanthanides are weakly affected by CF, band splitting can still be observed at sufficient spectral resolution, provided by the characteristic narrow bands that are not significantly broadened by the metal-ligand bond vibrations. As a result, a unique spectral shape for lanthanides in different coordination environments can serve as a 'fingerprint', suggesting its possible application in luminescent security tagging.

Table 1.2: Characterisation of common europium(III) transitions (Adapted from Binnemans (2015)).[3]

Transition	Dipole character	λ range /nm	Relative intensity*	Comments
$^5D_0 \rightarrow {}^7F_0$	ED	570-585	vw	Only observed in C_n, C_{nv} and C_s sym.
$^5D_0 \rightarrow {}^7F_1$	MD	585-600	s	Essentially environment-independent
$^5D_0 \rightarrow {}^7F_2$	ED	610-630	vw to vs	Hypersensitive to the environment
$^5D_0 \rightarrow {}^7F_3$	ED	640-660	vw to w	Forbidden transition
$^5D_0 \rightarrow {}^7F_4$	ED	680-710	m to s	Moderate environment dependence
$^5D_0 \rightarrow {}^7F_5$	ED	740-770	vw	Forbidden transition
$^5D_0 \rightarrow {}^7F_6$	ED	810-840	vw to m	Rarely measured

* vw = very weak, w = weak, m = medium, s = strong, vs = very strong.

I.7. Sensitization of trivalent lanthanides

Due to the previously discussed low ε of Laporte-forbidden IED *f-f* transitions, direct excitation of lanthanides is inefficient and instead requires a specifically designed system containing a light absorbing chromophore, for example, a macrocyclic organic ligand, that would effectively absorb the excitation light energy and then transfer it to a luminescent lanthanide centre. This multi-step processed is known as sensitised emission and requires a consideration of competing relaxation processes, further referred to as quenching, that reduce the overall quantum efficiency of the system.

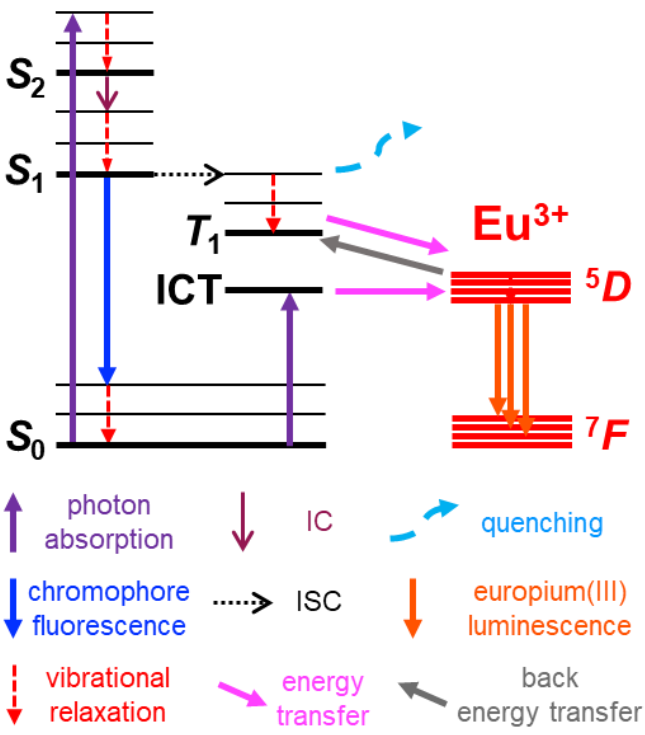

Figure 1.5: Jablonski diagram for europium(III) sensitisation.

Sensitisation can be expressed using an extended Jablonski diagram (Figure 1.5) which contains electronic states of both the sensitising chromophore and lanthanide, for instance, europium(III). Sensitisation commences with photon absorption (10^{15} s^{-1}) that populates higher vibrational levels of S_1 or S_2 electronic states of the sensitiser *via* a Laporte- and spin-allowed $\pi \rightarrow \pi^*$ or $n \rightarrow \pi^*$ transitions. This is followed by vibrational relaxation (10^{13} s^{-1}) to the ground vibrational state as well as IC from S_1 to S_2 in cases where S_2 was initially populated. After that, a relatively fast ISC is required to populate a long-lived T_1 in competition with sensitiser

fluorescence (~10^9 s^{-1}).[8] Such fast rates of ISC are observed when T_1 and S_1 states of the sensitising moiety are relatively close in energy.[9] The desired sensitisation pathway is then facilitated by electronic ET from the T_1 of the ligand to the lanthanide centre resulting in electronic excitation of the latter. Such ET can be modelled using the two established mechanisms - electron exchange (Dexter) and dipole-dipole (Förster).

Dexter mechanism involves a transfer of a high energy electron from the ligand in T_1 state to one of the excited states of the lanthanide, for example, $^5D_0$ of europium(III). Simultaneously, a 4*f* electron of the electronic ground state of the lanthanide, for example, $^7F_0$ of europium(III), is transferred to the S_0 of the ligand to recombine with the electron hole produced during the $S_0 \rightarrow T_1$ excitation. This creates another electron hole in $^7F_0$ that is recombined with an electron from $^5D_0$ during the PL of europium(III). Dexter mechanism is a short-range ET that strongly depends on the radial overlap between the wavefunctions of MOs of the ligand and the 4*f* orbitals. As a result, the ET rate decreases exponentially with the distance between the ligand energy donor and lanthanide acceptor (r_{DA}). For the $T_1 \rightarrow {}^5D_0$ ET in europium(III) complexes, the calculated rate was ~10^8 - 10^7 s^{-1}.[10]

Förster ET occurs *via* coupling between transition dipole moments of the ligand and the lanthanide. This depopulates T_1 of the ligand, returning the electron back to S_0. Förster ET is more long-range compared to Dexter. The rate of this dipole-dipole ET has r_{DA}^{-6} dependence, which justifies why Förster ET is considered 'long-range' and remains effective at larger r_{DA} (~5 to 6 Å) compared to Dexter (~3 Å).[10,11]

Apart from the distance between the ligand and the lanthanide, the rate of ET depends on the relative energies of the states involved, so that the smallest energy difference between the T_1 and $^5D_0$ would result in the highest rate of ET. On the contrary, when such energy difference is too small, non-radiative thermally activated back energy transfer (BET) repopulates the long-lived T_1 of a ligand at the expense of $^5D_0$, resulting in a competing with PL process. Since $^5D_0$ is generally longer lived (10^{-6} to 10^{-3} s) than T_1 (< 10^{-6} s), the former needs to be more than 10 k_BT (2050 cm^{-1}) higher in energy ($^5D_1$ and $^5D_0$ of europium(III) lie at 19050 and 17220 cm^{-1} respectively; $^5D_4$ of terbium(III) lies at 22 450 cm^{-1}) to minimise the thermally activated BET and therefore increase the sensitisation efficiency.[8] Otherwise, repopulation of the long-lived T_1 increases the probability of other NRR processes such as quenching by oxygen. As a consequence, BET allowed for practical applications of terbium(III) and europium(III) complexes as oxygen concentration and temperature sensors, where the luminescence τ and intensity decreased at increasing oxygen concentration and temperature.[12–17] This was achieved by using specifically designed sensitisers containing, for example, carbostyril and phenanthridine sensitisers (Figure 1.6) that possess T_1 states with the energies similar to the energy of $^5D_4$ excited state of terbium(III) to allow for the effective BET.

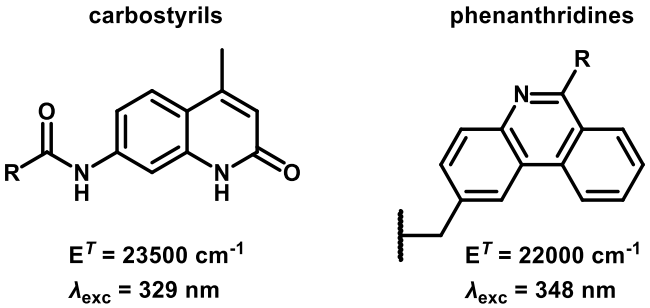

Figure 1.6: Structure, triplet state energy and optimal excitation λ (λ_{exc}) of carbosyril and phenanthridine sensitiser (adapted from Parker *et al.* (2021)).[8]

One of the advantageous consequences of sensitisation of lanthanide complexes is a large pseudo-Stokes shift (Figure 1.7).[18] Stokes shift in organic fluorophores results from PE and PL that are centred on a single chromophore. In contrast to that, sensitisation in lanthanide complexes often involves additional NRR, for instance, ET from the chromophore T_1 state to an excited state of a lanthanide, which are at least 10 k_BT apart for BET minimisation, that increases the magnitude of pseudo-Stokes. Although large pseudo-Stokes shift implies significant excitation energy loss *via* NRR, it brings a number of advantages that are crucial for some applications. For example, emission acquisition is simplified since the λ range of the emitted light is far from the optimal excitation λ, which is beneficial in bioimaging. Another advantage of large pseudo-Stokes' shift is that while the absorption λ falls into invisible to an unaided eye UV region, the PL λ range falls into visible light. This makes such system appear colourless until it is illuminated with low-energy UV to induce chromatically (colour) distinguished PL, suggesting applications in security inks.[18–22]

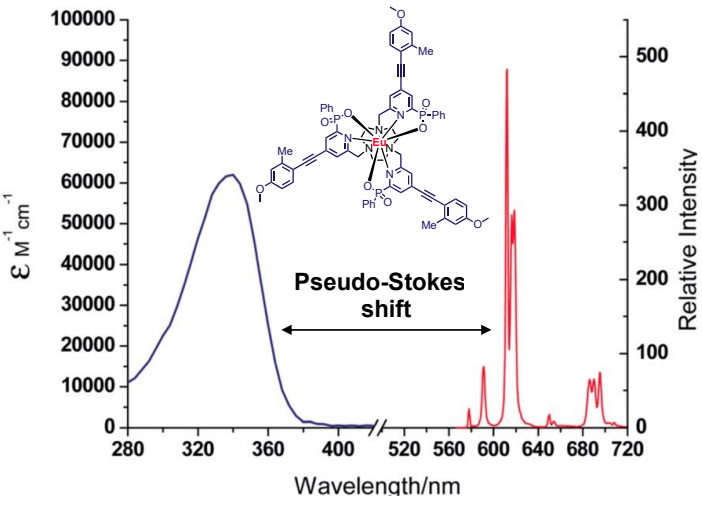

Figure 1.7: Pseudo-Stokes shift in alkylarylpyrydine-sensitised europium(III) complex (adapted from Butler et al. (2014)).[18]

Depending on the structure of the chromophore, the sensitisation can occur *via* an internal charge transfer (ICT) state rather than T_1. ICT state occurs when the structure of the chromophore contains conjugated spatially separated electron rich and electron depleted parts. In contrast to T_1, direct population of ICT state is spin-allowed, and therefore can be achieved *via* PE directly. One of the main advantages of sensitisation *via* a lower energy ICT state is the ability to excite the complex using a longer λ UV source, for instance, a commercially available 365 nm light emitting diode (LED).

One of the examples of the chromophore possessing an ICT state is arylalkynylpyridine. The ICT state in arylalkynylpyridines is facilitated by spatial separation of electron-rich aryl group and electron-depleted pyridyl group that are conjugated *via* an alkyne (Figure 1.8.A and B). According to density functional theory (DFT) calculations, the highest occupied MO (HOMO) is localised on the electron-rich aryl part of the chromophore, while the lowest unoccupied MO (LUMO) is found on the electron-depleted pyridyl part (Figure 1.8.C).[23]

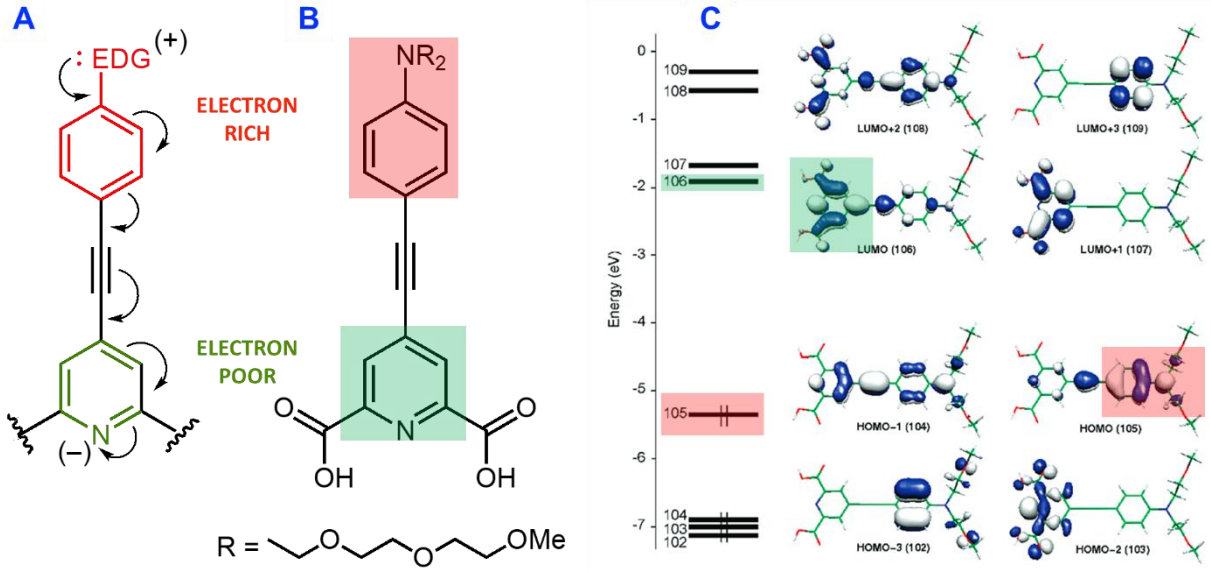

Figure 1.8. **A**: Resonance mechanism of ICT in arylalkynylpyridine. **B**: Example of an arylalkynylpyridine with an electron donor substituent on the aryl ring. **C**: Energy diagram for HOMO and LUMO, calculated for the species in **B** that demonstrates distribution of electron density in MOs (adapted from D'Aléo *et al.* (2008)).[23]

Upon closer examination, there are two LUMO orbitals that are very similar in energy and have slightly different distribution of electron density. A lower energy LUMO (106) appears to contain most but not all electron density on the pyridyl group, while in LUMO+1 (107), no electron density remains on the aryl 'top'. As a result, there is a possibility of populating two energetically similar LUMOs *via* PE since both have the ICT character and therefore produce high transition dipole moment.

It was also established that increasing the electron donating nature of the aryl ring substituents increases the energy of the HOMO and therefore decreases the HOMO-LUMO gap. This allows to fine-tune the λ of the absorption maximum that shifts bathochromically (red) when the aryl ring becomes more electron rich. Another advantage of large spatial separation of HOMO and LUMO is that PE results in a substantial displacement of electron charge. This increases the magnitude of the transition dipole moment and leads to larger values of ε. In addition to that, population of LUMO results in localisation of electron density on the pyridyl nitrogen atom which coordinates to the lanthanide centre in a complex. This results in a higher rate of ET that improves the material's Φ.

I.8. Chemical and photophysical properties of sensitisers

There is a large variety of chromophores that are used in sensitised lanthanide complexes (Figure 1.9) with certain structural similarities. Firstly, these molecules are highly conjugated which is a property of most organic fluorophores. In addition to good light absorption properties, extended conjugation brings their absorption λ maxima to the longer λ UV range. Secondly, sensitisers often contain lone pair donor atoms that can facilitate coordination to a metal centre. Lanthanides prefer coordination numbers of 8 or 9 and therefore require octa- or nonadentate ligands to form a stable with respect to dissociation complex. Coordinatively unsaturated lanthanide complexes are prone to coordination of the solvent molecules that can become a source of quenching.[24]

Multidenticity of macrocyclic ligands also results in stability towards dissociation of the complexes in solution since, for example, it would require association of 9 solvent molecules to detach a single nonadentate ligand, which is entropically unfavourable. Coordinational saturation of lanthanides can be achieved by using macrocyclic ligands with pre-arranged geometry which also minimises entropic penalty upon association to the metal centre. Macrocyclic ligands for lanthanides normally consist of one or multiple sensitisers covalently attached to a pre-arranged multidentate aza-crown ethers such as tetradentate 1,4,7,10-tetraazacyclododecane (cyclen) (Figure 1.9) and tridentate 1,4,7 - triazacyclononane (TACN).

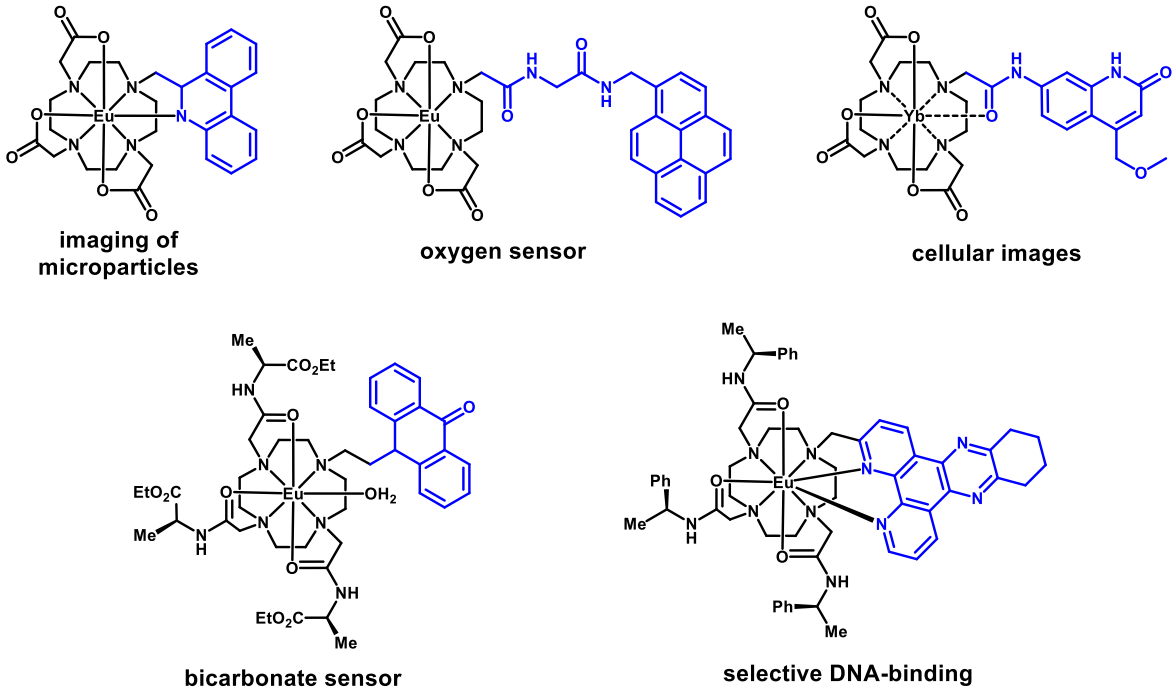

Figure 1.9: Several examples of lanthanide complexes with their sensitisers in blue.[17,25–28]

For example, in this work, a macrocyclic ligand comprising of a TACN with 3 sensitisers attached to it is used to sensitise europium(III). The ligand coordinates to europium(III) using 3 nitrogen atoms of the TACN, leaving 6 out of 9 coordination sites available for the chromophore donor atoms. This introduces chirality into the structure by the means of torsion angles and chiral centres, which then induces circularly polarised luminescence (CPL). Apart from aza-crown ethers, other unusual architectures (Figure 1.10) have been reported to effectively sensitise lanthanide complexes and produce strong CPL activity.[29,30]

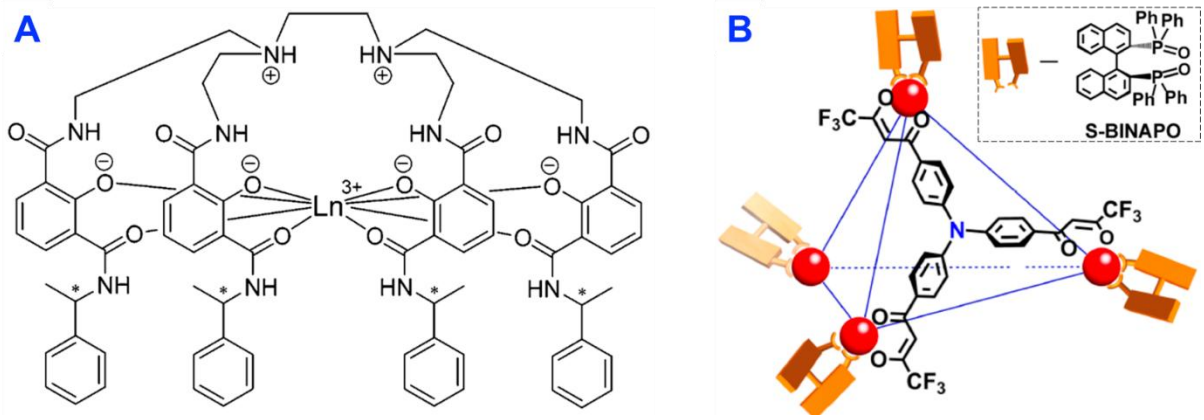

Figure 1.10: Examples of structures of some CPL-active lanthanide complexes. **A**: Chiral lanthanide complex comprising of octadentate 2-hydroxyisophthalamide containing ligand (adapted from Petoud *et al.* (2007).[29] **B**: $Eu_4L_4(L')_4$ tetrahedral cage made of four achiral C_3-symmetric tris(βdiketones) (4,4′,4″-tris(4,4,4-trifluoro-1,3-dioxobutyl)triphenylamine, L) as faces, four europium(III) as vertices and four chiral *R*-/*S*-bis(diphenylphosphoryl)-1,1′-binaphthyl (R/S BINAPO) as ancillary ligands (adapted from Zhou *et al.* (2019).[30]

I.9. Circularly polarised luminescence

In the context of quantum mechanical definition, all light is inherently circularly polarised (CP) and can possess two possible quantised spin angular momentum values of $+h/2\pi$ and $-h/2\pi$. If linearly polarised light (LPL) light is considered, the number of photons with spin angular momentum of $+h/2\pi$ is equal to those with $-h/2\pi$, resulting in net zero circular polarisation.[31–33] Therefore, all achiral luminescent species can be thought of producing equal amounts of left-handed CPL (L-CPL) and right-handed CPL (R-CPL) with no net helicity due to the equal probability of photons possessing either negative or positive values of the spin angular momentum, cancelling each other out. CPL can be also considered in terms of classical mechanics where light is an electromagnetic wave that consists of orthogonally oscillating electric and magnetic fields. For simplicity, magnetic field can be ignored and two orthogonally oscillating electric fields of the same λ considered. If such waves propagate in-phase, their combination will produce an electric field with a resulting vector that is at 45° with respect to the two orthogonal electric field components. If one of these two orthogonal waves is then shifted by a quarter of λ ($\lambda/4$) from the other, clockwise or anticlockwise rotation of the resulting electric field vector is produced as the wave propagates through space to give right-handed CP (R-CP) and left-handed CP (L-CP) light (Figure 1.11).

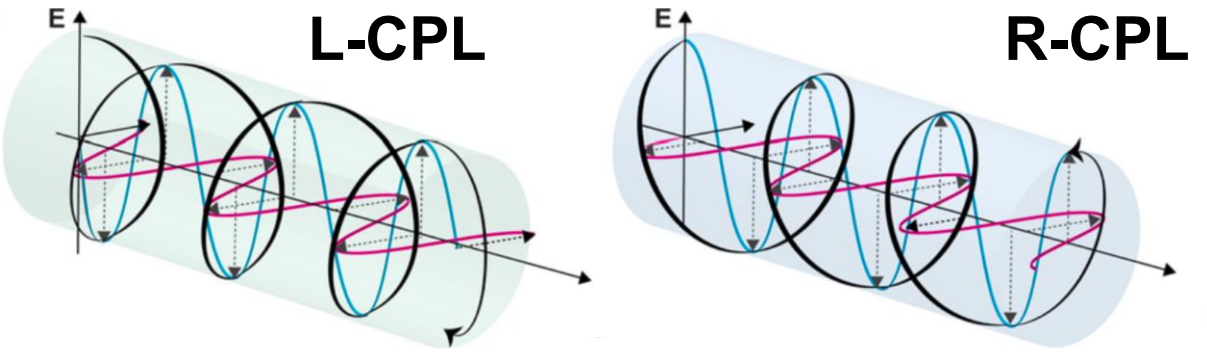

Figure 1.11: Classical interpretation of L- and R- CPL using vector model to describe the behaviour of the resulting electric field (adapted from Greenfield (2021)).[34]

L-CP and R-CP light can be generated by passing LPL through a quarter waveplate (QWP). QWPs contain a birefringent material such as quartz or liquid crystal polymers with light transmittance properties that are dependent on orientation, resulting in two orthogonally oriented fast and slow axes within. As a result, a wave that oscillates parallel two the slow axis will be retarded by $\lambda/4$ from a wave that oscillates parallel to the fast axis as both simultaneously passed through the QWP. Therefore, passing LPL at 45° to the fast axis will result in $\lambda/4$ retardation of the electric field component that is parallel to the slow axis, to induce CP light. The opposite helicity can be then achieved by passing LPL at -45° to the fast axis. Generation of L- and R-CP light is used in circular dichroism (CD) spectroscopy which is a technique that measures preferential absorption of L-CP or R-CP light by chiral materials.[35–38] CPL is the emission equivalent of CD. CPL-active materials usually emit unequal amounts of L-CPL and R-CPL with a different bias. Therefore, emission dissymmetry factor (g_{lum}) is used to describe the strength of CPL for different materials. In other words, a material that produces 99% L-CPL and 1% R-CPL will give a substantially stronger CPL signal compared to the one emitting 51% L-CP and 49% R-CP light. Therefore, g_{lum} can be expressed as a ratio between the L-CPL and R-CPL intensity (I) difference and a half of the total intensity (Equation 8).

$$g_{lum} = \frac{I_{L\text{-}CPL} - I_{R\text{-}CPL}}{0.5(I_{L\text{-}CPL} + I_{R\text{-}CPL})} = \frac{2(I_{L\text{-}CPL} - I_{R\text{-}CPL})}{(I_{L\text{-}CPL} + I_{R\text{-}CPL})} \quad [8]$$

As a result, theoretically possible values of g_{lum} are between 2 (only L-CPL) and -2 (only R-CPL), while $g_{lum} = 0$ indicates the absence of circular polarisation.

Practically useful CPL-active dyes must not only have high g_{lum} but also B. For example, a material can produce high g_{lum} and low total emission intensity due to poor B, which makes it inapplicable in rapid emission acquisition required for authentication of the CPL security feature. The product of g_{lum} and B is known as CPL brightness (CPB) (Equation 9).[22,39]

$$CPB = B\frac{g_{lum}}{2} = \varepsilon\Phi\frac{g_{lum}}{2} \quad [9]$$

CPB can also be used as a reference parameter to compare the performance of different CPL-active materials, where the maximal observed value of the g_{lum} is used. This, however, does not provide the most accurate representation of CPL performance, since g_{lum} is a function of emission λ. In other words, g_{lum} values can peak at λ of low total intensity that do not significantly contribute to the total emission and therefore *B*. This is particularly relevant for lanthanides, where some emission bands are more CPL-active than others. For example, the MD $\Delta J = 1$ transition in europium(III) demonstrates strong g_{lum} but contributes only ~5% to the total emission intensity. On the contrary, the most intense $\Delta J = 2$ transition often produces low g_{lum} values. Therefore, for a better measure *CPB* can be calculated for individual transitions (CPB_i) using a branching factor (β_i) which is the ratio of intensities of the emission band of interest and total emission (Equation 10).

$$CPB_i = \beta_i \times CPB \qquad [10]$$

For reference, the highest CPB_i to date was demonstrated by a recently developed europium(III) complex $[(Eu_4L_4)((R/S)\text{-BINAPO})_4]$ that was mentioned earlier (Section I.8, Figure 1.10.B).[30] CPB_i value of 3,000 M^{-1} cm^{-1} was produced by $\Delta J = 1$ transition.

There is a wide range of different classes of materials that are CPL active (Table 1.3.). Materials that were reported to produce the highest g_{lum} and *CPB* values are lanthanide(III) complexes, with particularly europium(III) producing the best results. The highest practically observed g_{lum} value of 1.38 were reported for the monomeric organometallic complex Cs[Eu(+)-(hfbc)$_4$] (hfbc = 3heptafluoro-butylryl-(+)-camphorato) (Figure 1.12).[40] In a separate publication, a helical polymeric form of Cs[Eu(+)-(hfbc)$_4$] resulted in the highest ever reported g_{lum} value of 1.45.[41] On the other hand, Cs[Eu(+)-(hfbc)$_4$] has relatively low CPB_i of just ~51 M^{-1} cm^{-1}, which is significantly lower than the average for europium(III) complexes 286 M^{-1} cm^{-1} ($\Delta J = 1$).[42] This highlights the superiority of CPB_i over g_{lum} in accurately estimating the performance of CPL-active materials for practical applications such as security inks.

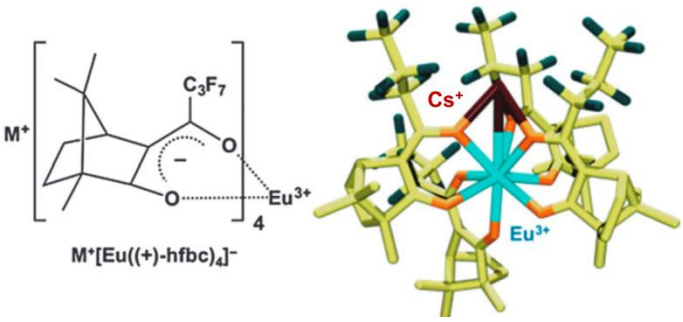

Figure 1.12. Schematic (left) and crystal (right) structure of CPL-active Cs[Eu(+)-(hfbc)$_4$] (adapted from Kumar et al. (2016)).[42]

Table 1.2: Overview of g_{lum}, *CPB* and Φ of CPL-active systems (adapted from MacKenzie and Pal (2021).[22,42]

CPL-active species	g_{lum} (best in class)	Average *CPB* / M^{-1} cm^{-1}	Φ / %
Lanthanide(III) complexes	0.1 – 1.4 (10^0)	Eu: 286 (ΔJ = 1), 69 (ΔJ = 2); Tb: 146; Yb: 4.	>50
Cr complexes	10^{-1}	174	~1
Helicenes	10^{-2}	5	3-65
Ketones	10^{-2}	1.1	<0.1
Cyclophanes	10^{-2}	68	>50
BODIPY derivatives	10^{-3}	47	15-70

I.10. Introduction to security inks

The focus of this project is on investigation of materials that can be used as security inks with 5 or more layers of security: spatial, chromatic, temporal, spectral and helicity-CPL. Spatial security layer is enclosed in a unique printed patter. Chromatic layer contains information on colours that are present within such pattern. Temporal layer contains information on the difference in emission lifetime of different security ink components which requires time time-gated authentication method. Spectral security layer is based on the total emission spectral shape that can serve as a unique fingerprint of the security ink structure. CPL security is based on the CPL sign and dissymmetry of the lanthanide(III) emission bands. While the first two levels – spatial and chromatic, can be easily verified using 'naked eye' and a conventional source of UV light, the rest would require a specially designed equipment. As a result, spatial and chromatic security layers are currently widely exploited in banknotes and identification documents such as driving licenses and passports.[22]

For example, a europium(III) complex of unknown structure is used in red emitting component of the luminescent pattern observed in the United Kingdom passports (Figure 1.13.A) under UV irradiation.[22] This was confirmed by the characteristic europium(III) emission spectral shape, while the wideband emission spectrum of the green component could be produced by some green fluorescing organic fluorophore such as fluorescein (**FIrscn**) (Figure 1.13.B).

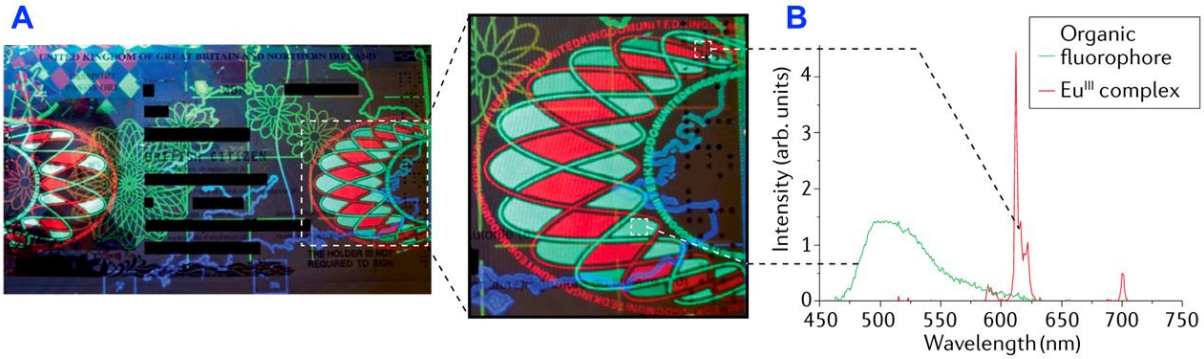

Figure 1.13. **A**: Luminescent security ink pattern on a contemporary United Kingdom passport that is only visible under 365 nm UV light. **B**: Emission spectrum recorded for green and red components of the pattern (adapted from MacKenzie and Pal (2021)).[22]

Another commonly known example are Euro banknotes that contain europium(III) and europium(II) complexes that produce red-orange and blue-green luminescent patterns under UV light. The presence of europium(III) was confirmed by recording the emission spectrum of the red-orange emission from a fragment of a 50 € banknote (Figure 1.14.A) to observe line-like spectral shape with characteristic for europium(III) band positions and relative intensities. The exact chemical composition of the sensitising ligand is kept secret to prevent counterfeiting.[5] This is an example of spectral security layer where identical relative intensities and splitting patterns of the emission bands can only be observed from lanthanide(III) complexes with the identical chemical composition. Although spectral fingerprinting is an effective anti-counterfeiting technique, it can't serve as a primary security layer since can only be authenticated using a high-resolution spectrometer.

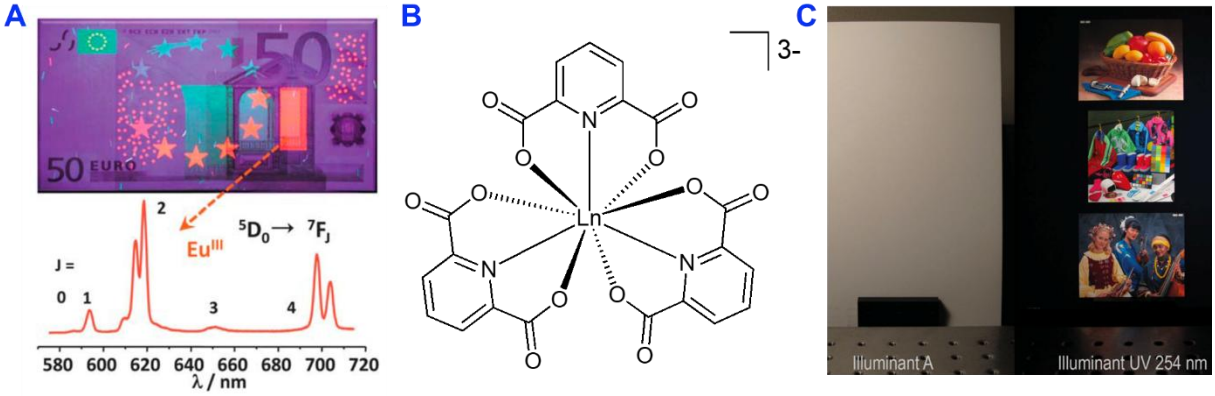

Figure 1.14. **A**: Emission spectrum (λ_{exc} = 366 nm) of the red-orange tag on a 50 € banknote (adapted from Bünzli and Eliseeva (2013)).[5] **B**: Structure of $[Ln(dpa)_3]^{3-}$ complex. **C**: Photograph of images printed using $[Ln(dpa)_3]^{3-}$ complexes of Eu and Tb and a blue fluorescent ink that are invisible (left) until illuminated with UV (254 nm) (right) (adapted from Andres *et al.* (2014)).[43]

Another promising example of security inks based on lanthanide(III) complexes for tags with spatial and chromatic security layers exploited water soluble $[Eu(dpa)_3]^{3-}$ and $[Tb(dpa)_3]^{3-}$ (dpa = dipicolinic acid) complexes producing red and green emission respectively (Figure 1.14.B). These two complexes together with a blue fluorescent ink were loaded into a standard inkjet printer to print full-colour images that were only visible under 254 nm UV irradiation (Figure 1.14.C). The obtained colour gamut was as large as the industry standard red-green-blue

(sRGB), which was achieved by mixing the three inks in different proportions using specially developed algorithms.[43]

A more recent example used zeolite particles doped with europium(III), terbium(III) and dysprosium(III) to create polyvinyl acetate (PVA) films containing a random multi-colour pattern.[44] High randomness of the particle distribution was obtained when preparing the films by spin-coating. Two possible ways to resolve the coloured pattern were discussed. Emission-based method required a spectrometer or band-pass filter-based detection to observe selected emission bands of the lanthanide(III) ions, which was not a reliable method due to spectral overlap of some europium(III) emission bands with the other two lanthanides (Figure 1.15.A). Excitation-based method was more reliable due to no significant overlap of the selected absorption bands of the three lanthanides. Therefore, 450, 465 and 488 nm laser lines were used to selectively excite dysprosium(III), europium(III) and terbium(III) respectively. The recorded emission intensity at each excitation λ was then assigned to R (europium), G (terbium) and B (dysprosium) channels (Figure 1.15.B) to generate digital versions of the random patterns. The selective excitation method avoided the need for a spectrometer and only required a single long pass filter (LPF) (optical filter that only transmits light above a specific λ) and a total intensity detector such as a charge-coupled device (CCD).

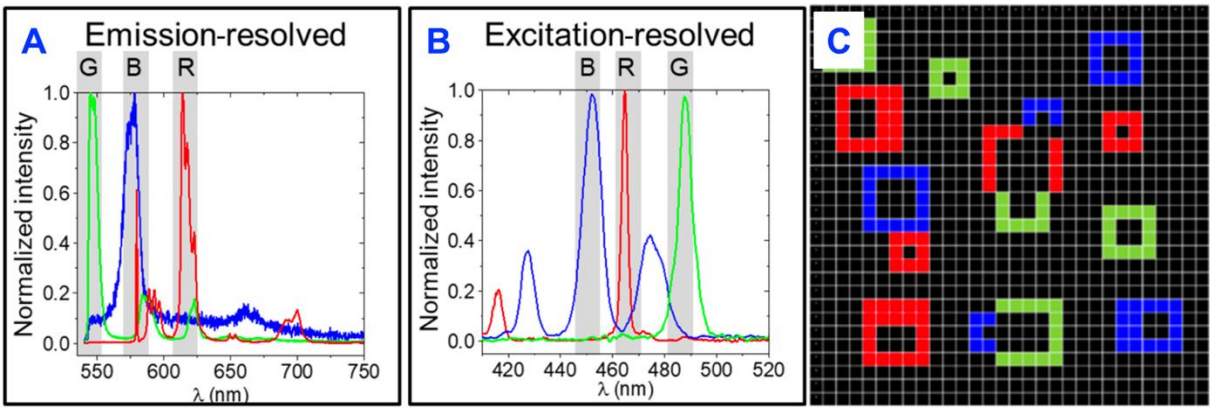

Figure 1.15: Emission (**A**) and excitation (**B**) spectra of zeolite particles doped with dysprosium(III) (blue), europium(III) (red) and terbium(III) (green) with the bands selected for G, B and R channels of the resolved images shaded in grey. **C**: GBR resolved image of a random pattern generated within a spin coated PVA film containing lanthanide(III) doped zeolite particles (adapted from Carro-Temboury *et al.* (2018)).[44]

The number of unique patterns with a size of 60×60 pixels was estimated as 7^{9000} which is essentially infinite for all practical purposes. Although this method of creating multi-colour security tags of unique patterns is promising in theory, practical implementation would encounter several challenges. Firstly, authentication of a single tag containing 3600 pixels would require a relatively long time, since the image acquisition was performed by sequential PE of each individual pixel. Secondly, this method exploited a confocal microscope which requires a high cost and space consuming laboratory-based setup. Thirdly, operation of a confocal microscope requires extensive training that would also contribute to additional costs.

Overall, this example of security tags demonstrates the importance of simultaneous development of both a security tag and equipment for its authentication that must be relatively inexpensive, easy to operate and sufficiently compact to be used in various settings and produce low level of authentication uncertainty.

I.11. Introduction to circularly polarised luminescence spectrometry

Current research in CPL-active materials is significantly limited by a relatively high cost of commercially available of CPL-spectrometers (>£100,000). Therefore, the use of 'home-built' CPL-spectrometers is currently predominant in CPL-related literature with the total cost of components of ~£50,000. Most set-ups, including the one exploited in this work, are similar and contain the same key components (Figure 1.16.A).

A CPL-spectrometer usually consists of a broad (i.e. laser-driven) excitation light source, two scanning monochromators (SM), for both excitation and emission, a photo-elastic modulator (PEM), a lock in amplifier (LIA), a linear polariser (LP) and a photomultiplier tube (PMT) or a photodiode (PD).[45] Excitation (SM (A)) and emission (SM (B)) SMs are used to select the λ of excitation light and emitted light respectively. Sample irradiation with unpolarised light triggers CPL of a chiral sample, which is then passed through a slit to minimise the amount of undesired scattered light reaching the PEM. It works by applying periodic physical stress at a frequency of 42 kHz to an optically transparent isotropic material such as quartz to induce birefringence. This makes PEM serve as an oscillating QWP that alternatively convert L- and R-CPL into LPL. This LPL is then then analysed using a static LP. Depending on the polarisation angle, different amount of such LPL will pass through the LP before reaching the detector.

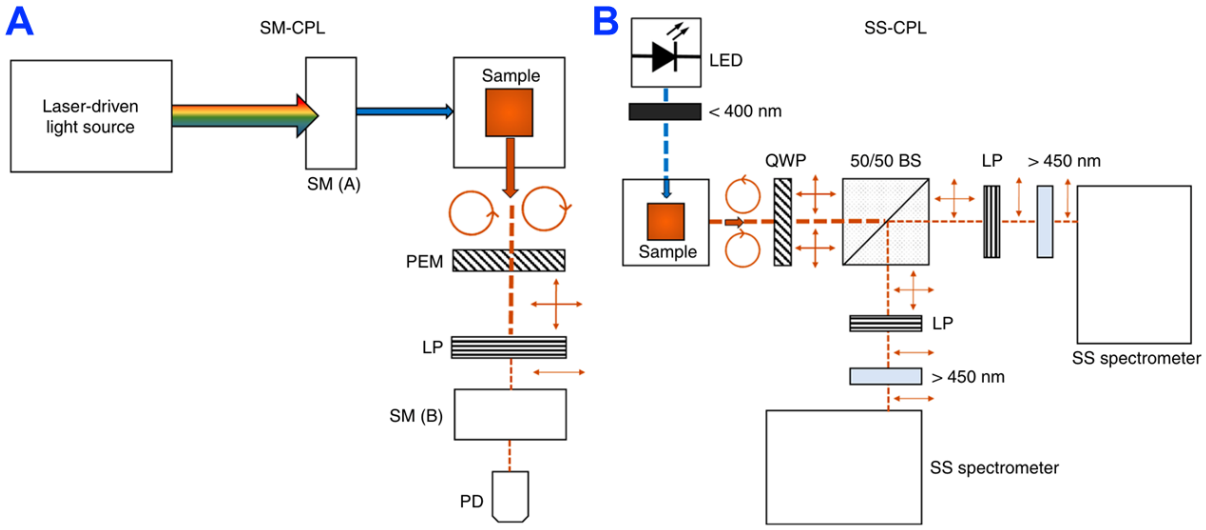

Figure 1.16: Schematic representation of two CPL spectrometer set-ups. **A**: Commonly exploited PEM based CPL-spectrometer. **B**: Newly introduced rapid CPL-spectrometer based on QWP, dual channel signal acquisition and CCD detectors (adapted from MacKenzie *et al.* (2020)).[46]

In order to accurately measure the intensity of L- and R-CPL, the detection must be synchronised with oscillations of the PEM. This is facilitated by a LIA in line with PMT that converts the recorded CPL signal into alternating current while total emission produces direct current signal. Since longer λ photons are lower energy, the intensity of the current they generate is lower compared to shorter λ photons. Therefore, red detection correction is applied to the recorded intensity. One of the main drawbacks of the above-described CPL-spectrometer is a long spectrum acquisition time which normally takes ~1 hour (5 averages, 100 nm spectral window, 0.5 nm intervals). In addition, the standard PEM set up is incompatible with time gating, which, on the other hand, could be facilitated by introduction of mechanical optical choppers that are synchronised to the PEM oscillating frequency (42 kHz).

Recently, a novel dual-channel CPL spectrometer that could acquire a single full λ-range spectrum in as little as 10 ms was proposed (Figure 1.16.B, SS-CPL).[46] It exploits a QWP instead of PEM and two solid-state CCD spectrometers instead of a PMT. When the emitted light is passed through a QWP, it is converts R- and L-CPL into two orthogonal LPL signals. The total signal is then equally split into two channels by a non-polarising beam splitter to be subsequently analysed by high-precision motorised rotation of LPs. The light was then diffracted inside the modules of the CCD spectrometers to simultaneously detect the light intensity at different λ within the 400-800 nm operating range. Another variation of the setup exploiting a polarising beam splitter was found to generate a larger error due to a non-linear polarisation differentiation by the prism which would require a more complex calibration and post-run correction of the recorded CPL spectra.

Overall, the dual-channel set-up allowed for a significantly faster (~5400 times with same parameters as above) acquisition rates with significantly larger signal to noise ratio compared to PEM CPL. This was achieved by accumulation of multiple spectra over a short period of time. Another advantage of fast acquisition rates was lower extent of sample degradation due to a reduced exposure of the sample to the excitation light. Most importantly, this setup was inherently capable of facilitating the time-resolved CPL detection for the first time.

The QWP-based multi-channel detection principle was further implemented in the recently developed CPL laser scanning confocal microscope (LSCM) for live-cell imaging and rapid handheld time-resolved CPL photography (CPLP) camera for authentication of CPL-active security inks.[20,47]

I.12. CPL laser scanning confocal microscope for enantioselective differential chiral contrast imaging

The previously discussed dual-channel CPL detection method was also implemented in CPL LSCM, where the light from the sample plane is passed through a QWP converting the L- and R-CPL into orthogonal linearly polarised states that are selected by precisely aligned LPs and detected by two avalanche hybrid PDs (Figure 1.17).[20] This allowed for simultaneous acquisition of images using the L- and R-CPL channels that could be then used for enantioselective differential chiral contrast (EDCC) imaging.

EDDC imaging is performed by subtracting the intensities recorded by the two polarisation-sensitive channels from one another in a pixel-by-pixel 3D raster pattern scanning method. Since the L- and R-CPL channels are more sensitive towards L-CP and R-CP light respectively, subtraction of the right channel intensity from the left channel intensity (L-R) will produce an EDDC image containing the surplus L-CPL and *vice versa*.

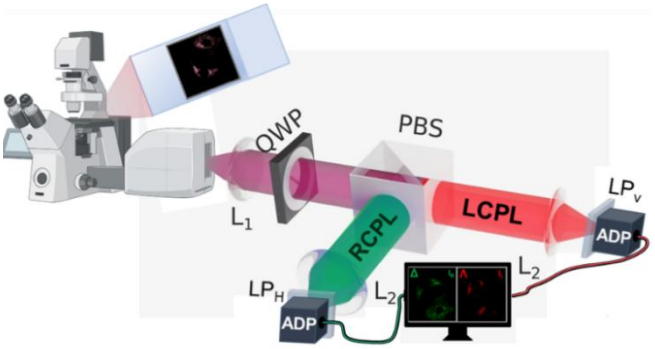

Figure 1.17: CPL LSCM set-up, where the light from LSCM is passed through a QWP, followed by equal splitting into two channels, where vertically and horizontally aligned LPs select L- and R-CPL before detection by avalanche photodiodes (ADP).

In a recent example, EDDC imaging was performed on live mouse skin fibroblast cells (NIH3T3) dosed with two enantiomers of a europium(III) complex **EuL^{b}** (Section III.6, Figure 3.8), where each demonstrated selective localisation in different organelles of the cell – either mitochondria (Figure 1.18.G) or lysosomes (Figure 1.18.B) which agreed with the total intensity images of the organelles targeting dyes MitoTracker™ Green (Figure 1.18.H) and LysoTracker™ Green (Figure 1.18.C) that possess selective mitochondrial and lysosomal localisation.[20] This demonstrates how CPL LSCM can be used to selectively image chiral CPL-active species in live-cells.

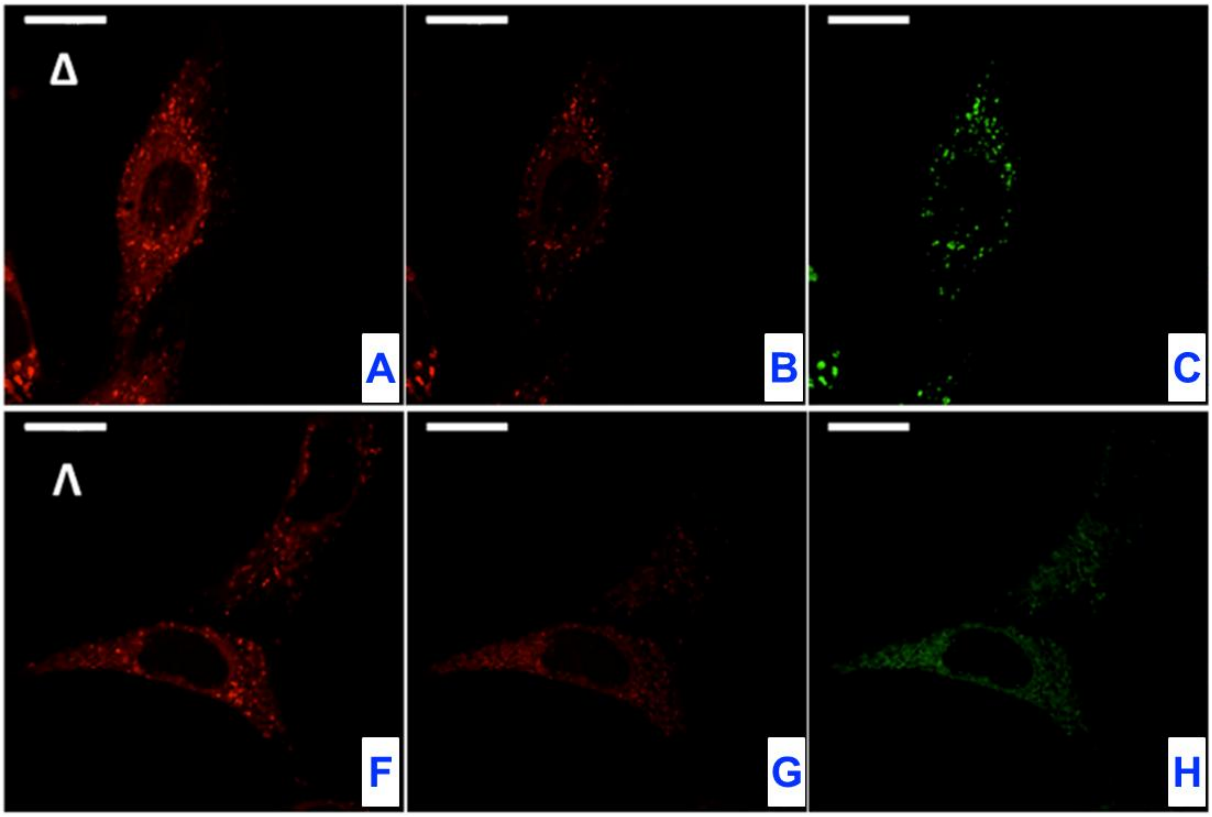

Figure 1.18: CPL-LSCM images of NIH3T3 cells doped with *Δ* (**A** and **B**) and *Λ* (**F** and **G**) enantiomers of **EuL^b** compared to LysoTracker^{TM} Green (**C**) and MitoTracker^{TM} Green (**H**) (λ_{ex} = 488 nm, 2 mW, λ_{em} = 500 to 530 nm) that selectively localise in lysosomes and mitochondria respectively. **A** and **F**: Total intensity images (λ_{exc} = 355 nm, 20mW, λ_{em} = 589 to 720 nm). **B**: EDCC R-CPL (R-L) image highlighting lysosomal localisation of *Δ* isomer. **G**: EDCC L-CPL (L-R) image highlighting mitochondrial localisation of the *Λ* isomer. Scale bar = 20 µm. (adapted from Stachelek *et al.*, 2022).[20]

Apart from live cell-imaging, CPL LSCM allows to record CPL of solid state materials (films, crystals, etc.) which allows to study the local and global chirality and therefore CPL properties with diffraction limited 3D resolution. One of the recent examples demonstrated how crystals of a *Δ* and *Λ* enantiomers of europium(III) complex containing chiral pyridyl-diamide (pda) (Section III.6 – Figure 3.15) ligands could be differentiated using EDCC imaging (Figure 1.19).[48]

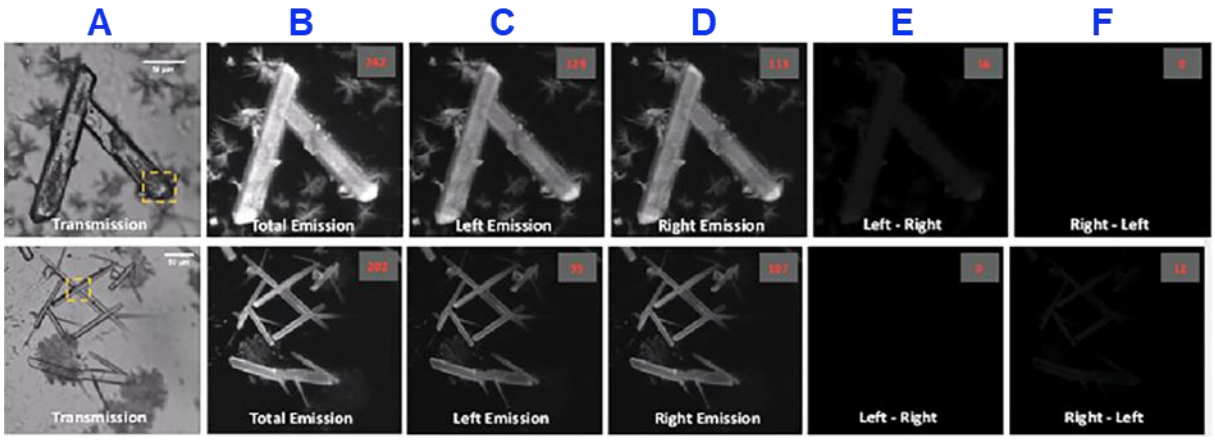

Figure 1.19: EDCC of crystals of *Δ* (top row) and *Λ* (bottom row) enantiomers of pda-containing europium(III) complex on a glass substrate: transmission image (**A**), total emission (λ_{ex}= 355 nm, 20 mW, λ_{em} = 589-599 nm) (**B**), images recorded using L- (**C**) and R- (**D**) CPL-sensitive channels (λ_{em} = 589-599 nm), calculated EDCC images: L-R (E) and R-L (F). (×40 0.7 numerical aperture (NA) air objective, 210 × 210 µm field of view (FOV), 100 averages, 1.5 µm axial section, scale bars = 50 µm, numbers in red are average 8-bit pixel intensity values for the regions of interest (ROI) (**A** in yellow) (adapted from Caffrey *et al.*, 2024).[48]

Another recent example demonstrated EDCC of crystalline L-valinol-based bis-perylene diimide macrocycle where chirality is induced by *π-π* stacking interactions. Here it was demonstrated how CPL LSCM could be used to study the dependence of CPL on local crystal morphology (Figure 1.20).[49] In this case, a higher dissymmetry of LCPL was observed when focusing on the edge of the crystal as opposed to the face, which was attributed to a lower extent of internal crystal reflections that randomise CPL signal. This was estimated by comparing the ratios of average intensities within the same ROIs on the raw images recorded using L- and R-CPL sensitive channels.

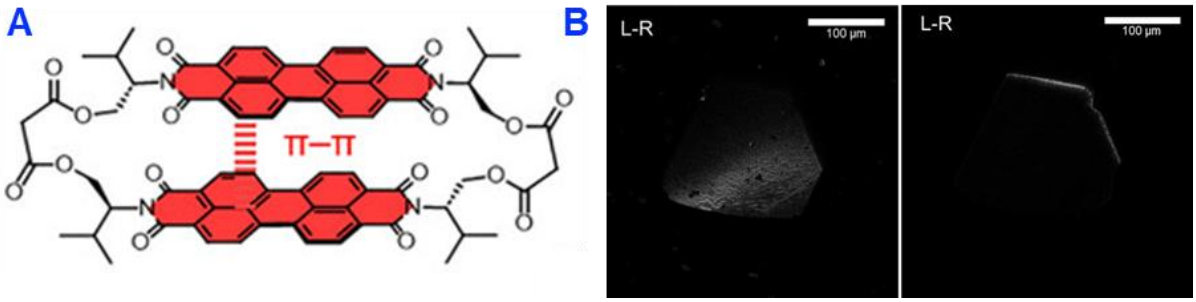

Figure 1.20: **A**: L-valinol-based bis-perylene diimide macrocycle structure; **B**: CPL LSCM L-R EDCC (λ_{ex} = 458 nm, λ_{em} > 570 nm (LPF570)) images of the L-valinol-based bis-perylene diimide macrocycle single crystal face (left) and edge (right) (adapted from Hartmann *et al.*, 2026).[49]

I.13. Rapid handheld time-resolved CPL photography camera

A novel polarisation-sensitive equipment for security ink authentication was proposed recently.[47] This rapid handheld time-resolved CPLP camera can be used for authentication four previously mentioned security features: spatial, chromatic, temporal and CPL. The set-up is based on a Kiralux® polarisation sensitive complementary metal-oxide-semiconductor (CMOS) USB camera (*CS505MUP1, Thorlabs*, Figure 1.21.A) that contains periodically repeating clusters of 4 pixels, each covered with an array of differently oriented LPs (Figure 1.21.B) at - 0°, 45°, -45° and 90°.

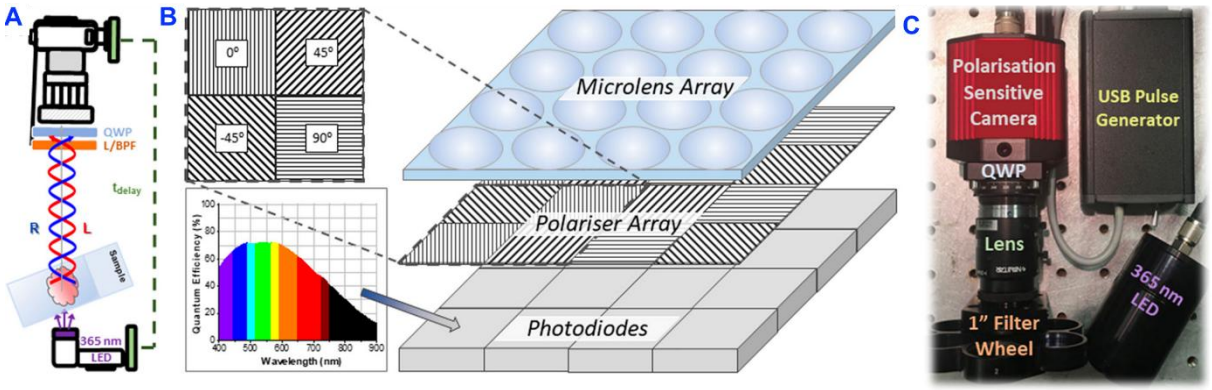

Figure 1.21. **A**: Schematic representation of the camera set-up. **B**: Shematic representaion of the distribution of LPs across the array of PDs in Kiralux® camera and its quantum efficiency λ dependence. **C**: Annotated photograph of the camera set-up (adapted from De Rosa *et al.* (2023)).[47]

In combination with a QWP that is precisely pre-aligned parallel to one of the LPs, L- and R-CPL can be rapidly distinguished in a single scan. For example, if the fast axis of the QWP is aligned with 0° LP, emission detected by the pixels covered with 45° and -45° LPs would be sensitive to R- and L-CPL respectively. In the proof-of-concept study, a chiral europium(III) complex **EuL^{b}** possessing a single-sign CPL ΔJ = 1 was selected to maximise the signal to noise ratio. The Δ and Λ enantiomers of the complex as well as CPL-inactive rhodamine B (**RhB**) were mixed with polymethylmethacrylate (PMMA) in dichloromethane (DCM) and drop-casted on a microscope slide (Figure 1.22.A)

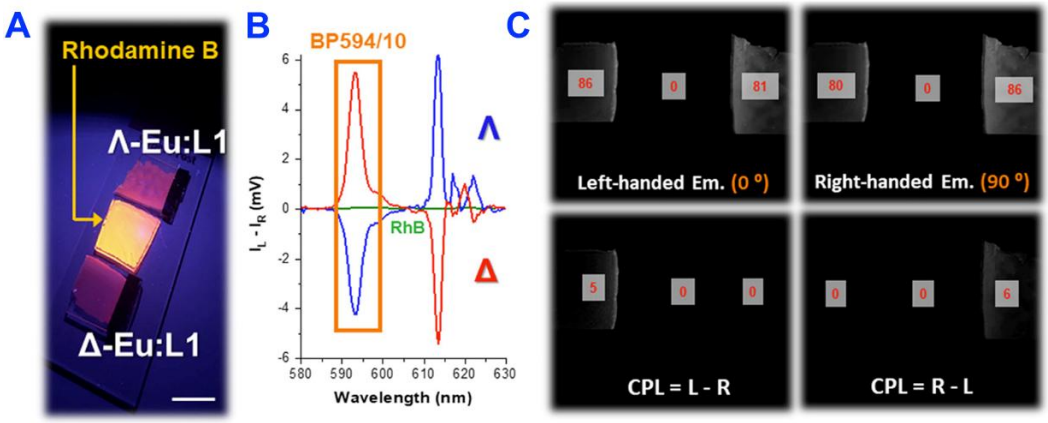

Figure 1.22. **A**: PMMA films doped with emissive species. **B**: Selection of ΔJ = 1 using BP594/10. **C**: Time resolved EDCC images (adapted from De Rosa *et al.* (2023)).[47]

Selective detection of the ΔJ = 1 band emission was achieved using a 594 ± 5 nm band bass filter (BPF) (BPF594/10) (Figure 1.22.B). Although **RhB** is also emissive within the selected BPF range, it would not be observed on the EDCC calculated images. As a result, the L-R image only contained the L-CPL of the *Δ* enantiomer, while R-L image only showed the R-CPL of the *Λ* enantiomer. This demonstrated a method of authenticating a CPL security layer facilitated by selectively recording the intensity of the two enantiomers of a europium(III) complex that could be placed in different parts of the total pattern. This was further demonstrated using a 'security tag' comprising of a smiling face, where the left and right eyes were drawn using the *Δ* and *Λ* enantiomers (Figure 1.23.A).

Apart from authenticating the CPL security feature using EDCC, the CPLP camera was compatible with authentication of other previously mentioned security layers such as temporal using time-gated photography. The image acquisition was performed after a 20 μs time delay following irradiation. This was facilitated using a combination of **EuL^{b}** with a millisecond-scale τ and organic dyes with nanosecond-scale τ in the tag. In the proof-of-concept study, three organic dyes (Figure 1.24): **RhB** (red), **FIrscn** (green) and anthracene (blue) together with racemic and enantiopure versions of **EuL^{b}** were used to draw different parts of the smiling face 'security tag' on optical brightener-free paper (Figure 1.23.A).

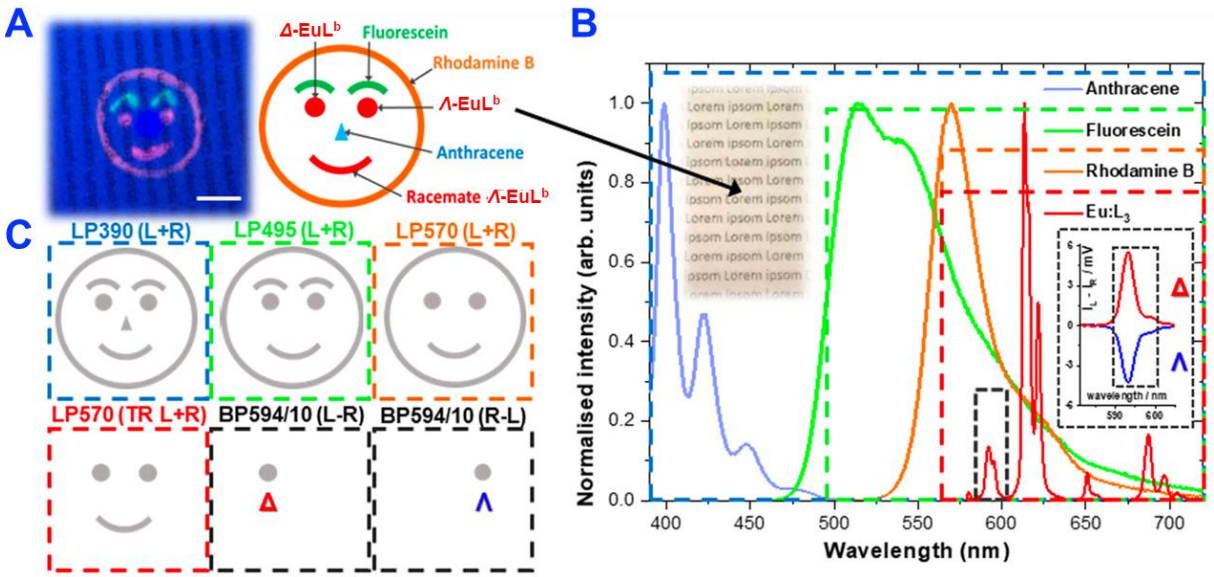

Figure 1.23. **A**: Photograph of a security tag embedded into an optical brightener free paper substrate (left) and the assignment of dyes to the tag features they were used for (right). **B**: Emission spectra of all materials present in the tag. **C**. Schematic representation of the tag features that can be selectively detected using time-gating, optical filters and chiral contrast (adapted from De Rosa *et al.* (2023)).[47]

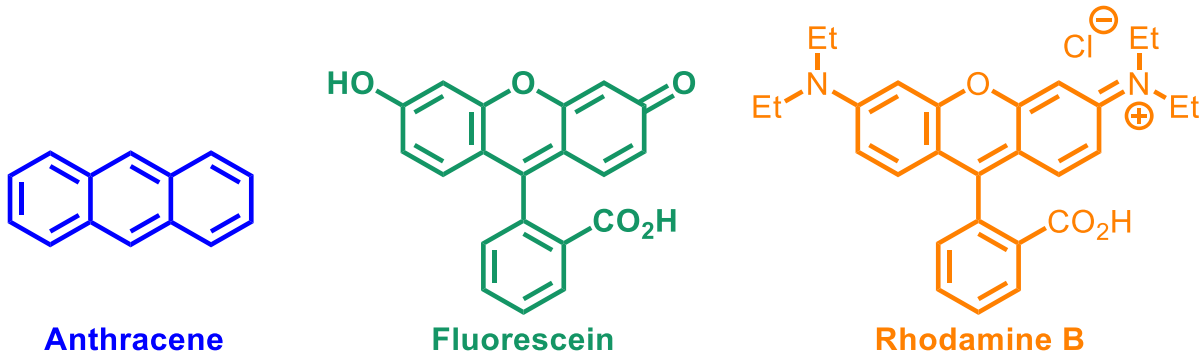

Figure 1.24: The structures of anthracene, **FIrscn** and **RhB** colour coded according to their emission.

The temporal security layer was then authenticated by acquiring the images with a 20 μs delay following the PE. As a result, the features containing organic dyes were invisible, while europium(III) containing features were still present (Figure 1.25.A). An extra security layer could be introduced using LP filters that sequentially remove the emission of individual dyes (Figure 1.23.C). For example, 495 nm LPF (LPF495) removed the anthracene component, while 570 nm LPF (LPF570) removed **FIrscn**. Most importantly, authentication of all security layers was achieved using a single light source – a commercially available 365 nm document reader that effectively excited all dyes present in the tag.

A simultaneous use of multiple authentication techniques was also explored, where EDCC calculations were performed with the images acquired using the time-gating method (Figure 1.25.A). Time gating alone allowed for a complete removal of the features containing organic dyes from the total emission image so that only europium(III) containing features remained (Figure 1.25.A). The two enantiomers (each of the eyes) could be then selected using the EDCC image calculation (Figure 1.25.B and C).

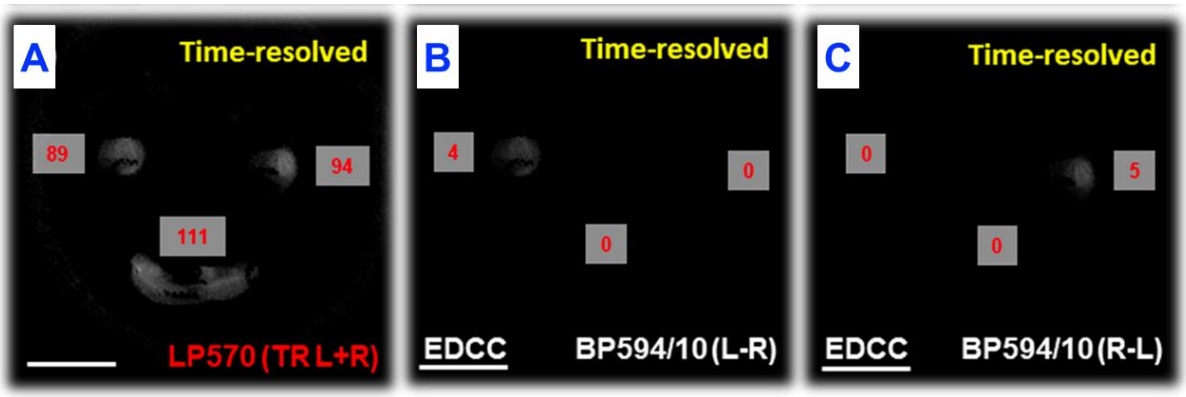

Figure 1.25: Time-resolved images of a laminated security tag that only show features produced by a long-lived europium(III) emission. **A**: Total intensity image using a LPF570 filter. **B** and **C**: Chiral contrast images using BPF594/10 filter, demonstrating ΔJ=1 emission from enantiopure europium(III) complexes that show net L-CPL (**B**) and R-CPL (**C**) (adapted from De Rosa *et al.* (2023)).[47]

II.14. Project aims and objectives

The overarching project objective is development of chameleon security inks that can be used to create a 'chameleon security tag' (CST) containing 5 or more layers of security. Such CST must be compatible with incorporation into banknotes, identification and other sensitive documents, certificates, military, medical and possibly other consumer goods where anti-counterfeiting features are necessary to prevent profit losses, fraud and even human deaths.[50] Therefore, for effective practical implementation of the CST, it needs to satisfy several requirements.

Firstly, the design of the tag must allow for its rapid authentication by the 'in-house' developed CPLP camera. Hence, incorporation of certain luminescent properties into the tag must be sensible in terms of functional capabilities of the camera such as emission detection limit, time-gating exposure as well as compatibility with commercially available optical filters and excitation light sources. For example, optimisation of the temporal security must exploit organic fluorophore that can be excited using the same λ of light as for the europium(III) complex; emission λ ranges of the fluorophore and the complex must sufficiently overlap within a fixed-in-place BPF is a simplified cheaper configuration is required for commercialisation; the concentrations of the materials must be brightness-optimised (at a measured λ range) to match their emission intensities that are governed by exposure times that are compatible with time-gating; if the materials are incorporated into the same host matrix such as PMMA film, reabsorption of europium(III) emission by the nearby organic fluorophores must be minimised to avoid the repeated PE of organic fluorophores after the time delay. Reasonable optimisation and simplification of the camera set-up and the automatization of the authentication procedure must also be considered when developing the CST.

Secondly, the physical nature of the tag needs to be considered. 43 world countries including China, New Zealand, Poland, Romania, Mexico, Egypt, Canada and Brazil switched to polymer banknotes starting with Australia in 1988.[51,52] Polymers are more resistant to mechanical and water damage which makes banknotes last longer compared to their paper alternatives. Therefore, the use of polymer matrix would make the CST more compatible with modern banknotes.

PL properties of materials are dependent on their environment, for example, solvatochromism, where the emission λ of the same fluorophore depends on the polarity of the solvent.[53] Generally, more polar solvents tend to reduce the energy of the S_1 by an ordered alignment of the solvent molecules surrounding the excited fluorophore to optimise the resulting dipole-dipole interactions, resulting in a bathochromic shift of absorption and emission bands. This can also occur in solid state polymer hosts, where the surrounding environment can affect the

energy of electronic states and induce splitting of states *via* symmetry reduction, affecting the emission spectral shape and potentially g_{lum}. Therefore, the key photophysical properties of the developed security inks must be studied in the solid-state polymer host as well. In addition, a high degree of reproducibility of the developed CSTs must be achieved to facilitate reliability of the authentication method. This is crucial for potential commercialisation of the CST in the future.

For the europium(III) complex to perform well in a CST, it needs to have photophysical properties that result in high CPB_i. Firstly, the sensitiser must effectively absorb excitation light which is characterised by a large value of ε. As mentioned earlier, arylalkynylpyridine chromophores have relatively high ε due to the structural feature facilitating the ICT excited state which results in a large transition dipole moment during PE. The systems containing arylalkynylpyridine chromophores demonstrated molar absorption coefficients of as large as 60000 M^{-1} cm^{-1}.[54] Another benefit of the arylalkynylpyridine based sensitising systems is the absorption maximum in low energy UV region, resulting in compatibility with the λ of a conventional 355 nm laser (3rd Harmonic of the Nd:YAG (neodymium-doped yttrium aluminium garnet) laser) or 365 nm UV LED. As a consequence, the ICT energy of the aryalkynylpyridines (~21300 cm^{-1}) is sufficiently close to the $^5D_0$ state of europium(III) at 19050 cm^{-1}, while also sufficiently far energetically (>10 k_BT (2050 cm^{-1})) to minimise the extent of thermally activated BET.[8] As a result, due to the efficient ET, aryalkynylpyridine-sensitised europium(III) complexes often demonstrated relatively high values of quantum yield of ~50%.[54] Another requirement for the sensitising ligand is the ability to coordinatively saturate the europium(III) centre (coordination number 9) to prevent undesired coordination of other species such as solvent molecules that destabilise the structure and serve as a source of vibrational relaxation, for example, *via* XH oscillators. In addition, the distribution of the lone pair donor atoms of the macrocyclic ligand must be optimised in terms of 'bite angles' to provide a sufficient overlap with the europium(III) centre without inducing too much strain during complex formation. Apart from that, the structure of the ligand must facilitate chirality which is a necessary requirement for the CPL activity. It is also necessary for the structure to provide a relatively high energy barrier for racemisation since enantiopurity needs to be maintained for a consistently high g_{lum} over longer periods of time at ambient temperatures and short exposures to higher temperatures such as 150°C which is commonly reached during document lamination.[22,55] Overall, aryalkynylpyridine-based sensitising ligand was chosen as a good candidate for europium(III) complexes targeting the main requirements of the novel CST.

CHAPTER II. The study of the arylalkynylpyridyl phenylphosphinate donor EuL^0 complex

II.1. Preparation and photophysical characterisation of the arylalkynylpyridyl-sensitised phenylphosphinate donor EuL^0 complex for security applications

The first target material of this work was a previously reported **EuL^0** complex (Figure 2.1). **EuL^0** is a good starting point to investigate arylalkynylpyridyl-sensitised europium(III) complexes as candidates for novel CPL active security inks. **EuL^0** has multiple useful photophysical properties that are governed by its structure. Firstly, and most importantly, **EuL^0** luminescence is facilitated by europium(III) which, as previously mentioned, is known to produce high g_{lum} values when placed in a chiral environment provided by macrocyclic ligands. High dissymmetry of CPL is necessary for an effective differentiation between the left and right handedness of the emitted light using commercially feasible instruments such as the CPLP camera to authorise the CPL security features. Another benefit of europium(III) emission is its relatively long lifetime (milliseconds) compared to organic dyes (nanoseconds). This allows for a selective time-gated detection of the europium(III) emission to enable the temporal security layer of a security tag containing a combination of **EuL^0** and organic fluorophores. In **EuL^0**, the emissive states of europium(III) are populated *via* the ligand sensitisation, which results in a large pseudo-Stokes shift. As a result, the material absorbs light in the UV region and emits visible light. Therefore, no absorption in visible light region makes the security ink invisible to an unaided eye unless illuminated with UV light. The aryl groups of the sensitising chromophores are 2,4,6-trimethoxy substituted, providing a bathochromic shift of the absorption maximum towards 365 nm for optimal excitation of the ink with a commercially available UV LED. An additional important benefit associated with the electron donating substituents on the 'top' of the chromophore is increase in ε due to a stronger transition dipole. Last, but not least, bulky phenyl substituents increase the energy barrier for inversion of the phosphorus chiral centres that are required for racemisation. Hence, the racemisation lifetime of **EuL^0** will be sufficiently large for CPL security inks which would increase their shelf life.

EuL^0 consists of a nonadentate macrocyclic ligand coordinated to the europium(III) centre *via* the pyridyl and TACN nitrogens and phosphinate donor oxygens. In this work, it was synthesised using procedures adopted from literature[47,54,56–61] From the retrosynthetic point of view, the whole macrocyclic ligand must be prepared separately prior to hydrolysis of the phosphinate esters followed by complexation to europium(III) (Scheme 2.1). The ligand is obtained by alkylation of the mesylated chromophore which can be obtained by Sonogashira cross coupling of two separately prepared 'top' and 'bottom' components.

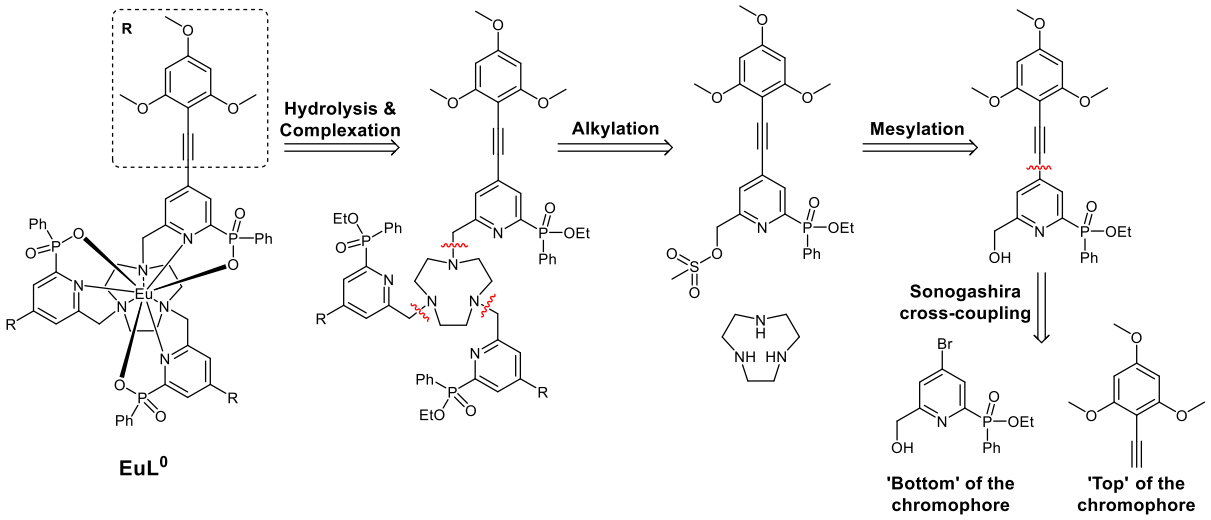

Scheme 2.1: Retrosynthetic analysis of **EuL⁰**.

In an alternative pathway, the complex containing only 'bottom' chromophore components could be prepared first, followed by Sonogashira cross coupling reaction with the 'top' components to give **EuL⁰**. This method was not attempted due to the entropic penalty associated with coupling three alkynes to each complex molecule. In other words, there was a possibility of the side products containing only one or two alkynes out of three.

The synthetic route towards the 'bottom' component was previously reported in literature (Scheme 2.2).[56,62] The first step was Pd-catalysed formation of C-P bond to attach phenylphosphinate group to 2-bromo-6-methyl-4-nitropyridine. This was achieved using $Pd(dppf)Cl_2$ (dppf = diphenyl phosphino ferrocene) as a to produce **1**. The mechanism of C-P bond formation using $Pd(dppf)Cl_2$ was not reported in literature but could be based on a similar reaction with aryl nonaflates using palladium(II) acetate (Scheme 2.3).[63]

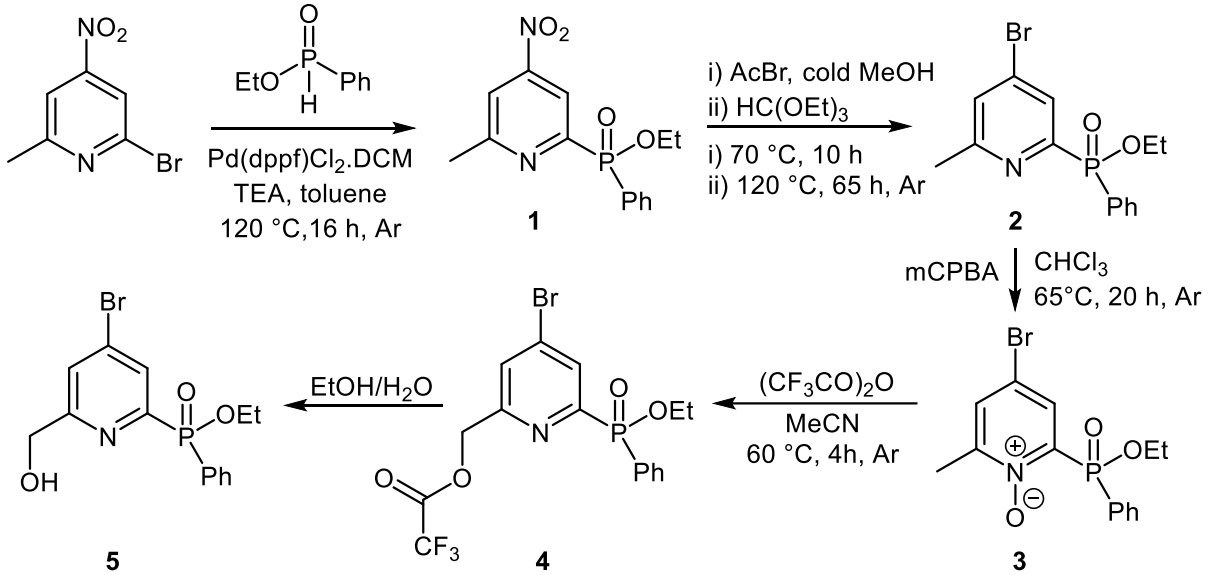

Scheme 2.2: The reaction sequence for the 'bottom' component of the phenylphospinate donor chromophore for **EuL⁰**.

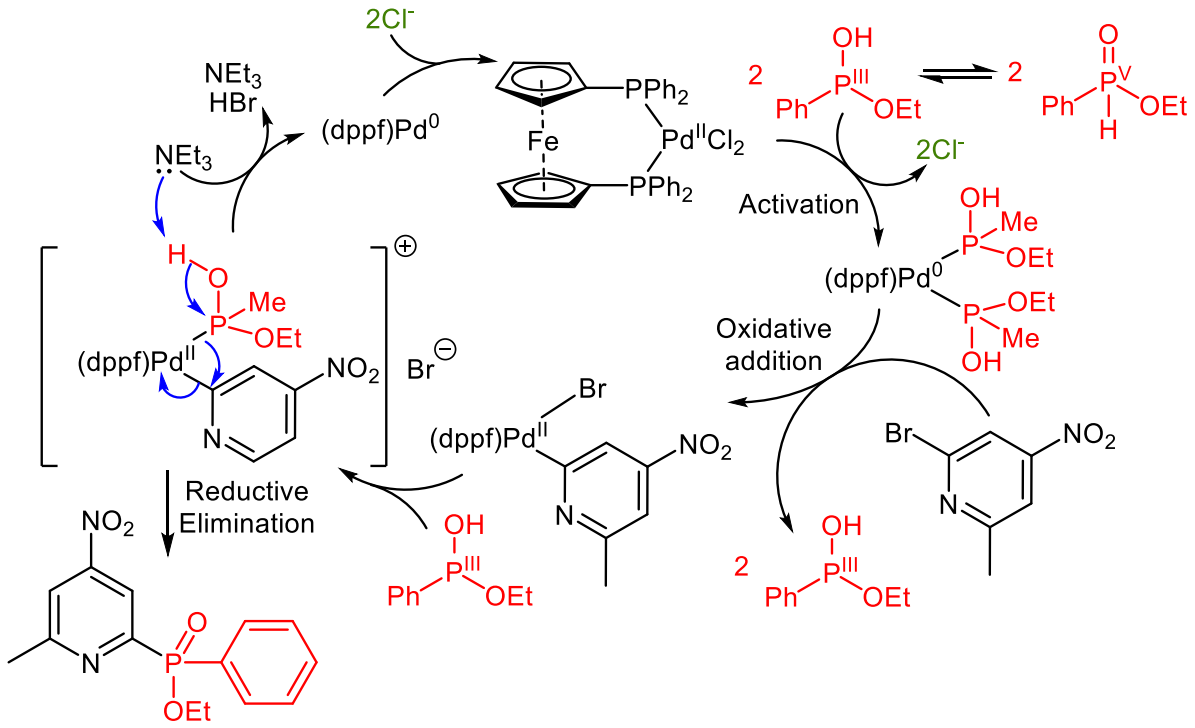

Scheme 2.3: Proposed mechanism for Pd-catalysed C-P bond formation.

In the next step, the nitro group on **1** was replaced with bromine using acetyl bromide (Scheme 2.4). In this transformation the phenylphosphinate ester undergoes undesired hydrolysis. Therefore, the ester needs to be restored using triethyl orthoformate to yield **2**. The following step involves a conversion of pyridine nitrogen into *N*-oxide using *meta*-chloroperoxybenzoic acid to produce **3**. Formation of *N*-oxide is necessary for introduction of alcohol functionality *via* Boekelheide rearrangement with trifluoroacetic anhydride.[64] Solvolysis of the obtained trifluoroacetic ester **4** in 50:50 mixture of water and ethanol (EtOH) yields the 'bottom' component of the sensitiser.

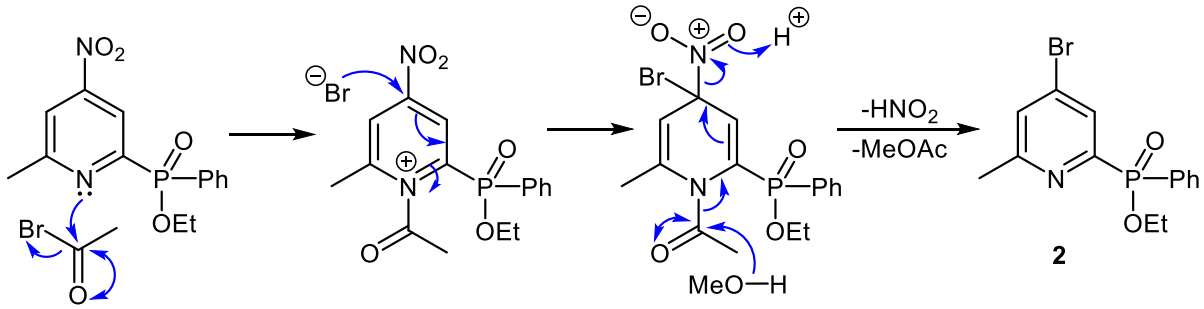

Scheme 2.4: Proposed mechanism for the nitro to bromo pyridine conversion using acetyl bromide (phenylphosphinate ester hydrolysis omitted for clarity).

The conversion of **3** to **5** could not be accurately monitored using liquid chromatography - mass spectrometry (LCMS) due to the same molecular mass of **3** and **5**. Therefore, the reaction was monitored using ^{1}H NMR, specifically, the proton environment at 6-methyl pyridine substituent of **3** at 2.32 ppm (3H, s, $CDCl_3$). Conversion of **3** into **4** results in

deshielding to produce a new resonance at 5.46 ppm (2H, s, $CDCl_3$). The final solvolysis step was monitored using the same ^1H environment that now resonated at 4.74 ppm (2H, s, $CDCl_3$).

The 'top' of the chromophore **7** was prepared in a two-step Corey-Fuchs transformation of 2,4,6-trimethoxybenzaldehyde (Scheme 2.5). According to literature, the first step of the original Corey-Fuchs method resulted in a complete conversion of an unsubstituted benzaldehyde into 2,2-dibromovinylbenzene intermediate in under 5 minutes at 0 °C.[65] In this work, the reaction took a significantly longer time to reach completion (20 hours). Such difference in the reaction rate could be explained by a substantially increased electron density and therefore a reduced electrophilicity of the aldehyde carbon due to conjugated electron-donating methoxy groups at the ortho and para positions. Therefore, the rate of the first step of the Wittig mechanism that involves an electrophilic attack on the aldehyde by the phosphorus ylid was substantially reduced. In addition, bulky methoxy substituents could also sterically hinder the approach of the bulky ylid containing three phenyl groups.

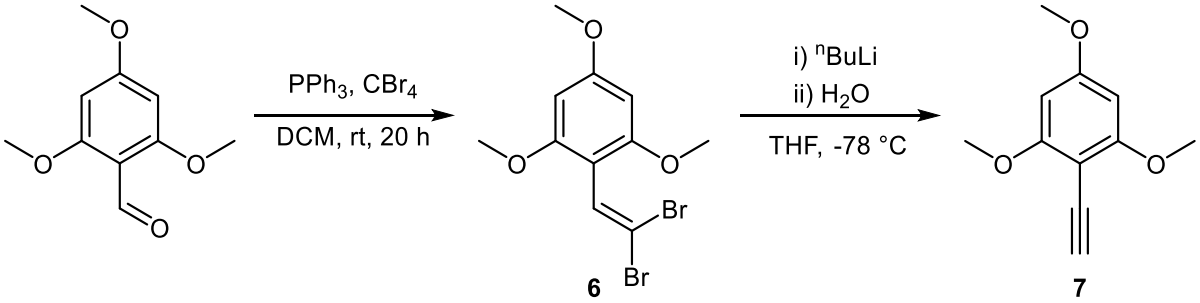

Scheme 2.5: The reaction sequence for the 'top' component of the chromophore.

In the next step, dibromoalkene **6** reacted with *n*-butyllithium, resulting in an elimination reaction to produce a bromoalkyne, followed by bromine-lithium exchange and aqueous work-up to yield **7.**

Once both 'top' and 'bottom' components are prepared, they can be linked together in a Sonogashira cross-coupling reaction. The classic Sonogashira reaction conditions require a combination of palladium(0) and copper(I) catalysts, resulting in high oxygen sensitivity.[66] In this work, a recently reported copper-free conditions were used, as they were believed to avoid homocoupling of the alkyne containing moieties. Although the exact role of the copper(I) co-catalyst is currently not fully understood, the homocoupled product would be formed in a copper-catalysed Glaser-Hay reaction in the presence of oxygen.[67] The general proposed mechanism of the palladium(0) and copper(I) catalysed Sonogashira cross-coupling involves 4 following steps (Scheme 2.6): oxidative addition of the aryl halide across the carbon (sp^2) – halide bond to the activated palldium(0) catalyst, resulting in a palladium(II) complex; substitution of the copper(I) halide with the alkyne species; transmetallation between the palladium(II) and copper(I) centres where the alkyne is transferred from copper(I) to the palladium(II), replacing the halogen to produce σ-alkynylpalladium(II) and restore the copper(I)

halide species; reductive elimination at the σ-alkynylpalladium(II) species that regenerates the palladium(0) catalyst and yields the cross-coupled product.[68–70]

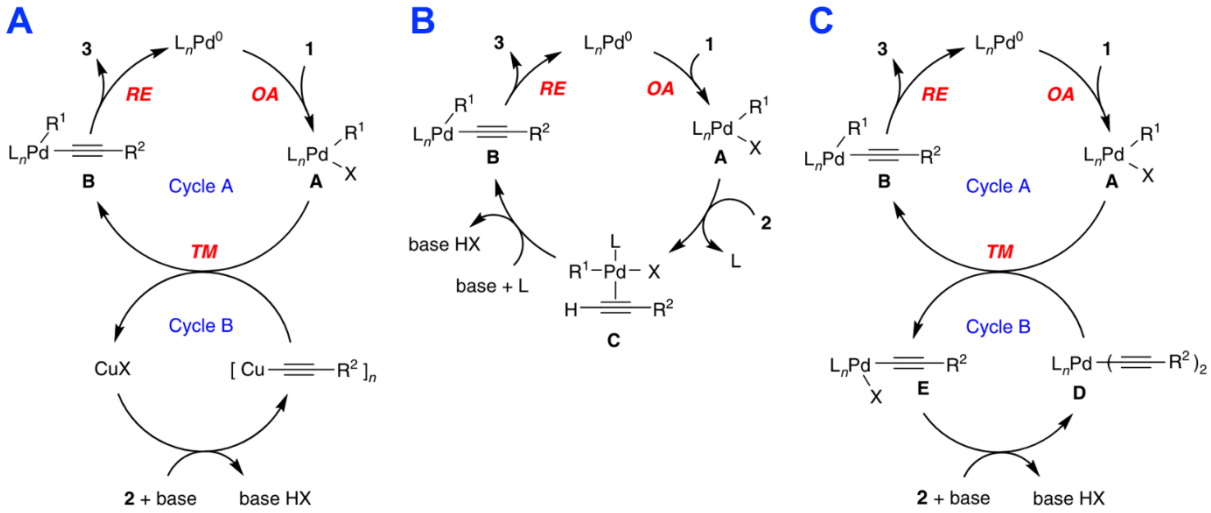

Scheme 2.6: Palladium-catalysed mechanisms for Sonogashira cross-coupling reaction. **A**: Copper co-catalysed mechanism. **B**: Copper-free mechanism. **C**: Copper-free mechanism containing an additional palladium catalytic cycle (adapted from Gazvoda *et al.* 2018).[70]

The copper-free mechanism (Figure 2.6.B and C) shares the oxidative addition and reductive elimination steps with the copper(I) co-catalysed mechanism described above. The rest of the mechanism is different due to the absence of copper(I) cycle. Instead, there are two possible ways of alkyne coordination to the palladium catalyst. One option is a side-on π-donation to the palladium(II) followed by a switch to σ-donation assisted by elimination of the halogen (Figure 2.7.B). The other option suggests a replacement of the copper(I) cycle with another palladium cycle that sources σ-alkynylpalladium(II) species for transmetallation (Figure 2.7.C).[70]

As it was mentioned above, the chromophore **8** was prepared using copper-free condition with allylpalladium(II) chloride dimer as a catalyst (Scheme 2.7). Once **8** is obtained, the alcohol needs to be mesylated to produce **9** which contains a good leaving group for the following alkylation of the TACN nitrogens *via* nucleophilic substitution.

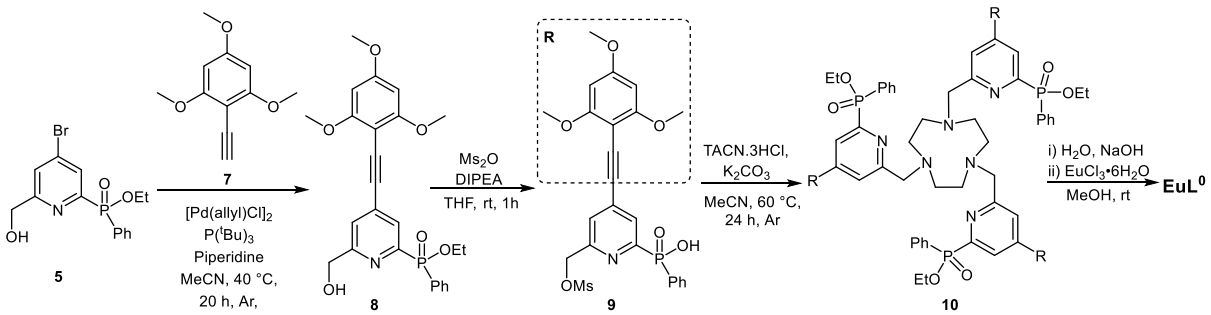

Scheme 2.7: The reaction sequence for the Sonogashira cross-coupling, mesylation, alkylation, hydrolysis and complexation of **EuL^0**.

To prevent the formation of TACN species that are mono- or di-substituted, a slight excess of **9** (3.5 eq.) was added to TACN.3HCl to produce **10**. A similar strategy was used for the final

complexation, where europium(III) chloride hexahydrate was used in a slight excess to avoid any free ligand in the crude **EuL^0**. Prior to complexation of **10** to europium(III), all three phosphinate esters must be hydrolysed. Base catalysed (rather than acid-catalysed) hydrolysis was used in order to prevent an undesired hydration of the alkyne bond that was previously reported to occur under acidic conditions (Scheme 2.8).[56] This was attributed to electron donating substituents on the aryl ring that are ortho and para to the alkyne providing resonance stabilisation of the protonated intermediate which was then susceptible to nucleophilic attack by water or other species.

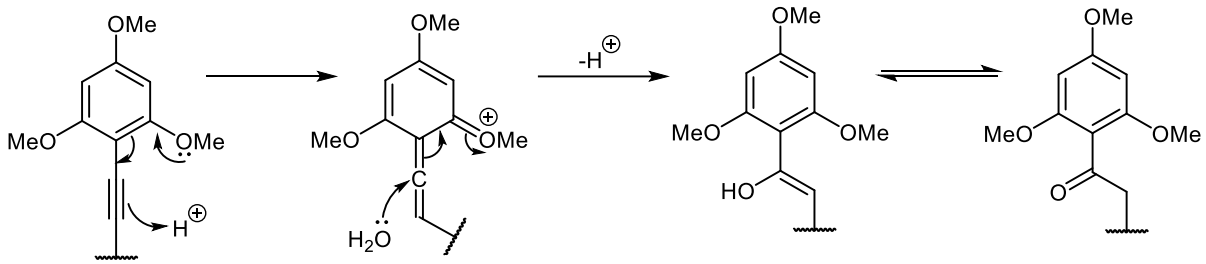

Scheme 2.8: Possible mechanism of acid-facilitated hydration of the alkyne bond of arylalkynylpyridine with electron-donating substituents (reproduced from Frawley (2017)).[56]

During hydrolysis, the pH of the solution was monitored and periodically adjusted with sodium hydroxide as the reaction proceeded, since the conversion of a phosphinate ester into a phosphinic acid lowered the pH, reducing the rate. Once hydrolysis of all three phosphinate esters was confirmed by LCMS, the solution was neutralised and europium(III) chloride was added to yield **EuL^0**.

II.2. General photophysical characterisation of EuL^0.

A sample of **EuL^0** in methanol (MeOH) was subjected to a range of standard photophysical experiments, some of which were also repeated in acetonitrile (MeCN) to investigate any solvent dependence.

As expected from a sensitised europium(III) complex, a large pseudo-Stokes shift of ~250 nm was observed (Figure 2.1.A). This is the consequence of multiple previously discussed NRR processes that occur during ET from the light-absorbing chromophores to europium(III) centre to populate the emissive $^5D_0$ state. As a result, the relatively broad absorption corresponds to the PE of the sensitising chromophore, while the emission is europium(III) centred, producing a lanthanide characteristic narrow-line spectral shape.

As expected from a chromophore with electron-rich 2,4,6-trimethoxy aryl ‘top’, the absorption maximum was shifted towards the desired 365 nm (Figure 2.1.A). In addition, the chromophore was susceptible to small positive solvatochromism which was evidenced (Figure 2.1.D) by a ~5 nm bathochromic shift of the absorption maximum when the solvent was changed from MeCN (λ_{max} = 355 nm) to MeOH (λ_{max} = 360 nm). Solvatochromism of **EuL^0** was expected,

since the arylalkynylpyridyl chromophores are 'push-pull' systems that possess an ICT state that can be stabilised in solvents that are polar and facilitate H-bonding. It is likely that the absorption spectrum contains two bands corresponding to the $S_0 \rightarrow S_1$ and $S_0 \rightarrow$ ICT, where S_1 and ICT states have similar MO configurations and energies, as discussed previously (Section I.7). A good overlap between the absorption and excitation spectra of **EuL^0** was obtained (Figure 2.1.A), confirming the sensitisation process.

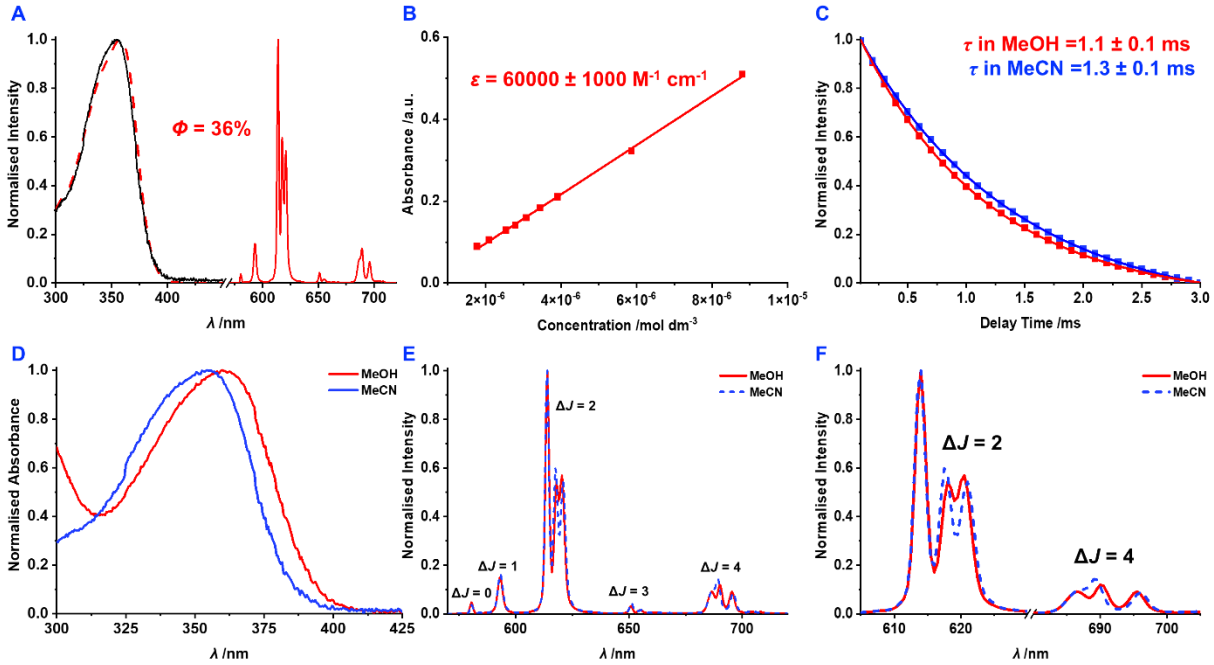

Figure 2.1. A: Normalised absorption (black), emission (solid red, λ_{exc} = 360 nm) and excitation (dashed red, λ_{em} = 614 nm) spectra of **EuL^0** in MeCN with the measured Φ (absolute method) annotated; **B:** Dependence of absorption (at 358 nm) on the **EuL^0** concentration in MeCN; **C:** Lifetime plots of **EuL^0** in MeOH and MeCN (0.1 abs solutions, λ_{exc} = 360 nm and 355 nm, λ_{em} = 614 nm); **D**: Normalised absorption spectra of **EuL^0** in MeOH (red) and MeCN (blue); **E**: Normalised emission spectra of **EuL^0** in MeOH (red, λ_{exc} = 360nm) and MeCN (blue, λ_{exc} = 355 nm); **F:** 605-630 and 680-720 nm sections of the spectrum in **E**.

As mentioned previously, population of the ICT state of chromophores provides a high value of ε due to a substantial displacement of electron density during PE, resulting in a strong transition dipole moment. The ε was measured (Figure 2.1.B) in MeCN as 60000 ± 1000 M^{-1} cm^{-1} (at 360 nm) which was similar to other previously reported arylalkynylpyridine -sensitised europium(III) complexes.[54,56] Such relatively high ε is provided by three light absorbing chromophores per each complex molecule. This is in agreement with previous work reporting the ε values of ~20000, ~40000 and ~60000 M^{-1} cm^{-1} for the complexes containing one, two and three sensitisers respectively.[71]

The measured τ of **EuL^0** were 1.3 ± 0.1 ms in MeCN and 1.1 ± 0.1 ms in MeOH (Figure 2.1.C) which agreed with the τ in isostructural europium(III) complexes. Such relatively long lifetime in beneficial when using **EuL^0** in combination with shorter-lived (nanoseconds) organic fluorophores, where the time-gated method can be facilitated to authenticate the temporal security layer. A slightly shorter τ in MeOH suggested a slight increase in the rate of BET from

$^5D_0$ to ICT, the energy of which is lower in polar protic solvents. Repopulation of the ICT state increases the extent of non-radiative vibrational quenching *via* solvent molecules.

EuL^0 emission spectral profile (Figure 2.1.E) consisted of sharp highly distinct bands as it was expected from a lanthanide(III) ion. Multiple $^5D_0 \rightarrow {}^7F_J$ electronic transitions of europium(III) (ΔJ = 0, 1, 2, 3 and 4) could be resolved on the recorded emission spectrum (Figure 2.1.E). The presence of the low intensity ΔJ = 0 transition suggested a relatively low symmetry at the europium(III) site. This agreed with the established *quasi*-C_3 symmetry of **EuL^0**, which only contained C_3 proper rotation symmetry element. Apart from that, *quasi*-C_3 symmetry of the complex resulted in high intensity of the ΔJ = 2 that clearly demonstrated a splitting pattern containing a singlet and a doublet (each ~ half intensity of the singlet) that corresponded to A+2E splitting of the $^7F_2$ (under C_3 symmetry).[3,7] One of the practical consequence of the relatively high intensity of ΔJ = 2 at 610-620 nm was the deep red colour of the emitted light. In contrast to europium(III) complexes of higher symmetry, the hypersensitive ΔJ = 2 band would be of a significantly lower intensity, resulting in an orange-biased emission. Deep red emission is beneficial in security applications where europium(III) needs to be easily differentiated from other blue and green light emitting fluorophores by an unaided eye for the chromatic security layer. The spectral profile was solvent dependent, suggested by a change in relative emission intensities of the bands within the ΔJ = 2 and ΔJ = 4 emission manifolds in MeCN and MeOH (Figure 2.1.F). The solvent effect will be further investigated when comparing the CPL spectra of **EuL^0** in both solvents.

Φ was initially determined using the relative method, with where coumarin 153 (Φ = 54.4% at 298 K in EtOH) was used as a reference.[72] As a result, the solutions of coumarin 153 in EtOH (refr. index = 1.3614) and **EuL^0** in MeCN (refr. index = 1.3441) were prepared, and their absorption and emission spectra were recorded to calculate the Φ of **EuL^0** as 41%. Further into the project, the Φ was remeasured using an integrating sphere that allowed to determine the ratio between the photons absorbed and photons emitted using the absolute method. This resulted in a slightly lower Φ value of 36%, suggesting that the error-prone relative method was slightly imprecise. Once both Φ and ε of **EuL^0** were obtained, B was calculated ($\Phi \times \varepsilon$) as 21600 M^{-1} cm^{-1} (at 355 nm). This value will be used in the following chapter for the *CPB* calculations.

Although not directly applicable for security inks at present time due to instrumental limitations (high cost and limited portability), a two-photon excitation (2PE) of **EuL^0** was performed to further explore its applicability for biological imaging applications, which was previously reported for compounds isostructural to **EuL^0**.[19,20,73,74] 2PE involves irradiation of a sample with two longer λ photons instead of one high energy photon. For example, instead of a single 355 nm photon, two 710 nm (half the energy - double the λ) photons separated by a very short

(femtosecond) time-delay can be exploited using a pulse train of highly focused photons. The benefit of using longer excitation light λ is deeper tissue penetration associated with lower absorption of NIR by haemoglobin which is beneficial in biomedical applications. For example, 710 nm falls into the first biological NIR window (700-900 nm). In bioimaging, the use of 2PE provides a better axial resolution due to a lower probability of simultaneous absorption of two photons compared to single photon absorption, which causes undesired out-of-focus excitation. 2PE spectrum of **EuL^0** was recorded and compared against the equivalent single photon excitation (1PE) spectrum (Figure 2.2).

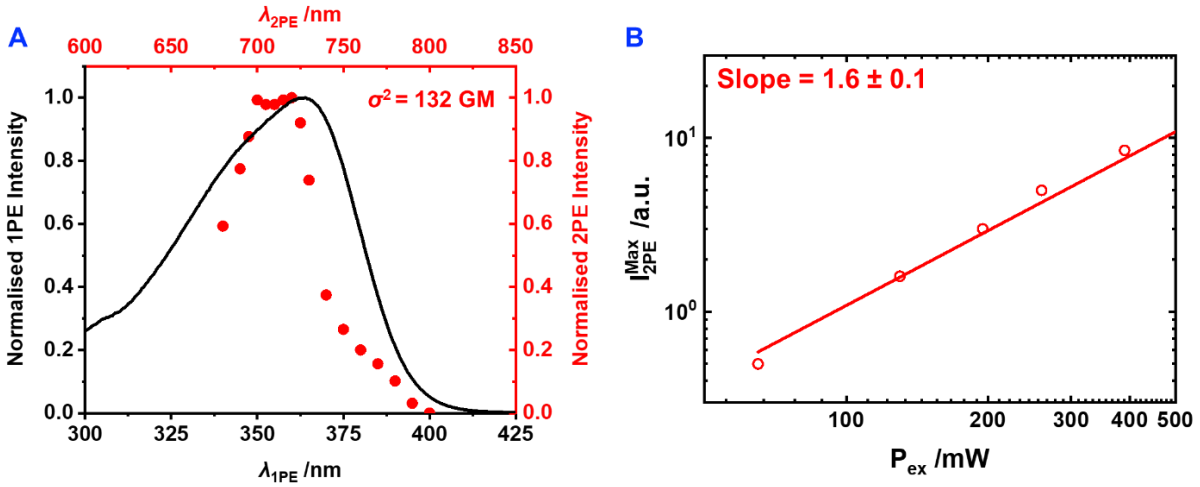

Figure 2.2. **A**: Normalised absorption (solid black) and 2PE (red spheres, λ_{em} = 614 nm) spectra of **EuL^0** in MeOH. **B**: Plot of integrated emission intensity at 614 nm against the excitation source power (λ_{exc} = 720 nm) on a logarithmic scale.

2PE spectrum appeared as two overlapping bands that are narrower and hypsochromically (blue) shifted with respect to the 1PE. The shift of the band is a result of the nonlinear effect of the non-degenerate 2PE, while the narrower band is associated with the quadratic relationship between the 2PE intensity and triggering of the emission.[20,75,76] As it was mentioned earlier, single photon absorption and excitation spectra contained two overlapping bands that correspond to $S_0 \rightarrow S_1$ and $S_0 \rightarrow$ ICT electronic transitions. This agrees with the 2PE excitation spectrum, where two distinct intensity peaks at 700 and 720 nm were observed.

Once the optimal 2PE λ was determined, the correlation between the excitation source power (at fixed λ_{2PE} = 720 nm) and emission intensity (λ_{em} = 614 nm) was recorded to produce the intensity against power plot on a logarithmic scale. The obtained slope of 1.6 suggested that the recorded emission was caused by absorption of two-photons, which slightly de*via*ted from an ideal quadratic relationship which would produce a slope of 2.

After that, 2PE absorption cross-section (σ^2) of **EuL^0** was determined as σ^2 = 132 GM (Goeppert-Mayer, 1 GM = 10^{-50} cm^4 s photon^{-1}) at 720 nm (Equation 11) in accordance with a standard procedure using **RhB** with a known σ^2 of 120 GM as a reference, where F is the

integrated emission intensity, *c* is concentration, *Φ* is quantum yield and *R* and *S* correspond to the reference and sample values respectively.[76,77]

$$\sigma^2 = \frac{F_s}{\phi_S C_s} \times \frac{\phi_R C_R \sigma_R^2}{F_R} \quad [11]$$

II.3. Investigation of EuL^0 CPL properties

The structure of **EuL^0** contains three sources of chirality. The first one is the tetra-substituted phosphorus atom (Figure 2.3.A – green) that can obtain either *R*- or *S*- configuration following the Cahn-Ingold-Prelog rules. Oxygen donor atom coordinated to europium(III) takes the highest priority, followed by the double-bonded oxygen atom, then pyridyl and finally phenyl. The second chirality source is the NCCN torsion angle within the TACN macrocycle that can have positive (*δ*) or negative (*λ*) rotation when viewed along the TACN C-C bond (Figure 2.3.A – red arrow). The third chirality source is the $NCCN_{pyr}$ torsion angle viewed along C-C bond connecting the TACN to the pyridyl (Figure 2.3.A – blue arrow indicated) that can have positive (*Δ*) or negative (*Λ*) helicity.

Although, there is a theoretical possibility of stereoisomers of **EuL^0** with all possible combinations of *R*/*S*, *δ*/*λ* and *Δ*/*Λ*, steric constrains imposed by bulky pyridine, phosphinate and phenyl groups limit their number to four practically possible stereoisomers (Figure 2.3.B – circled in red). This was confirmed in previous work, where two stereoisomers, *SSS*-*Δ*(*λλλ*) and *RRR*-*Λ*(*δδδ*), were experimentally observed and stereochemistry confirmed by single crystal x-ray diffraction.[56,78] In comparison, the other two theoretically possible *SSS*-*Δ*(*δδδ*) and *RRR*-*Λ*(*λλλ*) stereoisomers are destabilised by a steric clash or hindrance between the CH_2 of the TACN and pyridine nitrogen, reducing the probability of their formation. Therefore, interconversion between the enantiomers requires simultaneous rotation of the chromophore and inversion of the TACN ring and the phosphorus chiral centre. Although such racemisation mechanism avoids the high energy conformations, the racemisation energy barrier still remains relatively high, resulting in stability of the **EuL^0** enantiomers towards racemisation.[55]

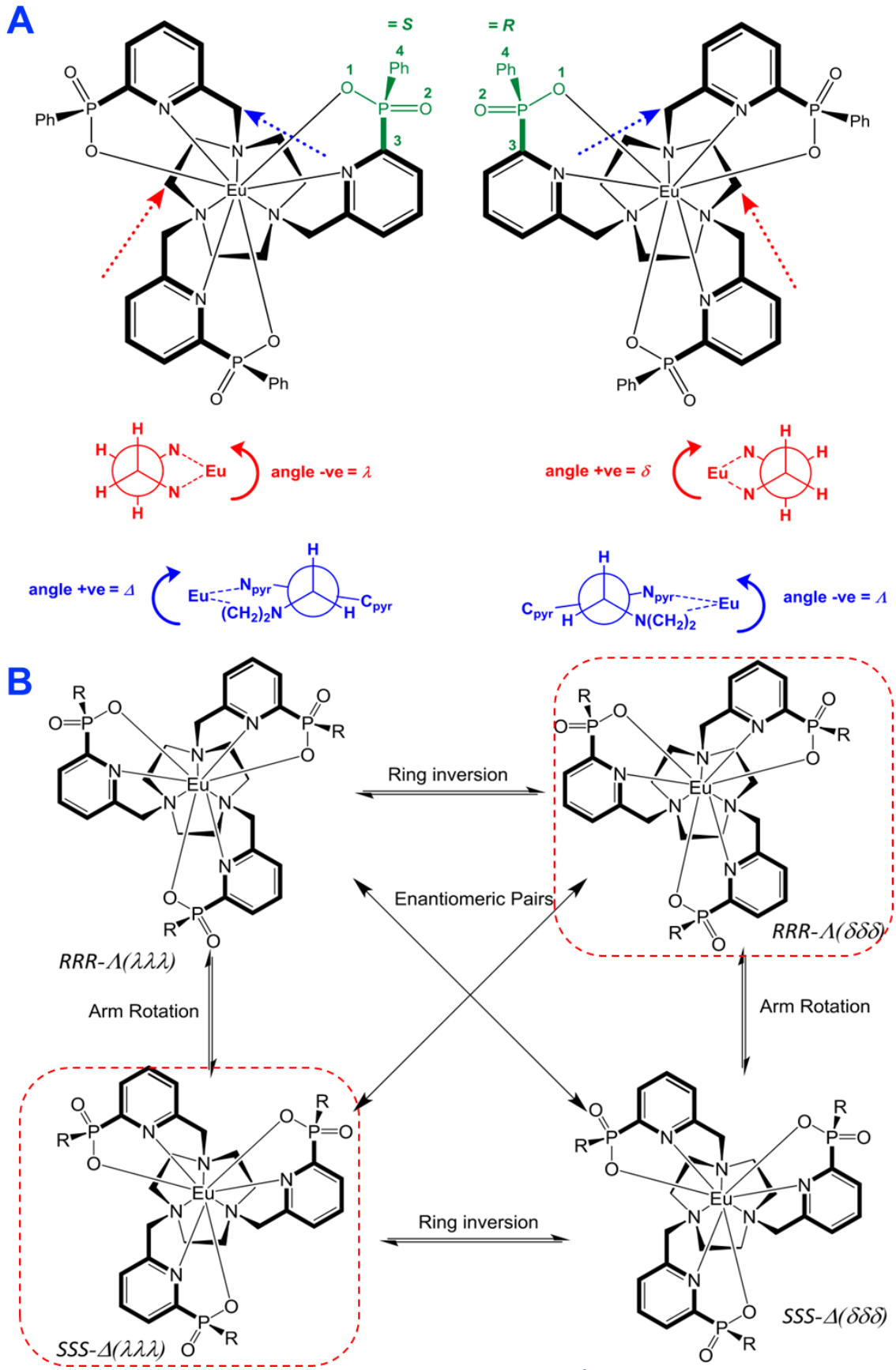

Figure 2.3. A: Demonstration of three sources of chirality in **EuL^0**: *R*/*S* configuration at phosphorus, *δ*/*λ* conformation of the TACN and *Δ*/*Λ* helicity of the complex. **B**: Four possible stereoisomers of **EuL^0** that minimise steric clash from bulky pyridine, phosphinate and phenyl groups with the two observed enantiomers in red boxes (both A and B were adapted from Dr Frawley (2017)).[56]

As expected, only two stereoisomers, assigned as *SSS-Δ*(*λλλ*) and *RRR-Λ*(*δδδ*) (further - *Δ* and *Λ* for short), were isolated by chiral high performance liquid chromatography (HPLC) of the **EuL^0** racemic mixture (Figure 2.4). This was possible due to a chiral stationary phase the column that produced stronger interactions with one of the enantiomers, resulting in its enhanced retention. From a large variety of chiral stationary phases, including synthetic and natural polymers such as methacrylates, cellulose, amylose and proteins, a cellulose based *CHIRALPAK IC* was known from previous work to result in optimal separation of the phosphinate donor complexes and therefore was used.[56]

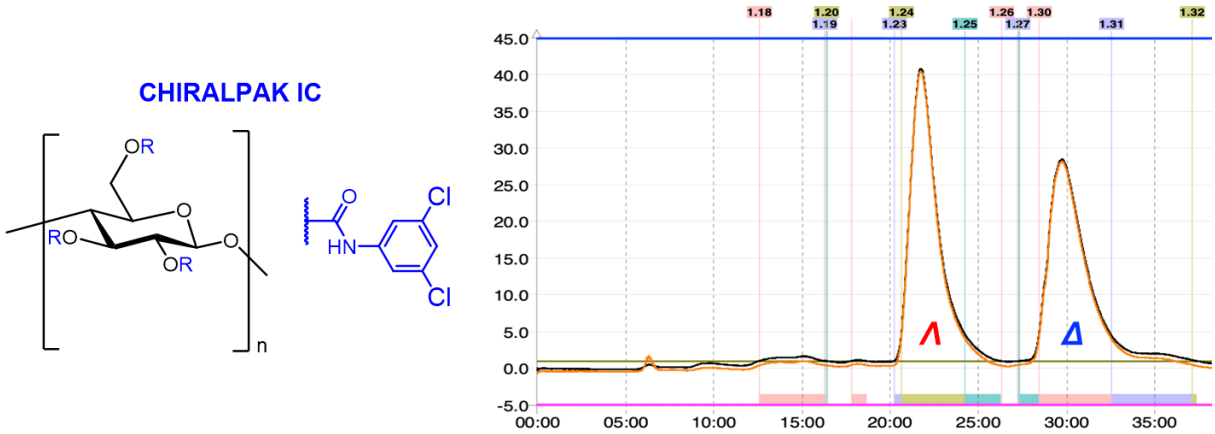

Figure 2.4: The structure of the *CHIRALPAK IC* chiral HPLC column stationary phase (left) and absorbance chromatogram (AC) (at 360 nm) for the separation of the **EuL^0** enantiomers (solvent: MeOH, injection: 20 µL of ~0.5 mg ml^{-1} in MeOH, 4.4 ml min^{-1}) (right). Performed by Dr. Aileen Congreve.

The assignment of the elution order of the two enantiomers (Figure 2.4) was based on the CPL sign of the *ΔJ* = 1 emission manifold. This was done by comparing their spectral profiles to the known isomers of isostructural complexes that were identified using x-ray diffraction (Figure 2.5). Specifically, *ΔJ* = 4 transition can serve as a CPL handedness 'fingerprint' due to multiple inversions of the CPL sign within a single transition.[78]

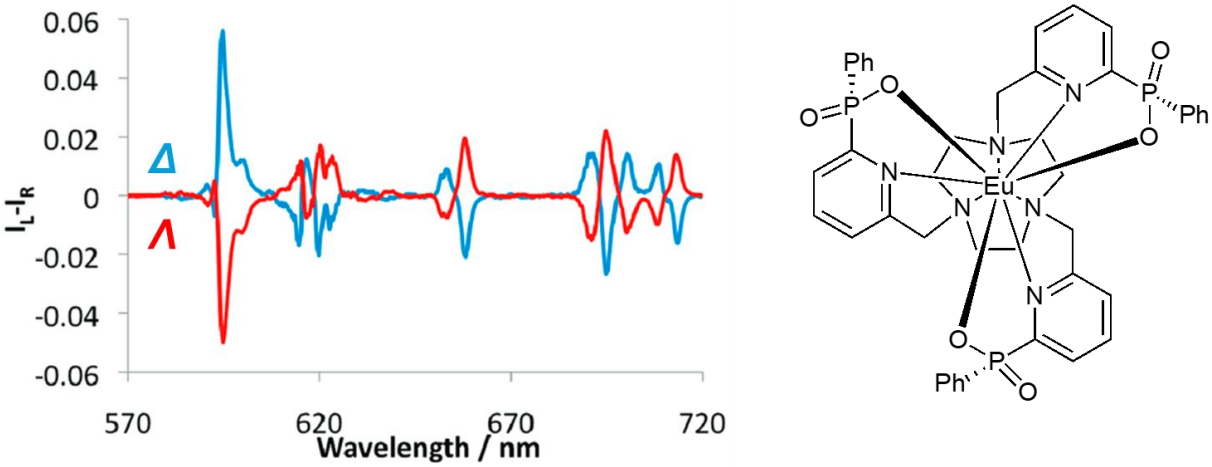

Figure 2.5: CPL spectrum (left) of the *RRR-Λ* (red) and *SSS-Δ* (blue) enantiomers in H_2O of the isostructural to **EuL^0** complex (right), λ_{ex} = 274 nm (adapted from Walton *et al.* (2012)).[78]

The CPL spectra of the enantiomers of **EuL^0** were recorded in MeCN and MeOH (Figure 2.6. A and C), demonstrating strong dependence of the spectral shape of the hypersensitive ΔJ = 2 emission manifold (~610-630 nm) on the solvent. This suggested that the solvent strongly interacts with the coordination environment of the europium(III) which alters the magnitude and orientation of the electric and magnetic transition dipole moments.

In MeCN, the ΔJ = 2 manifold contains 3 emission bands that correspond to the transitions from $^5D_0$ to 3 Starck states (A+2E) of $^7F_2$ (2J+1 = 5 maximal possible number states) that are no longer degenerate due to the CF effect under C_3 symmetry. In MeOH, however, 4 bands can be distinguished withing the ΔJ = 2 manifold on the CPL spectrum. It is likely that the highest CPL intensity band at 614 nm in MeCN splits into two bands of lower intensity and opposite sign when the solvent is changed to MeOH. Additional splitting could be a result of the phosphinate donor oxygen behaving as H-bond acceptor in protic solvents which significantly alters the europium(III) coordination environment. Overall, this is a great example of the use of CPL in investigation of the electronic structure of the emissive excited state of chiral species. CPL spectrum contains significantly more information compared to a standard emission spectrum, where only three emission bands could be distinguished within the ΔJ = 2 emission in MeOH.[3,7]

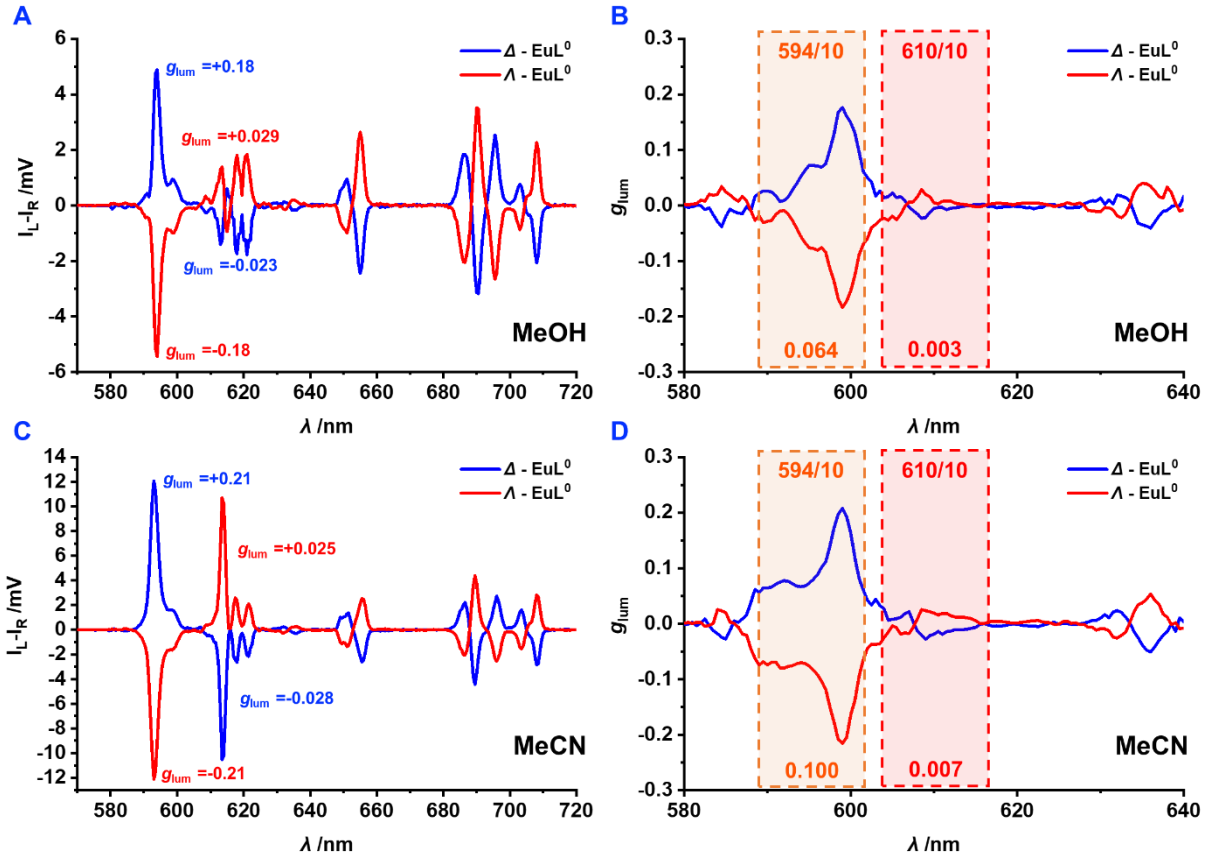

Figure 2.6: CPL spectra of ***Δ*-** (blue) and ***Λ*-EuL^0** (red) (with peak g_{lum} values stated) in MeOH (λ_{exc} = 365 nm, 5 avg.) (**A**) and MeCN (λ_{exc} = 360 nm, 5 avg.) (**C**) and the corresponding g_{lum} plots (**B** and **D**) with the relevant BPFs λ regions (orange – 594 ± 5 (594/10) and red – 610 ± 5 (610/10)) shown with their average g_{lum} stated.

In contrast to the solvent dependence of $\Delta J = 2$, the $\Delta J = 1$ manifold appeared of essentially the same shape in both solvents. This agreed with the fact that $\Delta J = 1$ is a magnetically allowed transition that only weakly depends on the environment. On the other hand, a slight reduction of the maximal g_{lum} was observed in MeOH (g_{lum} = ±0.18 at 599 nm) compared to MeCN (g_{lum} = ±0.21 at 599 nm), which can be attributed to a slight reduction in MD moment (orbital angular momentum driven).

To estimate the CPL performance of **EuL^0** as a security ink, a more practically useful CPB_i (rather than CPB) must be calculated. This is particularly relevant since CPB_i not only accounts for the total brightness of the material, but also the proportion of the total emission that produces a measurable CPL signal. More specifically, while the MD allowed $\Delta J = 1$ produced the strongest CPL signal with a significantly higher dissymmetry factor compared to the most intense $\Delta J = 2$ transition, its total emission is relatively low.

The previously discussed literature method of CPB_i determination uses β_i for the whole transition and the maximal g_{lum} point achieved within. Although a good estimate for a general comparison of CPL-active materials, it is not sufficiently accurate to estimate their performance in the context of CPLP, where a λ region is selected using a commercially available band pass filter (BPF) that sometimes doesn't cover the whole emission manifold of a transition. This is important since the sign of CPL is not always the same for all the bands within a single ΔJ emission manifold. Therefore, a more CPLP-relevant term CPB_F is introduced here for a more accurate CPL security ink performance estimation.

Instead of the β_i for the whole emission, a β_F for the λ range of BPF is used. In addition, the average g_{lum} value for the selected range ($\bar{x}g_{lum}$) is used instead of the maximal achieved (Equation 12). This provides a more accurate performance estimate since g_{lum} is not constant throughout the selected λ range.

$$CPB_{\mathrm{F}} = \beta_{\mathrm{F}} \times B \frac{\mathrm{x}\bar{g}_{\mathrm{lum}}}{2} \qquad [12]$$

As a result, both CPB_i and CPB_F were calculated (Table 2.1) for the $\Delta J = 1$ and $\Delta J = 2$ transitions, where the 589-599 nm and 605-615 nm regions were selected for CPB_F as they matched the commercially available 594 ± 10 nm (BPF594/10) and 610 ± 10 nm (BPF610/10) BPFs (Figure 2.6.B and D – orange and red boxes).

Table 2.3: CPB_i and CPB_F calculation for the ΔJ = 1 and ΔJ = 2 and BP594/10 and BP610/10 λ regions.

Solvent	Trans.	Trans. λ range /nm	β_i /%	max $\lvert g_{lum} \rvert$	CPB_i /M^{-1} cm^{-1}	Filter λ range /nm	β_F /%	$\bar{x}g_{lum}$	CPB_F /M^{-1} cm^{-1}
MeOH	**ΔJ = 1**	589-601	6.9	0.18	**134**	589-599	6.7	0.064	**46**
	ΔJ = 2	605-630	73	0.029	**228**	605-615	28	0.003	**9**
MeCN	**ΔJ = 1**	589-601	7.3	0.21	**166**	589-599	7.2	0.100	**78**
	ΔJ = 2	605-630	72	0.028	**218**	605-615	33	0.007	**25**

As expected, the calculated CPB_i and CPB_F values were significantly different, confirming the significance of the new term introduction. CPB_i values obtained in MeOH and MeCN were similar across the two transitions – 134 and 166 M^{-1} cm^{-1} for ΔJ = 1 and 228 and 218 for ΔJ = 2. The obtained CPB_i values were lower than average for ΔJ = 1 (286 M^{-1} cm^{-1}) and higher than average for ΔJ = 2 (69 M^{-1} cm^{-1}) compared to other europium(III) complexes. Based on CPB_i exclusively, a conclusion can be made that ΔJ = 2 is far more suitable for the authentication of the CPL security layer than ΔJ = 1. This, however, contradicts to the values of CPB_F obtained for the two transitions. As expected, the CPB_F values were significantly lower compared to CPB_i; however, most importantly, the relative magnitude of ΔJ = 1 and ΔJ = 2 was inverted. In other words, ΔJ = 1 is a far better transition for CPLP even though it's around 10 times dimmer than ΔJ = 2 in terms of the total emission. This is the case since a relatively high g_{lum} was maintained throughout the whole ΔJ = 1 λ range, increasing the $\bar{x}g_{lum}$. As a result, in both solvents CPB_F of ΔJ = 1 was around 5 times higher than that of ΔJ = 2, suggesting that only emission dissymmetry produced by ΔJ = 1 could be rapidly detected by the CPLP camera for CPL security authentication.

II.4. Discussion and future work

A previously reported **EuL^0** complex was synthesised and investigated in terms of its performance as a security ink for the first time. **EuL^0** is relatively bright material with a large pseudo-Stokes shift that makes the material invisible to a naked eye unless irradiated with a UV light source. The 'push-pull' structure of the chromophore containing spatially separated conjugated electron rich and electron depleted groups that are linearly oriented *via* an alkyne resulted in a large transition dipole moment that increased ε contributing to *B*. 2,4,6-

Trimethoxy substitution of the aryl group increases the HOMO energy, red shifting the absorption maximum towards the optimal 365 nm that matched the commercially available LED. Europium(III) emission demonstrated a characteristic millisecond-scale lifetime that allows to facilitate the temporal security layer when combined with nanosecond-scale emitting organic fluorophores. **EuL^0** was synthesised as a racemic mixture containing only two most conformationally stable enantiomers that were separated using chiral HPLC and investigated in terms of their CPL properties. Strong CPL signal with high g_{lum} was observed, which was characteristic for europium(III) in a chiral environment. The advantage of the use of CPL to study the electronic structure of the excited state was demonstrated by a comparison between the recorded total emission and CPL spectra. In the latter, a larger number of emission bands were observed in ΔJ = 2, suggesting a de*via*tion of the **EuL^0** symmetry from C_3. The highest g_{lum} values were obtained from the low intensity MD allowed ΔJ = 1 transition, the spectral shape of which was essentially independent on the environment. On the contrary, the most intense 'hypersensitive' ΔJ = 2 demonstrated a strong dependence of CPL on the solvent in terms of both the spectral profile and g_{lum}. The CPL performance of **EuL^0** was analysed in terms of recently introduced in literature CPB_i and herein proposed CPB_F, which provided a more realistic estimate of CPL performance in the context of CPLP. As a result, while CPB_i suggested ΔJ = 2 as the best candidate for CPL security authentication, CPB_F contradicted that by providing a more accurate estimate of the detectability of the CPL signal produced by the two transitions. While the CPL security could be facilitated using the ΔJ = 1 transition, it was not ideal since it only contributes around 7% to the total emission. This makes the **EuL^0** based security ink more expensive as more material is required to surpass the detection limit. An ideal europium(III) complex for security applications would produce ΔJ = 2 emission manifold that maintains a relatively high g_{lum} throughout a λ range of a commercially available BPF. Since the brightest ΔJ = 2 emission contributes ~70% to the total emission, such ink would be around 7 times cheaper, based on the amount of material required to produce the same amount of signal. Simultaneously, the material must retain other previously mentioned photophysical properties that are beneficial in security applications. The investigation into the design and preparation of such material follows in the next chapter.

CHAPTER III. The investigation into a novel EuL^1 carboxylate donor complex to achieve monosign circularly polarised luminesce

III.1. Introduction to the structural modifications of EuL^1

In the previous chapter, the photophysical characterisation of **EuL^0** suggested its suitability for a novel CPL active CST using ΔJ = 1. On the other hand, the ΔJ = 2 transition produced a relatively low CPB_F (BPF610/10) value which was unlikely to be sufficient for a rapid authentication by the CPLP camera. In addition, **EuL^0** demonstrated a strong solvent dependence of the ΔJ = 2 emission manifold CPL spectral shape and average g_{lum} ($\bar{x}g_{lum}$) on the solvent, where protic solvent resulted in an additional band splitting and CPL sign variation. This is a critical issue for security application as the material must be universally compatible with a range of commercially used host materials. The need for a repeated investigation of the photophysical properties in each host material followed by optimisation increases costs and decreases the reproducibility of CST.

This leads to the main requirement for a CPL-active security ink – conservation of the CPL sign across the emission manifold to maximise the $\bar{x}g_{lum}$ within the selected wavelength region. Therefore, it is important to consider the symmetry at the europium(III) emitting centre that affects the multiplicity of the electronic states involved in a transition. For europium(III), the emissive $^5D_0$ state has a multiplicity of 1 (J = 0) in all symmetries unlike the multiplicities of the $^7F_1$ and $^7F_2$ which contain 3 and 5 (2J+1) degenerate Starck states respectively. Once europium(III) experiences the CF of the surrounding environment, the degeneracy of certain states is lifted and multiple emission bands within each ΔJ emission manifold are observed. For example, under the C_3 symmetry, the $^7F_1$ splits into 2 (A+E) and $^7F_2$ splits into 3 states (A+2E), resulting in 2 and 3 bands within the ΔJ = 1 and ΔJ = 2 emission manifolds respectively.[3] Such multiplicity is the same across other high symmetry classes such as hexagonal and octagonal but can increase when the symmetry is lowered. This increases the probability of CPL sign variation, since the consecutive bands can possess opposite helicity, which then reduces the $\bar{x}g_{lum}$. In addition, CF splitting decreases the overall MD moment and hence the rotatory strength of the molecule, also resulting in a lower g_{lum}.

Although macrocyclic nonadentate arylalkynylpyridine-sensitised europium(III) complexes are well-known in literature as bright, long-lived and chemically stable inorganic emitters,[18,19,58,59,78,79] the research focusing on their CPL-properties is relatively recent. So far, europium(III) complexes that were the most widely explored for their CPL activity contained phosphinate donor groups.[20,59,80,81] In this work, CPL spectra of the previously reported isostructural with **EuL^0** materials were analysed in terms of the CPL sign variation within the

ΔJ = 2 manifold.[20,47,56,59,82] It was established that, similarly to **EuL^0**, most phosphinate containing materials demonstrated multiple low-intensity bands that possessed sequentially opposite CPL sign. An exception from this observation was two recently reported methylphosphinate containing europium(III) complexes (Figure 3.1).

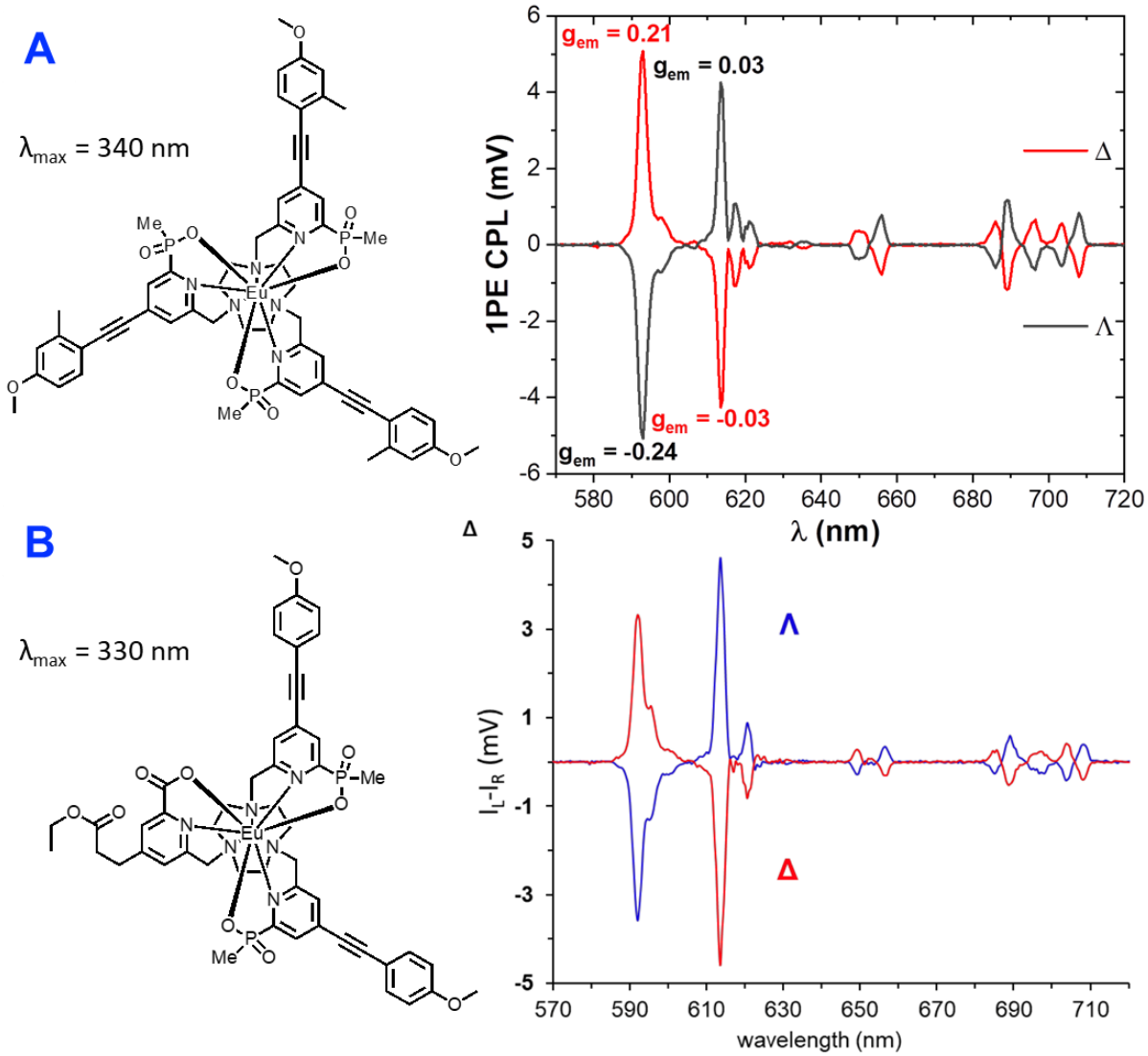

Figure 3.1: Structures of the two europium(III) complexes (left) and their CPL spectra (right) demonstrating monosignate ΔJ = 2 manifold in *N*-methyl-2-pyrrolidone (NMP) solvent (adapted from Stachelek *et al.* (2022)[20] (**A**) and De Rosa *et al.* (2023) (**B**)).[47]

The first example was very structurally similar to **EuL^0** and contained three methylphosphinate donor groups (Figure 3.1.A),[20] while the second one was a mixed donor complex containing two methylphosphinate donors and one carboxylate donor (Figure 3.1.B).[47] Both complexes demonstrated a single sign ΔJ = 2 manifold when recorded in NMP (Figure 3.1) which is a monomer unit for the polyvinylpyrrolidone (PVP). The CPL spectrum of the second complex recorded in ethyl acetate (EtOAc), which is a monomer unit for PMMA, was also reported with a single sign ΔJ = 2. CPL spectra of these two complexes are solvent dependent and do not demonstrate monosign ΔJ = 2 in some other solvents such as MeOH or water.

The observed conservation of the CPL sign within the ΔJ = 2 manifold in NMP and EtOAc, which are monomer units of the commercially available PVA and PMMA polymer host materials, is beneficial for application in security. On the contrary, the absorption maxima of these materials were 340 nm and 330 nm, resulting in sub-optimal PE of these materials using the commercially available 365 nm LED, reducing the practically observed CPB_i. Therefore, the new target material must retain the 2,4,6-trimethoxy substitution on the top of the chromophore which causes the bathochromic shift of the absorption maximum.

Currently, the literature reporting EuL-type complexes is dominated by examples containing phosphinate donor groups, while their carboxylate containing counterparts are underrepresented. This could be associated with a more challenging separation of the enantiomers by chiral HPLC, which is necessary to enable the CPL-activity (racemic mixture is not CPL active). In contrast to carboxylates, phosphinate donors bring in additional phosphorus chiral centres that can facilitate selective interactions of the enantiomers with chiral stationary phases of the columns.

To the knowledge of the author, the only reported example of a CPL-active all-carboxylate europium(III) complex contained no arylalkyl chromophore arms. Nevertheless, the ΔJ = 2 manifold was dominated by a strong monosign band (Figure 3.2).[59]

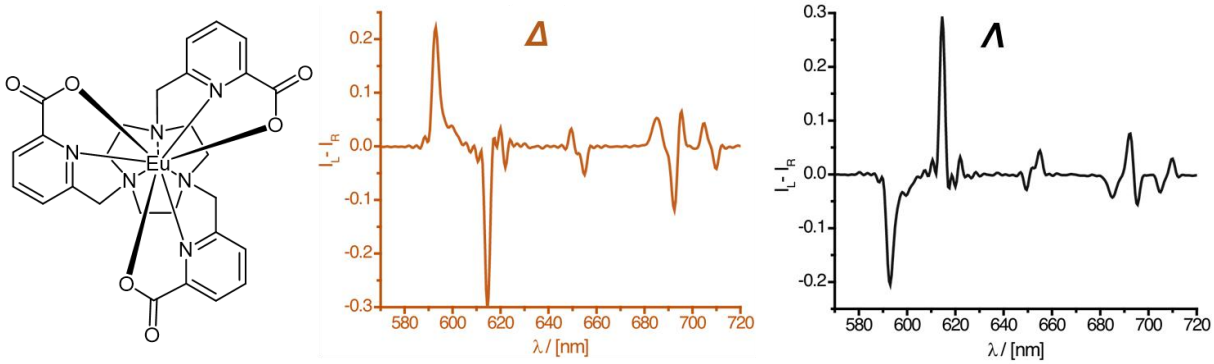

Figure 3.2: The structure of all-carboxylate europium(III) complex and CPL spectra of its enantiomers in water (adapted from Evans *et al.* (2013)).[59]

Although a direct relationship between the complex structure and its observed CPL spectrum is not fully understood, it was proposed that substitution of chiral phosphinate donors with achiral centrosymmetric bidentate carboxylate donors would increase the MD moment induced (total angular momentum driven). This would greatly affect the overall rotatory strength of the molecule and the variation of CPL sign within the ΔJ = 1 and ΔJ = 2 manifold. An increase in rotatory strength improves emission dissymmetry, leading to higher values of g_{lum} and therefore *CPB*. In contrast to the pseudo-tetrahedral geometry of phosphinate donors in **EuL^0**, trigonal planar geometry of carboxylate donors does not allow the oxygen atom to approach the luminescent europium(III) centre as closely. This leads to a weaker CF experienced by europium(III) which reduces the CF splitting of the individual ^7F_J electronic

states (especially relevant for the 'hypersensitive' ΔJ = 2 transition). As a result, the transition multiplet is simplified on both the total emission spectrum and the CPL spectrum. This increases the probability of the CPL sign conservation within a transition manifold by decreasing the total number of individual bands that can produce sequentially opposite sign of CPL. Apart from the donor groups, the rest of the structure was set to remain the same with **EuL^0**, which also allowed to directly study the isolated effect of the carboxylate donor group on photophysical properties of the complex, including CPL.

In this work, the design of the novel europium(III) complex was aimed on conservation of the CPL sign within both ΔJ = 1 and ΔJ = 2 transition manifolds to achieve high CPB_F. Strong g_{lum} of ΔJ = 2 would generate an additional CPL security layer to the existing multi-coloured, multi-spectral, opposing helicity security, combined with high spatial and temporal resolution five-tier security. In addition, the ability to use the brightest ΔJ = 2 transition for CPL security authentication would reduce the amount of material required to benefit potential commercialisation.

III.2. Synthesis of the novel carboxylate donor EuL^1 complex

The synthetic approach towards **EuL^1** was equivalent to that for **EuL^0**, where the 'top' and 'bottom' components of the chromophore are separately prepared before undergoing Sonogashira cross-coupling reaction. Three chromophores are then attached to TACN *via* alkylation to prepare a macrocyclic ligand that coordinates to europium(III) after all three esters are hydrolysed.

The bottom pyridine component was prepared from commercially available chelidamic acid, which is brominated using phosphorus pentabromide to yield **11** (Scheme 3.1), which then undergoes esterification with EtOH to restore the esters in **12**. One of the two esters is then reduced to alcohol with sodium borohydride in a kinetically controlled reaction to give **13**, which is the complete 'bottom' component of the sensitising chromophore.

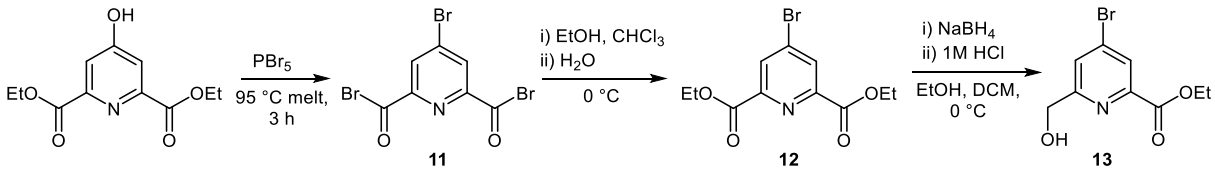

Scheme 3.1: The reaction sequence for the 'bottom' of the carboxylate donor sensitising chromophore for **EuL^1**.

This three-step synthesis of the bottom component of the sensitiser for the **EuL^1** is shorter than that of **EuL^0** and exploits a cheaper starting material while also avoiding the palladium catalysed C-P coupling reaction. The 'top' of the chromophore **7**, however, is shared between **EuL^0** and **EuL^1**.

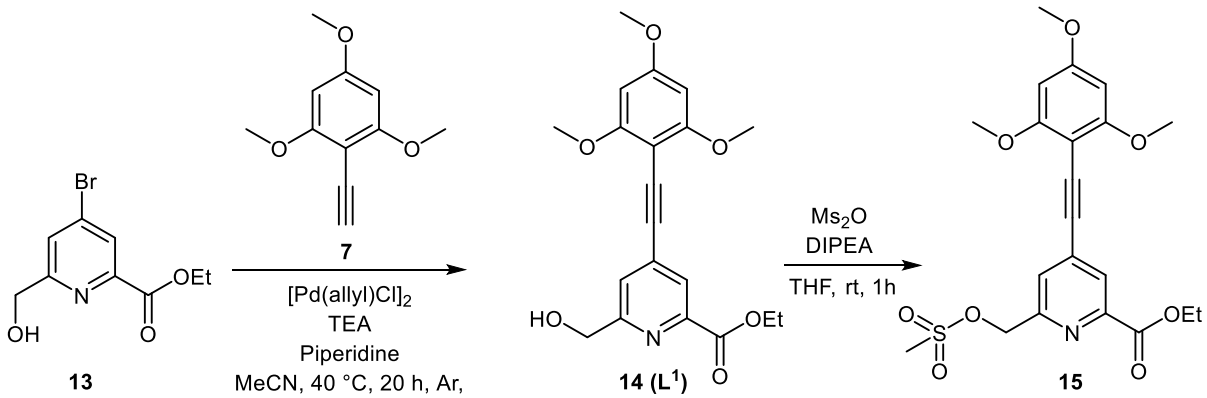

Scheme 3.2: The reaction sequence for the carboxylate donor sensitising chromophore for **EuL^1**.

Once the 'top' and the 'bottom' components are prepared, they undergo copper-free Sonogashira cross-coupling to yield the chromophore **14** (Scheme 3.2). Once **14** is mesylated, 3 equivalents of **15** are attached to TACN *via* nucleophilic substitution to give the macrocyclic ligand precursor 1**6** (Scheme 3.3). Once all esters on **16** are hydrolysed, complexation to europium(III) yields **EuL^1**.

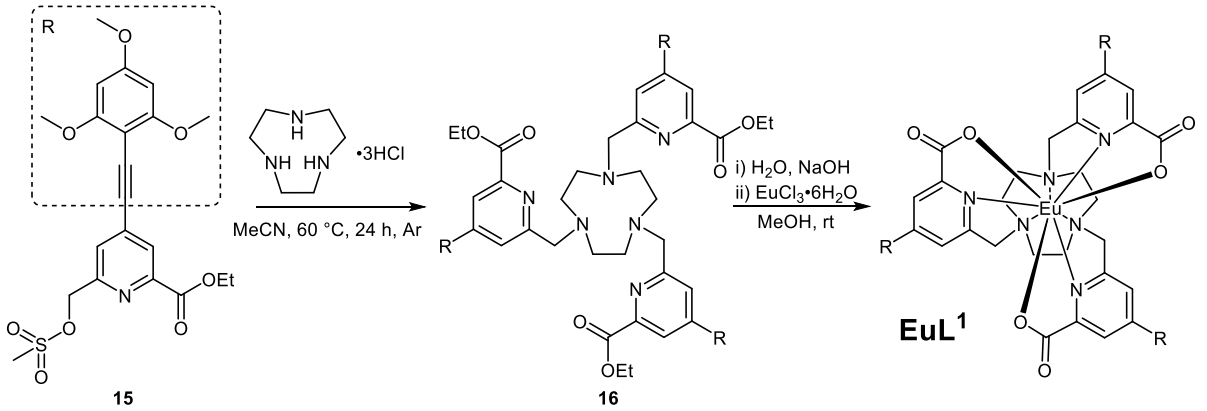

Scheme 3.3: The reaction sequence for the alkylation, hydrolysis and complexation steps for **EuL^1**.

III.3. General photophysical characterisation of EuL^1

Similarly to other sensitised lanthanide complexes, including **EuL^0**, a large pseudo-Stokes shift (~257 nm) was observed for **EuL^1** (Figure 3.3.A). The band shape match between the absorption and excitation spectra of **EuL^1** confirmed the sensitised nature of the europium(III) emission. Φ of **EuL^1** was measured as 45% (in MeCN) *via* absolute method using the integrating sphere. As a result, Φ of **EuL^1** was 25% higher than that of **EuL^0** (36% in MeCN), suggesting a lower rate of non-radiative decay during the sensitisation process.

The ε of **EuL^1** was determined as 77000 ± 1000 M^{-1} cm^{-1} (λ_{exc} = 358 nm) in MeCN (Figure 3.3.B), which was ~28% higher than 60000 ± 1000 M^{-1} cm^{-1} (λ_{exc} = 355 nm) recorded for **EuL^0** in MeOH. In order to confirm the accuracy of the determined ε, the experiment was repeated with a single chromophore **14** to produce 27000 ± 200 M^{-1} cm^{-1} (λ_{exc} = 340 nm) in MeCN, which, as expected, was approximately one third of that measured for **EuL^1** containing three chromophores.

As a result, **EuL^1** was found to be a significantly brighter material compared to **EuL^0**, since both Φ and ε were higher. The calculated B value for **EuL^1** was 34650 M^{-1} cm^{-1} (λ_{exc} = 358 nm), resulting in a ~60% increase compared to **EuL^0** (21600 M^{-1} cm^{-1}, λ_{exc} = 355). B directly impacts CPB, CPB_i and, most importantly, CPB_F, suggesting that **EuL^1** was likely to perform significantly better than **EuL^0** as a security ink.

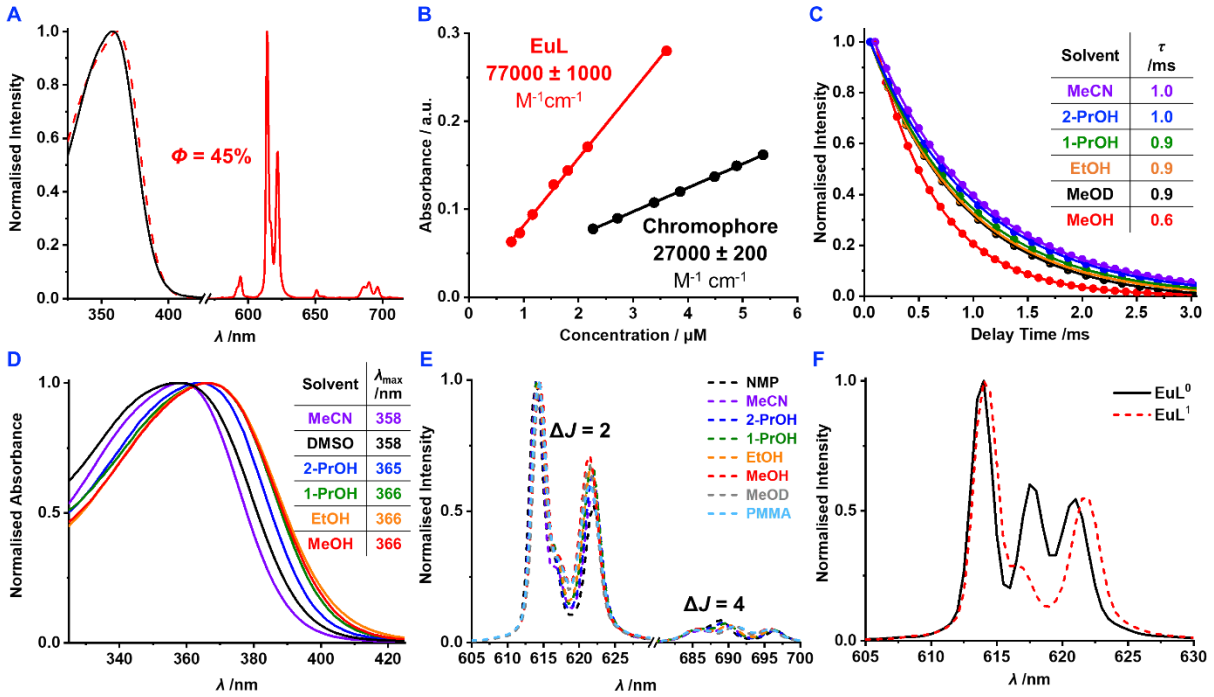

Figure 3.3: A: Normalised absorption curves (black), emission (solid red, λ_{exc} = 360 nm) and excitation (dashed red, λ_{em} = 614 nm) spectra of **EuL^1** in MeCN with the measured Φ (absolute method) annotated; **B:** Dependence of absorption (at 358 nm) on the **EuL^1** concentration in MeCN; **C:** Lifetime plots of **EuL^1** in different solvents (0.1 abs solutions, λ_{em} = 614 nm); **D**: Normalised absorption spectra of **EuL^1** in different solvents; **E**: Normalised emission spectra (ΔJ = 2 and 4 only) of **EuL^1** in different solvents and solid PMMA film; **F:** 605-630 nm section of the spectrum in **E** demonstrating ΔJ = 2 transition.

As previously discussed, the arylalkynylpyridyl containing chromophores sensitise europium(III) *via* an ICT state, where electron donating substituents on the HOMO-containing aryl group result in HOMO-LUMO energy gap decrease and therefore a bathochromic shift of the absorption maximum. The absorption maximum of **EuL^1** at 358 nm demonstrated a small 3 nm red shift from the absorption maximum of **EuL^0** at 355 nm which is beneficial for the CPB_F under CPLP parameters due to a slight increase in the relative absorbance at the desired 365 nm.

As the only structural difference between the two chromophores is the donor group on the pyridyl 'bottom' of the chromophore, the observed red shift was attributed to a more electron withdrawing carboxylate group reducing the LUMO energy.

In MeOH, a larger bathochromic shift of 6 nm was observed (from 360 nm in **EuL^0** to 366 nm in **EuL^1**), suggesting a stronger ICT-stabilising interaction between the protic solvent and the chromophore containing carboxylate donor compared to the phosphinate donor. Since the ICT state stabilisation is believed to occur *via* a pyridyl nitrogen accepting a H-bond, it was proposed that enhanced stabilisation is facilitated by a less sterically hindered approach of the H-bond donating solvent molecules provided by a less bulky (compared to phenylphosphinate) carboxylate group. This proposal agrees with a significantly shorter τ of **EuL^1** in MeOH (0.6 ms) compared to other solvents, where τ remained at a constant ~1 ms in solvents with different polarity as well as in deuterated MeOH (MeOD) (Figure 3.3.C). Since τ in MeOD was similar to that in the rest of the alcohols, it was supposed that that emission quenching is not a product of vibrational relaxation *via* O-H oscillators. Instead, small protic solvents stabilise the ICT *via* H-bonding, which decreases the energy gap between the ICT state and the lower-lying $^5D_0$, and therefore increases the rate of thermally activated BET. This depopulates $^5D_0$, resulting in europium(III) emission quenching. The τ of **EuL^1** in a 200 nm thick PMMA film (discussed later in Chapter IV) was measured as 0.8 ± 0.1 ms, which is slightly shorter compared to the solution state. The likely cause of this was a higher concentration of **EuL^1** in PMMA (~650μM) compared to solution (~1μM), resulting in NRR *via* concentration quenching, where the energy can be transferred between the europium(III) centres in proximity to one another.

Stabilisation of the ICT state can also be evidenced by the positive solvatochromism observed from the **EuL^1** absorption spectra in solvents with increasing polarity and H-bond donating capabilities (Figure 3.3.D). Importantly, no significant dependence of the **EuL^1** emission spectral shape on the solvent was observed (Figure 3.3.E), including solid-state PMMA film. The emission spectral profile remained the same while the relative intensity of the emission bands in the ΔJ = 2 slightly changed in different solvents. This was the opposite to what was observed for **EuL^0**, where the relative intensities and positions of the bands within the ΔJ = 2

and 4 emission manifolds significantly differed between the measurements performed in MeOH and MeCN. As previously mentioned, this poses a disadvantage for the use in security tagging where the emission properties would not remain consistent across different host materials, requiring additional optimisation every time. In the case of **EuL^1**, the total emission profile essentially remained constant in different host materials, improving the versatility of such security ink.

Similarly to **EuL^0**, the environmentally 'hypersensitive' ΔJ = 2 emission manifold appeared as 3 bands (Figure 3.3.F), where the central band appeared significantly lower intensity compared to **EuL^1**.

The 2PE spectrum of **EuL^2** (Figure 3.4.A) produced a narrow hypsochromically shifted band when compared against the 1PE spectrum. As previously mentioned, the blue shift of the band is a result of the nonlinear effect of the non-degenerate photons in 2PE, while narrower band results from the quadratic relationship between the intensity of 2PE and triggering of the emission event.[20] Similarly to **EuL^0**, 2PE spectrum of **EuL^1** demonstrated two peaks at 700 and 720 nm that could correspond to population of S_1 and the ICT states of the arylalkynylpyridine chromophore respectively. The plot of the integrated emission intensity against the laser power (Figure 3.4.B) on a logarithmic scale produced a slope of 2.0, confirming the 2PE, since the excitation rate scales as the square of the laser power at a constant beam area. 2PE cross-section (σ^2) of **EuL^1** was calculated as 308 GM at 700 nm using **RhB** as a reference (σ^2 = 240 at λ_{2PE} = 700 nm).[77]

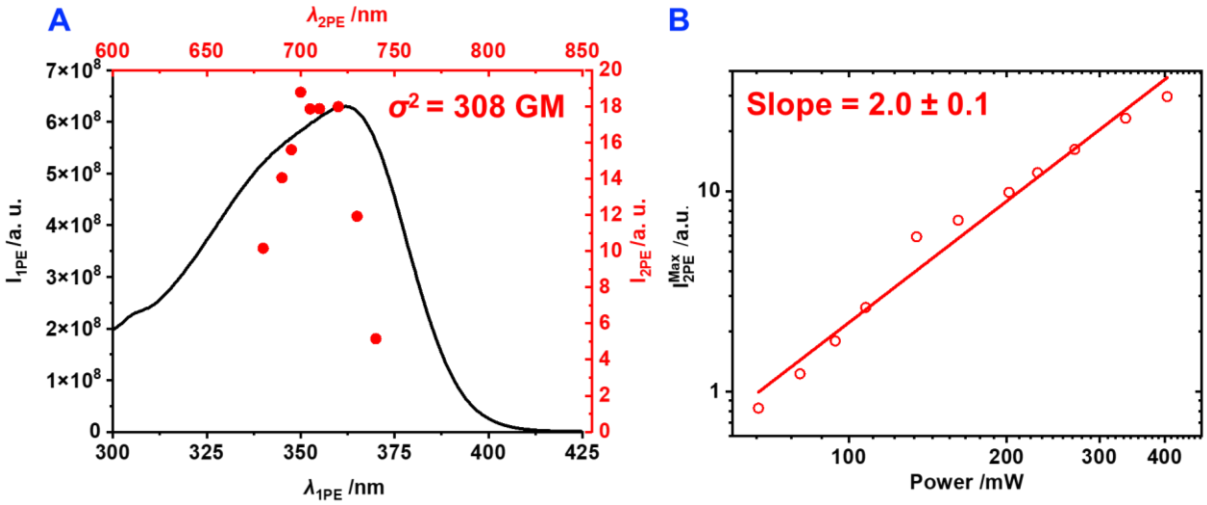

Figure 3.4: A: Normalised absorption (solid black) and 2PE (red spheres, λ_{em} = 614 nm) spectra of **EuL^1** in MeCN. **B**: Plot of integrated emission intensity at 614 nm against the excitation source power (λ_{exc} = 700 nm) on a logarithmic scale.

III.4. Chiral separation of the EuL[1]

Since it was not possible to accurately predict which combination of a chiral stationary phase and mobile phase would provide the best separation of **Δ-** and **Λ-EuL[1]** in a time and cost efficient manner (initially available CHIRALPAK IC and ID did not result in separation of enantiomers), the method development was performed by *Daicel*, the manufacturer of *CHIRALPAK* chiral columns. A racemic mixture of **EuL[1]** was tested against the commercially available range of the HPLC columns based on amylose and cellulose (Figure 3.5).

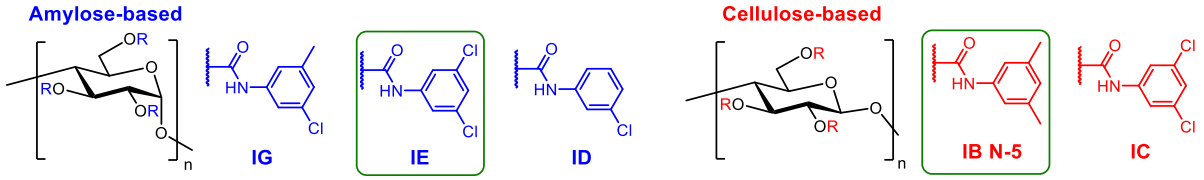

Figure 3.5: The structures of the chiral stationary phases of the *CHIRALPAK* columns which were tested against separation of **Δ-** and **Λ-EuL[1]** with the columns providing the optimal separation in green boxes.

As a result, the *CHIRALPAK IE* and *IB N-5* columns (Figure 3.5 – green boxes) provided the best separation with 35 minutes and 4 minutes retention time difference of the two enantiomers respectively (Figure 3.6).

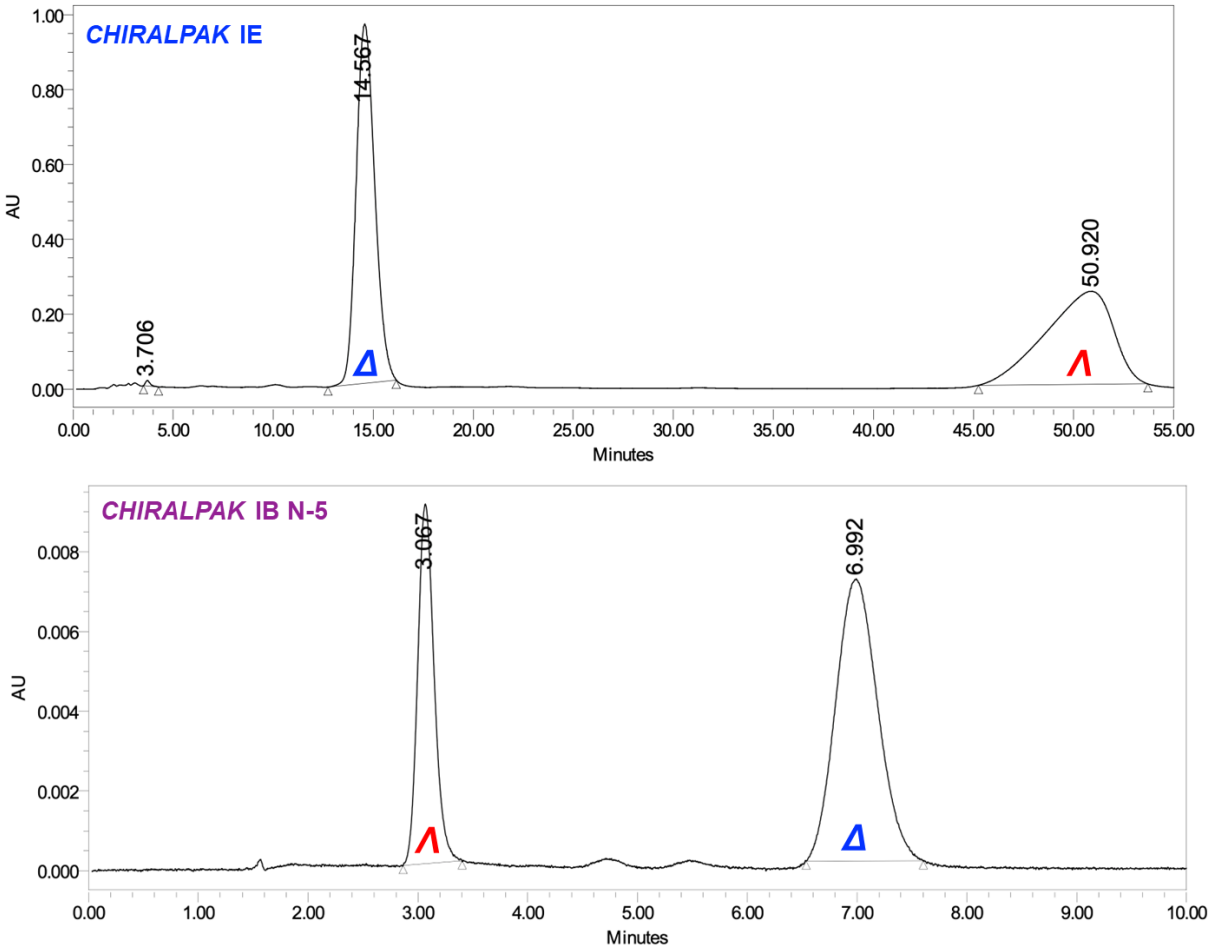

Figure 3.6: Chiral HPLC ACs (at 360 nm) for the chiral separation of the **EuL[1]** enantiomers using *CHIRALPAK* IE (top) and IB N-5 (bottom) (solvent: EtOH/MeOH/TEA/TFA at 50/50/0.5/0.3, injection: 10 µL of ~0.5 mg ml^{-1} in MeOH, 2 ml min^{-1}). Performed by Dr. Aileen Congreve.

The method required triethylamine (TEA) and trifluoroacetic acid (TFA) additives in the mobile phase for ion-pairing. Therefore, the obtained samples of ***Δ*-** and ***Λ*-EuL^1** were isolated from the additive using reverse-phase HPLC (C_{18}, Method A, Section V.II). TFA and TEA could not be removed by heating the enantiopure samples under reduced pressure as this posed a risk of racemisation. The two chiral columns resulted in the enantiomers eluting in a different order (Figure 3.6). As expected, the racemic **EuL^1** sample contained only two enantiomers. Similarly to **EuL^0**, the chirality of the enantiomers was assigned based on the relative sign of the bands on the CPL spectra, using a previously reported isostructural material as a reference.[59]

III.5. Investigation of EuL^1 CPL properties

Similarly to **EuL^0**, the CPL spectra of ***Δ*-EuL^1** and ***Λ*-EuL^1** are mirror images with the opposite sign (Figure 3.7.A). The spectra were recorded in a range of different solvents (Figure 3.7.C) and as a PMMA film, where no dependence of the spectral shape on the solvent properties was observed. This suggested that **EuL^1** is a more versatile security ink than **EuL^0** since it can be used in a wide range of host materials without changing its luminescent properties. The observed g_{lum} slightly varied (±0.07) in different solvents (Figure 3.7.D) which could be mostly related to a change in signal to noise ratio with variation in total emission intensity.

In contrast to the previously reported CPL spectra of various phosphinate donor complexes,[47,56,59,82] the ΔJ = 2 band produced a stronger than ΔJ = 1 CPL signal with a significant sign retention (Figure 3.7.A). This resulted in the peak CPL intensity of the ΔJ = 2 (at 615 nm) around 2.5 times higher than that of ΔJ = 1 (at 594 nm). The only example with such strongly CPL-active monosign ΔJ = 2 band was Eu:BPEPC, a commonly known CPL-standard.[83] Similarly to **EuL^0**, the whole ΔJ = 1 manifold (588-605 nm) of **EuL^1** was single sign, producing the highest g_{lum} values of +0.30 (at 597 nm) and +0.29 (at 601 nm) for ***Δ*-EuL^1** and -0.29 (at 597 nm) and -0.29 (at 601 nm) for ***Λ*-EuL^1** (Figure 3.7). Such outstanding g_{lum} values of **EuL^1** were higher than those of most other reported europium(III) complexes including **EuL^0**, which produced a lower g_{lum} of ±0.21 (at 599 nm). Although there are few examples reporting g_{lum} values higher than 0.30 for the ΔJ = 1 transition, they often have significantly lower values of Φ and ε, resulting in overall lower CPB_i that limits their security application.[39,84] For example, one material demonstrated the g_{lum} values of ±0.33 (at 600 nm) but a relatively low Φ of 11%.[85] Another example reported similar g_{lum} values of +0.298 and -0.294 but much lower ε (23000 mol^{-1} dm^3 cm^{-1}) and Φ (11%).[29] The material (Cs[Eu(+)-(hfbc)$_4$) with the highest ever reported g_{lum} of 1.38 (at 595 nm) also has a significantly lower ε (35000 mol^{-1} dm^3 cm^{-1}) and Φ (3 %).[41] This, again, highlights the superiority of CPB_i and CPB_F over g_{lum} to assess the performance of the CPL emitters for practical applications.

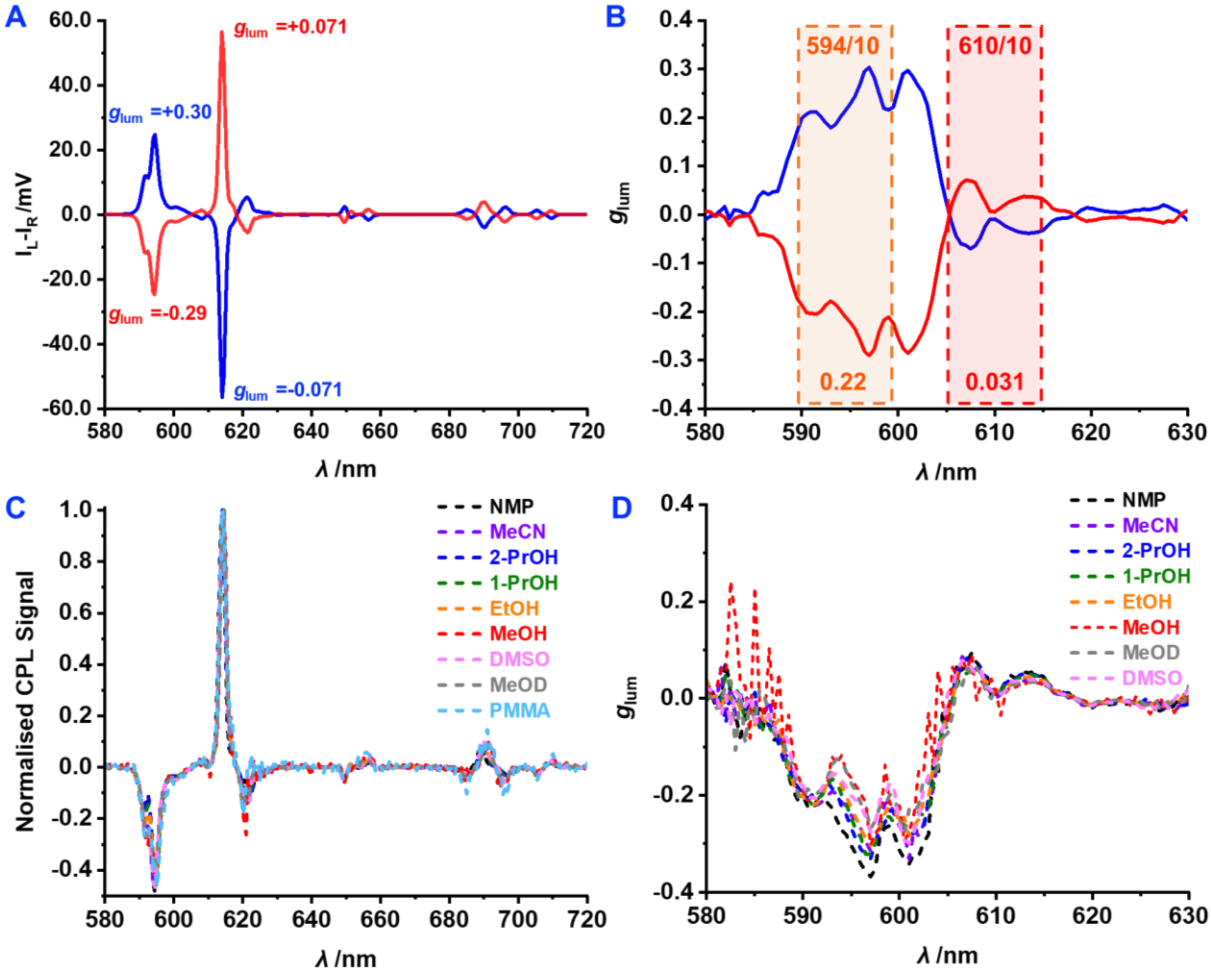

Figure 3.7. A: CPL spectra of ***Δ*-** (blue) and ***Λ*-EuL^1** (red) (with peak g_{lum} values stated) in MeCN (λ_{exc} = 365 nm, 5 avg.) and the corresponding g_{lum} plots (**B**) with the relevant BPFs λ regions (orange and red) shown and their $\bar{x}g_{lum}$ shown; **C**: Normalised CPL spectra of ***Λ*-EuL^1** in different solvents and solid-state PMMA film; **D**: g_{lum} plots for the CPL spectra of ***Λ*-EuL^1** in different solvents.

Half of the ΔJ = 2 manifold (606-618 nm) contained a strong single sign band with the highest g_{lum} values of -0.071 (at 607.5 nm) for ***Δ*-EuL^1** and +0.071 (at 607 nm) for ***Λ*-EuL^1**. This is more than double the maximal g_{lum} produced by ΔJ = 2 in **EuL^0** (+0.025 at 608.5 nm and -0.028 at 609 nm in MeCN). Overall, **EuL^1** is the third best in terms of literature reported g_{lum} for ΔJ = 2 after the previously mentioned Cs[Eu(+)-(hfbc)$_4$] producing g_{lum} of 0.25 (at 614 nm) and another material with 0.11 at (616 nm).[41,83] The latter also has significantly lower values of ε (55000 mol^{-1} dm^3 cm^{-1}) and Φ (11%) which reduces the CPB_i.

To access and compare the CPL performance of **EuL^1**, the CPB_i was calculated for both ΔJ = 1 and ΔJ = 2 transitions (Table 3.1). Similarly to the calculations for **EuL^0**, β_i was calculated for the 585-605 and 605-630 wavelength regions as 5.4% and 80% respectively, even though ΔJ = 2 did not remain single sign throughout the whole manifold. As a result, the maximal CPB_i for ΔJ = 1 and ΔJ = 2 was calculated as 307 (at 596 nm) and 984 (at 607 nm) mol^{-1} dm^3 cm^{-1} respectively. This puts CPB_i of **EuL^1** above the average for both ΔJ = 1 and ΔJ = 2 (287 and 69 mol^{-1} dm^3 cm^{-1} respectively) in previously reported europium(III) complexes.[39]

Table 3.1: CPB_i and CPB_F calculation for the ΔJ = 1 and ΔJ = 2 and BP594/10 and BP610/10 λ regions.

Trans.	Trans. λ range /nm	β_i /%	max $\lvert g_{lum} \rvert$	CPB_i /M^{-1} cm^{-1}
ΔJ = 1	585-605	5.9	0.30	**307**
ΔJ = 2	605-630	80	0.071	**984**
	605-618	48		**590**

Filter λ range /nm	β_F /%	$\bar{x}g_{lum}$	CPB_F /M^{-1} cm^{-1}	
			EuL^1	**% inc. comp. to EuL^0**
589-599	5.3	0.22	**202**	**159%**
605-615	33	0.033	**189**	**656%**

EuL^1 is the third best in terms of the CPB_i for ΔJ = 1 after the recently reported tetrahedral $Eu_4L_4(L')_4$ cages with CPB_i of 3240 and 1122 M^{-1} cm^{-1}.[30] On the other hand, CPB_i for the ΔJ = 2 transition in these materials was not reported. The unprecedented CPB_i of 984 M^{-1} cm^{-1} (at 607 nm) produced by the ΔJ = 2 of **EuL^1** is the highest ever reported to the knowledge of the author with the second best producing more than four times lower value of 213 M^{-1} cm^{-1}.[83] The CPB_i calculation for the ΔJ = 2 transition used a branching factor for the whole transition, even though it's not completely single sign. In order to make a more accurate representation of the ΔJ = 2 CPB_i, it was recalculated using β_i of 48% for the 605-618 nm wavelength region where the CPL sign is conserved. This gave a value of 590 M^{-1} cm^{-1}, which was still the highest reported for the ΔJ = 2 transition.

In order to assess the applicability of **EuL^1** for the use in security tags authenticated by CPLP, CPB_F values for the single-sign regions of ΔJ = 1 and ΔJ = 2 selected by the BPF594/10 and BPF610/10 were determined (Table 3.1). Similarly to the calculations for **EuL^0**, $\bar{x}g_{lum}$ and β_F were determined for the wavelength regions selected by the BPFs. As a result, the calculated values of CPB_F for ΔJ =1 and ΔJ =2 transitions were similar (202 and 189 M^{-1} cm^{-1}), suggesting that both transitions could be simultaneously used for CPLP. The obtained CPB_F values were significantly higher compared to **EuL^0**, with the CPB_F increase of 159% for ΔJ = 1 and 656% for ΔJ = 2. Most importantly, these values would also remain the same in different host materials due to conservation of the relative intensity and spectral shape of CPL in different solvents as well as nearly identical associated g_{lum} plots, which was not the case for **EuL^0**.

III.6. Racemisation study of EuL[1]

Strong CPL signal requires enantiopurity of the measured sample, since racemic mixtures produce CPL signal of opposing helicity, resulting in self-cancellation. Therefore, for a material to maintain its CPL properties over time, it must be stable towards racemisation, the rate of which is temperature dependent. This is particularly important for a security ink, since it must produce a consistent CPL signal over prolonged periods of time. For instance, British passports are valid for 10 years after issue, and, therefore, the embedded security features they contain must be robust and stable. For optimal authentication of the **EuL[1]** containing security ink, it needs to be resistant towards racemisation at rt over prolonged periods of time and during short exposures to high temperature such as 150°C that is commonly used during document lamination.[22,55] Therefore, stability of the enantiomers of **EuL[1]** towards racemisation was investigated in solution state at both rt (25 °C) and elevated 60 °C (for example, high-temperature laundry cycle) to determine the racemisation half-life ($\tau_{1/2}$). Racemisation $\tau_{1/2}$ in solid state material such as PMMA was the expected to be longer due an increased racemisation energy barrier provided by the lower mobility state.

Racemisation of **EuL[1]** was monitored by CPL-spectroscopy using g_{lum} as the main variable. This was used to establish when racemisation resulted in a detectable amount of a newly formed enantiomer, at which point a solution sample was taken for further analysis by chiral HPLC. Integration under the retention peaks areas was used to precisely determine the relative amounts of each enantiomer in the mixture to calculate racemisation $\tau_{1/2}$. For example, when racemisation of the enantiopure sample with 100 % enantiomeric excess of the *Λ* enantiomer is considered, an equilibrium is established:

$$\Delta \underset{k_{-1}}{\overset{k_1}{\rightleftharpoons}} \Lambda \qquad [13]$$

where the rates of interconversion for each enantiomer are assumed to be equal ($k_1 = k_{-1} = k$). Therefore, the rate expression for the racemisation can be written as

$$\frac{-\mathrm{d}[\Lambda]}{\mathrm{d}t} = k[\Lambda] - k[\Delta] = k([\Lambda] - [\Delta]) \qquad [14]$$

$$\frac{1}{[\Lambda] - [\Delta]}\,\mathrm{d}[\Lambda] = -k\mathrm{d}t \qquad [15]$$

Since $[\Delta] = [\Lambda]_0 - [\Lambda]$, integration of the rate equation gives

$$\int_{[\Lambda]_0}^{[\Lambda]} \frac{1}{2[\Lambda] - [\Lambda]_0}\,\mathrm{d}[\Lambda] = \int_{t_0}^{t} -k\,\mathrm{d}t \qquad [16]$$

$$\frac{\ln(2[\Lambda] - [\Lambda]_0) - \ln(2[\Lambda]_0 - [\Lambda]_0)}{2} = -kt \qquad [17]$$

$$\ln\left(\frac{[\Lambda]_0}{2[\Lambda]-[\Lambda]_0}\right) = 2kt \qquad [18]$$

which allows for determination of $2k$ by taking gradient of the plot of $\ln\left(\frac{[\Lambda]_0}{2[\Lambda]-[\Lambda]_0}\right)$ against t.

The half-life for racemisation ($\tau_{1/2}$) is a time during which the enantiomeric excess of 50% is reached, which can be interpreted as a mixture containing 75% of the starting enantiomer and 25% of the other enantiomer which was formed by interconversion. Substitution of 1 and 0.75 into $[\Lambda]_0$ and $[\Lambda]$ respectively gives equation for the relationship between the experimentally obtained $2k$ and $\tau_{1/2}$.

$$2k\tau_{1/2} = \ln\left(\frac{1}{2\times 0.75-1}\right) = \ln 2 \qquad [19]$$

$$\tau_{1/2} = \frac{\ln 2}{2k} \qquad [20]$$

As mentioned earlier, racemisation was initially monitored by CPL spectroscopy using the $\bar{x}g_{lum}$ values for the single-sign regions of both ΔJ =1 (585 - 605 nm) and ΔJ =2 (605.5 – 618 nm) transitions (Figure 3.8). The rt racemisation experiment was performed for both ***Δ*-EuL^1** and ***Λ*-EuL^1** in MeCN at ~4μM concentration. After stirring both solutions for a total of 336 hours, no significant change in the magnitude of $\bar{x}g_{lum}$ of either ΔJ = 1 or ΔJ = 2 (Figure 3.8). The enantiopurity was also confirmed by chiral HPLC (*CHIRALPAK* IE) where only one enantiomer retained before and after the experiment.

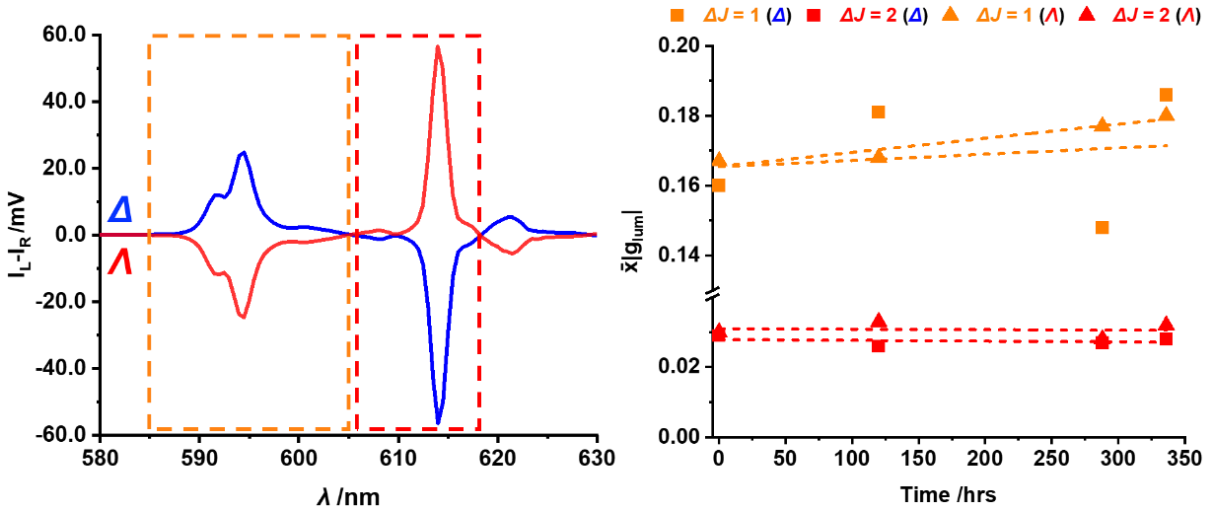

Figure 3.8: CPL spectrum of **EuL^1** in MeCN with the selected single CPL sign regions for the $\bar{x}g_{lum}$ calculations (left); $\bar{x}g_{lum}$ values for the single-sign regions of the ΔJ =1 (585 - 605 nm, orange) and ΔJ =2 (605.5 – 618 nm, red) transitions of ***Δ*-EuL^1** (squares) and ***Λ*-EuL^1** (triangles) after stirring in MeCN at rt.

The experiment was then repeated at 60°C where the samples were collected every 25 hours for the total of 200 hours for the chiral HPLC analysis. The ratio of the integrated peak intensities was used in calculations (Equation 18) as they were equivalent to their concentration ratio due to the same ε. The resulting plot (Figure 3.10 left plot – purple line) produced the gradient of 0.0018(2) which was used to calculate (Equation 11) the $\tau_{1/2}$ as 195 ± 22 hours. This is almost double than 99 ± 1 hours previously reported for **EuL^{a}** carboxylate complex without extended chromophores and similar to the previously reported 180 ± 10 hours for the isostructural methylphosphinate donor containing **EuL^{b}** (Figure 3.9).[56,59]

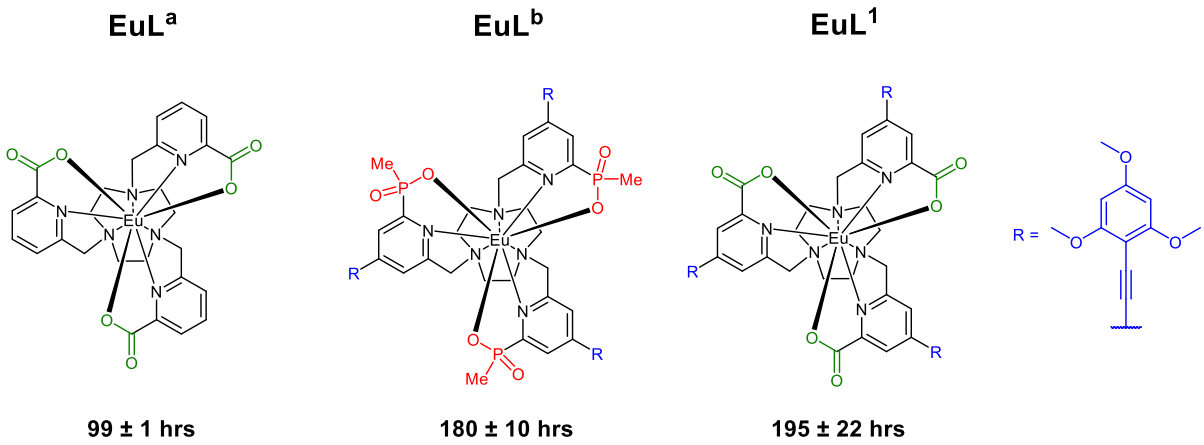

Figure 3.9: The structures of arylalkynyl-free carboxylate **EuL^{a}** (left), methylphosphinate **EuL^{b}** (middle) and **EuL^{1}** complexes and their reported racemisation half-life.

In contrast to that, no racemisation of **EuL^{0}** was observed in the previous work after heating at 60°C in MeOH for 3 weeks. Such dependence of racemisation $\tau_{1/2}$ on structure agrees with the racemisation mechanism that requires simultaneous inversion of the chiral phosphorus centre as well as inversion of the TACN ring and rotation of the sensitising chromophores. As a result, bulky donor groups and extended chromophores result in an increased racemisation energy barrier, increasing the $\tau_{1/2}$. When comparing **EuL^{1}** to **EuL^{b}**, which are only different in terms of the donor groups, a similar $\tau_{1/2}$ could be a result of a combination of two factors: steric bulk of the donor (phenylphosphinate is bulkier than carboxylate) and the strength of coordination to europium(III) (bidentate carboxylate binds stronger).

The study also compared **EuL^{1}** racemisation $\tau_{1/2}$ in a range of solvents of increasing polarity: isopropanol (2-PrOH), MeOH, MeCN, NMP and dimethyl sulfoxide (DMSO). The experiment was also repeated in deuterated MeOD to investigate the effect of hydrogen bonding. Excessive solubility of **EuL^{1}** in NMP and DMSO resulted in nearly immediate elution of both enantiomers with no chiral resolution. From the chiral HPLC analysis of **EuL^{1}** solutions in 2-PrOH, MeOH and MeCN, an inverse dependence of racemisation on increasing solvent polarity was observed (Figure 3.10 - left). The calculated racemisation $\tau_{1/2}$ was 14 ± 2 and 48 ± 4 hours in 2-PrOH and MeOH respectively, which is significantly lower than 195 ± 22 hours in MeCN.

To compare the racemisation of **EuL^1** in the above-mentioned solvents to more polar NMP and DMSO where the chiral HPLC experiment failed, CPL spectra were recorded for the heated **EuL^1** solutions after 142, 190 and 259 hours and the $\bar{x}g_{lum}$ of the ΔJ =1 (585-605 nm) compared (Figure 3.10 - right).

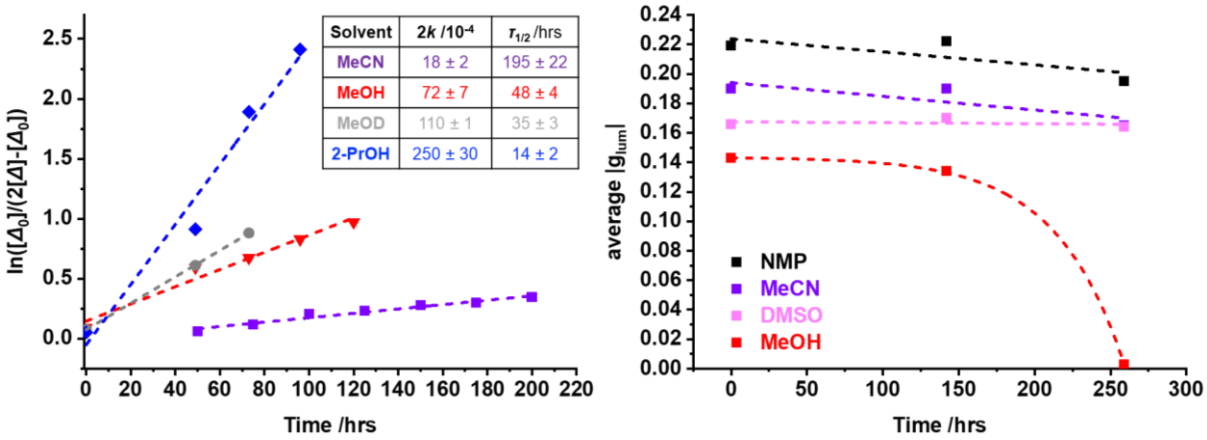

Figure 3.10: ln([Λ_0]/(2[Λ]-[Λ_0]) against heating time at 60 °C in MeCN (purple), MeOH (red), MeOD (grey) and 2-PrOH (blue) with obtained gradients (2k) and calculated racemisation $\tau_{1/2}$. (left); $\bar{x}g_{lum}$ values for ΔJ =1 (585 - 605 nm) of **EuL^1** after stirring at 60 °C in NMP (black), MeCN (purple), DMSO (pink), MeOH (red).

During the 259 hours at 60 °C the enantiopure sample of **EuL^1** fully racemised in less polar MeOH while remained essentially enantiopure (based on g_{lum}) in more polar MeCN, NMP and DMSO. This correlates with the previously observed inverse dependence of racemisation rate on solvent polarity.

When comparing the $\tau_{1/2}$ data recorded in alcohols, the racemisation $\tau_{1/2}$ could be correlated with the hydrogen bonding ability of the solvents, where MeOH is a better hydrogen bond donor than 2-PrOH due to a more electron donating isopropyl group. However, repeating the experiment in MeOD resulted in a slightly shorter racemisation $\tau_{1/2}$ (35 ± 3 hours) compared to that in MeOH (48 ± 4 hours). This isolated the effect of solvent H-bonding on the racemisation $\tau_{1/2}$ since MeOH and MeOD have a similar polarity, while MeOD is a worse H-bond donor due to a shorter O-D bond compared to the O-H. This demonstrated that hydrogen bonding reduced the rate of **EuL^1** racemisation.

Overall, both high polarity and strong H-bonding reduced the rate of racemisation. This observation agreed with the racemisation mechanism that requires rotation of the chromophores. Since the chromophores are polar, they can experience orientation dependent dipole-dipole interactions with polar solvent molecules. Such interaction adds to the racemisation activation energy barrier, since it gets disturbed when the chromophores are rotated. The same principle applies to the H-bonding dependence, where the carboxylate oxygens and pyridyl nitrogens can behave as H-bond acceptors. Since H-bonds prefer linear orientation, rotation of the chromophores would disturb the H-bonds and, again, increase the racemisation energy barrier.

Overall, the established stability of the **EuL^1** towards racemisation at 60 °C in solution with polar solvents suggested that it would not significantly racemise during short-term exposure to 150 °C lamination temperature (1 cm per second) in a polar solid-state PMMA film due to a relatively high racemisation energy barrier. No racemisation at rt in solution state is advantageous for application of **EuL^1** for a CPL tag with a long 'shelf life'.

III.7. Discussion and Future work

A novel bright CPL-active quasi-C_3 symmetric **EuL^1** complex containing all carboxylate donor groups was prepared, chirally separated and photophysically characterised. **EuL^1** was exceptionally bright (B = 34650 M^{-1} cm^{-1}) due to high values of Φ (45 %) and ε (77000 M^{-1} cm^{-1}) while its near 365 nm maximal absorbance suggested optimal excitation by commercially available 365 nm UV LEDs. Invisible to the unaided naked eye, their large pseudo-Stokes shift allowed for absorption in the UV and emission in the visible light regions. Emission lifetime on the millisecond time scale allows for temporal separation by time gating out nanosecond time-scale emission of the applied organic dyes. Both ΔJ = 1 and ΔJ = 2 transitions demonstrated strong monosign CPL with CPB_i values of 307 mol^{-1} cm^{-1} at 596 nm and 984 mol^{-1} cm^{-1} at 607 nm respectively, rendering it to be the best known candidate for a CPL security ink so far. The CPB_F was also calculated for the single-sign spectral regions selected by the BPF594/10 (594 ± 5 nm) and BPF610/10 (610 ± 5 nm) to confirm the suitability of both transitions for authentication by CPLP. No racemisation of an enantiopure sample of **EuL^1** was observed in MeCN at rt, while the racemisation $\tau_{1/2}$ of 195 ± 22 hours was recorded at 60°C. This suggested an optimal stability of **EuL^1** towards racemisation that is likely to be sufficient for the application in CSTs that maintain their CPL security features over prolonged periods of time with occasional exposures to higher temperatures.

The only structural modification that was made to **EuL^0** to produce **EuL^1** was the phenylphosphinate donor replacement with the carboxylate donor. Such modification significantly improved the photophysical properties (Table 3.2), creating a promising security ink candidate. Not only **EuL^1** is brighter than **EuL^0**, but also it is more CPL active with significantly higher values of g_{lum} for both ΔJ = 1 and ΔJ = 2 transitions. This could be attributed to a poorer overlap between the europium(III) *f* orbitals and the orbitals of carboxylate donor due to its trigonal planar geometry, as opposed to pseudo-tetrahedral geometry of the phenylphosphinate donor. This reduced the strength of the CF experienced by europium(III), resulting in a lower extent of the MD moment quenching that contributes to the rotatory strength.

Table 3.2: Comparison of the key photophysical properties and racemisation of **EuL^0** and **EuL^1** in MeCN.

Parameter		EuL^0	EuL^1	% increase
λ_{max} /nm		356 nm	358 nm	-
ε / M^{-1} cm^{-1}		60000	77000	28%
Φ		0.36	0.45	25%
B / M^{-1} cm^{-1}		22000	34650	58%
τ		1.3 ± 0.1 ms	1.0 ± 0.1 ms	-30%
σ^2 /GM		132 (at 720 nm)	308 (at 700 nm)	133%
max $\lvert g_{lum} \rvert$	ΔJ = 1	0.21	0.30	43%
	ΔJ = 2	0.028	0.071	154%
CPB_i / M^{-1} cm^{-1}	ΔJ = 1	166	307	85%
	ΔJ = 2	218	984	351%
CPB_F / M^{-1} cm^{-1}	BP594/10	78	202	159%
	BP610/10	25	189	656%
Racemisation $\tau_{1/2}$	r. t.	unknown	unknown	-
	60°C	unknown	195 ± 22 hrs	-

The main drawback of such modification was a decrease in racemisation energy barrier that was provided by a bulky phenyl group. Although there is no direct evidence that racemisation stability of **EuL^1** was insufficient for its potential application, a further structural modification could be implemented to increase the racemisation energy barrier. The idea of attaching a bulky phenyl group near the TACN ring to limit its inversion was adopted from **EuL^0**. Since the carboxylate donor carbon cannot be functionalised, the pyridine nitrogen α-carbon on the chromophore can be functionalised instead with the phenyl group (Figure 3.11). As a result, the phenyl group would create the steric bulk necessary to prevent the simultaneous TACN ring inversion and chromophore arm rotation, while potentially not affecting the CF experienced by europium(III) centre.

To achieve such functionalisation, one of the esters of **12** can be reduced to an aldehyde rather than alcohol (Figure 3.11). This would allow to attach a phenyl group to the carbonyl carbon using, for instance, phenyl magnesium bromide Grignard reagent. Such nucleophilic attack is not stereoselective since the sp^2 – hybridised aldehyde carbon can be approached equally from both sides to result in a chiral centre. As a result, the chromophore would be obtained as a racemic mixture of *S* and *R* enantiomers. The enantiomers must be separated before they undergo alkylation, since complexation to europium(III) would only be achieved if the TACN containing macrocyclic ligand has the same stereochemistry on all three chromophores. Since alkylation of mesylated chromophores would likely proceed *via* the S_N2 mechanism with inversion of stereochemistry, the *S* chromophore would give the *RRR* ligand

and *vice versa*. The final complexation step would also be stereospecific (*RRR* to give *Δ*, *SSS* - *Λ*) due to the steric bulk of the phenyl groups that are set to point away from the carboxylate donor groups.

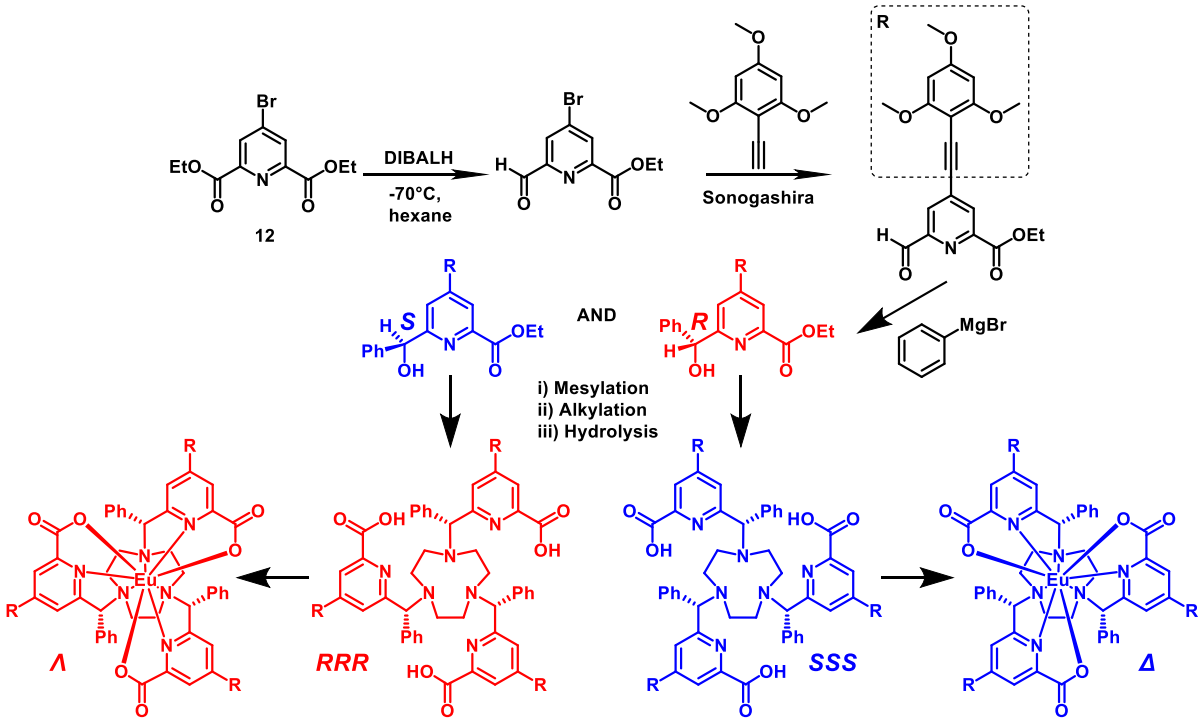

Figure 3.11: Synthetic sequence proposal towards a phenyl-functionalised **EuL**[1].

The same strategy of chirality transfer from a chiral ligand to the resulting complex was recently demonstrated in the previously mentioned example (Section I.12) using enantiopure (*S*, *S*) and (*R*, *R*) pda ligands that resulted in complexation with *Δ* and *Λ* chirality respectively (Figure 3.12).[48] The resulting europium(III) complexes demonstrated a relatively high g_{lum} of ±0.3 for the *ΔJ* = 2 transition in both solution and sold state (single layer of crystals confirmed by LSCM).

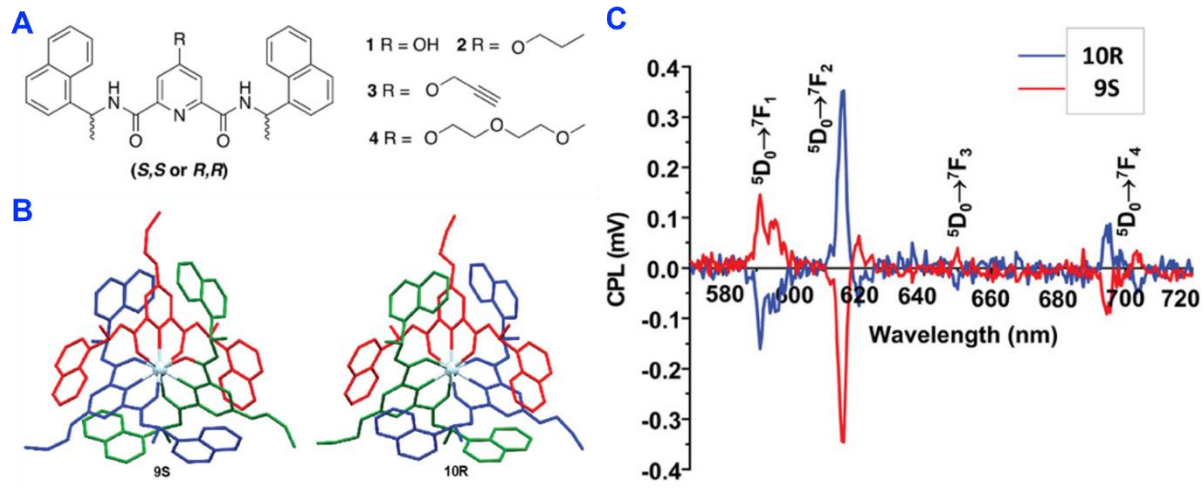

Figure 3.12: Structures of chiral pda ligands (**A**) and the resulting europium (III) complexes (**B**) with their solid-state film CPL spectra shown (λ_{exc} = 325 nm, 50 averages) (**C**) (adapted from Caffrey *et al.*).[48]

CHAPTER IV. The design and development of a thin film-based chameleon security tag

IV.1. Introduction to the chameleon security tag host material requirements

The overall target of this project was a development of a CPL security ink that can be incorporated into a tag that combines already existing security features (spatial, chromatic, spectral) with the newly proposed (temporal and CPL) to create a multi-layer security chameleon security tag (CST) that can be authenticated using the newly developed CPLP camera.[47] Such tag must be compatible with the existing items that require anti-counterfeiting, for example, banknotes, identification and other sensitive documents, certificates, military, medical and possibly other consumer goods where anti-counterfeiting features are necessary to prevent profit losses, fraud and even human deaths.[50]

As it was discussed earlier, the modern identification documents and banknotes are made of polymeric materials that provide mechanical durability and water resistance. Therefore, for a material to be considered a practically applicable security ink, it must be compatible with materials of the current trade. In other words, the security ink must maintain its photophysical properties in polymeric host materials. For example, the host must not create NRR pathways for luminescence quenching of the guest material. This could occur, for instance, *via* positive solvatochromism that would over-stabilise the ICT state which could result in a dramatically increased rate of BET. Luminescence quenching by the host material that would significantly reduce the Φ and therefore *CPB*. Another factor to consider is the interaction of the host material with europium(III) coordination environment which can lead to the undesired decrease in MD moment and therefore the magnitude of g_{lum}.

For the optimal real-world security performance, the host polymer must be durable, transparent, low absorbing in UV region, non-luminescent, colourless, soluble in the same solvent with the guest species, insoluble in water and resistant to lamination temperatures (~150 °C). In addition to that, the host must be suitable for preparation of a smooth film with uniform thickness that can be used in CST. The smooth surface is necessary to minimise scattering of the emitted light that would cause randomisation of the CPL signal. The uniform thickness provides consistent distribution of the light-emitting species for elimination of the areas with different emission intensity that can either fall below the detection limit or oversaturate the detector. In addition, variation in thickness leads to a variation in signal to noise ratio which can compromise the authentication precision. Therefore, solid-state polymeric thin films were chosen as an optimal starting point in development of the CST.

IV.2. Development of the reproducible method for thin film fabrication

To reliably study the performance of the prepared security inks in the context of a CST, a reproducible thin-film preparation method was developed. Importantly, a method of controlling film thickness was established as it might be necessary for adaptations of CST to fulfil the potential future requirements for commercialisation.

PMMA was chosen as host material for the CSTs due to its successful application in security tags in previous work.[20,47] PMMA is a polyacrylic ester (Figure 4.1) that has found a wide application in many fields due to its transparency, light weight and low cost. For example, PMMA is often used as a glass substitute in optical devices, including optical lenses, gratings and waveguides.[86,87] Due to a necessity to produce polymer films doped with emissive materials, solution coating method was exploited. There are multiple solution coating methods such as dip coating (dipping substrate into the solution), slot-die coating (direct coating of a moving substrate through a coating 'head'), blade coating (a blade moves at a small distance from a substrate containing solution).[88] In this work, spin coating method was used due to uniformity of the films, wide range of achievable thicknesses, fast drying time and cost effectiveness (no heating required).[89] In spin coating, a polymer solution is dispensed onto a flat substrate prior or during its rotation at frequencies of thousands of rotations per minute (rpm). Rotation of the substrate forces the solution to evenly distribute across the substrate under the influence of centripetal force, which is proportional to rotational frequency. Variable parameters that affect the thickness and homogeneity of the film include PMMA molecular weight concentration of the polymer solution, boiling point of the solvent, the dispensed solution volume, rotational frequency and rotational time. Therefore, the development of a reproducible spin-coating method required keeping certain parameters fixed while varying the others in a trial-and-error study.

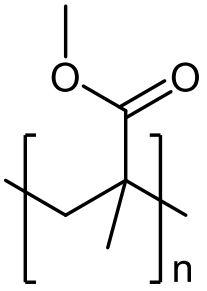

Figure 4.1: PMMA.

In this work, the solution is dispensed on the substrate that is rotating at different frequencies (7000-12000 rpm). DCM with a relatively low boiling point of 39.6 °C that was exploited due to its fast evaporation from the substrate. This avoided the need for post-annealing of the films to evaporate residual solvent with higher boiling points such as chlorobenzene (132 °C).[89] Although very short spinning times could be used due to rapid evaporation of DCM (visually complete few seconds after deposition), the spinning time was kept at constant 40 seconds. The size and material of the substrate was also kept constant. The substrate was regular microscope slides were cut into rectangular pieces (1.5 × 1.0 cm) with a surface area of 1.5 cm^2. A low weight average molecular weight (~15 kDa) PMMA was used to aim for the 50-1000 nm film thickness. The PMMA solution was mixed with **RhB** that gave the films purple colour for a convenient visual control of the film uniformity.

The variation in dispensed solution volume was optimised so that it is sufficient to cover most of the substrate surface. At the same time, the volume should not be excessive to minimise the waste, since the excess solution is sheared from the substrate during spinning. The studied dispensing volumes ranged from 5 to 30 µL, where 10 µL resulted in the highest success rate of producing smooth films (Figure 4.2.A) across the studied range of PMMA solution concentration, while the volumes above that often caused a multi-layered film (Figure 4.2.B). Therefore, 10 µL dispensing volume was kept constant for further optimisation of other parameters

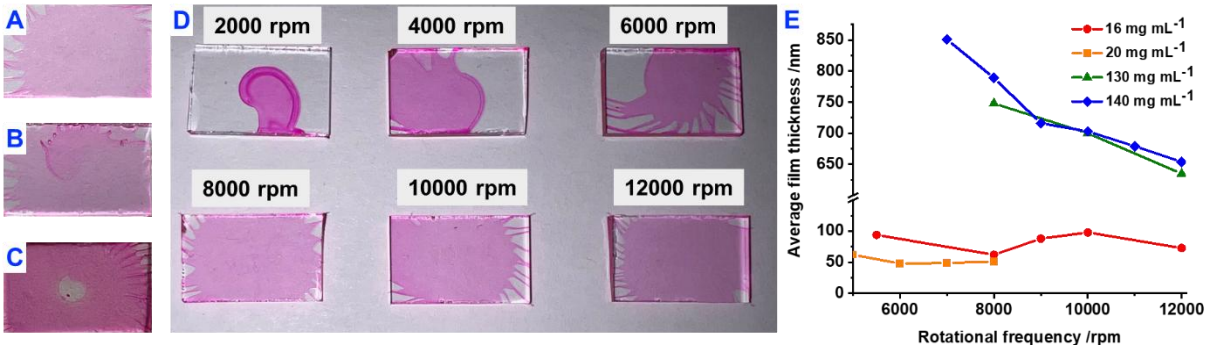

Figure 4.2: Photographs of **RhB** doped spin-coated PMMA films on a glass substrate where the quality of the produced films was studied in terms of dispensing volume: 10 µL (**A**) and 20 µL (**B**); excessive PMMA concentration [~150 mg mL^{-1}] (**C**) and rotational frequency (D) (PMMA concentration in DCM = 140 mg mL^{-1} in **A**, **B** and **D**); as well as the plot of the film thickness against rotational frequency of the spin-coater stage at different PMMA concentrations in DCM.

The two main variables affecting the film thickness were PMMA solution concentration and rotational frequency. While the solution concentration was a dominating factor affecting the film thickness, rotational frequency altered it to a significantly lower extent and therefore could be used for fine thickness adjustments.

At first, very dilute solutions of PMMA in DCM were used for spin coating to explore the film thickness dependence on concentration. Film thickness measurements were performed using atomic force microscopy (AFM) discussed in the following section (Section IV.3). The PMMA concentrations from 16 to 140 mg mL^{-1} were explored, where 16 mg mL^{-1} resulted in the thickness range of ~40 to ~60 nanometres, 20 mg mL^{-1} gave ~60 to ~100 nm, while 140 mg mL^{-1} produced thicker films with a greater range of thickness between ~650 and ~850 nm (Figure 4.2.E). The higher concentrations of PMMA up to 300 mg mL^{-1} were also explored; however, above 140 mg mL^{-1}, the quality of the films considerably decreased, thickness uniformity was lost, and surface coverage was not consistent, for example, an uncoated surface area was often observed in the centre where the solution was dispensed (Figure 4.2.C). This was attributed to insufficient shear due to excessive viscosity of the resulting spin-coating solution.

Rotational frequency variation study was performed for further optimisation of the fabrication procedure, where it was established that optimal surface coverage at 140 mg mL^{-1} PMMA

concentration required a 7000-12000 rpm frequency regime (Figure 4.2.D) Film thickness dependence on the rotational frequency was more significant at high PMMA concentrations, with faster spinning producing thinner films.

IV.3. Film thickness determination using atomic force microscopy

AFM is a technique of nanoscale surface morphology determination based on intermolecular forces including adhesion strength, magnetic forces and mechanical properties. Atomic force microscope (Figure 4.3.A) consists of a sharp tip that is around 10-20 nm in diameter which declares the resolution of surface imaging. The tip is attached to a cantilever that contains a light reflective surface. Both tip and cantilever are made of silicon or silicon nitride. During imaging, a laser beam is aimed at the surface of the cantilever, from which its reflected onto a position-sensitive photo detector containing four sections. The position of the reflected laser beam is then calculated as the difference between the intensities detected by each of the four segments.

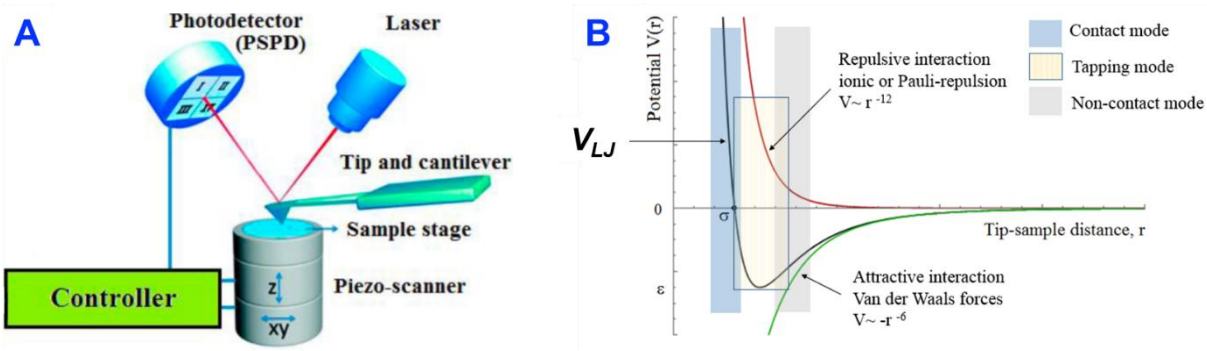

Figure 4.3 A: Standard AFM set-up. **B**: Lennard-Jones potential (V_{LJ}) and its components with highlighted regions relevant for the three main AFM modes (both adapted from Kaman (2020)).[90]

A combination of distance-dependent attractive and repulsive forces acts on the tip as it moves along the sample surface in proximity (in practice the substrate moves). These forces can be summarised using the Lennard-Jones potential (Figure 4.3.B). At long distances (>1 nm) between the tip and the surface, the attractive van der Waal's forces are dominant (r^{-6} distance dependence). When the tip approaches the surface closer, Pauli-repulsion (two electrons can't occupy the same quantum state) interactions rapidly increase and become dominant (r^{-12} distance dependence). Combination of the two forces produces a Lennard Jones potential energy ($V(r)$) curve that is a function of distance between the tip and the surface (Equation 21), where σ is van der Waals radius (minimal distance between the two particles non-interacting particles), k is a constant that measures force of attraction between the species (potential well depth).

$$V(r) = 4k\left[\left(\frac{\sigma}{r}\right)^{12} - \left(\frac{\sigma}{r}\right)^{6}\right] \qquad [21]$$

Since most surfaces are not perfectly flat on the atomic scale, the distance between the tip and the surface (z) is a function of the tip position (xy). As a result, surface features cause variation in z that disturbs the equilibrium of the attractive and repulsive forces, causing oscillations of the cantilever. These oscillations are then detected using the reflected laser beam and converted into z-contrast images of the surface. A typical maximal surface area covered in a single scan is 100 × 100 μm.

There are three most common AFM modes: contact, tapping and non-contact, which operate at different distances between the tip and the surface. The choice of the AFM mode depends on the surface roughness. In this work, contact mode operating in repulsive force regime was used due to a relatively smooth surface of the film. Contact mode creates a direct contact of the tip with the surface and therefore provides a better resolution.

To determine the thickness of the film, three equally distributed cuts were made across the film surface (Figure 4.4.A) using a scalpel in a single swing to minimise tearing of the film resulting in jagged edges near the cut.

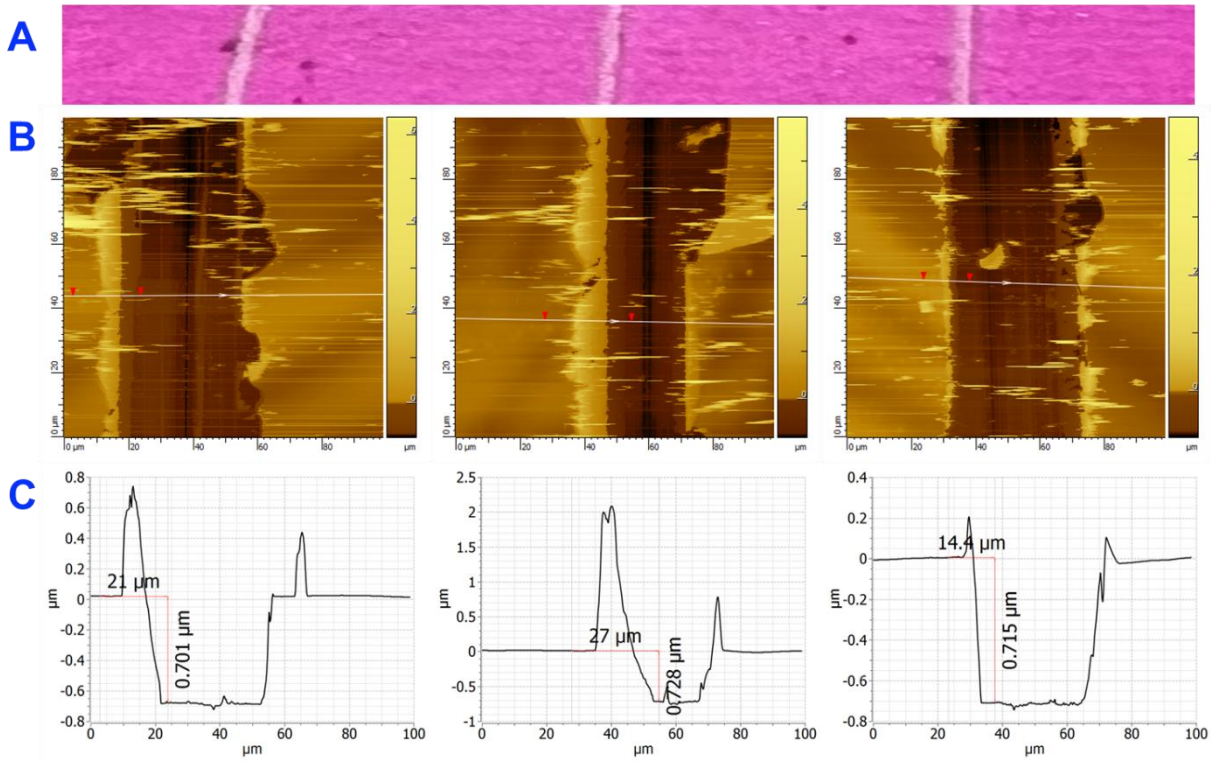

Figure 4.4. A: Cropped photo of three cuts made on spin-coated PMMA film. **B**: AFM images of the film surface centred at the cuts with coloured-coded depth profile (darker = further away). **C**: Depth profiles with calculated differences between the height of a glass substrate and film surface to determine film thickness.

Since PMMA is softer than glass, no damage to the glass was made when applying a relatively weak force to cut the film, allowing for an accurate determination of the thickness profile. Each of the three cuts was then imaged using AFM (Figure 4.4.B), centring the scan area on the cut in order to cover both the film and PMMA-free area of the glass. This was repeated for each prepared film, with the thicknesses expressed as an average of the three cuts. Average

de*via*tion of thickness across the length of the measured films was ~5%, for example, ~40 nm for the ~700-800 nm films. There was no observed corelation between the relative position of the cut (centre or edge) with respect to the substrate thickness. In other words, a possible trend for the films, for example, to be consistently thicker on the edges than in the centre of the substrate where the solution is dispensed, was not observed.

The next stage of the method development was aimed on determining the correlation between the concentration of PMMA and film thickness. If there is a trend that can be expressed using an equation, then any target film thickness can be achieved directly by simply using a calculated concentration of PMMA, while keeping all other parameters kept constant. Therefore, the thickness of the films prepared by spin coating at a fixed 8000 rpm frequency was plotted against PMMA concentration of these solutions. As a result, a linear dependence (Figure 4.5.A) was established, which was believed to hold for the PMMA concentrations between 16 and 300 mg mL^{-1}.

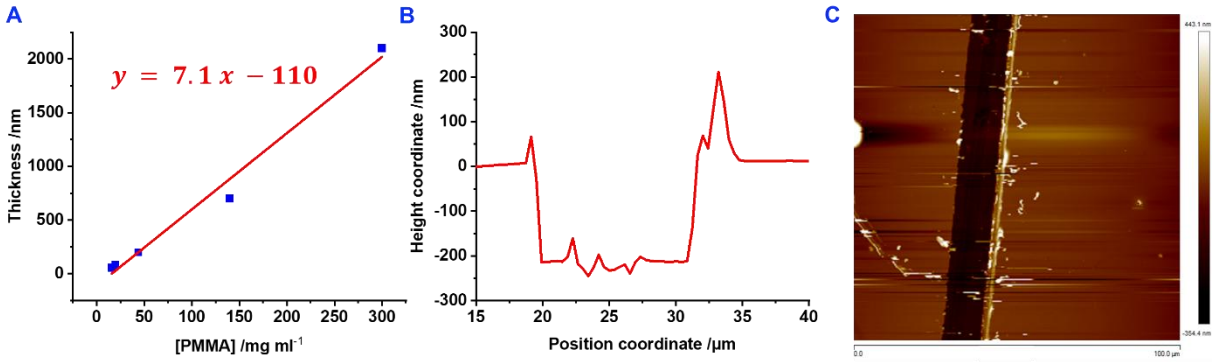

Figure 4.5. A: At 8000 rpm spin-coated film thickness against PMMA concentration plot with linear fit and the corresponding equation with the errors reported; The depth profile (**B**) and the corresponding AFM image (**C**) of an incision on a spin-coated PMMA film using the calculated 44 mg ml^{-1} [PMMA] for a target 200 nm thickness.

The obtained equation was used to prepare a test 200 nm thick film using a calculated concentration of 44 mg mL^{-1}. As a result, the obtained film thickness was measured as 210 nm which de*via*ted by only 5% from the target thickness (Figure 4.5.B and C). This was within the average thickness de*via*tion observed previously for the films that were consecutively spin-coated using the same stock solution and all other parameters fixed.

As a result, a reproducible method of spin-coating PMMA films with uniform thickness in the range of ~50-1000 nm was developed. In the next step of the CST development, the PMMA films contained the enantiomers of **EuL^0** and **EuL^1** instead of **RhB**. This allowed to test the CPL security performance of the prepared materials in a close-to real life scenario, where the security ink is placed in a polymeric host material.

IV.4. Preparation of the EuL^0 and EuL^1 containing PMMA thin films

From the optimisation study it was established that at the same **RhB** concentration, the thicker films provided a brighter emission compared to thinner films. On the other hand, thinner films appeared more uniform, contained less artifacts and gave a lower rate of defective films during spin coating. In addition, thinner films, when spin-coated on a flexible substrate, were less likely to crack during substrate deformation. Importantly, thinner films decreased the probability of internal reflection of the emitted light that would lead to CPL randomisation and diminishing of chiral contrast. As a result, 200 nm film thickness was chosen as a starting point for the CST.

To calculate the concentration of **EuL^1** in PMMA film required to produce a sufficient emission intensity for detection by the CPLP camera emission under PE with two 500w 365 nm LEDs, a solution of **EuL^1** in MeCN with 0.1 absorbance was taken as a reference. Since the path length in 200 nm film is 2×10^5 shorter compared to that of a 1 cm cuvette, the required **EuL^1** concentration was calculated (Equation 22).

$$c = \frac{A}{\varepsilon l} = \frac{0.1}{77000\ \mathrm{cm^{-1}\ M} \times 2 \times 10^{-5}\mathrm{cm}} = 65\ \mathrm{mM} \quad [22]$$

Since the required concentration of PMMA in DCM is 44 mg mL^{-1}, 0.5 ml of such spin coating solution would require 22 mg of PMMA which would take up around 1.9×10^{-5} dm^{-3} (PMMA density 1.18 g cm^{-3}). The mass of **EuL^1** required for such solution could be then calculated (Equation 23).

$$mass = n \times M_r = cVM_r = 65 \times 10^{-3}\mathrm{M} \times 1.9 \times 10^{-5}\mathrm{dm^{-3}} \times 1254.11\ \mathrm{g\ mol^{-1}} = 1.5\ \mathrm{mg} \quad [23]$$

Since 10 µl of the 0.5 ml solution (2% of total volume) was dispensed during spin coated at a time, each individual film would then require 0.03 mg of **EuL^1**. Such consumption of the material is excessive since the implemented multistep synthesis currently yields the product on the milligrams scale. This makes such security tag overly expensive for a wide commercial application.

It was hypothesised that the emission of the **EuL^1** in solid state PMMA film could be brighter than in solution due to a reduced rate of photophysical quenching processes promoted by molecular motion, for example, collisional quenching and vibrational quenching. Therefore, it was proposed that a visible emission could be achieved by a film at a lower concentration than that of a solution. The first test solution was prepared at 100 times lower concentration of **EuL^1** than calculated for a 0.1 abs solution in a '200 nm wide cuvette'. Since this would require a mass of less than a milligram for such solution, the desired amount of **EuL^1** was obtained by preparing its stock solution with a calculated target absorbance and volume. The required

amount of **EuL^1** was calculated from its concentration of 0.65 mM in 1.9×10^{-5} dm^{-3} (22 mg) of PMMA (Equation 24).

$$n = cV = 0.65 \times 10^{-3}\ \text{mol dm}^{-3} \times 1.9 \times 10^{-5}\ \text{dm}^{-3} = 12\ \text{nmol} \quad [24]$$

This can be then used to calculate the concentration and then target absorbance for a **EuL^1** solution of a given volume. For example, a 5 ml solution containing 12 nanomoles of **EuL^1** would have the concentration of 2.4 μM which can be used to calculate the desired absorbance (Equation 25).

$$A = \varepsilon cl = 77000\ \text{cm}^{-1}\ \text{M} \times 2.4 \times 10^{-6} \times 1\ \text{cm} = 0.18 \quad [25]$$

Once such 5 ml solution with 0.18 absorbance is prepared, the solvent can be evaporated and the residual **EuL^1** redissolved in 0.5 ml solution of 22 mg PMMA in DCM. Once the film was prepared, it was found to produce visible emission under irradiation with a two 500 mW 365 nm LEDs. Based on the emission brightness of the film, it was evident that the concentration of the **EuL^1** could be reduced even further as part of future optimisation studies. The films containing **EuL^0** were prepared in the same way and using the same concentration of **EuL^0**.

IV.5. Circularly polarised photography and enantioselective differential contrast imaging method development for authentication of EuL^0 and EuL^1

The CSTs containing enantiopure **EuL^1** would be authenticated with the recently developed CPL photography (CPLP) camera .[47] Its working principle is based on precise alignment of a QWP with 4 different orientations (0°, 45°, 90° and -45°) LPs covering an array of PDs. QWP converts CPL into LPL with polarisation planes at 45° (R-CPL) and -45° (L-CPL) with respect to the fast axis. This LPL then passes through the LPs before sensitising the underlying PDs. This generates sensitivity of the camera towards the CPL sign where 4 simultaneously taken images contain different information on chirality of the light emitted by the probe. For example, if the QWP is aligned with the 45° polarisers, then 0° and 90° channels will be more sensitive towards L-CPL (L image) and R-CPL (R image) respectively while 45° and -45° will each contain half of the total emitted light intensity. For example, an image containing ***Δ*-** and ***Λ*-EuL^1** as well as their racemic mixture in three separate containers (Figure 4.6.A) will all produce the same intensity in +45° and -45° channels, as these correspond to half of total intensity (1/2TE) (Figure 4.6.C). On the contrary, only racemic sample will produce the same intensity in the polarisation sensitive 0° and 90° channels (Figure 4.6.C), since it will emit equal amounts of L- and R-CPL. The use of BPF594/10 selects the ΔJ=1 emission band, which has a positive CPL sign (L-CPL) for ***Δ*-EuL^1** and negative sign (R-CPL) for ***Λ*-EuL^1** (Figure 4.6.A). Therefore, the relative emission intensity from the two enantiomers will be different in the 0° and 90° channels: ***Δ*-EuL^1** will appear brighter in the 0° L-CPL channel and ***Λ*-EuL^1** – in the

90° R-CPL (Figure 4.6.C). In order to isolate exclusively L- or R-CPL signal, image subtraction is necessary, the procedure of which was previously reported as enantioselective differential chiral contrast (EDCC).[20]

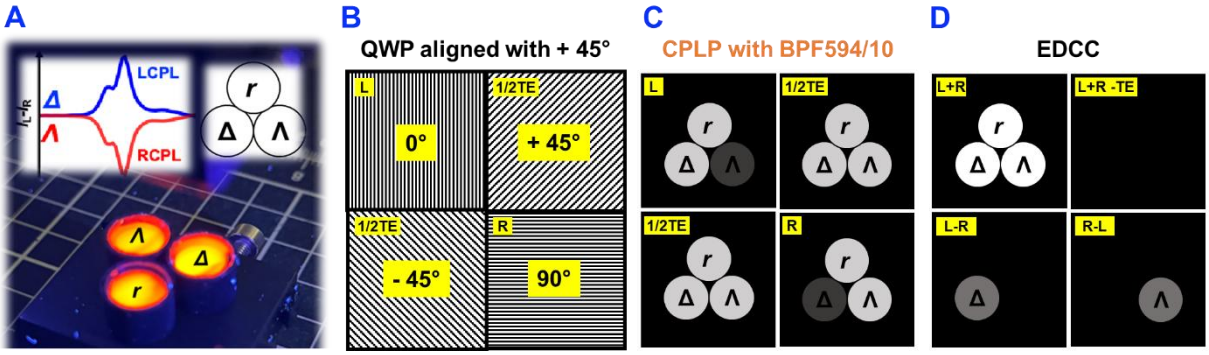

Figure 4.6. A: Photograph of *Δ*, *Λ* and racemic solutions of **EuL¹** in MeCN in three separate wells under the CPLP camera with the 365 nm UV excitation light source on, with an insert of the ΔJ = 1 emission band and position of the wells on the image; **B:** A scheme of one of the 4-pixel cluster with 4 orientations of LPs and channel assignment shown; **C:** A scheme of a recorded (through the BPF594/10) 4-channel CPLP image with relative intensities of the 3 emitting species in each channel shown; **D:** EDCC processed image with relative intensities of the 3 emitting species in each calculated image shown.

For example, subtracting the R image from the L image will generate L-R image where only the signal produced by ***Δ*-EuL¹** will appear, while ***Λ*-EuL¹** will show near zero intensity (Figure 4.6.D) (not zero due to directional light guided reflection). The opposite will occur when the L image is subtracted from the R image. Limited by *Fiji* (version 1.53q) image processing software,[91] image subtraction can't result in negative intensity. For example, the R-L calculation of the L-CPL emitting species will result in zero rather than negative value.

Therefore, for R-CPL-active probes the R-L image will be relevant. The total intensity can be calculated by L+R and used to obtain the CPLP specific dissymmetry factor (g_{CPLP}):

$$g_{CPLP} = 2 \times \frac{(L - R)}{(L + R)} \qquad [26]$$

Importantly, when R-L image was used in calculation, the g_{CPLP} value must be multiplied by -1 to account for the negative CPL sign of R-CPL:

$$g_{CPLP} = -2 \times \frac{(R - L)}{(L + R)} \qquad [27]$$

The choice of the correct formula is based on relative intensity of the L-R and R-L images, where the brighter image is used, which can also be computer-automated if necessary.

In theory, g_{CPLP} must correlate with g_{lum} due to a similar light polarisation information acquisition principle between the CPLP camera and PEM CPL spectrometer. In a CPLP camera, the QWP is fixed and orientations of the LP clusters are used to distinguish the L- and R-CPL, whilst the conventional CPL spectrometer exploits a PEM that serves as a QWP with a variable angular orientation in combination with a fixed LP.

To check whether correlation between g_{CPLP} and g_{lum} is genuine, black, non-reflective, non-emissive plastic containers (sample bottle caps) were filled with ***Δ*-EuL^1**, ***Λ*-EuL^1** and racemic **EuL^1** solutions in MeCN of similar concentration and placed within a single frame for CPLP and EDCC (Figure 4.7). The L+R, L-R and R-L calculated images were then used for g_{CPLP} calculations. In contrast to measuring the intensity of the whole image, a specific ROI was chosen to avoid the error associated with rough edges of the containers which is a source of undesired reflections of the emitted light.

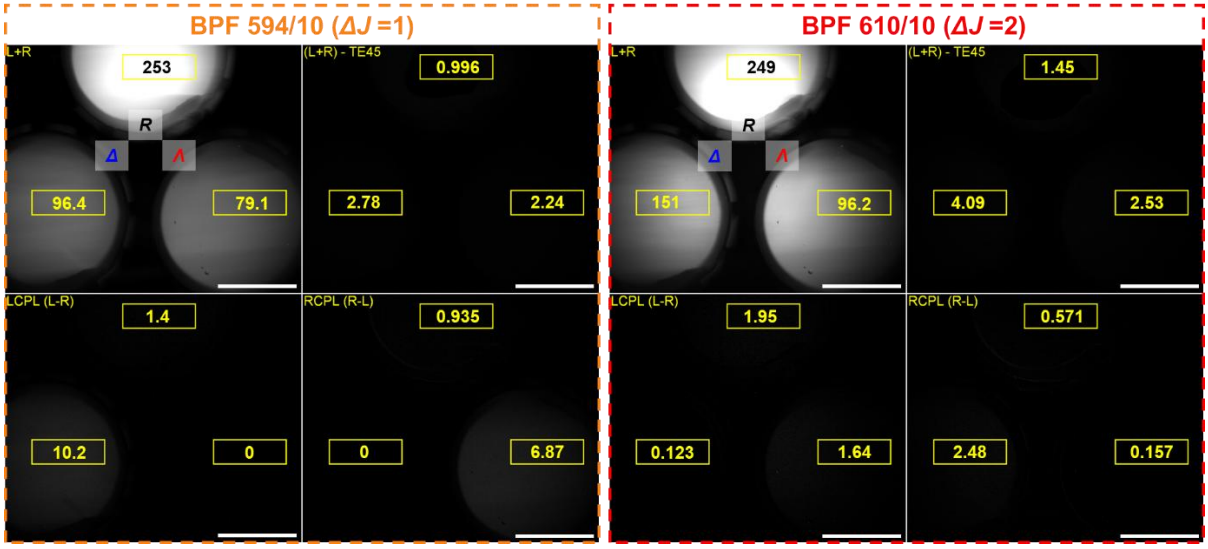

Figure 4.7: 2 sets (using BPF594/10 and BPF610/10) of 4 CPLP images: (L+R, (L+R)-TE45*, L-R, R-L) of the *Δ* (bottom left), *Λ* (bottom right) and racemic (*R*) (centre top) samples of **EuL^1** under 365 nm excitation with the regions of interest for g_{CPLP} and their average intensities shown in yellow. Scale bar = 5 mm. *TE45 image is a sum of the two images generated from 45° and -45° channels that have no CPL sign preference (QWP aligned with 45° polarisers) and record half of the total intensity each; subtraction of TE45 from (L+R) should theoretically produce an image with zero intensity, which is practically non-zero due to experimental error.

As expected, each enantiomer produced intensity in either L-R or R-L depending on the BPF used. This correlated with the CPL sign of each enantiomer within the selected wavelength regions of the ΔJ = 1 and ΔJ = 2 manifolds. For example, the CPL spectrum of ***Δ*-EuL^1** has a positive sign in 589-599 nm region (BPF594/10, ΔJ = 1) and a negative sign in 605-615 nm region (BPF610/10, ΔJ = 2), which correlated with non-zero intensities observed on L-R and R-L images when using BPF594/10 and BPF=610/10 respectively. The relevant areas of the calculated images were then used to calculate g_{CPLP} values of 0.21 and -0.17 for ***Δ*-EuL^1** and ***Λ*-EuL^1** respectively when using the BPF594/10 and ±0.031 for the BPF610/10. This correlated with the g_{lum} values obtained from the PEM-CPL spectrometer data within the experimental error, where the difference between the two dissymmetry factors was around ±0.02 (~ 11 %) for the ΔJ = 1 and around ±0.003 (~ 9 %) for ΔJ = 2. The racemate did not produce a significant intensity in either L-R or R-L images as expected. The nearly equivalent errors obtained for both g_{CPLP} values could be due to similar CPB_F values obtained for the ΔJ = 1 and ΔJ = 2 transitions (202 and 189 mol^{-1} dm^3 cm^{-1}) using BPF594/10 and BPF610/10.

The experimental error associated with CPLP could arise from the PE of the stage not being perfectly homogenous leading to unequal spatial excitation of the sample. As a result, certain pixels of the camera module might get oversaturated, serving as a source of error in image calculation. Moreover, the pixels within the module are not identical and might have slightly different sensitivity. The same applies to the imperfect alignment of the LPs at each pixel. If distribution of such pixels is not random, the error is generated when a specific area of an image is selected for the average intensity measurement. Another source of error could be associated with inelastic scattering of the excitation light by the sample, making it fall into the detection wavelength range. Such light would likely be linearly polarised, and therefore L and R channels would be subjected to linear dichroism.

IV.6. Circularly polarised luminescence photography of chameleon security tags

Due to the superiority of **EuL^1** over **EuL^0** in terms of g_{lum} and CPB_F for both ΔJ = 1 and ΔJ = 2, this study focused on the CSTs containing **EuL^1**. To test the CPL security performance of **EuL^1**, polymethyl methacrylate thin films (200 nm) containing ***Δ*-EuL^1** and ***Λ*-EuL^1** (labelled as ***Δ*** and ***Λ***) were spin coated on glass and subjected to CPLP followed by EDCC (Figure 4.8).

The g_{CPLP} values were then calculated from the L-R and R-L images as +0.10 and -0.024 respectively. When compared to the average g_{lum} values recorded using a PEM-CPL spectrometer for the equivalent wavelength regions (+0.21 for 589-599 nm and -0.033 for 605-615 nm and), it was evident that the magnitude of dissymmetry factor produced by the ***Δ*-EuL^1** containing film in ΔJ = 1 and ΔJ = 2 decreased by ~50 % and ~30 % respectively. Similar results were obtained for the film containing ***Λ*-EuL^1**, where the g_{CPLP} value of -0.11 decreased by ~ 50 % compared to g_{lum} of -0.22 for ΔJ = 1; however, remained essentially the same for the ΔJ = 2 where g_{CPLP} = +0.035 and g_{lum} = +0.033.

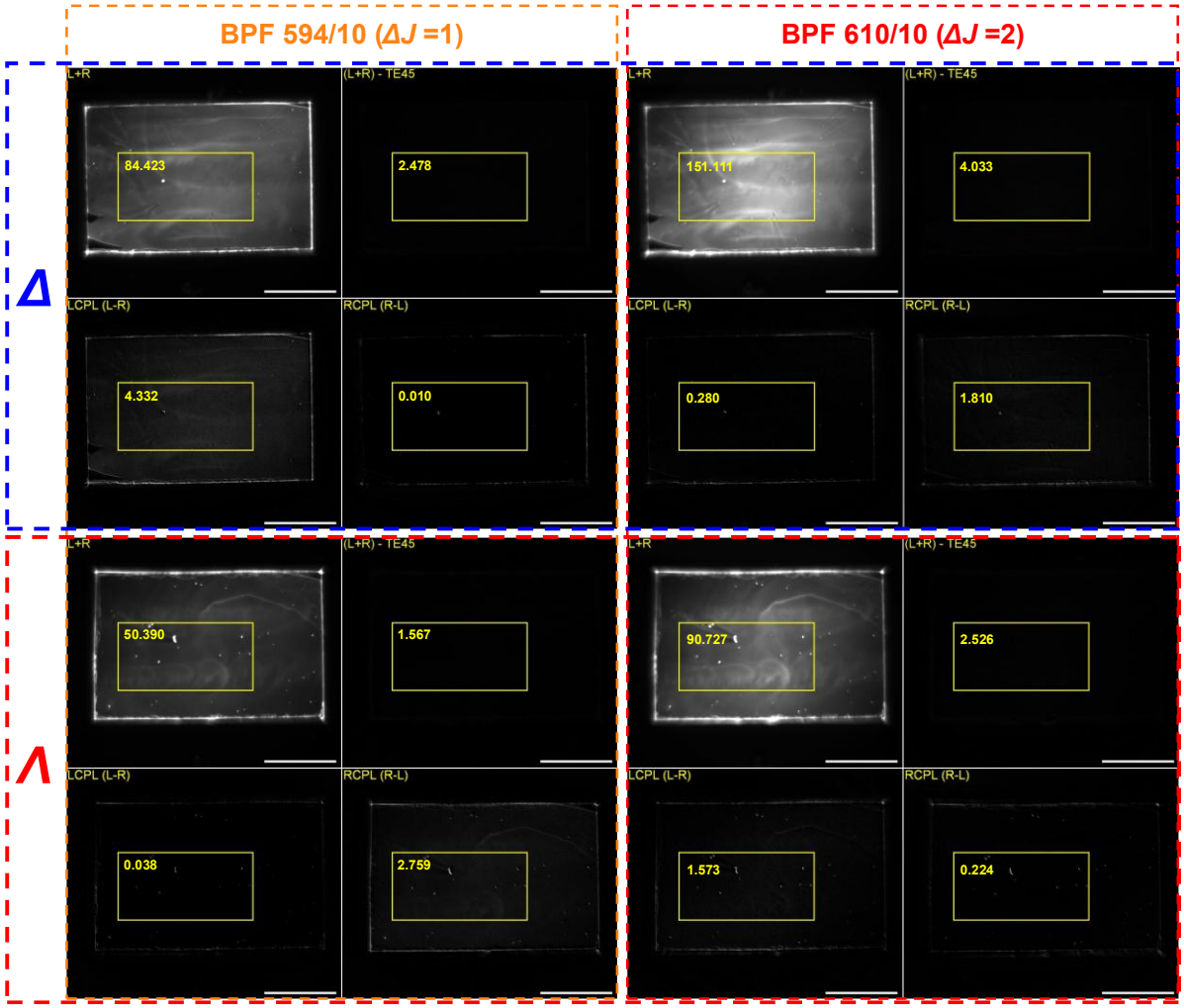

Figure 4.8: EDCC images (L+R, (L+R)-TE45*, L-R and R-L) of the spin coated PMMA films under 365 nm excitation containing ***Δ*-EuL^1** (top two rows) and ***Λ*-EuL^1** (bottom two rows) using BPF594/10 (two left columns) and BPF610/10 (two right columns) with the regions of interest for g_{CPLP} calculations and their average intensities shown in yellow. Scale bar = 5 mm. R-L and L-R images are 6 times contrast enhanced for display.

To confirm that the reduction in g_{CPLP} is not a product of a random error, the calculation was repeated for multiple sequentially spin-coated films using the same method as for the original film (Figure 4.9).

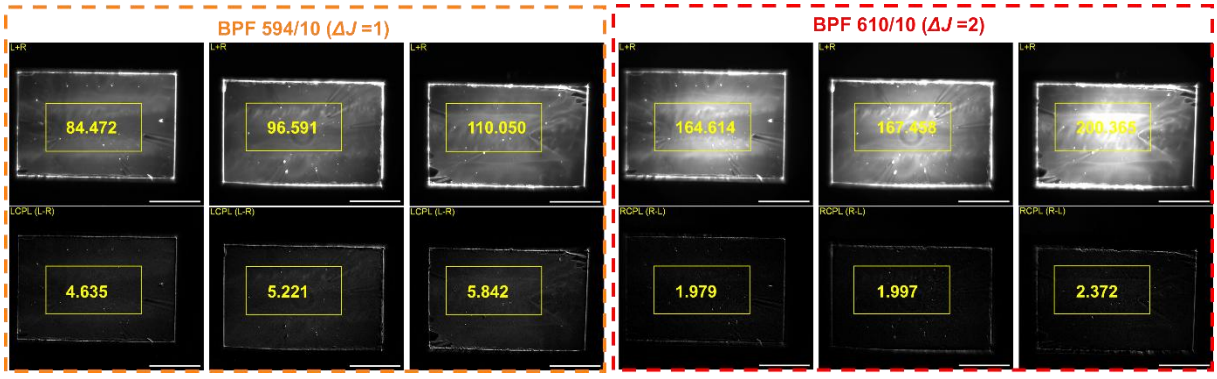

Figure 4.9: EDCC images of three sequentially spin coated PMMA films containing ***Δ*-EuL^1** using BPF594/10 (left side) and BPF610/10 (right side) where L+R (top row) and L-R (bottom row) with the regions of interest for g_{CPLP} calculations and their average intensities shown in yellow. Scale bar = 5 mm. R-L and L-R images are 6 times contrast enhanced for display.

This could also determine whether structural imperfections of the spin-coated films significantly could impact the g_{CPLP}. As a result, all 4 films consistently produced nearly identical g_{CPLP} values when using the same BPF, resulting in 50% and 30% g_{CPLP} reduction for the ΔJ = 1 (BPF594/10) and ΔJ = 2 (BPF610/10) respectively compared that of the **Δ-EuL[1]** solution (Table 4.1). It was hypothesised that such reduction in g_{CPLP} resulted from reflection of CPL from the underlying glass substrate that led to the sign inversion. The stronger effect observed in the 589-599 nm region could be attributed to the shorter wavelength light being more susceptible to scattering compared to that of the longer wavelength (605-610 nm), which is known as Rayleigh scattering.

Table 4.1: Summary of the g_{CPLP} for spin-coated on glass PMMA films with **Δ-EuL[1]** and for solution of **Δ-EuL[1]**.

Filter	Glass Substrate				Solution state	% g_{CPLP} reduction
	1	2	3	4		
BPF594/10	+0.10	+0.10	+0.11	+0.11	+0.21	50%
BPF610/10	-0.024	-0.024	-0.024	-0.024	-0.031	30%

To test this proposal, prior to spin-coating, the glass substrate was covered with black matt tape, which is non-reflective in the λ ROI, non-emissive under 365 nm irradiation and not soluble in DCM. The same solution of **Δ-EuL[1]** was then used to prepare 6 spin-coated PMMA films for CPLP (Figure 4.10).

Figure 4.10: EDCC images of six sequentially spin coated PMMA films containing **Δ-EuL[1]** using BPF594/10 (top two rows) and BPF610/10 (bottom two rows) where L+R (1st and 3rd rows) and L-R (2nd and 4th rows) with regions of interest for g_{CPLP} calculations and their average intensities shown in yellow. Scale bar = 5 mm. R-L and L-R images are 6 times contrast enhanced for display.

Similarly to the films spin-coated on glass, the obtained g_{CPLP} values (Table 4.2) were consistent across the 6 films using both BPFs which suggested high reproducibility of the

method. The change of substrate increased the g_{CPLP} for the ΔJ = 1 (BPF594/10); however, they are slightly lower (20%) compared to the solution. Similarly to that, the g_{CPLP} for the ΔJ = 2 increased (BPF610/10) to become essentially equal to its g_{lum} equivalent.

Table 4.2: g_{CPLP} for 6 sequentially spin-coated on tape PMMA films containing ***Δ*-EuL^1** and for solution of ***Δ*-EuL^1**.

Filter	Black Tape Substrate						Solution state	% g_{CPLP} reduction
	1	2	3	4	5	6		
BPF594/10	0.17	0.17	0.16	0.17	0.17	0.16	0.21	20%
BPF610/10	-0.038	-0.039	-0.037	-0.041	-0.037	-0.038	-0.031	none

Since each enantiomer of **EuL^1** produced ΔJ = 1 and ΔJ = 2 of mutually opposite CPL signs, a single enantiomer appeared exclusively in (L-R) or (R-L) images depending on the filter used. This makes ***Δ*-EuL^1** and ***Λ*-EuL^1** unique security inks that simultaneously incorporate two CPL security layers. In contrast to this, most other reported CPL-active europium(III) complexes, could only produce sufficient CPB_F in the λ region of the ΔJ = 1 band.

As a proof of concept, two films spin coated on the non-reflective matt black tape containing either ***Δ*-EuL^1** or ***Λ*-EuL^1** were imaged together. For example, an authentic CST tag could be designed to contain ***Δ*-EuL^1** on the left-hand side section and ***Λ*-EuL^1** on the right-hand side sectionσ (or can be found in different parts of a pattern). As a result, when observing the ΔJ =1 emission through the BPF594/10, only the left-hand side section appeared on the L-R image and only the right-hand side section on the R-L image (Figure 4.11).

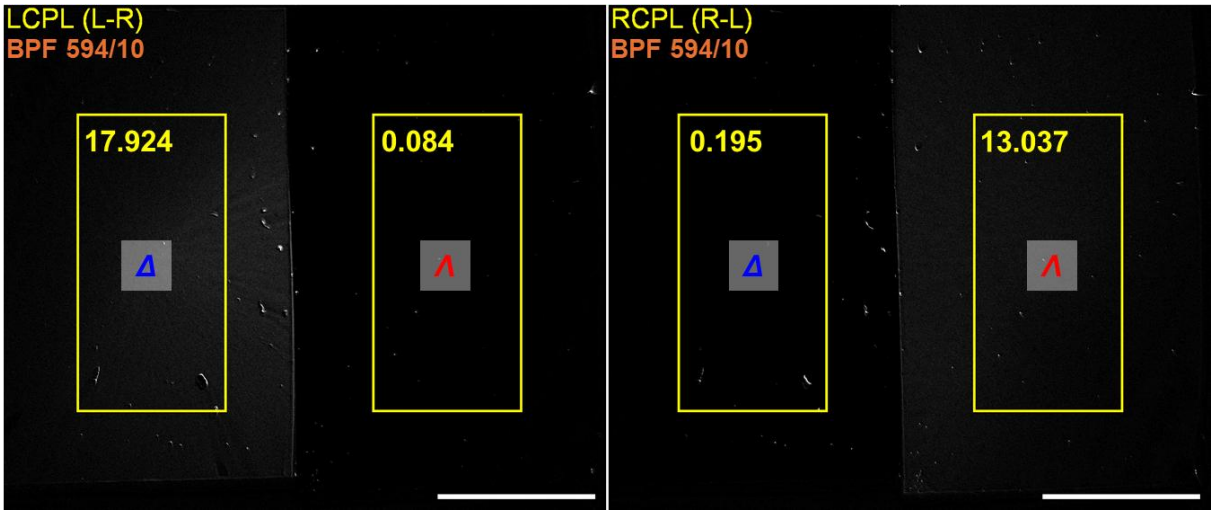

Figure 4.11: L-R (left) and R-L (right) EDCC images used for authentication of the proof-of-concept CST containing ***Δ*-EuL^1** (left section) and ***Λ*-EuL^1** (right section) under 365 nm excitation with average intensities of the regions of interest shown in yellow. Scale bar = 5 mm, BPF594/10.

Simultaneously, switching to the BP610/10 filter to select the ΔJ =2 emission resulted in the opposite distribution of sections: the left-hand side section appeared only on the R-L image and the right-hand side section on the L-R image (Figure 4.12).

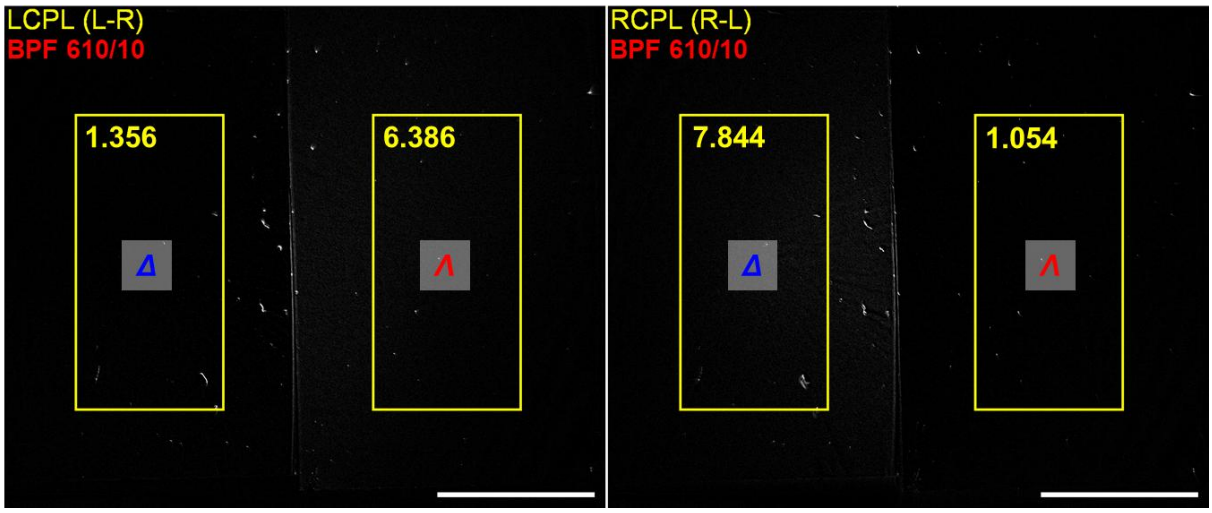

Figure 4.12: L-R (left) and R-L (right) EDCC images used for authentication of the proof-of-concept CST containing ***Δ*-EuL^1** (left section) and ***Λ*-EuL^1** (right section) under 365 nm excitation with average intensities of the regions of interest shown in yellow Scale bar = 5 mm, BPF610/10.

Since sequentially produced films resulted in consistent g_{CPLP} values in both BPF594/10 and BPF610/10, the tag can be further secured by cross-checking the g_{CPLP} numerical values for each spatial region with the expected threshold. Moreover, a CST can contain multiple CPL active materials that produce different g_{CPLP} values within the selected sections of the total pattern. Fine tuning of the g_{CPLP} can be also achieved by mixing the two enantiomers in secret proportions to further enhance the anticounterfeiting properties of the tag. To demonstrate the g_{CPLP} resolving power of the current setup, ***Δ*-EuL^0** containing film was prepared by spin-coating the black tape and subjected to CPLP.

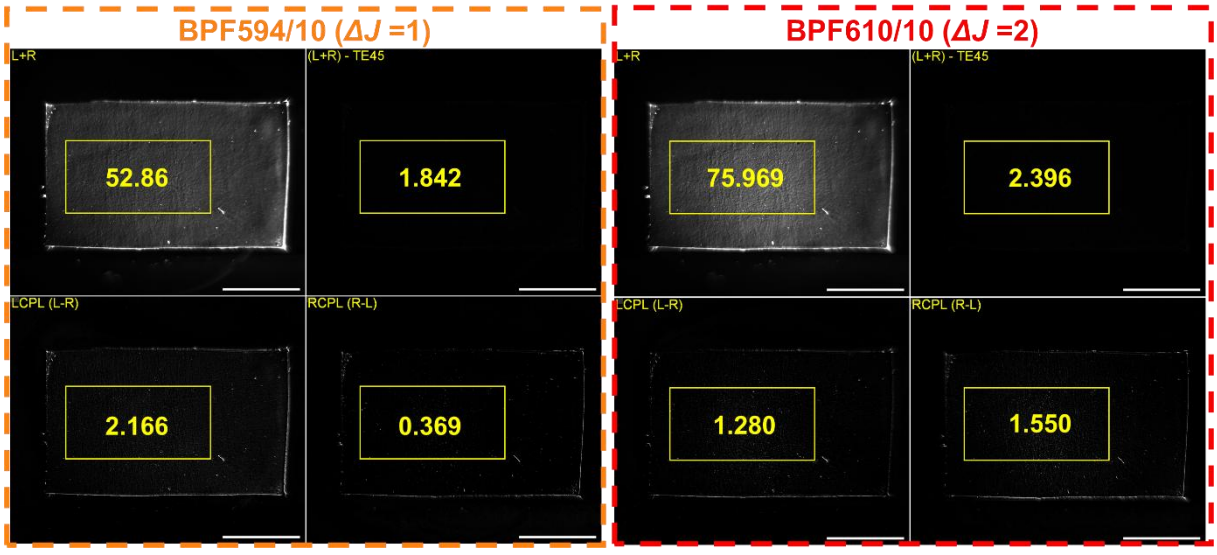

Figure 4.13: EDCC images of PMMA films under 365 nm excitation containing ***Δ*-EuL^0** using BPF594/10 and BPF610/10 with the regions of interest for g_{CPLP} calculations and their average intensities shown in yellow. Scale bar = 5 mm. R-L and L-R images are 6 times contrast enhanced for display.

The g_{CPLP} values obtained for the ΔJ = 1 transition using BPF594/10 (Figure 4.13) was 0.082 which was similar to the average g_{lum} of 0.10 (589-599 nm range) obtained for ***Δ*-EuL^0** solution in MeCN. CPLP was repeated with another equivalent film to produce g_{CPLP} of 0.073 (Figure 4.14), which differed from the first measured film by ~12%. In contrast to that, the g_{CPLP} values

obtained earlier for the ΔJ = 1 transition of **Δ-EuL^1** containing films did not differ by more than ~6%. The doubling of the error corresponded to a decrease in CPB_F when using **Δ-EuL^0** instead of **Δ-EuL^1.** It was suggested that CPB_F is more important for the signal to noise ratio than just g_{CPLP} alone. This is supported by the fact that the g_{CPLP} error produced by recording the ΔJ = 2 transition of **Δ-EuL^1** using BPF610/10 was ~7% (based on comparing the average of 6 films). The average g_{CPLP} for ΔJ = 2 transition of **Δ-EuL^1** (~0.038) is lower than g_{CPLP} for ΔJ = 1 transition of **Δ-EuL^0** (~0.077); however, the former produces a significantly lower error (~7% vs ~12%). Moreover, for **Δ-EuL^1**, the g_{CPLP} errors for ΔJ = 2 and ΔJ = 1 were the same (~6%). This suggested that the error of g_{CPLP} is a function of CPB_F rather than just average g_{CPLP}, since CPB_F values of **Δ-EuL^1** for the BPF594/10 and BPF610/10 are similar (202 and 189 M^{-1} cm^{-1} respectively). At the same time, CPB_F of **Δ-EuL^1** for BPF610/10 is ~2.5 higher CPB_F of **Δ-EuL^0** for BPF594/10, which was in agreement with the relative errors.

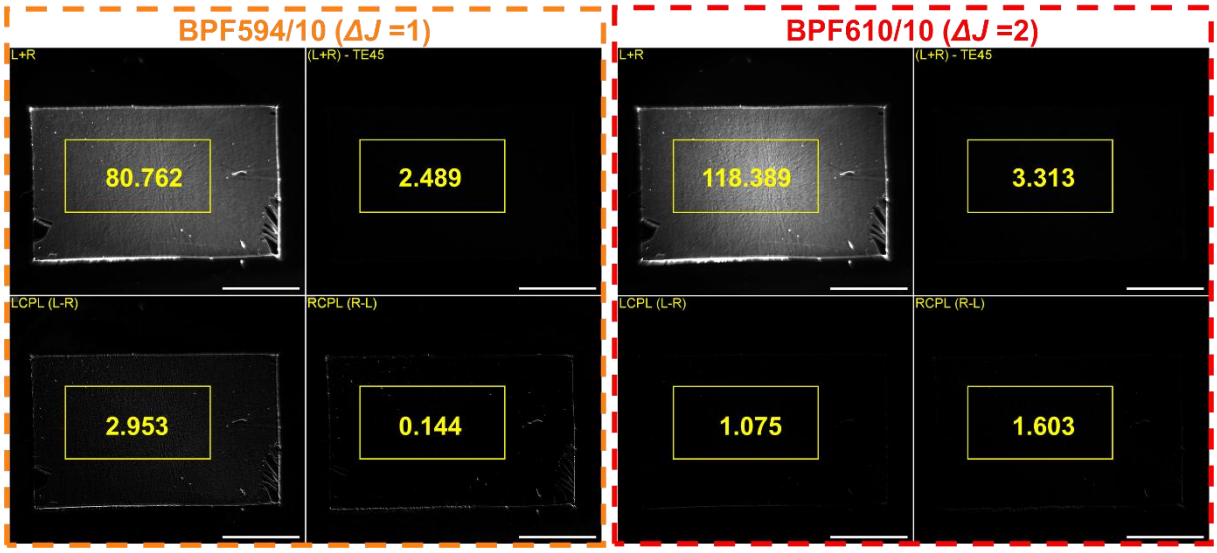

Figure 4.14: EDCC images of PMMA films under 365 nm excitation containing **Δ-EuL^0** using BPF594/10 and BPF610/10 with the regions of interest for g_{CPLP} calculations and their average intensities shown in yellow. Scale bar = 5 mm. R-L and L-R images are 6 times contrast enhanced for display.

The two films containing **Δ-EuL^0** produced totally different values of g_{CPLP} using BPF610/10 to target the ΔJ = 2 transition: -0.041 (Figure 4.13) and -0.014 (Figure 4.14)) both of which are significantly different from the average solution-state g_{lum} of 0.007. This suggests that in this case, the signal to noise ratio is too low for sufficient accuracy of the measurement. This correlates with the previously measured CPB_F of just 25 M^{-1} cm^{-1} for **Δ-EuL^0** in BPF610/10 range. Further tests with a larger number of films containing the enantiomers of **EuL^0** and **EuL^1** are necessary to determine the g_{CPLP} uncertainty precisely; however, at this stage, it can be concluded that, limited by the current CPLP setup, only chiral emitters producing the CPB_F value of more or equal to ~100 M^{-1} cm^{-1} are suitable for the use is CSTs that can be quantitatively authenticated using numerical g_{CPLP} values.

To demonstrate that the substrate itself does not introduce an additional error, the black tape alone was subjected to CPLP. As a result, no significant intensity was observed on the calculated images under 365 nm excitation (Figure 4.15). The same was done for the caps that were filled with the solutions of **EuL^1** for the CPLP method validation (Section IV.5).

No photodegradation or loss of CPL signal of the studied was observed during prolonged experiments in excess of 1 hour using the 365 nm UV LED irradiation source (1W total power, collimated and focused to a 1 cm diameter circle).

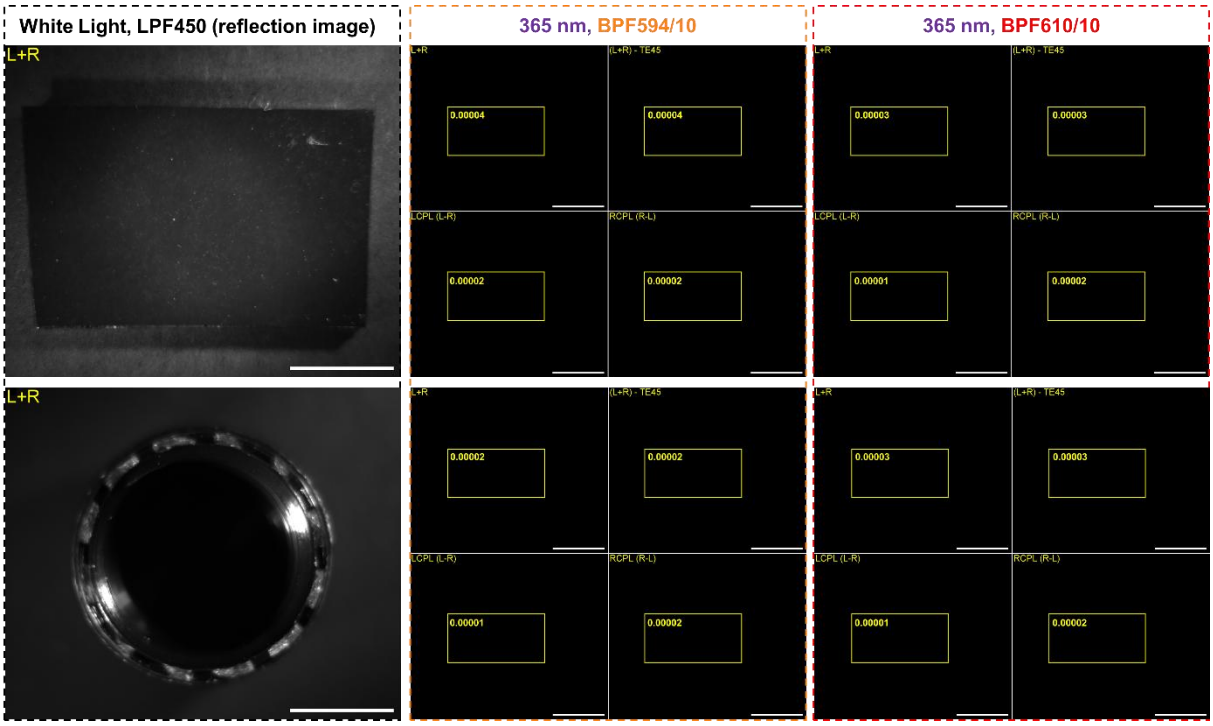

Figure 4.15: EDCC images of black tape substrate (top) and black plastic cap (bottom) using BPF594/10 and BPF610/10 under 365 nm excitation with the regions of interest and their average intensities shown in yellow. The corresponding L+R images under white light using LPF450; Scale bar = 5 mm.

IV.7. Discussion and future work

EuL^1 was embedded into solid-state PMMA spin-coated thin films for a proof-of-concept security tag. Both enantiomers were successfully authenticated *via* CPLP and EDCC, where dissymmetry of both ΔJ = 1 and ΔJ = 2 transitions was rapidly detected. The recorded dissymmetry was also quantified using the newly introduced term g_{CPLP}, and the results compared to the average g_{lum} values recorded by the PEM CPL spectrometer in the same λ regions. The g_{CPLP} values calculated from the EDCC images of solutions of **EuL^1** enantiomers were in good agreement with the g_{lum} values; however, the g_{CPLP} significantly reduced in PMMA films spin-coated on a glass substrate. The proposed hypothesis of dissymmetry reduction *via* reflection-induced CPL sign cancellation from substrate was confirmed by replacing glass with black non-reflective tape that recovered the magnitude of g_{CPLP}. The g_{CPLP} values remained consistent across multiple sequentially spin-coated films, suggesting high repeatability and consistent CPL security feature. An attempt to repeat the g_{CPLP} measurements with multiple **EuL^0** containing PMMA films did not result in consistency of the observed g_{CPLP} for either ΔJ = 1 or ΔJ = 2, suggesting that its CPB_F was too low for a reliable CPL active security ink.

Reproducibility of the g_{CPLP} values for the BPF594/10 and BPF610/10 that remained consistent across multiple consecutively spin-coated films suggested a possibility of authentication of a fine-tuned g_{CPLP} value achieved by a blend of the two enantiomers of **EuL^1** in a secret ratio. This would create a unique value of g_{CPLP} only known to the manufacturer of CSTs. In addition, this can be further sophisticated by CST authentication using a set of different unknown BPFs and LPFs of unknown λ range. In the same way as the $\bar{x}g_{lum}$ is unique for each randomly selected λ range of the CPL spectrum, g_{CPLP} will also change depending on the optical filter used during authentication. This introduces an additional CPL security layer which incorporates CPL intensity and spectral features.

As mentioned earlier, the security tag must not racemise during lamination, which exposes ***Δ*-EuL^1** and ***Λ*-EuL^1** to 150°C (1 cm min^{-1}). Although the racemisation study performed at 60°C demonstrated a high racemisation stability in solution state, it could not accurately predict the extent of racemisation during lamination. Therefore, a 200 nm thick PMMA film containing ***Δ*-EuL^1** was spin-coated on the black tape substrate and subjected to CPLP. After that, it was laminated, and CPLP was repeated (Figure 4.16). The g_{CPLP} values for both ΔJ = 1 and ΔJ = 2 transitions before and after lamination were determined and compared (Table 4.3).

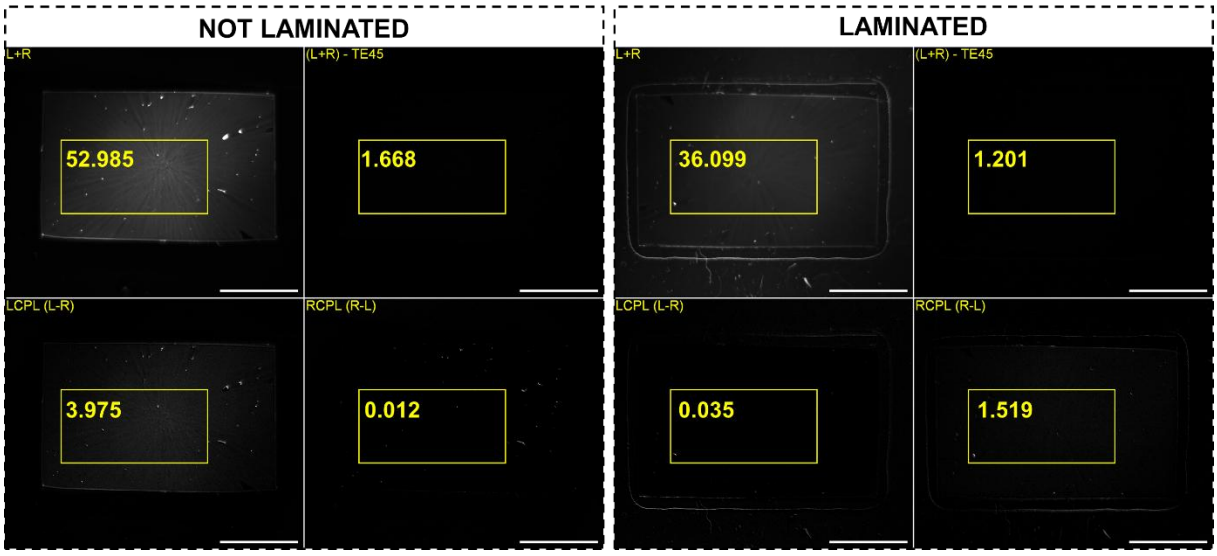

Figure 4.16: EDCC images of the ***Δ*-EuL[1]** containing PMMA films spin-coated on black electrical tap substrate before (left) and after (right) lamination using BPF594/10 with the areas selected for g_{CPLP} calculations and their average intensities shown in yellow. Scale bar = 5 mm, R-L and L-R images are 6 times contrast enhanced for display.

Lamination produced unexpected results, where the CPL sign inversion occurred for both ΔJ = 1 and ΔJ = 2 transitions. At the same time, a significant decrease of g_{CPLP} magnitude in ΔJ = 1 was observed while that of ΔJ = 2 remained essentially the same (Table 4.3). Further photophysical investigation of the laminated sheet alone suggested that it behaved as a half-waveplate, which could completely invert the CPL sign.

Table 4.3: comparison of the g_{CPLP} obtained for PMMA films with *Δ*-EuL[1] before and after lamination.

Lamination	g_{CPLP} BPF594/10 (ΔJ = 1)	g_{CPLP} BPF594/10 (ΔJ = 2)
Before	+0.15	-0.035
After	-0.084	+0.033
% magnitude decrease	44%	6%

A perfect half-waveplate would invert the sign without affecting the magnitude of g_{CPLP}. In this case, since only the magnitude of g_{CPLP} for the ΔJ = 1 transition significantly decreased, the half-waveplate properties of the sheet could be wavelength dependent, which is common even for the commercially available waveplates. On the other hand, the g_{CPLP} decrease could be caused by the reflections introduced by the laminating sheet. From the previous results, the ΔJ = 2 was less susceptible to reflections-caused dissymmetry decrease, which was attributed to the longer wavelength of light being less prone to scattering. Further tests are required to determine whether the g_{CPLP} magnitude decrease is due to the laminating sheet acting as an imperfect half waveplate or due to the reflections from the glossy surface of the sheet. Once the half-waveplate properties of commercially used laminating sheets are fully characterised, lamination could serve as an additional security layer that inverts the CPL sign of the inks.

One of the possible future directions of the CST development is introduction of CPL-inactive organic fluorophores into the tag that are imaged simultaneously with ***Δ*-EuL^1** and ***Λ*-EuL^1**. This will facilitate all previously mentioned security layers and potentially introduce new ones. For example, alongside the enantiomers of europium(III) complex, a CST can contain the commercially available organic dyes **FIrscn** and **RhB** that can be also replaced with other fluorophores of choice (Figure 4.17).

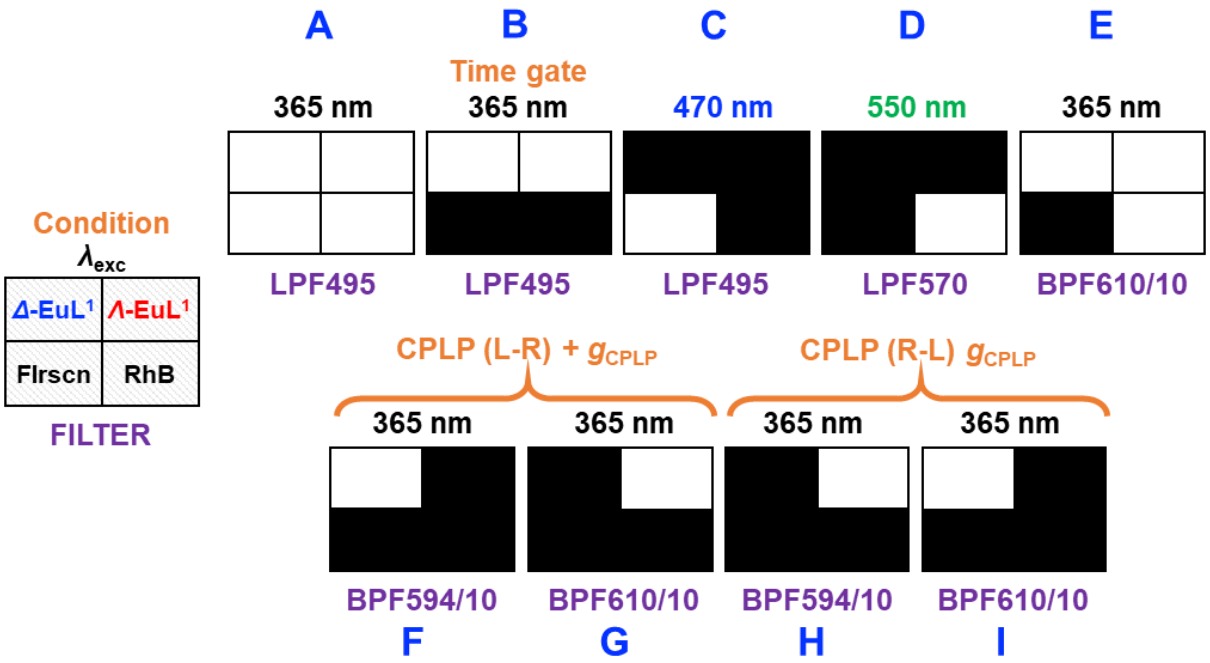

Figure 4.17: Sequence of the unique CST patterns and their variables (excitation wavelength, optical filter and method) suitable for digital authentication, where the areas of the high and near zero intensity are shown in white and black respectively.

As a result, all present materials can be photoexcited at 365 nm, resulting in green, orange and red emission from **FIrscn**, **RhB** and **EuL^1** respectively, that can be recorded by the camera using a 495 nm long-pass filter (LPF495) (Figure 4.17.A). This simultaneously authenticates spatial and chromatic security layers. If the same procedure is repeated, but with a nanosecond scale time delay between the PE and the shutter introduced, only europium(III) containing sections of the tag will produce intensity, authenticating the temporal security layer (Figure 4.17.B). The next step could be illumination of the CST using 470 nm LED at a specific power to selectively excite only **FIrscn** (Figure 4.17.C). The same can be repeated with 550 nm LED to selectively excite **RhB**; however, a LPF570 would be necessary to avoid detection of the reflected excitation light (Figure 4.17.D). The use of different wavelength LEDs to selectively excite individual sections of the CST pattern provides an additional security layer that can be implemented. Another security layer can be facilitated by using different BPFs to observe only those sections of the tag that contain the dyes emitting in the selected wavelength range of filter transmission window. For example, when the whole tag excited with 365 nm LED, the use of BPF610/10 will only transmit orange and red emitting

RhB and **EuL^1** (Figure 4.17.C). Finally, the CPL security layer can be authenticated using L-R-CPL EDCC images in combination with BPF594/10 and BPF610/10 to select the ΔJ = 1 and ΔJ = 2 emission manifolds. As a result, L-R image will show the ***Δ*-EuL^1** *via* BPF594/10 (Figure 4.17.F) and ***Λ*-EuL^1** *via* BPF610/10 (Figure 4.17.G). The opposite will be observed when R-L calculation is performed (Figure 4.17.H and I).

The whole sequence (Figure 4.17.A-I) can be computer-automated for a rapid authentication of multi-layer security of the proposed CST. The flexibility of the design allows for introduction of other dyes and the use of other combinations of the excitation light wavelength, optical filter and time gating. Once the design is confirmed, further optimisation of various parameters such as LED power and camera exposure time can be performed.

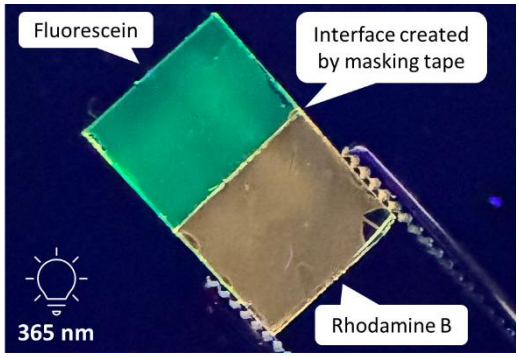

Figure 4.18: Photograph of a sectioned PMMA film under 365 nm PE (containing **FIrscn** and **RhB** on a single substrate

To practically achieve multiple sections containing different luminescent materials, a templating method can be used. This is done by covering individual parts of the substrate with a masking tape while spin-coating with solutions containing different dyes. The material used to cover the substrate must be moderately sticky in order to remain attached during spinning while also detach freely without damaging the existing film. In addition, it must be insoluble in DCM. A polyethylene terephthalate (PET) film *E-MASK RP301* by *Nitto* was found to have just the right adhesive strength of 10 mN mm^{-1}. A proof-of concept PMMA film containing two separate sections was spin-coated using the templating method (Figure 4.18). The sections contained **FIrscn** and **RhB** that produce green and orange emission respectively under 365 nm PE. The potential disadvantage of the templating method was expected to be a bleed of the second spin-coated film into the first one during the spin coating. Although the section corners can be avoided during the image calculation by selecting only smooth central parts of the sections, the film was subjected to LSCM to investigate the extent of the bleed as well as to test the possibility of selectively exciting different sections of the film using the excitation sources of different wavelengths. Therefoe, the area centred on the interface between the two sections was excited using 355 nm light that resulted in PE of both sections. The images were then taken using 495-515 nm detection window to exclusively observe **FIrscn** emission (Figure 4.19.A) and 660-680 nm to observe only **RhB** emission (Figure 4.19.E). As a result, the interface between the two sections was relatively smooth with no significant mixing of the two films, which was determined from the overlay of both mission images with the transmission image (Figure 4.19.H). The selective excitation security feature was then tested using 458 nm and

543 nm excitation to selectively excite **FIrscn** (Figure 4.19.B) and **RhB** (Figure 4.19.F) respectively. The images were taken using both detection windows to confirm that only one of the sections glows at each excitation λ (Figure 4.19.F and C).

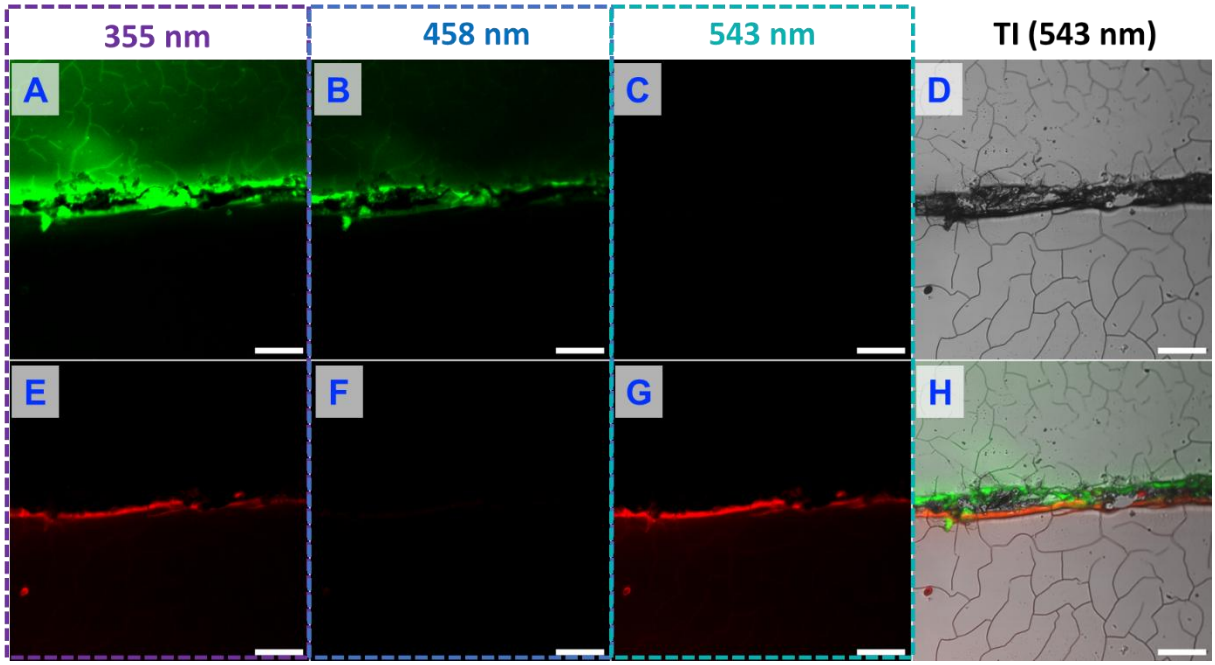

Figure 4.19: LSCM of **FIrscn** (green coloured) and **RhB** (red coloured) containing sections of a spin-coated PMMA(×10/0.40 objective, 620×620 µM FOV) showing total emission using 495-515 nm (**A**-**C**) and 660-680 nm (**E**-**F**) detection windows and λ_{ex} = 355 nm (**A** and **E**), λ_{ex} = 458 nm (**B** and **F**) and λ_{ex} = 543 nm (**C** and **G**). Overlay of the transmission image (**D**) with A and F is shown in **H**. Scale bar = 100 µm. Performed by Dr. Dominic Black.

In order to facilitate authentication of the above-proposed selective excitation security layer using the CPLP camera, the set-up was modified by incorporation of different λ LEDs. Before the new multi-LED unit was introduced, the PE of CSTs was performed using two 365 nm LEDs placed at the opposite sides of the sample stage and oriented at ~45° angle with respect to the sample. Apart from availability of just a single excitation λ, such setup resulted in such problems as uneven irradiation of the sample stage at low LED power and PE of some filters in the filter wheel which produced circular artifacts on the images. Therefore, in cooperation with Durham University electrical workshop, a novel multi-LED PE module was designed and built. The module contained pairs of multiple wavelength LEDs (400-1000 white, 365 nm UV, 470 nm blue, 525 nm green, 660 nm red and 760 nm NIR) that are mounted on a trapezium-shaped aluminium ring at 45° with respect to the sample stage plane using a thermally conductive adhesive to facilitate heat sinking (Figure 4.20).

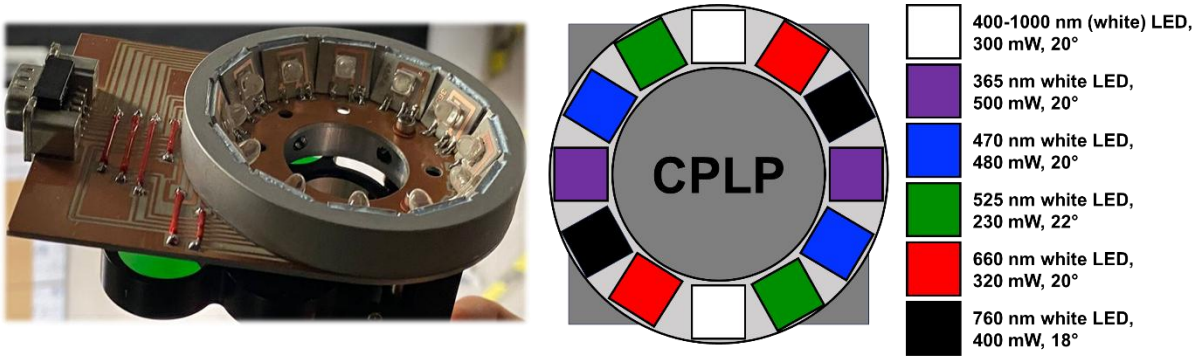

Figure 4.20: Photograph of the multi-LED excitation module (left) and its schematic representation (right).

The LED pairs were necessary to provide an even illumination of the sample, which is crucial for quantitative authentication methods. Such broad λ range of LEDs was chosen to improve the compatibility of the system with selective PE of most available luminescent dyes. The LED pairs were then connected to pulse width modulation drivers that allowed to individually adjust the brightness of each λ LED pair to account for the difference in power specification. In addition, the brightness adjustability is essential when switching between the optical filters to keep the recorded intensity within the dynamic range. In other words, optical filters select λ regions where the measured light intensity might differ, potentially resulting in oversaturation of the detector unless PE power corrected. Apart from that, pulse modulation is inherently compatible with time gating that is necessary for authentication of the previously mentioned temporal security layer.

In order to test the new CPLP camera multi-LED module, the previously reported security tag[47] was irradiated with two different λ LEDs. More specifically, the combination of the 470 nm LEDs with LPF495 and 525 nm LEDs with LPF570. As a result, in the first combination, only the features containing **RhB** and **FIrscn** emission were detected, since both dyes absorbed in the green region. In the second sequence, out of all dyes present only **RhB** absorbed in green (525 nm) light, resulting in only the contour of the tag appear on the image (Figure 4.21).

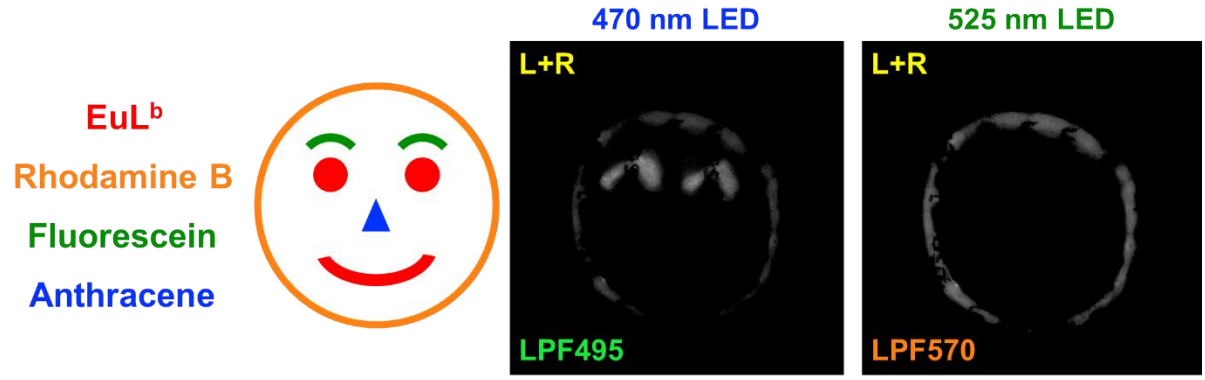

Figure 4.21: Schematic representation of the luminescent species forming the security tag pattern (left) and two total intensity EDCC images recorded using the different stated parameters - PE λ and optical filter.

The modular setup of the camera has proven advantageous for its adaptability to new authentication methods that increase the complexity of the CST security which minimises its susceptibility to counterfeiting. Therefore, to improve the commercialisation prospects of the camera, other potential applications apart from the CST authentication were investigated, taking into consideration the required camera hardware modifications. The camera could be integrated into processes where it would either demonstrate significant improvements over the existing instrumentation or introduce a completely new analytical method that would bring commercial value. The areas of science that most commonly study chiral materials are biochemistry, pharmaceutical chemistry and molecular biology. For example, pharmaceutical chemistry aims on replication of biologically active molecules such as enzymes and receptors that are chiral and demonstrate only stereospecific interactions. This leads to one of the great challenges in drug discovery, where the control of stereochemistry at the chiral centres, which need to match that of a biological target, is crucial for the potency and toxicity of the drug. Moreover, metabolic pathways for the administered drugs are also stereospecific, which can lead to undesired accumulation of the wrong enantiomer in patients. In molecular biology, for example, nucleic acids are chiral, for instance, deoxyribonucleic acid (DNA) and ribonucleic acid (RNA). Therefore, one of the simple indicators of a successful DNA replication or modification procedure could be determination of chirality of the resulting species. Currently, CD spectroscopy is used for these purposes, since chiral species preferentially absorb either R-CP or L-CP light. The main disadvantage of this method is that is it relatively time consuming, since only one sample can be measured at a time. This significantly reduces the method efficiency in scenarios where multiple different targets need to be screened at once, for instance, in time-resolved studies, where rapid screening of multiple samples needs to be performed simultaneously. In this chapter the capability of the camera to analyse the whole sample stage by simultaneous detection of both L-CP and R-CP light was confirmed. It was demonstrated how image processing allowed to select individual ROIs for the g_{CPLP} calculations, for example, for three containers containing solutions of **EuL^{1}** enantiomers (Figure 4.7). Therefore, by replacing them with, for example, a 96 well plate, 96 samples could be screened by the CPLP camera in a single shot. This would require a lens with a longer focal length, which would allow to fit the well plate footprint with appropriately large FOV. Since the resolution of the CMOS sensor is 2448 × 2048 pixels, which produce a ratio of 12 × 10, and the 96 well plate contains 12 × 8 wells, the longest side of the well plate containing 12 wells would be matched with the longest side of the FOV containing 2448 pixels (Figure 4.22 - left). Otherwise, if 8 wells were matched with 2048 pixels, the plate would not fully fit into the FOV (Figure 4.22 – right).

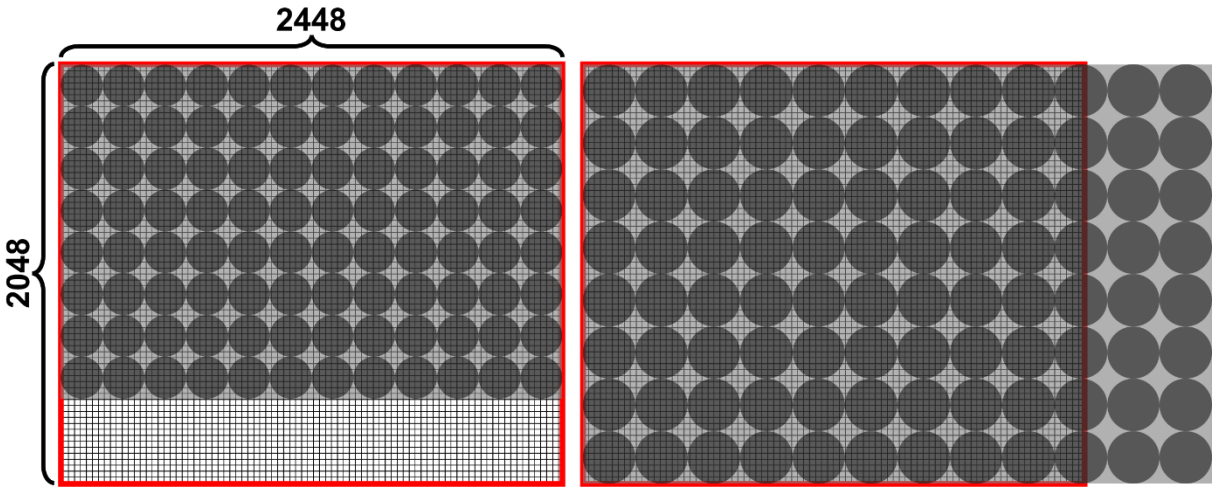

Figure 4.22: Relative dimensions of the CMOS 2448 × 2048 pixels FOV (red borders) and 12 × 8 well plate at different zoom settings of the lens to match long sides (left) and short sides (right) of the FOV and well plate.

As a result, each well would fit into a 204 × 204-pixel cluster, however, zero intensity areas covering the space in-between the circular well plates needs to be accounted for. Therefore, the size of the largest possible square-shaped cluster of pixels that would fit into a well with the diameter corresponding to 204 pixels can be calculated by setting the diagonal of such square as 204 pixels (diagonal = side × $\sqrt{2}$). As a result, each well would fit 144 × 144-pixel corresponding to 72 sets of 2 × 2-pixel clusters covered by 4 differently oriented LPs. In other words, each g_{CPLP} calculation would be a result of 72 averages, suggesting a high precision of the method.

In order to achieve an even illumination of all 96 wells, the PE excitation module needed to be redesigned to account for the bigger sample size. In addition, the illumination of the plastic well plate from above could result in reflection of PE light reflection that would generate a longer λ LPL that could introduce an additional error to the measurements. Therefore, it was decided to illuminate the sample from underneath using multiple LEDs of different λ that are covered by a light diffuser. It will have the same power control functionality as the previously mentioned ring module (Figure 4.23); however, might require LEDs with a wider angular intensity distribution for an even illumination due to their proximity to the sample. The project is currently at the development stage in collaboration with Durham University electrical workshop.

This will turn the CPLP camera into a CPLP plate reader which will allow to simultaneously measure the CPL of 96 solutions in a single shot. The plate reader will be compatible with a wide range of the PE λs, emission will be measured through the relevant LPFs or BPFs to avoid the detection of the excitation light and select the λ range with single sign CPL for a given species.

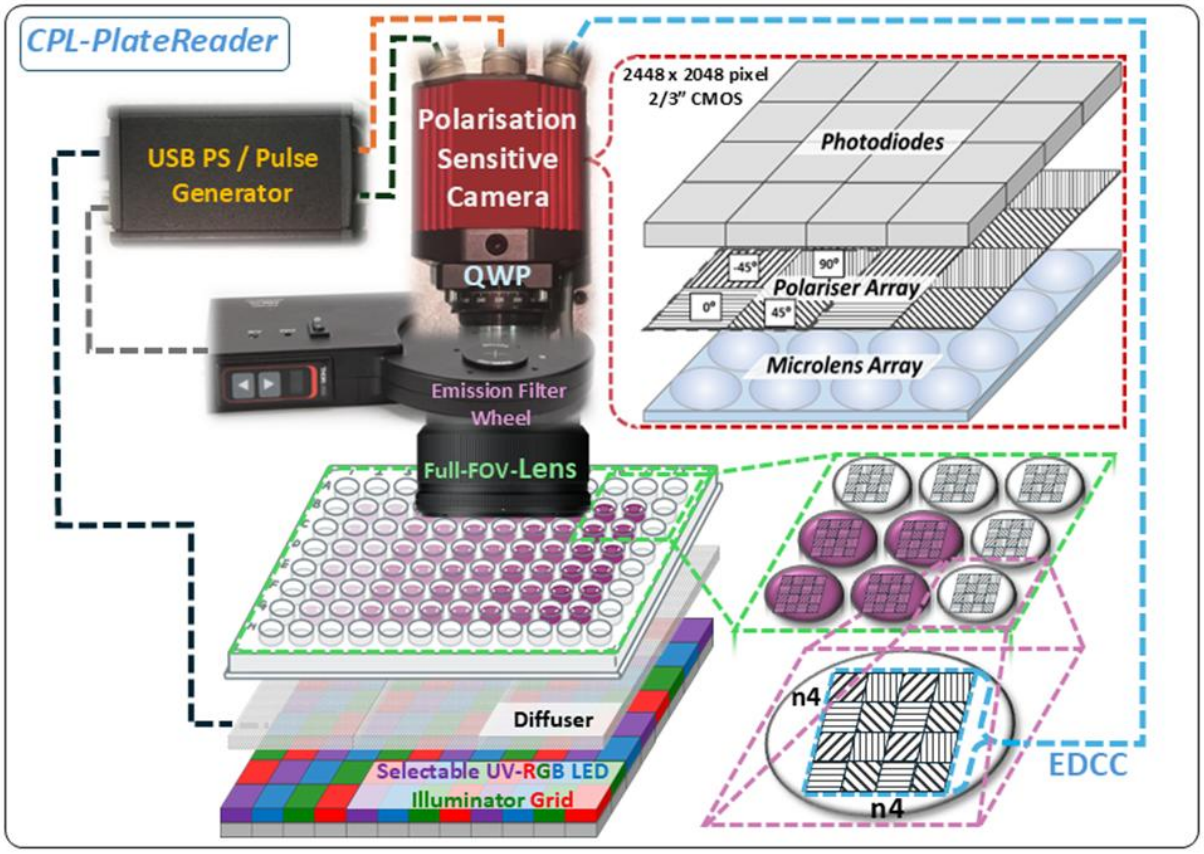

Figure 4.23: Schematic representation of the modified CPLP camera setup for the use as a 96 well plate reader.

In addition to this, the setup can be explored in CD spectroscopy mode, where the sample is illuminated to directly measure the helicity of the excitation light after it passes through the sample using a BPF matched with the LED λ range. When LED light with no polarisation bias passes through a solution containing a chiral material, it becomes CP. For example, if a material shows positive CD, it will absorb more L-CP light than R-CP light. As a result, the camera would record a greater intensity in the R-CPL-sensitive channel, while the calculated g_{CPLP} will correspond to the negative of the g_{abs}, which is the absorption equivalent of g_{lum} (Equation 28).

$$g_{abs} = \frac{2(A_L - A_R)}{(A_L + A_R)} = -g_{CPLP} \qquad [28]$$

Therefore, the method of CD detection of the CPLP plate reader will be opposite to that of a CD spectrometer. While CD spectrometer measures the intensity of the instrument-generated CP light that is transmitted through the sample, CPLP plate reader measures the intensity of the originally unpolarised light that becomes polarised when passing through the sample. The implementation of the CD mode would significantly broaden the application scope of the plate reader as there are significantly more materials that show strong CD rather than strong CPL.

CHAPTER V. The design of novel CPL emitters for late-stage functionalisation

V.1. Investigation of the novel EuL^2 nitro-functionalised complex and its derivatives

V.1.1. Introduction to the series of complex intermediates for the late-stage functionalisation

Modular synthetic strategy towards the EuL-type materials affords flexibility to introduce various structural modifications into the system for desired chemical and photophysical properties. For instance, as previously discussed, introduction of electron-donating groups to the aryl ring of the arylalkynylpyridyl chromophore resulted in bathochromic shift of the absorption maximum. Another example of phosphinate to carboxylate donor replacement significantly altered the CPL properties, resulting in strong monosign band within the ΔJ =2 manifold with 656% CPB_F increase. Such structural modifications need to be introduced at an early stage of chromophore 'top' and 'bottom' components synthesis. As a result, the main limitation of this strategy is a potential sensitivity of the introduced functional group towards the downstream reaction sequence that, apart from others, includes a two-step Corey Fuchs homologation, mesylation, nucleophilic substitution and base-catalysed hydrolysis steps. Therefore, each new modification would likely require a careful consideration of the reaction sequence as well as additional synthetic steps to introduce and cleave protecting groups, adding to the complexity and costs. In addition, the need for a brand-new synthesis for each desired modification is not feasible in terms of commercialisation. This creates demand for a new approach where a versatile **EuL^1**-type material susceptible to a late complex-stage functionalisation *via* functional group interconversions. Such complex, for instance, could be functionalised with glucose units for a better cellular uptake for cellular bioimaging.[19] Alternatively, it can be conjugated with various peptide sequences for targeting specific organelles such as endoplasmic reticulum with "AcCFFKDEL" or trans-golgi targetting "AcGASDYQRLGC".[92] Such complex could be also used for conjugation to chiral self-assembly systems or chiral polymers for CPL enhancement.[93–95]

This idea was previously investigated using europium(III) complexes that either contained a nitro leaving group or an amino-propyl group at the pyridyl for the late-stage conversion (Figure 5.1).[92] On the contrary the design allowed sensitisation *via* only 2 chromophore 'arms' while the third arm only served functionalisation purpose. As a result, such materials demonstrated a guaranteed reduction in molar extinction coefficient and therefore *CPB* by ~33%. Another disadvantage came from the complex symmetry reduction near the europium(III)

luminescence centre that would negatively affect CPL sign conservation within the 'hypersensitive' ΔJ =2 manifold.

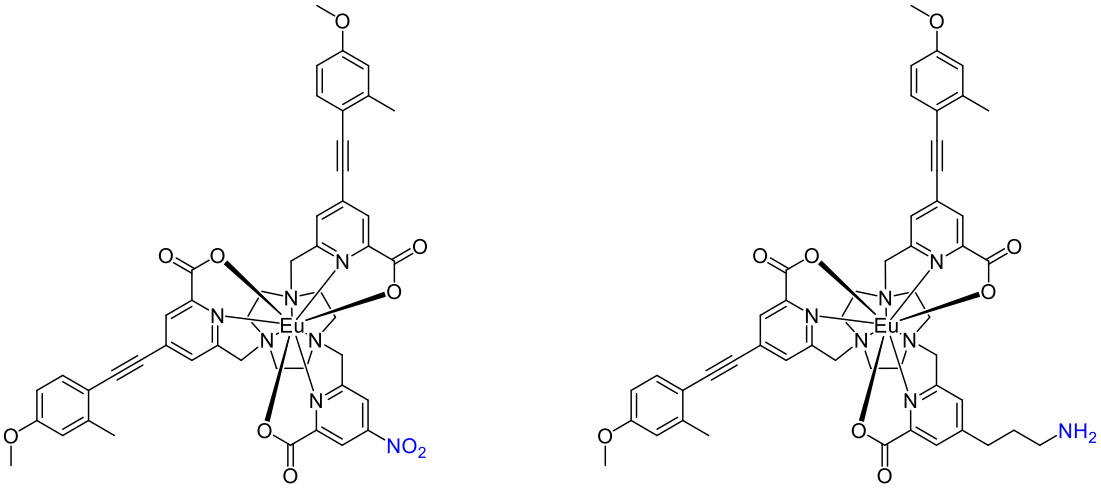

Figure 5.1: The structures of literature examples of europium(III) complexes for the late-stage modification.[92]

To improve upon the above-mentioned downsides, the new convertible functional group must be structurally distant from the europium(III) centre and not conjugated with the rest of the chromophore to minimise the effect on photophysical properties by alteration of ICT state energy that could shift the maximal absorption wavelength. It was also important to maintain 2,4,6-trimethoxy substitution of the aryl ring for the absorption maximum near 365 nm.

All things considered, the meta position of the aryl was chosen for functionalisation with a nitro group **EuL^{2}** that can be converted into an azide **EuL^{2b}** *via* an amine intermediate **EuL^{2a}** at a complex stage (Figure 5.2). It was proposed that **EuL^{2a}** can be functionalised by forming a amide bond to a carboxylic acid bearing moiety, and **EuL^{2b}** can undergo click-chemistry cycloaddition to alkyne containing substrates.

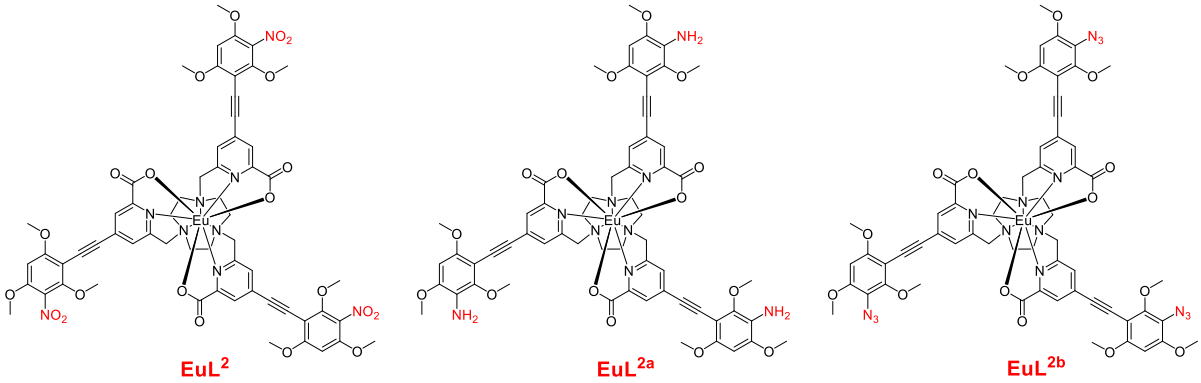

Figure 5.2: The proposed structures for the novel europium(III) complexes for the late-stage modification.

The main drawback of such design is large steric hindrance at the meta- position due to adjacent methoxy groups which could significantly reduce reactivity. This would not only affect the **EuL^{2}** to **EuL^{2a}** to **EuL^{2b}** interconversion but also the amide formation and cycloaddition. Therefore, it was important to test the reaction conditions using early chromophore precursors.

V.1.2. Proposed late-stage functional group interconversion

Nitro to amino to azido functional group interconversion was proposed to be carried out at the complex stage. Firstly, it was advantageous to afford both **EuL^{2a}** and **EuL^{2b}** to make the system more versatile towards functionalisation with different substrates (containing carboxylic acid or alkyne). Secondly, the nitro to amine reduction had to be performed at the **EuL^{2}** complex stage due to reactivity of the amine group towards the mesylation step of the ligand synthesis. On the contrary, nitro group attached to the electron-rich trimethoxy-substituted aryl group is relatively inert and was expected to remain intact throughout all subsequent synthetic steps. In addition, introduction of unprotected primary amines complicates purification of the complex precursors *via* normal-phase column chromatography. Therefore, both complex-stage functional group interconversion reactions had to be compatible with **EuL^{2}** chemical stability.

The two standard methods for nitro to amino reduction are catalytic hydrogenation and metal reduction under acidic conditions. They both are incompatible with the alkyne functionality causing its hydrogenation or hydration. Therefore, an acid-free method of nitro reduction using tin (II) chloride in MeOH at an elevated temperature (60°C) was adapted from literature (Scheme 5.1).[96,97] The following amino to azido group conversion followed a recently published method that used tert-butyl nitrite in combination with trimethylsilyl azide (Scheme 5.1).[98] Other factors such as purification simplicity, catalyst cost and solvent compatibility were also prioritised during method selection.

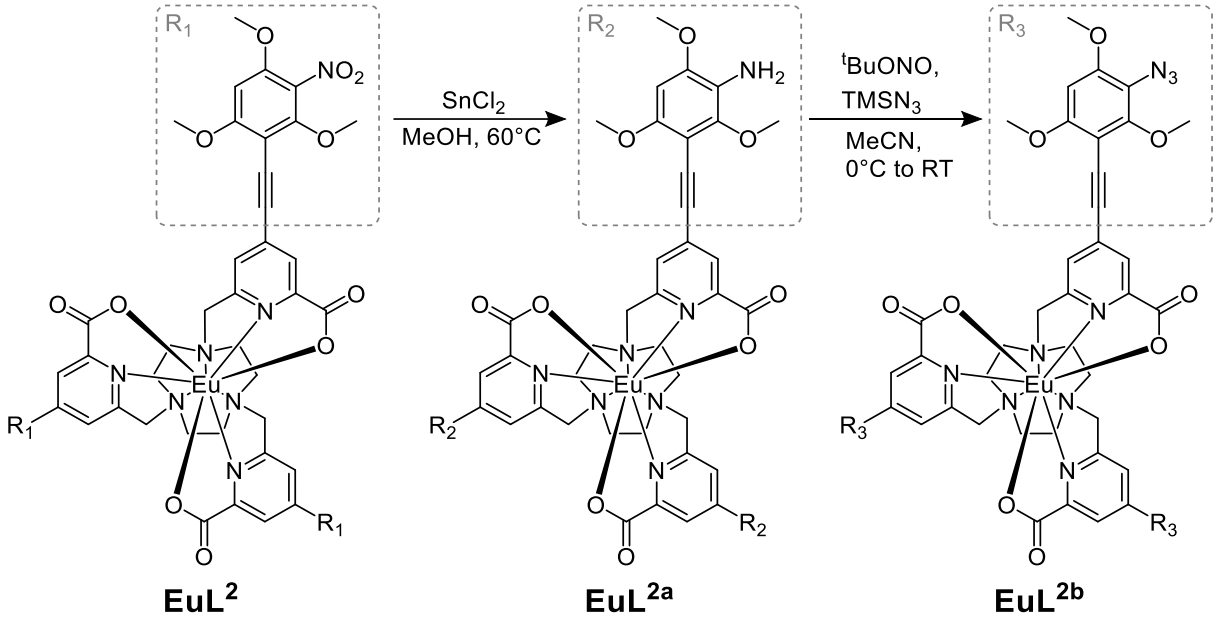

Scheme 5.1: The proposed reaction sequence for the complex-stage functional group interconversion of **EuL^{2}**.

V.1.3. Preparation of EuL^2

The total synthesis of **EuL^2** was equivalent to that of the **EuL^1**, where where 'top' and 'bottom' components of the chromophore were prepared separately prior to Sonogashira cross-coupling reaction. While the 'bottom' pyridyl component of the chromophore was shared between the **EuL^1** and **EuL^2**, the 'top' was modified by introduction of a nitro group. As mentioned earlier, it was decided to nitrate the aryl group at an early stage (the first synthetic step) due to its chemical inertness towards further steps (Scheme 5.2). In addition, nitration requires harsh acidic conditions which could affect other functional groups if performed at a later stage.

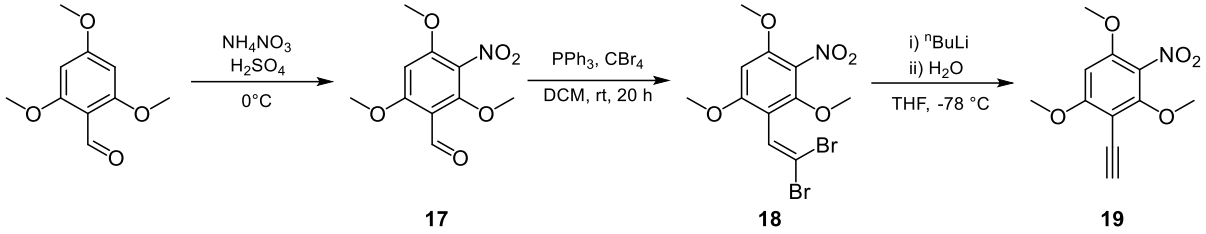

Scheme 5.2: The reaction sequence for the 'top' component of the chromophore in **EuL^2**.

2,4,6 - Trimethoxybenzaldehyde was nitrated in a standard electrophilic aromatic substitution reaction using a mixture of nitric and sulfuric acids to give **17**. The probability of the unwanted double nitration at both meta positions was reduced by a short reaction time (10 minutes) and low temperature (0°C). The second nitration was likely due to the ortho-para activating nature of the methoxy groups. On the other hand, once one electron withdrawing nitro group is added, the substrate was deactivated toward the second electrophilic aromatic substitution. The method for the following 2-step Corey-Fuchs reaction remained unchanged from the previously reported procedure towards the 'nitro-free' equivalent of **19**. The same applied to the following sequence to prepare the sensitising chromophore **20** which was then mesylated to give **21** (Scheme 5.3).

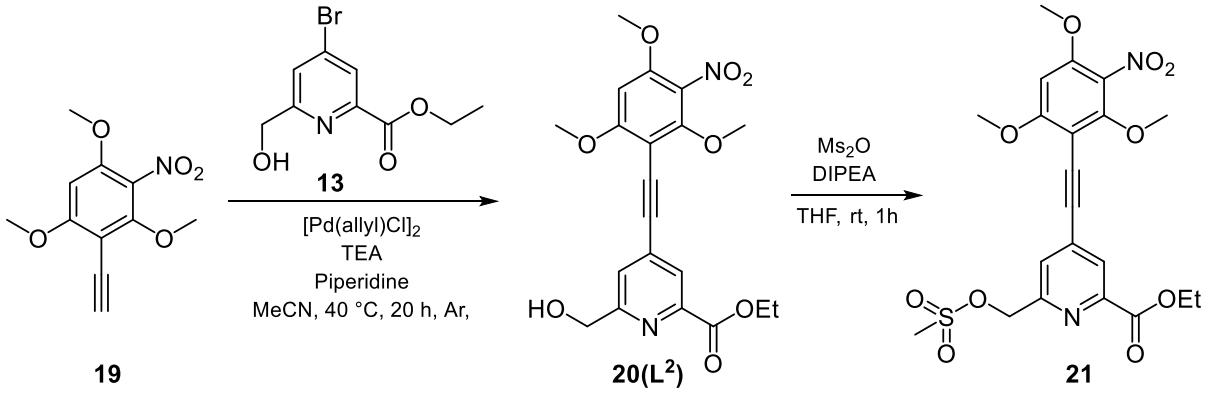

Scheme 5.3: The reaction sequence for the sensitising chromophore of **EuL^2**.

Purification of **20** using reverse-phase HPLC with MeCN-water of MeOH-water solvent gradient was inefficient due to poor solubility, and therefore it was purified by flash chromatography (silica, 3% MeOH in DCM) instead. The rest of the synthetic procedure was also the same with that reported for **EuL^1** (Scheme 5.4). The above-mentioned solubility problem also affected the purification of **EuL^2**. Therefore, similarly to **20**, it was purified by flash chromatography (silica, 5% MeOH in DCM).

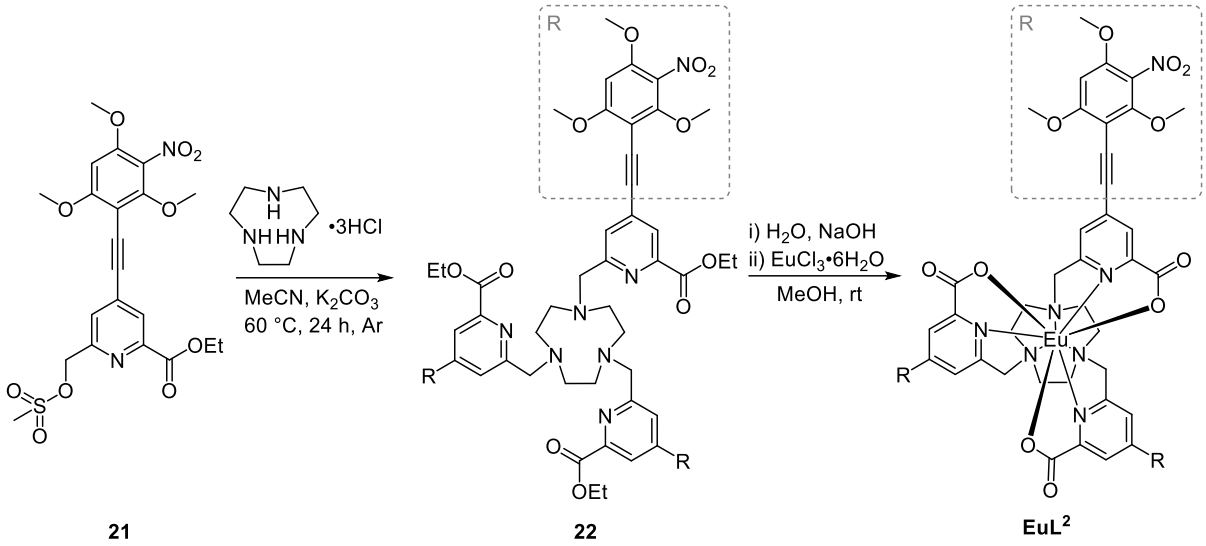

Scheme 5.4: The reaction sequence for the alkylation, hydrolysis and complexation steps for **EuL^2**.

V.1.4. Photophysical study of EuL^2

Apart from being a late precursor for functionally prominent **EuL^{2a}** and **EuL^{2b}**, **EuL^2** was photophysically evaluated to study the effect of structural modification on the far end from the europium(III) centre. Introduction of the electron withdrawing nitro group on the 'top' of the chromophore would decrease the energy of the HOMO resulting in an undesired hypsochromic (blue) shift of the absorption maximum. Since **EuL^2** was meant to be just a precursor complex for the practically useful **EuL^{2a}** and **EuL^{2b}**, blue shifted absorption maximum did not pose a problem. **EuL^{2a}** would contain electron donating amine in addition to trimethoxy substitution that would potentially red shift the absorption maximum closer to the 365 nm (depending on solvent) compared to **EuL^1**. Although **EuL^{2b}** contains electron withdrawing azide, it would form a triazole ring upon cycloaddition to a functional moiety. Therefore, both **EuL^{2a}** and **EuL^{2b}** would maintain the optimal absorption at 365 nm, enabling the highest possible luminescence brightness when excited with a commercially available UV LED or 355 nm Nd:YAG laser line.

As expected, the excitation maximum of the **EuL^2** hypsochromically shifted from around 360 nm (for **EuL^1**) to around 340 nm (Figure 5.3.C, both in MeCN). Such increase in the HOMO-LUMO gap can be due to a decrease in HOMO energy which is a result of electron withdrawing nature of the nitro group. Both materials produced nearly identical emission spectra (Figure

5.3.D), including the 'hypersensitive' ΔJ = 2 manifold. This confirmed near zero influence of such distant structural modification on the symmetry at the europium(III) site. This also suggested a high possibility of CPL spectral shape conservation.

Φ of the **EuL²** (10 ± 1%) was around 4 times lower than that of **EuL¹** (45 ± 1%). On the other hand, the emission lifetime of **EuL²** in MeCN remained the same with that of **EuL¹** (both 1.0 ± 0.1 ms). Both factors suggested that the emission of **EuL²** was quenched by an additional (in contrast to **EuL¹**) non-radiative relaxation of the short-lived first singlet (S_1) or ICT excited states of the chromophore rather than europium(III) $^5D_0$ long-lived state. In addition, the chromophore of **EuL²** (**L²**) was not emissive in contrast to **L¹**, supporting the claim of the S_1 quenching.

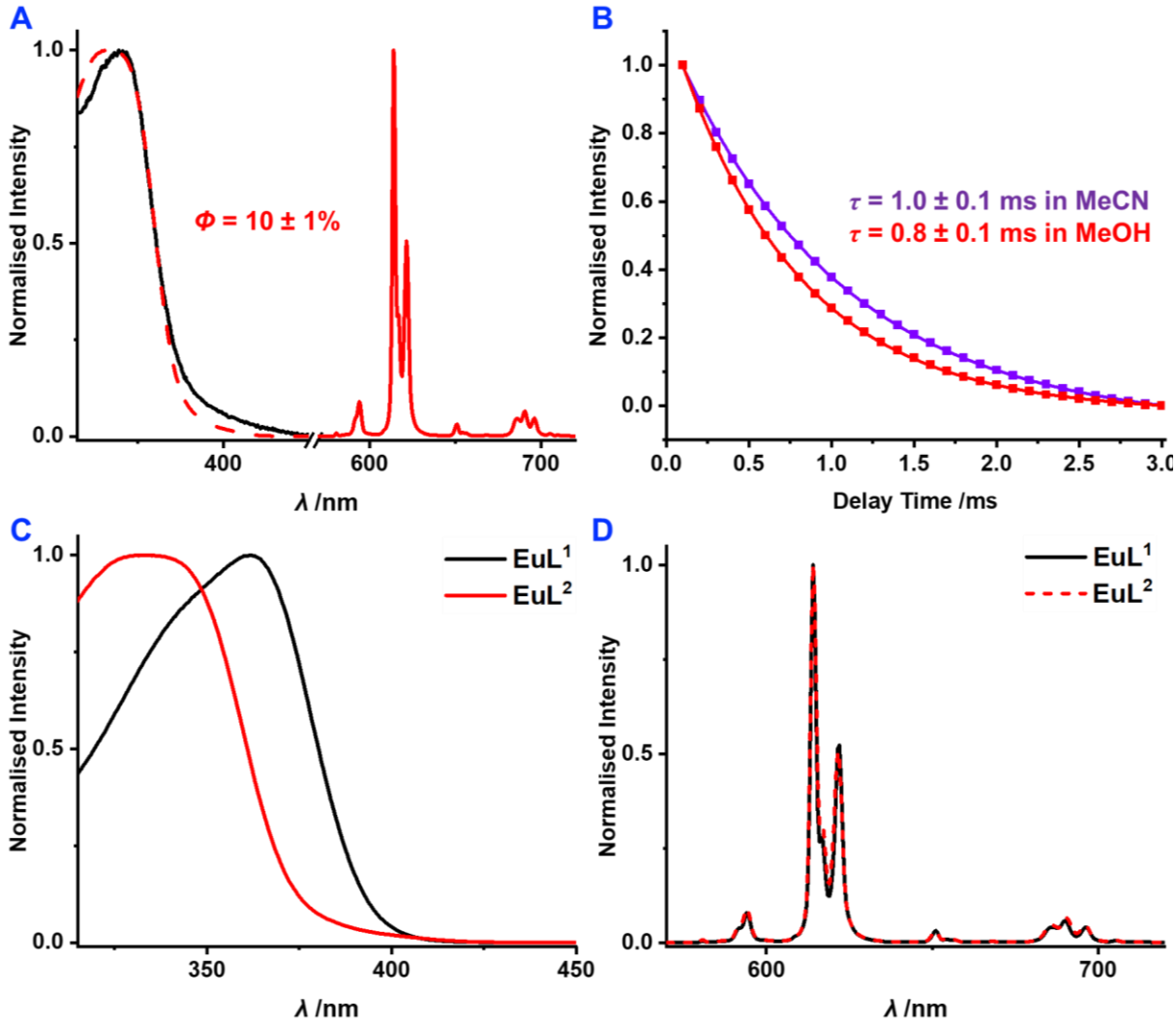

Figure 5.3. A: Normalised absorption (black), emission (solid red, λ_{exc} = 340 nm) and excitation (dashed red, λ_{em} = 614 nm) spectra of **EuL²** in MeCN with the measured Φ (absolute method) annotated; **B:** Lifetime plots of **EuL²** in MeCN and MeOH (0.1 abs solutions, λ_{exc} = 340 nm, λ_{em} = 614 nm); **C**: Normalised excitation spectra of **EuL¹** (black) and **EuL²** (red) in MeCN (λ_{em} = 614 nm); **D**: Normalised emission spectra of **EuL¹** (black) and **EuL²** (dashed red) in MeCN (λ_{exc} = 360 nm and 340 nm respectively).

From previous τ experiments it was evident that τ of the parent **EuL^1** significantly decreased in MeOH (but not in MeOD). The quenching was therefore attributed ICT stabilisation *via* H-bonding, promoting the thermally activated BET. In this study of **EuL^2**, τ in MeOH was recorded as 0.8 ± 0.1 ms, which was higher compared to 0.6 ± 0.1 ms for **EuL^1** (~33% increase) (Figure 5.3.B). This was attributed to destabilisation of the ICT by electron withdrawing nitro group, which increased the ICT - $^5D_0$ energy gap, which decreased the rate of BET and therefore increased τ in protic solvents. More specifically, the ICT state of the chromophore is likely to exist in a form of charge separated species with a negative charge localised on the electron-pulling pyridyl nitrogen and a positive charge on the electron-pushing aryl (Figure 5.4). Once a nitro group is attached to the aryl, it can withdraw electrons from the partially positive aryl ring (ICT state) *via* both induction and resonance, resulting in a possibility of a high-energy resonance form with two positive charges in proximity.

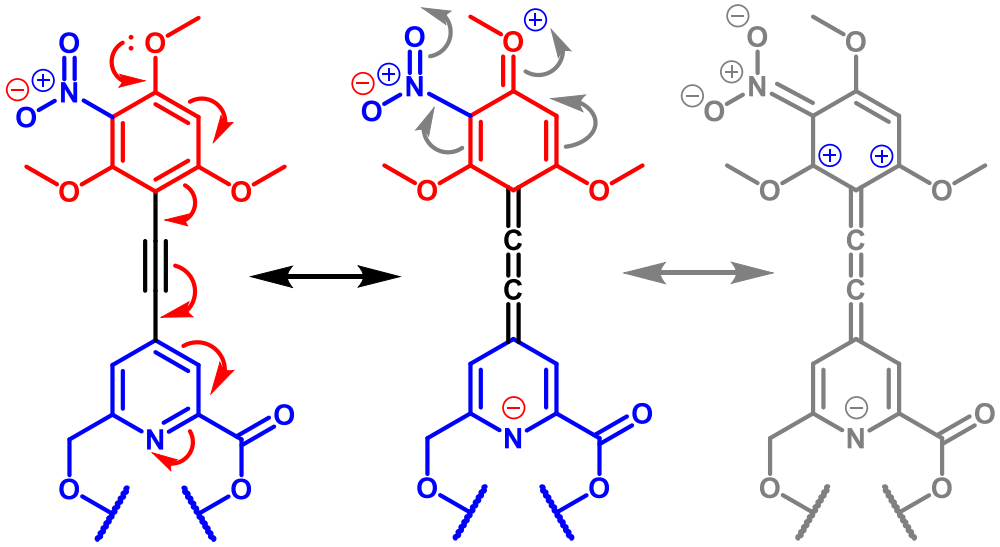

Figure 5.4: Potential resonance mechanism of the ICT state destabilisation by the nitro group.

The molar extinction coefficient (ε) of **EuL^2** could not be accurately determined due to its generally poor solubility in organic solvents. In order to estimate how it would compare to that of **EuL^1**, the ε of the **EuL^2** chromophore **L^2** was measured and compared to that of **L^1**. As a result, the introduction of the electron withdrawing nitro group at the aryl ring decreased the ε of **L^2** by around 40% (Figure 5.5 - left). This agreed with the previously mentioned effect of spatially separated electron rich (bearing HOMO) and electron depleted (bearing LUMO) regions on the transition dipole moment. In the case of **EuL^2**, the nitro group depletes the aryl from electrons resulting in a weaker dipole and hence lower ε (Figure 5.5 - right).

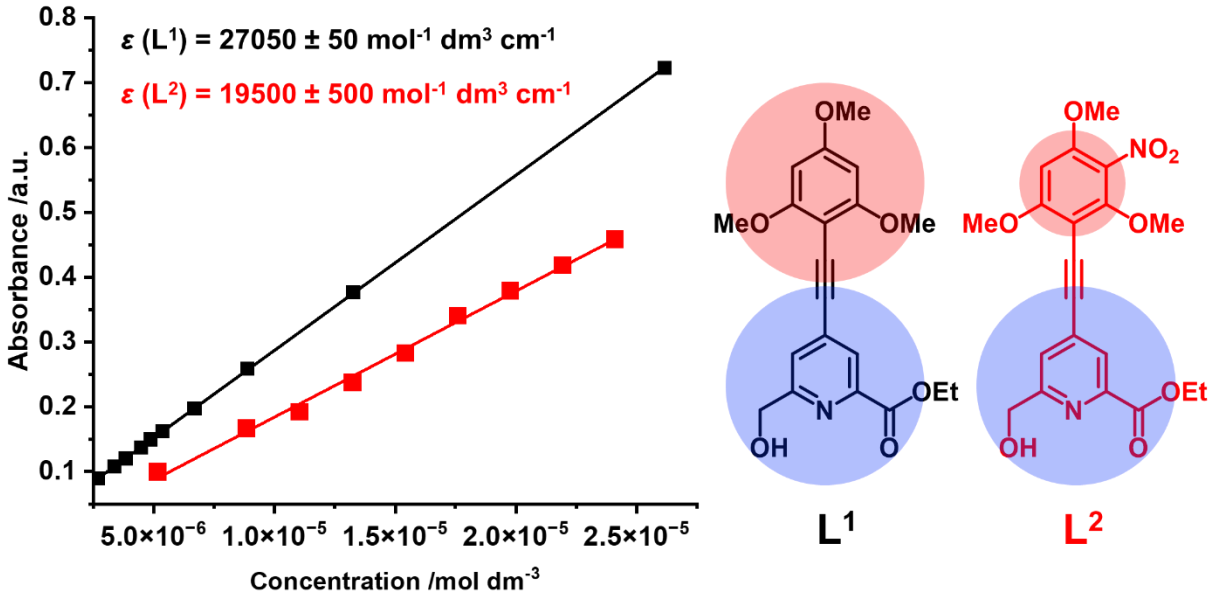

Figure 5.5: Dependence of **L¹** and **L²** absorbance on the concentration in MeCN (left); Structures of **L¹** and **L²** with the coloured circles representing the relative magnitudes of charge densities (right) (blue – electron depleted, red – electron rich regions).

The quenching effect could be directly related to the nitro group which was the only structural component that differed between **EuL²** and **EuL¹**. As discussed earlier, a number of different quenching pathways can occur during sensitisation. In this case, the most likely quenching type that can be attributed to the presence of a nitro group is vibrational relaxation *via* N-O stretching modes. These normally have the vibrational wavenumbers of 1600-1530 and ~1380-1310 cm^{-1} for the asymmetric and symmetric N-O modes in nitro compounds respectively.[99,100] Since the nitro group is in proximity to the HOMO of the chromophore, there is a high probability of the chromophores' excited state quenching *via* vibrational ET to the N-O stretching overtones. Since **EuL²** absorption maximum in MeCN is around 340 nm (29412 cm^{-1}), while the N-O bond dissociation energy is around 200-250 kJ mol^{-1} (~17000-21000 cm^{-1}), which is significantly lower than 29412 cm^{-1}), it is impossible to relax the chromophore back to the ground state *via* N-O stretching alone. However, there is a possibility of a cascade vibrational ET from the N-O vibrational levels into the C≡N stretching in MeCN. The energies of the N-O vibrational levels can be compared to the vibrational overtones of the C≡N stretching (vibrational wavenumber of 2240-2260 cm^{-1}) to determine whether there is an energy match required for the effective vibrational ET (Table 5.1). As evident form the calculations, there are multiple energy matches between the vibrational transitions of N-O and C≡N stretching, suggesting an effective vibrational relaxation pathway.

Table 5.4: The energy match between the N-O and C≡N vibrational overtones calculated using 1530 and 2240 cm^{-1} vibrational wavenumbers and 0.0074 and 0.0063 anharmonicity constants respectively.[101]

N-O vibrational overtone energy /cm^{-1}		C≡N vibrational overtone energy /cm^{-1}		% energy match
$v_6 \rightarrow v_0$	8704	$v_0 \rightarrow v_4$	8678	99.7%
$v_7 \rightarrow v_0$	10076	$v_0 \rightarrow v_5$	10777	93.5%
$v_9 \rightarrow v_0$	12751	$v_0 \rightarrow v_6$	12847	99.3%

A similar process would be also observed in other solvents that can produce a good energy match of the vibrational overtones to behave as an efficient energy sink. A recent example demonstrated similar quenching properties of the nitro group that are attributed to its electron withdrawing nature which destabilised the excited state by electron transfer.[102]

V.1.5. CPL properties of EuL^2

An attempt to separate the *Δ* and *Λ* enantiomers of the **EuL²** using the same chiral HPLC method as for the **EuL¹** using the *CHIRALPAK IE* column was successful and produced similar retention times and the same elution order for the enantiomers (Figure 5.6). The experiment was then repeated with the *CHIRALPAK IB-N5* column but showed no signs of separation.

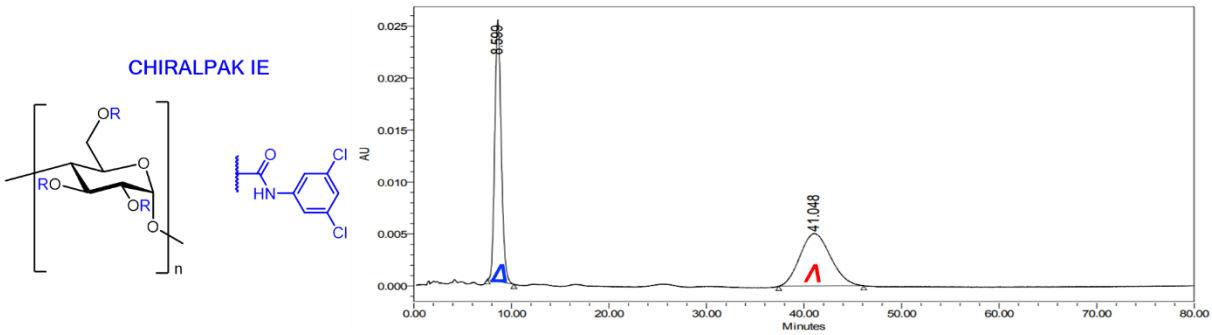

Figure 5.6: The structure of the *CHIRALPAK IE* chiral HPLC column stationary phase (left) and chiral HPLC AC (at 340 nm) for the separation of the **EuL²** enantiomers (solvent: EtOH/MeOH/TEA/TFA at 50/50/0.5/0.3, injection: 20 µL of ~0.5 mg ml^{-1} in MeCN, 2 ml min^{-1}) (right). Performed by Dr. Aileen Congreve.

As expected, there was no significant difference between the CPL spectra (Figure 5.7.A and C) and g_{lum} plots (Figure 5.7.B and D) of the enantiomers of **EuL²** and **EuL¹**. It was particularly interesting that even the 'hypersensitive' $\Delta J = 2$ emission manifolds of the two materials did not produce a significant difference in spectral shape and relative intensity of the bands.

The maximum g_{lum} was recorded as +0.310 (at 601 nm) for ***Δ*-EuL²** and -0.326 (at 601 nm) for ***Λ*-EuL₂** that were similar to ±0.290 for **EuL¹** (at 601 nm). The highest g_{lum} values recorded for the $\Delta J = 2$ were -0.074 and +0.067 (both at 607.5 nm) for the ***Δ*-** and ***Λ*-EuL²** respectively, which were similar to ±0.071 for **EuL¹** (at 607.5 nm).

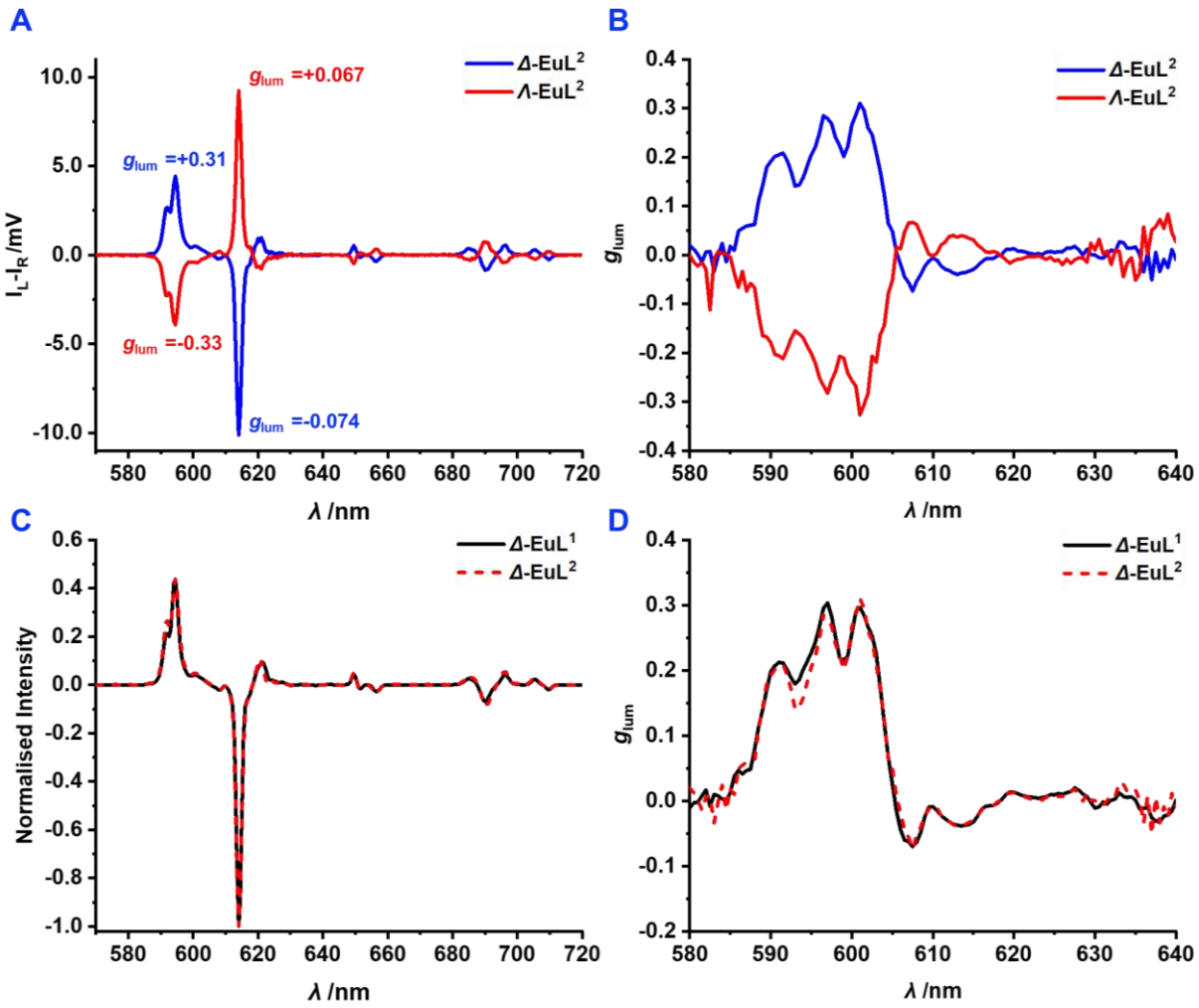

Figure 5.7. A: CPL spectra of **Δ-EuL²** (blue) and **Λ-EuL²** (red) in MeCN (λ_{exc} = 340 nm, 5 averages); **B**: g_{lum} plots for the CPL spectra in **A** (ΔJ = 1 and 2 only)**; C:** The normalised (to the intensity at 614 nm) CPL spectra of the **Δ** enantiomers of **EuL¹** (solid black) and **EuL²** (dashed red) in MeCN (λ_{exc} = 360 nm for **EuL¹** and 340 nm for **EuL²**, 5 averages); **D**: g_{lum} plots for the CPL spectra in **C** (ΔJ = 1 and 2 only).

Since ε could not be accurately determined, the *CPB* for the **EuL²** was not calculated. However, it was expected to be at least 6 times lower than that of **EuL¹** due to 4.5 times lower Φ and ~40% lower ε of each of the three **L²** chromophores. Although photophysical properties of **EuL²** were not planned to be practically useful, its lower CPL performance, when compared to that of **EuL¹** could be confirmed. This serves as an additional example of the superiority of *CPB* over g_{lum}, which is identical for both materials.

This photophysical study of **EuL²** evidenced how structural modifications on the far end from the europium(III) centre did not result in perturbation of the local symmetry that would affect the CF splitting of the ^7F_J states, and, as a result, the CPL spectral band shape and relative intensity remained unaffected. This suggested that **EuL²ᵃ**, **EuL²ᵇ** and their functionalised versions would unlikely demonstrate any significant changes in CPL properties.

V.1.6. Investigation of the proposed functional group interconversion reactions

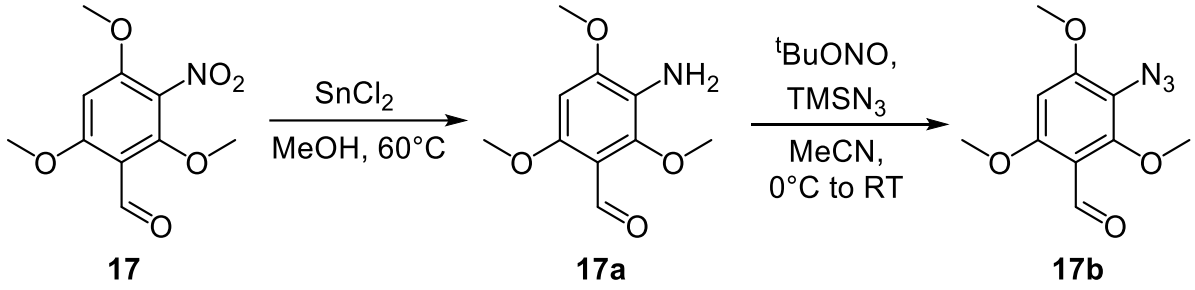

Scheme 5.5: The proposed reaction sequence for the functional group interconversion test reactions.

Prior to functional group conversion on **EuL²**, the reaction conditions were tested on the relevant chromophore precursors on the analytical scale and hence analysed using LCMS. The first reaction was a reduction of the nitro group on **17** to produce an amine **17a**. As previously mentioned, the presence of the alkyne functionality in **EuL²** introduced limitations on the choice of the reduction method (section V.1.2). Therefore, an adapted literature procedure was used to yield amine using tin(II) chloride in MeOH at 60°C (Scheme 5.5).[96,97] At the start, 5 equivalents of tin(II) chloride were added to 1 equivalent of **17** and stirred overnight (20 hrs) at 60°C under argon. After 20 hours, only ~50% conversion was achieved (Figure 5.8 – left). The reaction was further monitored for additional 4 hours with no further conversion observed. Therefore, an additional 5 equivalents of tin(II) chloride were added, and the reaction was stirred for another 20 hours which resulted in full conversion (Figure 5.8 – right). It was proposed that the need for a large excess of tin(II) chloride was due to a relatively low reaction rate associated with steric hindrance at the reaction site generated by the ortho-methoxy groups.

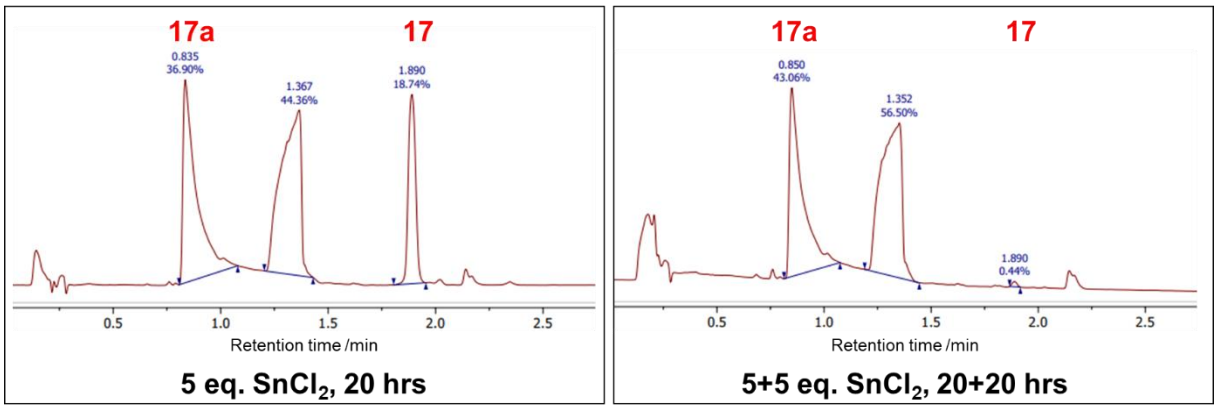

Figure 5.8: LCMS (Method E, Section VI.2.) AC (210-400 nm) of the **17** to **17a** reaction mixture after 20 hours with 5 equivalents of tin(II) chloride (left) and after an additional 20 hours and 5 equivalents (right).

Once completed, the reaction mixture was concentrated under reduced pressure and poured over ice, where the resulting acidic solution was neutralised using 1 M sodium hydroxide (NaOH). It was essential to neutralise the mixture promptly to avoid any hydration of the alkyne under acidic conditions. The product was then extracted with EtOAc followed by an aqueous wash. This step was also repeated with DCM since it was expected to be a better solvent for the **EuL**^{2a} than EtOAc.

The next reaction step targeted conversion of the amine **17a** to the azide **17b**. The recent literature suggested the use of tert-butyl nitrite with trimethyl silyl azide in MeCN at rt (Scheme 5.5).[98] Initially, the exact literature procedure was applied to **17a** (1.5 eq. of tert-butyl nitrite and 1.2 eq. of trimethyl silyl azide) but resulted in no conversion after the suggested 3 hours. Similarly to the previous step, the sterically hindered approach to the reaction site was expected to significantly reduce the reaction rate. Therefore, the mixture was left stirring for over 20 hours to produce a small amount of product. Another 5 equivalents of each reagent were added to push the reaction forward, resulting in no further conversion after 20 hours (Figure 5.9).

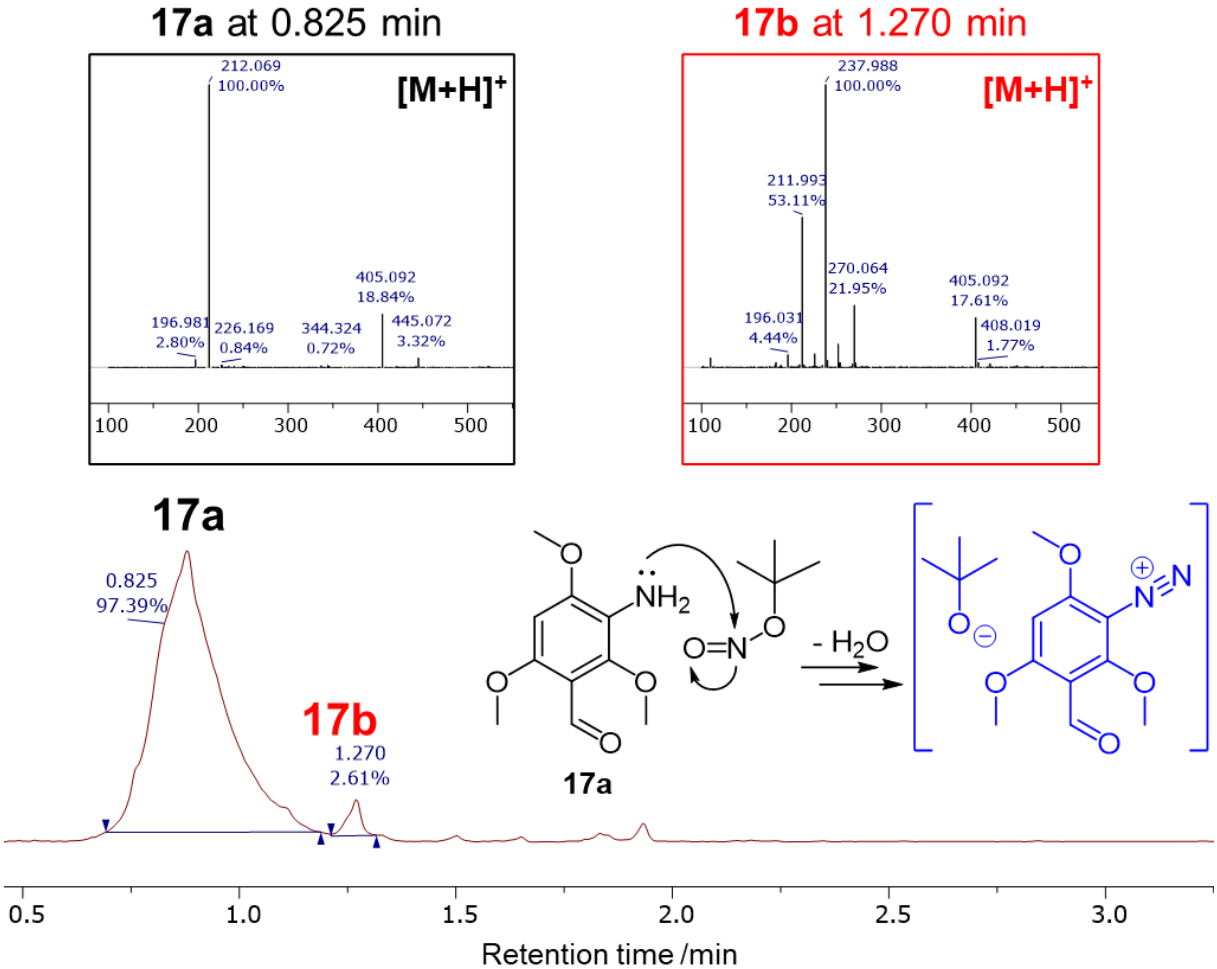

Figure 5.9: LCMS (Method E, Section VI.2) AC (210-400 nm) of the **17a** to **17b** reaction mixture with the mass spectrum (MS) inserts recorded for the eluted materials after the total of 43 hours and ~6 equivalents of the reagents added and the proposed first mechanistic step of the **17a** to **17b** reaction mechanism.

Although the mechanism for this reaction was not reported in the original literature, it was assumed that the first mechanistic step would involve a nucleophilic attack of the tert-butyl nitrite nitrogen by the amine nitrogen to form a diazonium salt (Figure 5.9 - blue) which can be then substituted by the azide. The diazonium formation is likely to be a rate limiting step which depends on the electronic properties of the substrate. In the case of **17a**, the reaction rate depends on the nucleophilicity of the amine that is affected by the nearby functional groups. Although not conjugated with the amine, the aldehyde substituent is electron-withdrawing with respet to the aryl ring. This results in a decrease of the amine nucleophilicity and therefore the reaction rate reduction.

To confirm this, the amine to azide conversion was repeated with a more electron rich **18a**, where the electron withdrawing aldehyde was transformed into a dibromo alkene to restore the amine nucleophilicity. Therefore, the reaction conditions for the nitro to amino conversion were successfully applied to convert **18** into **18a** (Figure 5.10) using the same method as for the reduction of **17** but only 5 equivalents of tin (II) chloride.

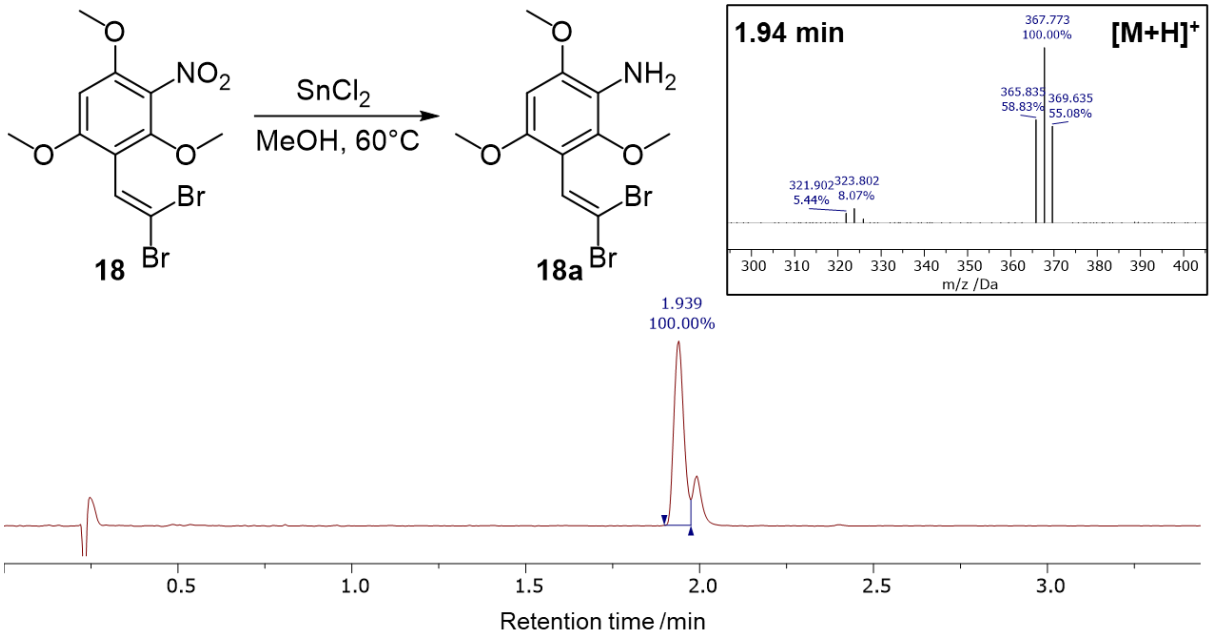

Figure 5.10: LCMS (Method E, Section VI.2.) AC (210-400 nm) of the **18** to **18a** reaction mixture (after purification) with the reaction scheme and the MS insert at 1.939 min.

18a was then reacted with 5 equivalents of tert-butyl nitrite and trimethyl silyl azide to give **18b** after stirring under argon overnight (Figure 5.11). Since the aryl rings of the **EuL^2** sensitising chromophores did not contain electron withdrawing substituents, both reactions of functional group interconversions were expected to work for the **EuL^2** to **EuL^{2a}** to **EuL^{2b}** transformations.

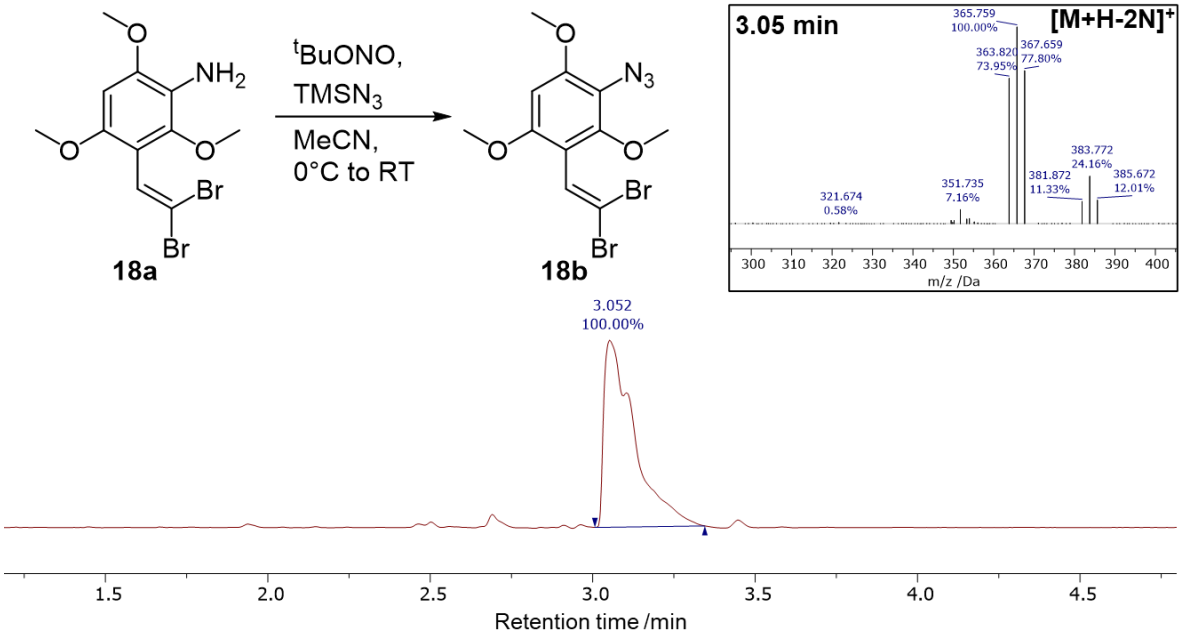

Figure 5.11: LCMS (Method E, Section VI.2.) AC (210-400 nm) of **2a** to **2b** reaction mixture with the reaction scheme and the MS insert at 3.05 min.

The next reaction was aimed on testing standard 'click' chemistry conditions with the azide **18b** (Figure 5.12). Trimethyl silyl acetylene was chosen as a simple substrate to be added to **18b** *via* copper(I) catalysed cycloaddition. Sodium ascorbate was also added to act as reducing agent to maintain low oxidation state of copper. The reaction was subjected to LCMS after 1 hour, which revealed the formation of the triazole-containing **18c**. This confirmed the susceptibility of the sterically hindered azide towards click-chemistry, suggesting the possibility of the complex-stage functionalisation of **EuL**^{2b}.

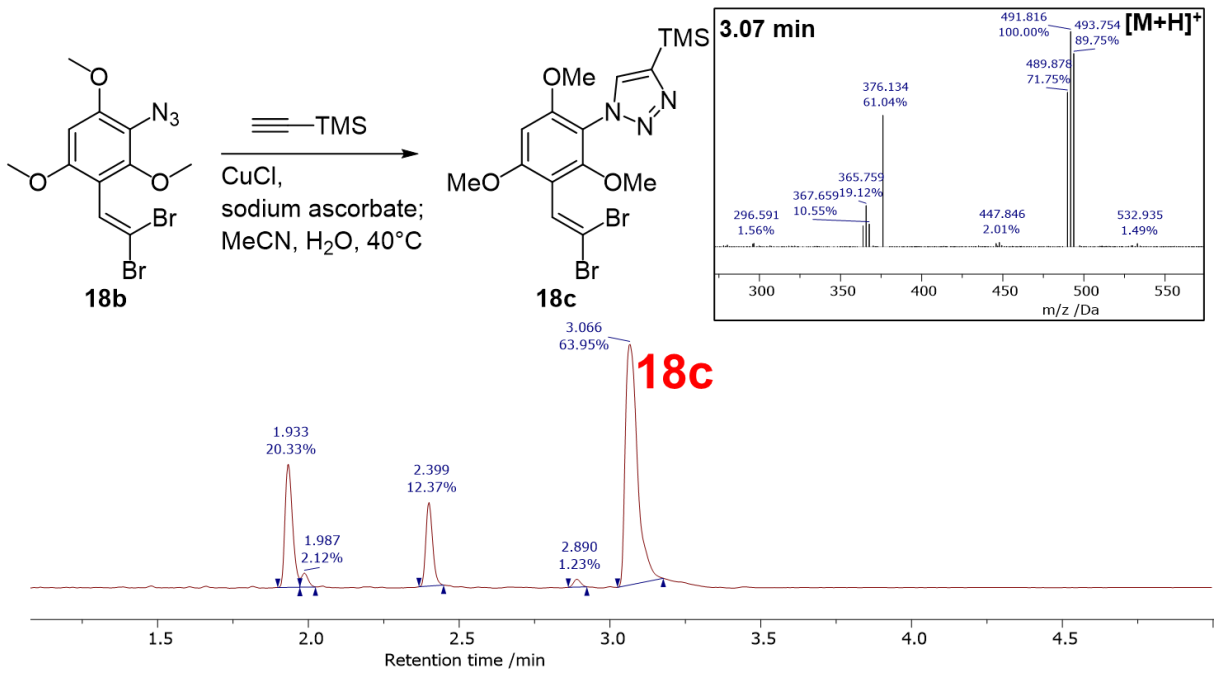

Figure 5.12: LCMS (Method E, Section VI.2.) AC (210-400 nm) of **18b** to **18c** reaction mixture after 1 hour with the reaction scheme and the MS insert at 3.07 min.

V.1.7. Preparation of EuL^{2a} *via* late-stage functional group interconversion of EuL^{2}

Once the nitro to amino to azido interconversion reaction conditions were tested on the chromophore precursors, they could be further tested on **EuL^{2}**. For the nitro to amine conversion reaction, the solvent system was changed from isocratic MeOH to a DCM/MeOH mixture due to low solubility. Once **EuL^{2}** was suspended in MeOH, DCM was added dropwise until the solution became clear. 30 equivalents of tin(II) chloride were then added (10 eq. for each nitro group) and the solution was stirred at 40 °C overnight. As a result, a mixture of **EuL^{2a}** and the intermediates containing just one (**EuL$^{2a'}$**) and two (**EuL$^{2a''}$**) amino groups were obtained (Figure 5.13).

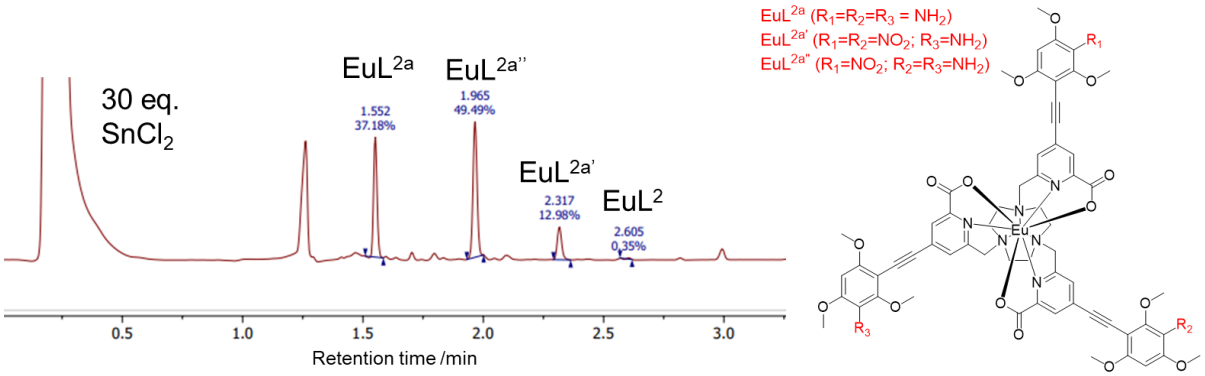

Figure 5.13: LCMS (Method E, Section VI.2.) AC (210-400 nm) of **EuL^{2} to EuL^{2a}** reaction mixture after 20 hours with 30 eq. of tin(II) chloride (left) and the structures of the reaction intermediates (right).

It was noted that upon irradiation with a 365 nm light the intensity of red europium(III) emission gradually decreased as the reaction proceeded. A significant drop in intensity was observed during the first 3 minutes after tin(II) chloride addition and then remained constant. Since the emission intensity did not drop immediately after tin(II) chloride was added (and instantly dissolved), the quenching effect was not attributed to tin cations. Instead, it could be a result of the reaction progression, where the electron-withdrawing nitro groups were converted into electron-donating amines, resulting in ICT stabilisation, promoting BET. Therefore, it was hypothesised that the reaction rate is strongly dependent on the concentration of tin(II) chloride where the rate is the highest once tin(II) chloride is added, and then sharply decreases.

To test this, the reaction was repeated with 30 equivalents of tin(II) chloride. The reaction mixture was analysed by LCMS after 10 minutes and then was left overnight to be analysed again. As a result, there was no difference in the composition of the reaction mixture after 10 minutes and 20 hours. This suggested a strategy to bring the reaction to completion by adding the tin(II) chloride every 10 minutes portion-wise until no emission is observed. Overall, it required ~170 equivalents of tin(II) chloride to reduce all three nitro groups of **EuL^{2}** (Figure 5.14).

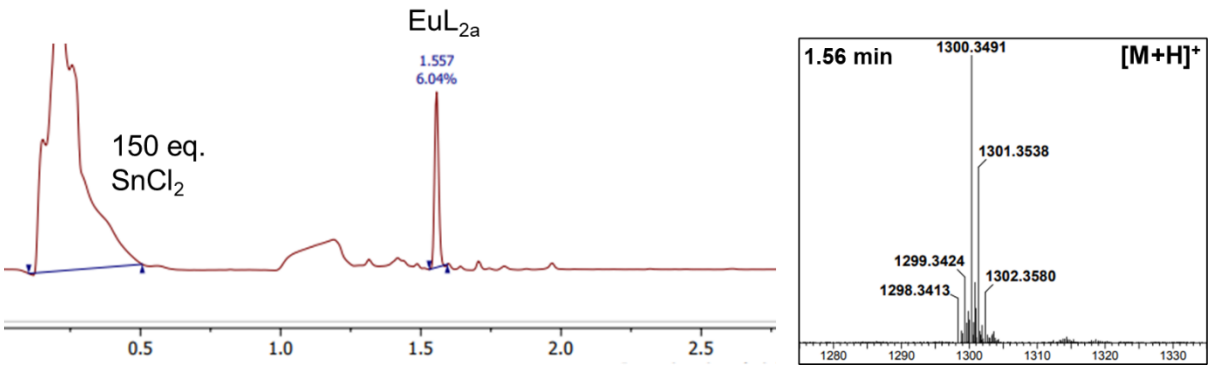

Figure 5.14: LCMS (Method E, Section VI.2.) AC (210-400 nm) for the **EuL^2 to EuL^{2a}** reaction mixture after 10 minutes with 150 eq. of tin(II) chloride and the accurate MS insert at 1.557 min.

This significantly complicated the purification procedure since tin(II) chloride and related tin containing side products had similar solubility with **EuL^{2a}** in alcohols and MeCN. Preparatory scale HPLC was not feasible due to rapid precipitation of tin byproducts in water, which complicated the use of a solvent gradient method. In addition, once water is added to the crude mixture, it would react with tin(II) chloride to form HCl, leading to a pH = 0 which was incompatible with the alkyne groups of **EuL^2**. Apart from that, neutralisation of HCl with sodium hydroxide could lead to decomposition of the complex near the endpoint where europium could be removed from the macrocyclic ligand by complexation to hydroxide ions. During one of the neutralisation attempts performed under 365 nm UV irradiation, the endpoint was unintentionally passed by adding too much base to result in pH = 10. At that point, europium(III) red emission was no longer observed, and the attempt to recover the emission by carefully bringing the pH back to neutral and then slightly acidic was not successful. Nevertheless, even if neutralisation of the aqueous suspension without **EuL^{2a}** decomposition succeeded by using, for instance, a weaker base to minimise the possibility of hydroxide coordination, the following extraction step would fail since **EuL^{2a}** was insoluble in water immiscible DCM, EtOAc and diethyl ether (confirmed by LCMS). An attempt to purify **EuL^{2a}** using normal-phase column chromatography was also unsuccessful since a solvent system, which would efficiently move the bulky complex containing three hydrogen bond accepting amines through silica, was not found.

A modification of the method, aimed at reducing the tin to product ratio, where **EuL^2** was drop-wise added into a concentrated solution of tin(II) chloride (50 eq.) over the period of 20 hours did not result in full conversion.

Standard nitro group conditions using a combination of a metal and strong acid were only tested on the terminal alkyne containing ‘top’ of the chromophore, resulting in formation of a product with a mass corresponding to a hydrated alkyne. The same was observed when a weak acetic acid or ammonium chloride were used instead of HCl. Therefore, these conditions were not further tested on the complex.

At that point, it was decided to attempt the nitro group reduction at the stage of the chromophore since the normal extraction method with DCM or EtOAc that gave pure products **17a** and **18a** would not be yet limited by solubility. To avoid protection and then deprotection of the amine using such functional group as tert-butyloxycarbonyl (Boc) or fluorenylmethyloxycarbonyl (Fmoc), it was decided to produce the amine at the latest possible stage of the chromophore **20**. Therefore, **20** was exposed to the same conditions as for the synthesis of **17a** and **17a**, resulting in nearly complete conversion after reacting with 10 equivalents of tin(II) chloride overnight to give **20a** (Figure 5.15).

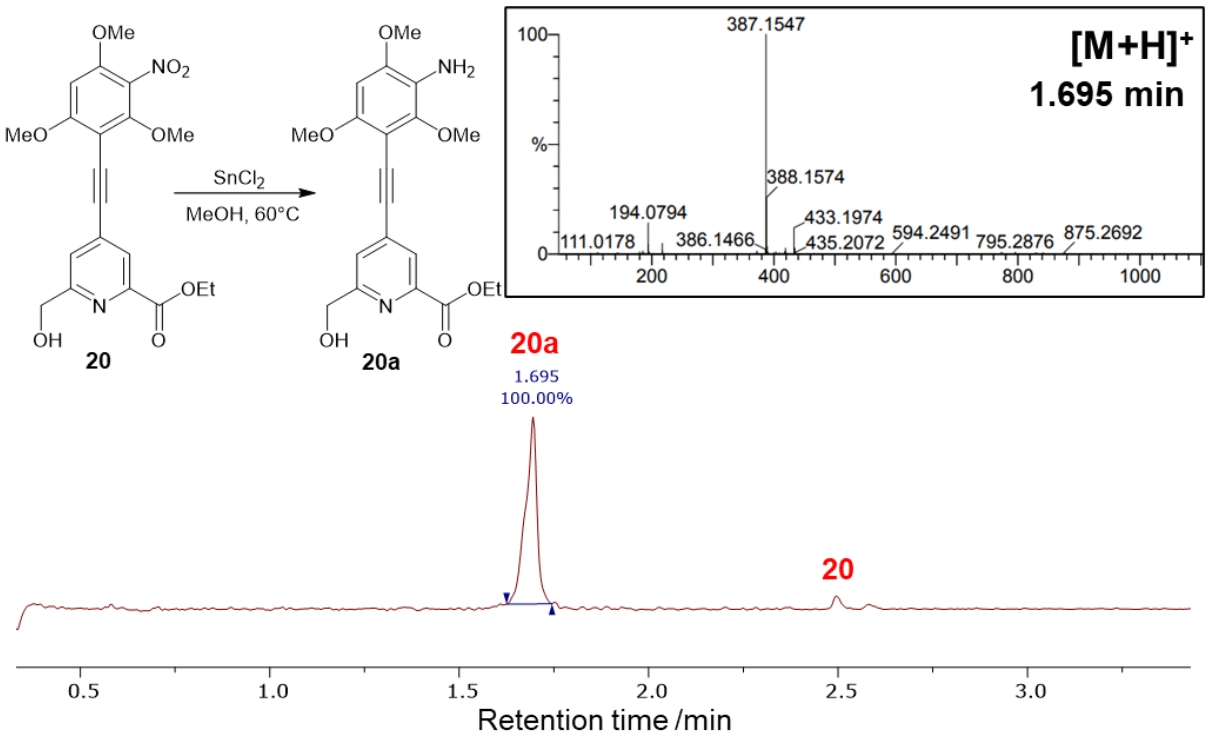

Figure 5.15: LCMS (Method E, Section VI.2.) AC (210-400 nm) of **20** to **20a** reaction mixture after 20 hours with 10 eq. of tin(II) chloride with the reaction scheme and the MS insert at 1.695 min.

If done earlier in the reaction sequence, the free amine would complicate the purification of the chromophores' 'top' precursors by normal-phase chromatography. Producing the amine at the stage of the 'three-armed' ligand containing three chromophores would generate the same incomplete conversion and solubility problems as with **EuL^{2a}**. Deprotection of the amine from Boc would require acidic conditions which are not compatible with the alkyne, while Fmoc would get cleaved under basic conditions, for instance, in the Sonogashira reaction step to make the chromophore.

Unfortunately, the amine was sensitive towards the following mesylation step. As the reaction proceeded, the amine on **21a** reacted with the methanesulfonic anhydride to produce methanesulfonamide (Figure 5.16). At this stage, it would be nearly impossible to restore the amide due to a very strong sulfonamide bond N-S that requires very harsh reductive or acidic conditions.[103,104] To mitigate this, nosylation could be used instead to result in a p-nitrobenzenesulfonamide with a more labile N-S group that can be cleaved using a thiolate *via* nucleophilic aromatic substitution releasing SO_2.[104,105] This would require further test reactions and introduce additional reaction steps as well as potentially challenging purification of the free amine.

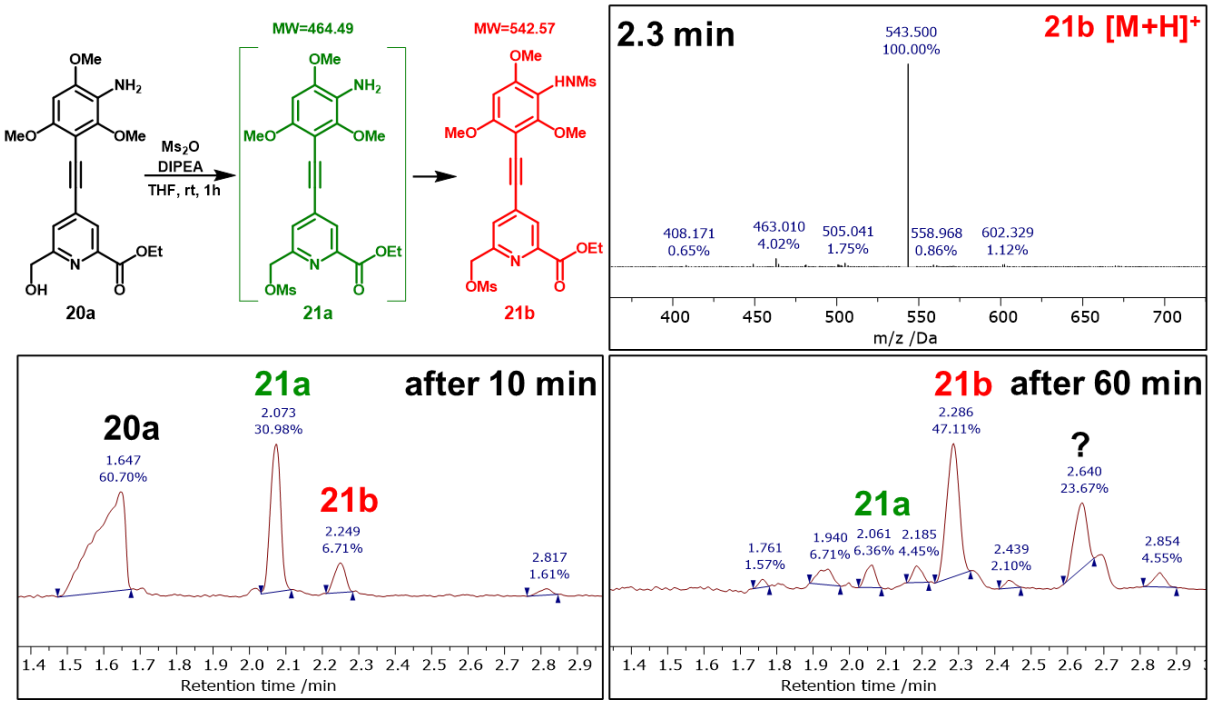

Figure 5.16: 20a to **21a** reaction scheme with the undesired **21b** product shown (top left); LCMS (Method E, Section VI.2.) AC (210-400 nm) for the **20a** mesylation reaction mixture after 10 minutes (bottom left) and 60 minutes (bottom right) with a MS of the major **21b** product shown (top right).

As a last resort, standard nitro group reduction conditions using a combination of a metal and strong acid were tested on the terminal alkyne containing 'top' of the chromophore, resulting in formation of a product with a mass corresponding to a hydrated alkyne. The same was observed when a weak acetic acid was used instead of HCl. It could still be possible to produce **EuL^{2b}** by converting the **20a** amine into azide which would remain intact during the following reaction steps towards the complex. This was not further explored since the position of the azide and therefore the potential triazole-linked functionalities would affect the photophysical properties of the resulting chromophore. Although the click-chemistry test reaction worked successfully with trimethylsilylacetylene, it could be challenging for larger functional groups to approach the sterically hindered azide due to the two ortho- methoxy groups. At this point, it was decided to suspend further investigation into the synthesis of **EuL^{2a}** and **EuL^{2b}** in favour of a novel structurally improved target **EuL^{3}** complex.

V.2. Structurally improved novel EuL^3 for complex-stage functionalisation

V.2.1. Introduction to the structural modifications of EuL^3

From the photophysical study of **EuL^2** it was established that the introduction of a functional group directly on the aryl ring of the chromophore negatively impacted its photophysical properties. In the case of **EuL^2**, the nitro group resulted in a significant reduction in Φ and therefore brightness that would make the material less practically useful. Although not prepared, **EuL^{2a}** and **EuL^{2b}** derivatives could also produce lower Φ as well as τ values due to the electron donating nitrogen lone pair that would lower the ICT state energy and therefore promote BET. Another problem with the **EuL^2** design was related to the steric hindrance arising from the trimethoxy substitution of the aryl ring which could not be removed due to a necessity to maintain the optimal excitation wavelength (near 365 nm). This could pose a problem when bulky functional substituents such as peptide sequences for cell organelle targeting need to be introduced. In order to address both issues, a novel **EuL^3** complex was proposed, where the functionalisation site was separated from the chromophore by a moderately long alkyl chain originating from the alkoxy oxygen (Scheme 5.5). This would maintain high electron density of the aryl ring, structurally separate the variable functional group from the areas of HOMOs and LUMOs while also mitigating the steric hindrance affecting the complex-stage functionalisation reactions.

Similarly to **EuL^{2b}**, **EuL^3** would contain the azide functionality to perform click-chemistry cycloadditions. If needed, it could also be reduced to a primary amine using Staudinger reaction at the complex stage (Scheme 5.5). Similarly to **EuL^{2a}**, **EuL^{3a}** would allow to expand the application scope of the complex by introducing compatibility with carboxylic acid bearing moieties.

There were two positions available for the addition of an alkyl chain to the aryl component of the chromophore – either ortho or para oxygen (with respect to the alkyne). Para position was preferred as it was the most distant from the europium(III) centre and the alkyne than ortho position, which could allow intramolecular cyclisation under click-chemistry conditions. The alkyl chain was chosen to be attached using a nucleophilic substitution reaction between a phenol and dibromo alkane. The second bromine was needed for azide substitution on the other end of the chain. Due to a relatively high stability of the azide, it could be introduced at the early stage of the chromophore synthesis and remain intact during the following reactions.

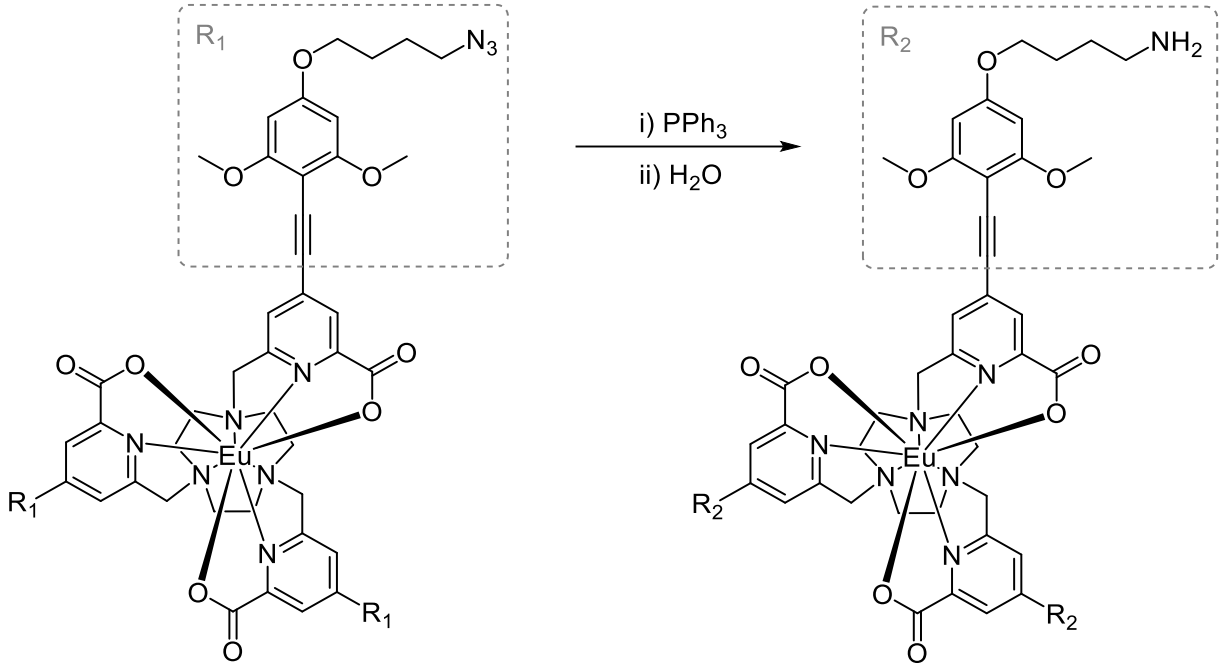

Scheme 5.5: The proposed reaction sequence for a complex-stage transformation of **EuL^3** to **EuL^{3a}** *via* Staudinger reduction.

V.2.2. Development of the synthetic procedure for EuL^3

The starting material for the following transformation was commercially available 3,5 – dimethoxyphenol that was formylated using a Vilsmeier-Haack reaction (Scheme 5.6). The method was adapted from a large-scale synthesis using a combination of phosphorus oxychloride and DMF.[106] This reaction was kinetically controlled to minimise the formation of the 2-hydroxy-4,6-dimethoxybenzaldehyde, which could conveniently be removed by a simple recrystallisation of **23** from ethanol.

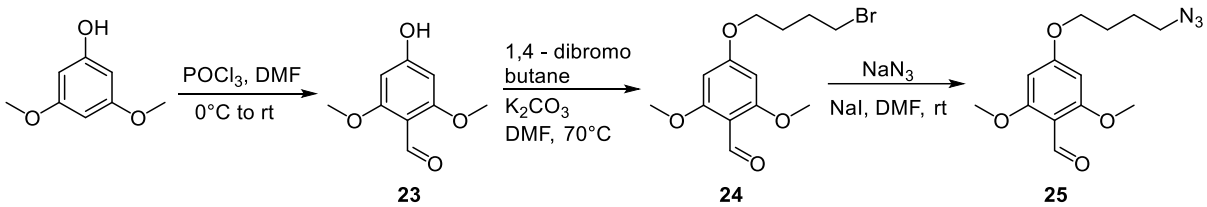

Scheme 5.6: The reaction sequence to introduce an alkyl azide on the precursor of the chromophore 'top'.

Since it was not obvious whether the free alcohol would affect the following two-step Corey-Fuchs transformation, it was decided to functionalise the alcohol with the alkyl azide at this stage. To accomplish this, **23** was dropwise added to a solution of 1,4-dibromobutane and potassium carbonate in DMF at 70°C. This was necessary to prevent double substitution product resulting from two phenols attached to each end of a single alkyne chain by substitution of both bromines. As a result, **24** containing an alkyl chain with a terminal bromine that was substituted with an azide in the next step to give **25**. In this case, the reaction was

accelerated using iodide ions which, when replaced bromine on the alkyl chain, created a better leaving group which increased the reaction rate.

Once the alcohol functionalisation was complete, the standard two-step Corey-Fuchs transformation was performed on **25** (Scheme 5.7). The first step did not work as well as it did with 2,4,6-trimethoxybenzaldehyde. The reaction proceeded slowly and required very high concentration of the Wittig reagent provided by an excess of the tetrabromomethane (2 eq.) and triphenylphosphine (4 eq.) as well as minimal solvent volume. Only ~50% conversion was achieved after stirring the solution overnight with no further progress made during additional 24 hours. Therefore, another 4 eq. of triphenylphosphine and 2 eq. of carbon tetrabromide were added and the solution was stirred for additional 3 hours to result in complete conversion of **25** into **26**, which agreed with strong dependence of the reaction rate on concentration of the starting material.

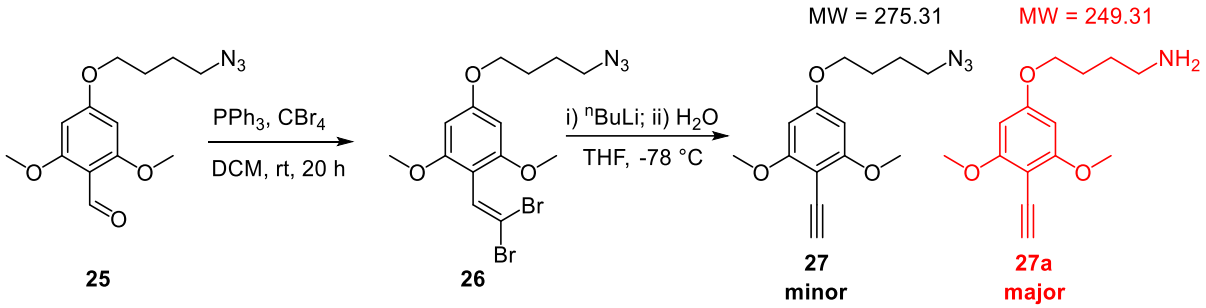

Scheme 5.7: The reaction sequence for the 2-step Corey-Fuchs transformation of **25**.

The next step aimed at transforming the dibromoalkene **26** into a terminal alkyne **27**; however, it gave a product with an incorrect mass which instead corresponded to that of **27a** (Figure 5.17). The mass corresponding to **27** was not observed from the LCMS of the crude sample. To the knowledge of author, the method of azide reduction to amine using n-butyl lithium was not reported in literature, whereas other reduction methods such as using sodium borohydride or lithium aluminium hydride were common.

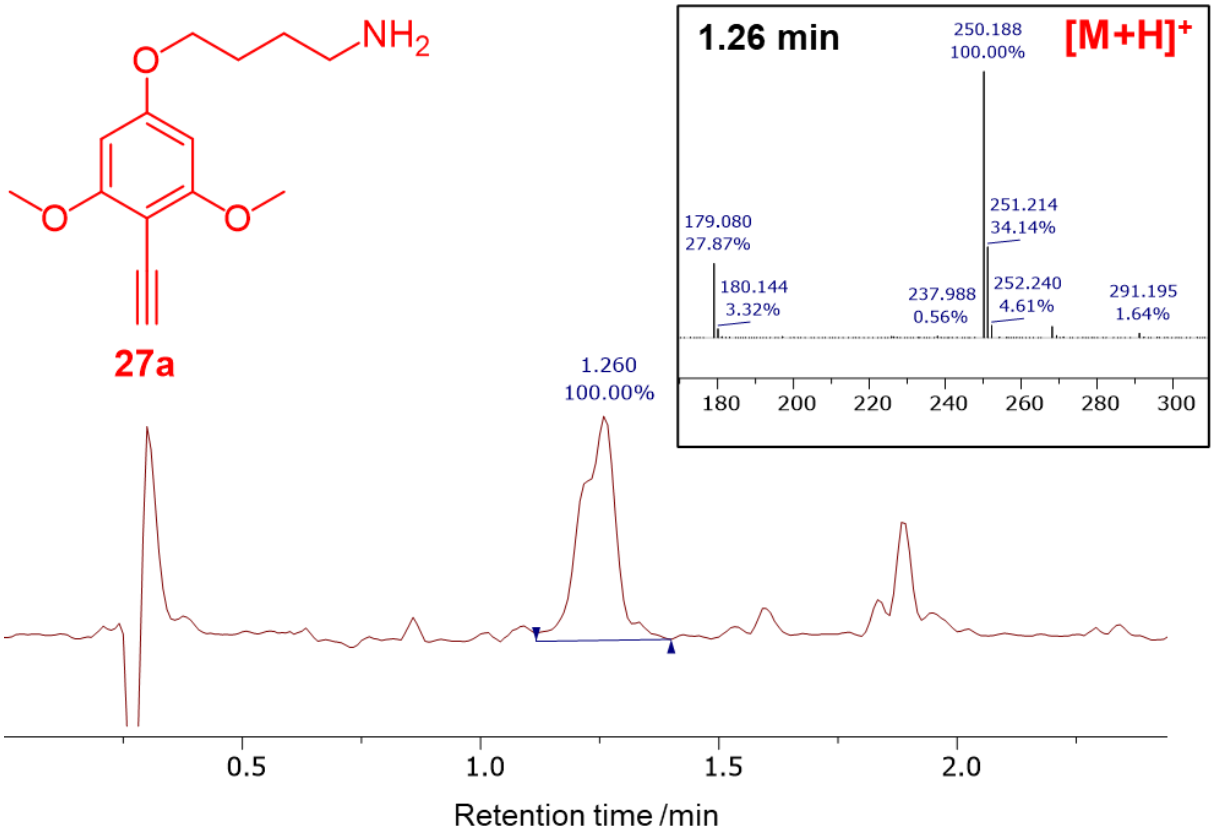

Figure 5.17: LCMS (Method E, Section VI.2.) AC (210-400 nm) of **26** to **27** reaction mixture with the MS insert at 1.260 min corresponding to the major product **27a**.

In order to confirm the efficacy of the new azide reduction method, the experiment would need to be repeated on a larger scale followed by purification of **27a** to confirm the structure by NMR. Instead, the synthesis of **27** was prioritised and, an alternative reaction sequence was investigated to avoid the exposure of the azide to n-butyl lithium.

The alternative reaction sequence would introduce the azide after the Corey-Fuchs transformation. Therefore, it was performed on **23** to give **28** in the first step (Scheme 5.8).

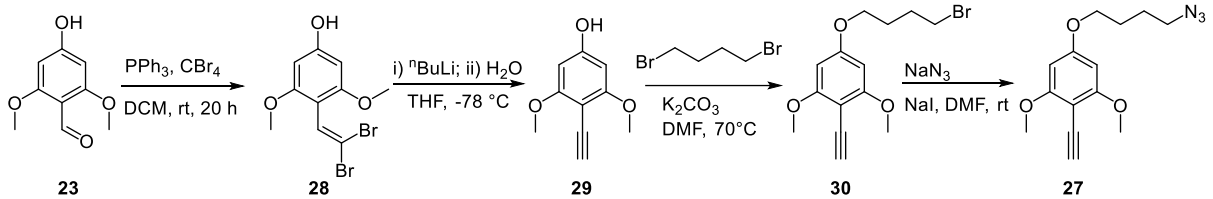

Scheme 5.8: The reaction sequence for the alkyl azide functionalised 'top' of the chromophore.

Substitution of the hydroxy group with bromine was not expected since the potential Appel reaction was not expected to work for halogenation of phenols. The yield of this transformation remained relatively low (15%) which was also the case in **26**. In the synthesis of **26**, the yield could be low due to abstraction of triphenyl phosphine by the azide, which is the first mechanistic steps in Staudinger reaction (Scheme 5.9 - top). A similar process could occur when preparing **28**, which is the first step of Appel reaction (Scheme 5.9 - bottom).

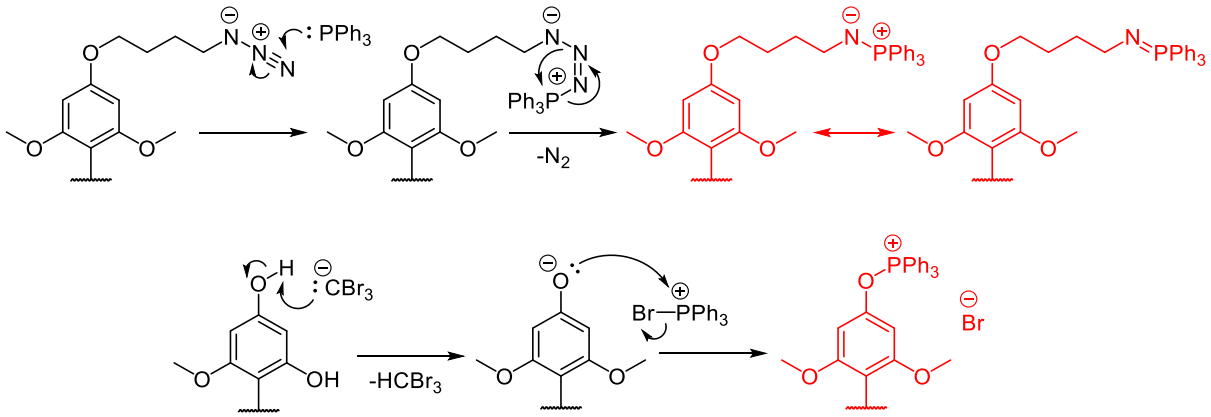

Scheme 5.9: Two possible side-processes of the first step of Corey-Fuchs transformation that could affect the yield of the reactions of **25** to give **26** (top) and **23** to give **28** (bottom).

Both processes could reduce the concentration of 'free' triphenylphosphine in the mixture, resulting in a slower rate of product formation. In addition, they could lead to irreversible formation of side products as well as reduce the efficiency of purification by chromatography (simultaneous elution of the product and impurities), leading to a low yield. Therefore, it was hypothesised that protecting the alcohol group to prevent it from interacting with the reagents would lead to a substantial yield increase. To test this, **23** was protected with a triisopropylsilane (TIPS) group and subjected to the first step of the Corey-Fuchs reaction. As a result, the product was obtained with a 25% yield, which was higher than that for the unprotected alcohol but still relatively low. In comparison, the same reaction with trimethoxybenzaldehyde produced a 36% yield. Moreover, an additional TIPS deprotection step would be needed, which could result in further total yield decrease. Therefore, no further optimisations were made at this stage, and **28** was subjected to the second step of the Corey-Fuchs reaction to produce **29**. Normally, after the reaction is quenched with water, followed by the extraction of the alkyne product from the aqueous solution with DCM or EtOAc. The use of the same procedure for **29** was unsuccessful as it remained in the aqueous phase. Therefore, once the reaction was stirred for 10 minutes after quenching, the crude **29** was isolated from solvents under reduced pressure and redissolved in DMF for the next reaction with 1,4-dibromobutane to give **30**, followed by a nucleophilic substitution to yield the azide containing 'top' of the chromophore **27**.

The next reaction step was Sonogashira cross-coupling reaction between **27** and the 'bottom' component (**13**) of the chromophore (Scheme 5.10). Although copper-free reaction conditions were used, where palladium(I) acted as both catalyst and co-catalyst, there was still a concern over a possibility of **27** undergoing intramolecularself-polymerisation *via* click-chemistry cycloaddition of azide to alkyne, since each molecule contained both functionalities, or , more likely, intermolecular cyclisation. To prevent this, **27** was added dropwise to a solution containing the **13** and the catalyst over 5 hours. Once the addition was complete, LCMS

revealed the presence of a small amount of the product **31**, roughly equal amounts of **27** and the **13** in the reaction mixture and no trace of the cycloaddition product.

The reaction was then left overnight, resulting in complete conversion of the starting materials with no evidence of cycloaddition product. This suggested that copper-free Sonogashira reaction conditions were suboptimal for the anticipated click-chemistry cycloaddition. Therefore, dropwise addition of **27** was not necessary, which was confirmed by the absence of the cycloaddition product when the reaction was repeated with equivalent concentration of both chromophore components from the start.

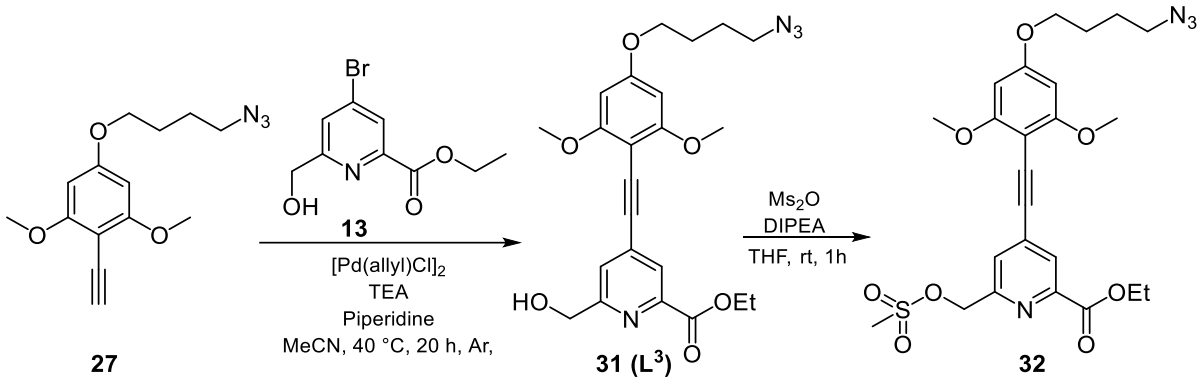

Scheme 5.10: The reaction sequence for the formation of the alkyl azide functionalised chromophore **16** and its mesylated version **17**.

The rest of the synthesis towards **EuL^3** was performed without any modifications (Scheme 5.11) since the azide remained unaffected by mesylation to give **32**, alkylation to give **33** and hydrolysis of the ethyl esters to facilitate complexation in the following step. As a result, **EuL^3** was prepared with three azide groups per complex molecule to be used for attachment of various functionalities at the stage of the complex *via* click-chemistry cycloaddition. The proof-of-concept functionalisation of **EuL^3** with a D-glucose-containing moiety for an improved live-cell uptake was described in the following section.

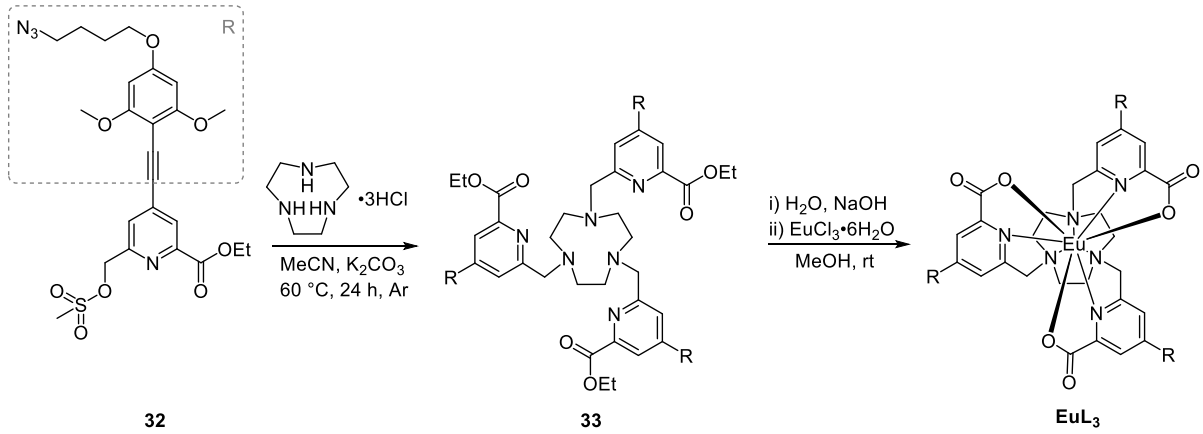

Scheme 5.11: The reaction sequence for the alkylation, hydrolysis and complexation steps for **EuL^3**.

V.2.3. Proof of concept EuL^3 functionalisation with a D-glucose derivative

As mentioned earlier, the azide functionality allowed to attach various functional moieties containing an alkyne group *via* click-chemistry cycloaddition. To demonstrate this, **EuL^3** was reacted with a commercially available D-glucose derivative containing an alkyne group under click-chemistry conditions. The previously tested conditions for the conversion of **18b** into **18c** were not suitable for **EuL^3** due to its negligible solubility in water, which was necessary for solvation of copper-reducing sodium ascorbate. Therefore, a different catalytic system compatible with such organic solvents as MeCN or DCM-MeOH mixture was used, where copper(I) chloride was replaced with tetrakis(MeCN)copper(I) hexafluorophosphate ($[Cu(MeCN)_4]PF_6$). The use of ($[Cu(MeCN)_4]PF_6$) avoided the need for a separate reducing agent since copper(I) was stabilised by the nitrogen lone pairs provided by MeCN ligands.[107] In addition, ($[Cu(MeCN)_4]PF_6$) is unstable in MeCN-water mixture, where it disproportionates to produce copper(II) hexahydrate, elemental copper and acetonitrile. This aids the separation of the water-insoluble europium(III) complex product from the residual catalyst.

The commercially available source of D-glucose functional moiety 2-propynyl-tetra-O-acetyl-β-D glucopyranoside contained acetylated alcohols that could be deprotected to release the sugar (Scheme 5.12). Since the deprotection procedure was relatively straightforward, it was decided to attach the glucopyranoside in its acetylated form and then remove the acetyl groups at the complex stage.

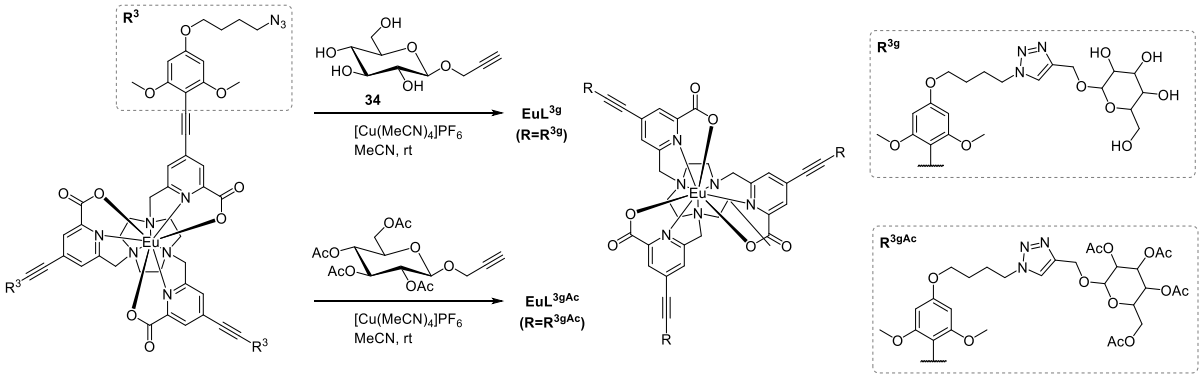

Scheme 5.12: The reaction sequences for the proof-of-concept complex-stage functionalisation of **EuL^3** with propargyl glucopyranoside.

Therefore, **EuL^3** and the excess of 2-propynyl-tetra-O-acetyl-β-D-glucopyranoside (4 eq.) were dissolved in MeCN, and $[Cu(MeCN)_4]PF_6$ was added and stirred at rt overnight to yield **EuL^{3gAc}**. Interestingly, the reaction solution would stop glowing red under UV (365 nm) when the copper(I) catalyst was added. This feature was used to check if the purified solution of **EuL^{3gAc}** was free from copper at a purification stage.

The sugars on **EuL^{3gAc}** were then deacetylated using a standard literature procedure – stirring in 0.1 M solution of sodium methoxide in MeOH.[108,109] After ~1 hour, the reaction completion was confirmed with LCMS, and the solution was neutralised using Amberlite H^+ ion exchange

resin. Once the resin was added, the solution no longer glowed red under UV (365 nm). The repeated LCMS experiment revealed a significant decrease in product concentration. An attempt of redissolving the product in different solvents, including, MeCN, DCM, DMF, MeOH and water was not successful, suggesting a possible irreversible adsorption of the complex to the resin. This was not investigated further since an alternative reaction sequence was used instead.

In this new attempt, 2-propynyl-tetra-O-acetyl-β-D-glucopyranoside was first deacetylated to give the 1-propargyl-β-D-glucopyranoside **34**. After that, 4 equivalents of **34** were reacted with **EuL^{3}** using the same cycloaddition reaction conditions to yield **EuL^{3g}**. Successful preparation of **EuL^{3g}** was a practical example of the proposed complex-stage functionalisation of **EuL^{3}**, where mild cycloaddition conditions would allow to use a wide range of substrates. This makes **EuL^{3}** a bright versatile material that can be tailored by the end-user to match the desired application without affecting any photophysical properties, including its CPL-activity.

V.2.4. Photophysical characterisation of EuL^{3}, EuL^{3g} and EuL^{3gAc}

In order to confirm the conservation of the photophysical properties in functionalised versions of **EuL^{3}**, the essential photophysical properties were compared across the **EuL^{1}**, **EuL^{3}** and **EuL^{3g}** series.

The absorption and emission profiles of the **EuL^{3}** in MeCN matched those of the **EuL^{1}** (Figure 5.18.A). The absorption maxima (~360 nm, MeCN) matched due to conservation of the chromophores' electronic structure and hence the HOMO-LUMO energy gap provided by a similar electron donating effect of the methoxy (in **EuL^{1}**) and butoxy (in **EuL^{3}** series) substituents on the para position of the aryl ring. This also agrees with similar values of Φ (45 ± 1% in **EuL^{1}** and 42 ± 1% in **EuL^{3}**) and τ (both 1.0 ± 0.1 ms) for both materials (Figure 5.18.A and C). The molar extinction coefficient (Figure 5.18.B) recorded for **EuL^{3}** (81000 ± 500 mol^{-1} cm^{-1}) was slightly higher than that of **EuL^{1}** (77000 ± 500 mol^{-1} cm^{-1}) which could be due to a butoxy group being slightly more electron donating than methoxy, providing a stronger transition dipole. The matching emission band-shapes agreed with the equivalent local symmetry at the europium(III) centre. The photophysical measurements for the glucose-functionalised **EuL^{3g}** were performed in MeOH since the material was practically insoluble in MeCN. The data for **EuL^{3g}** was, again, compared to the reference **EuL^{1}** to confirm that the complex-stage functionalisation of the **EuL^{3}** did not alter the desired photophysical properties. As expected, both emission and absorption band shapes matched. The absorption maximum of **EuL^{3g}** red shifted from 360 to 365 nm, which was also the case in **EuL^{1}**. This agrees with the previous discussion on the dependence of the ICT energy of the chromophore on the H-bond donating ability of the solvent.

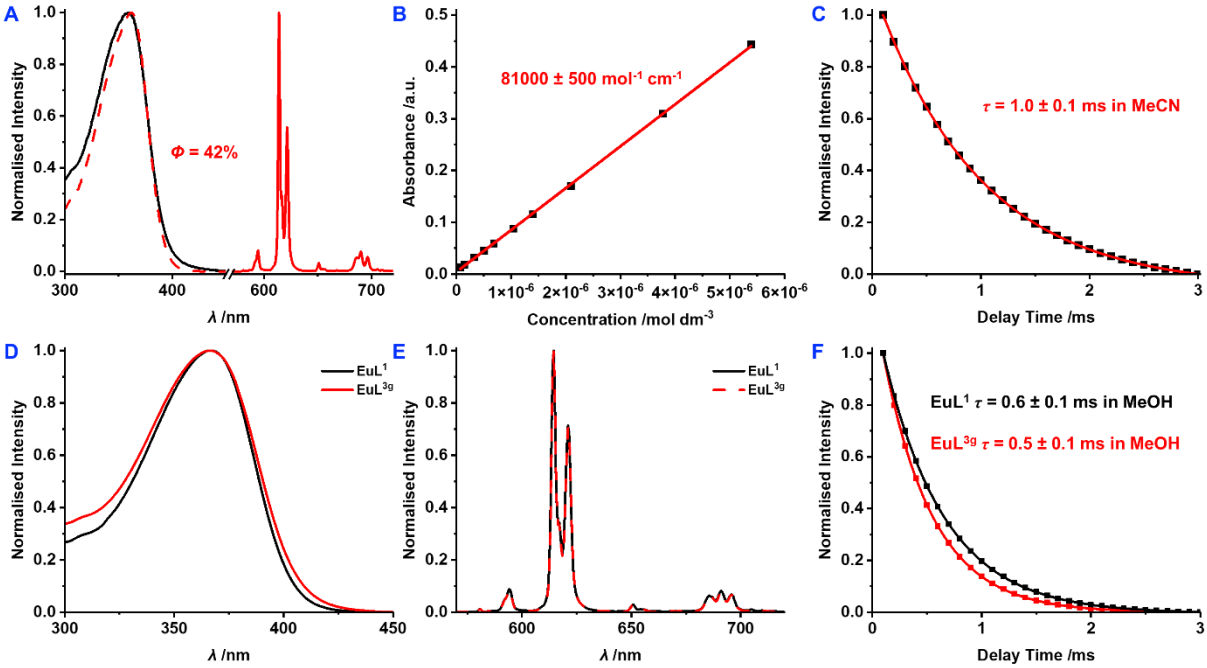

Figure 5.18. A: Normalised absorption (black), emission (solid red, λ_{exc} = 360 nm) and excitation (dashed red, λ_{em} = 614 nm) spectra of **EuL^3** in MeCN with the measured Φ (absolute method) annotated; **B:** Dependence of absorption on the **EuL^3** concentration in MeCN **C:** Lifetime plot of **EuL^3** in MeCN (0.1 abs solutions, λ_{exc} = 360 nm, λ_{em} = 614 nm); **D**: Normalised excitation spectra of **EuL^1** (black) and **EuL^{3g}** (red) in MeOH (λ_{em} = 614 nm); **E**: Normalised emission spectra of **EuL^1** (black) and **EuL^{3g}** (dashed red) in MeOH (λ_{exc} = 365 nm); **F:** Lifetime plots of **EuL^1** (black) and **EuL^{3g}** (red) in MeOH (0.1 abs solutions, λ_{exc} = 365 nm, λ_{em} = 614 nm);

Analytical chiral HPLC of **EuL^3** was successfully performed using the *CHIRALPAK* IE column, where the enantiomers eluted slightly later compared to **EuL^1** (Figure 5.19). This could be a result of an additional steric bulk of the butyl chain that slowed down the elution. The experiment was not repeated on the preparatory scale, since the CPL properties of the **EuL^3** series were expected to be equivalent to **EuL^1** and **EuL^2**. Functionalisation of the **EuL^2** chromophore did result in any changes in the CPL spectra and the g_{lum} plots, which were equivalent to **EuL^1**. In the case of **EuL^3**, the chromophore **L^3** was functionalised even further away from the europium(III) centre than in **EuL^2**, suggesting a very high probability of the conservation of the CPL properties.

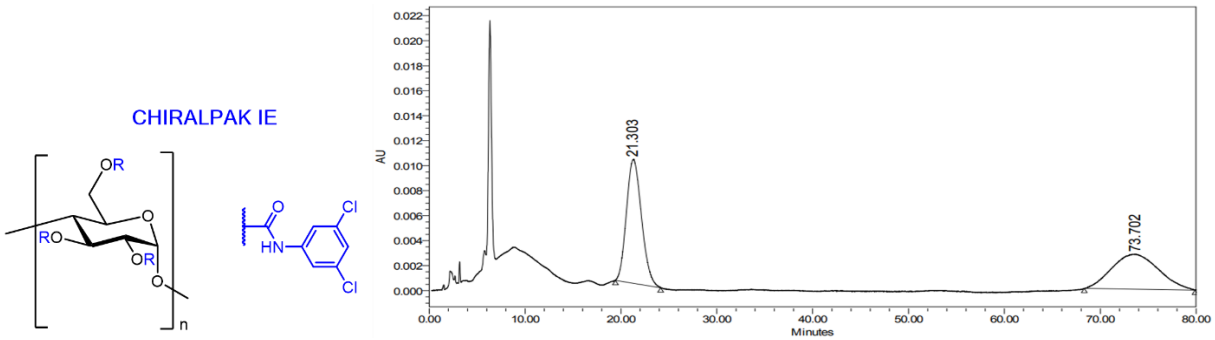

Figure 5.19: The structure of the *CHIRALPAK IE* chiral HPLC column stationary phase (left) and chiral HPLC AC (at 360 nm) for the separation of the **EuL^3** enantiomers (solvent: EtOH/MeOH/TEA/TFA at 50/50/0.5/0.3, injection: 10 µL of ~0.5 mg ml^{-1} in MeCN, 2 ml min^{-1}) (right). Performed by Dr. Aileen Congreve.

V.2.5. Comparison of EuL^3 and EuL^{3g} bioimaging performance

As a proof of concept study, NIH3T3 cells were dosed with **EuL^3** and **EuL^{3g}** and subjected to laser scanning confocal microscopy (LSCM). The cell dosing parameters such as complex concentration (5 μM) and incubation time (30 mins) were kept constant. The cell images were obtained using the same parameters such as the power and wavelength (355 nm) of the laser excitation source and the λ of the emission detection window (600-720nm). As mentioned previously, complex-stage functionalisation of **EuL^3** with a glucose derivative was expected to improve the cell uptake. In addition, at least 12 additional hydroxyl groups (15 groups if glucose takes linear form) were expected to improve the solubility of **EuL^{3g}** in aqueous media. As a result, D-glucose-functionalised **EuL^{3g}** demonstrated a significantly better uptake by live cells with primarily mitochondrial localisation (Figure 5.20).

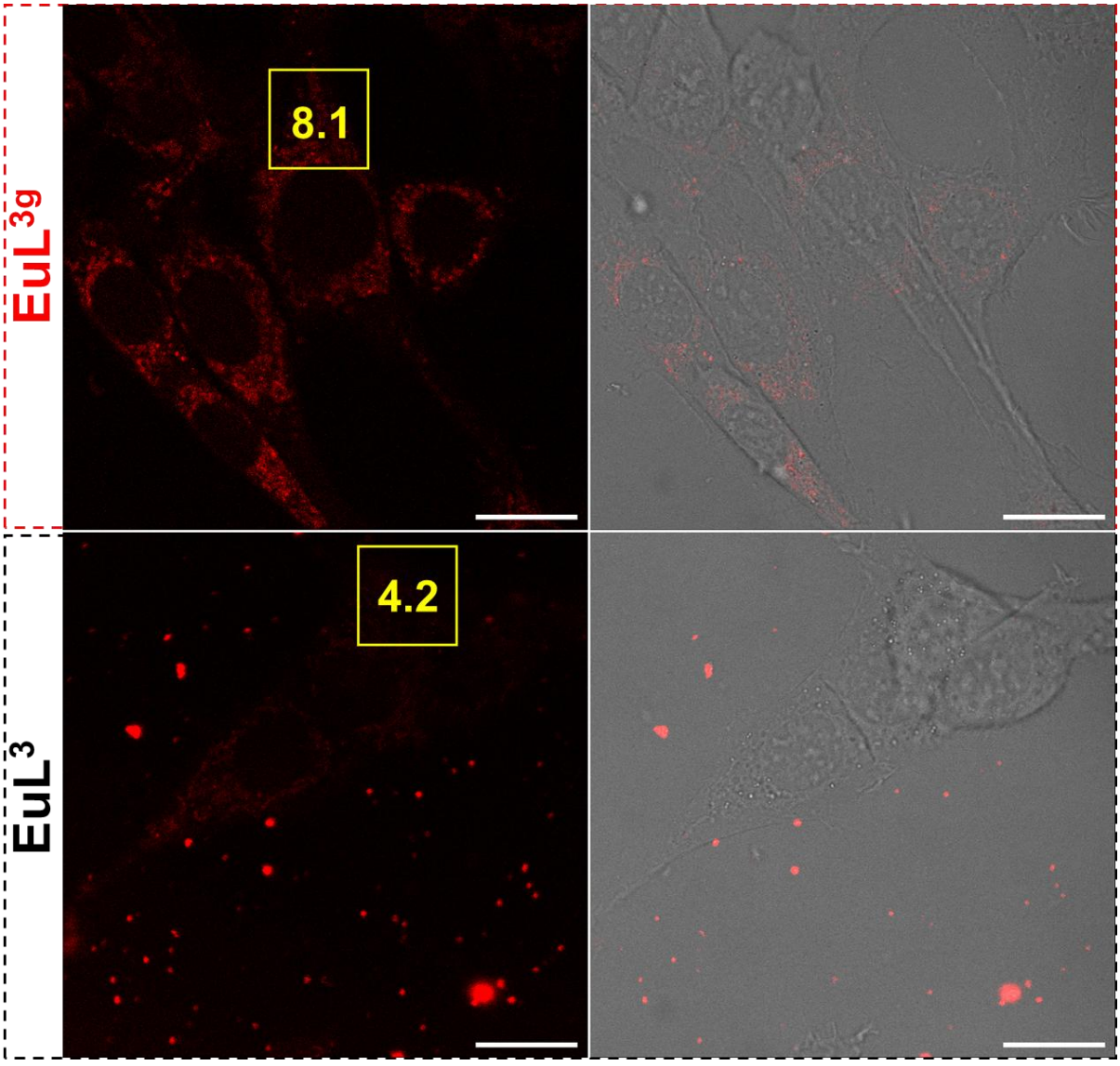

Figure 5.20: LSCM of **EuL^3** (bottom row) and **EuL^{3g}** (top row) (5 μM, 30 mins loading, ×63/1.4 NA oil objective, 96×96 μM FOV, 790 nm axial section) in NIH-3T3 cells, showing total emission (left images, λ_{ex} = 355 nm, 20 mW, λ_{em} = 600–720 nm) and overlay between the total emission and transmission. The ROIs (yellow squares) and their average intensity values are shown. Scale bar = 20 μm.

In contrast to that, the experiment with **EuL^3** under the same conditions failed, resulting in a large number of precipitated red-emitting clusters with no spatial selectivity, which was in agreement with very poor solubility of **EuL^3** in aqueous media. In order to quantitatively compare the difference in performance of **EuL^3** and **EuL^{3g}** as luminescent dye for live cell imaging, the average intensities of the two essentially equivalent ROIs (targeting cell mitochondrial network) of the same size were measured on the recorded images. As a result, the intensity recorded from the cells dosed with **EuL^{3g}** was nearly double that for **EuL^3**. Although this method was relatively imprecise due to just a single comparison of two different cells, it provided a sufficiently accurate estimate of the cell uptake improvement due to functionalisation of the complex with D-glucose containing functional moieties.

Further optimisation of the **EuL^{3g}** for bioimaging could involve preparation of the equivalent material with shorter alkyl chains to improve water solubility and reduce the steric bulk which could decrease the rate of cell uptake. Water solubility could also be improved by functionalising the complex with polyethylene glycol (PEG) moieties.

V.3. Unsymmetric EuL^4 complex for single-arm functionalisation

V.3.1. Investigation of the standard procedure for the preparation of unsymmetric complexes

So far, the new **EuL^2** and **EuL^3** materials designed for the complex-stage functionalisation have been symmetrical in terms of the structure of three chromophore arms. This, however, can be a disadvantage in scenarios where complex functionalisation with different groups is desired. Such design also imposes limitations on selective attachment of the complex molecules to other moieties, for example, chiral macrocycles, nanoparticles or even viruses, where the attachment *via* two or three functionalised chromophores simultaneously could result in complex geometry distortion or cause undesired aggregation.

The standard method for preparing the unsymmetric complexes (containing different chromophores on the TACN ring) is selective Boc protection of one or two of the TACN nitrogen atoms. After that, the alkylation of the partially protected TACN with the arm of one type is performed, followed by Boc deprotection to allow for the arm of the other type to be attached. The main issue with such method is the sensitivity of the chromophore alkyne towards the deprotection conditions that require the use of trifluoroacetic acid. Such acidic conditions are incompatible with chromophores that contain electron donating substituents at the para and ortho positions of the aryl ring due to conjugation to the alkyne (Scheme 5.13). This provides resonance stabilisation for the product of alkyne hydrogenation, which is susceptible to electrophilic attack of other species such as solvent molecules or the in-situ formed tert-butoxide.

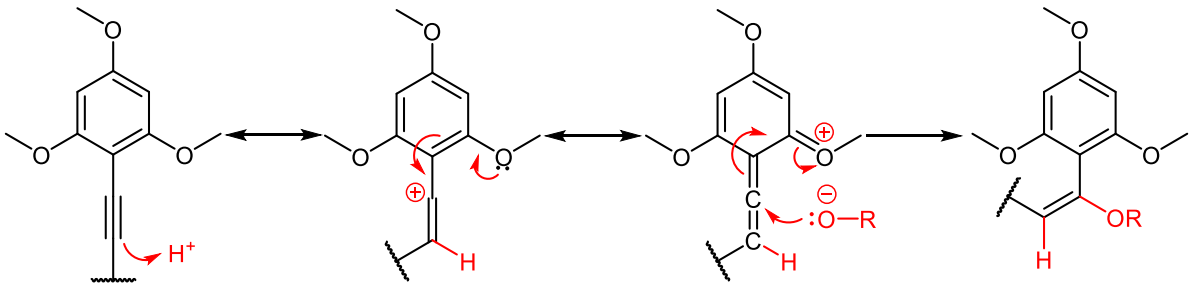

Scheme 5.13: A possible mechanism for electrophilic addition to alkyne facilitated by resonance stabilisation from electron donating ortho and para substituents.

A recent literature example provided a new mild method for Boc deprotection using oxalyl chloride and MeOH at relatively high yields.[110] This method was tested on two complex ligand precursors that comprised of a mono-protected TACN containing chromophore arms with different combinations of 'top' substituents. In the case when a less electron-donating combination of substituents (2-methyl, 4- methoxy), the TACN nitrogen deprotection left the alkynes intact, producing a single peak on the LCMS chromatogram (Scheme 5.21 – left, 2.259 min) On the contrary, the same reaction conditions resulted in multiple alkyne substitution products with a more electron rich combination of the substituents (Figure 5.21 – right). As a result, a different synthetic strategy towards an unsymmetric complex with 2,4,6-trialkoxy substitution of the chromophore was necessary.

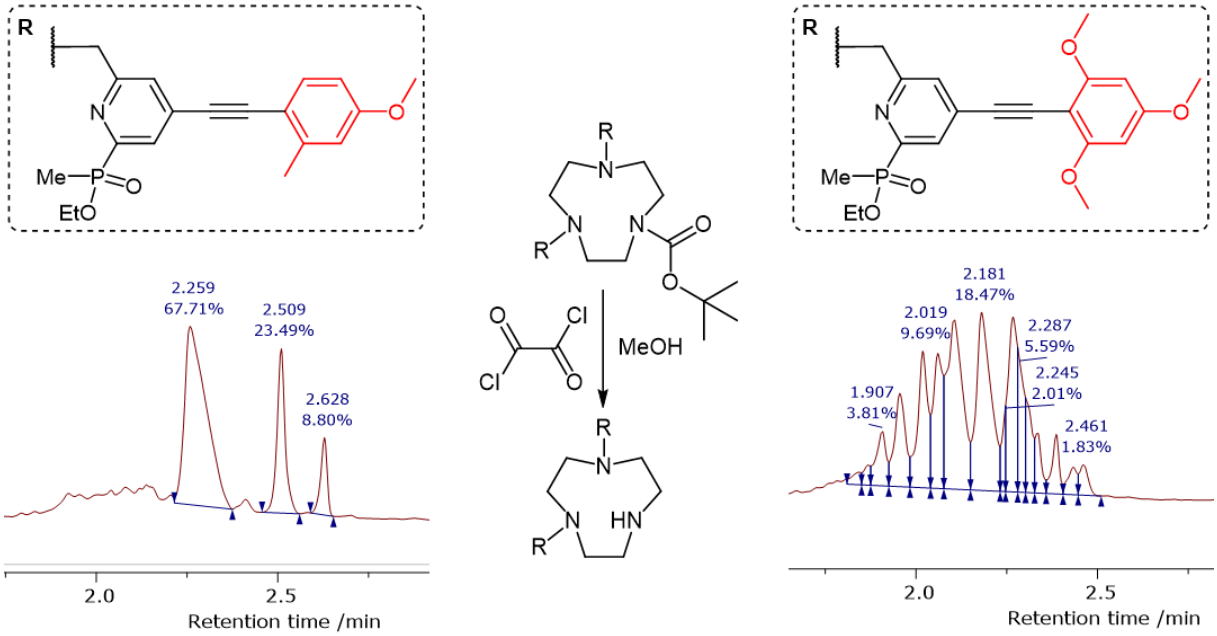

Figure 5.21: LCMS (Method E, Section VI.2.) AC (210-400 nm) sections demonstrating the product of the Boc deprotection of the complex ligand precursors with a less (left) and more (right) electron donating combination of 'top' substituents, and the reaction scheme shown (middle).

V.3.2. Preparation of EuL^4 *via* sequential alkylation

Normally, alkylation of the TACN proceeds relatively slowly due to the entropic penalty associated with attaching 3 chromophores to each TACN molecule. Therefore, a slight excess of the mesylated chromophore (3.5-4 eq.) to push the reaction to completion is used. Based on this, the unsymmetric complex could be achieved by sequential alkylation of TACN, where different mesylated chromophores are sequentially added to the reaction mixture. Therefore, to minimise the extent of the symmetrical complex formation, 1 equivalent of the functionalised arm could be added first, followed by slightly more than 2 equivalents of the unfunctionalised chromophore. This, in theory, would yield a singly functionalised complex as a major product.

In order to add another interconvertible functional group to the library of the **EuL^1** based materials, a carboxylic acid containing chromophore was chosen for the new unsymmetric **EuL^4** complex. This will provide another example of the versatility of the modular synthetic approach that allows most common functionalities to be introduced to the chromophore. So far, such methods as cycloaddition *via* azide and nucleophilic substitution *via* amine were proposed for the complex-stage functionalisation of **EuL^3** with alkyne and carboxylic acid containing moieties. **EuL^4** will expand the range of compatible functional groups to allow for the amine containing structures to be attached.

The preparation of the carboxylic acid functionalised chromophore followed the approach as for the **EuL^3** chromophore, where **29** is prepared first *via* the two-step Corey-Fuchs reaction (Scheme 5.8). In order to improve the solubility of the chromophore precursor in organic solvents and simplify purification of the intermediates, the carboxylic acid functionality was introduced in a form of ethyl ester. The carboxylic acid can then be obtained at the hydrolysis stage prior to the complexation. Therefore, **29** was reacted with ethyl 4-bromobutyrate to give **35**, which was then coupled with **13** to give the chromophore **36** (Scheme 5.14).

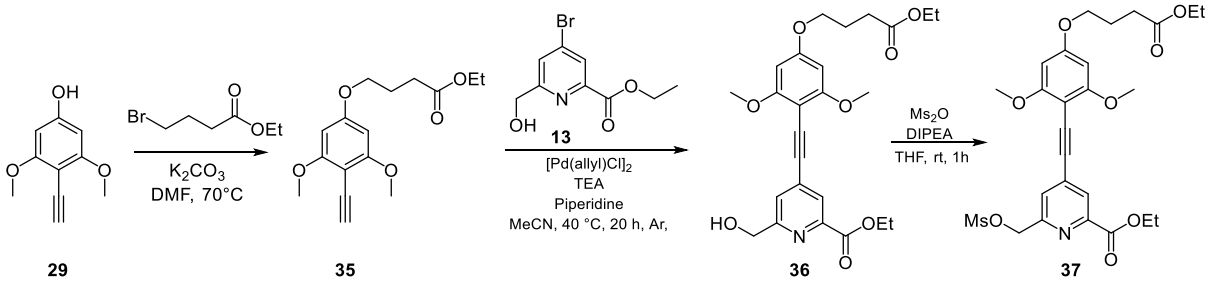

Scheme 5.14: The reaction sequence for the sensitising chromophore of **EuL^4**.

As discussed earlier, once **36** was mesylated to give **37**, only 1 equivalent of it was first added to TACN, expecting **38i** as a major intermediate product (Scheme 5.15). After that, 2.1 equivalents of the mesylated **37** were added to the reaction mixture to alkylate the remaining two nitrogen positions with unfunctionalised chromophores **15** to give **38**.

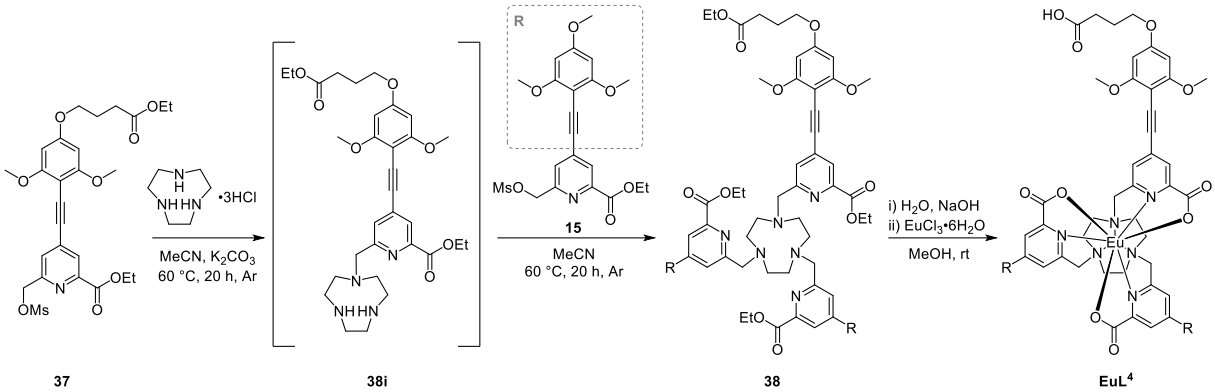

Scheme 5.15: The reaction conditions for the sequential alkylation of the TACN with different chromophores, followed by hydrolysis and complexation.

Once TACN was reacted with 1 equivalent of **37** for 20 hours, a mixture of the singly, doubly and triply alkylated products was observed, with **38i** not being a major product. It was not possible to determine the relative ratio of the products in the mixture using LCMS, as the material with the mass corresponding to **38i** eluted for a duration of ~1 minute, producing a very broad low intensity absorbance peak. This can be rationalised by the presence of two secondary amines that often lead to peak broadening. On the other hand, the lower UV absorbance could also be a result of lower molar absorption coefficient of a molecule containing a single chromophore compared to those with two and three chromophores. Regardless, the reaction did not proceed as expected, suggesting that the rate of the first alkylation was not faster compared to the second and third alkylation. Although the first alkylation would be the least sterically hindered, the rate of the first alkylation could drop due to a reduction in the concentration of the unsubstituted TACN as the reaction proceeded; however, a further investigation into reaction kinetics was necessary to determine the reaction order. As a first stage improvement, **37** could be slowly added to the stirring mixture containing TACN over 20 hours. In addition, a high dilution of the reaction mixture could be implemented. This would maintain a low ratio of **37** to TACN and **37** to **38i**, limiting the extent of the undesired repeated alkylation.

Nevertheless, the obtained reaction mixture was exposed to a slight excess of mesylated **L**[1] to produce a mixture of products, containing different combinations of the chromophores attached to the TACN (Figure 5.22).

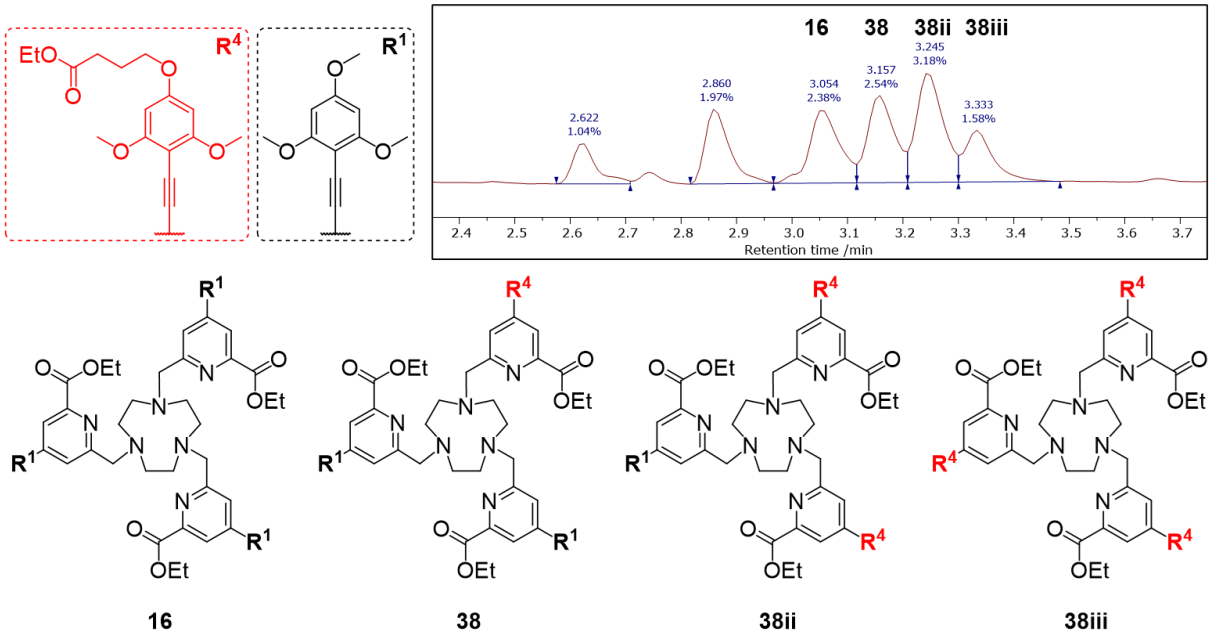

Figure 5.22: Annotated section of the LCMS (Method E, Section VI.2.) AC for the **37** to **38** alkylation reaction mixture with the structures matching the observed $[M+H]^+$ shown.

The mixture was then exposed to hydrolysis, followed by complexation to yield a mixture of complexes (Figure 23). One of the key points to note is a strong dependence of the solubility of the complexes on the number of the carboxylic acid functionalised chromophores. Hence, **EuL^{4ii}** and **EuL^{4iii}** were insoluble in organic solvents at neutral pH, while **EuL^{4}** was sparingly soluble. Therefore, after the crude mixture was sonicated in MeOH, only **EuL^{4}** and **EuL^{1}** were dissolved and were then separated by reverse-phase HPLC (Method C, Section VI.2.). The residue in MeOH, which mostly contained **EuL^{4ii}** and **EuL^{4iii}**, was then found to be soluble in a 1:1 mixture of MeOH and water by adding 0.1 M NaOH until pH = 8. Therefore, if needed, the two additional materials could be purified using reverse-phase HPLC with a solvent system containing a small amount of mild base. For example, a previously mentioned literature example used a gradient of 5 to 70% MeOH in 0.1 M aqueous solution of ammonium bicarbonate for a phosphinate donor complex containing carboxylate functionalised chromophores.[18]

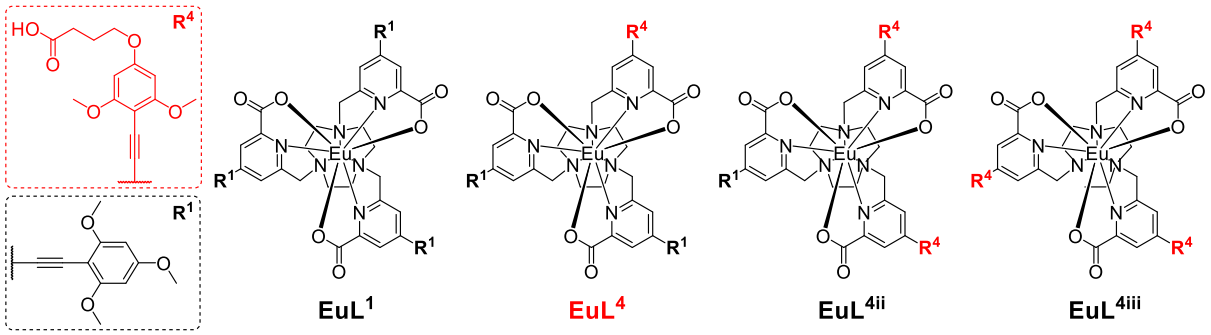

Figure 5.23: The structures of the complexes obtained during preparation of **EuL^{4}**.

V.3.3. Photophysical study of EuL^4

Up until **EuL^4**, structural modifications of parent **EuL^1** complex did affect global complex symmetry, since all three chromophores were equivalent. In this study, inequivalence of the chromophores was introduced. In small organic chromophores, the whole structure often contributes to the MOs of the electronic states involved in transitions associated with light absorption and emission. As a result, most structural modifications are likely to affect the orbital energies and therefore photophysical properties. In EuL-type complexes, coordination environment of europium(III) emitting centre is affected by proximal donor groups (phosphinate or carboxylate), pyridyl group and the TACN ring. Therefore, structural modifications or replacement of these proximal structural components would affect CF splitting of ^7F_J electronic states. This has been previously evidenced by comparing the regular emission and CPL spectra of **EuL^0** and **EuL^1** where replacement of a phosphinate donor with a carboxylate donor altered the bandshape of the ΔJ = 2 manifold. Other distant structural modifications, such as that on **EuL^2** and **EuL^3** did not affect the europium(III) total emission and CPL spectra. The same was expected from **EuL^4,** even though formally the overall complex symmetry was lowered. Therefore, **EuL^4** was expected to have identical photophysical properties to that of **EuL^4**, suggesting another example of EuL-type functional material with fixed photophysical properties that are independent on the structural modifications on the top of the chromophore. As expected, there were no significant difference between the emission, absorption and excitation (Figures 5.24 and 5.25) spectra of **EuL^4** and **EuL^1**, suggesting no detectable effect of the overall molecular symmetry reduction on the energy and splitting of europium(III) electronic states. No significant difference was observed for the emission lifetime (Figure 5.24.B) of **EuL^4** (0.8 ± 0.1 ms), which was the same with **EuL^1** (1.0 ± 0.1 ms) within the experimental error.

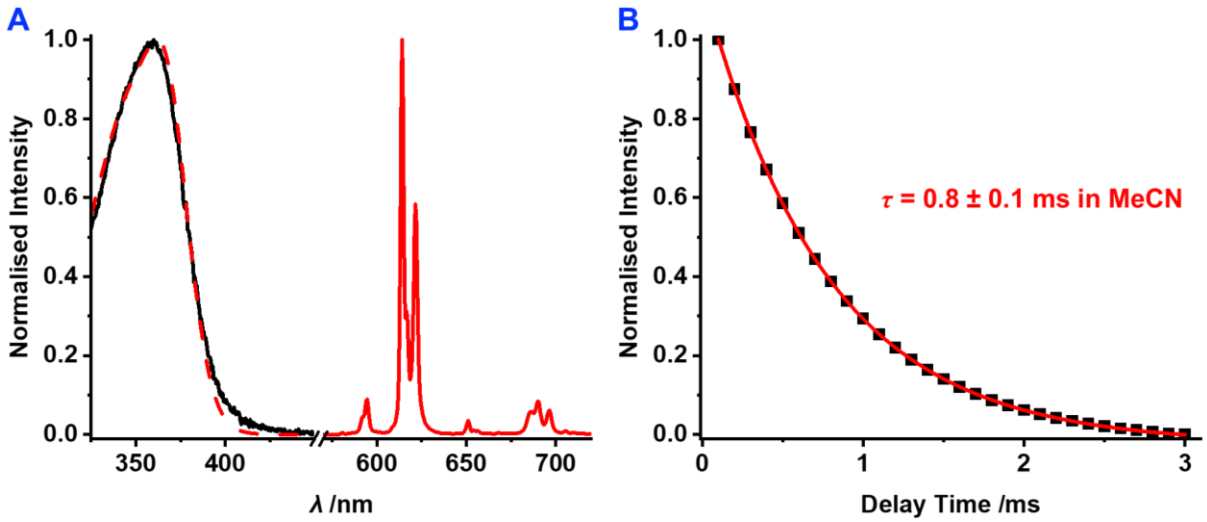

Figure 5.24. **A:** Normalised absorption (black), emission (solid red, λ_{exc} = 360 nm) and excitation (dashed red, λ_{em} = 614 nm) spectra of **EuL^4** in MeCN; **B:** Emission lifetime plot (0.1 abs solutions, λ_{exc} = 360 nm, λ_{em} = 614 nm) of **EuL^4** in MeCN.

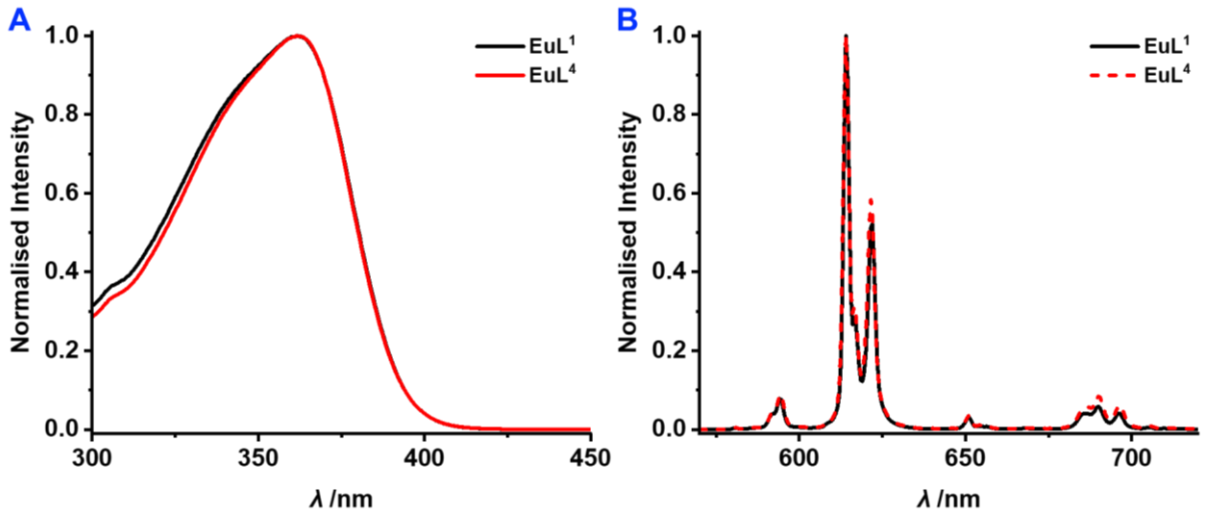

Figure 5.25. A: Normalised excitation spectra (λ_{em} = 614 nm) of **EuL^1** (black) and EuL^4 (red) in MeCN; **B:** Normalised emission spectra (λ_{exc} = 360 nm) of **EuL^1** (solid black) and **EuL^4** (dashed red) in MeCN.

V.3.4. CPL properties of EuL^4

Due to the structural similarity between the **EuL^1** and **EuL^4**, the racemic mixture of **EuL^4** enantiomers was tested against the chiral HPLC conditions previously used for **EuL^1**. As a result, both *CHIRALPAK IE* and *IB-N5* columns resulted in successful enantiomeric separation of **EuL^4** (Figure 5.26) with similar to **EuL^1** retention times.

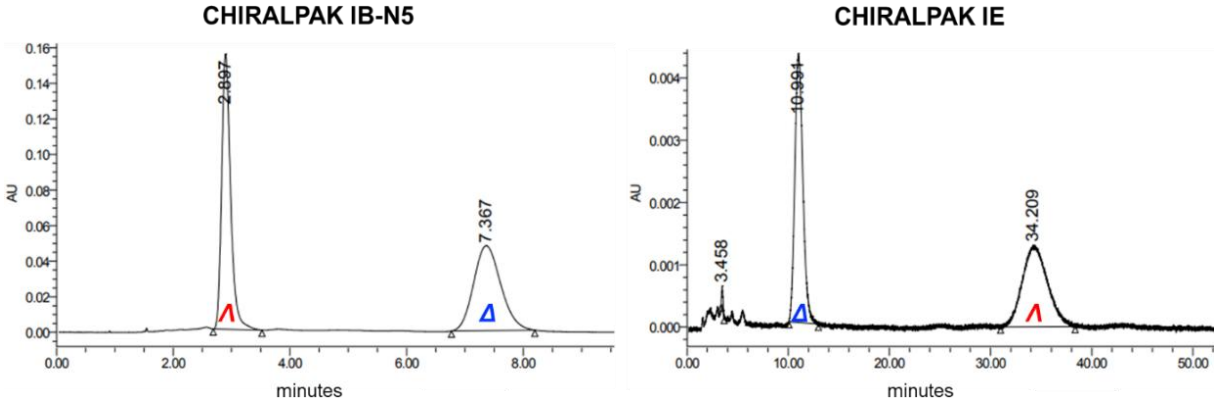

Figure 5.26: Chiral HPLC ACs (at 360 nm) for the chiral separation of the **EuL^4** enantiomers using *CHIRALPAK IB-N5* (left) and *IE* (right) (solvent: EtOH/MeOH/TEA/TFA at 50/50/0.5/0.3, injection: 10 µL of ~0.5 mg ml^{-1} in MeOH, 2 ml min^{-1}). Performed by Dr. Aileen Congreve.

In order to predict whether the structural modification introduced in **EuL^4** would affect the CPL spectral shape, it is necessary to estimate whether the rotatory strength of the molecule, governed by electric and MD moments, is affected. For the sensitised lanthanide complexes, where absorption and emission processes are centred at different parts of the molecule, only transition dipole moments associated with the emitting lanthanide centre affect CPL (on the contrary, CD would be dependent on the whole ligand structure). Since the coordination environment of the europium(III) centre remained the same, the CF splitting of the ^7F_J electronic states and therefore the CPL spectral shape must remain unaffected. The same principle applies to the environment-dependent magnetic and electric transition dipole

moments that directly affect the rotatory strength of the complex and, therefore, the same g_{lum} values were expected.

As expected, the reduction of overall complex symmetry *via* a structural modification from the europium(III) centre did not affect the CPL properties. The CPL spectral shape of **EuL⁴** (Figure 5.28. A) matched **EuL¹** exactly (Figure 5.27.C) within the experimental error. Similarly, the g_{lum} plots (Figure 5.27.B) of the two complexes nearly matched (Figure 5.27.D), while **EuL⁴** produced marginally lower maximal g_{lum} values of +0.29 (***Δ*-EuL⁴**) and -0.28 (***Λ*-EuL⁴**) (both at 601 nm) for ΔJ = *1* and -0.066 (***Δ*-EuL⁴** at 607 nm) and +0.069 (***Λ*-EuL⁴** at 607.5 nm) for ΔJ = *2*. For comparison, the maximum g_{lum} values for **EuL¹** were ±0.290 at 601 nm and ±0.071 at 607.5 nm.

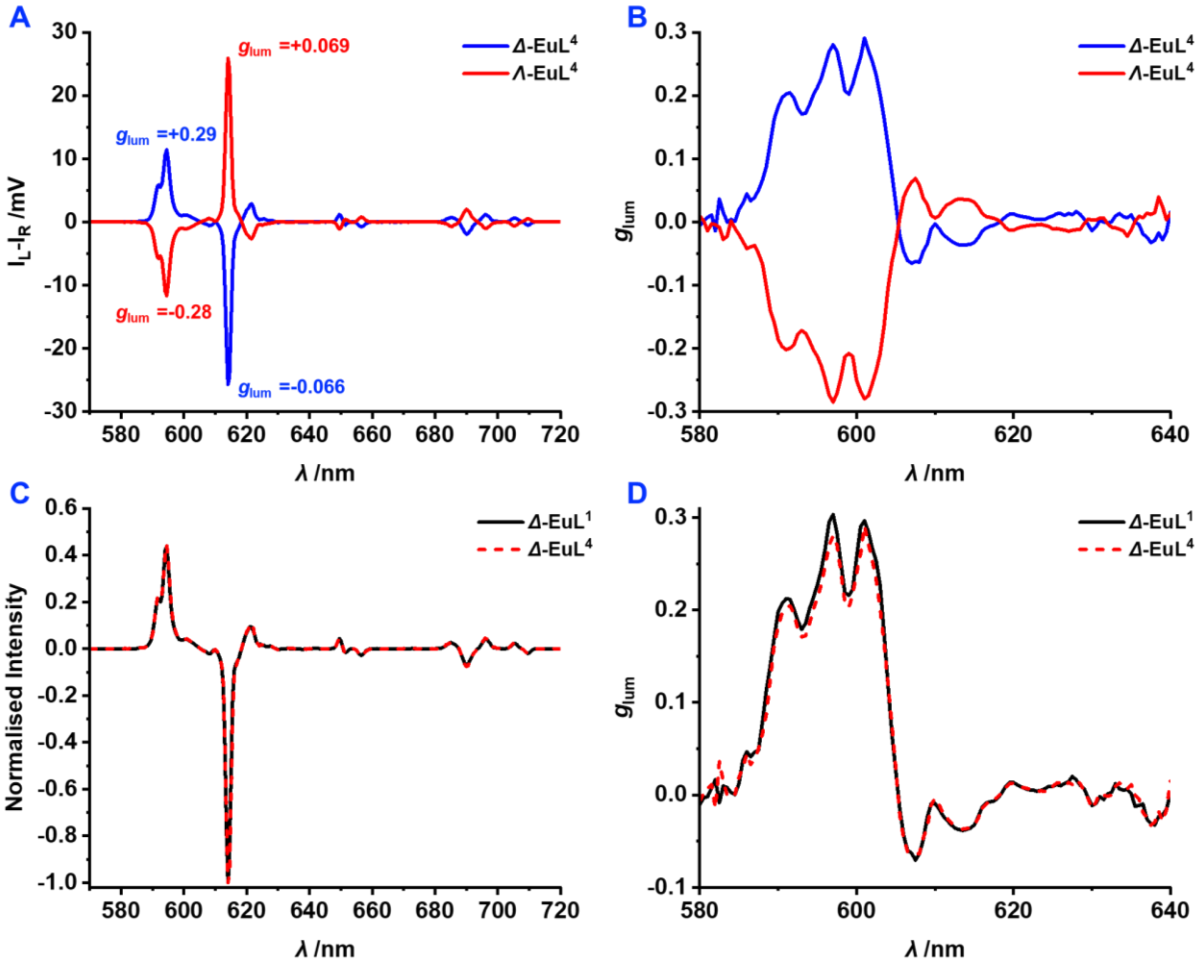

Figure 5.27: **A**: CPL spectra of the ***Δ*-EuL⁴** (blue) and ***Λ*-EuL⁴** (red) in MeCN (λ_{exc} = 360 nm, 5 averages); **B**: g_{lum} plots for the CPL spectra in **A** (ΔJ=1 and 2 only); **C:** Normalised (to the intensity at 614 nm) CPL spectra of the ***Δ*** enantiomers of **EuL¹** (solid black) and **EuL⁴** (dashed red) in MeCN (λ_{exc} = 360 nm, 5 averages); **D**: g_{lum} plots for the CPL spectra in **C** (ΔJ = 1 and 2 only).

V.4. Discussion and future work

Overall, the comparison of the CPL properties across the **EuL^0**, **EuL^1**, **EuL^2** and **EuL^4** series provided a great insight into the relationship between the CPL spectral shape and structural features of the complexes. It was established that only those structural modifications that are proximal to the europium(III) coordination site can significantly impact the luminescent properties. The electronic transitions that give rise to photoemission relax europium(III) from the $^5D_0$ electronic excited state to different ^7F_J states, each containing $2J+1$ degenerate Stark states for each value of J. When the 4*f* orbitals of europium(III) experience the CF of the ligand, the degeneracy of the Stark states is lifted, resulting in a characteristic fingerprint spectral shape of each ΔJ emission manifold. Therefore, in order to alter the spectral shape, the CF experienced by the 4*f* orbitals must be changed by structural modifications at the europium(III) coordination site or close to it. This was observed when the phenylphosphinate donor groups in **EuL^0** were swapped with carboxylate groups in **EuL^1**, resulting in a completely different photophysical characteristics, including CPL (Chapter III). The further structural modifications of the top aryl component of the chromophore, such as introduction of a nitro group in **EuL^2** and functionalisation of the para- alkoxy group in **EuL^3** series did not alter the europium(III) luminescence. Even when the total complex symmetry was lowered by functionalising just one of the three chromophores in **EuL^4**, the CPL properties remained the same. This demonstrated excellent versatility of such complex-stage functionalisation-compatible europium(III) complexes that maintained their photophysical properties in different environments and upon functional group interconversion. This suggested that **EuL^3** and **EuL^4** complexes were likely to find application in a number of areas such as security inks, bioimaging and optoelectronics. These areas are likely to benefit from these environmentally independent bright CPL emitters that can be covalently linked to practically any functional moiety containing one of the common potent functional groups such as amine, thiol, carboxylic acid and alkyne. An example of such modification was the attachment of propargyl glucopyranoside to the azide-functionalised **EuL^3** *via* click-chemistry cycloaddition, while the attachment of other specific organelle-targeting functionalities can be explored in the future. This significantly improved the live cell uptake which made **EuL^{3g}** suitable for live cell bioimaging. The unsymmetric **EuL^4** can be functionalised in the same way *via* nucleophilic substitution at the carboxylic acid linker. The modular synthesis of such complexes allows the ease of their structural modification to achieve high compatibility with the commercially available functional moieties such as the ones that are used for specific cell organelle targeting.

On the contrary, **EuL^2** could not be effectively functionalised due to the reactivity issues caused by large steric hindrance generated by adjacent methoxy groups. On the other hand, it demonstrated an additional way of modifying the electronic structure of the sensitising

chromophore in order to induce the dependence of the complex photophysical properties such as Φ on some of the external environmental factors such as pH, temperature, solvent polarity or oxygen concentration. Introduction of the nitro group on the aryl ring in **EuL^2** decreased the Φ ~4 times, while the τ remained essentially the same with that of **EuL^1**. This suggested that the nitro group facilitated additional NRR pathways during the sensitisation process prior to the population of the $^5D_0$ emitting state, for instance, vibrational relaxation *via* solvent bond oscillators. Since vibrational relaxation is also a temperature-dependent process, future work would involve the study of **EuL^2** photophysical dependence on both solvent and temperature. At the same time, the g_{lum} plots for the enantiomers of **EuL^1** and **EuL^2** remained the same, suggesting that if an external factor dependence of some photophysical quantity of **EuL^2** such as total emission is established, the constant g_{lum} value could then serve as an internal reference for using **EuL^2** as a reliable self-calibrating sensor.

Conclusions

A novel bright CPL-active *quasi-C_3* symmetric **EuL^1** complex containing all carboxylate donor groups was prepared as a racemic mixture of two practically achievable enantiomers. The enantiomers were then separated using chiral HPLC and photophysically characterised. The design of **EuL^1** was based on the previously reported **EuL^0** complex which was also prepared and characterised as part of this work. The only structural difference between **EuL^0** and **EuL^1** was replacement of all three phenylphosphinate donor groups in **EuL^0** with the carboxylate equivalents. Such structural modification resulted in significant improvements of photophysical properties that resulted in **EuL^1** being the best CPL active security ink candidate reported so far. **EuL^1** was exceptionally bright due to a combination of high values of the Φ (45 %) and ε (77000 M^{-1} cm^{-1}) which resulted in 58% brightness increase compared to **EuL^0**. Apart from the high value of ε, sensitisation *via* the lower-energy ICT state, facilitated by the conjugated linearly oriented electron rich and depleted structural components of the chromophore, resulted in **EuL^1** absorption maximum near the 365 nm which suggested the optimal excitation of the security ink using the commercially available 365 nm UV LED. The occurrence of multiple NRR processes during the sensitisation resulted in a large pseudo-Stokes shift, which made **EuL^1** colourless and therefore invisible to the unaided eye unless irradiated with UV light. In addition, due to the formally Laporte forbidden nature of $^5D_0 \rightarrow {}^7F_J$ transitions, a relatively long millisecond τ of **EuL^1** provided compatibility with the temporal security layer, authenticated using a microsecond scale delay between the sample illumination (once the LED rise time has passed) and triggering the exposure. This allows to filter-out any nanosecond-scale emission of organic fluorophores present in the CST.

Introduction of the bidentate carboxylate donor groups that are more symmetric than phosphinate donors and have no chrial centre resulted in a significant increase of the hypersensitive ΔJ = 2 relative CPL intensity and a substantial CPL sign conservation. The calculated CPB_{i} values (at 607 nm) of 984 M^{-1} cm^{-1} (using β_i for the whole transition) and 590 (using β_i for the first single-sign part of the transition) were higher than that of any other previously reported material, rendering it to be the best-known candidate for the CPL security ink so far. As a result, the most intense ΔJ = 2 could now be used for authentication of the CPL security instead of ΔJ = 1 that only contributes ~5% to the total emission. This is commercially advantageous since ~7 times less material would be required to reach the detection limit. The CPB_{i} value for ΔJ = 1 was calculated as 307 M^{-1} cm^{-1}, which was the third best in terms of ΔJ = 1 and the best among materials with the same structure type. The CPB_F values for BPF594/10 and BPF610/10 were calculated as 202 and 189 M^{-1} cm^{-1} respectively. This enabled the use of both ΔJ = 1 and ΔJ = 2 opposite-sign transitions for the double CPL security layer. To demonstrate this, both enantiomers of **EuL^1** were dissolved with PMMA to

produce thin (~200 nm) films that were subjected to CPLP. Apart from a simple CPL sign determination *via* EDCC, the CPLP-specific g_{CPLP} was derived and calculated for the consecutively prepared films. As a result, the obtained g_{CPLP} values corresponded to the average g_{lum} values recorded by a PEM CPL spectrometer in the λ regions of the corresponding BPFs. This created a possibility of further sophistication of the CPL security feature *via* mixing the two enantiomers in secret proportions to create a unique value of g_{CPLP} for a genuine CST. In addition, secret λ BPFs and LPFs could be used to observe unique g_{CPLP} values, incorporating the CPL spectral features into the CPL security layers.

Since the films were transparent, the underlying spin-coating glass substrate introduced a significant error into the g_{CPLP} measurements due to the reflections of the CP light emitted by films which resulted in 50% and 30% g_{CPLP} reduction for the 594 ± 5 nm and 610 ± 5 nm λ regions respectively. The proposed hypothesis of dissymmetry reduction *via* reflection induced CPL sign cancellation from substrate was confirmed by replacing glass with black non-reflective tape that recovered the magnitude of g_{CPLP}. The g_{CPLP} values remained consistent across multiple sequentially spin-coated films, suggesting high repeatability and consistent CPL security feature. From the racemisation studies it was established that **EuL^1** would not racemise at rt and would remain enantiopure over short exposures to elevated temperatures in solid-state PMMA film based on a relatively long racemisation $\tau_{1/2}$ of ~190 hours in MeCN at 60°C. The racemisation barrier in **EuL^1** was energetically lower compared to **EuL^0** containing bulky phenylphosphinate donor groups which prevented racemisation at 60°C entirely.

Due to the outstanding *CPB* of the novel **EuL^1**, the structure was used as a platform for novel **EuL^2**, **EuL^3** and **EuL^4** that were designed to be compatible with the complex-stage functionalisation. This would broaden the scope of practical applications where a CPL-active material can be covalently linked to different functional moieties, for example, to live-cell organelle targeting groups for bioimaging, to chiral polymers for chirality transfer, to other light absorbing chromophores for tuning the λ of sensitisation *via* Förster resonance ET, to gold nanoparticles to study the effect of surface plasmon resonance on the CPL and other applications. The conservation of CPL properties and their insensitivity towards the environment (solvent) observed across the **EuL^1** – **EuL^4** range suggested positive commercialisation prospects while also gave an insight into the understudied structure-CPL relationship in sensitised lanthanide(III) complexes. It was found that functionalisation of the complex chromophores away from the europium(III) coordination environment resulted in no effect on the CPL spectral shape and therefore the rotatory strength of the molecule. Even when the overall complex symmetry was reduced by introduction of a structurally different chromophore in the unsymmetric **EuL^4**, CPL properties remained identical to those in **EuL^1**.

CHAPTER VI. Experimental methods

VI.1. General procedures

All starting materials are commercially available and distributed by *Merck*. Analytical grade and HPLC grade solvents were used and degassed using freeze-pump-thaw or cycling where appropriate.

Silica gel plates on aluminium support (0.2 mm thick, 60 F254, *Merck*) were used in thin layer chromatography (TLC) and resolved under UV radiation source at 254 or 365 nm. Flash column chromatography was manually prepared using silica gel (60 (230-400 mesh, *Flourochem*).

^{1}H and ^{13}C NMR was performed on a *Bruker Advance-400* (^{1}H at 400.06 MHz and^{13}C at 100.61 MHz), a *Mercury 400* (^{1}H at 399.95 MHz), a *Varian VNMRS-600* (^{1}H at 599.67 MHz and ^{13}C at 150.79 MHz) or a *Varian VNMRS-700* (^{1}H at 699.73 MHz and ^{13}C at 175.95 MHz) using $CDCl_3$ and MeOD (*Merck*). Chemical shifts and J-couplings were reported in ppm and Hz respectively.

LCMS experiments were performed on Waters Single Quadrupole Detector (SQD) spectrometer exploiting *Acquity* ultra-performance liquid chromatography (UPLC) and electrospray ionisation (ESI) source. The instrument is set up for alternate positive / negative ion MS scans plus PD array detection. The UPLC exploits *Acquity* UPLC ethylene bridged hybrid C_{18} 1.7 µm (2.1 × 50 mm) analytical column with MeCN – water gradient (Method E – section VI.2, Table 6.1). Accurate mass measurements were performed on Waters Quadrupole Time-of-Flight (QToF) mass spectrometer configured for ESI and coupled to an *Acquity* UPLC.

VI.2. HPLC separation

V.2.1. Preparative and analytical reverse-phase HPLC and UPLC

Preparative reverse-phase HPLC was performed using a Shimadzu module comprising of a vacuum degasser (*DGU-20AR5*), a *Prominence* liquid chromatography pump *(LC-20AP*), a *Prominence* UV-Vis detector (*SPD-20A*) and a communications bus module (*CBM-20A*). Sample separation was performed using a preparative *XBridge* C_{18} OBD column (19 × 100 mm, 5 µm, flow rate = 17 cm^3 min^{-1}) with fractions collected manually. The solvent system was a mixture of water and MeCN, where the proportion of the two solvents was varied in time (Table 6.1, Methods A-D). Analytical UPLC was performed as part of LCMS experiments as per above (Section VI.1.).

Table 6.1: Time dependent solvent gradients for HCPL and UPLC.

Method	Time/ mins	Water fraction /%	MeCN fraction /%
Method A (10 min gradient from 10%)	0	90	10
	4	90	10
	14	0	100
	19	0	100
	21	90	10
Method B (15 min gradient from 10%)	0	90	10
	4	90	10
	19	0	100
	24	0	100
	27	90	10
Method C (20 min gradient from 10%)*	0	90	10
	4	90	10
	24	0	100
	29	0	100
	32	90	10
Method D (15 min gradient from 30%)	0	70	30
	4	70	30
	19	0	100
	23	0	100
	26	70	30
Method E (Analytical)*	0	95	5
	0.2	95	5
	4	5	95
	4.5	5	95
	5	95	5

*0.1% formic acid in water was used instead of water

V.2.2. Chiral HPLC.

Chiral HPLC was performed using a *Perkin Elmer Series 200* module consisting of a *Perkin Elmer Series 200* pump, autosampler, UV-Vis detector and *CHIRALPAK* IC column (10 × 250 mm, flow rate = 4.4 cm^3 min^{-1}, isocratic MeOH) for **EuL⁰** and either *CHIRALPAK* IE or IB N-5 columns (4.6 × 250 mm, flow rate = 2 ml min^{-1} at 40 °C, EtOH/MeOH/TEA/TFA at 50/50/0.5/0.3 ratio) for the rest of the materials as specified.

VI.3. Photophysical measurements

VI.3.1. Absorption, emission and lifetime measurements

All solution state optical analyses were carried out in quartz cuvettes with a path length of 1.0000 cm. Solid state (PMMA) samples were recorded using a custom-built holder. UV-vis absorption was measured on an *ATI Unicam* UV-vis spectrometer using *Vision* software (version 3.33). Emission experiments were performed on an *ISA Jobin-Yvon Spex Fluorolog-3* luminescence spectrometer using *DataMax* software (version 2.2.10). Lifetime was measured with a *Perkin Elmer LS55* spectrometer using *FL Winlab* software. All emission experiments were performed at 1 μM solution concentration. Absolute photoluminescent quantum yields were determined using a *Horiba FluoroMax Plus* fitted with a *QuantaPhi-2* integrating sphere. Excitation and emission slits were fixed at 2 nm with neutral density filters (*ThorLabs, NEK01S*) used at the excitation aperture to maintain a signal of approximately 10^6 cps at the excitation wavelength.

VI.3.2. CPL spectroscopy

CPL was measured with a home-built (modular) spectrometer.[45] The excitation source was a broad band (200 – 1000 nm) nitrogen purged, laser - driven light source *EQ 99* (*Elliot Scientific*). The excitation wavelength was selected by feeding the broadband light into an *Acton SP-2155* monochromator (*Princeton Instruments*); the collimated light was focused into the sample cell (1.0000 cm quartz cuvette). Sample PL emission was collected perpendicular to the excitation direction with a lens (f = 150 mm). The emission was fed through a PEM (*Hinds Series II/FS42AA*) and through a linear sheet polariser (*Comar*). The light was then focused into a second SM (*Acton SP2155*) and subsequently on to a PMT (*Hamamatsu H10723 series*). The detection of the CPL signal was achieved using the field modulation lock-in technique. The electronic signal from the PMT was then fed into a lock-in amplifier (*Hinds Instruments Signaloc Model* 2100). The reference signal for the lock-in detection was provided by the PEM control unit. The monochromators, PEM control unit and lock-in amplifier were interfaced to a desktop PC and controlled by a custom-written *LabVIEW 2014b* graphic user interface. The lock-in amplifier provided two signals, an alternating current signal

corresponding to (I_L- I_R) and a direct current signal corresponding to (I_L+ I_R) after background subtraction. Spectral calibration of the scanning monochromator was performed using a Hg-Ar calibration lamp (*Ocean Optics*, *HG-2*). A correction factor for the wavelength dependence of the detection system was constructed using a calibrated lamp (*Ocean Optics*, *HL-2000*). The measured raw data was subsequently corrected using this correction factor. The validation of the CPL detection systems was achieved using LEDs at various emission wavelengths (i.e. 650/50 nm). The LED was mounted in the sample holder and the light from the LED was fed through a broad band polarising filter and QWP (*ThorLabs, LPVISE100-A* and *AQWP05M-600*) to generate CP light. The emission spectra were recorded with 0.5 nm step size, and the slits of the detection monochromator were set to a slit width corresponding to a spectral resolution of 0.25 nm. CPL and total emission spectra were obtained through an averaging procedure of 5 scans. Prior to all measurements, the QWP and an LED were used to set the phase of the lock-in amplifier correctly.

VI.3.3.Circularly polarised luminescence photography (CPLP) and enantioselective differential chiral contrast (EDCC)

The CPLP handheld instrument for EDCC comprises of an externally triggered *Kiralux*® polarisation 5.0 Megapixel CMOS USB camera (*CS505MUP1, Thorlabs*). It is synchronised to 2 standalone 365 nm LEDs (*Nichia*, 5.2V, 500mW) or custom multi-RGB-LED flash illuminator module (described in Figure 4.20) driven by an internal custom built signal generator module operating at master frequencies of 0.1, 1 or 10 Hz. This device has been constructed to be able to provide both a variable illumination (1 ms - 1 s) and image acquisition (0.027 ms – 14 s) sequence with a constant 20 µs time delay between the two pulses to allow discrimination of short lived organic (ns- µs) and long-lived lanthanide pseudo phosphorescence (ms). The chiroptical separator of the apparatus comprises of the built in pixel decoded wire grid polariser array complemented by a precisely aligned broad wavelengths (λ = 400 – 800 nm) QWP (*Thorlabs AQWP05M-600*), a machine vision (*Navitar* f = 25mm/F1.4) objective lens (interchangeable to a *LWD* f = 50 mm/F2.8 lens and 0.63x video relay lens (*Edmund Optics*) for epifluorescence microscopy) and a selectable filter wheel containing high precision narrow BPFs (such as *Edmund Optics* BPF546/10, BPF589/10, BPF594/10, and BPF610/10) to achieve chromatic discrimination.

Camera control and image acquisition were performed with *ThorLab*'s commercial camera software *ThorCam*™ or an adapted custom *LabView* code to facilitate time-resolved detection and controlled external camera triggering. The camera was operated in quad where the 16-bit overlayed total image has been split up into four individual 8-bit images decoding each wire grid polariser state orientation (0, 90, +45 and -45 degree) captured image as a 2 x 2 array in

one captured frame. These images were generated by the area-defined crop and paste image generation without pixel position reassignment, followed by EDCC image calculations using a custom written macro operating the *ImageJ* software (v1.53) software pre-installed image calculation plugin:

```
original = getImageID; title = getTitle; height = getHeight; width = getWidth; halfWidth = width / 2; halfHeight = height / 2 makeRectangle(0, 0, halfWidth, halfHeight); run("Duplicate...", "title=TE1"); selectImage(original); makeRectangle(halfWidth+1, 0, width, halfHeight); run("Duplicate...", "title=R"); selectImage(original); makeRectangle(0, halfHeight+1, halfWidth, height); run("Duplicate...", "title=L"); selectImage(original); makeRectangle(halfWidth+1, halfHeight+1, width, height); run("Duplicate...", "title=TE2"); Stack.setXUnit("mm"); Stack.setYUnit("mm"); run("Properties...", "channels=1 slices=1 frames=1 pixel_width=0.0156250 pixel_height=0.0156250 voxel_depth=25.4001000 global"); imageCalculator("Add create", "TE1","TE2"); selectImage("Result of TE1"); rename("TE45.tif"); imageCalculator("Subtract create", "TE1","TE2"); selectImage("Result of TE1"); rename("T1-T2.tif"); imageCalculator("Subtract create", "TE2","TE1"); selectImage("Result of TE2"); rename("T2-T1.tif"); imageCalculator("Add create", "L","R"); selectImage("Result of L"); rename("L+R.tif"); imageCalculator("Subtract create", "L+R.tif","TE45.tif"); selectImage("Result of L+R.tif"); rename("(L+R)-TE45.tif"); imageCalculator("Subtract create", "L","R"); selectImage("Result of L"); rename("LCPL.tif"); imageCalculator("Subtract create", "R","L"); selectImage("Result of R"); rename("RCPL.tif"); selectImage("TE1"); close(); selectImage("TE2"); close(); selectImage("L"); close(); selectImage("R"); close(); selectImage("TE45.tif");//setTool("rectangle"); makeRectangle(0, 0, 36, 25); run("Fill", "slice"); //setTool("text"); setFont("Arial", 55, " antialiased"); setColor("yellow"); Overlay.drawString("TE45", 5, 45, 0.0); Overlay.show(); selectImage("L+R.tif");//setTool("rectangle"); makeRectangle(0, 0, 36, 25); run("Fill", "slice"); //setTool("text"); setFont("Arial", 55, " antialiased"); setColor("yellow"); Overlay.drawString("L+R", 5, 45, 0.0); Overlay.show(); selectImage("(L+R)-TE45.tif"); //setTool("rectangle"); makeRectangle(0, 0, 36, 25); run("Fill", "slice"); //setTool("text"); setFont("Arial", 55, " antialiased"); Overlay.drawString("(L+R) - TE45", 5, 45, 0.0); Overlay.show(); selectImage("LCPL.tif"); //setTool("rectangle"); makeRectangle(0, 0, 36, 25); run("Fill", "slice"); //setTool("text"); setFont("Arial", 55, " antialiased"); setColor("yellow"); Overlay.drawString("LCPL (L-R)", 5, 45, 0.0); Overlay.show(); selectImage("RCPL.tif"); //setTool("rectangle"); makeRectangle(0, 0, 36, 25); run("Fill", "slice"); //setTool("text"); setFont("Arial", 55, " antialiased"); setColor("yellow"); Overlay.drawString("RCPL (R-L)", 5, 45, 0.0); Overlay.show(); selectImage("T1-T2.tif"); //setTool("rectangle"); makeRectangle(0, 0, 36, 25); run("Fill", "slice"); //setTool("text"); setFont("Arial", 55, " antialiased"); setColor("yellow"); Overlay.drawString("T1-T2", 5, 45, 0.0); Overlay.show(); selectImage("T2-T1.tif"); //setTool("rectangle"); makeRectangle(0, 0, 36, 25); run("Fill", "slice"); //setTool("text"); setFont("Arial", 55, " antialiased"); setColor("yellow"); Overlay.drawString("T2-T1", 5, 45, 0.0); Overlay.show(); selectImage("TE45.tif"); selectImage("RCPL.tif"); selectImage("TE45.tif"); run("Flatten"); selectImage("TE45.tif"); close(); selectImage("LCPL.tif"); run("Scale Bar...", "width=5 height=10 thickness=30 hide overlay"); run("Flatten"); selectImage("LCPL.tif"); close(); selectImage("(L+R)-TE45.tif"); run("Scale Bar...", "width=5 height=10 thickness=30 hide overlay"); run("Flatten"); selectImage("(L+R)-TE45.tif"); run("Scale Bar...", "width=5 height=10 thickness=30 hide overlay"); close(); selectImage("T2-T1.tif"); run("Scale Bar...", "width=5 height=10 thickness=30 hide overlay"); run("Flatten"); selectImage("T2-T1.tif"); close(); selectImage("T1-T2.tif"); run("Scale Bar...", "width=5 height=10 thickness=30 hide overlay"); run("Flatten"); selectImage("T1-T2.tif"); close(); selectImage("RCPL.tif"); run("Scale Bar...", "width=5 height=10 thickness=30 hide overlay"); run("Flatten"); selectImage("RCPL.tif"); close(); selectImage("L+R.tif"); run("Scale Bar...", "width=5 height=10 thickness=15 hide overlay"); run("Flatten"); selectImage("L+R.tif"); close(); selectImage("LCPL-1.tif"); rename("LCPL.tif"); selectImage("T2-T1-1.tif"); rename("T2-T1.tif"); selectImage("(L+R)-TE45-1.tif"); rename("(L+R)-TE45.tif"); selectImage("RCPL-1.tif"); rename("RCPL.tif"); selectImage("T1-T2-1.tif"); rename("T1-T2.tif"); selectImage("L+R-1.tif"); rename("L+R.tif"); selectImage("TE45-1.tif"); rename("TE45.tif"); run("Concatenate...", " title=Stack keep open image1=L+R.tif image2=(L+R)-TE45.tif image3=LCPL.tif image4=RCPL.tif image5=[-- None --]"); run("Make Montage...", "columns=2 rows=2 scale=1 border=5"); rename("CPLP"); selectImage("Stack"); close(); selectImage("TE45.tif"); close();
```

Images were recorded with the camera's native 2448 x 2048-pixel FOV without image cropping with total accumulated integration time varied from 20 ms to 1 s with 5 – 32 frame averaged sequences. The total integration time has been determined case by case by careful monitoring of maximum 8-bit pixel values to eliminate pixel saturation and achieve maximum overall image brightness for EDCC calculations.

The all-important 8-bit average pixel chiroptical contrast value calculations were facilitated by selecting and averaging equal size and shape arbitrary area portions of the sample using a custom written macro operating the *ImageJ* analyse-measure plugin with mean ROI intensity

value mode that employs a maximum average value ROI histogram methodology that is based on a standard Gaussian distribution profiling of the average intensity values:

```
makeRectangle(580, 400, 250, 250); run("Properties... ", "  width=5"); run("Add Selection..."); run("Measure");
makeRectangle(580, 1425, 250, 250); run("Properties... ", "  width=5"); run("Add Selection..."); run("Measure");
makeRectangle(1805, 1425, 250, 250); run("Properties... ", "  width=5"); run("Add Selection..."); run("Measure");
makeRectangle(1805, 400, 250, 250); run("Properties... ", "  width=5"); run("Add Selection..."); run("Measure");
```

VI.3.4. Two photon cross section determination

The two photon cross-section (σ^2) is calculated according to the established procedures:[111]

$$\sigma^2 = \frac{F_S}{\phi_S C_S} \times \frac{\phi_R C_R \sigma_R^2}{F_R}$$

where *S* is sample, *R* is reference, ϕ is the total emission quantum yield of the sample (ϕ_S), *C* is the concentration, *n* is the refractive index and F_S (λ) and F_R (λ) are the integrated total emission spectra for the sample and reference, respectively. Additionally, the two-photon nature of the excitation process was proven by recording an excitation power dependence; the resulting line has a slope of two on a logarithmic scale.[76] The cross sections were calculated with reference to **RhB** in methanol.

Two photon spectroscopy was performed using a tuneable femtosecond pulsed laser (680 – 1300 nm, *Coherent Discovery TPC*, 100 fs, 80 MHz) perpendicularly mounted to an *Ocean Optics HR2000Pro* (2048- pixel linear CCD *Sony ILX5* chip, 200 µm slit, H3 grating, 350 – 850 nm spectral region) spectrometer.[20] The laser beam was focused onto the centre of the 1.0000 cm path sample holder (*Thor labs CVH100*) by a dedicated ultrafast laser lens (*Edmund Optics 11711*, f = 50 mm). The spectrometer was also equipped with a perpendicularly mounted 365 nm LED *Nichia*, 1W) and been operated using a modified version of the above-mentioned custom time resolved detection and accumulation algorithm written in *Labview2013* software. In order to eliminate unwanted artefacts associated with stray light from multiphoton excitation the spectrometer was equipped with a rotating filter wheel (*Thor Labs*, *CFW6*) housing an LPF420 (*Comar Optics*, for 365 nm UV-LED excitation) and SPF650 and SPF700 (*Edmund Optics*, *8472* and *8474*) short pass filters.

VI.4. Spin coating and atomic force microscopy

Spin coating solutions contained 22 mg PMMA (average M_w ~15000 by gel permeation chromatography, density 1.18 g cm^{-3}) and ~15 µg of EuL (obtained by preparing 5 ml of 0.18 max absorbance solution and then evaporating the solvent) dissolved in 0.500 ml of DCM. This resulted in PMMA concentration of 44 mg mL^{-1} in DCM and 650 µM EuL concentration in PMMA. The solutions were spin coated on 1*1.5 cm cut glass microscope slides. To prepare films on the black electrical tape substrate, the tape was attached to the glass substrates and

cut to size. Each film was prepared by casting 10 µl of the solution on the substrate spinning at 8000 rpm.

AFM was performed on an *SPM SmartSPM™-1000* (*AIST-NT*) which consisted of the base and scanning head, both operated by a scanning probe microscopy controller. The base contained the sample metal holder that allowed for magnetic attachment of the SPM specimen discs (15 mm, *Agar Scientific*) containing a sample that was attached to the specimen discs using carbon tabs (9 mm, *Agar Scientific*). The metal holder was attached to a digitally controlled (*SmartSPM* software) motorised positioning system allowing for translation of the sample holder vertically (18 mm range) and horizontally (5 × 5 mm). The scanning head comprised of a cantilever probe holder, laser and a four-sectional PD. The probe was a silicon tip with the 10 nm diameter and force constant of 0.02 - 0.77 N/m designed for contact-mode (*NANOSENSORS™*).

VI.5. Live cell imaging using laser scanning confocal microscopy

LSCM experiments were conducted using NIH3T3 embryonic mouse skin fibroblast cell line (*ATCC*, CRL-1658), established and maintained in a category 2 cell culture facility. Cells were maintained in exponential growth as monolayers in DMEM F-12 (Dulbecco's Modified Eagle Medium) supplemented with 10% foetal bovine serum. Cells were grown in 75 cm^2 plastic culture flasks and incubated at 37 °C, 10% humidity and 5% (v/v) CO_2. Cells were harvested by treatment with 0.25% (v/v) trypsin solution in phosphate-buffered saline for 5 min at 37 °C. The cells were dosed with 1 mM stock solutions of **EuL^3** and **EuL^{3g}** in DMSO that were diluted to 5 µM in DMEM, maintaining less than 1% (v/v) DMSO concentration. The cells were grown in *ibidi* chamber slides until ~80% confluency for dosing and 30 minutes. The **EuL^3** and **EuL^{3g}** containing media was replaced with the media lacking phenol red.

LSCM was performed using *Leica Microsystems SP5 II* microscope with PE provided by a fibre coupled 80 mW variable power 355 nm Nd:YAG continuous wave laser. The intensity of emission was quantified by fibre-coupled high performance matched tandem avalanche PDs (*Leica ADP*s, *Becker & Hickl* ID-120). Images were processed using *ImageJ* software (version 1.53q) and its associated plugins.

VI.6. Synthetic Procedures

Ethyl (6-methyl-4-nitropyridin-2-yl)(phenyl)phosphinate, **1**[80]

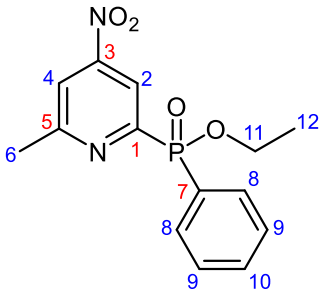

2-bromo-6-methyl-4-nitropyridine (4.00 g, 18.4 mmol, 1 eq.) was dissolved in anhydrous toluene. The solution was degassed (freeze-pump-thaw × 3) before TEA (9 ml), ethyl phenylphosphinate (3.20 ml, 21.2 mmol, 1.2 eq.) and [1,1′-bis(diphenylphosphino) ferrocene]dichloropalladium (II) (0.756 g, 0.926 mmol, 0.05 eq.) were added. The resulting red solution was stirred at 120 °C for 16 hours under argon to produce a black residue. The solvent was then removed under reduced pressure, and the residue dissolved in DCM. The solution was washed with 1 M HCl (20 ml × 3) and water (20 ml × 2), followed by extraction of the combine aqueous layers with DCM (10 ml × 3). The combined organic layers were dried over Na_2SO_4 and filtered. The solvent was removed under reduced pressure to result in a black solid that was then purified by flash chromatography (solid loading, silica, 1:3 to 3:2 EtOAc to hexane) to yield a yellow oil (1.15 g, 3.748 mmol, 20%).

^{1}H NMR (400 MHz, $CDCl_3$) δ 8.47 (1 H, dd, $^3J_{H\text{-}P}$ 6.2, $^4J_{H\text{-}H}$ 2.0, H^2), 7.89 (2 H, ddd, $^3J_{H\text{-}P}$ 12.3, $^3J_{H\text{-}H}$ 8.2, $^4J_{H\text{-}H}$ 1.5, H^8), 7.84 (1 H, t, $^4J_{H\text{-}H}$ 1.5, H^4), 7.46 (1 H, td, $^3J_{H\text{-}H}$ 7.5, $^4J_{H\text{-}H}$ 1.5, H^{10}), 7.38 (2 H, td, $^3J_{H\text{-}H}$ 7.7, $^4J_{H\text{-}P}$ 3.8, H^9), 4.14-4.03 (2 H, m, H^{11}), 2.64 (3 H, s, H^6), 1.29 (3 H, t, 7.1, H^{12}).

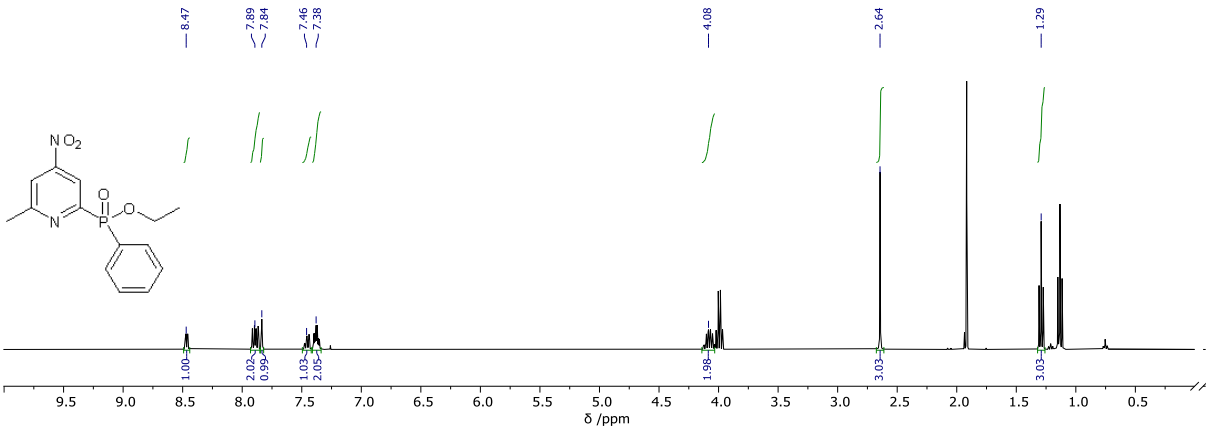

Figure 6.1: ^{1}H NMR (400 MHz, $CDCl_3$) spectrum of **1**.

Ethyl (4-bromo-6-methylpyridin-2-yl)(phenyl)phosphinate, **2**[80]

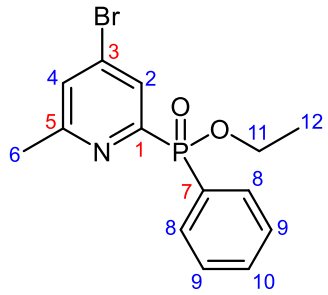

Ethyl(6-methyl-4-nitropyridin-2-yl)(phenyl)phosphinate, **1** (1.15 g, 3.748 mmol, 1 eq.) was dissolved in acetyl bromide (12.0 ml, 162 mmol, 43 eq.), and the solution was stirred at 70 °C for 10 hours. After the reaction mixture was allowed to cool to rt., it was dropwise added to stirring ice-cold MeOH (30 ml). Once added, the mixture was stirred at rt for further an additional 1 hour before the solvent was removed under reduced pressure to yield dark red oil. The oil was then dissolved in triethyl orthoformate (30.0 ml, 180 mmol, 48 eq.) and refluxed at 120 °C for 65 hours under argon. The solvent was then removed under reduced pressure to yield brown oil which was purified by flash chromatography (silica, DCM to 0.8 % MeOH in DCM) to yield pale yellow oil (442 mg, 1.30 mmol, 35 %).

LCMS (ESI$^+$) *m/z* 340.144 $[M+H]^+$.

^{1}H NMR (400 MHz, $CDCl_3$) δ 8.04 (1 H, dd, $^3J_{H\text{-}P}$ 6.2, $^4J_{H\text{-}H}$ 1.8, H^2), 7.95 (2 H, ddd, $^3J_{H\text{-}P}$ 12.2, $^3J_{H\text{-}H}$ 8.1, $^4J_{H\text{-}H}$ 1.5, H^8), 7.50 (1 H, td, $^3J_{H\text{-}H}$ 7.5, $^4J_{H\text{-}H}$ 1.5, H^{10}), 7.42 (2 H, td, $^3J_{H\text{-}H}$ 7.4, $^4J_{H\text{-}P}$ 3.7, H^9), 7.36 (1 H, t, $^4J_{H\text{-}H}$ 1.4, H^4) 4.18-4.03 (2 H, m, H^{11}), 2.51 (3 H, s, H^6), 1.33 (3 H, t,$^3J_{H\text{-}H}$ 7.1, H^{12}).

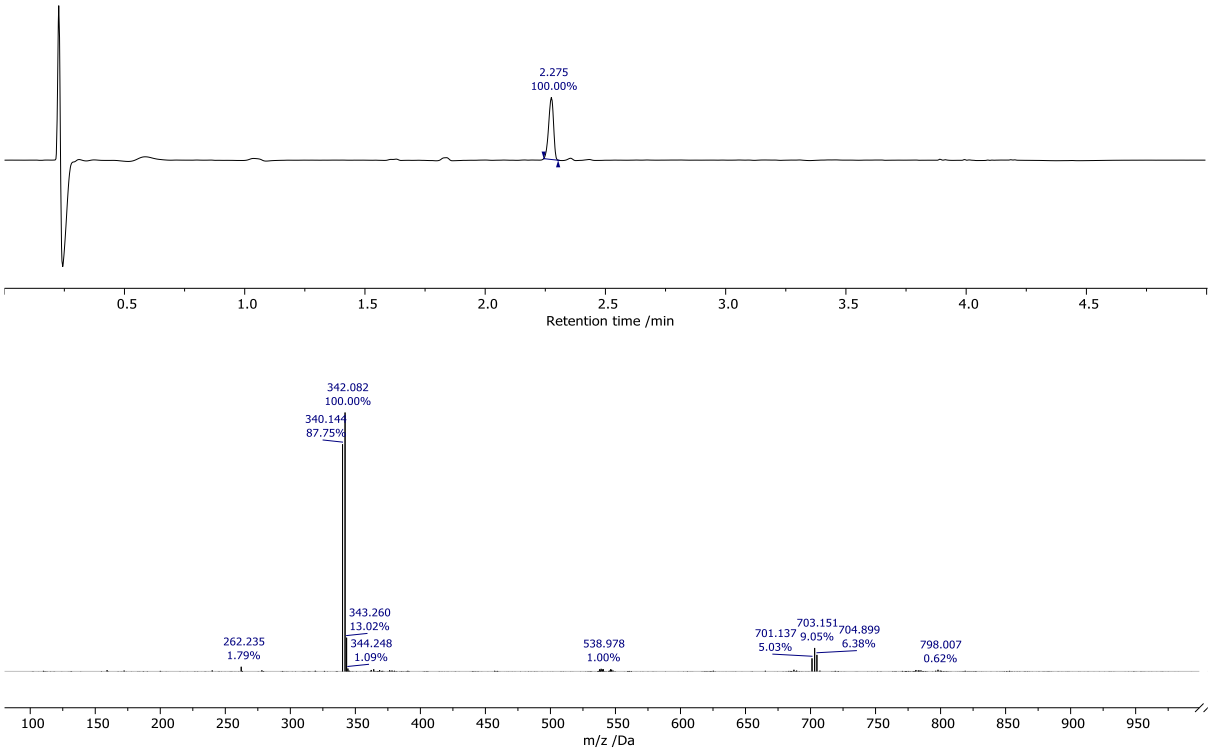

Figure 6.2: LCMS (Method E) of **2** AC (210-400 nm) (top) and the MS (ESI$^+$) at 2.275 min (bottom).

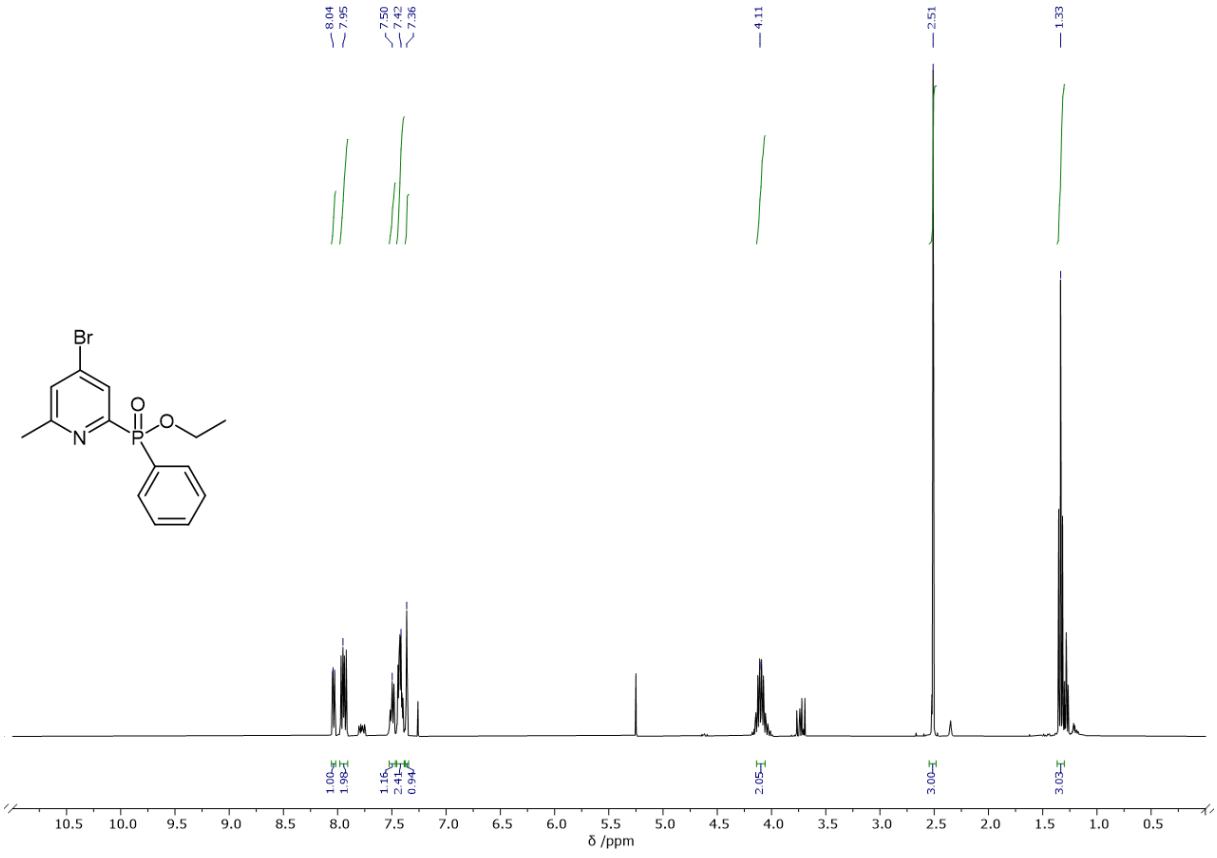

Figure 6.3: ^{1}H NMR (400 MHz, $CDCl_3$) spectrum of **2**.

Ethyl (4-bromo-6-methyl-1-oxo-pyridin-2-yl)(phenyl)phosphinate, **3**[80]

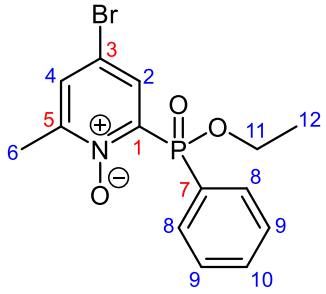

Ethyl (4-bromo-6-methylpyridin-2-yl)(phenyl)phosphinate, **2** (442 mg, 1.30 mmol, 1 eq.) and meta-chloroperoxybenzoic acid (500 mg, 2.90 mmol, 2.2 eq.) were dissolved in anhydrous $CDCl_3$ (8 ml) and refluxed at 65°C for 20 hours under argon. After that, solvent was removed under reduced pressure to give yellow residue which was redissolved in DCM (15 ml) and washed with 0.5 M sodium bicarbonate (15 ml × 4), followed by extraction of the combined aqueous layers with DCM (15 ml × 3). The combined organic layers were then dried over Na_2SO_4, filtered and concentrated. The crude product was purified by flash chromatography (DCM to 2.5 % MeOH in DCM) to yield yellow oil (245 mg, 0.689 mmol, 53%);

LCMS (ESI^+) *m/z* 356.144 $[M+H]^+$.

^1H NMR (400 MHz, $CDCl_3$) δ 8.05 (1 H, dd, $^3J_{H-P}$ 7.8, $^4J_{H-H}$ 2.9, H^2), 7.97 (2 H, ddd, $^3J_{H-P}$ 13.7, $^3J_{H-H}$ 8.3, $^4J_{H-H}$ 1.5, H^8), 7.50 (1 H, td, $^3J_{H-H}$ 7.5, $^4J_{H-H}$ 1.5, H^{10}), 7.45 (1 H, d, $^4J_{H-H}$ 3.0, H^4), 7.41 (2 H, td, $^3J_{H-H}$ 7.7, $^4J_{H-P}$ 4.1, H^9), 4.17-4.08 (2 H, m, H^{11}), 2.32 (3 H, s, H^6), 1.34 (3 H, t, $^3J_{H-H}$ 7.1, H^{12}).

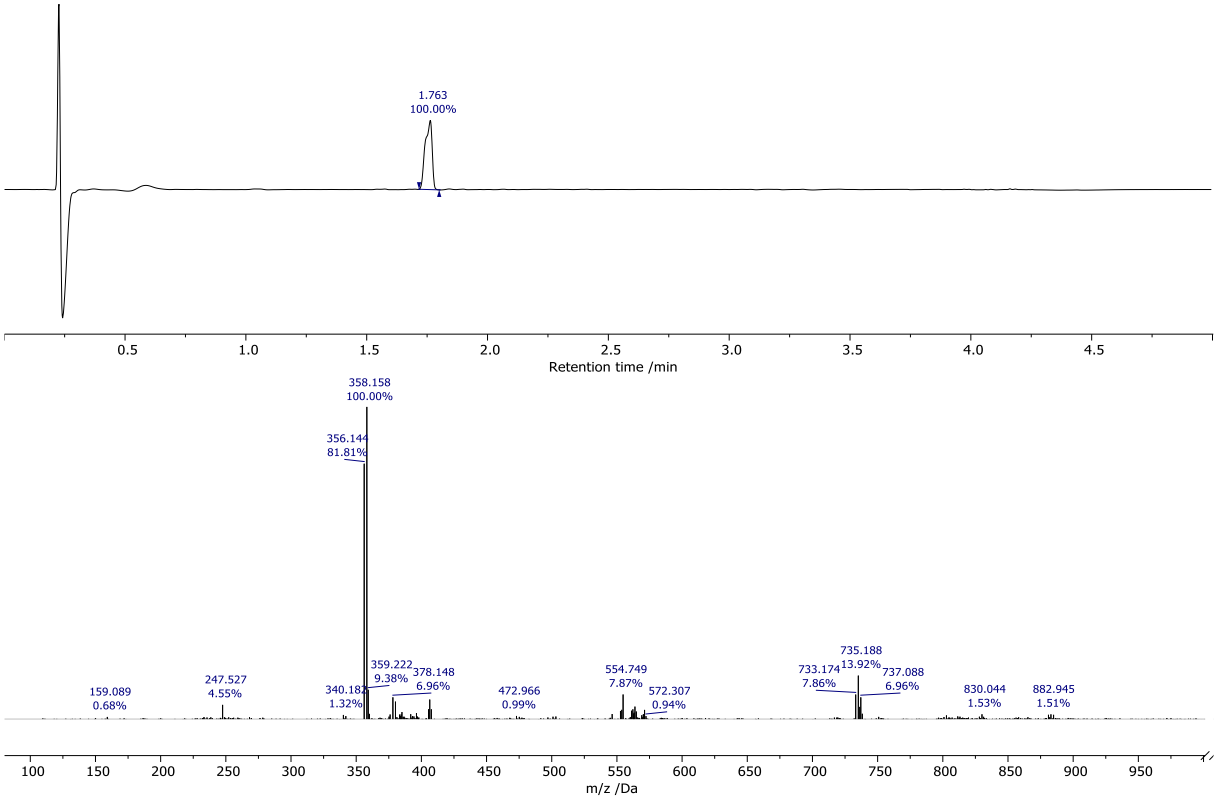

Figure 6.4: LCMS (Method E) of **3** AC (210-400 nm) (top) and the MS (ESI⁺) at 1.763 minutes (bottom).

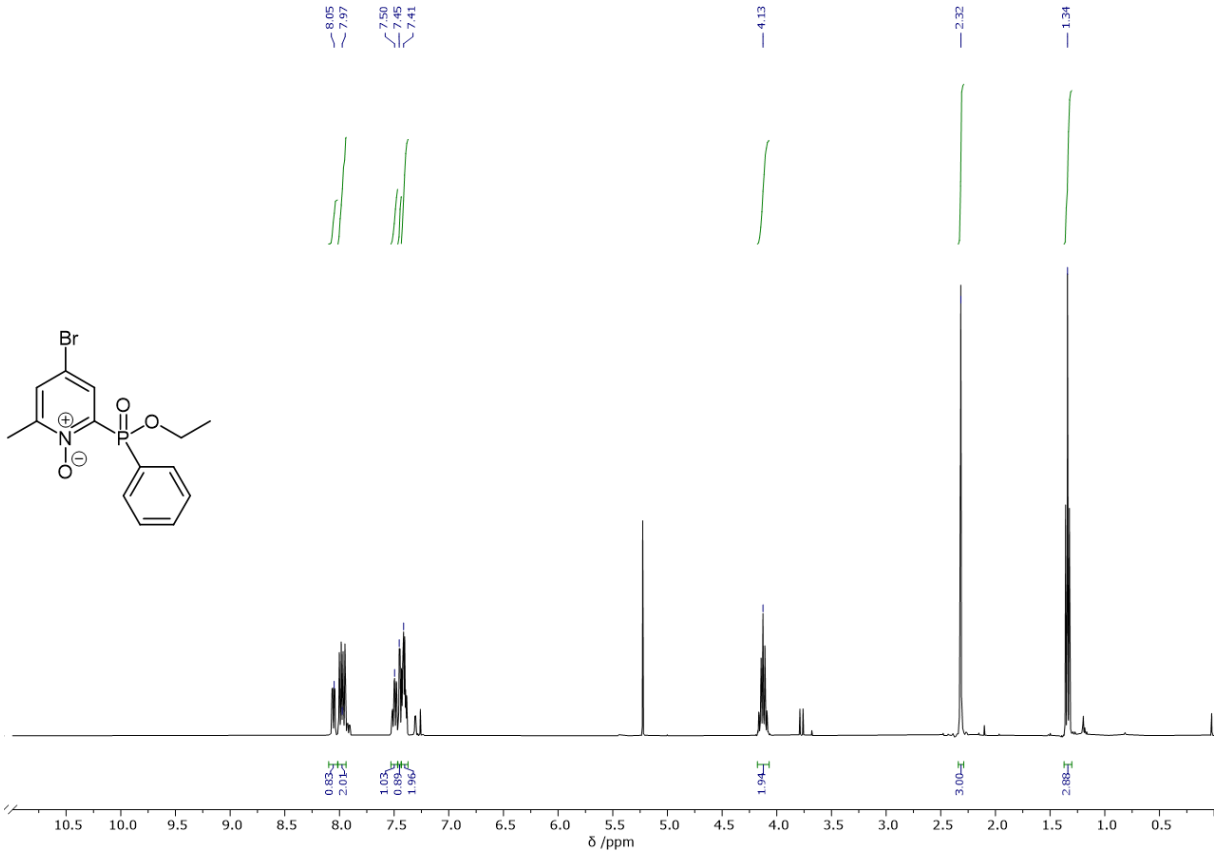

Figure 6.5: ^{1}H NMR (400 MHz, $CDCl_3$) spectrum of **3**.

Ethyl [4-bromo-6-(hydroxymethyl)pyridin-2-yl](phenyl) phosphinate, **5**[80]

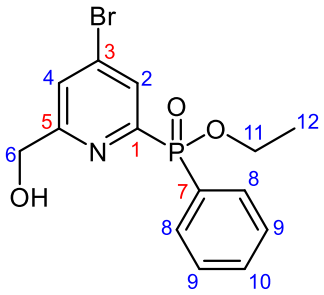

Trifluoroacetic acid anhydride (2.00 ml, 14.4 mmol, 21 eq.) was added to the solution of ethyl (4-bromo-6-methyl-1-oxo-pyridin-2-yl)(phenyl)phosphinate, **3** (245 mg, 0.689 mmol, 1 eq.) in anhydrous MeCN (5 ml). The resulting green solution was refluxed at 60°C for 6 h under argon until the formation of trifluoroacetate ester **4** was complete (^{1}H NMR: δ H^3 2.32 $\rightarrow$ 5.46 ppm). The solvent was removed under reduced pressure, and the residue was redissolved in a 1:1 solution of ethanol and water (10 ml). The resulting solution was stirred at rt for 17 hours followed by evaporation of the organic solvent under reduced pressure. The resulting aqueous solution was extracted with DCM (20 ml × 3), and the combined organic layers were dried over Na_2SO_4, filtered and concentrated. The crude product was purified by flash chromatography (silica, DCM to 2.5 % MeOH in DCM) to yield yellow oil (104 mg, 0.292 mmol, 42 %).

^{1}H NMR (400 MHz, $CDCl_3$) δ 8.10 (1 H, dd, $^3J_{H\text{-}P}$ 6.0, $^4J_{H\text{-}H}$ 1.8, H^2), 7.92 (2 H, ddd, $^3J_{H\text{-}P}$ 12.3, $^3J_{H\text{-}H}$ 8.3, $^4J_{H\text{-}H}$ 1.4, H^8), 7.61 (1 H, t, $^4J_{H\text{-}H}$ 1.4, H^4), 7.54 (1 H, td, $^3J_{H\text{-}H}$ 7.5, $^4J_{H\text{-}H}$ 1.5, H^{10}), 7.46 (2 H, td, $^3J_{H\text{-}H}$ 7.7, $^4J_{H\text{-}P}$ 3.7, H^9), 4.74 (2 H, s, H^6), 4.19-4.05 (2 H, m, H^{11}), 1.36 (3 H, t, $^3J_{H\text{-}H}$ 7.0, H^{12}).

LCMS (ESI$^+$) *m/z* 356.144 [M+H]$^+$.

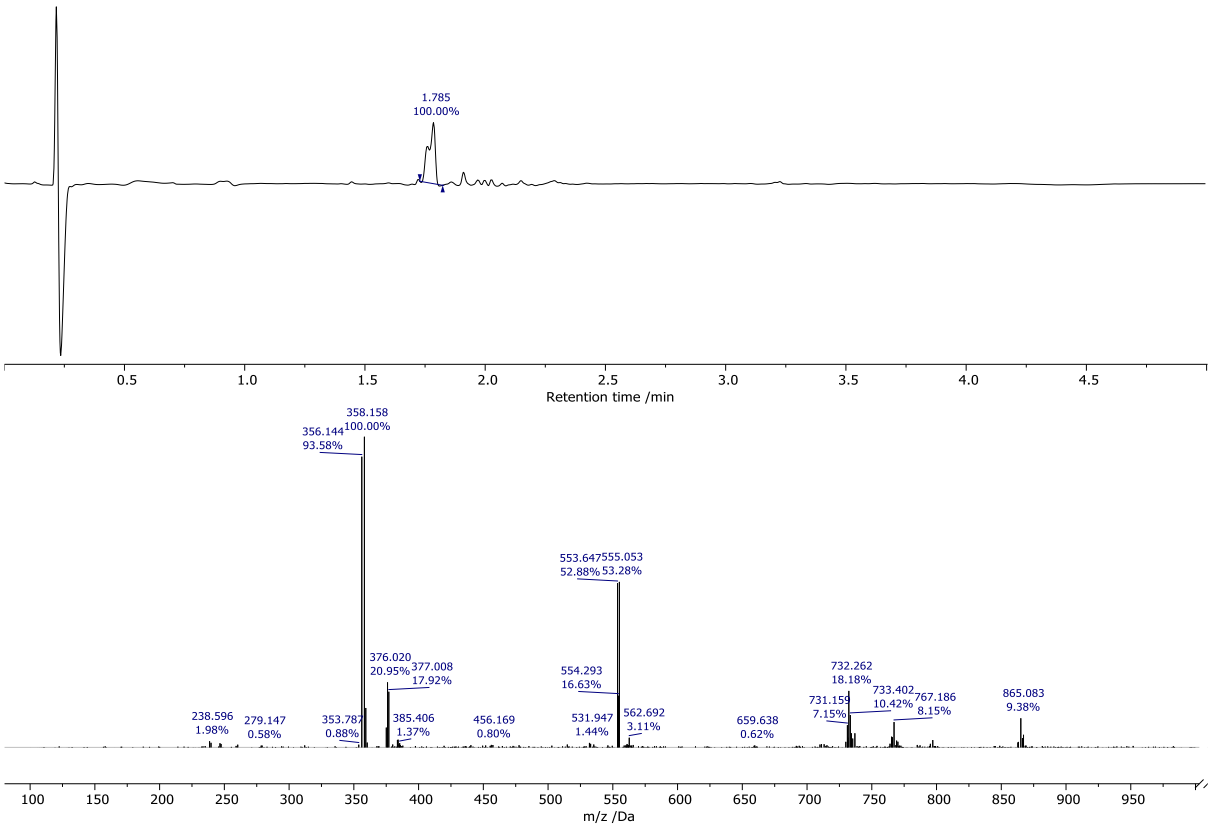

Figure 6.6: LCMS (Method E) of **5** AC (210-400 nm) (top) and the MS (ESI$^+$) at 1.785 minutes (bottom).

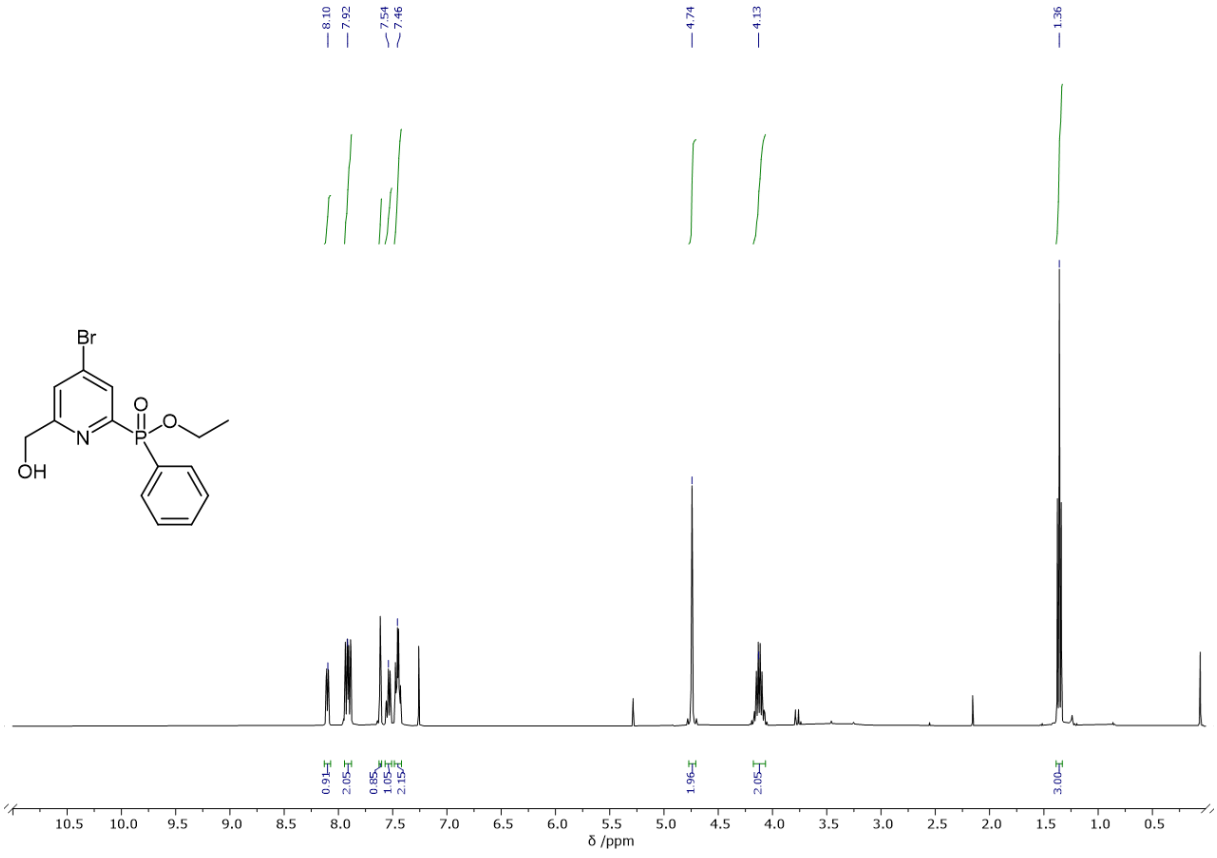

Figure 6.7: ^{1}H NMR (400 MHz, $CDCl_3$) spectrum of **5**.

2-(2,2-Dibromovinyl)-1,3,5-trimethoxybenzene, **6**[80]

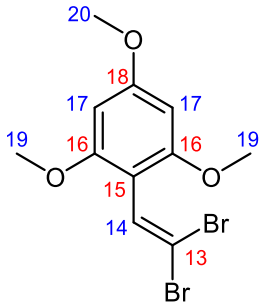

A solution of CBr_4 (1.69 g, 5.10 mmol, 2 eq.) in anhydrous DCM (3 ml) was dropwise added to a cooled (ice bath) solution of 2,4,6-trimethoxybenzaldehyde (0.5 g, 2.5 mmol, 1 eq.) and PPh_3 (5.36 g, 20.5 mmol, 10 eq.) in anhydrous DCM (3 ml), and the resulting solution was stirred at rt for 20 hours under argon. After that, the solution was washed with water (10 ml × 5) followed by extraction of combined aqueous layers with DCM (10 ml × 3). The combined organic layers were dried over Na_2SO_4, filtered and concentrated. The crude product was purified by column chromatography (silica, 30 to 50 % DCM in hexane) to yield white solid (321 mg, 0.912 mmol, 36%).

LCMS (ESI^+) *m/z* 351.051 $[M+H]^+$.

^1H NMR (400 MHz, $CDCl_3$) δ 7.19 (1 H, s, H^{14}), 6.11 (2 H, s, H^{17}), 3.83 (3 H, s, H^{20}), 3.81 (6 H, s, H^{19});

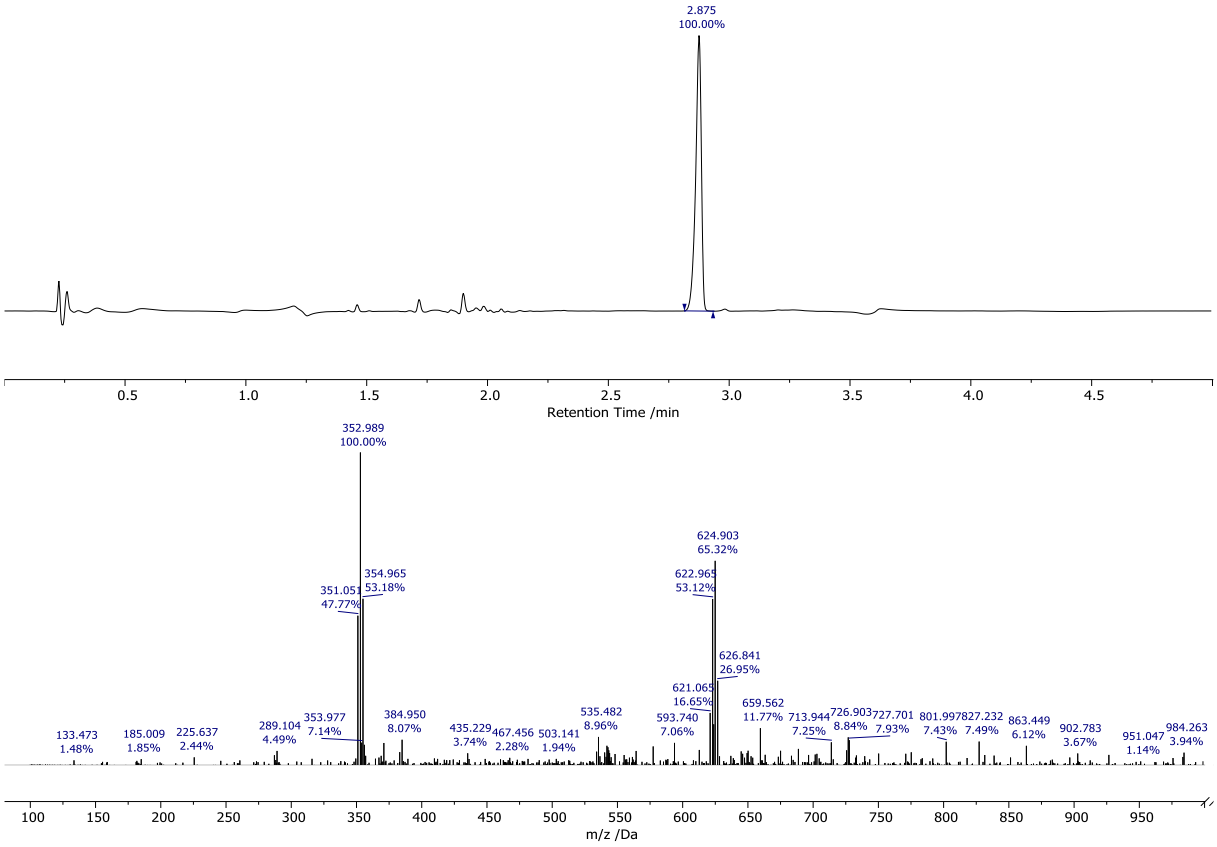

Figure 6.8: LCMS (Method E) of **6** AC (210-400 nm) (top) and the MS (ESI⁺) at 2.875 minutes (bottom).

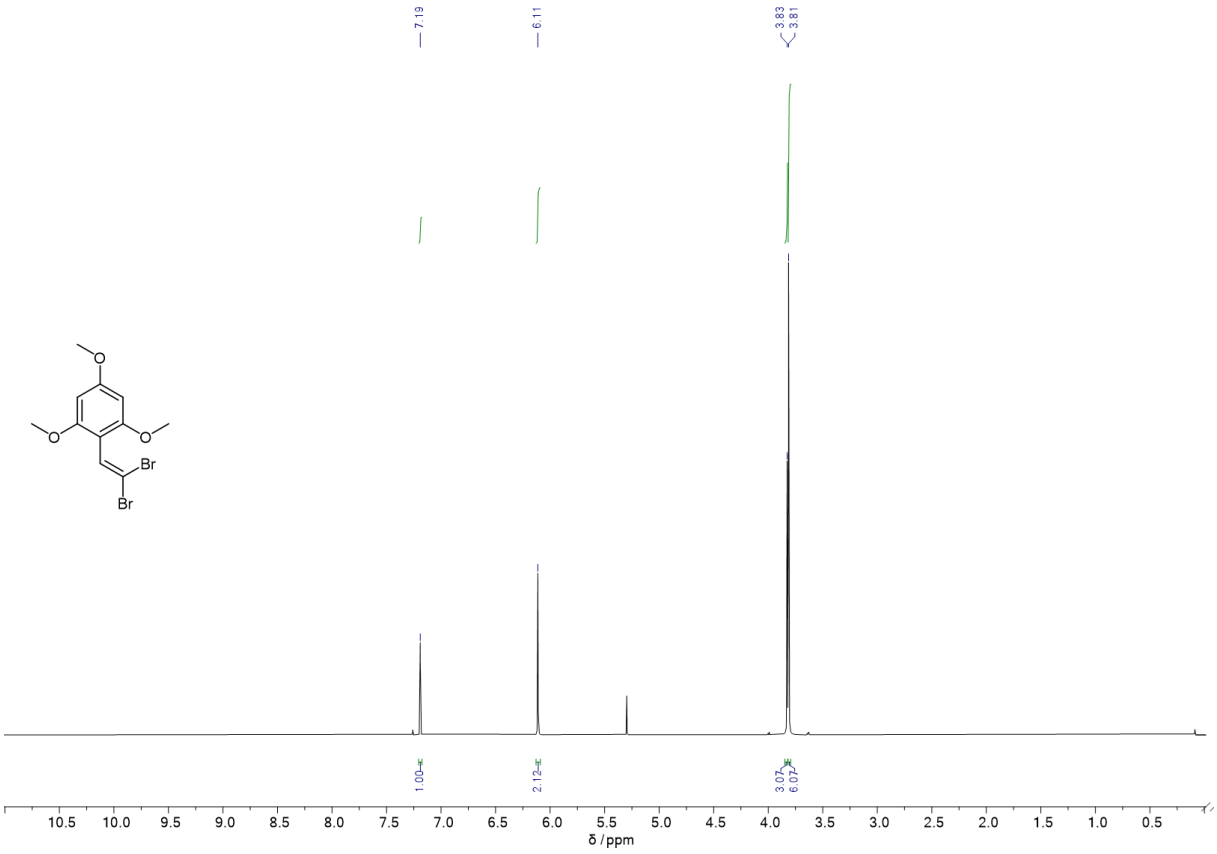

Figure 6.9: ^{1}H NMR (400 MHz, $CDCl_3$) spectrum of **6.**

2-Ethynyl-1,3,5-trimethoxybenzene, **7**[80]

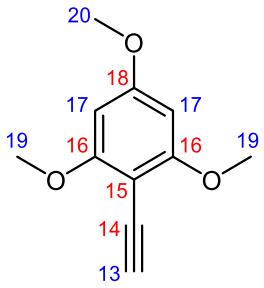

2-(2,2-dibromovinyl)-1,3,5-trimethoxybenzene, **6** (321 mg, 0.912 mmol, 1 eq.) was dissolved in anhydrous THF and cooled to -78 °C (acetone, dry ice). 1.6 M solution of n-butyllithium in hexane (1.5 ml, 2.4 mmol, 2.6 eq.) was then added dropwise, and the resulting orange solution was stirred for 20 minutes at -78 °C. After that, water (4 ml) was added dropwise, and the resulting green solution was stirred at rt for additional 30 minutes. After that, the organic solvents were removed under reduced pressure, and the resulting aqueous solution was extracted with ethyl acetate (20 ml × 3). The combined organic layers were washed with brine, dried over Na_2SO_4, filtered and dried under reduced pressure to yield yellow solid that was used without further purification (0.171 g, 0.890 mmol, 98%).

LCMS (ESI$^+$) *m/z* 193.104 $[M+H]^+$.

^{1}H NMR (400 MHz, $CDCl_3$) δ 6.10 (2 H, s, H^{17}), 3.88 (6 H, s, H^{19}), 3.83 (3 H, s, H^{20}), 3.50 (1 H, s, H^{13}).

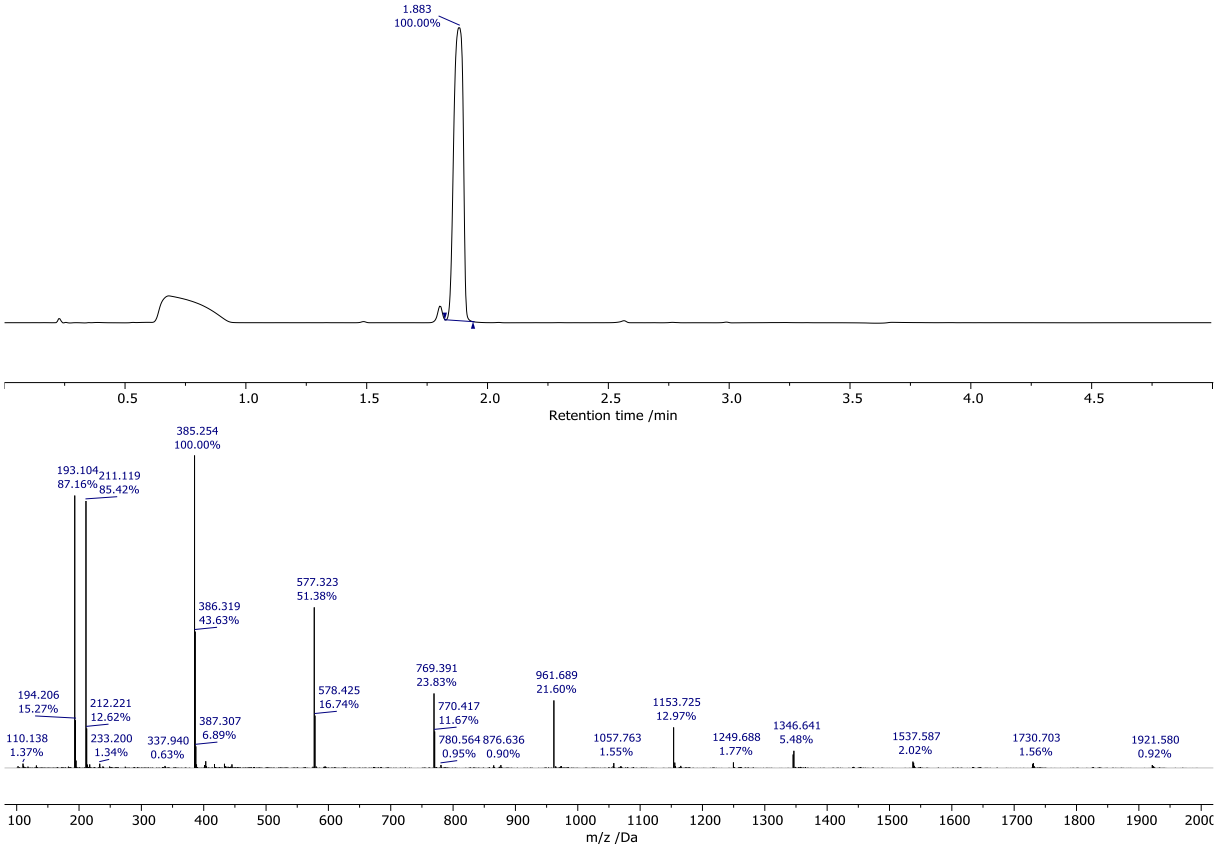

Figure 6.10: LCMS (Method E) of **7** AC (210-400 nm) (top) and the MS (ESI$^+$) at 1.883 minutes (bottom).

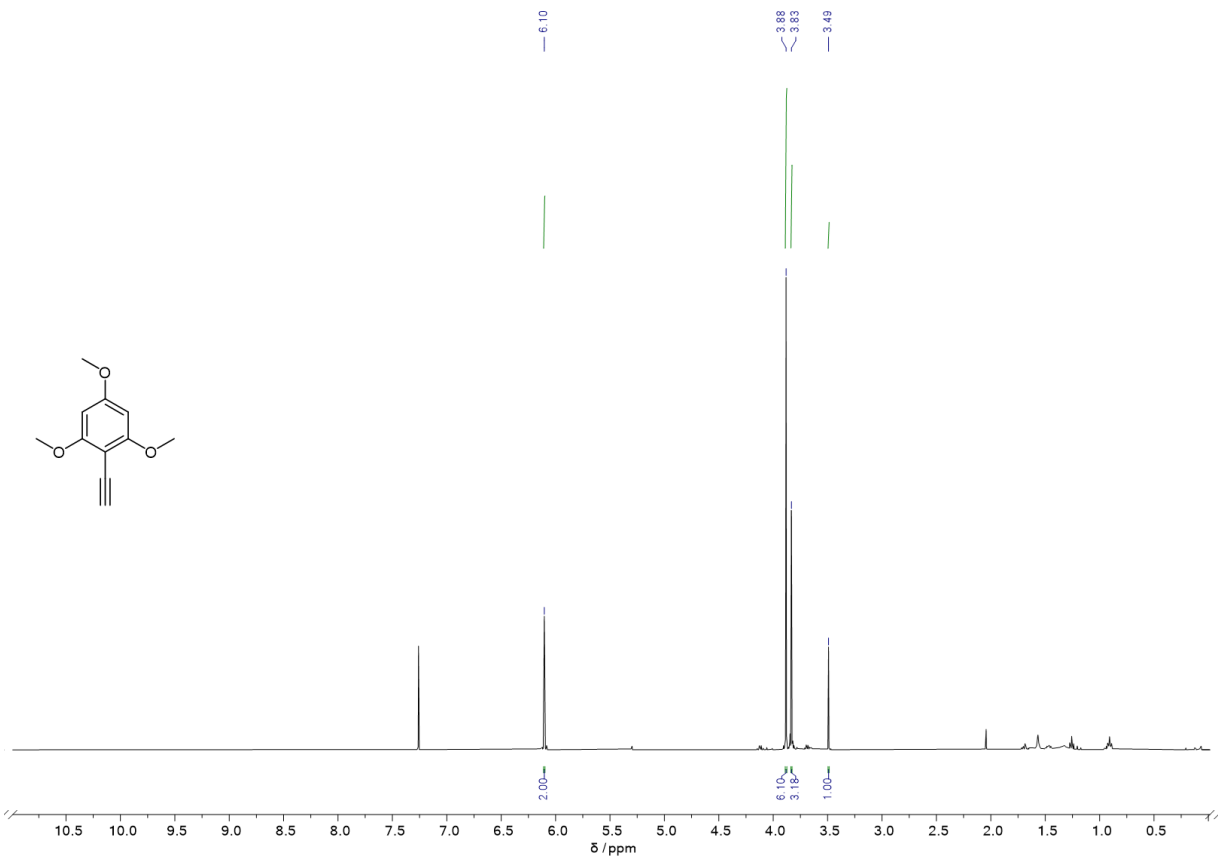

Figure 6.11: ^{1}H NMR (400 MHz, $CDCl_3$) spectrum of **7**.

Ethyl [6-(hydroxymethyl)-4-[2-(2,4,6-trimethoxyphenyl)ethynyl] pyridin-2-yl](phenyl)phosphinate, **8**

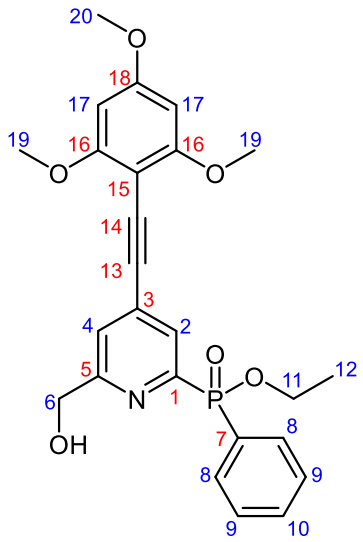

2-ethynyl-1,3,5-trimethoxybenzene **7** (0.0613 g, 0.319 mmol 1.1 eq.), ethyl [4-bromo-6-(hydroxymethyl)pyridin-2-yl](phenyl) phosphinate **5** (0.104 g, 0.290 mmol, 1 eq.) and $[Pd(allyl)Cl]_2$ (0.0106 g, 0.0290 mmol, 0.1 eq.) were dissolved in anhydrous MeCN (3 ml) and degassed (freeze-pump-thaw × 3). After that, $P(^tBu)_3$ (20 µl, 0.087 mmol, 0.3 eq.) and piperidine (110 µl,1.16 mmol, 4 eq.) were added, and the resulting solution was stirred at 40°C for 20 hours under argon. Organic solvents were then evaporated under reduced pressure, and the residue was dissolved in DCM (3 ml). The resulting solution was washed with water (5 ml × 3), followed by extraction of the combined aqueous layers with DCM (5 ml × 3). The combined organic layers were then dried over Na_2SO_4, filtered and isolated from solvent under reduced pressure. The resulting dark red oil was purified using reverse-phase HPLC (C_{18}, Method B, retention time = 10 minutes) to yield yellow oil (32 mg, 0.068 mmol, 23%).

LCMS (ESI^+) *m/z* 468.292 $[M+H]^+$.

^1H NMR (400 MHz, $CDCl_3$) δ 8.15 (1 H, d, $^3J_{H-P}$ 6.5, H^2), 7.97 (2 H, ddd, $^3J_{H-P}$ 12.3, $^3J_{H-H}$ 8.3, $^4J_{H-H}$ 1.4, H^8), 7.54 (1 H, td, $^3J_{H-H}$ 7.5, $^4J_{H-H}$ 1.5, H^3), 7.47 (2 H, td, $^3J_{H-H}$ 7.7, $^4J_{H-P}$ 3.7, H^9), 7.40 (1 H, t, $^4J_{H-H}$ 1.4 H^4), 6.10 (2 H, s, H^{17}), 4.74 (2 H, d, $^4J_{H-H}$ 1.4, H^6), 4.19-4.05 (2 H, m, H^{11}), 3.89 (6 H, s, H^{19}), 3.85 (3 H, s, H^{20}), 1.38 (3 H, t, $^3J_{H-H}$ 7.1, H^{12});

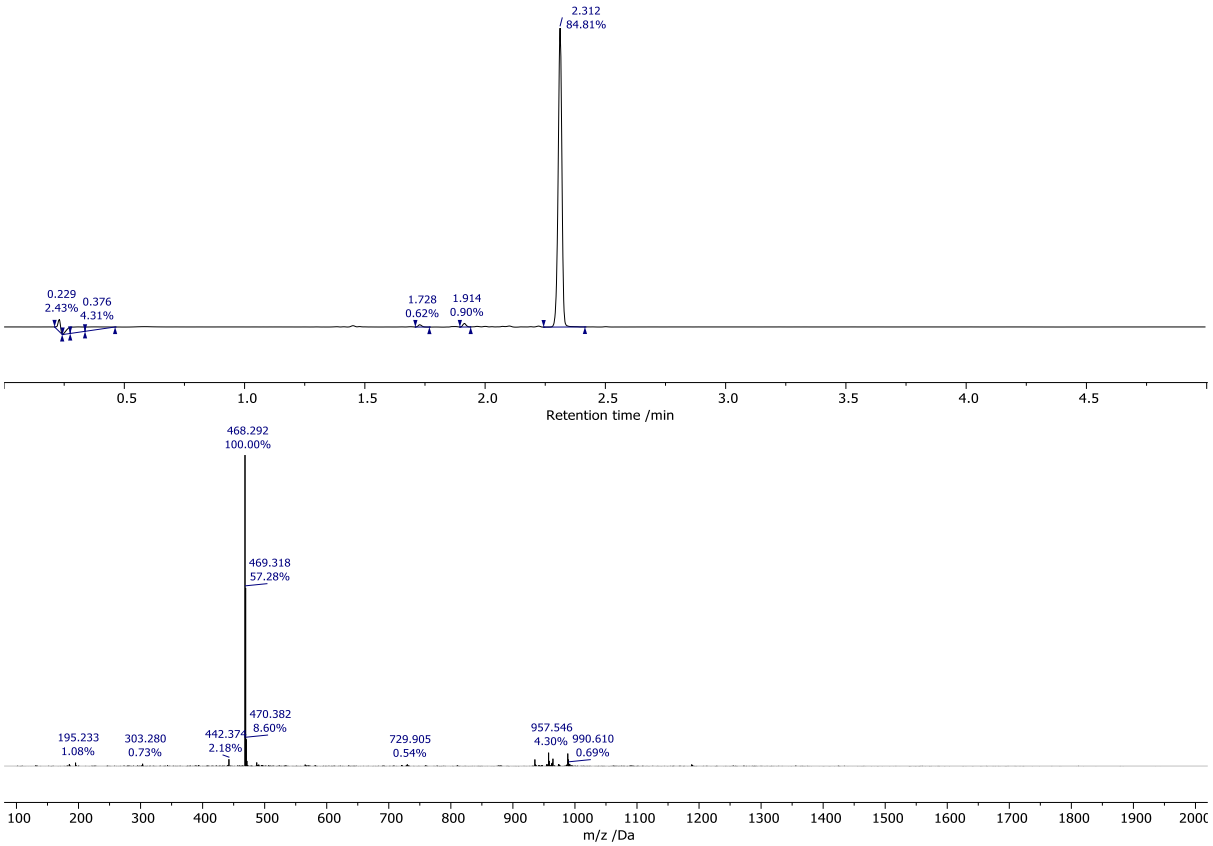

Figure 6.12: LCMS (Method E) of **8** AC (210-400 nm) (top) and the MS (ESI^+) at 2.312 minutes (bottom).

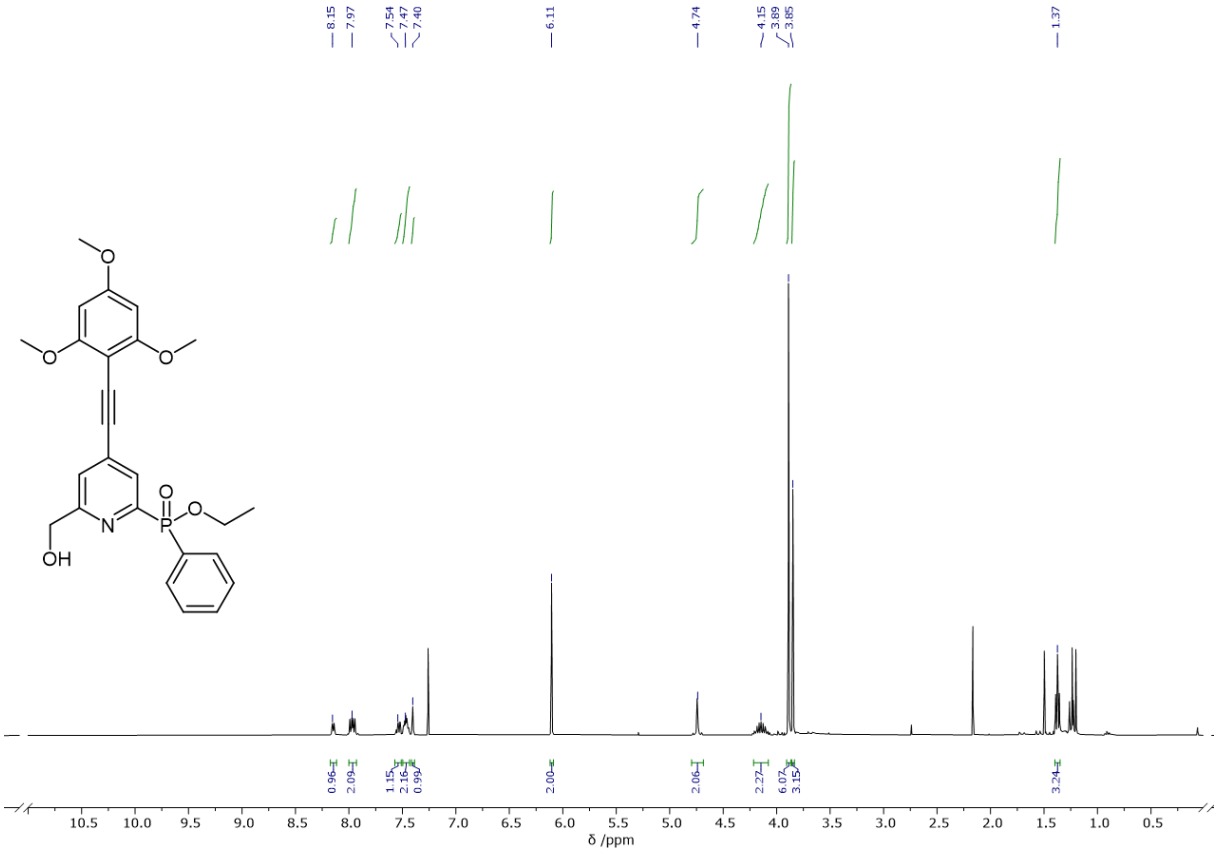

Figure 6.13: ^1H NMR (400 MHz, $CDCl_3$) spectrum of **8**.

{4-[2-(2,4,6-Trimethoxyphenyl)ethynyl]-6-[ethoxy(phenyl)phosphoryl] pyridin-2yl}methyl methanesulfonate, **9**[80]

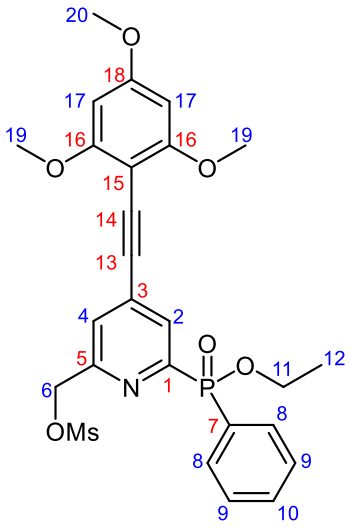

Ethyl [6- (hydroxymethyl)-4-[2-(2,4,6-trimethoxyphenyl) ethynyl] pyridin-2-yl] (phenyl) phosphinate **8** (32 mg, 0.068 mmol, 1 eq.) was dissolved in anhydrous THF (3 ml). *N,N*-Diisopropylethylamine (DIPEA) (120 µl, 0.520 mmol, 7.6 eq.) and methanesulfonic anhydride (48 mg, 0.278 mmol, 4 eq.) were added, and the resulting solution was stirred at rt for 4h under argon. After that, organic solvents were then evaporated under reduced pressure, and the residue dissolved in DCM (10 ml). The resulting solution was washed with water (15 ml × 3), followed by extraction of the combined aqueous layers with DCM (15 ml × 3). The combined organic layers were then dried over Na_2SO_4, filtered and isolated from solvent under reduced pressure to yield dark yellow oil that was used in the next step without further purification.

^{1}H NMR (400 MHz, $CDCl_3$) δ 8.22 (1 H, dd, $^3J_{H\text{-}P}$ 6.2, $^4J_{H\text{-}H}$ 1.4, H^2), 7.97 (2 H, ddd, $^3J_{H\text{-}P}$ 12.3, $^3J_{H\text{-}H}$ 8.3, $^4J_{H\text{-}H}$ 1.4, H^8), 7.60 (1 H, t, $^4J_{H\text{-}H}$ 1.5, H^4), 7.57 (1 H, td, $^3J_{H\text{-}H}$ 7.5, $^4J_{H\text{-}H}$ 1.5, H^{10}), 7.47 (2 H, td, $^3J_{H\text{-}H}$ 7.7, $^4J_{H\text{-}P}$ 3.7, H^9), 6.14 (2 H, s, H^{17}), 5.32 (2 H, s, H^6), 4.19-4.05 (2 H, m, H^{11}), 3.93 (6 H, s, H^{19}), 3.88 (3 H, s, H^{20}), 1.40 (3 H, t, $^3J_{H\text{-}H}$ 7.1, H^{12}).

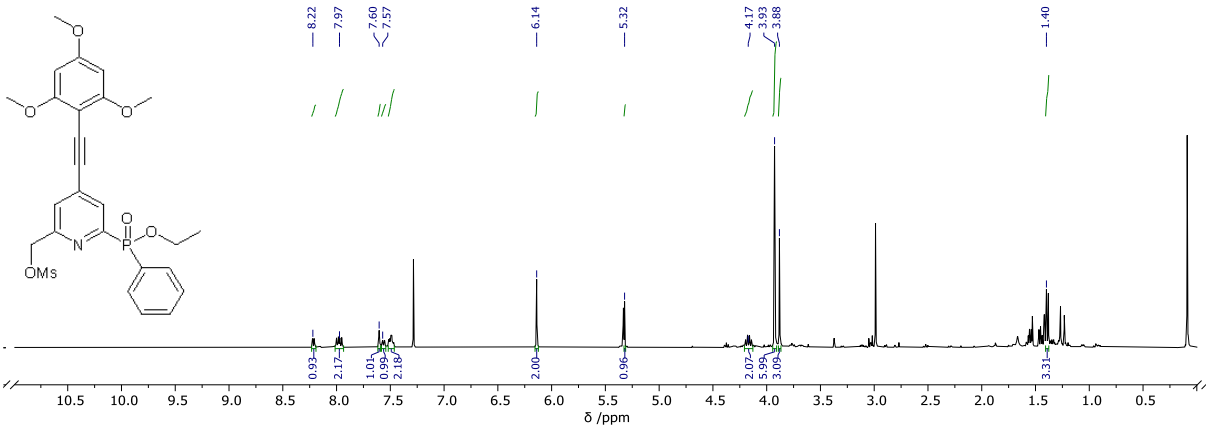

Figure 6.14: ^{1}H NMR (400 MHz, $CDCl_3$) spectrum of **9**.

1,4,7-Tris({4-[2-(2,4,6-trimethoxyphenyl)ethynyl]-6[ethoxy(phenyl)phosphoryl]pyridin-2-yl}methyl)-1,4,7-triazacyclononane, **10**[80]

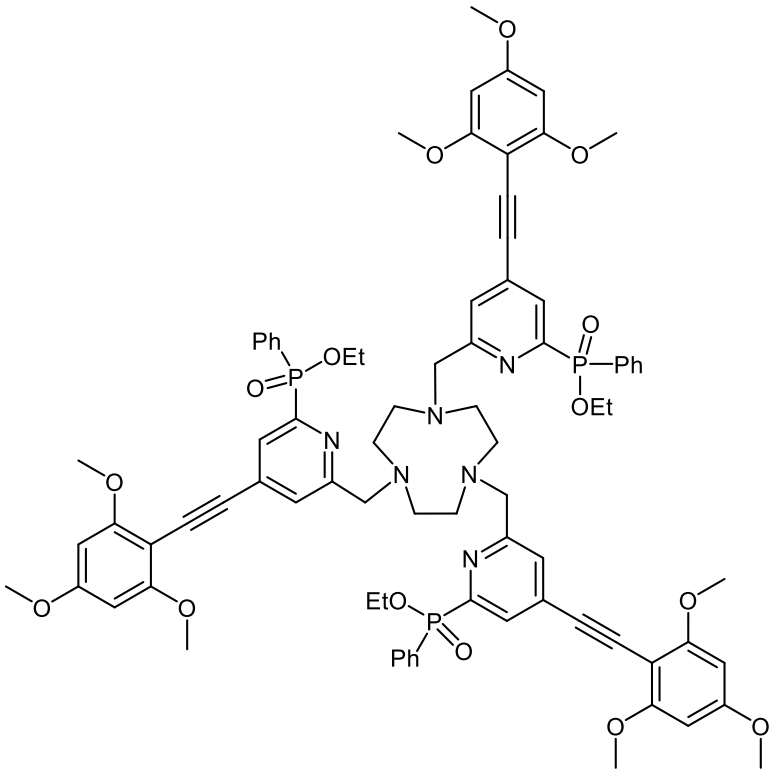

Ethyl [6-(hydroxymethyl)-4-[2-(2,4,6-trimethoxyphenyl)ethynyl] pyridin-2yl](phenyl) phosphinate, **9** (*0.068* mmol, 3.4 eq.), TACN.3HCl (4.7 mg, 0.020 mmol, 1 eq.) and K_2CO_3 (19.2 mg, 0.139 mmol, 7 eq.) were dissolved in anhydrous MeCN (2 ml) and stirred at 60°C for 20 hours under argon. After that, MeCN was removed under reduced pressure, and the crude was redissolved in MeOH for the use in the next step without purification. LCMS (ESI^+) *m/z* 1477.840 $[M+H]^+$.

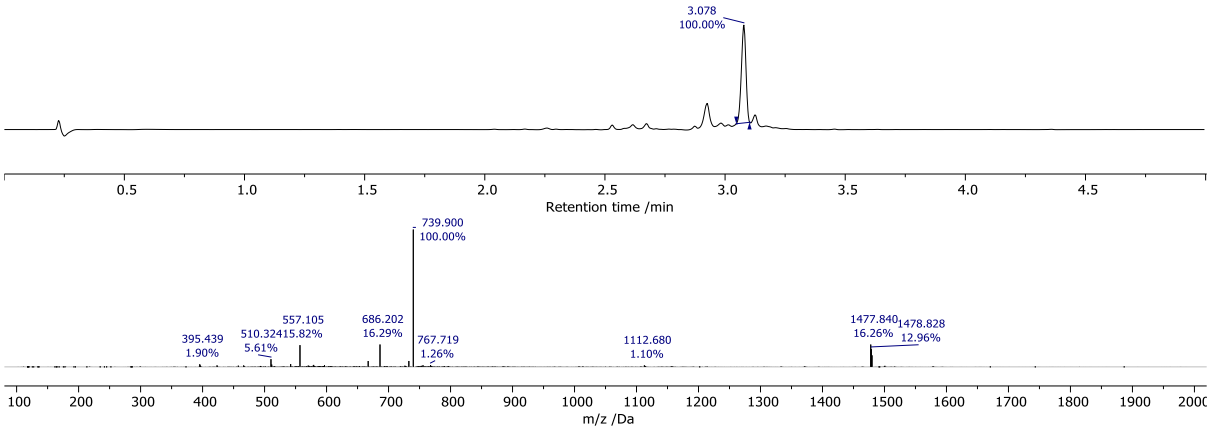

Figure 6.15: LCMS (Method E) of **10** AC (210-400 nm) (top) and the MS (ESI^+) at 3.078 minutes (bottom).

EuL^{0} [80]

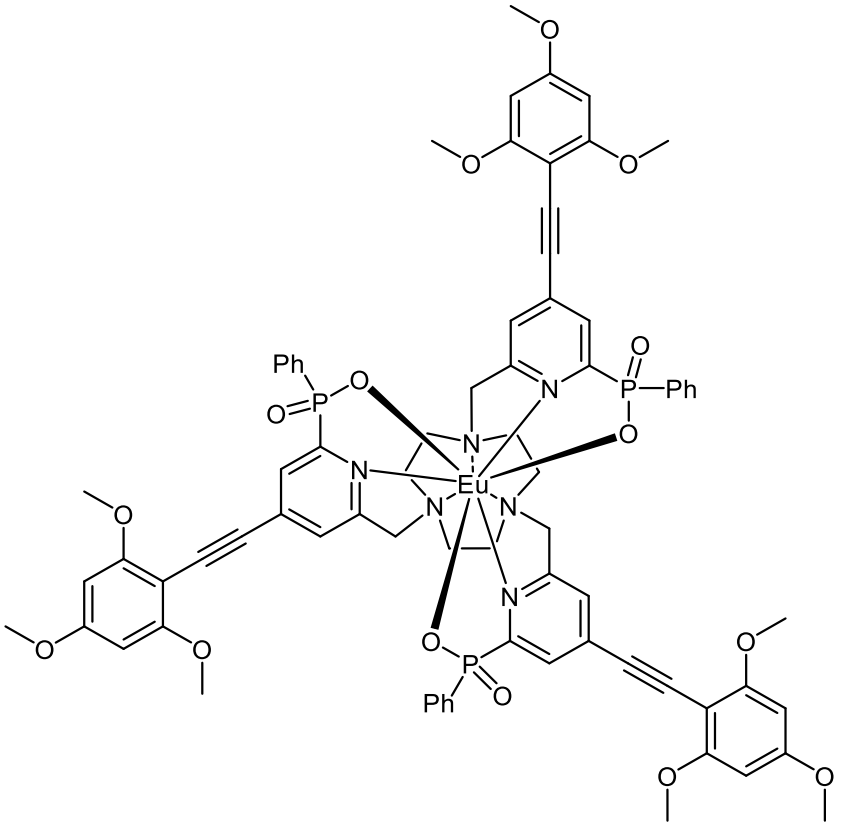

1,4,7-Tris({4-[2-(2,4,6-trimethoxyphenyl)ethynyl]-6[ethoxy(phenyl)phosphoryl]pyridin-2-yl}methyl)-1,4,7-triazacyclononane **12** (*0.020* mmol) was dissolved in MeOH (2 ml) and water until white precipitate persisted. The pH of the resulting solution was adjusted to 12.5 using 1M NaOH, and the solution was stirred at 60°C for 72 hours, while its pH was monitored and periodically adjusted to 12.5 until hydrolysis completion was confirmed by LCMS. After that, the solution pH was readjusted to 6.5 using 0.5 M HCl. $EuCl_3.6H_2O$ was then added (8.0 mg, 0.022 mmol, 1.1 eq.) and the resulting solution was stirred at rt for 18 hours. The solvents were then evaporated under reduced pressure to yield white solid which was purified using reverse-phase HPLC (C18, Method A, retention time = 13.5 minutes) to yield white solid (13 mg, 0.0084 mmol, 42% over three steps).

HRMS (ESI$^+$) *m/z* 1541.3539 $[M+H]^+$ ($C_{75}H_{72}{}^{151}EuN_6O_{15}P_3$ requires 1541.3545).

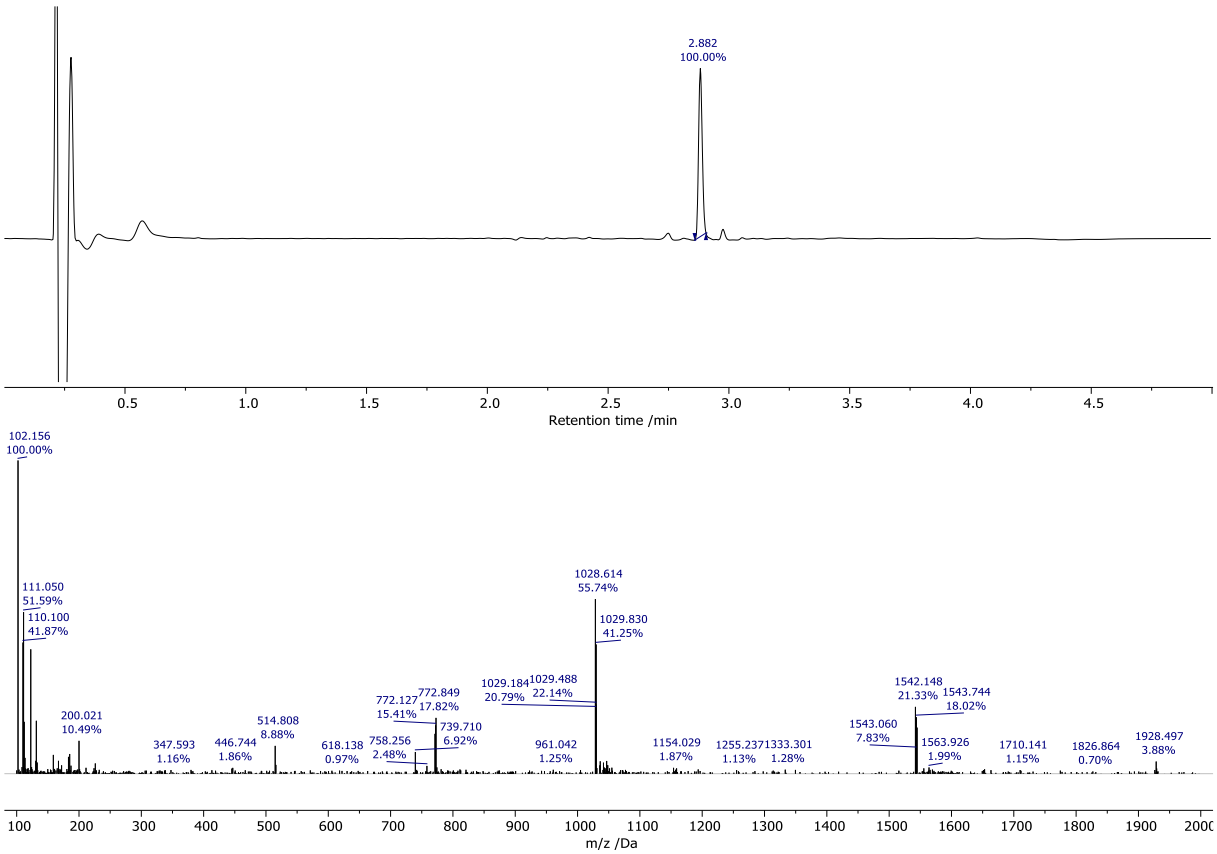

Figure 6.16: LCMS (Method E) of **EuL^{0}** AC (210-400 nm) (top) and the MS (ESI^{+}) at 2.882 minutes (bottom).

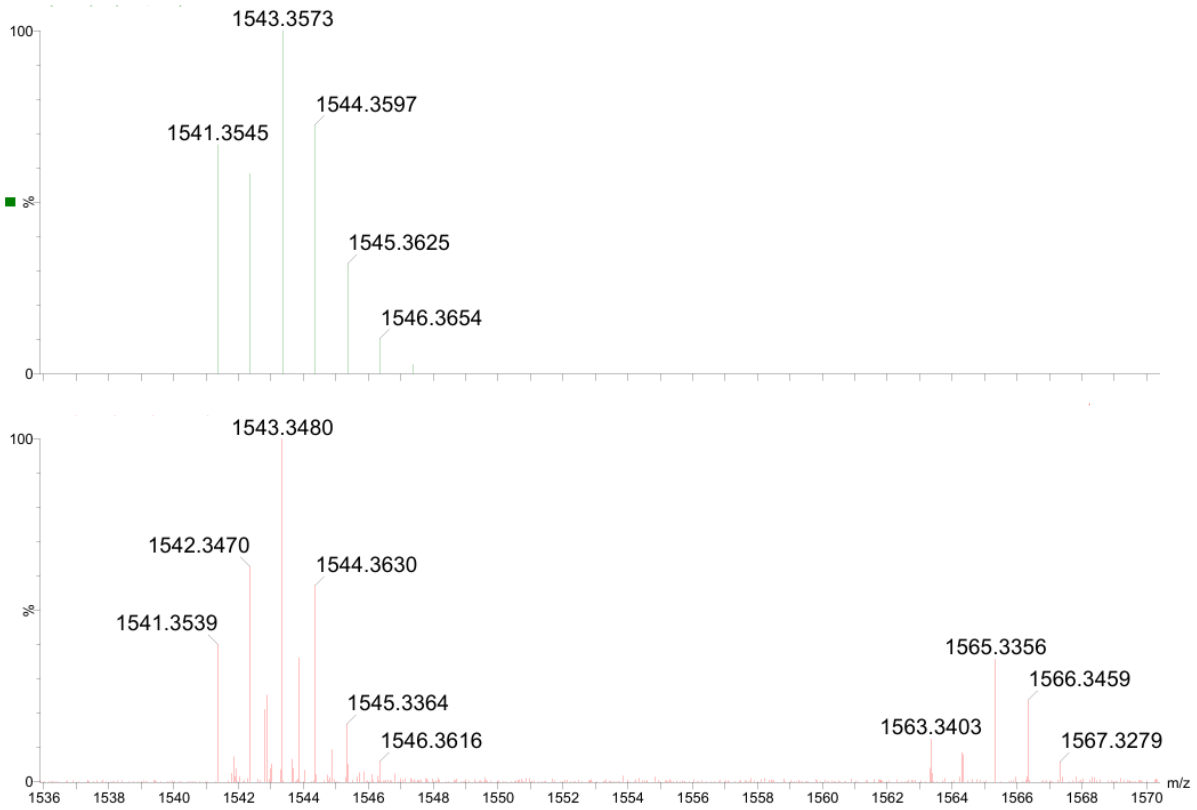

Figure 6.17: Simulated (top) and recorded (bottom) accurate MS (ESI^{+}) of **EuL^{0}**.

Diethyl 4-bromopyridine-2,6-dicarboxylate, **12**[61]

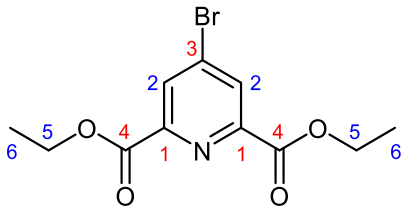

A solid mixture of chelidamic acid (1.64 g, 8.97 mmol, 1 eq.) and phosphorus pentabromide (11.6 g, 26.9 mmol, 3 eq.) was melted and heated at 95 °C for 3 hours. After that, anhydrous $CHCl_3$ (30 ml) was added, and the resulting hot mixture was filtered and cooled in an ice batch to yield **11**. This was followed by drop-wise addition of cold EtOH (20 ml) to the reaction mixture which was then stirred at rt for 15 minutes. After that, the solvents were evaporated under reduced pressure to yield brown oil. The oil was then dissolved in ice-cold water and stirred at 0 °C for 1 hour to allow for precipitation of the crude **12**. The resulting brown solid was dried and recrystallised from hexane to yield light-brown solid (1.23 g, 4.07 mmol, 45%).

HRMS (ESI$^+$) *m/z* 302.0023 ($C_{11}H_{13}NO_4Br$ requires 302.0028).

^{1}H NMR (400 MHz, $CDCl_3$) δ 8.42 (2 H, s, H^2), 4.50 (4 H, q, $^3J_{H\text{-}H}$ 7.1, H^5), 1.46 (6 H, t, $^3J_{H\text{-}H}$ 7.4, H^6).

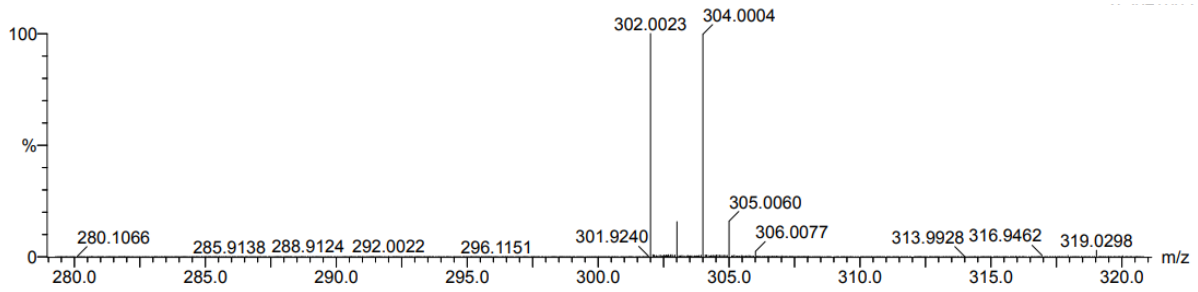

Figure 6.18: Accurate MS (ESI$^+$) of **12**.

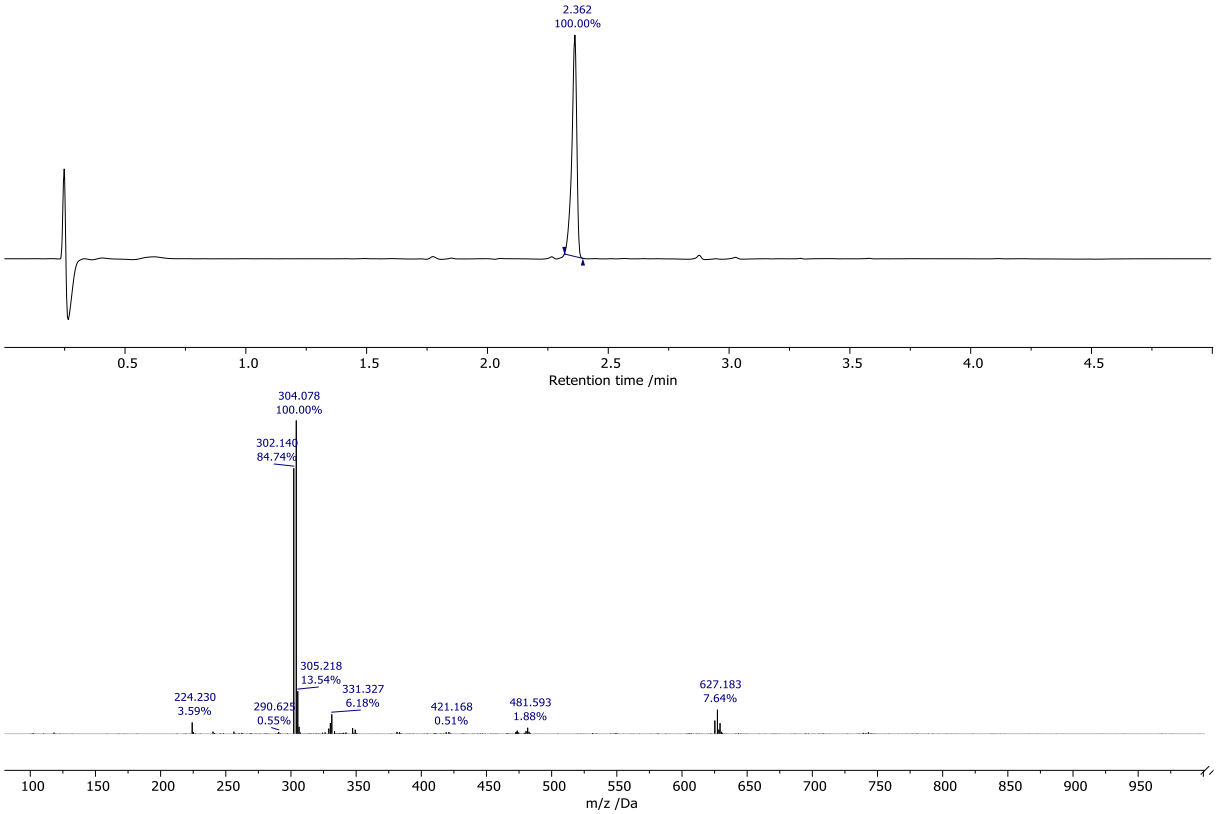

Figure 6.19: LCMS (Method E) of **12** AC (210-400 nm) (top) and the MS (ESI^+) at 2.362 minutes (bottom).

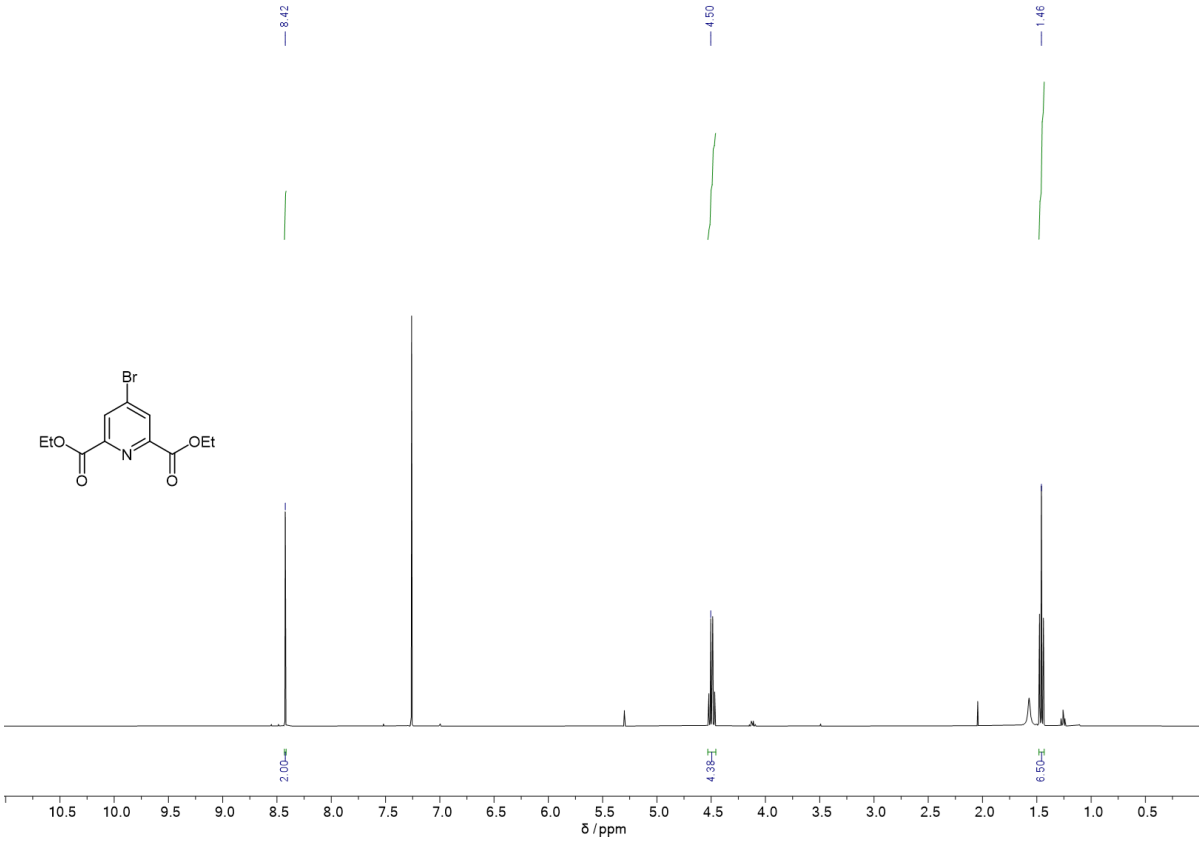

Figure 6.20: ^1H NMR (400 MHz, $CDCl_3$) spectrum of **12**.

Ethyl 4-bromo-6-(hydroxymethyl)picolinate**, 13**[112]

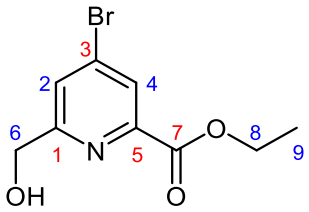

Diethyl diethyl 4-bromopyridine-2,6-dicarboxylate, **12** (1.23 g, 4.07 mmol, 1 eq.) was dissolved in a solution of DCM (7 ml) and ethanol (9 ml) and cooled in an ice bath. After that, solid sodium borohydride (0.23 g, 6.11 mmol, 1.5 eq.) was slowly added and the resulting solution was stirred at 0 °C for 4 hours under argon, while monitoring the reaction using TLC (silica, 3% MeOH in DCM). Once the starting material was consumed, a solution of 1 M HCl (6 ml) was added to the reaction mixture, followed by water (25 ml) and DCM (20 ml). The resulting aqueous layer was separated and washed with DCM (10 ml × 3). After that, the combined organic layers were washed with water (10 ml × 3), dried over $MgSO_4$, filtered and concentrated under reduced pressure. The crude solution was then purified by flash chromatography (silica, DCM to 2.5% MeOH in DCM) to yield white solid (0.675 g, 2.60 mmol, 64%).

LCMS (ESI^+) *m/z* 260.102 $[M+H]^+$.

^1H NMR (400 MHz, $CDCl_3$) δ 8.17 (1 H, d, $^4J_{H\text{-}H}$ 1.83, H^4), 7.73 (1 H, d, $^4J_{H\text{-}H}$ 1.83, H^2), 4.84 (2 H, s, H^6), 4.46 (2 H, q, $^3J_{H\text{-}H}$ 6.9, H^8), 1.43 (6 H, t, $^3J_{H\text{-}H}$ 7.1, H^9).

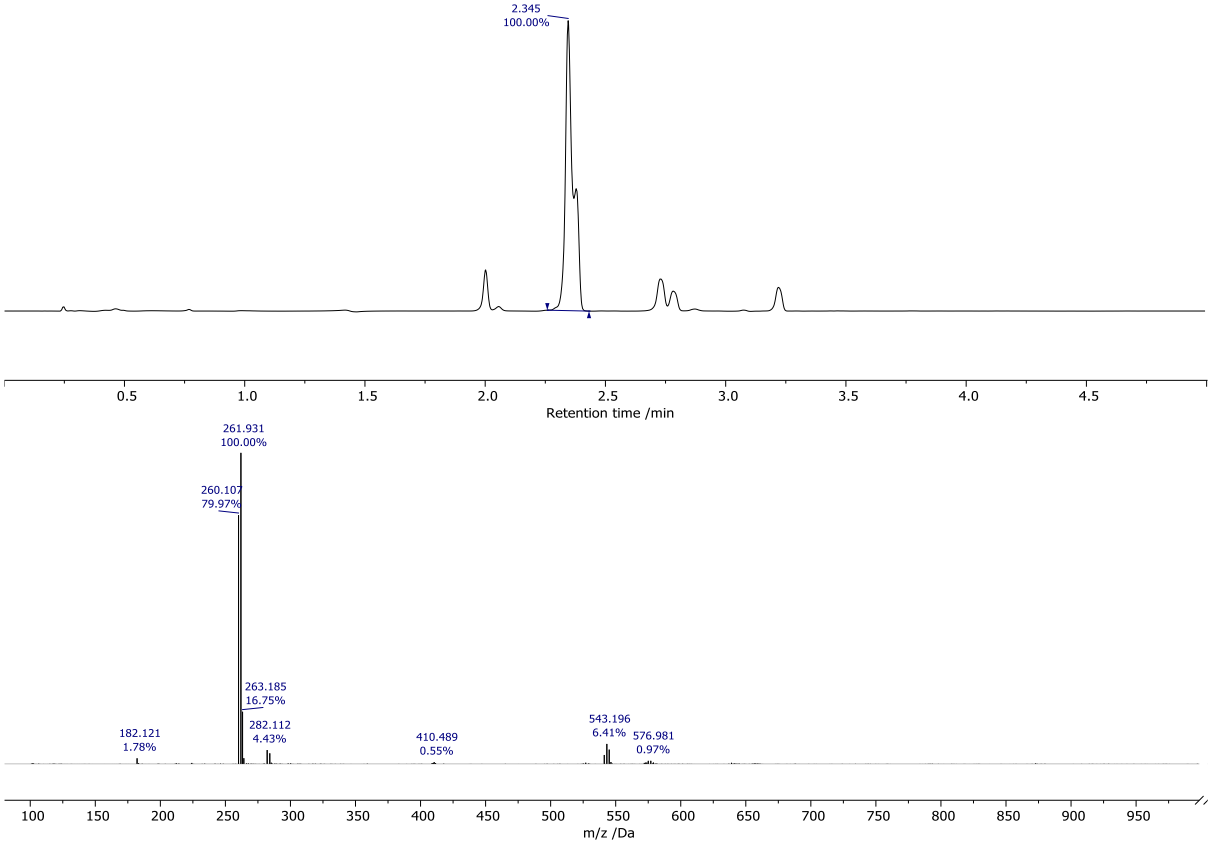

Figure 6.21: LCMS (Method E) of **13** AC (210-400 nm) (top) and the MS (ESI^+) at 2.345 minutes (bottom).

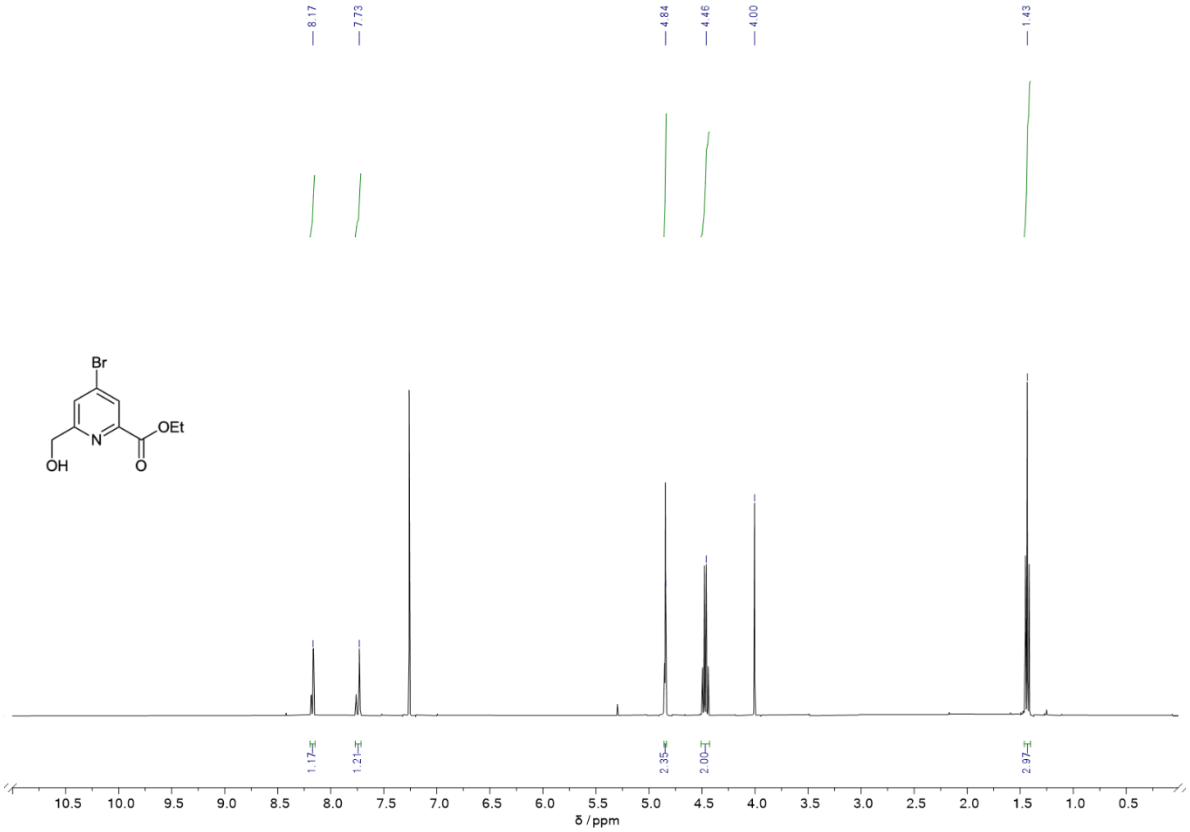

Figure 6.22: ^1H NMR (400 MHz, $CDCl_3$) spectrum of **13**.

Ethyl 6-(hydroxymethyl)-4-((2,4,6-trimethoxyphenyl)ethynyl)picolinate, **14**

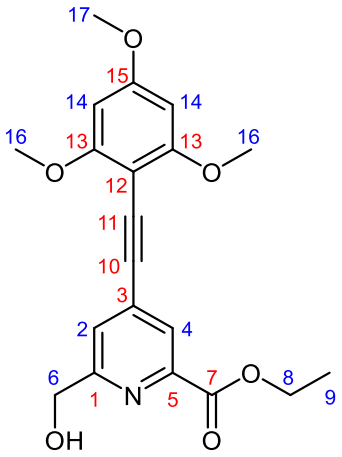

2-ethynyl-1,3,5-trimethoxybenzene, **7** (300 mg, 1.56 mmol, 1 eq.), ethyl 4-bromo-6-(hydroxymethyl)picolinate, **13** (446 mg, 1.72 mmol, 1.1 eq.) and $[Pd(allyl)Cl]_2$ (60 mg, 0.164 mmol, 0.1 eq.) were dissolved in anhydrous acetonitrile (5 ml) and degassed freeze-pump-thaw × 3). After that, TEA (2.16 ml, 15.6 mmol, 10 eq.) and piperidine (0.6 ml, 6.24 mmol, 4 eq.) were added, and the resulting solution was stirred at 40°C for 12 hours under argon. Organic solvents were then removed under reduced pressure, and the residue was dissolved in DCM (10 ml). The resulting solution was washed with water (5 ml × 3), and the combined aqueous phases were extracted with DCM (5 ml × 3). The combined organic layers were dried over $MgSO_4$, filtered and isolated from the solvent under reduced pressure. The crude product was then purified by column chromatography (silica, 4% MeOH in DCM) to yield yellow solid (204 mg, 0.550 mmol, 35%). HRMS (ESI^+) *m/z* 372.1443 ($C_{20}H_{22}NO_6$ requires 372.1447).

^1H NMR (600 MHz, $CDCl_3$) δ 8.10 (1 H, d, $^4J_{H\text{-}H}$ 1.4, H^4), 7.58 (1 H, d, $^4J_{H\text{-}H}$ 1.4, H^2), 6.11 (2 H, s, H^{14}), 4.82 (2 H, s, H^6), 4.47-4.43 (2H, m, H^8), 3.90 (6 H, s, H^{16}), 3.85 (3 H, s, H^{17}), 1.42 (3 H, t, $^3J_{H\text{-}H}$ 7.1, H^9).

^{13}C NMR (151 MHz, $CDCl_3$) δ 164.86 (C^7), 162.87 (C^{15}), 162.82 (C^{13}), 159.92 (C^1), 147.14 (C^5), 134.48 (C^3), 125.61(C^4), 125.14 (C^2), 93.35 (C^{10}), 93.07 (C^{11}), 90.44 (C^{14}), 89.26 (C^{12}), 64.38 (C^6), 61.94 (C^8), 56.07 (C^{16}), 55.48 (C^{17}), 14.27 (C^9).

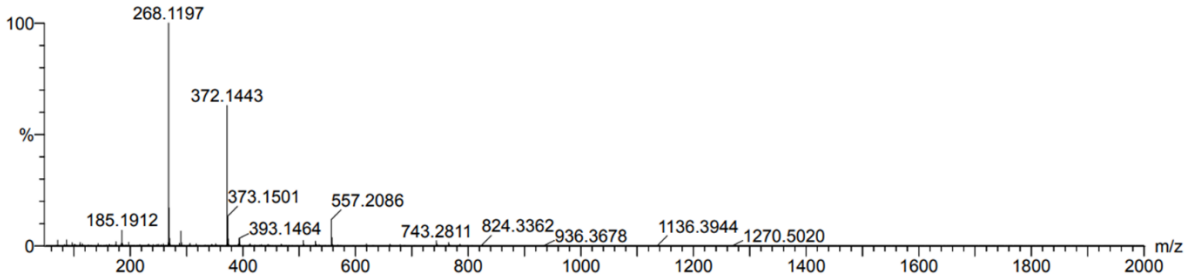

Figure 6.23: Accurate MS (ESI^+) of **14**.

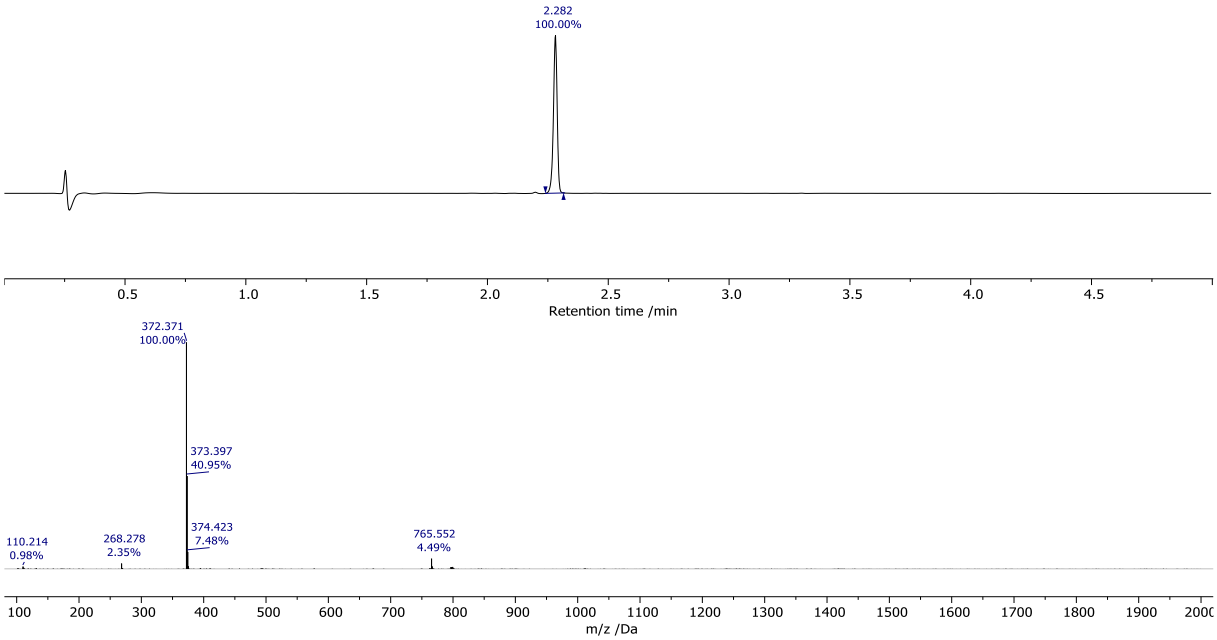

Figure 6.24: LCMS (Method E) of **14** AC (210-400 nm) (top) and the MS (ESI$^+$) at 2.282 minutes (bottom).

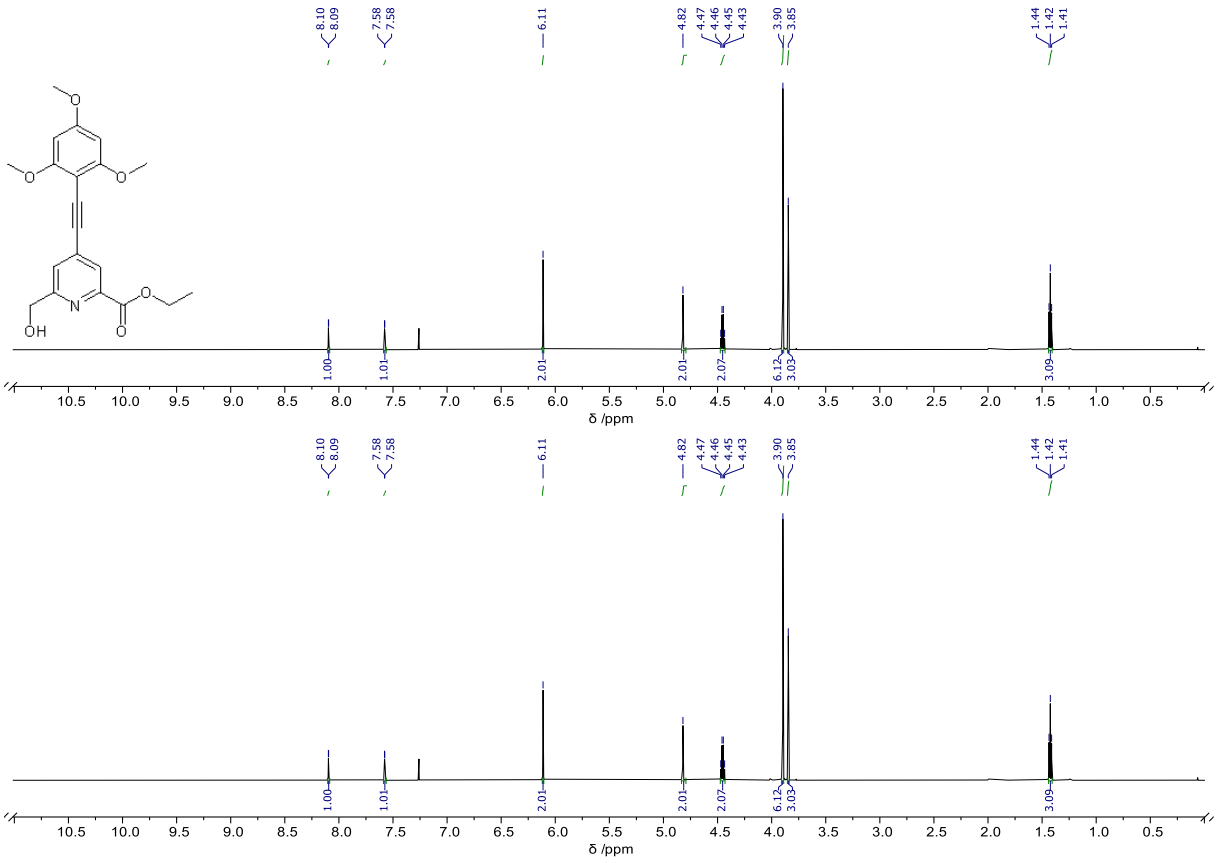

Figure 6.25: ^{1}H NMR (600 MHz, $CDCl_3$) (top) and ^{13}C NMR (151 MHz, $CDCl_3$) (bottom) spectra of **14**.

Ethyl 6-(((methylsulfonyl)oxy)methyl)-4-((2,4,6-trimethoxyphenyl)ethynyl)picolinate, **15**

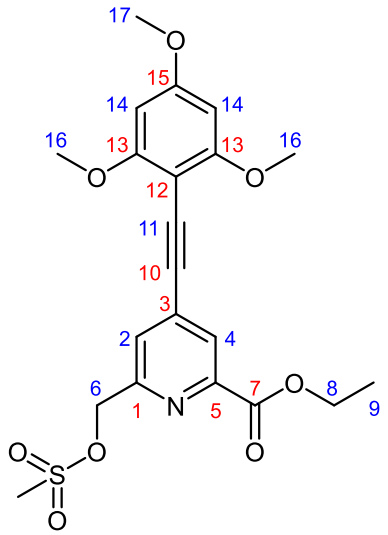

Ethyl 6-(hydroxymethyl)-4-((2,4,6-trimethoxyphenyl)ethynyl)picolinate, **14** (119 mg, 0.320 mmol, 1 eq.) was dissolved in anhydrous THF (3.5 ml). DIPEA (0.17 ml, 0.960, 3 eq.) and methanesulfonic anhydride (0.223 g, 1.280 mmol, 4 eq.) were added, and the resulting mixture was stirred at rt for 1 hour under argon. Once the reaction completion was confirmed by TLC (silica, 5% MeOH in DCM), organic solvents were evaporated under reduced pressure, and the residue was redissolved in DCM (10 ml). The resulting solution was washed with water (10 ml × 3), and the combined aqueous phases were extracted with DCM (5 ml × 3). The combined organic layers were dried over $MgSO_4$, filtered and isolated from solvent under reduced pressure to yield pale yellow solid that was used in the next step without further purification.

^{1}H NMR (400 MHz, $CDCl_3$) δ 8.17 (1 H, s, H^4), 7.72 (1 H, s, H^2), 6.12 (2 H, s, H^{14}), 5.44 (2 H, s, H^6), 4.58-4.47 (2H, m, H^8), 3.91 (6 H, s, H^{16}), 3.86 (3 H, s, H^{17}), 1.44 (3 H, t, $^3J_{H\text{-}H}$ 7.5, H^9).

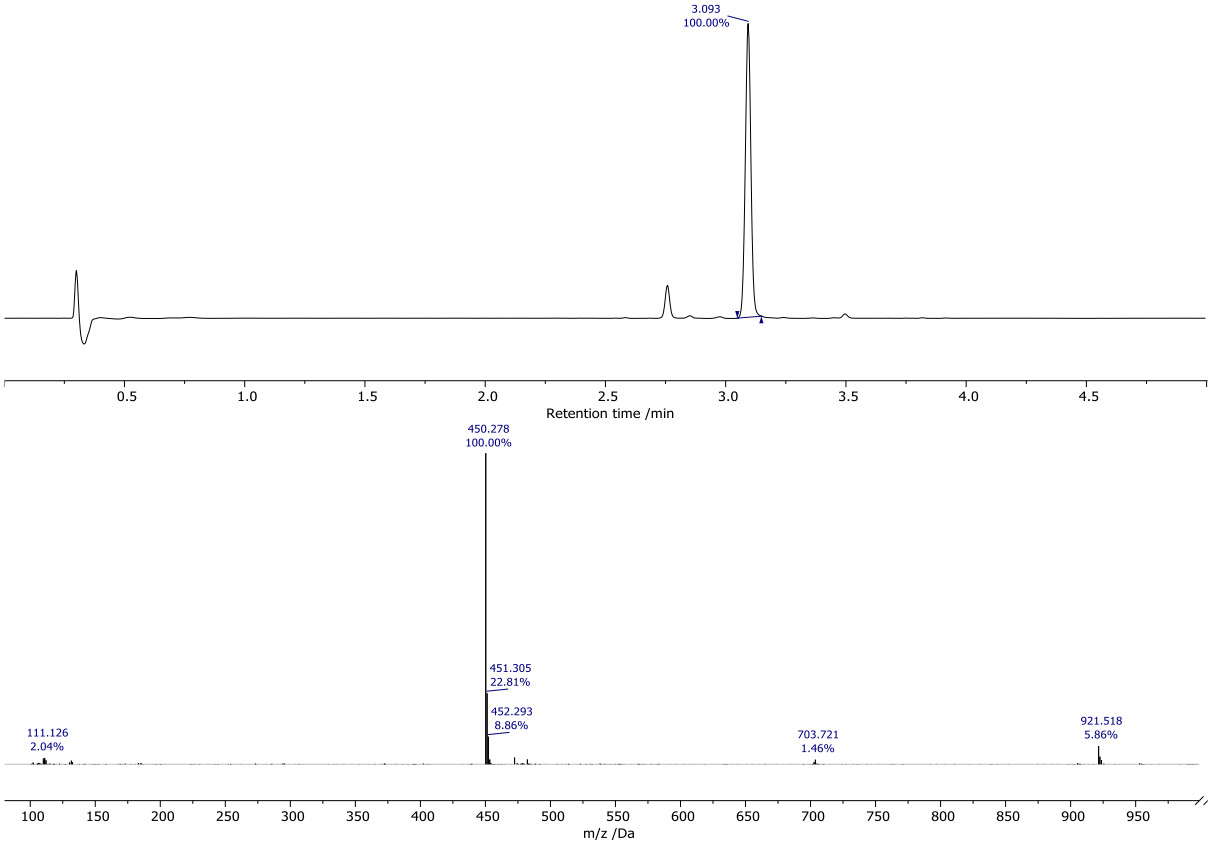

Figure 6.26: LCMS (Method E) of **15** AC (210-400 nm) (top) and the MS (ESI^+) at 3.093 minutes (bottom).

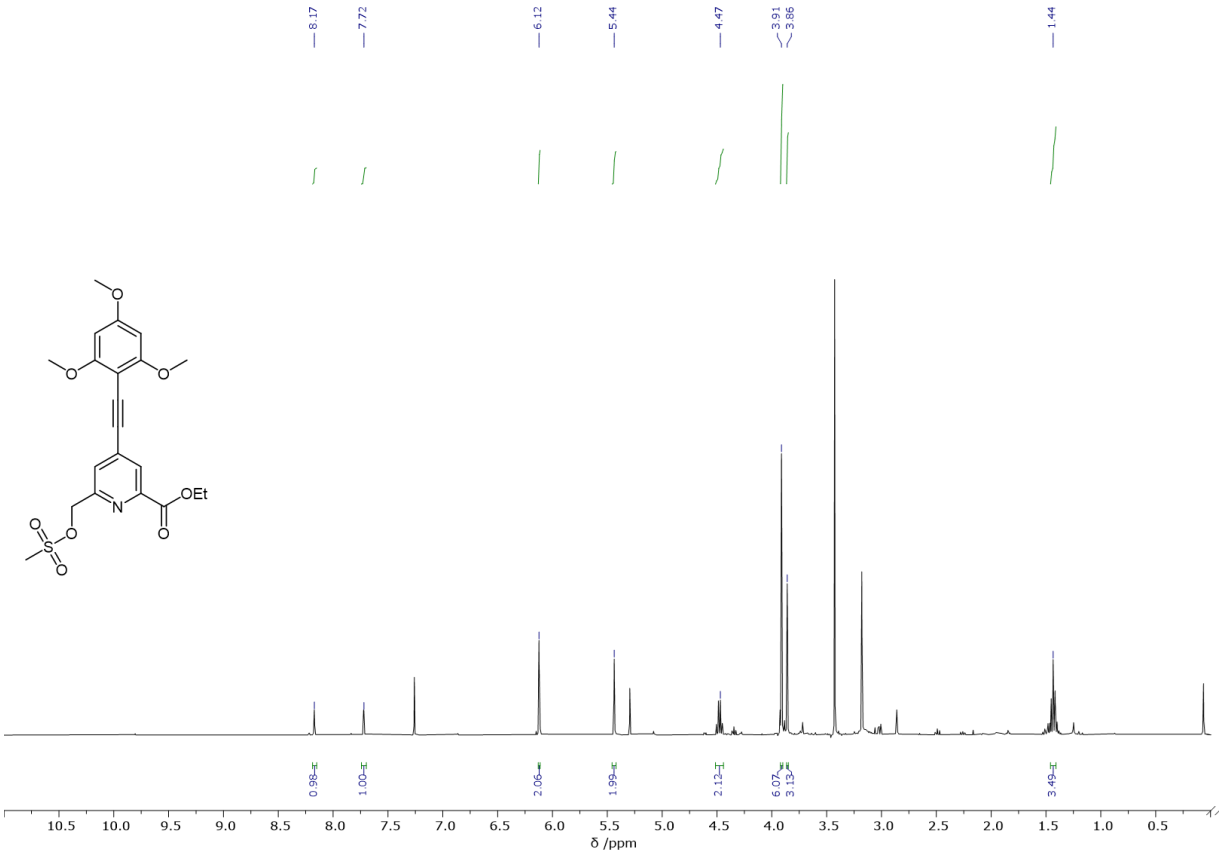

Figure 6.27: ^1H NMR (400 MHz, $CDCl_3$) spectrum of **15**.

Triethyl 6,6',6''-((1,4,7-triazonane-1,4,7-triyl)tris(methylene))tris(4-((2,4,6-trimethoxyphenyl)ethynyl)picolinate), **16**

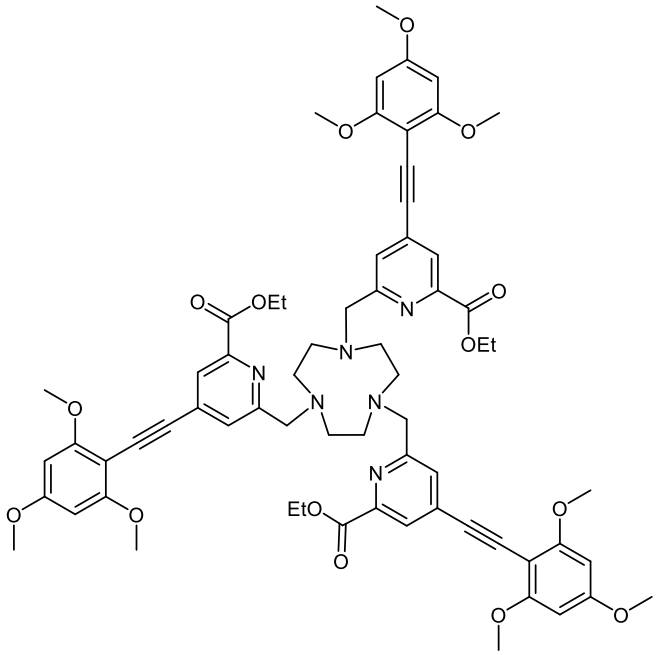

Ethyl 6-(((methylsulfonyl)oxy) methyl)-4-((2,4,6-trimethoxyphenyl) ethynyl) picolinate, **15** (*0.144 g*, *0.320 mmol,* 3.5 eq.), TACN.3HCl (22 mg, 0.0914 mmol, 1 eq.) and K_2CO_3 (88 mg, 0.6398 mmol, 7 eq.) were dissolved in anhydrous acetonitrile (5 ml) and stirred at 60°C for 20 hours under argon. The crude was then isolated from solvent under reduced pressure and redissolved in MeOH for the use in the next step without purification.

HRMS (ESI$^+$) *m/z* 1189.5195 $[M+H]^+$ ($C_{66}H_{72}N_6O_{15}$ requires 1189.5134).

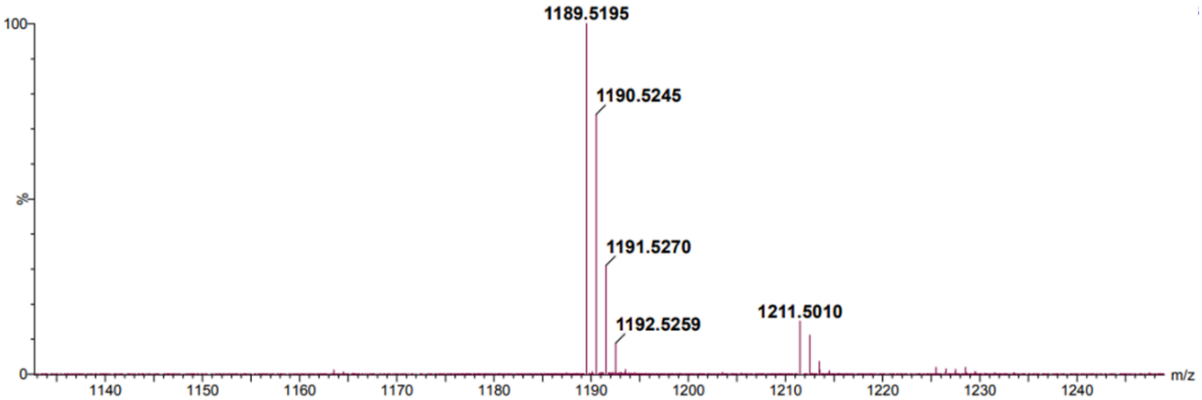

Figure 6.28: Accurate MS (ESI$^+$) of **16**.

EuL[1]

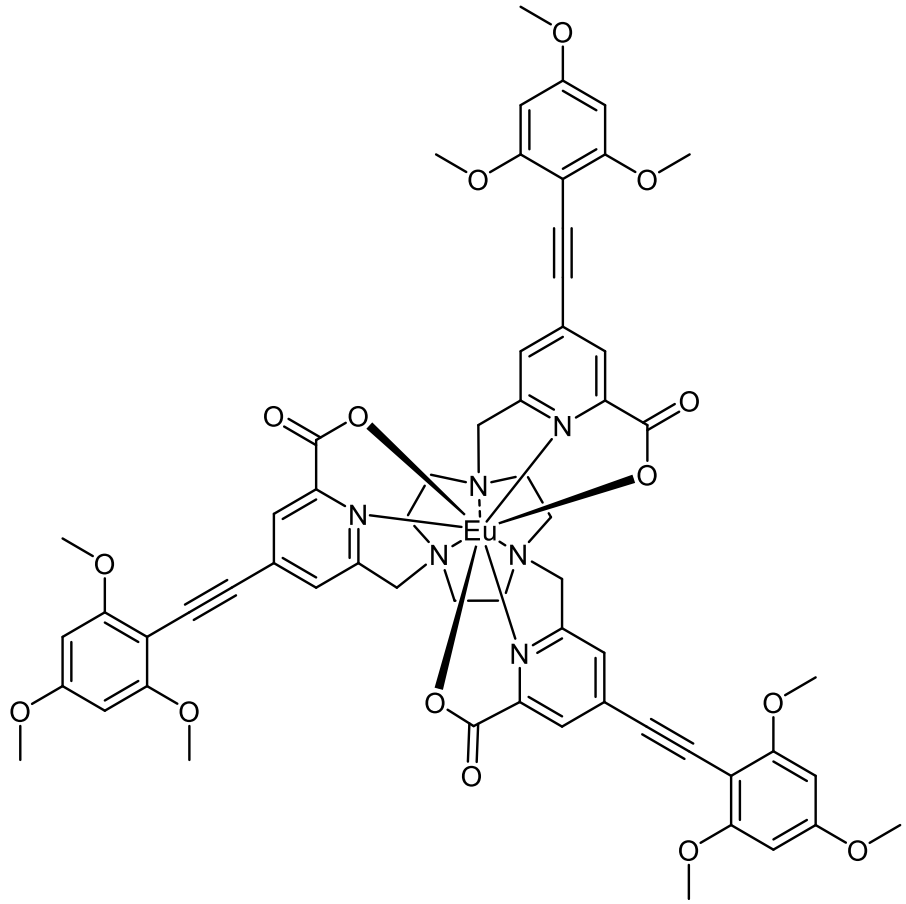

Triethyl 6,6',6''- ((1,4,7-triazonane-1,4,7-triyl) tris (methylene)) tris (4-((2,4,6-trimethoxyphenyl) ethynyl)picolinate), **16** (*0.0914* mmol) was dissolved in MeOH (5 ml). Water was then drop-wise added to the resulting solution until the white precipitate remained undissolved. The pH of the resulting solution was adjusted to 12.5 using 1M NaOH. The resulting solution was stirred at rt for 72 hours, while its pH was monitored and periodically adjusted to 12.5 until hydrolysis completion was confirmed by LCMS. After that, the solution pH was readjusted to 6.5 using 1 M HCl. $EuCl_3.6H_2O$ was then added (37 mg, 0.101 mmol, 1.1 eq.), and the resulting solution was stirred at rt for 18 hours. Solvents were then removed under reduced pressure, and the resulting pale yield yellow solid was purified by reverse-phase HPLC (C18, Method B, retention time = 11.4 minutes) to yield yellow solid (67 mg, 58% over 3 steps).

HRMS (ESI^+) *m/z* 1253.3190 $[M+H]^+$ ($C_{60}H_{57}{}^{151}EuN_6O_{15}$ requires 1253.3159).

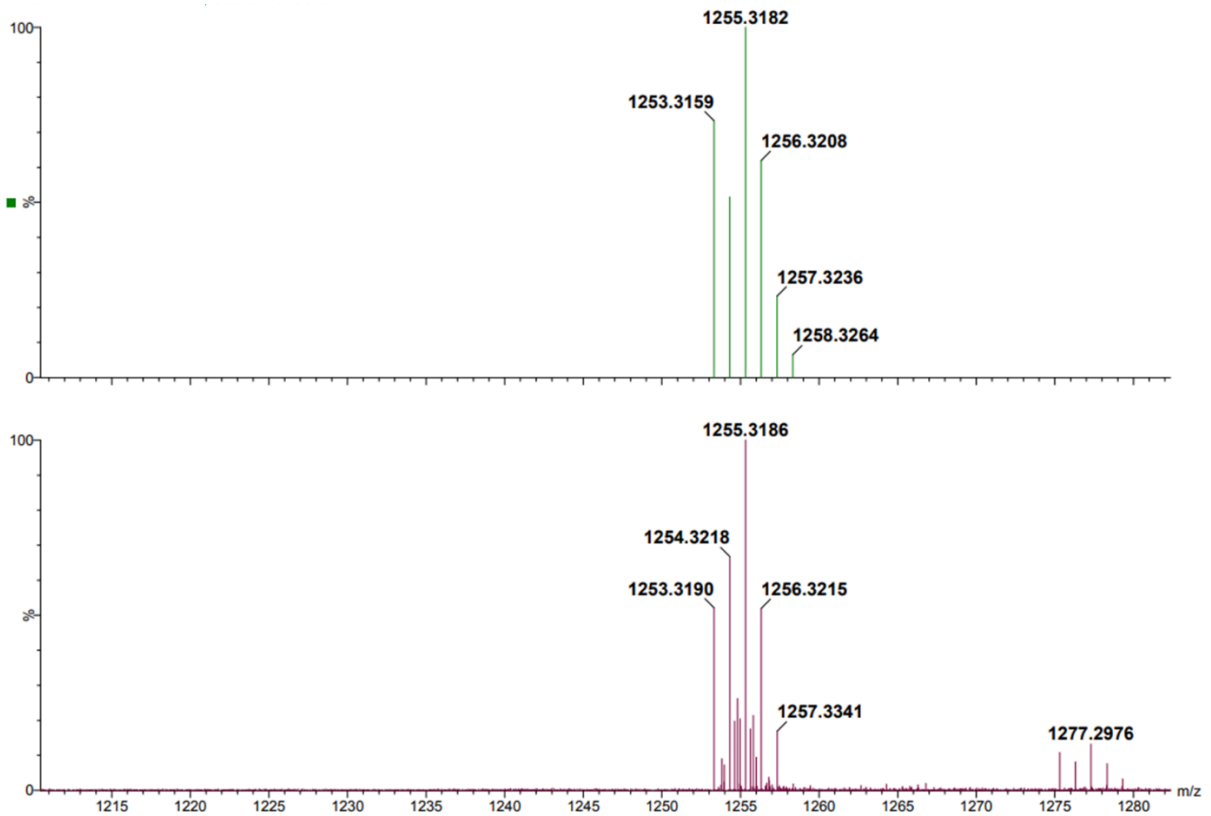

Figure 6.29: Simulated (top) and recorded (bottom) accurate MS (ESI⁺) of **EuL¹**.

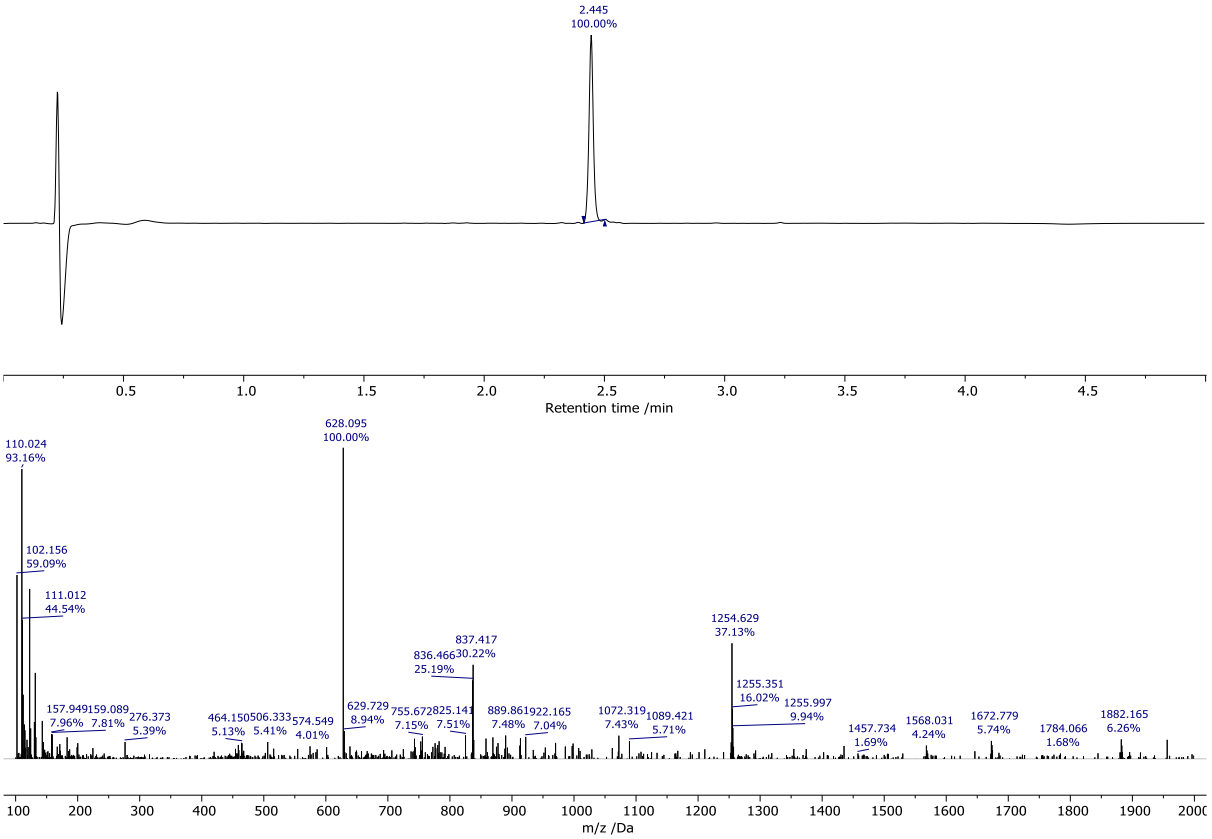

Figure 6.30: LCMS (Method E) of **EuL¹** AC (210-400 nm) (top) and the MS (ESI⁺) at 2.445 minutes (bottom).

2,4,6-Trimethoxy-3-nitrobenzaldehyde, **17**

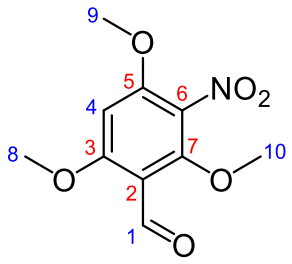

To an ice-cold solution of 2,4,6-trimethoxybenzaldehyde (1.00 g, 5.10 mmol, 1 eq.) in concentrated sulfuric acid (5 ml) the solution of ammonium nitrate (0.450 g. 5.61 mmol, 1.1 eq.) in concentrated sulfuric acid (5 ml) was dropwise added over 10 minutes, and the resulting mixture was poured over ice. The resulting suspension was then filtered, and the solid residue was washed with water (10 ml × 3) and dried to yield beige solid (1.157 g, 4.80 mmol, 94%) which was used in the next step without further purification.

HRMS (ESI$^+$) *m/z* 242.0673 ($C_{10}H_{12}NO_6$ requires 242.0673)

^{1}H NMR (700 MHz, $CDCl_3$) δ 10.25 (1H, s, H^1), 6.31 (1H, s, H^4), 3.96 (3H, s, H^9) 3.95 (3H, s, H^8), 3.91 (3H, s, H^{10}).

^{13}C NMR (151 MHz, $CDCl_3$) δ 186.37 (C^1), 164.86 (C^5), 156.88 (C^3), 155.38 (C^7), 131.22 (C^6), 111.96 (C^2), 91.39 (C^4), 64.74 (C^{10}), 56.85 (C^8), 56.66 (C^9).

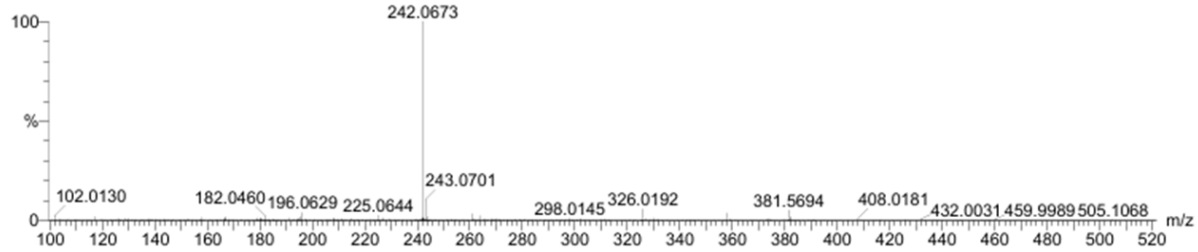

Figure 6.31: Accurate MS (ESI$^+$) of **17**.

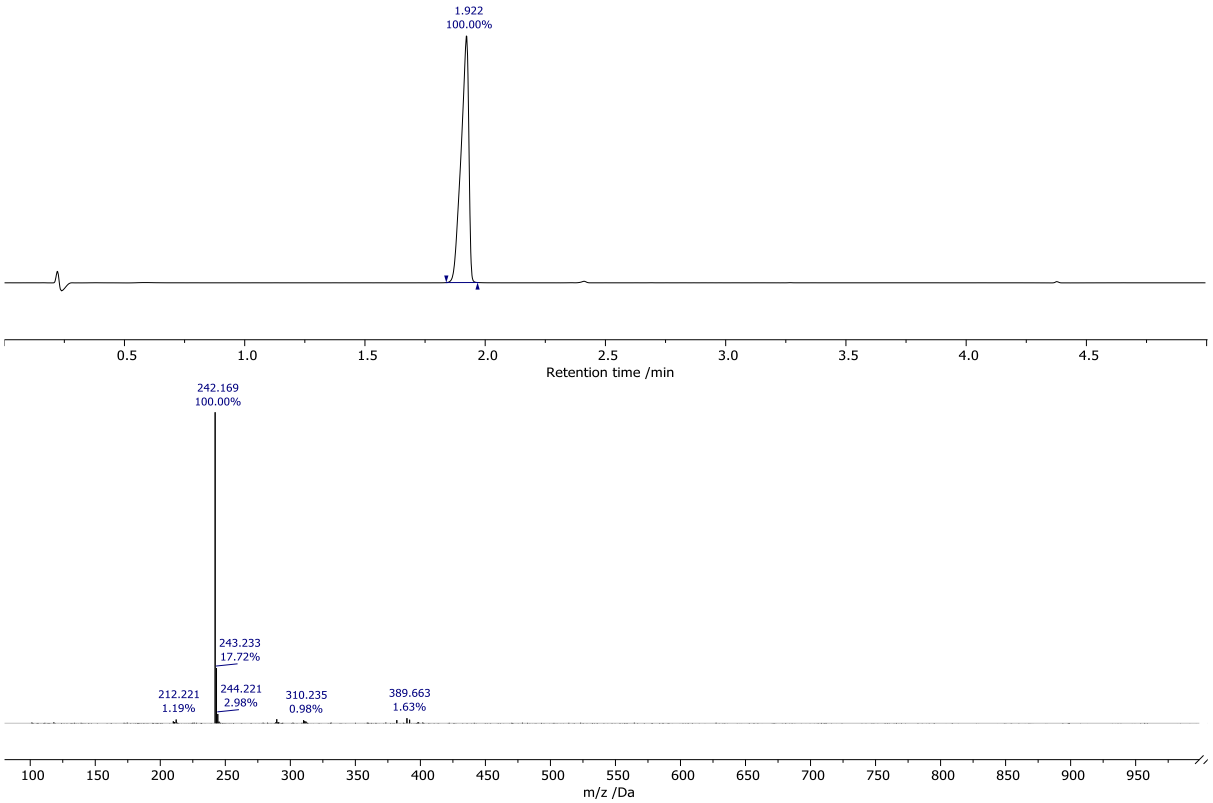

Figure 6.32: LCMS (Method E) of **17** AC (210-400 nm) (top) and the MS (ESI^+) at 1.992 minutes (bottom).

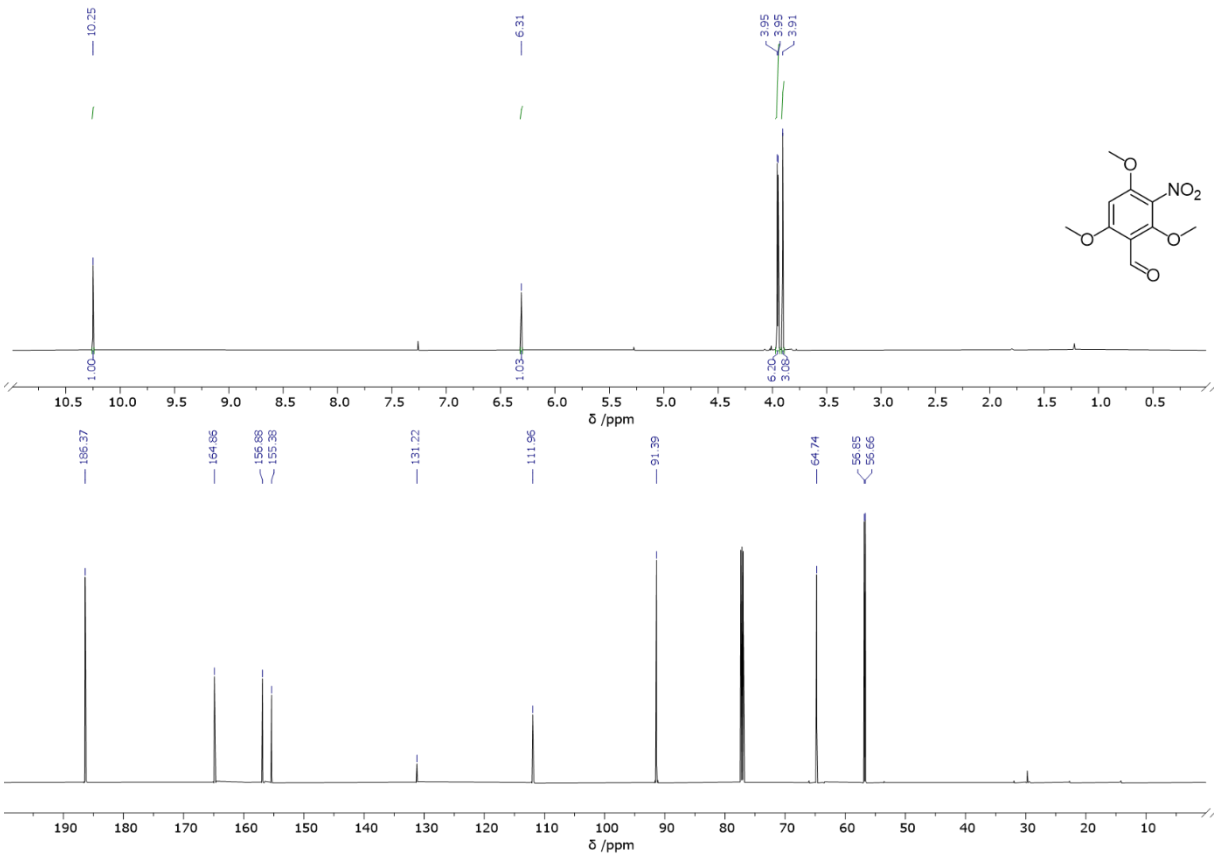

Figure 6.33: ^{1}H NMR (700 MHz, $CDCl_3$) (top) and ^{13}C NMR (151 MHz, $CDCl_3$) (bottom) spectra of **17**.

2-(2,2-Dibromovinyl)-1,3,5-trimethoxy-4-nitrobenzene, **18**

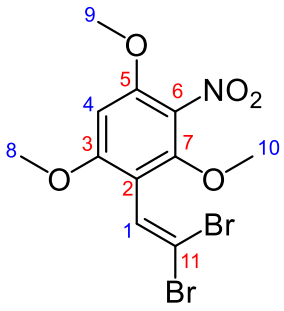

A solution of CBr_4 (2.07 g, 6.23 mmol, 1.5 eq.) in anhydrous DCM (10 ml) was dropwise added to an ice-cold solution of 2,4,6-trimethoxy-3-nitrobenzaldehyde, **17** (1.00 g, 4.15 mmol, 1 eq.) and PPh_3 (3.27 g, 12.5 mmol, 3 eq.) in anhydrous DCM (5 ml), and the resulting solution was stirred at rt for 20 hours under argon. The crude mixture was then purified by column chromatography (silica, 50% DCM in hexane) to yield beige solid (1.20 g, 3.04 mmol, 73%).

^{1}H NMR (700 MHz, $CDCl_3$) δ 7.19 (1H, s, H^1), 6.27 (1H, s, H^4), 3.91 (3H, s H^8), 3.88 (3H, s, H^9), 3.82 (3H, s, H^{10}).

^{13}C NMR (151 MHz, $CDCl_3$) δ 158.95 (C^5), 153.10 (C^7), 151.48 (C^7), 130.68 (C^6), 129.14 (C^1), 111.88 (C^2), 95.80 (C^{11}), 91.34 (C^4), 62.77 (C^{10}), 56.65 (C^8).

HRMS (ESI$^+$) *m/z* 395.9080 ($C_{11}H_{12}Br_2NO_5$ requires 395.9082)

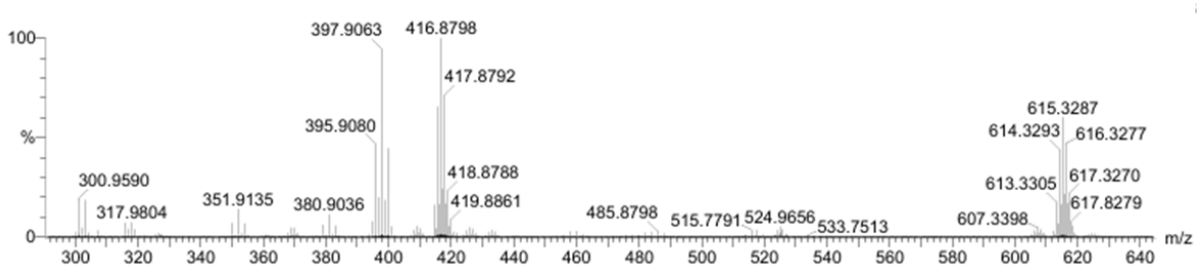

Figure 6.34: Accurate MS (ESI$^+$) of **18**.

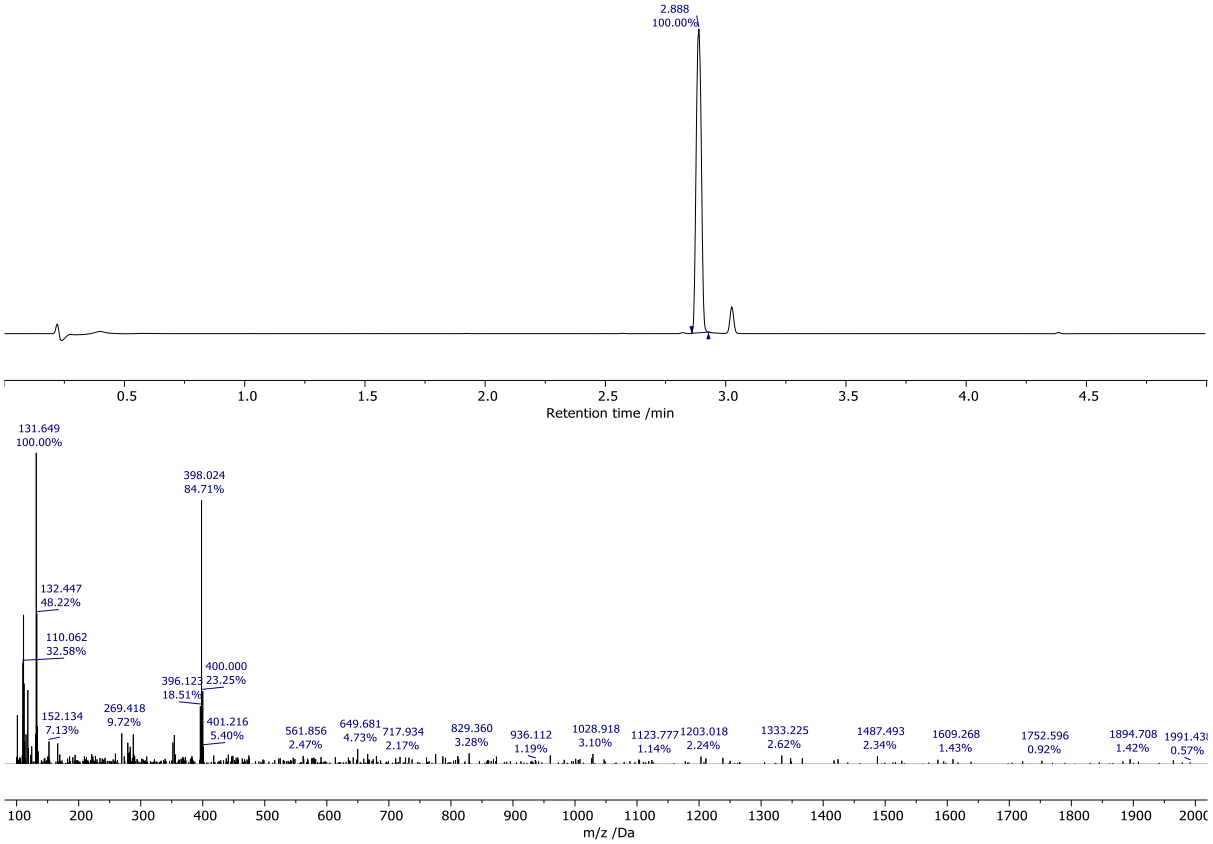

Figure 6.35: LCMS (Method E) of **18** AC (210-400 nm) (top) and the MS (ESI^+) at 2.888 minutes (bottom).

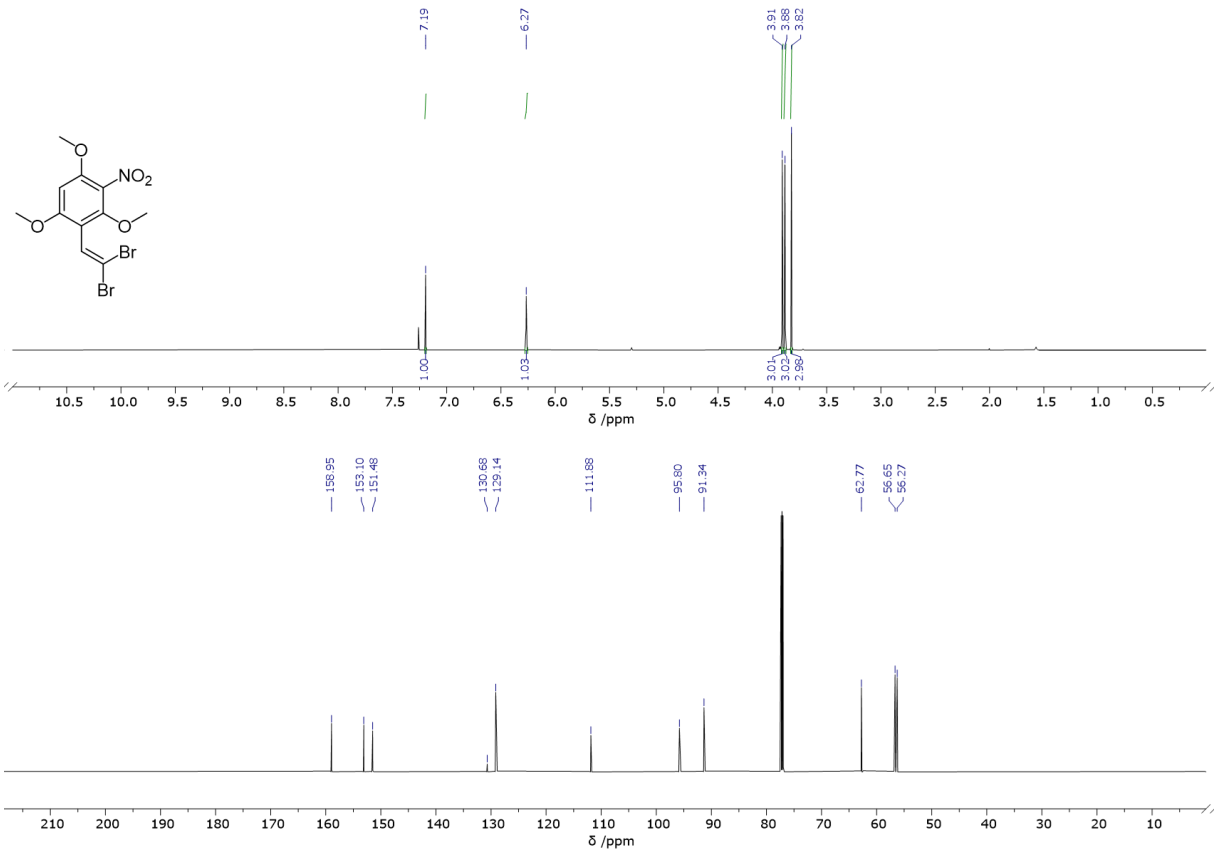

Figure 6.36: ^1H NMR (700 MHz, $CDCl_3$) (top) and ^{13}C NMR (151 MHz, $CDCl_3$) (bottom) spectra of **18**.

1-Ethynyl-2,4,6-trimethoxy-3-nitrobenzene, **19**

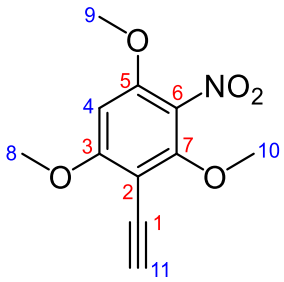

2-(2,2-dibromovinyl)-1,3,5-trimethoxy-4-nitrobenzene, **18** (1.13 g, 2.83 mmol, 1 eq.) was dissolved in anhydrous THF (10 ml) and cooled to -78 °C (acetone, dry ice). 2.5 M solution of n-butyllithium in hexane (2.30 ml, 5.67 mmol, 2 eq.) was then added dropwise, and the resulting orange solution was stirred for 30 minutes at -78 °C. Water (20 ml) was then added dropwise, and the resulting solution was stirred at rt for another 30 minutes. After that, the organic solvents were removed under reduced pressure, and the resulting aqueous solution was extracted with DCM (20 ml × 3). The combined organic layers were washed with brine (10 ml) and water (15 ml × 3), dried over $MgSO_4$ and filtered. DCM solvent was removed under reduced pressure to yield yellow oil that was purified by column chromatography (silica, 30% hexane in DCM) to yield yellow solid (0.163 g, 24%).

HRMS (ESI$^+$) *m/z* 238.0718 ($C_{11}H_{12}NO_5$ requires 238.0715)

^{1}H NMR (700 MHz, $CDCl_3$) *δ* 6.25 (1H, s, H^4), 4.05 (3H, s, H^{10}), 3.94 (3H, s, H^9), 3.91 (3H, s, H^8), 3.52 (1H, s, H^{11}).

^{13}C NMR (151 MHz, $CDCl_3$) *δ* 163.53 (C^5), 156.16 (C^7), 153.00 (C^3), 130.61 (C^6), 98.54 (C^1), 90.88 (C^4), 86.34 (C^{11}), 74.51 (C^2), 62.65 (C^{10}), 56.60 (C^8), 56.54 (C^9).

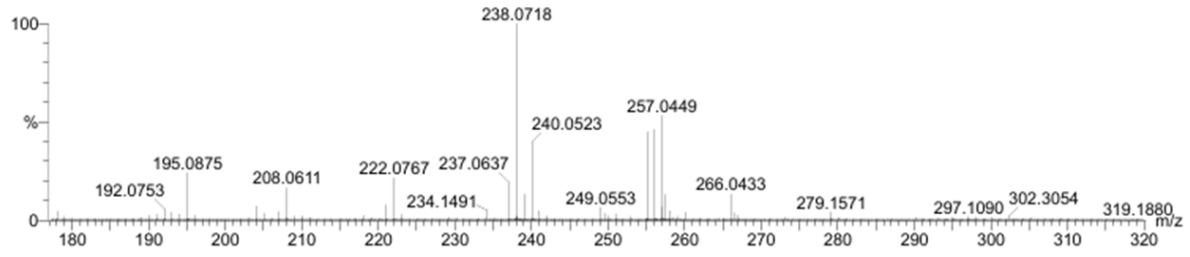

Figure 6.37: Accurate MS (ESI$^+$) of **19**.

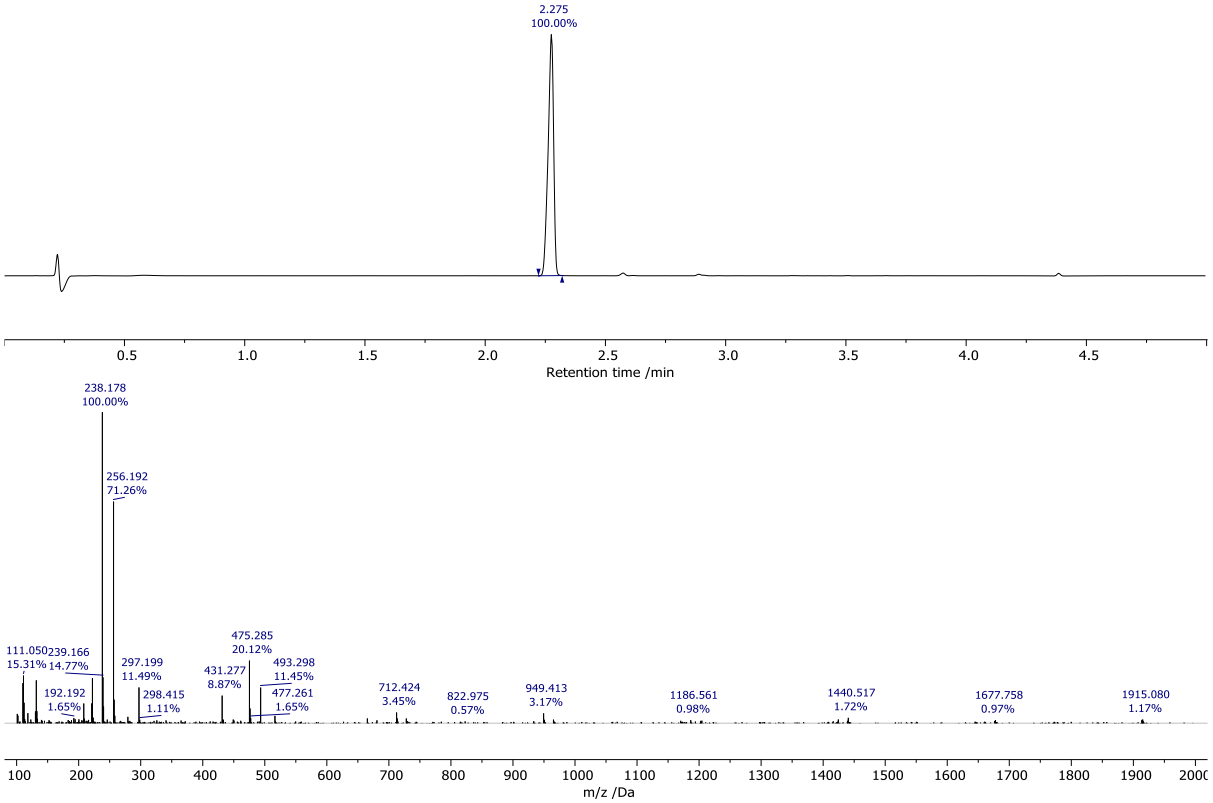

Figure 6.38: LCMS (Method E) of **19** AC (210-400 nm) (top) and the MS (ESI^+) at 2.275 minutes (bottom).

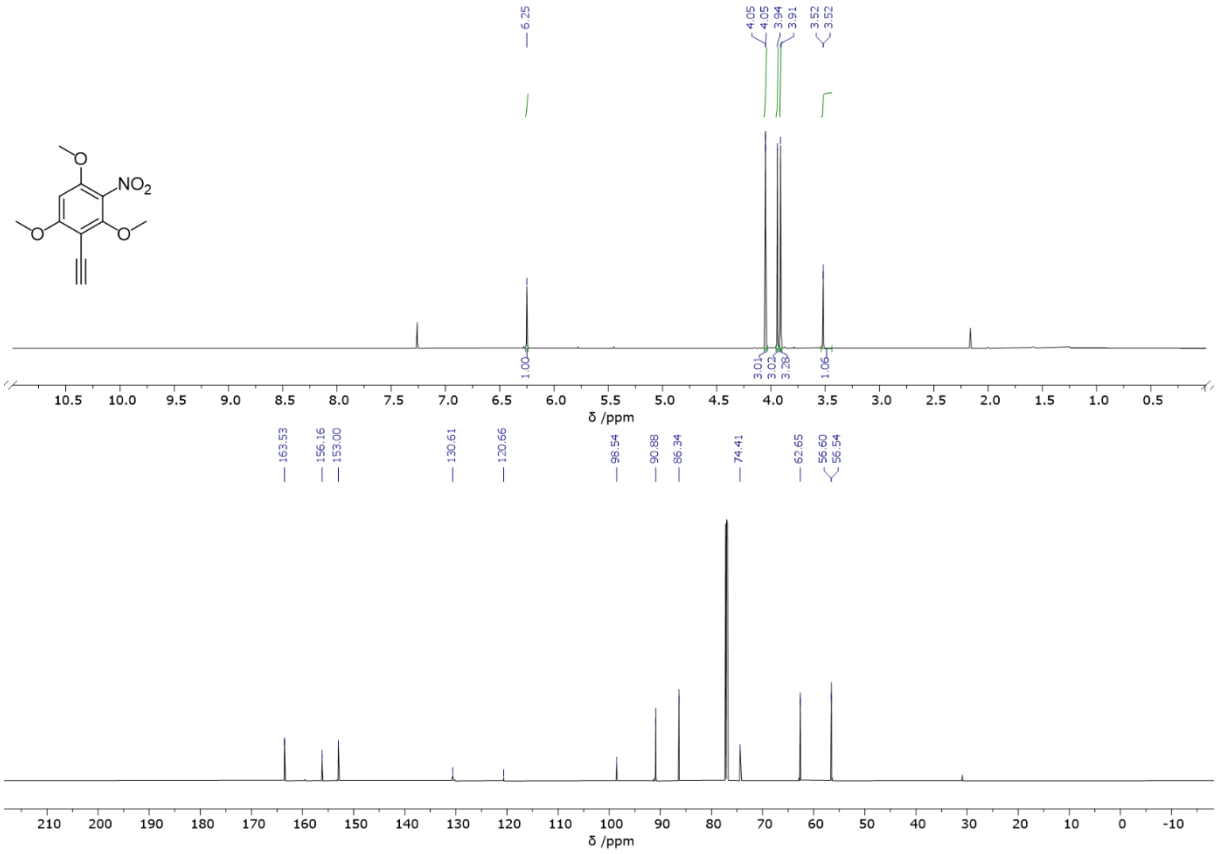

Figure 6.39: ^1H NMR (700 MHz, $CDCl_3$) (top) and ^{13}C NMR (151 MHz, $CDCl_3$) (bottom) spectra of **19**.

Ethyl 6-(hydroxymethyl)-4-((2,4,6-trimethoxy-3-nitrophenyl)ethynyl)picolinate, **20**

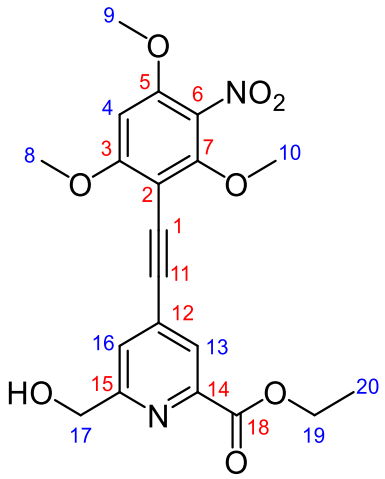

2-(2,2-dibromovinyl)-1,3,5-trimethoxy-4-nitrobenzene, **18** (150 mg, 0.632 mmol, 1 eq.), ethyl 4-bromo-6-(hydroxymethyl)picolinate, **13** (181 mg, 0.695, 1.1 eq.) and $[Pd(allyl)Cl]_2$ (23 mg, 0.0632 mmol, 0.1 eq.) were dissolved in anhydrous acetonitrile (3 ml) and degassed (freeze-pump-thaw × 3). After that, TEA (1.00 ml, 7.22 mmol, 11 eq.) and piperidine (0.25 ml, 2.6 mmol, 4 eq.) were added, and the resulting solution was stirred at 40°C for 20 hours under argon). Organic solvents were then removed under reduced pressure, and the resulting yellow solid was purified by column chromatography (silica, 3 % MeOH in DCM) to yield beige solid (0.207 g, 0.497 mmol, 79%).

HRMS (ESI$^+$) *m/z* 417.1288 ($C_{20}H_{21}N_2O_8$ requires 417.1298).

^{1}H NMR (700 MHz, CD_2Cl_2) δ 8.06 (1H, s, H^{13}), 7.58 (1H, s, H^{16}), 6.33 (1H, s, H^4), 4.81 (2, q, $^3J_{H\text{-}H}$ 7.1, H^{17}), 4.43 (2H, q, $^3J_{H\text{-}H}$ 7.1, H^{19}), 4.11 (3H, s, H^{10}) 3.99 (3H, s, H^9), 3.95 (3H, s, H^8), 1.42 (3H, t, $^3J_{H\text{-}H}$ 7.1, H^{20}).

^{13}C NMR (151 MHz, CD_2Cl_2) δ 164.90 (C^{18}), 163.85 (C^5), 160.92 (C^{15}), 156.00 (C^7), 154.16 (C^3), 148.11 (C^{14}), 133.52 (C^{12}), 125.49 (C^{13}), 125.19 (C^{16}), 98.52 (C^1), 95.15 (C^{11}), 91.64 (C^4), 86.54 (C^2), 64.67 (C^{17}), 63.29 (C^{10}), 62.35 (C^{19}), 57.23 (C^8), 57.11 (C^9), 14.47 (C^{20}).

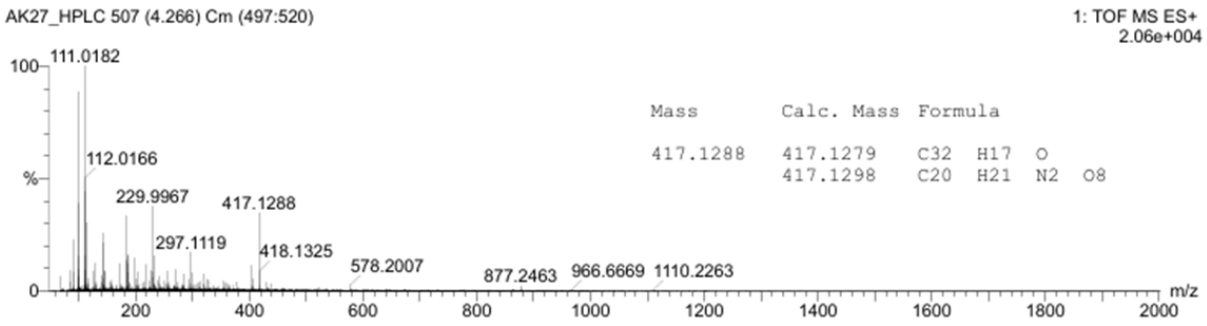

Figure 6.40: Accurate MS (ESI$^+$) of **20**.

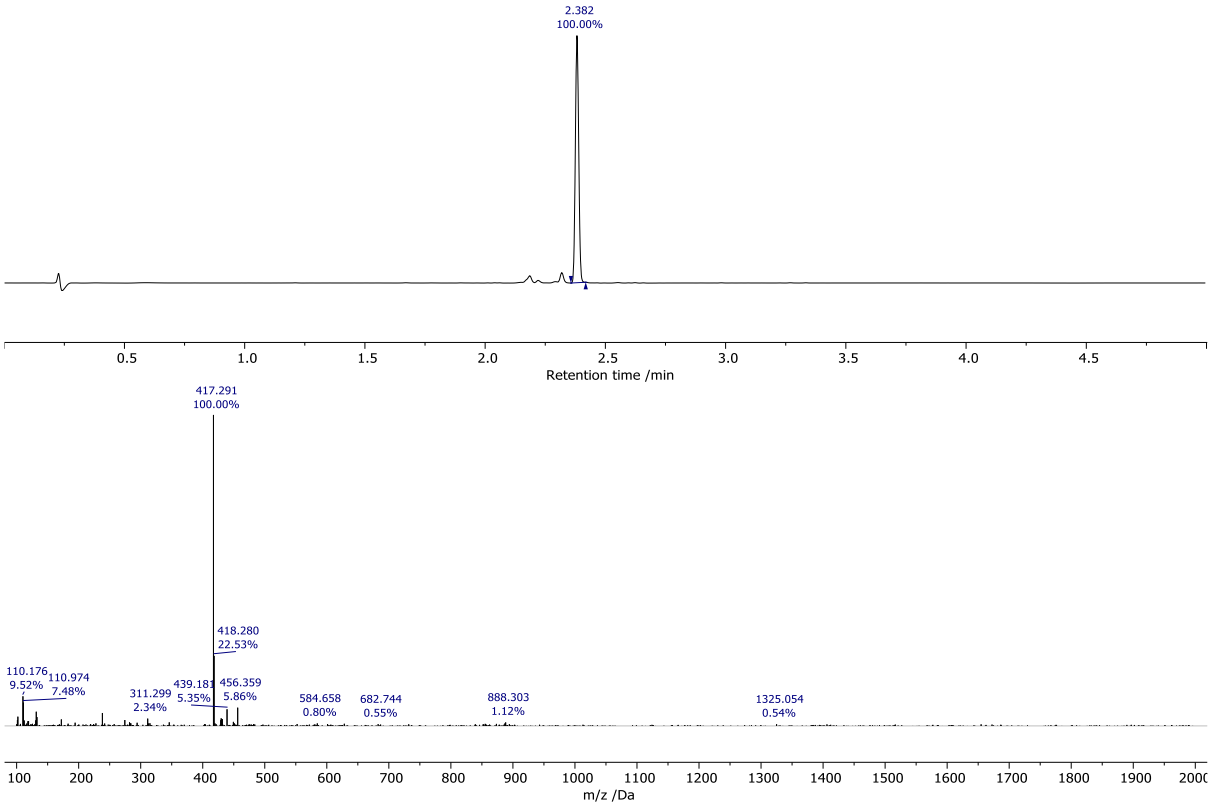

Figure 6.41: LCMS (Method E) of **20** AC (210-400 nm) (top) and the MS (ESI$^+$) at 2.382 minutes (bottom).

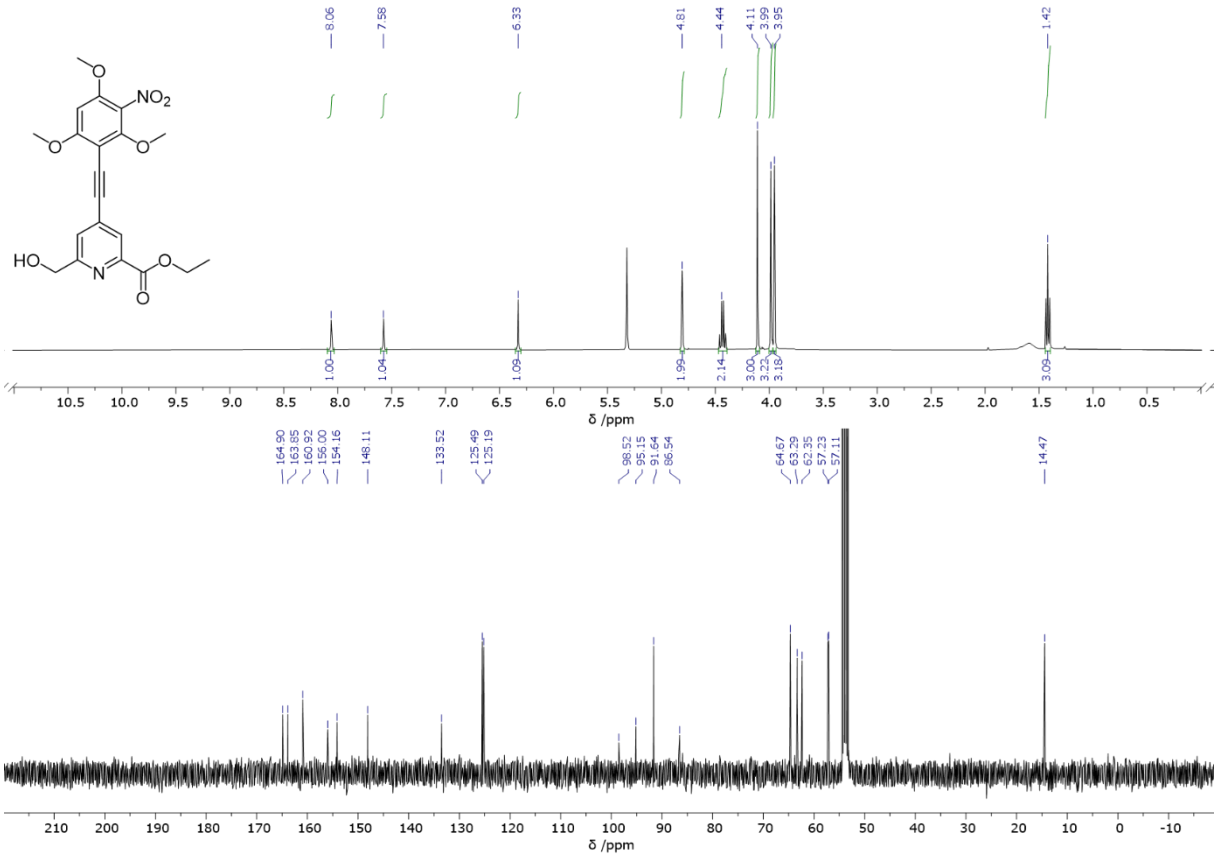

Figure 6.42: ^{1}H NMR (700 MHz, $CDCl_3$) (top) and ^{13}C NMR (151 MHz, $CDCl_3$) (bottom) spectra of **20**.

Ethyl 6-(((methylsulfonyl)oxy)methyl)-4-((2,4,6-trimethoxy-3-nitrophenyl)ethynyl)picolinate, **21**

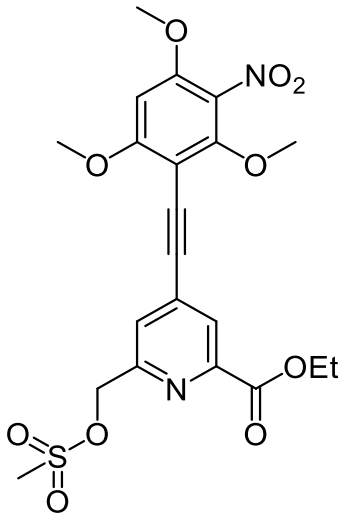

Ethyl 6-(hydroxymethyl)-4-((2,4,6-trimethoxy-3-nitrophenyl)ethynyl)picolinate, **20** (200 mg, 0.480 mmol, 1 eq.) and methanesulfonic anhydride (335 mg, 1.921 mmol, 4 eq.) were dissolved in anhydrous THF (10 ml) and DIPEA (0.250 ml, 1.44 mmol, 3 eq.) was added. The resulting solution was stirred at rt for 1 hour under argon). Once the reaction completion was confirmed by TLC (silica, 5% MeOH in DCM), the volatile organic materials were evaporated under reduced pressure, and the obtained yellow oil was dissolved in DCM (10 ml). The resulting solution was washed with water (10 ml × 3), and the combined aqueous phases were extracted with DCM (5 ml × 3). The combined organic layers were dried over $MgSO_4$, filtered and isolated from the solvent under reduced pressure to yield pale yellow solid that was used in the next step without further purification.

LCMS (ESI^+) *m/z* 495.388 $[M+H]^+$

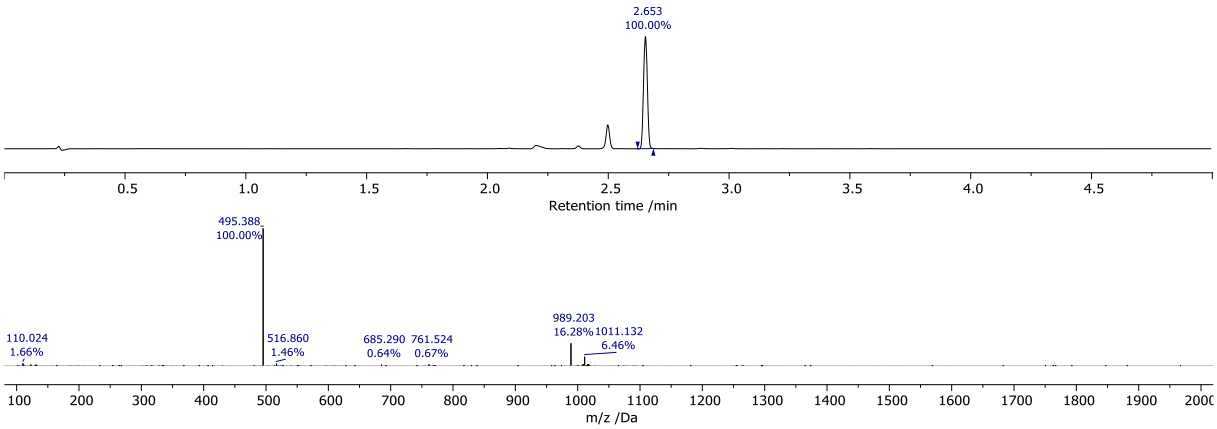

Figure 6.43: LCMS (Method E) of **21** AC (210-400 nm) (top) and the MS (ESI^+) at 2.653 minutes (bottom).

Triethyl 6,6',6''-((1,4,7-triazonane-1,4,7-triyl)tris(methylene))tris(4-((2,4,6-trimethoxy-3-nitrophenyl)ethynyl)picolinate), **22**

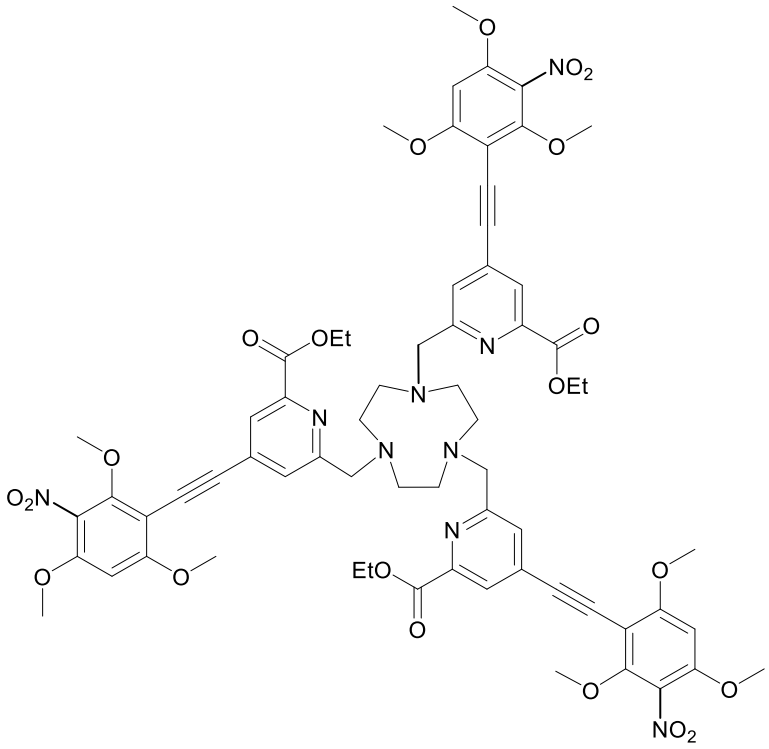

Ethyl 6-(((methylsulfonyl)oxy)methyl)-4-((2,4,6-trimethoxy-3-nitrophenyl)ethynyl)picolinate **21** (*0.480 mmol,* 3.5 eq.), TACN.3HCl (32 mg, 0.137 mmol, 1 eq.) and K_2CO_3 (133 mg, 0.960 mmol, 7 eq.) were dissolved in anhydrous acetonitrile (5 ml) and stirred at 60°C for 12 hours under argon. The crude was isolated from the solvent under reduced pressure and dissolved in DCM. It was then washed with water (5 ml × 3), and the combined aqueous phases were extracted with DCM (5 ml × 3). The combined organic layers were dried over $MgSO_4$, filtered and isolated from the solvent under reduced pressure to yield pale yellow solid (*0.137 mmol*) that was used in the next step without further purification.

HRMS (ESI$^+$) *m/z* 1324.4679 $[M+H]^+$ ($C_{66}H_{69}N_9O_{21}$ requires 1324.4686).

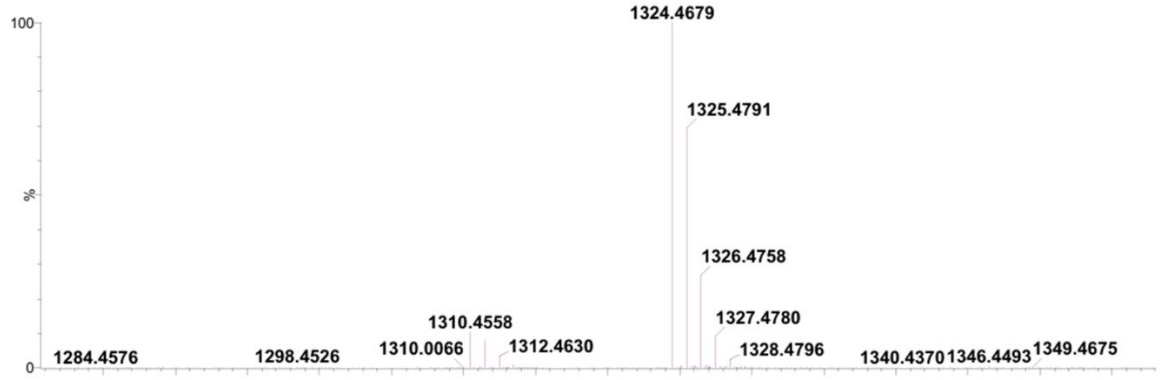

Figure 6.44: Accurate MS (ESI$^+$) of **22**.

EuL²

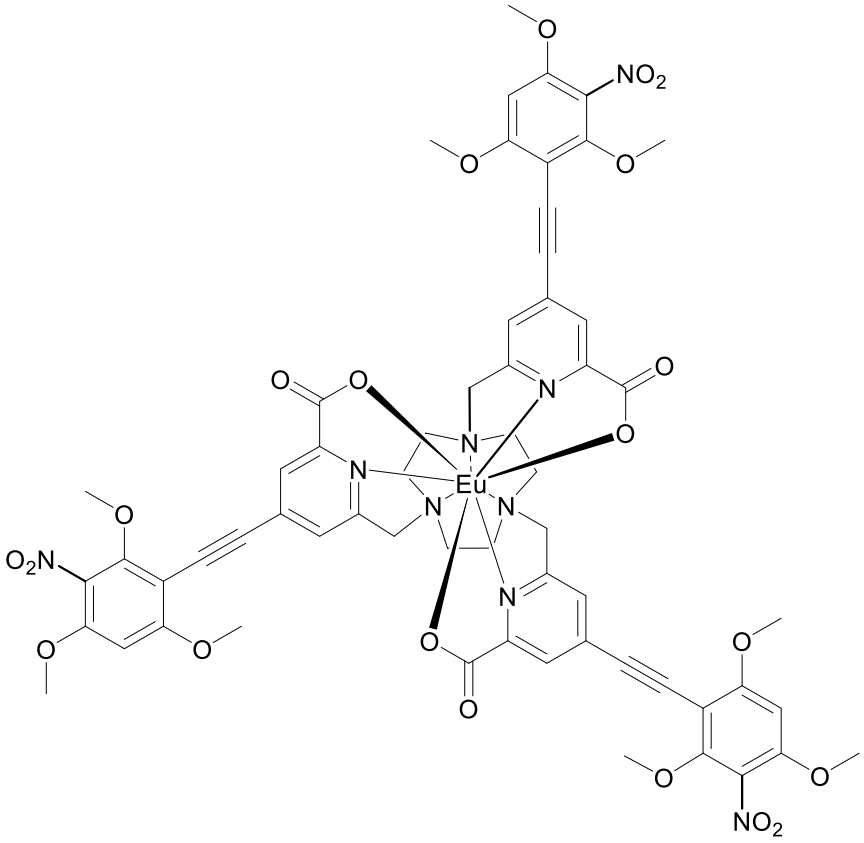

Triethyl 6,6',6''-((1,4,7-triazonane-1,4,7-triyl) tris (methylene)) tris (4-((2,4,6-trimethoxy-3-nitrophenyl) ethynyl) picolinate) **6** (*0.137 mmol*) was dissolved in MeOH (5 ml) and water was dropwise added until white precipitate remained undissolved. The pH of the resulting solution was adjusted to 12.5 using 1M NaOH, and it was then stirred at rt for 3 hours, while its pH was periodically adjusted to 12.5 until hydrolysis completion was confirmed by LCMS. After that, the solution pH was readjusted to 6.5 using 1M HCl. $Eu(OAC)_3$ was then added (50 mg, 0.151 mmol, 1.1 eq.) and the resulting solution was stirred at rt for 20 hours. The solvent was then removed under reduced pressure to yield yellow solid which was purified by flash chromatography (silica, 5% MeOH in DCM) to yield yellow solid (31 mg, 0.022 mmol, 16% over two steps).

HRMS (ESI^+) *m/z* 1388.2751 $[M+H]^+$ ($C_{60}H_{54}{}^{151}EuN_9O_{21}$ requires 1388.2711).

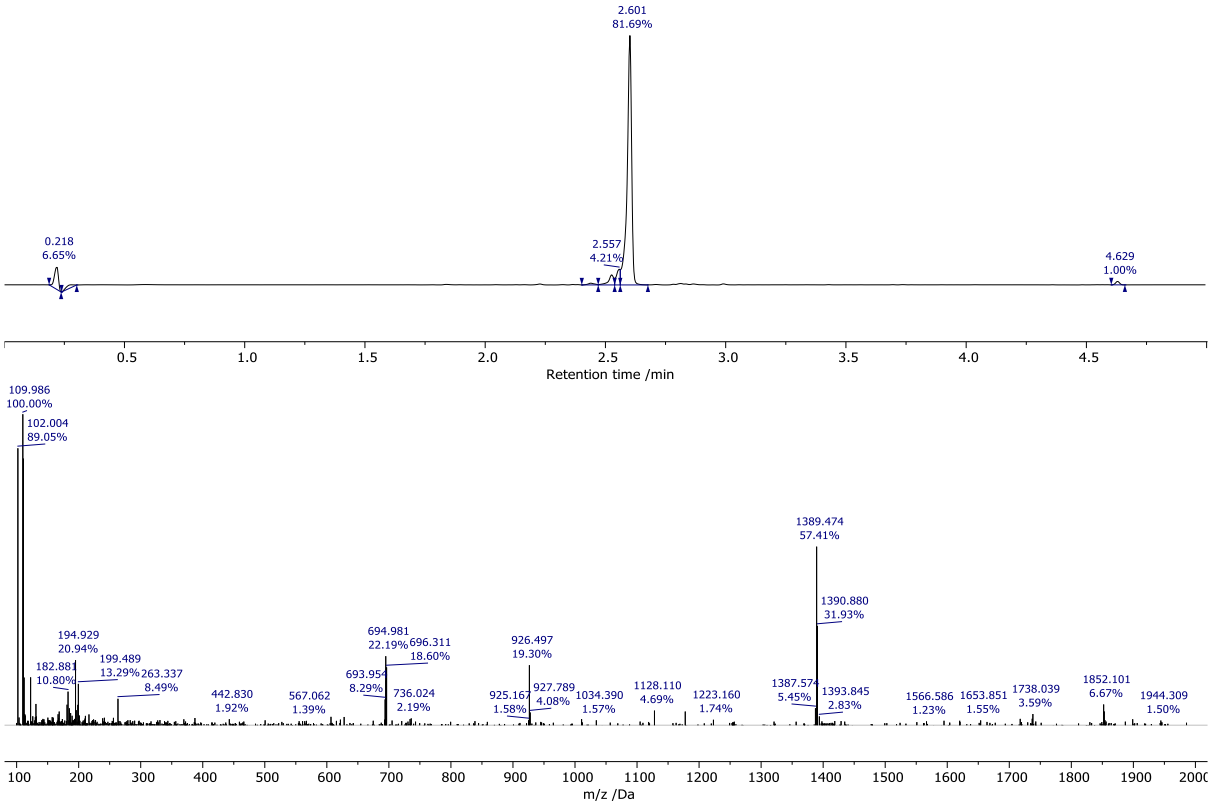

Figure 6.45: LCMS (Method E) of **EuL²** AC (210-400 nm) (top) and the MS (ESI⁺) at 2.601 minutes (bottom).

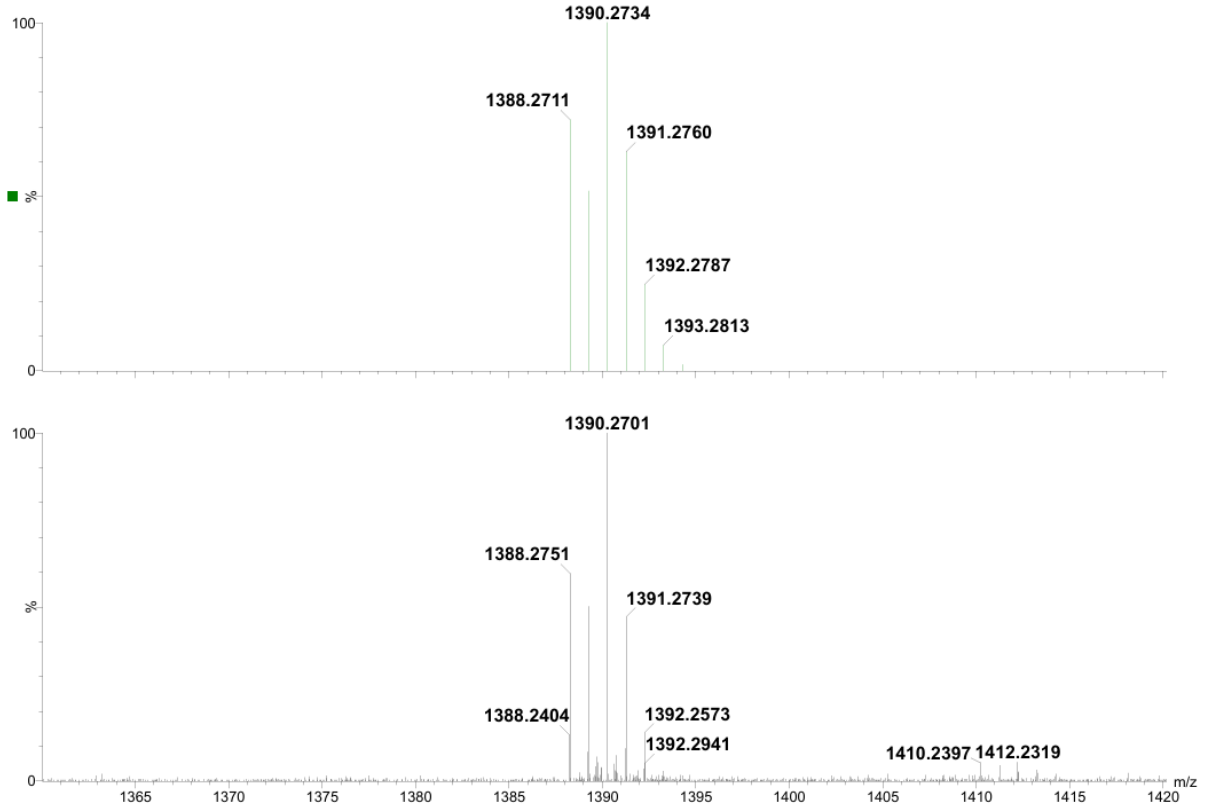

Figure 6.46: Simulated (top) and recorded (bottom) accurate MS (ESI⁺) of **EuL²**.

3-Amino-2,4,6-trimethoxybenzaldehyde, **17a**

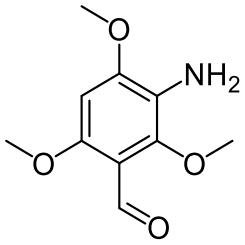

$SnCl_2$ (2.40 g, 12.7 mmol, 15 eq.) was added to a stirring solution of 2,4,6-trimethoxy-3-nitrobenzaldehyde, **17** (204 mg, 0.846 mmol, 1 eq.) in EtOH (10 ml), and the resulting solution was stirred for 20 hours at 60°C under argon. After that, the reaction mixture was poured over ice, neutralised using 1 M NaOH and extracted with EtOAc (20 ml × 3). The combined organic fractions were then washed with water (20 ml × 3) and dried over $MgSO_4$. The product was isolated from the solvent under reduced pressure to give yellow oil (113 mg, 0.535 mmol, 63%).

HRMS (ESI$^+$) *m/z* 212.0913 $[M+H]^+$ ($C_{10}H_{14}NO_4$ requires 212.0923).

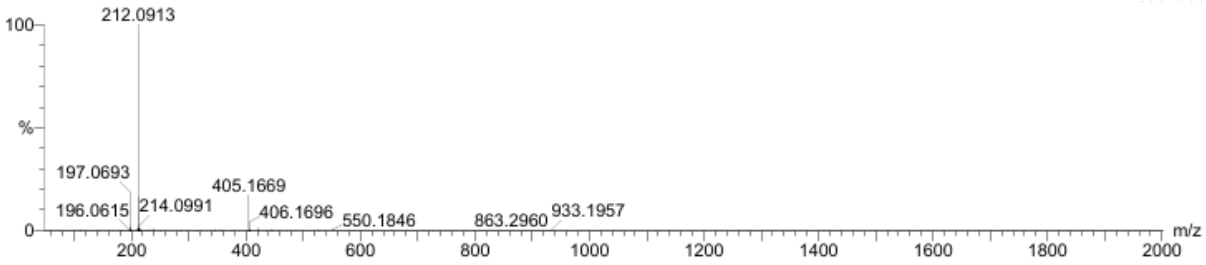

Figure 6.47: Accurate MS (ESI$^+$) of **20**.

3-Azido-2,4,6-trimethoxybenzaldehyde, **17b** (unsuccessful)[98]

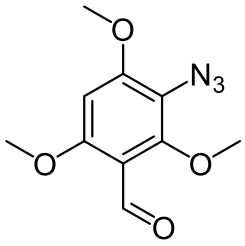

Tert-butyl nitrite (45 µl, 0.377 mmol, 1.5 eq.) followed by trimethylsilyl azide (40 µl, 0.301 mmol, 1.2 eq.) were dropwise added to an ice-cold solution of 3-amino-2,4,6-trimethoxybenzaldehyde, **17a** (53 mg, 0.251 mmol, 1 eq.) in MeCN (2 ml). The resulting solution was stirred for 20 hours at rt under argon before another portion of tert-butyl nitrite (150 µl, 1.26 mmol, 5 eq.) and trimethylsilyl azide (167 µl, 1.25 mmol, 5 eq.) was added. The reaction mixture was then stirred for further 20 hours to result in marginal conversion.

3-(2,2-Dibromovinyl)-2,4,6-trimethoxyaniline, **18a**

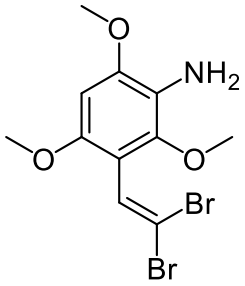

$SnCl_2$ (355 mg, 1.87 mmol, 5 eq.) was added to a stirring solution of 2-(2,2-dibromovinyl)-1,3,5-trimethoxy-4-nitrobenzene, **18**, (148 mg, 0.373 mmol, 1 eq.) in EtOH (8 ml), and the resulting solution was stirred for 20 hours at 60°C under argon. After this time, the reaction mixture was poured over ice, neutralised using 1 M NaOH and extracted with EtOAc (20 ml × 3). The combined organic fractions were then washed with water (20 ml × 3) and dried over $MgSO_4$). The product was isolated from the solvent under reduced pressure to give yellow oil (99 mg, 0.27 mmol, 72%).

LCMS (ESI+) *m/z* 365.835 $[M+H]^+$.

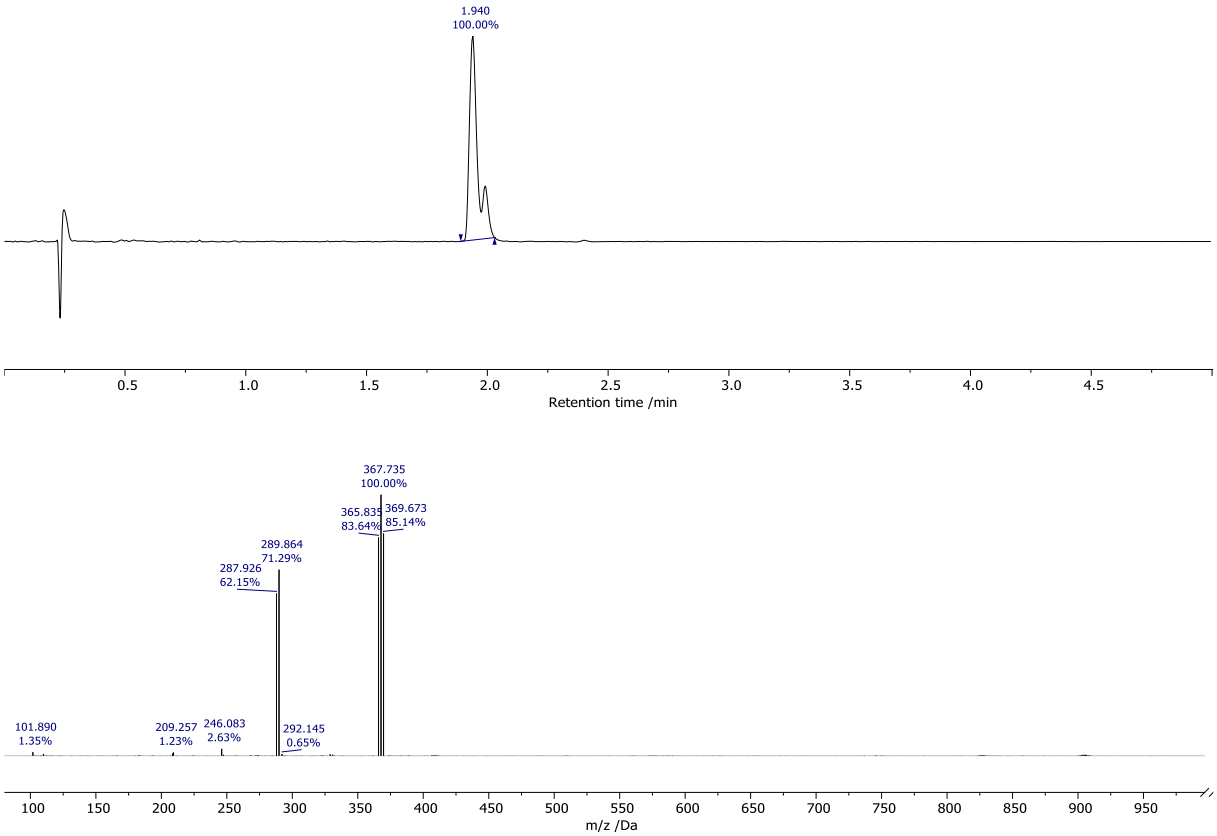

Figure 6.48: LCMS (Method E) of **18a** AC (210-400 nm) (top) and the MS (ESI^+) at 1.940 minutes (bottom).

2-Azido-4-(2,2-dibromovinyl)-1,3,5-trimethoxybenzene, **18b**

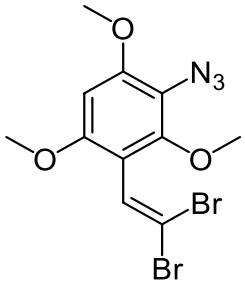

Tert-butyl nitrite (137 µl, 1.09 mmol, 5 eq.) followed by trimethylsilyl azide (146 µl, 1.09 mmol, 5 eq.) were dropwise added to an ice-cold solution of 3-amino-2,4,6-trimethoxybenzaldehyde, **17a** (80 mg, 0.22 mmol, 1 eq.) in MeCN (2 ml). The resulting solution was stirred for 20 hours at rt under argon. After that, the crude product was dried under reduced pressure and then redissolved in DCM. The solution was washed with water (20 ml × 3), and the aqueous fractions were extracted with DCM (20 ml × 3). The product was then isolated from solvent under reduced pressure to yield pale-yellow oil (64 mg, 0.16 mmol, 74 %).

LCMS (ESI+) *m/z* 363.820 $[M+H-2N]^+$.

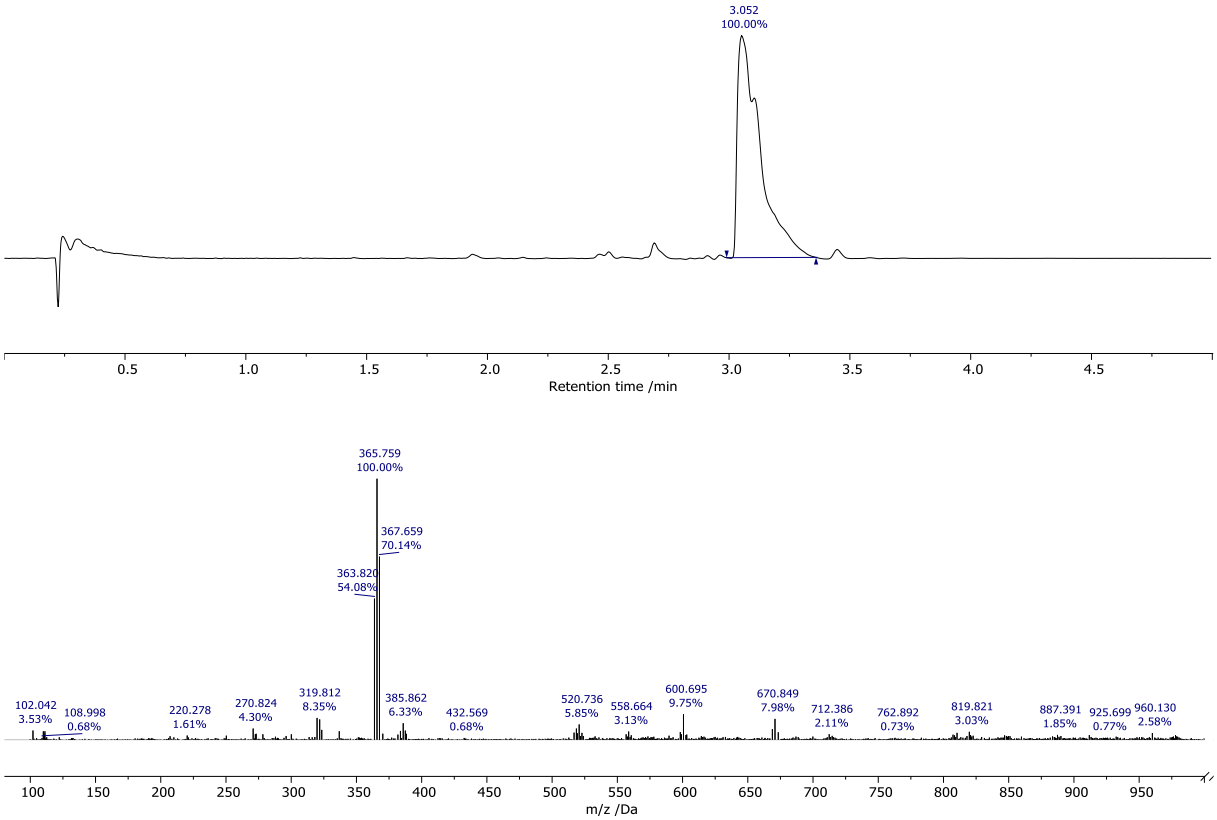

Figure 6.49: LCMS (Method E) of **18b** AC (210-400 nm) (top) and the MS (ESI^+) at 3.052 minutes (bottom).

1-(3-(2,2-Dibromovinyl)-2,4,6-trimethoxyphenyl)-4-(trimethylsilyl)-1H-1,2,3-triazole, **18c**

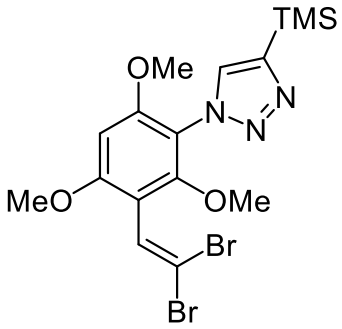

To a solution of 2-azido-4-(2,2-dibromovinyl)-1,3,5-trimethoxybenzene, **18b** (20 mg, 0.054 mmol, 1 eq.), CuCl (1.0 mg, 0.011 mmol, 0.2 eq.) and sodium ascorbate (2.2 mg, 0.011 mmol, 0.2 eq.) in a mixture of MeCN (1 ml) and water (1 ml) was added trimethylsilyl azide (36 µl,0.27 mmol, 5 eq.). The resulting solution was stirred at 40°C for 1 hour under argon. All volatile components of the product mixture were evaporated under reduced pressure to yield dark brown oil (23 mg, 0.047 mmol, 87%).

LCMS (ESI$^+$) 489.878 $[M+H]^+$.

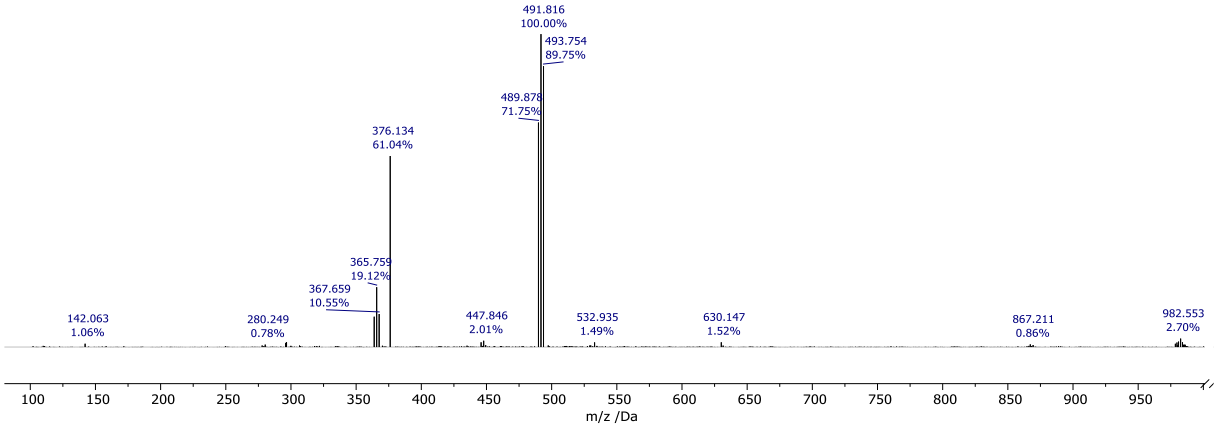

Figure 6.50: MS (ESI$^+$) for **18c**.

EuL^{2a}

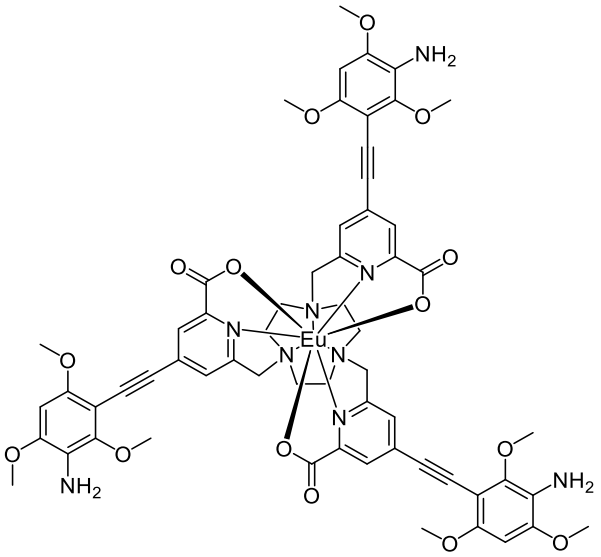

To a stirring suspension of **EuL^{2}** (5.0 mg, 0.0036 mmol, 1 eq.) in MeOH (5 ml) at 40°C was drop-wise added DCM (~5 ml) until a clear solution was obtained. The solution was irradiated with 365 nm LED resulting in a red glow. $SnCl_2$ was then added to a stirring solution under argon in small portions (71 mg, 0.61 mmol, 169 eq.) until the solution no longer glowed under the UV light irradiation. The feasible purification method from tin(II) byproducts was not found.

HRMS (ESI$^+$) *m/z* 1298.3413 $[M+H]^+$ ($C_{60}H_{60}{}^{151}EuN_9O_{15}$ requires 1298.3486).

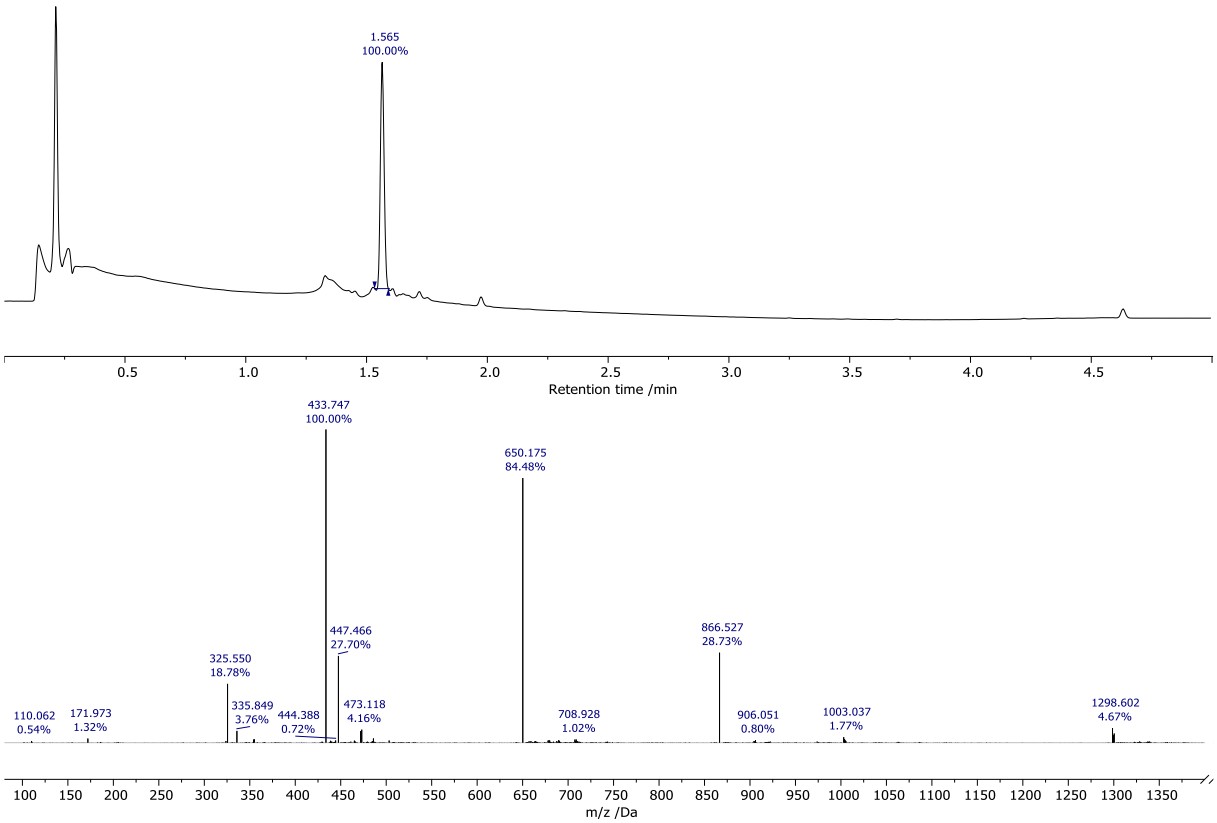

Figure 6.51: LCMS (Method E) of **EuL^{2a}** AC (210-400 nm) (top) and the MS (ESI$^+$) at 1.565 minutes (bottom).

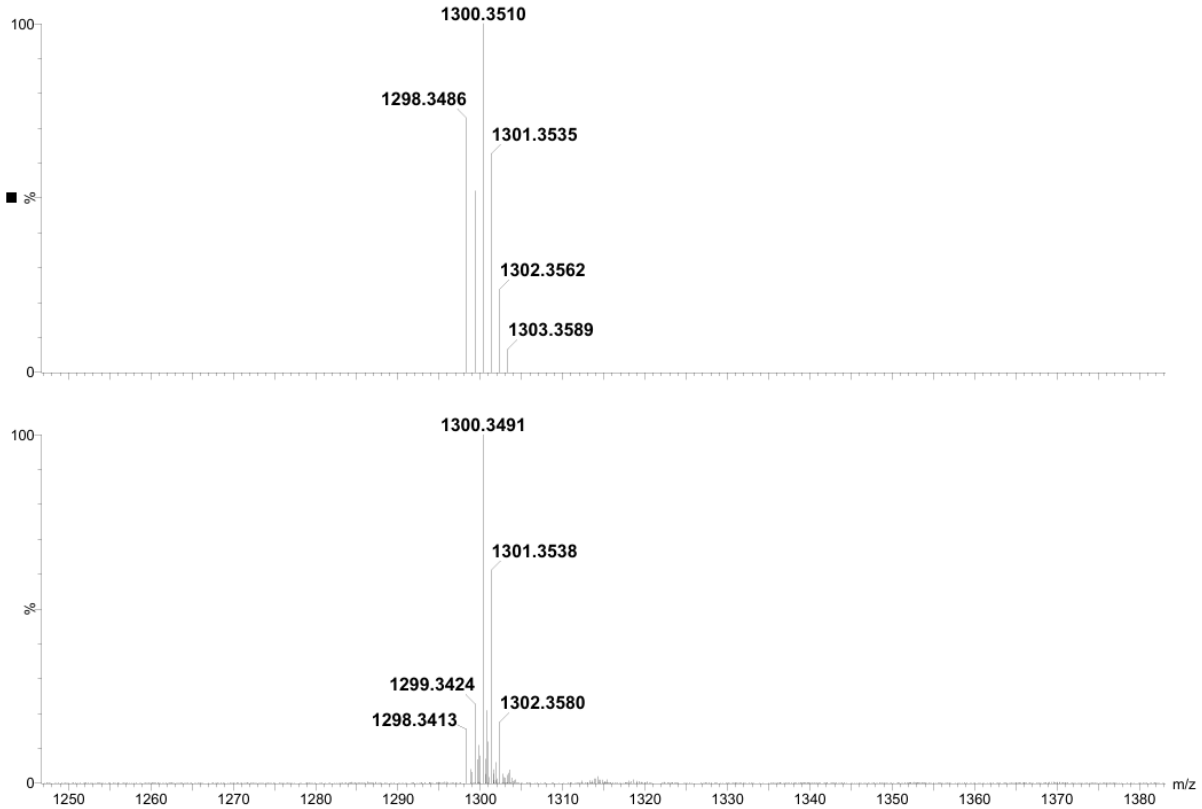

Figure 6.52: Simulated (top) and recorded (bottom) accurate MS (ESI$^+$) of **EuL^{2a}**.

Ethyl 4-((3-amino-2,4,6-trimethoxyphenyl)ethynyl)-6-(hydroxymethyl)picolinate, **20a**

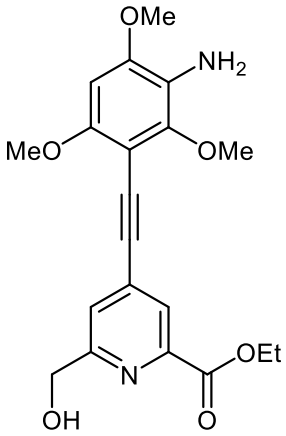

$SnCl_2$ (91 mg, 0.48 mmol, 10 eq.) was added to a stirring solution of ethyl 6-(hydroxymethyl)-4-((2,4,6-trimethoxy-3-nitrophenyl)ethynyl)picolinate, **20** (20 mg, 0.048 mmol, 1 eq.) in EtOH (5 ml), and the resulting solution was stirred for 20 hours at 60°C under argon. After this time, the reaction mixture was poured over ice, neutralised using 1 M NaOH and extracted with EtOAc (20 ml × 3). The combined organic fractions were then washed with water (20 ml × 3) and dried over $MgSO_4$. The product was isolated from the solvent under reduced pressure to yield yellow oil (13 mg, 0.034 mmol, 70%).

LCMS (ESI+) *m/z* 387.345 $[M+H]^+$.

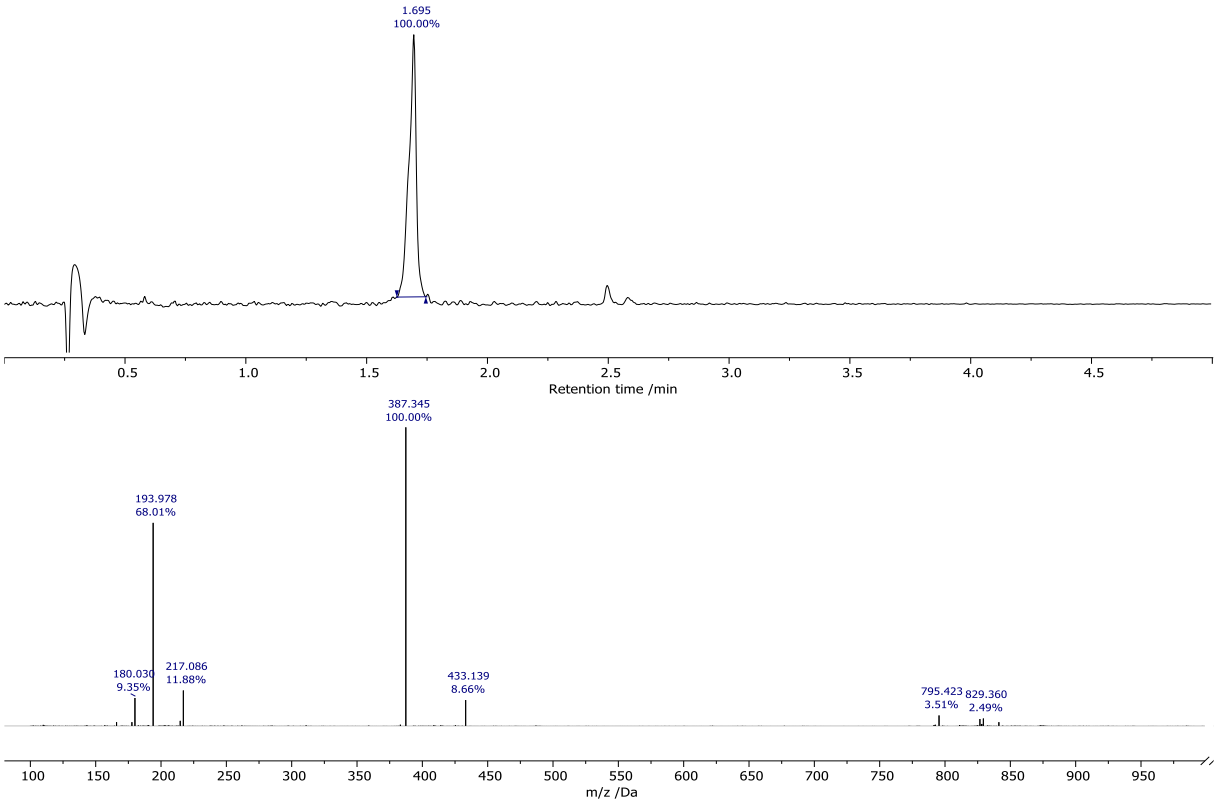

Figure 6.53: LCMS (Method E) of **20a** AC (210-400 nm) (top) and the MS (ESI^+) at 1.695 minutes (bottom).

Ethyl 4-((3-amino-2,4,6-trimethoxyphenyl)ethynyl)-6-(((methylsulfonyl)oxy)methyl)picolinate, **21a** and ethyl 6-(((methylsulfonyl)oxy)methyl)-4-((2,4,6-trimethoxy-3-(methylsulfonamido)phenyl)ethynyl)picolinate, **21b**

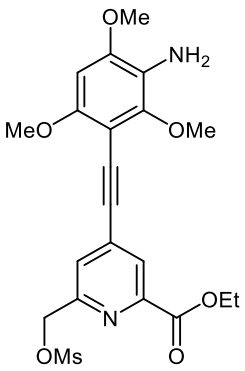

21a
minor

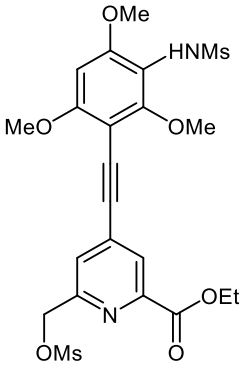

21b
major

DIPEA (18.0 µl, 0.102, 3 eq.) and methanesulfonic anhydride (47 mg, 0.27 mmol, 8 eq.) were added to a solution of ethyl 4-((3-amino-2,4,6 trimethoxyphenyl) ethynyl)-6-(hydroxymethyl)picolinate, **20a** (13 mg, 0.034 mmol, 1 eq.) in anhydrous THF (2 ml). The resulting solution was stirred for 1 hour at rt before it was subjected to LCMS to reveal the formation of the unwanted **21b** major product.

LCMS (ESI+) *m/z* 543.500 $[M+H]^+$.

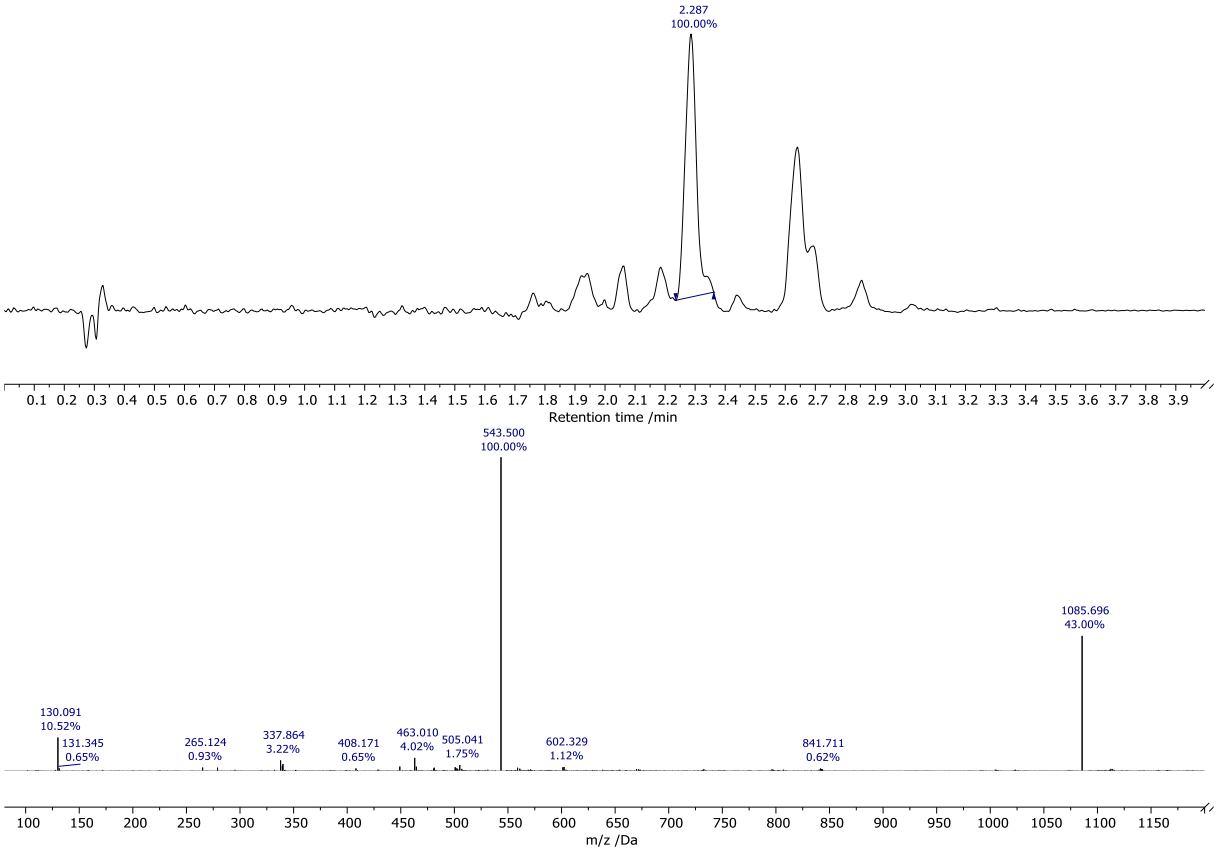

Figure 6.54: LCMS (Method E) of **20a** AC (210-400 nm) (top) and the MS (ESI^+) at 2.287 minutes (bottom).

4-Hydroxy-2,6-dimethoxybenzaldehyde, **23**[106]

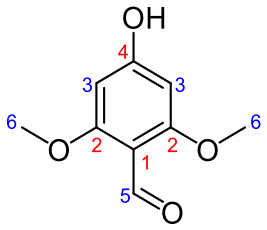

An ice-cold solution of phosphorus oxychloride (9.0 ml, 97 mmol, 1.5 eq.) in DCM (30 ml) was dropwise added to an ice-cold solution 3,5-dimethoxyphenol (10 g, 65 mmol, 1 eq.) in DCM (30 ml), and the resulting solution was stirred for 10 minutes in an ice bath. To the resulting solution DMF (5.5 ml, 71 mmol, 1.1 eq.) was added dropwise over 40 minutes and stirred for further 1 hour in an ice bath once addition was completed. After that, water (250 ml) was slowly added to the mixture which was then stirred vigorously for 15 minutes at rt. The resulting solution was washed with DCM (100 ml × 3), and the aqueous layer was then basified with 1M NaOH until pH = 6 and then stirred for 10 minutes. The resulting suspension was filtered, and the residue was dried under reduced pressure. The crude product was then recrystallised from ethanol to yield pale-yellow solid (3.9 g, 21 mmol, 32%).

LCMS (ESI+) *m/z* 543.500 $[M+H]^+$.

^{1}H NMR (400 MHz, MeOD) δ 10.14 (1H, s, H^5), 6.09 (2H, s, H^3), 3.83 (6H, s, H^6).

^{13}C NMR (100 MHz, MeOD) δ 191.61, 187.68, 166.46, 164.80, 91.31, 54.72.

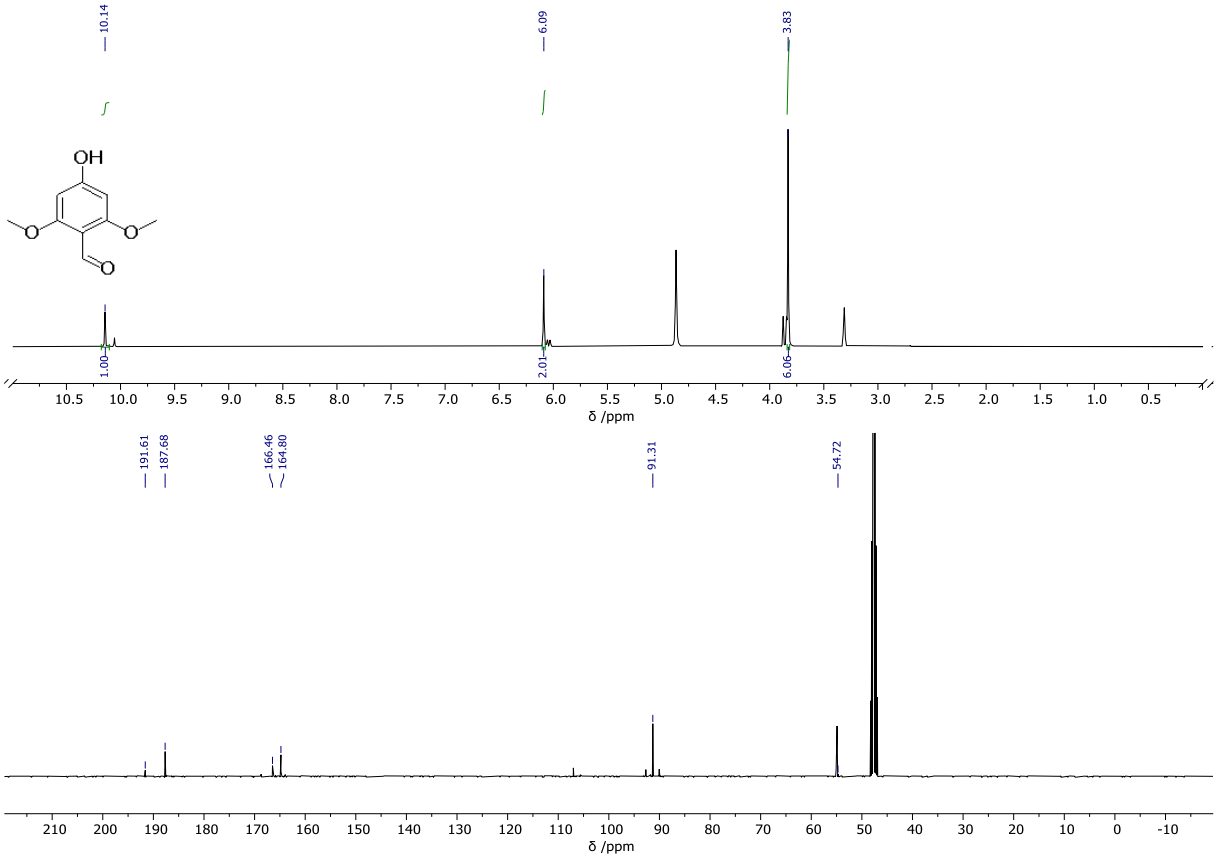

Figure 6.55: ^{1}H NMR (400 MHz, MeOD) (top) and ^{13}C NMR (100 MHz, MeOD) (bottom) spectra of **23**.

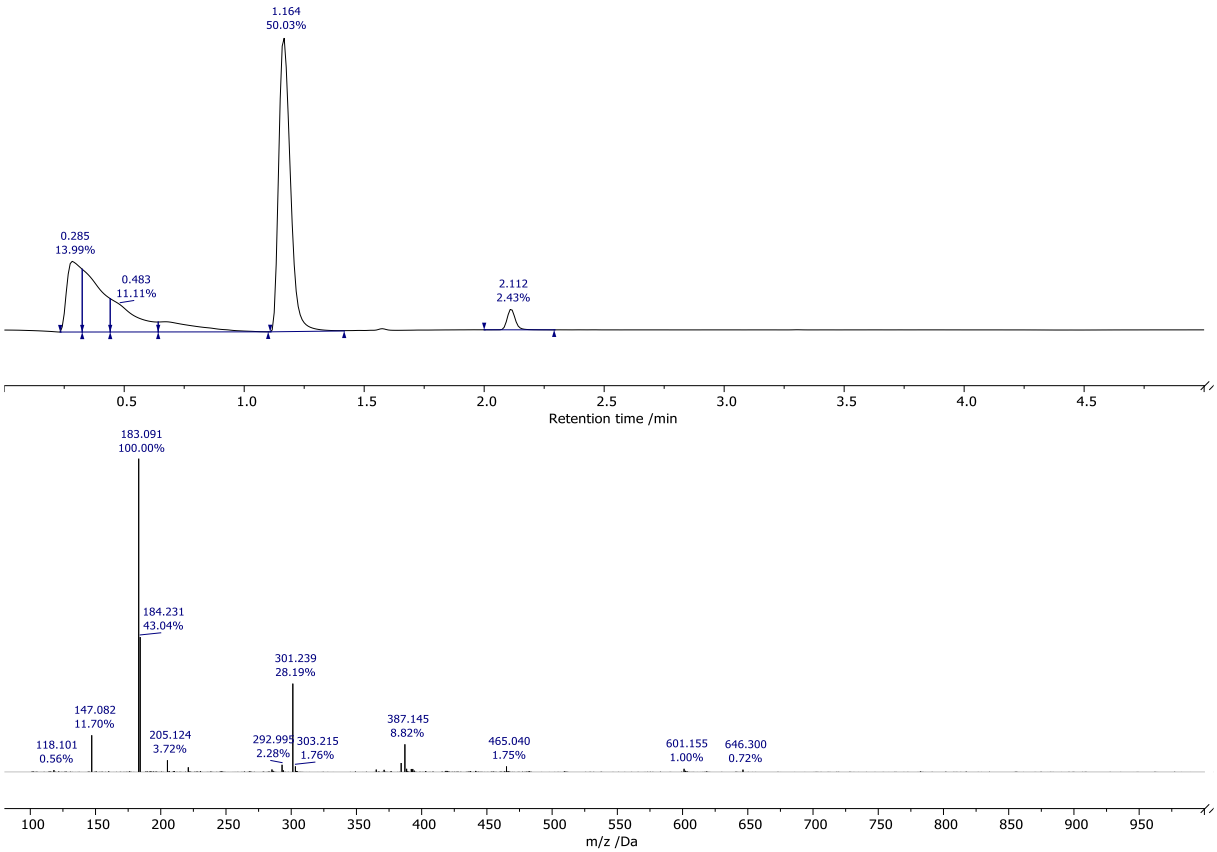

Figure 6.56: LCMS (Method E) of **23** AC (210-400 nm) (top) and the MS (ESI^{+}) at 1.164 minutes (bottom).

4-(4-Bromobutoxy)-2,6-dimethoxybenzaldehyde, **24**

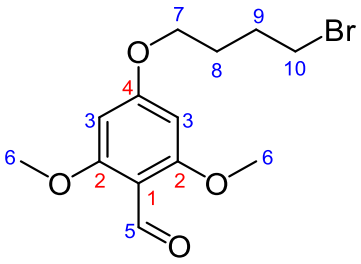

A solution of 4-hydroxy-2,6-dimethoxybenzaldehyde, **23** (504 mg, 2.77 mmol, 1 eq.) in DMF (20 ml) was dropwise added over 1 hour to a solution of 1,4-dibromobutane (3.3 ml, 27.7 mmol, 10 eq.) and K_2CO_3 (574 mg, 4.16 mmol, 1.5 eq.) in DMF (5 ml) stirring at 70°C. Once the addition was completed, the resulting solution was stirred for additional 10 minutes before DMF solvent was removed under reduced pressure. The crude product was purified by flash chromatography (silica, 1:2 hexane - EtOAc) to yield pale yellow solid (853 mg, 2.69 mmol, 97%).

LCMS (ESI$^+$) *m/z* 282.986 $[M+H]^+$.

^{1}H NMR (400 MHz, $CDCl_3$) δ 10.29 (1H, s, H^5), 6.02 (2H, s, H^3), 4.02 (2H, t, $^3J_{H\text{-}H}$ 6.2, H^7), 3.83 (6H, S, H^6), 3.45 (2H, t, $^3J_{H\text{-}H}$ 6.5, H^{10}), 2.03 (2H, m, H^8), 2.03 (2H, m, H^9).

^{13}C NMR (100 MHz, $CDCl_3$) δ 187.66, 165.56, 164.08, 108.76, 90.65, 67.21, 56.02, 33.25, 29.26, 27.66.

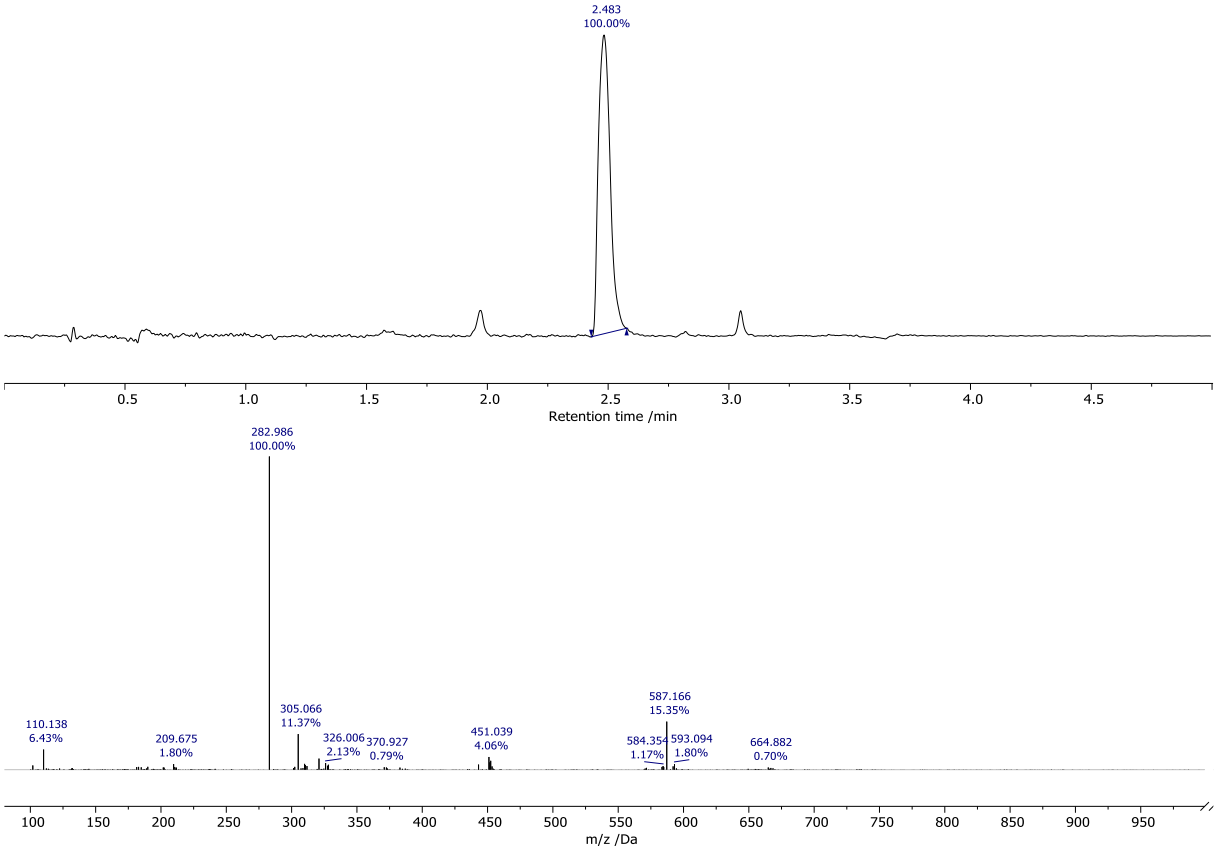

Figure 6.57: LCMS (Method E) of **24** AC (210-400 nm) (top) and the MS (ESI$^+$) at 2.483 minutes (bottom).

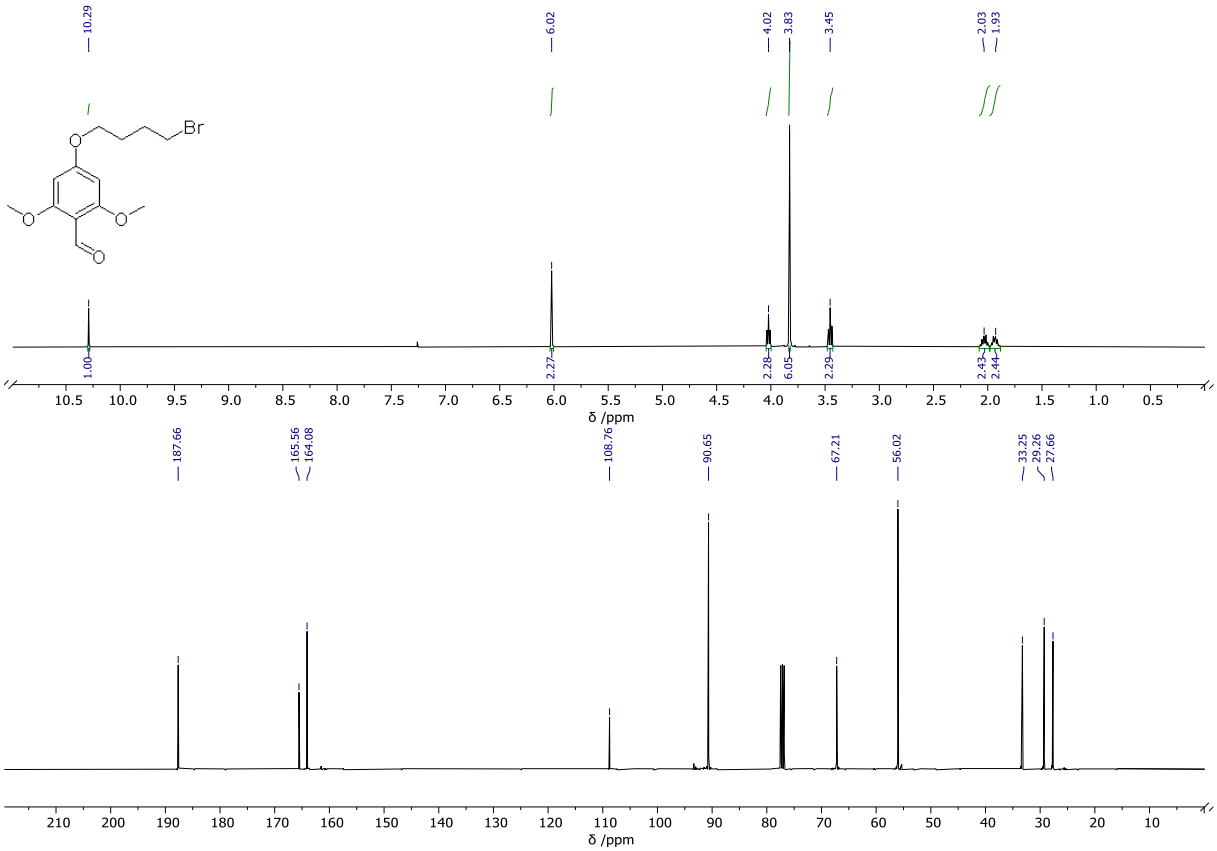

Figure 6.58: ^{1}H NMR (400 MHz, $CDCl_3$) (top) and ^{13}C NMR (100 MHz, $CDCl_3$) (bottom) spectra of **24**.

4-(4-Azidobutoxy)-2,6-dimethoxybenzaldehyde, **25**

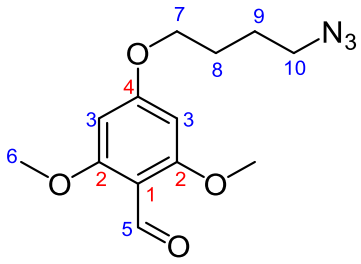

4-(4-bromobutoxy)-2,6-dimethoxybenzaldehyde, **24** (300 mg, 0.946 mmol, 1 eq.), sodium azide (246 mg, 3.78 mmol, 4 eq.) and sodium iodide (142 mg, 0.947, 1 eq.) were dissolved in DMF (10 ml) and stirred for 20 hours at rt. The resulting mixture was isolated from DMF solvent under reduced pressure and redissolved in DCM (50 ml). The resulting solution was washed with water (20 ml × 3), and the combined aqueous fractions were extracted with DCM. The combined organic fractions were dried over $MgSO_4$ and filtered. The product was isolated from DCM solvent under reduced pressure to give pale-yellow solid (220 mg, 0.789 mmol, 83%).

HRMS (ESI$^+$) *m/z* 280.1277 $[M+H]^+$ ($C_{13}H_{18}N_3O_4$ requires 280.1297).

^{1}H NMR (400 MHz, $CDCl_3$) δ 10.29 (1H, s, H^5), 6.05 (2H, s, H^3), 4.04 (2H, t, $^3J_{H\text{-}H}$ 6.2, H^7), 3.85 (6H, S, H^6), 3.37 (2H, t, $^3J_{H\text{-}H}$ 6.5, H^{10}), 1.88 (2H, m, H^8), 1.79 (2H, m, H^9).

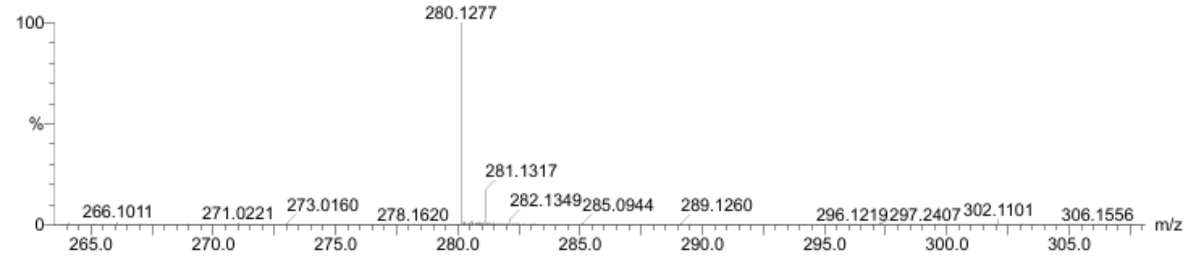

Figure 6.59: Accurate MS (ESI$^+$) of **25**.

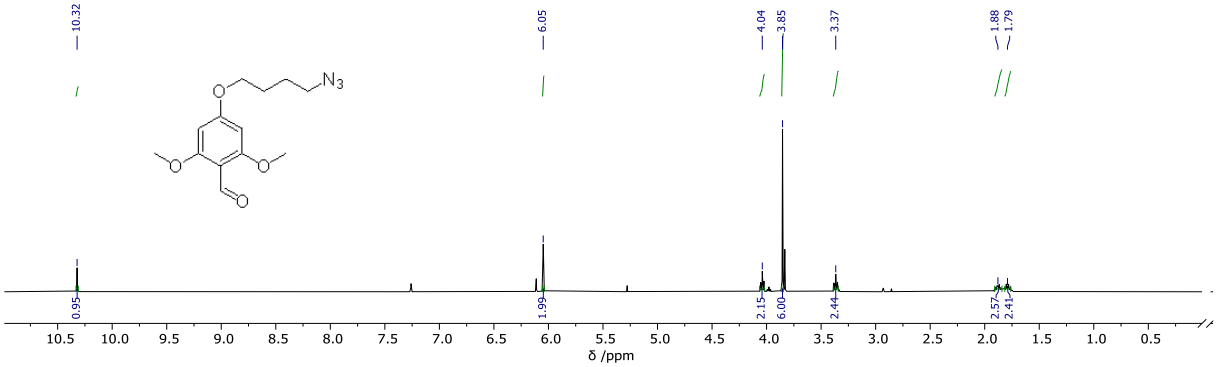

Figure 6.60: ^{1}H NMR (400 MHz, $CDCl_3$) spectrum of **25**.

5-(4-Azidobutoxy)-2-(2,2-dibromovinyl)-1,3-dimethoxybenzene, **26**

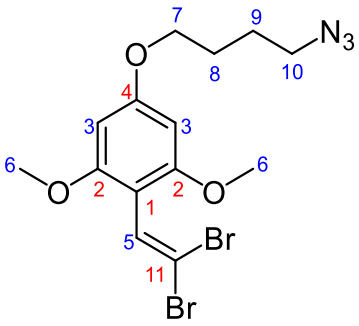

A solution of CBr_4 (321 mg, 0.968 mmol, 2 eq.) in anhydrous DCM (10 ml) was dropwise added to an ice-cold solution of 4-(4-azidobutoxy)-2,6-dimethoxybenzaldehyde, **25,** (135 mg, 0.484 mmol, 1 eq.) and PPh_3 (508 mg, 1.936 mmol, 4 eq.) in anhydrous DCM (5 ml), and the resulting solution was allowed to warm to rt and stirred for 20 hours under argon. The resulting mixture was subjected to LCMS to establish ~50% conversion. Therefore, the reaction mixture was cooled in an ice bath, and another portion of CBr_4 (321 mg, 0.968 mmol, 2 eq.) and PPh_3 (508 mg, 1.936 mmol, 4 eq.) were added. The resulting mixture was stirred for additional 3 hours at rt to result in full conversion. After that, the product mixture was washed with water (10 ml × 5) followed by extraction of the combined aqueous layers with DCM (20 ml × 3). The combined organic layers were dried over $MgSO_4$, filtered and the crude product was isolated from DCM under reduced pressure. The crude was purified by flash chromatography (silica, 70% DCM in hexane) to yield white solid (32 mg, 0.074 mmol, 15%).

HRMS (ESI$^+$) *m/z* 433.9725 $[M+H]^+$ ($C_{14}H_{18}N_3O_3Br_2$ requires 433.9715).

^{1}H NMR (400 MHz, $CDCl_3$) δ 7.18 (1H, s, H^5), 6.10 (2H, s, H^3), 4.00 (2H, t, $^3J_{H\text{-}H}$ 6.2, H^7), 3.81 (6H, S, H^6), 3.38 (2H, t, $^3J_{H\text{-}H}$ 6.5, H^{10}), 1.87 (2H, m, H^8), 1.81 (2H, m, H^9).

^{13}C NMR (100 MHz, $CDCl_3$) δ 161.03, 158.05, 130.96, 106.90, 92.75, 90.91, 67.28, 55.68, 51.17, 26.51, 25.78.

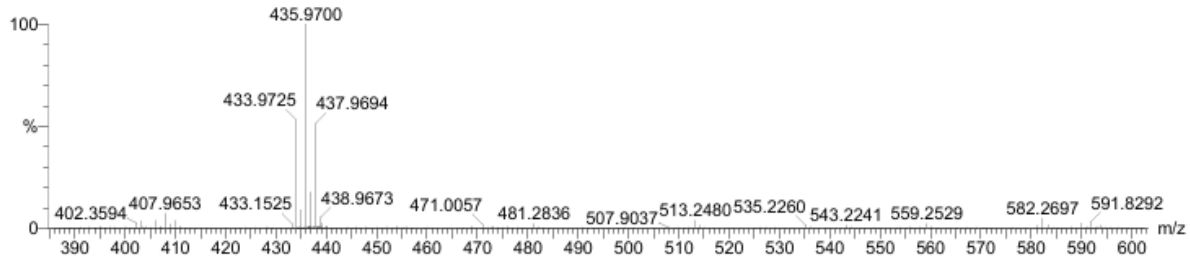

Figure 6.61: Accurate MS (ESI$^+$) of **26**.

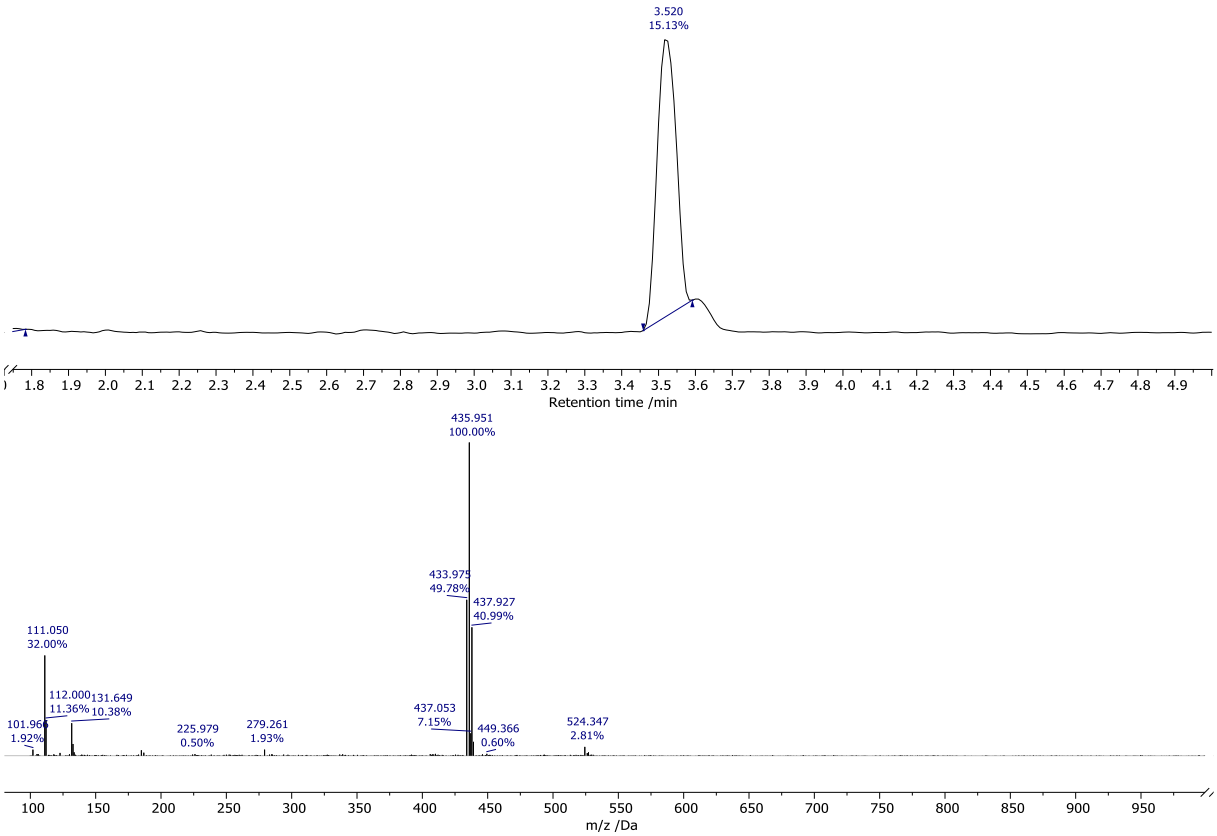

Figure 6.62: LCMS (Method E) of **26** AC (210-400 nm) (top) and the MS (ESI$^+$) at 3.520 minutes (bottom).

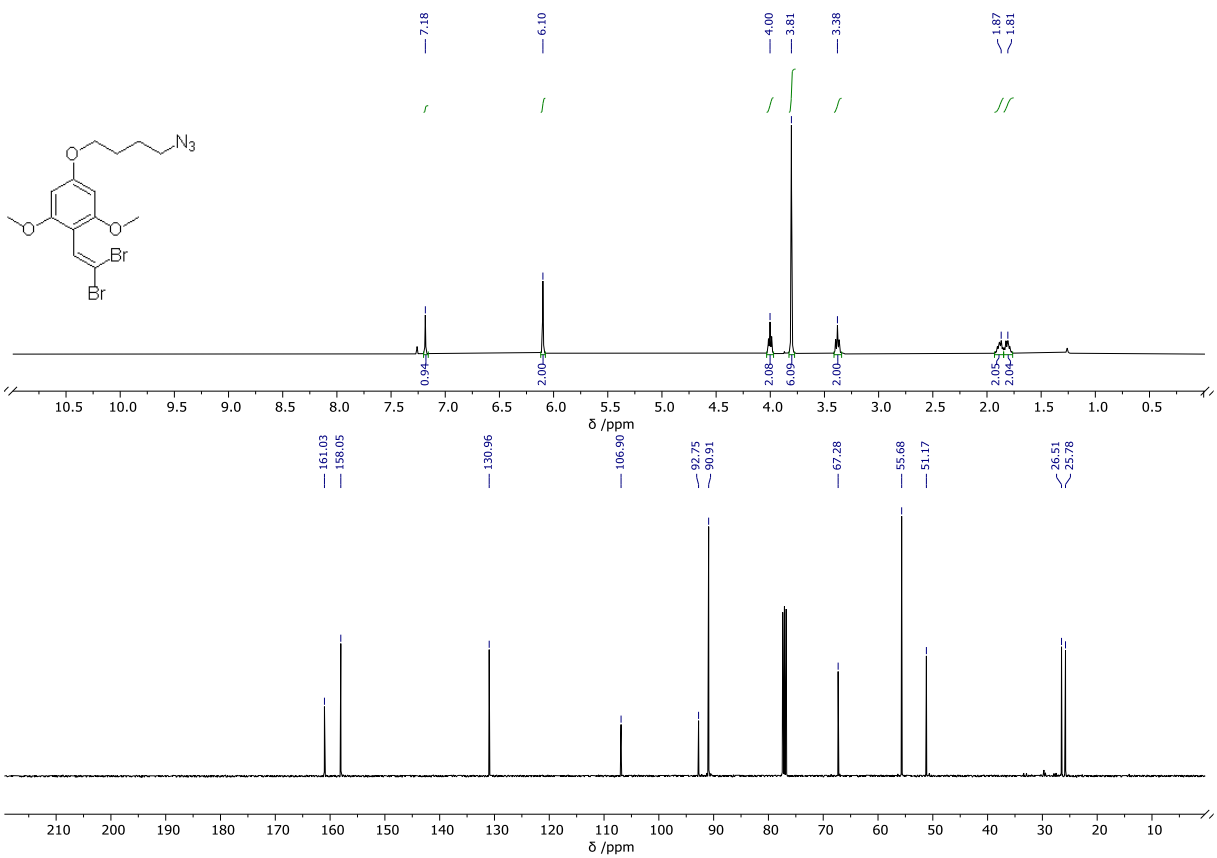

Figure 6.63: ^{1}H NMR (400 MHz, $CDCl_3$) (top) and ^{13}C NMR (100 MHz, $CDCl_3$) (bottom) spectra of **26**.

5-(4-Azidobutoxy)-2-ethynyl-1,3-dimethoxybenzene, **27**, and
4-(4-ethynyl-3,5-dimethoxyphenoxy)butan-1-amine, **27a**

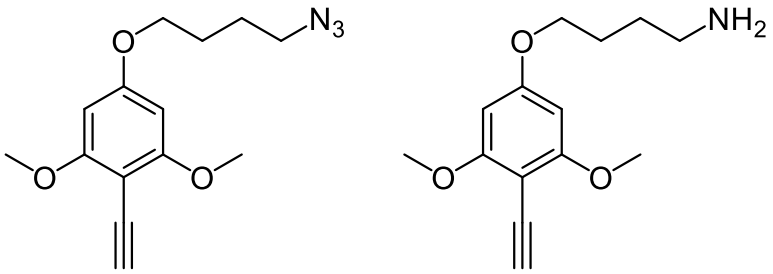

27
minor

27a
major

5-(4-azidobutoxy)-2-(2,2-dibromovinyl)-1,3-dimethoxybenzene, **26** (27 mg, 0.062 mmol, 1 eq.) was dissolved in anhydrous THF (5 ml) and cooled to -78 °C (acetone, dry ice). 2.5 M solution of n-butyllithium in hexane (50.0 µl, 0.124 mmol, 2 eq.) was then added dropwise, and the resulting orange solution was stirred for 30 minutes. Water (10 ml) was then added dropwise, and the resulting solution was stirred for additional 30 minutes at rt. The major product was determined (based on *m/z*) to be the undesired amine **27a**.

LCMS (ESI$^+$) *m/z* 250.18 $[M+H]^+$.

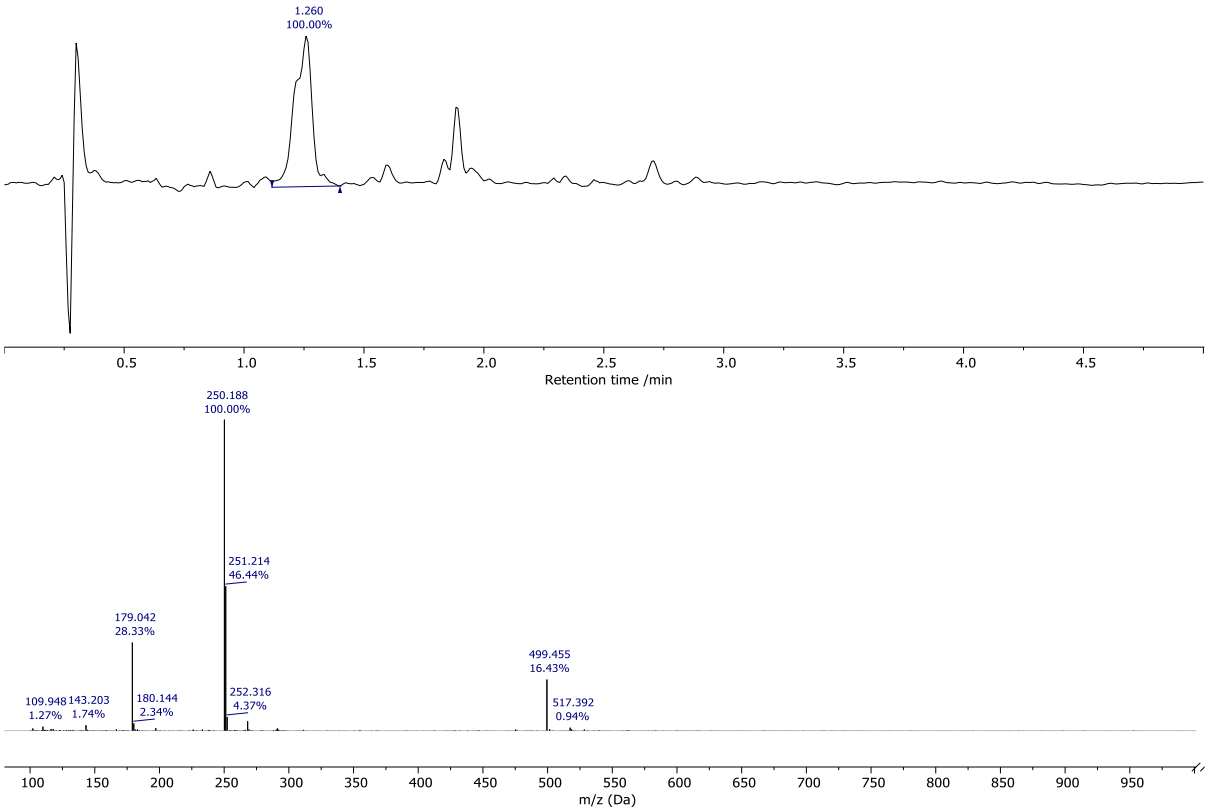

Figure 6.64: LCMS (Method E) of **27a** AC (210-400 nm) (top) and the MS (ESI$^+$) at 3.520 minutes (bottom).

4-(2,2-Dibromovinyl)-3,5-dimethoxyphenol, **28**

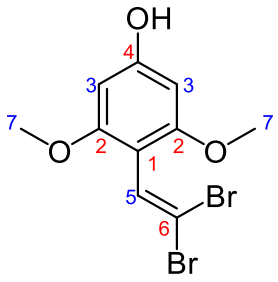

A solution of CBr_4 (2.46 g, 7.41 mmol, 1.5 eq.) in anhydrous DCM (30 ml) was dropwise added to an ice-cold solution of 4-hydroxy-2,6-dimethoxybenzaldehyde, **23** (900 mg, 4.94, 1 eq.) and PPh_3 (3.90 g, 14.82 mmol, 3 eq.) in anhydrous DCM (10 ml), and the resulting solution was stirred at rt for 20 hours under argon. After that, the solution was concentrated and the crude was purified by column chromatography (silica, from 2:3 to 1:3 hexane to DCM) to yield pale yellow solid (250 mg, 0.740 mmol, 15%).

HRMS (ESI$^+$) *m/z* 336.9081 $[M+H]^+$ ($C_{14}H_{18}N_3O_3Br_2$ requires 336.9075).

^{1}H NMR (400 MHz, $CDCl_3$) δ 7.16 (1H, s, H^5), 6.05 (2H, s, H^3), 3.78 (6H, S, H^7).

^{13}C NMR (100 MHz, $CDCl_3$) 158.18, 157.64, 130.82, 106.81, 92.87, 91.90, 55.70.

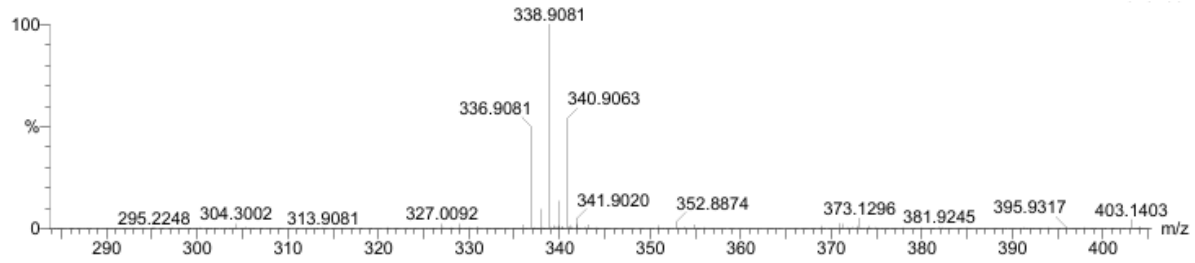

Figure 6.65: Accurate MS (ESI$^+$) of **28**.

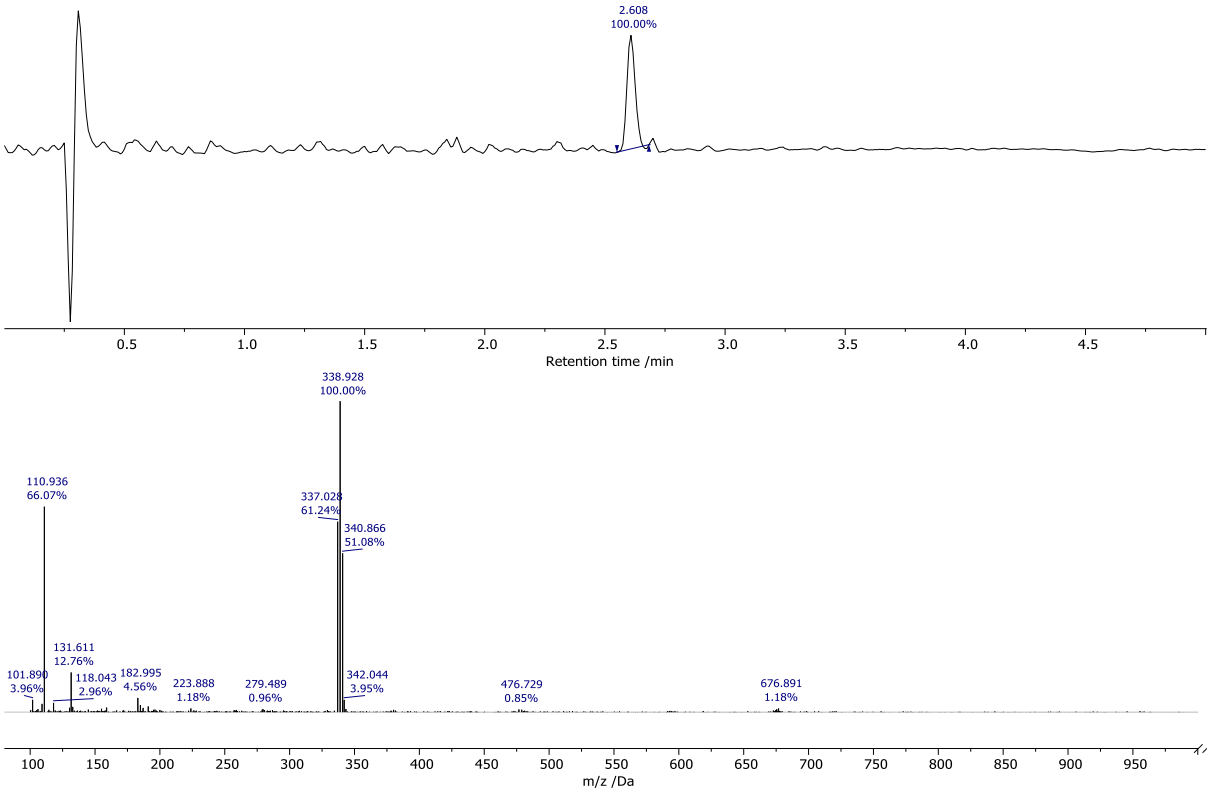

Figure 6.66: LCMS (Method E) of **28** AC (210-400 nm) (top) and the MS (ESI^+) at 2.608 minutes (bottom).

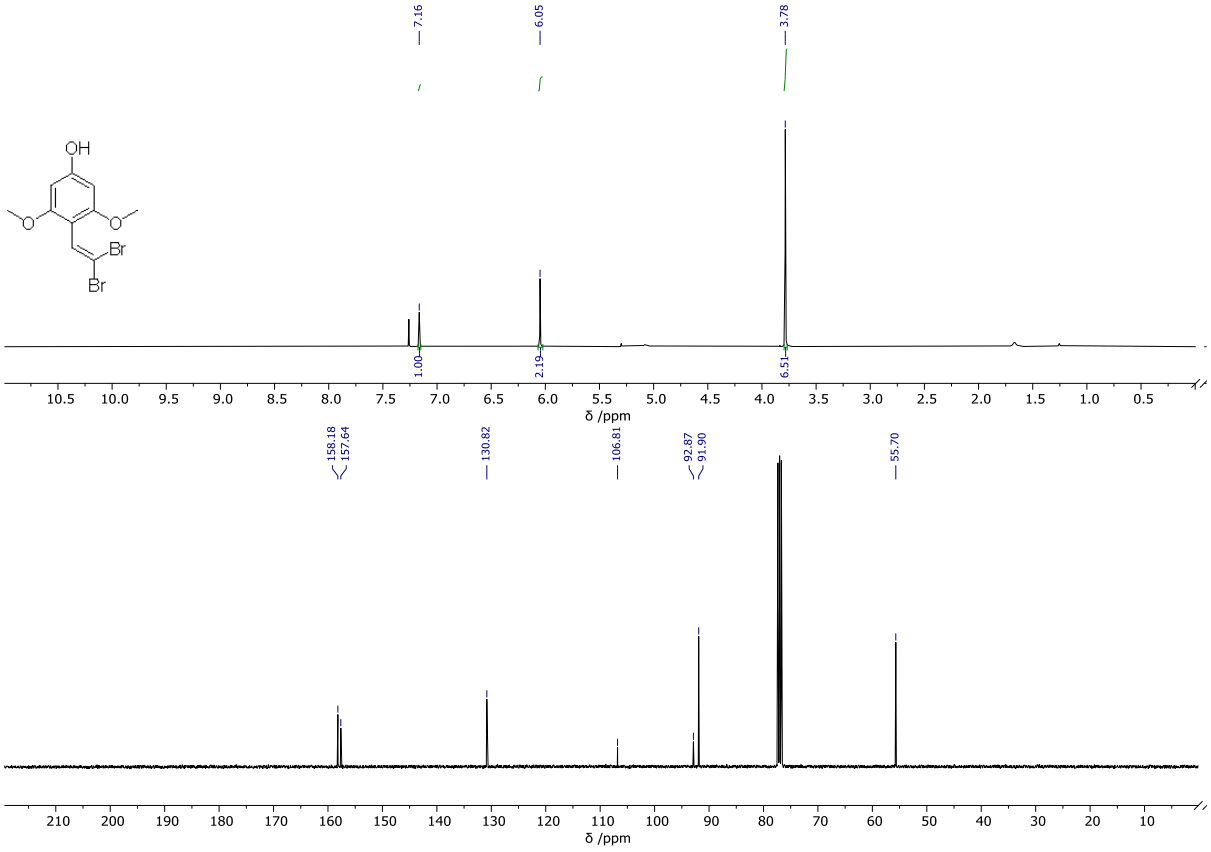

Figure 6.67: ^1H NMR (400 MHz, $CDCl_3$) (top) and ^{13}C NMR (100 MHz, $CDCl_3$) (bottom) spectra of **28**.

4-Ethynyl-3,5-dimethoxyphenol, **29**

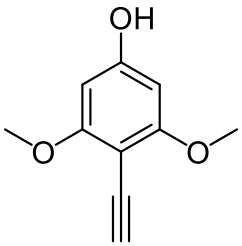

4-(2,2-dibromovinyl)-3,5-dimethoxyphenol, **28** (240 mg, 0.710 mmol, 1 eq.) was dissolved in anhydrous THF (10 ml) and cooled to -78 °C (acetone, dry ice). 2.5 M solution of n-butyllithium in hexane (1.15 ml, 2.84 mmol, 4 eq.) was then added dropwise, and the resulting orange solution was stirred at -78°C for 20 minutes under argon. Water (20 ml) was then added dropwise, and the resulting solution was stirred at rt for further 20 min. After that, the organic solvents were removed under the reduced pressure, and the crude was recrystallised from MeOH to give orange solid which was used in the next step without further purification.

HRMS (ESI$^+$) 179.0721 $[M+H]^+$ ($C_{10}H_{11}O_3$ requires 179.0708)

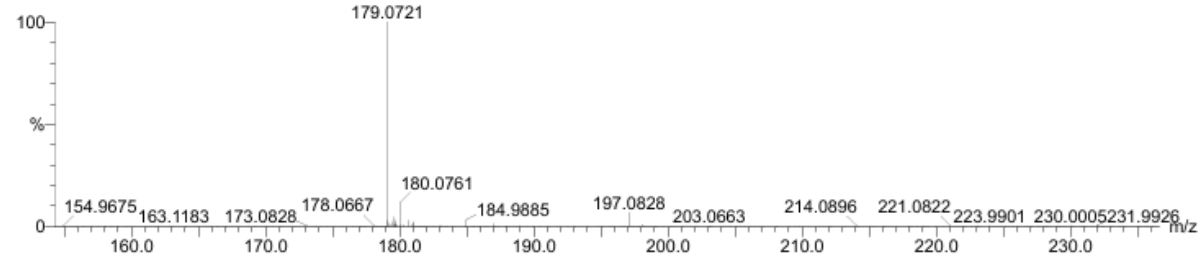

Figure 6.68: Accurate MS (ESI$^+$) of **29**.

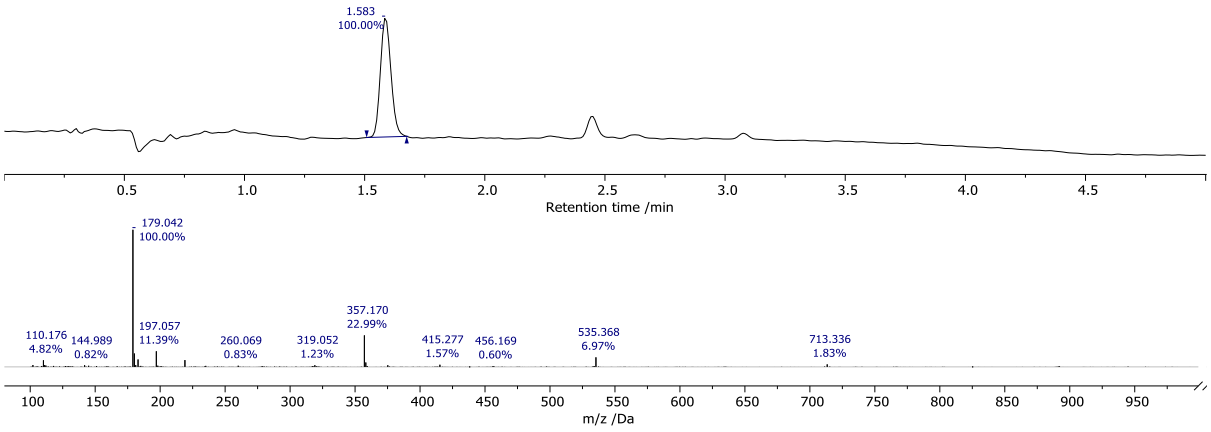

Figure 6.69: LCMS (Method E) of **29** AC (210-400 nm) (top) and the MS (ESI$^+$) at 1.583 minutes (bottom).

5-(4-Bromobutoxy)-2-ethynyl-1,3-dimethoxybenzene, **30**

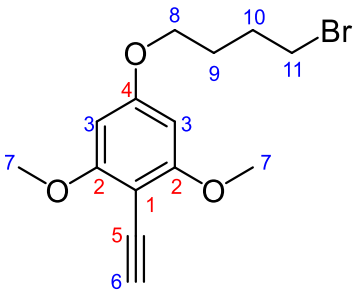

A solution of 4-ethynyl-3,5-dimethoxyphenol, **29** (*0.710 mmol, 1 eq.*) in DMF (5 ml) was dropwise added over 1 hour to a solution of 1,4-dibromobutane (3 ml, 25.0 mmol, 35 eq.) and K_2CO_3 (143 mg, 1.04 mmol, 1.5 eq.) in DMF (5 ml) stirring at 70°C. Once the addition was completed, the resulting solution was stirred for additional 10 minutes before DMF solvent was removed under reduced pressure. The crude product was purified by flash chromatography (silica, 3:7 EtOAc - hexane) to yield pale yellow solid (142 mg, 0.453 mmol, 64% over two steps).

HRMS (ESI$^+$) *m/z* 313.04340 [M+H]+ ($C_{14}H_{17}BrO_3$ requires 313.04338).

^{1}H NMR (400 MHz, $CDCl_3$) δ 6.09 (2H, s, H^3), 4.02 (2H, t, $^3J_{H\text{-}H}$ 6.1, H^8), 3.87 (6H, s, H^7), 3.49 (3H, t, $^3J_{H\text{-}H}$ 6.5, H^{11}), 3.49(1H, s, H^6) 2.07 (2H, m, H^9), 1.96 (2H, m, H^{10}).

^{13}C NMR (100 MHz, $CDCl_3$) δ 163.02, 161.22, 93.14, 90.84, 83.81, 67.06, 56.11, 33.31, 29.37, 27.79.

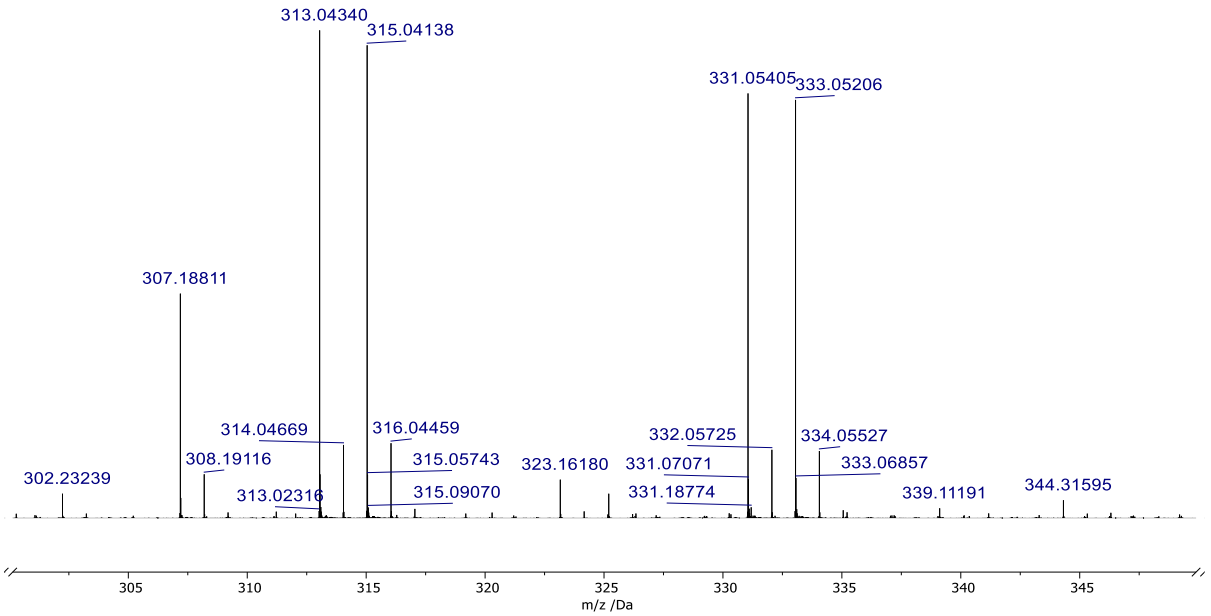

Figure 6.70: Accurate MS (ESI$^+$) of **30**.

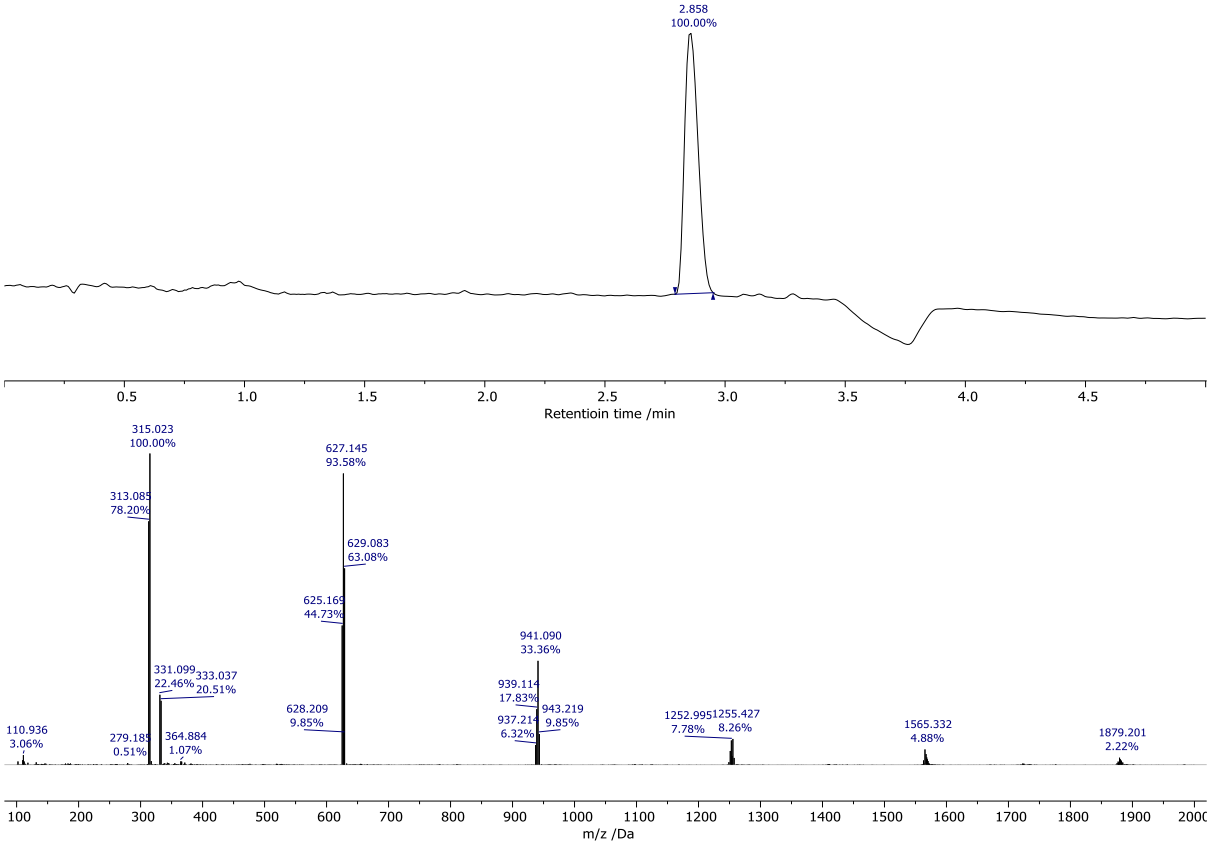

Figure 6.71: LCMS (Method E) of **29** AC (210-400 nm) (top) and the MS (ESI^+) at 2.858 minutes (bottom).

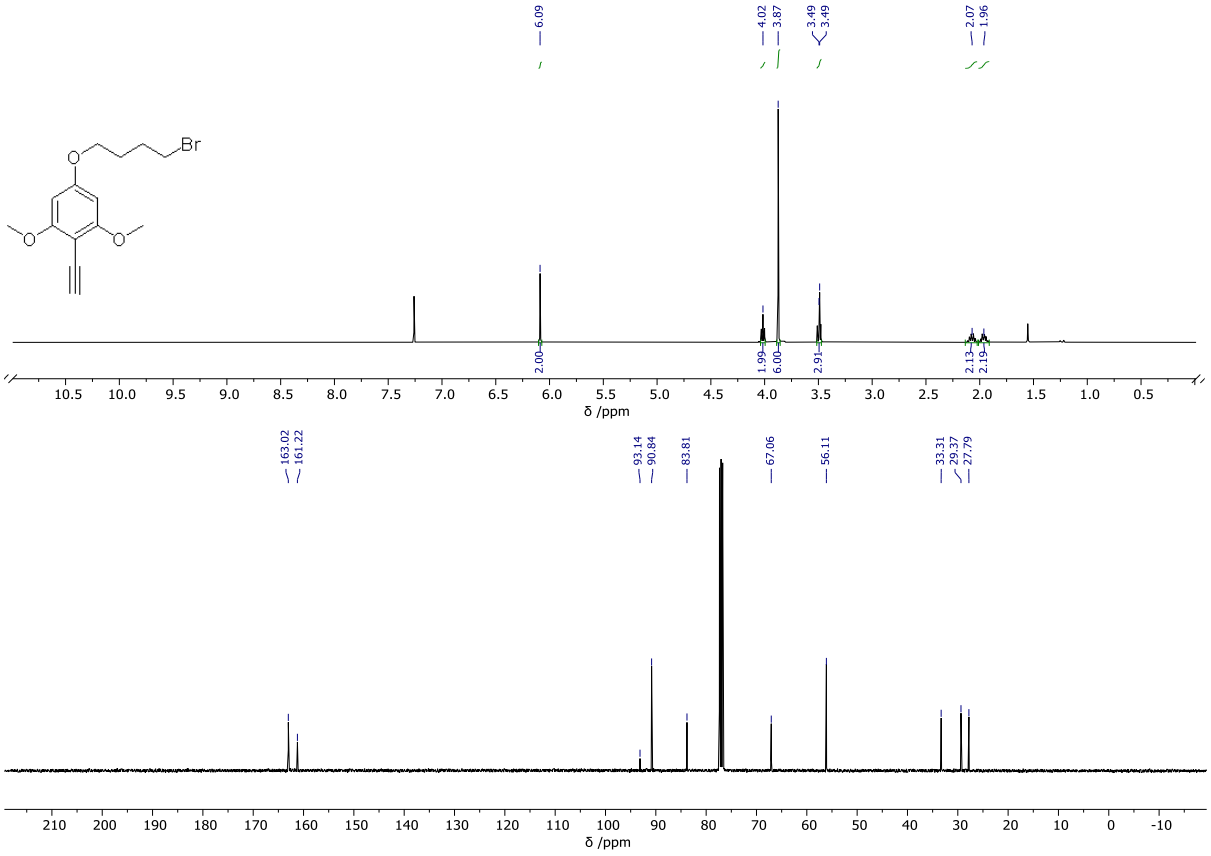

Figure 6.72: ^1H NMR (400 MHz, $CDCl_3$) (top) and ^{13}C NMR (100 MHz, $CDCl_3$) (bottom) spectra of **29**.

5-(4-Azidobutoxy)-2-ethynyl-1,3-dimethoxybenzene, **27**

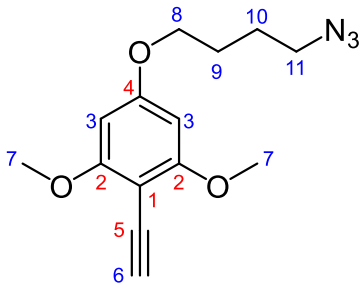

5-(4-bromobutoxy)-2-ethynyl-1,3-dimethoxybenzene, **30** (122 mg, 0.390 mmol, 1 eq.), sodium azide (100 mg, 1.54 mmol, 4 eq.) and sodium iodide (58 mg, 0.39, 1 eq.) were dissolved in DMF (10 ml) and stirred for 20 hours at rt. The resulting mixture was then isolated from DMF solvent under reduced pressure and redissolved in DCM (50 ml). The resulting solution was washed with water (20 ml × 3), and the combined aqueous fractions were extracted with DCM. The combined organic fractions were dried over $MgSO_4$ and filtered. The product was isolated from DCM solvent under reduced pressure to give pale-yellow solid (98 mg, 0.356 mmol, 91%).

HRMS (ESI$^+$) *m/z* 276.1345 $[M+H]^+$ ($C_{14}H_{18}N_3O_3$ requires 276.1348).

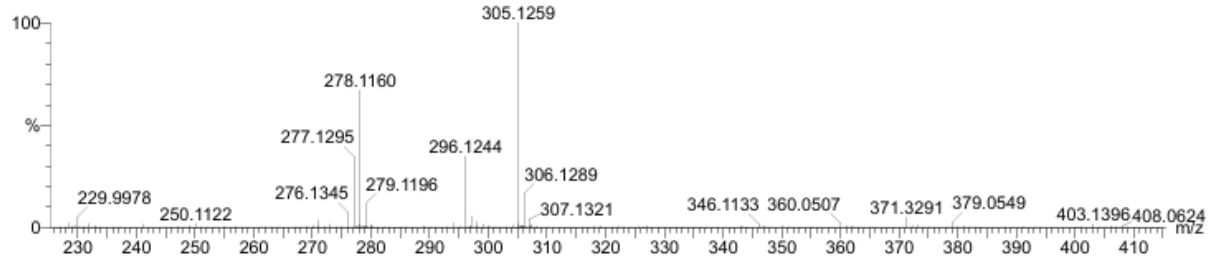

Figure 6.73: Accurate MS (ESI$^+$) of **27**.

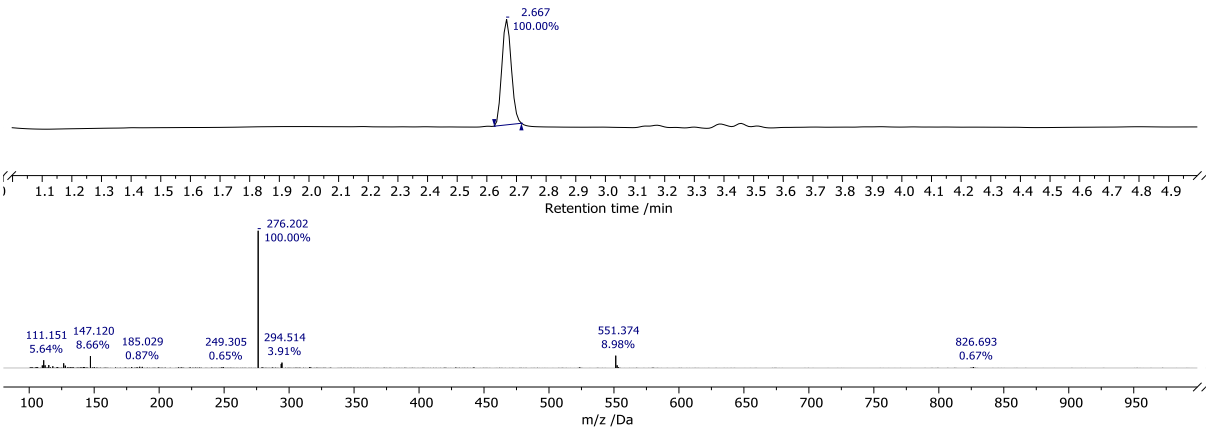

Figure 6.74: LCMS (Method E) of **27** AC (210-400 nm) (top) and the MS (ESI$^+$) at 2.667 minutes (bottom).

Ethyl 4-((4-(4-azidobutoxy)-2,6-dimethoxyphenyl)ethynyl)-6-(hydroxymethyl)picolinate, **31**

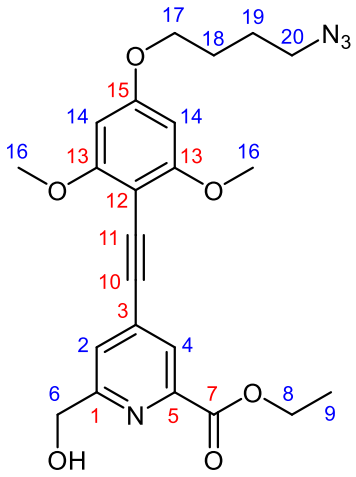

5-(4-azidobutoxy)-2-ethynyl-1,3-dimethoxybenzene, **27** (75 mg, 0.272 mmol, 1 eq.) ethyl 4-bromo-6-(hydroxymethyl)picolinate, **13** (73 mg, 0.281 mmol, 1.03 eq.) and $[Pd(allyl)Cl]_2$ (10 mg, 0.027 mmol, 0.1 eq.) were dissolved in anhydrous acetonitrile (2 ml) and degassed (freeze-pump-thaw × 3). After that, TEA (0.380 ml, 2.70 mmol, 10 eq.) and piperidine (0.105 ml, 1.09 mmol, 4 eq.) were added, and the resulting solution was stirred at 40°C for 20 h under argon. Organic solvents were then removed under reduced pressure, and the resulting yellow solid was purified by column chromatography (silica, 3% MeOH in DCM) to yield yellow solid (56 mg, 0.123 mmol, 45%).

HRMS (ESI$^+$) *m/z* 455.1914 $[M+H]^+$ ($C_{14}H_{17}BrO_3$ requires 455.1931).

^{1}H NMR (700 MHz, $CDCl_3$) δ 8.11 (1H, s, H^4), 7.57 (1H, s, H^2), 6.11 (2H, s, H^{14}), 4.83 (2H, s, H^6), 4.47 (2H, q, $^3J_{H\text{-}H}$ 7.2 H^8), 4.04 (2H, t, $^3J_{H\text{-}H}$ 6.0, H^{17}), 3.90 (6H, s, H^{16}), 3.39 (2H, t, $^3J_{H\text{-}H}$ 7.0, H^{20}), 1.90 (2H, m, H^{18}), 1.82 (2H, m, H^{19}), 1.44 (3H, t, $^3J_{H\text{-}H}$ 7.3, H^9)

^{13}C NMR (151 MHz, $CDCl_3$) δ 164.94 (C^7), 162.99 (C^{13}), 162.33 (C^{15}), 159.91 (C^1), 147.24 (C^5), 134.74 (C^3), 125.84 (C^4), 125.30 (C^2), 93.35 (C^{10}), 93.27 (C^{12}), 91.03 (C^{14}), 89.59 (C^{11}), 67.61 (C^{17}), 64.46 (C^6), 62.15 (C^8), 56.26 (C^{16}), 51.25 (C^{20}), 26.55 (C^{18}), 25.84 (C^{19}), 14.45 (C^9).

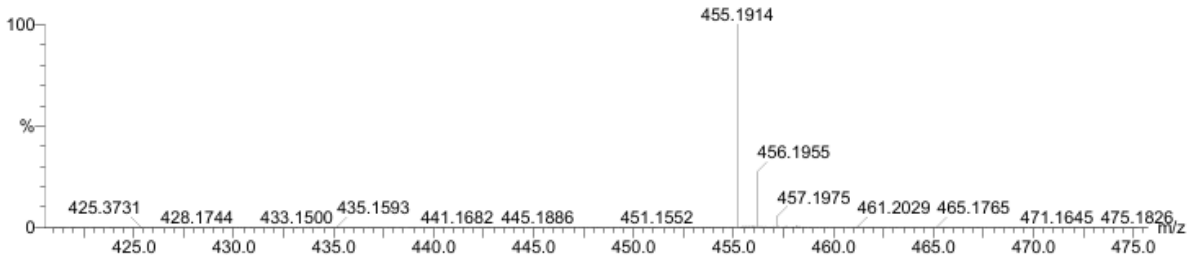

Figure 6.75: Accurate MS (ESI$^+$) of **31**.

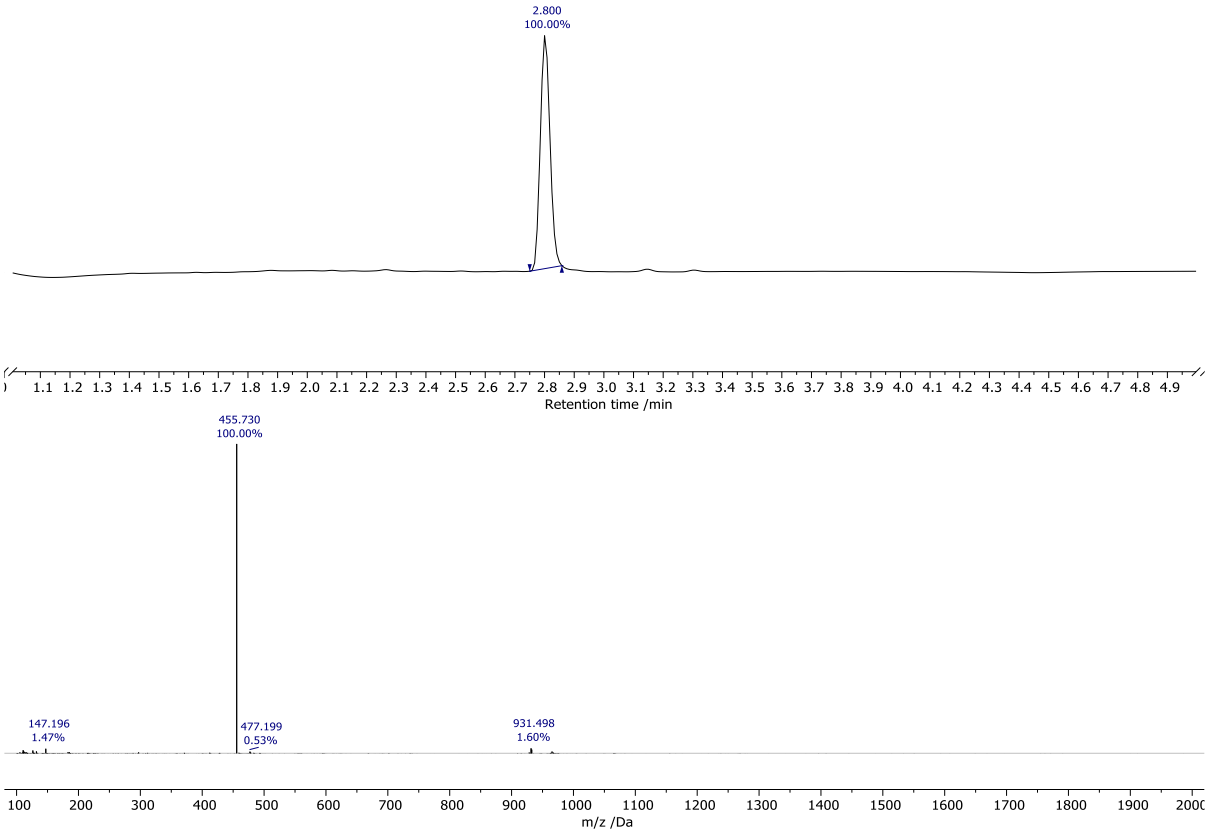

Figure 6.76: LCMS (Method E) of **31** AC (210-400 nm) (top) and the MS (ESI$^+$) at 2.800 minutes (bottom).

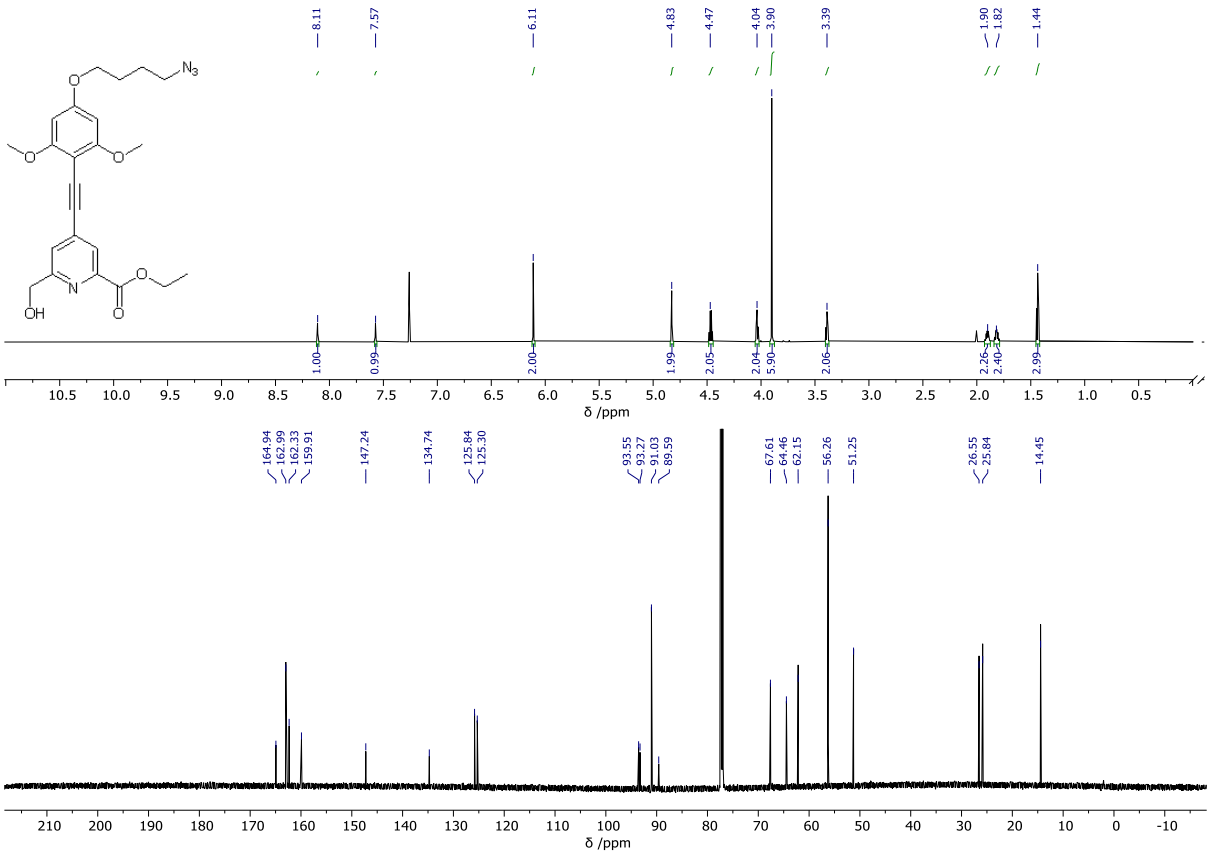

Figure 6.77: ^{1}H NMR (700 MHz, $CDCl_3$) (top) and ^{13}C NMR (151 MHz, $CDCl_3$) (bottom) spectra of **31**.

Ethyl 4-((4-(4-azidobutoxy)-2,6-dimethoxyphenyl)ethynyl)-6-(((methylsulfonyl)oxy)methyl)picolinate, **32**

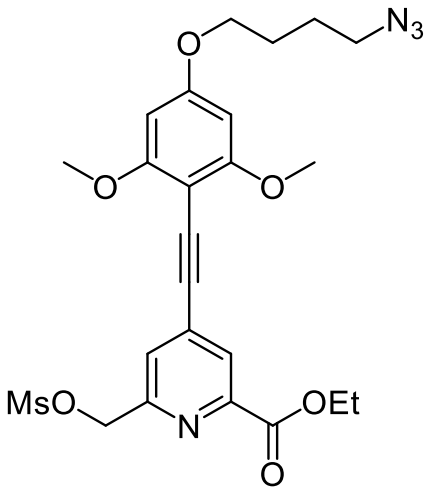

Ethyl 4-((4-(4-azidobutoxy)-2,6-dimethoxyphenyl)ethynyl)-6-(hydroxymethyl)picolinate, **31** (32 mg, 0.071 mmol, 1 eq.) and methanesulfonic anhydride (44 mg, 0.25 mmol, 3.5 eq.) were dissolved in anhydrous THF (7 ml) and DIPEA (37 µl, 0.212 mmol, 3 eq.) was added. The resulting solution was stirred at rt for 1 hour under argon. After that, volatile organic materials were evaporated under reduced pressure, and the obtained yellow oil was redissolved in DCM (10 ml). The resulting solution was washed with water (10 ml × 3), and the combined aqueous layers were extracted with DCM (5 ml × 3). The combined organic layers were dried over $MgSO_4$ and filtered. DCM solvent was evaporated under reduced pressure to yield pale yellow solid that was used in the next step without further purification.

HRMS(ESI$^+$) *m/z* 533.16950 $[M+H]^+$ ($C_{24}H_{28}N_4O_8S$ requires 533.17006)

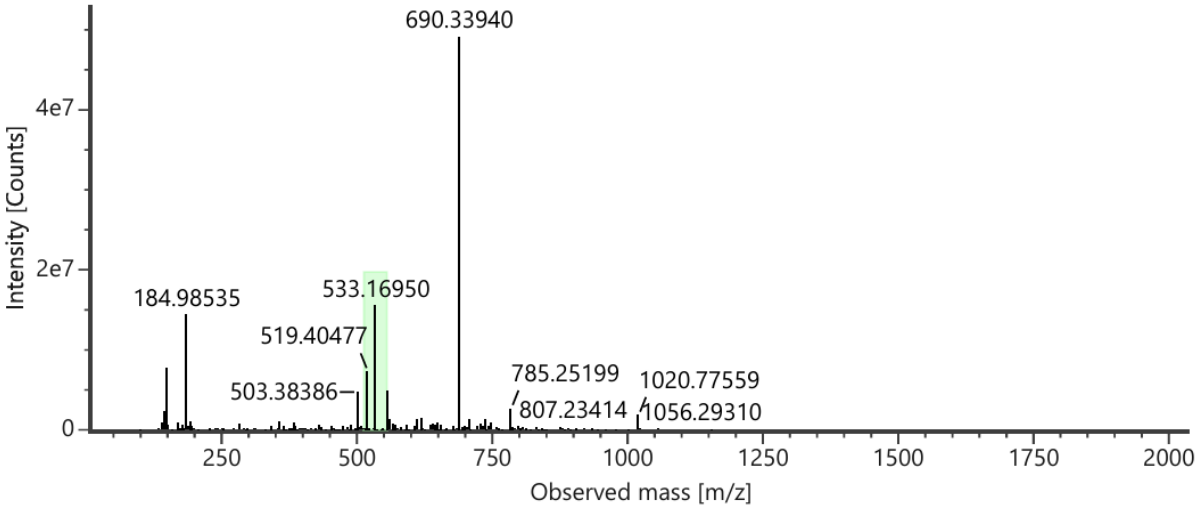

Figure 6.78: Accurate MS (ESI$^+$) of **23**.

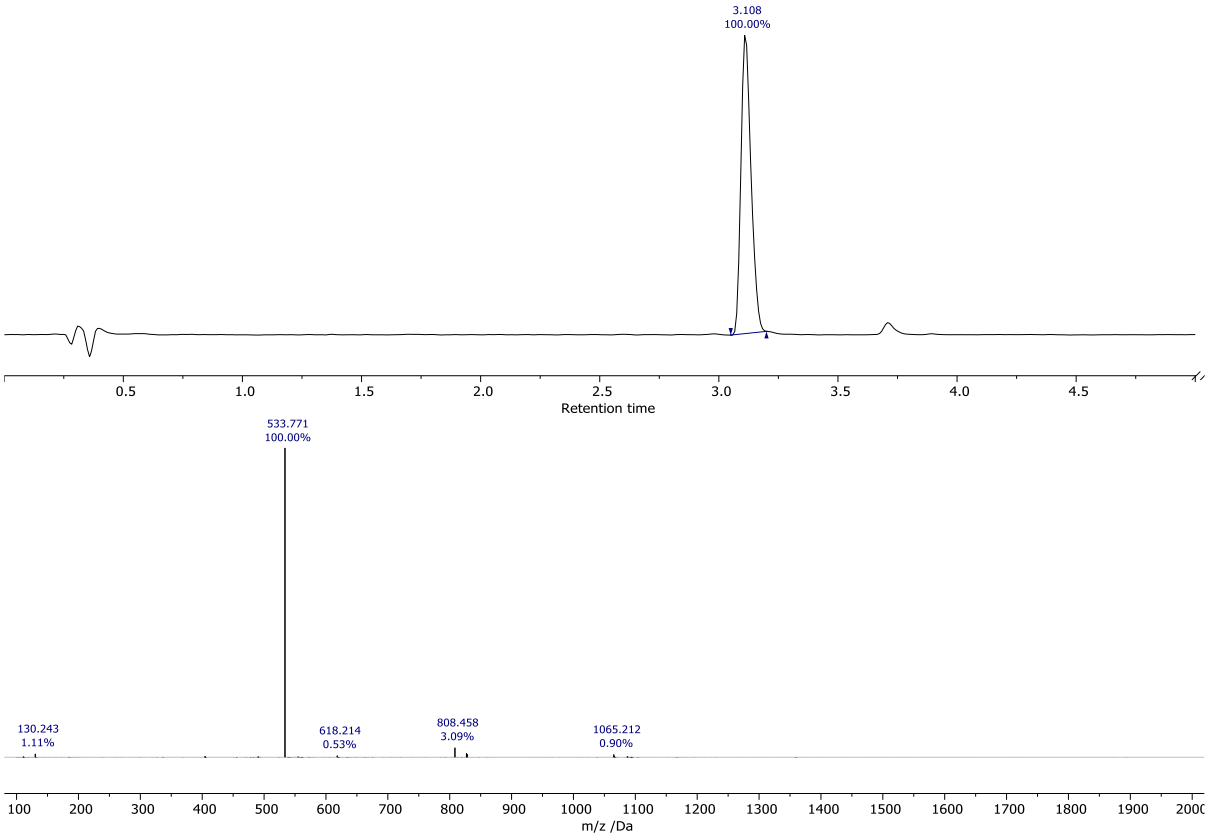

Figure 6.79: LCMS (Method E) of **31** AC (210-400 nm) (top) and the MS (ESI^+) at 3.108 minutes (bottom).

Triethyl 6,6',6''-((1,4,7-triazonane-1,4,7-triyl)tris(methylene))tris(4-((4-(4-azidobutoxy)-2,6-dimethoxyphenyl)ethynyl)picolinate), **33**

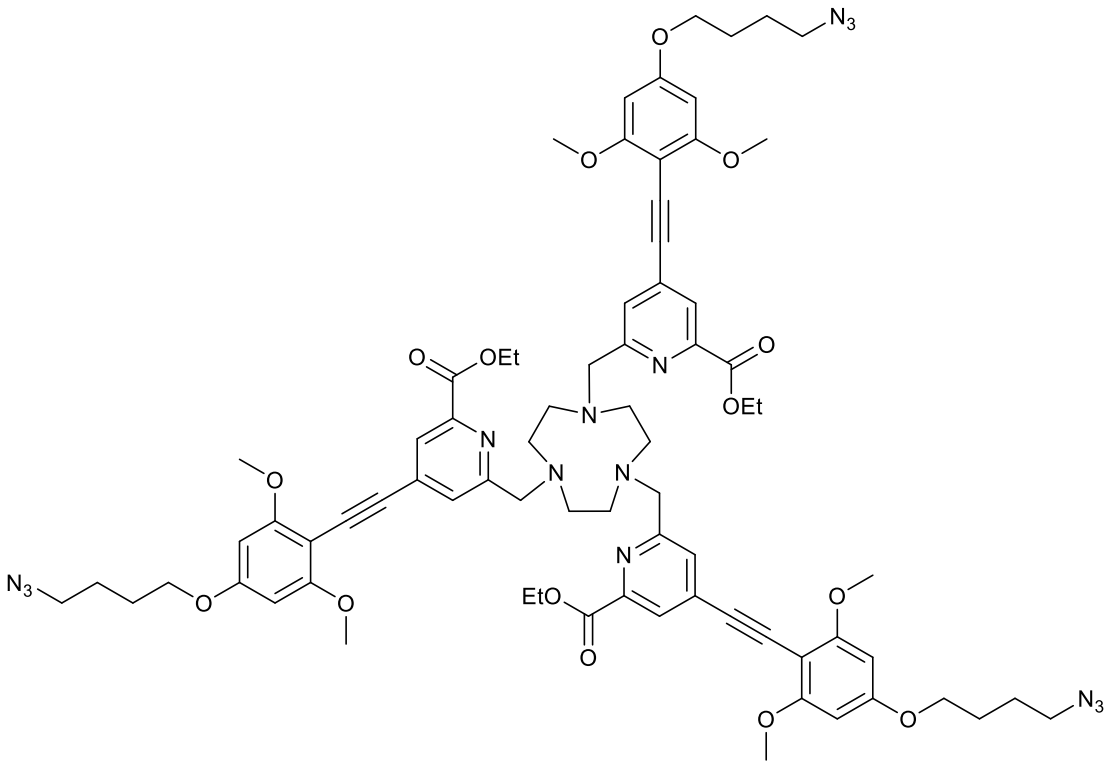

K_2CO_3 (68 mg, 0.49 mmol, 7 eq.), ethyl4-((4-(4-azidobutoxy)-2,6-dimethoxyphenyl)ethynyl)-6 (((methylsulfonyl)oxy)methyl)picolinate, **32** (*0.071 mmol,* 3.5 eq.) and TACN.3HCl (4.8 mg, 0.020 mmol, 1 eq.) were dissolved in MeCN (5 ml) and stirred at 60°C for 12 h under argon. After that, MeCN was removed under reduced pressure, and the crude was redissolved in MeOH and used in the next step without further purification.

HRMS (ESI$^+$) *m/z* 1438.6527 $[M+H]^+$ ($C_{75}H_{87}N_{15}O_{15}$ requires 1438.6584).

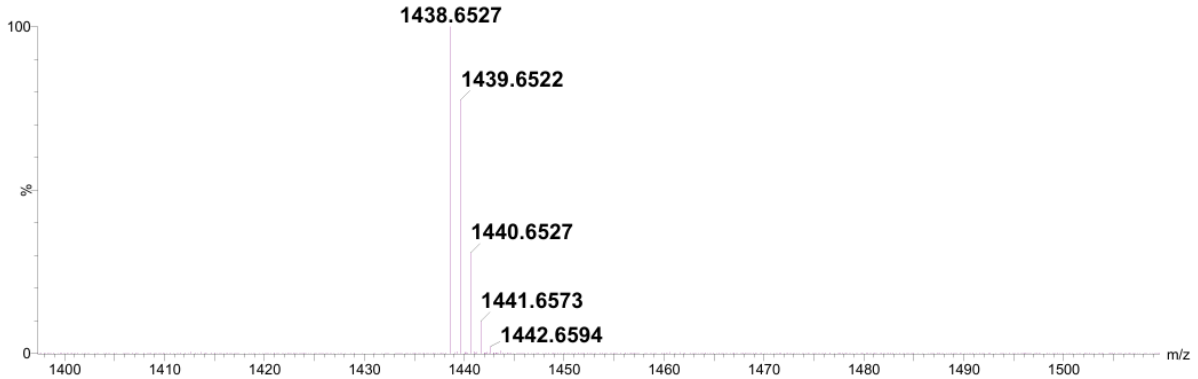

Figure 6.80: Accurate MS (ESI$^+$) of **23**.

EuL^3

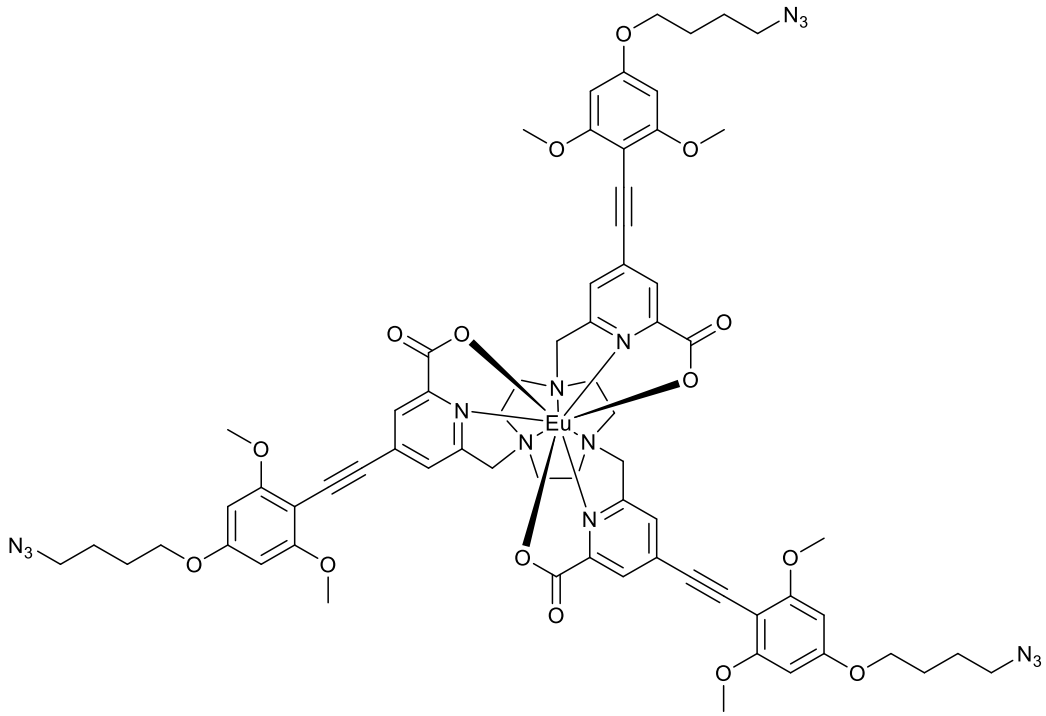

Triethyl 6,6',6''-((1,4,7-triazonane-1,4,7-triyl)tris(methylene)) tris(4-((4-(4-azidobutoxy)-2,6-dimethoxyphenyl)ethynyl)picolinate), **33** (*0.020 mmol*) was dissolved in MeOH (5 ml) and water was dropwise added until the precipitate remained undissolved. The pH of the resulting solution was adjusted to 12.5 using 1M NaOH. The solution was stirred at 60 °C for 3 hours while its pH was periodically adjusted to 12.5 until hydrolysis completion was confirmed by LCMS. After that, the solution pH was readjusted to 6.5 using 1 M HCl, and $EuCl_3.6HCl$ was added (7.5 mg, 0.020 mmol, 1 eq.). The resulting solution was stirred at rt for 20 hours. After that, the solvent was removed under pressure to yield yellow solid which was purified by reverse-phase HPLC (C_{18}, Method B, retention time = 14.3 minutes) to yield yellow solid (6.8 mg, 0.0045 mmol, 23% over two steps).

HRMS (ESI$^+$) 1502.4485 [M+H$^+$] ($C_{69}H_{72}{}^{151}EuN_{15}O_{15}$ requires 1502.4609)

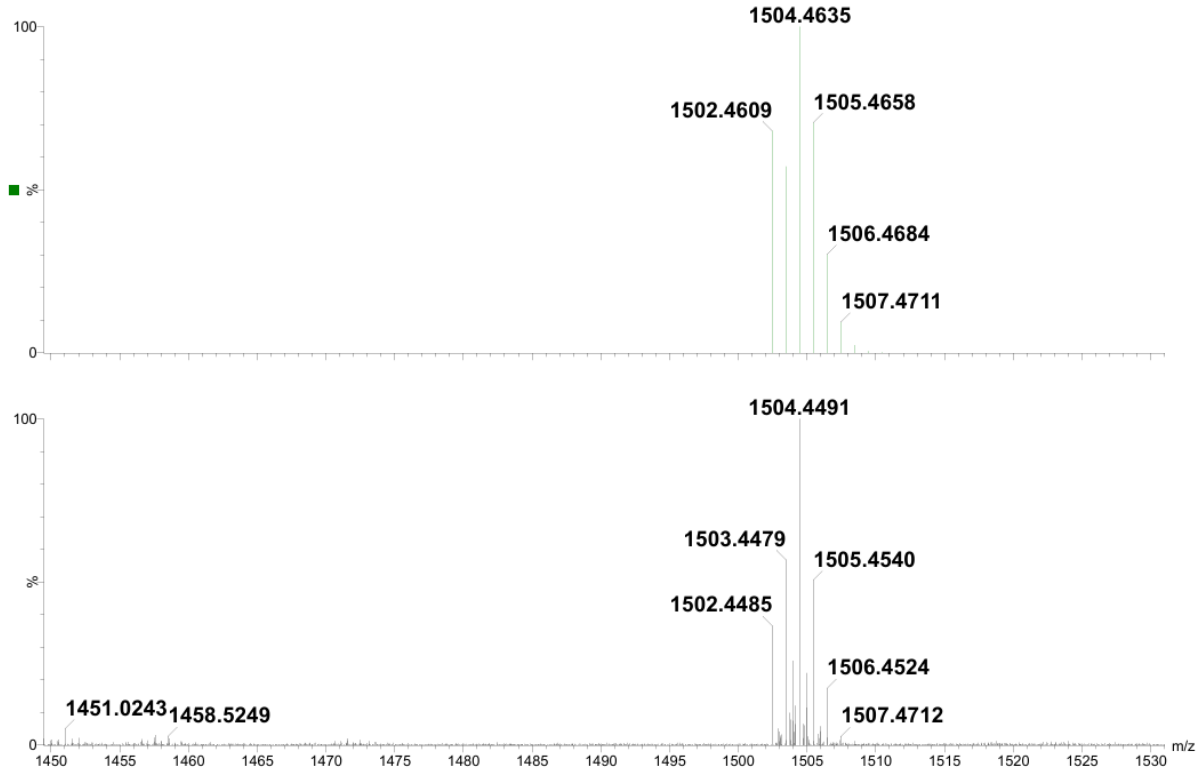

Figure 6.81: Simulated (top) and recorded (bottom) accurate MS (ESI⁺) of **EuL³**.

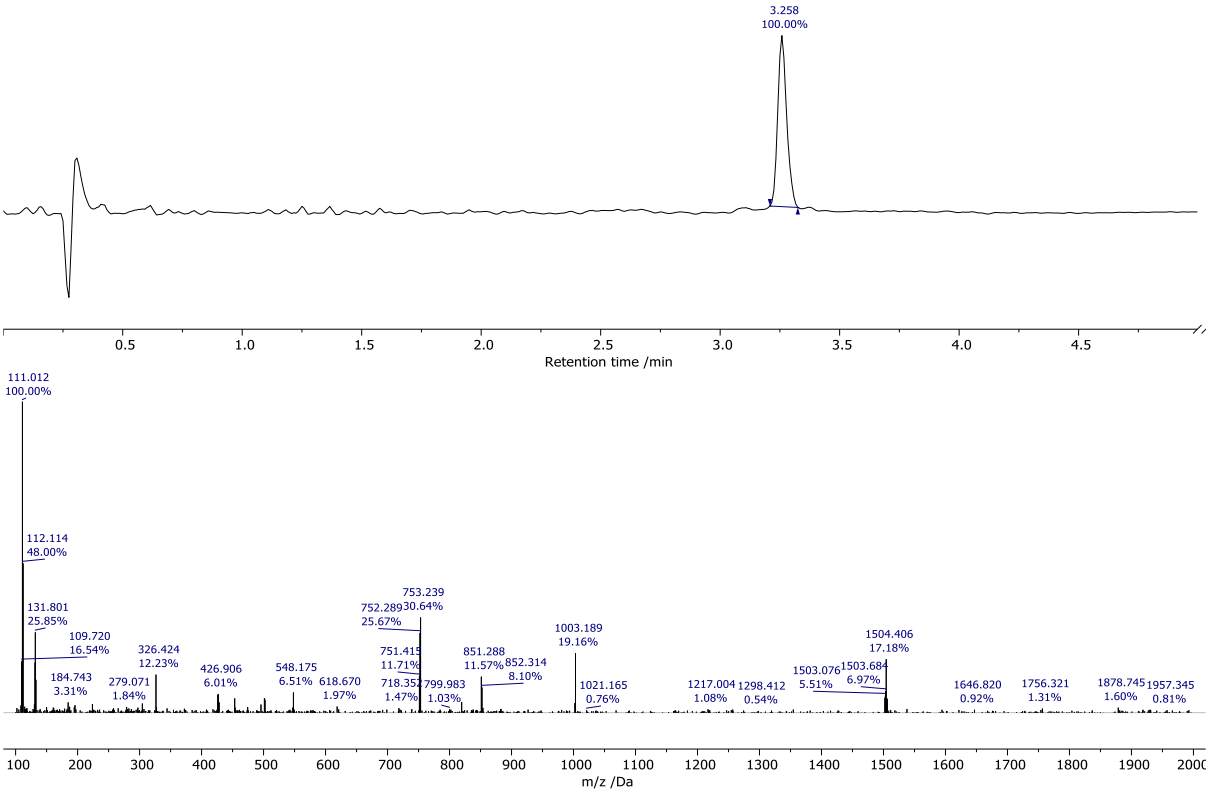

Figure 6.82: LCMS (Method E) of **EuL³** AC (210-400 nm) (top) and the MS (ESI⁺) at 3.258 minutes (bottom).

EuL^{3gAc}

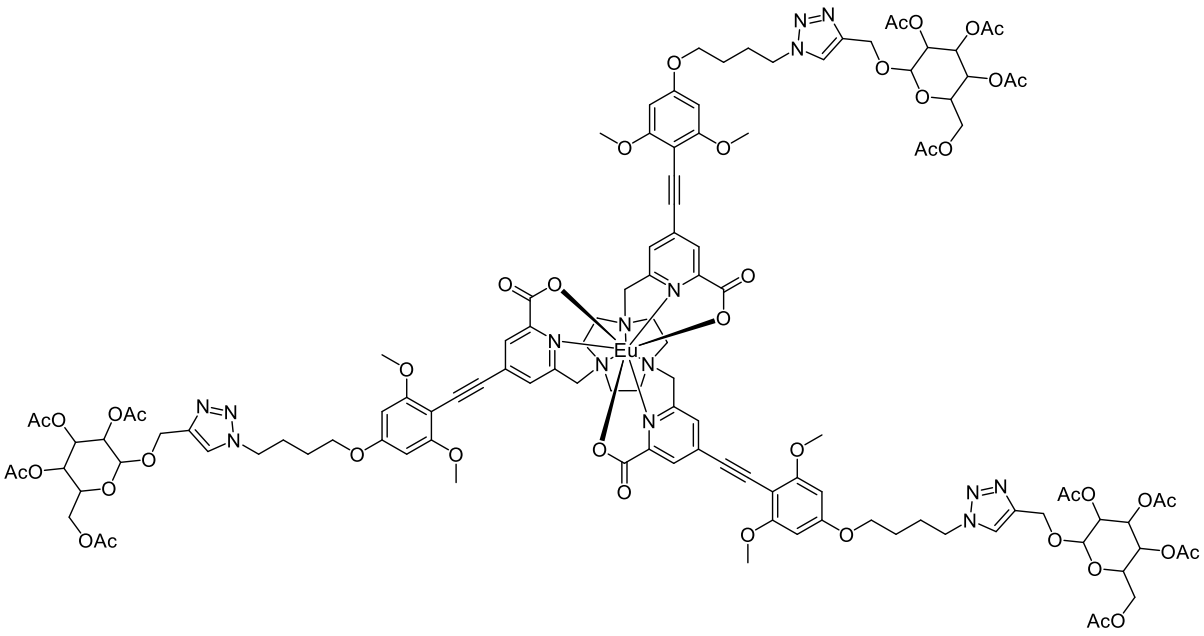

To a solution of 2-propynyl-tetra-O-acetyl-β-D-glucopyranoside (2.0 mg, 0.0052 mmol, 4 eq.) and **EuL^{3}** (2.0 mg, 0.0013 mmol, 1 eq.) in MeCN (5 ml) was added $[Cu(MeCN)_4]PF_6$ (1.0 mg, 0.0027 mmol, 2 eq.). The resulting solution was stirred at rt for 20 hours under argon. After that, water was added (5 ml), and the reaction mixture was stirred for further 30 minutes. MeCN was then evaporated and the resulting suspension was centrifuged (6000 rpm). Once water was removed, the residue was resuspended in MeOH and centrifuged again. The resulting product solution was separated from the grey residue, and MeOH was then removed under reduced pressure to yield yellow solid (3.2 mg, 0.0012 mmol, 92%).

HRMS (ESI$^+$) 1330.91394 $[M+2H]^{2+}$ ($C_{120}H_{140}{}^{151}EuN_{15}O_{45}$ requires 1330.91576)

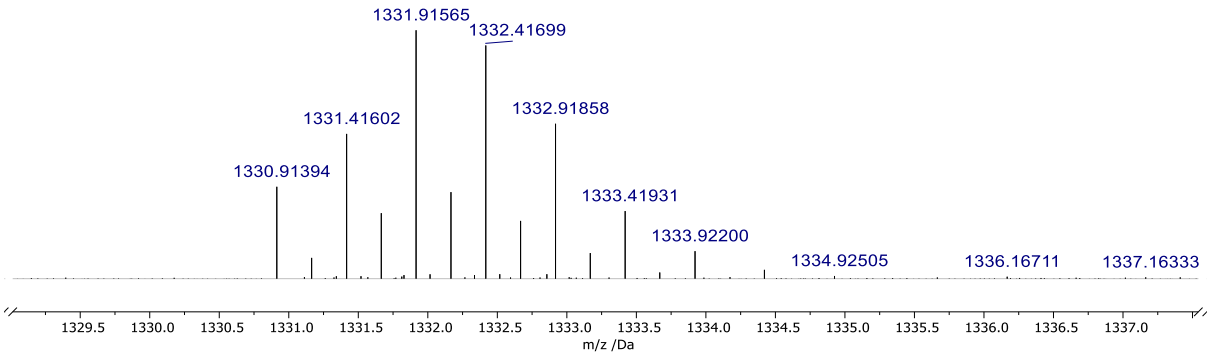

Figure 6.83: Accurate MS (ESI$^+$) of **EuL^{3gAc}** ([M+2H]$^{2+}$, *m*/2).

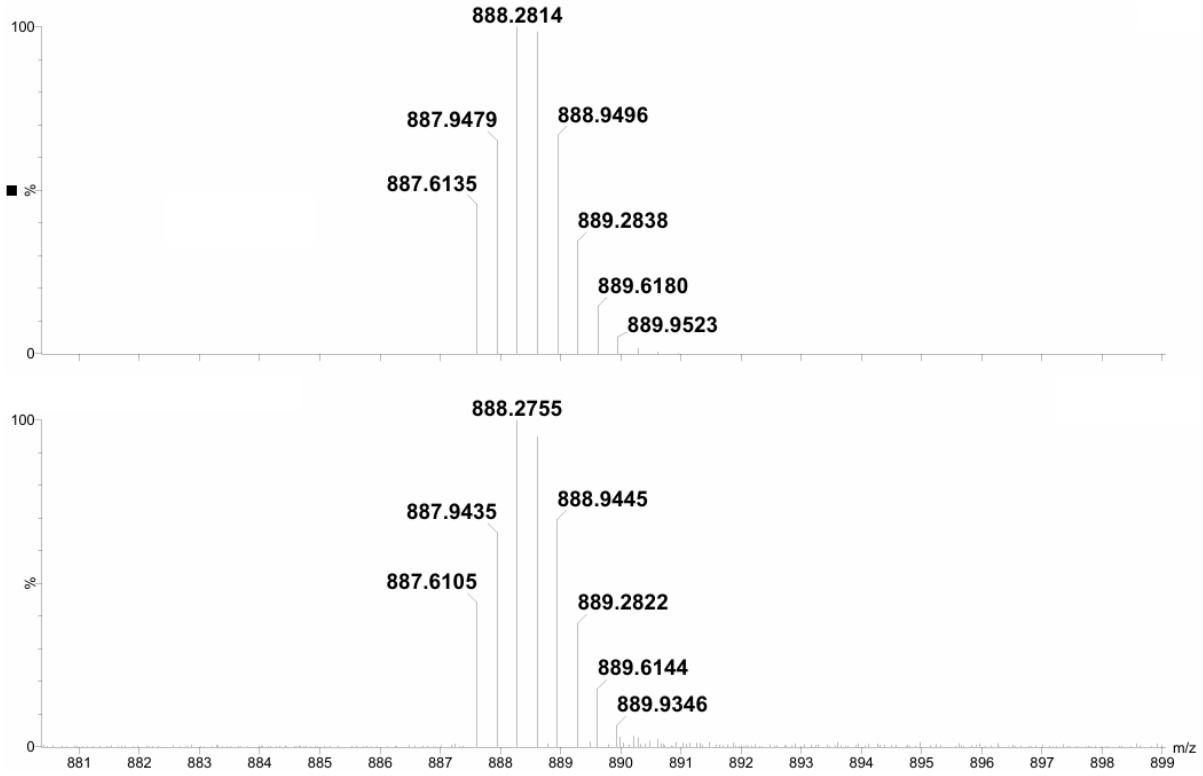

Figure 6.84: Simulated (top) and recorded (bottom) accurate MS (ESI$^+$) of **EuL^{3gAc}** ([M+3H]$^{3+}$, *m*/3)

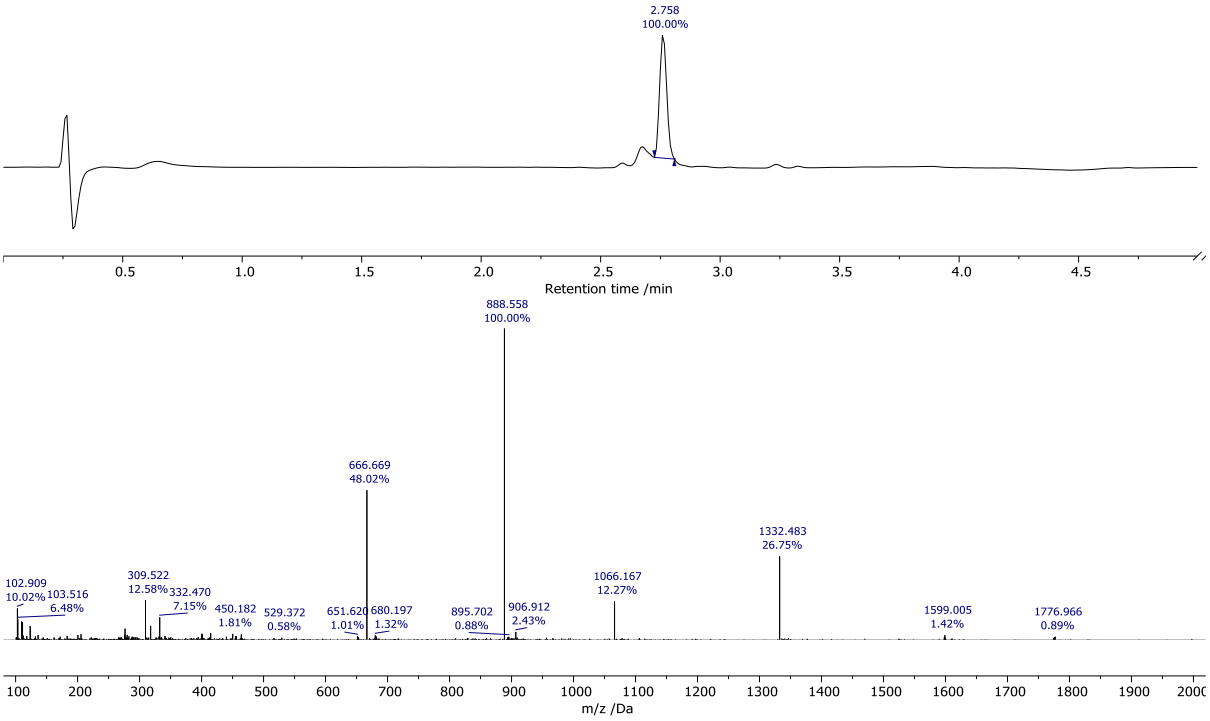

Figure 6.85: LCMS (Method E) of **EuL^{3gAc}** AC (210-400 nm) (top) and the MS (ESI$^+$) at 2.758 minutes (bottom).

1-Propargyl-β-D-glucopyranoside, **34**

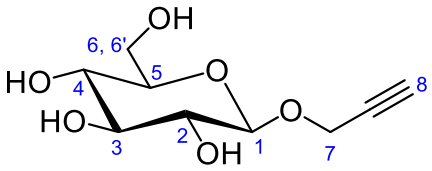

2-propynyl-tetra-O-acetyl-β-D-glucopyranoside (50 mg, 0.055 mmol) was added to a 0.1 M solution of NaOMe in MeOH (3 ml) and stirred at rt for 1 hr. After that, the reaction mixture was neutralised using *Amberlite* H^+ resin and filtered. MeOH was then removed under reduced pressure to yield white solid (12 mg, 0.054 mmol, 98%).

^{1}H NMR (400 MHz, MeOD) 4.50 (1H, d,$^3J_{H\text{-}H}$ 7.9, H^1), 4.46 (2H, t, $^3J_{H\text{-}H}$ 2.8, H^7), 3.92 (1H, d, $^2J_{H\text{-}H}$ 12.2, H^6), 3.71 (1H, dd, $^3J_{H\text{-}H}$ 12.2, $^3J_{H\text{-}H}$ 5.7, $H^{6'}$), 3.40 (1H, t, $^3J_{H\text{-}H}$ 8.4, H^3), 3.32 (1H, m, H^4), 3.31 (1H, m, H^5), 3.23 (1H, t, $^3J_{H\text{-}H}$ 7.5, H^2), 2.90(1H, t, $^4J_{H\text{-}H}$ 2.4, H^8).

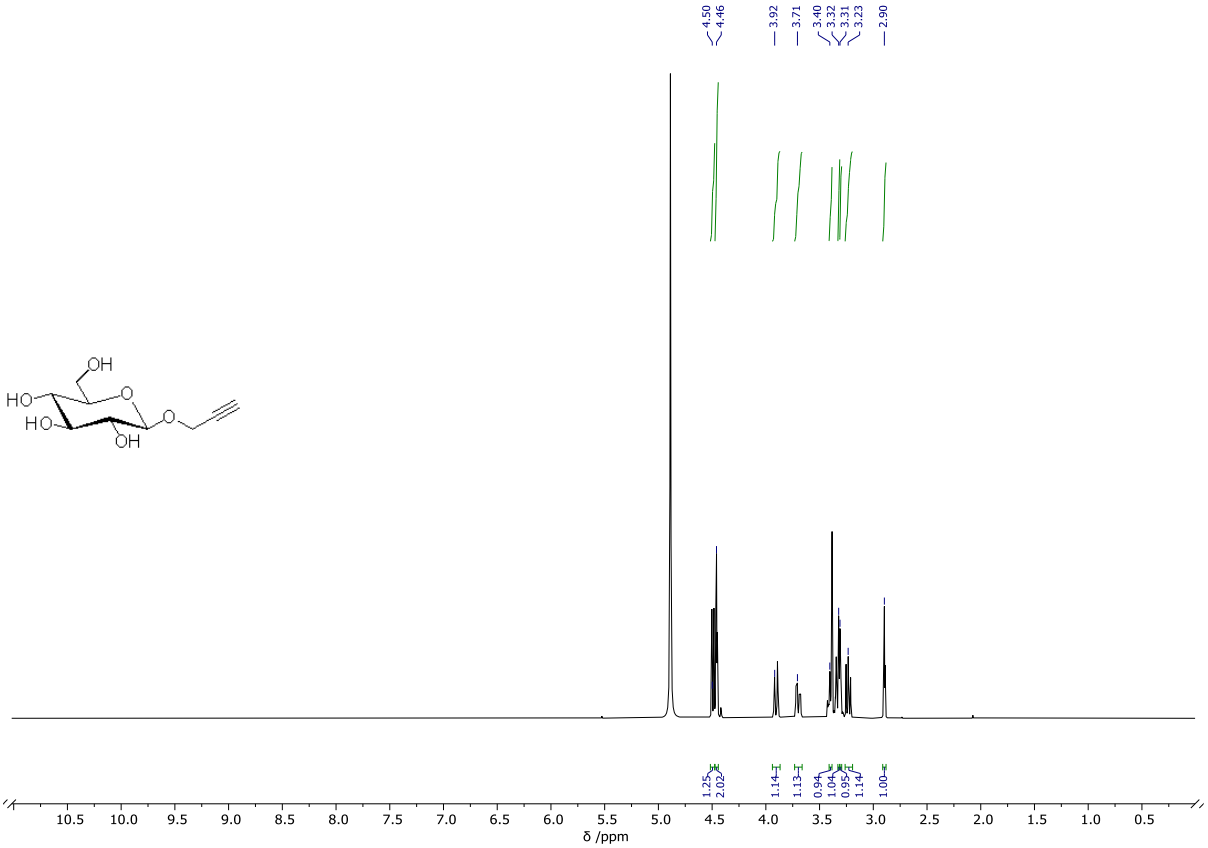

Figure 6.86: ^{1}H NMR (400 MHz, $CDCl_3$) spectrum of **34**.

EuL^{3g}

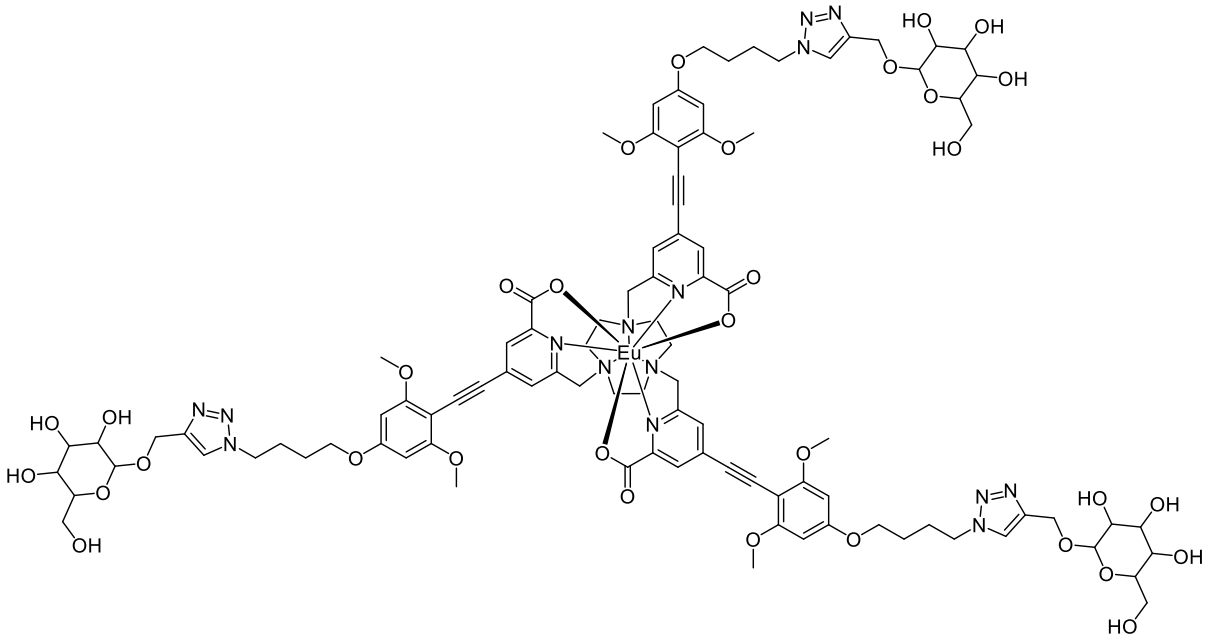

To a solution of 1-propargyl-β-D-glucopyranoside, **34** (12 mg, 0.0054 mmol, 4.2 eq.) and **EuL^3** (2.0 mg, 0.0013 mmol, 1 eq.) in MeCN (5 ml) was added $[Cu(MeCN)_4]PF_6$ (1.0 mg, 0.0027 mmol, 2 eq.). The resulting solution was stirred at rt for 20 hours under argon. After that, water was added (5 ml), and the reaction mixture was stirred for further 30 minutes. MeCN was then evaporated and the resulting suspension was centrifuged (6000 rpm). Once water was removed, the residue was resuspended in MeOH and centrifuged again. The resulting product solution was then separated from the grey residue, and MeOH was removed under reduced pressure to yield yellow solid (2.6 mg, 0.0012 mmol, 92%).

HRMS (ESI$^+$) 1078.8431 $[M+2H]^{2+}$ ($C_{96}H_{114}{}^{151}EuN_{15}O_{33}$ requires 1078.8529)

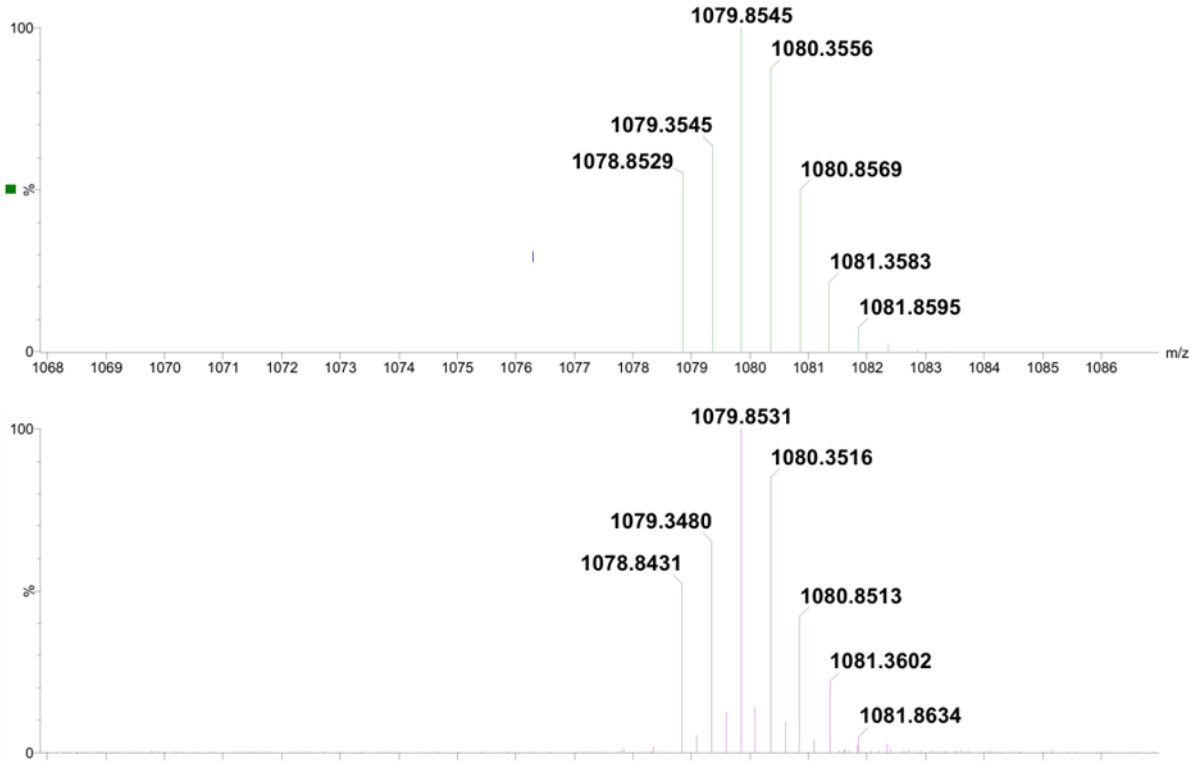

Figure 6.87: Simulated (top) and recorded (bottom) accurate MS (ESI$^+$) of **EuL^{3g}** ([M+2H]$^{2+}$, *m*/2)

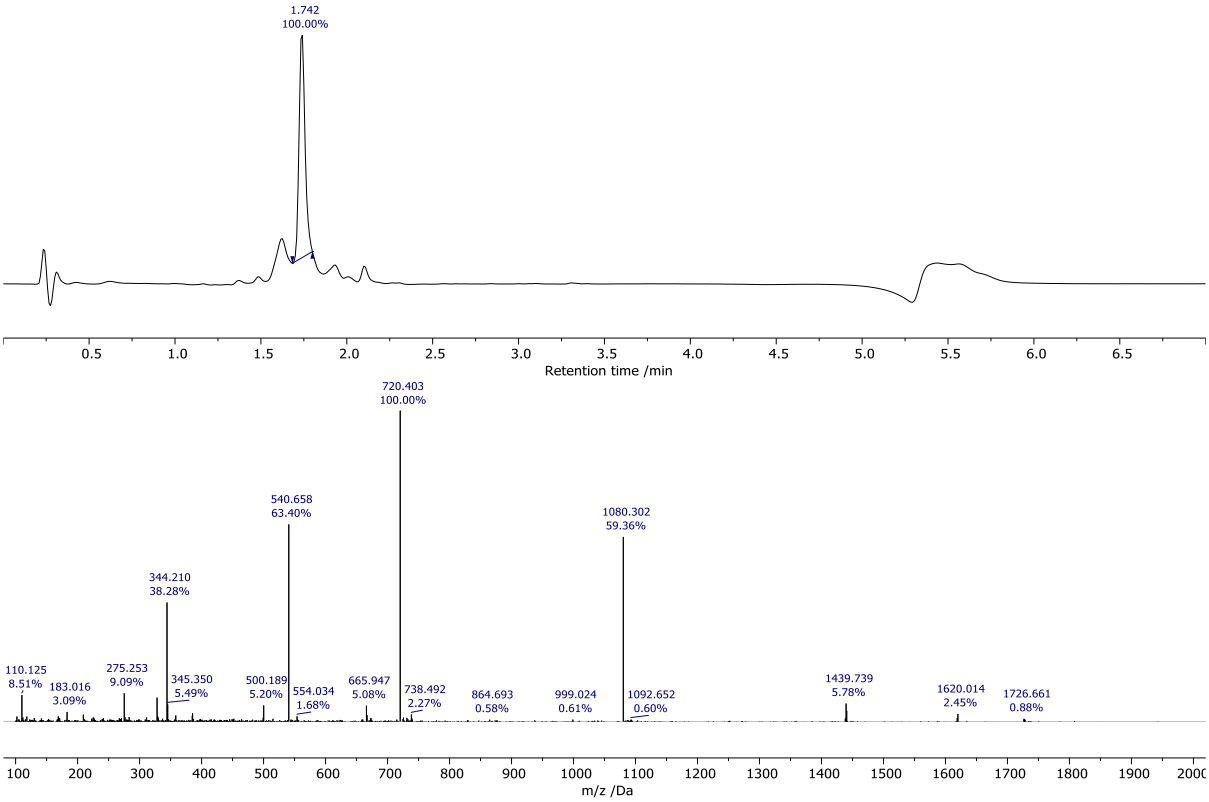

Figure 6.88: LCMS (Method E) of **EuL^{3g}** AC (210-400 nm) (top) and the MS (ESI$^+$) at 1.742 minutes (bottom).

Ethyl 4-(4-ethynyl-3,5-dimethoxyphenoxy)butanoate, **35**

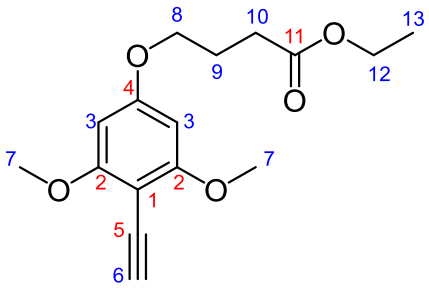

A solution of 4-ethynyl-3,5-dimethoxyphenol, **29** (*0.864 mmol, 1 eq*., prepared from 292 mg of **28**) in DMF (5 ml) was dropwise added over 1 hour to a solution of 4-bromobutyrate (1.24 ml, 8.64 mmol,10 eq.) and K_2CO_3 (143 mg, 1.04 mmol, 1.5 eq.) in DMF (5 ml) stirring at 60°C. Once the addition was completed, the resulting solution was stirred for additional 10 minutes before DMF solvent was removed under reduced pressure. The crude product was purified by flash chromatography (silica, 3:7 EtOAc - hexane) to yield pale yellow solid (58 mg, 0.198 mmol, 23% over two steps).

HRMS (ESI$^+$) *m/z* 293.14148 [M+H]+ ($C_{25}H_{30}NO_8$ requires 293.13835).

^{1}H NMR (700 MHz, $CDCl_3$) δ 6.08 (2H, s, H^3), 4.12 (2H, q, $^3J_{H\text{-}H}$ 7.2, H^{12}), 4.02 (2H, t, $^3J_{H\text{-}H}$ 6.1, H^8), 3.86 (6H, s, H^7), 3.47 (1H, s, H^6), 2.50 (2H, t, $^3J_{H\text{-}H}$ 7.2, H^{10}), 2.10 (2H, m, H^9), 1.25 (3H, t, $^3J_{H\text{-}H}$ 7.2, H^{13})

^{13}C NMR (151 MHz, $CDCl_3$) δ 173.18 (C^{11}), 163.08 (C^2), 161.27 (C^4), 93.13 (C^5), 90.93 (C^3), 83.86 (C^6), 76.65 (C^1) 67.01 (C^8), 60.61 (C^{12}), 56.17 (C^7), 30.68 (C^{10}), 24.57 (C^9), 14.33 (C^{13}).

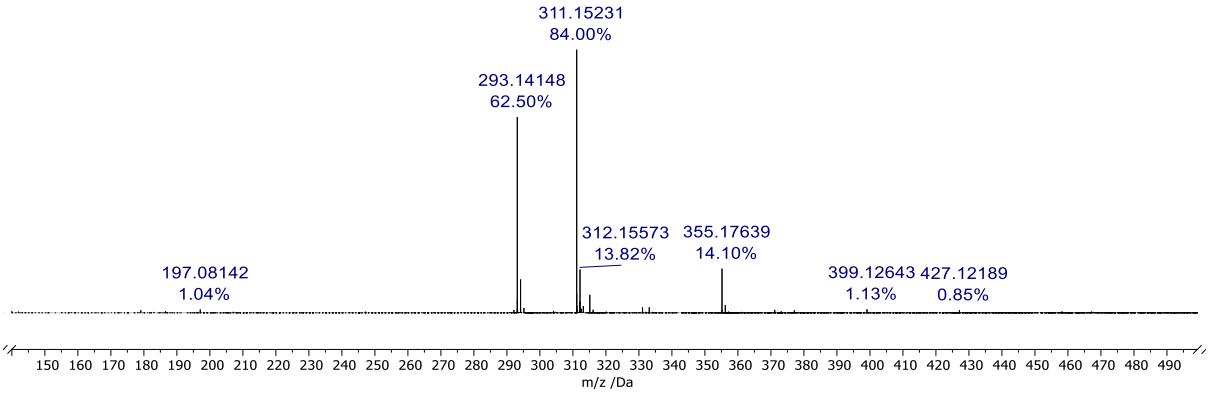

Figure 6.89: Accurate MS (ESI$^+$) of **35**.

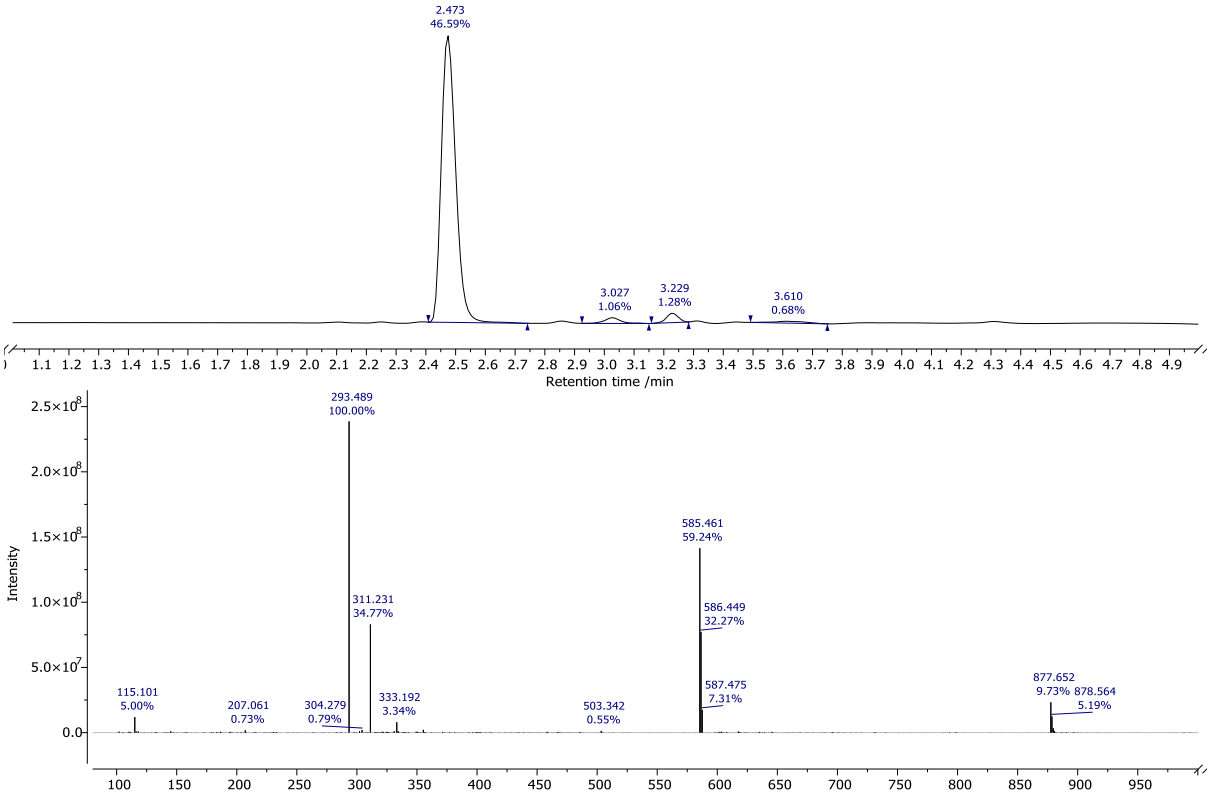

Figure 6.90: LCMS (Method E) of **35** AC (210-400 nm) (top) and the MS (ESI$^+$) at 2.473 minutes (bottom).

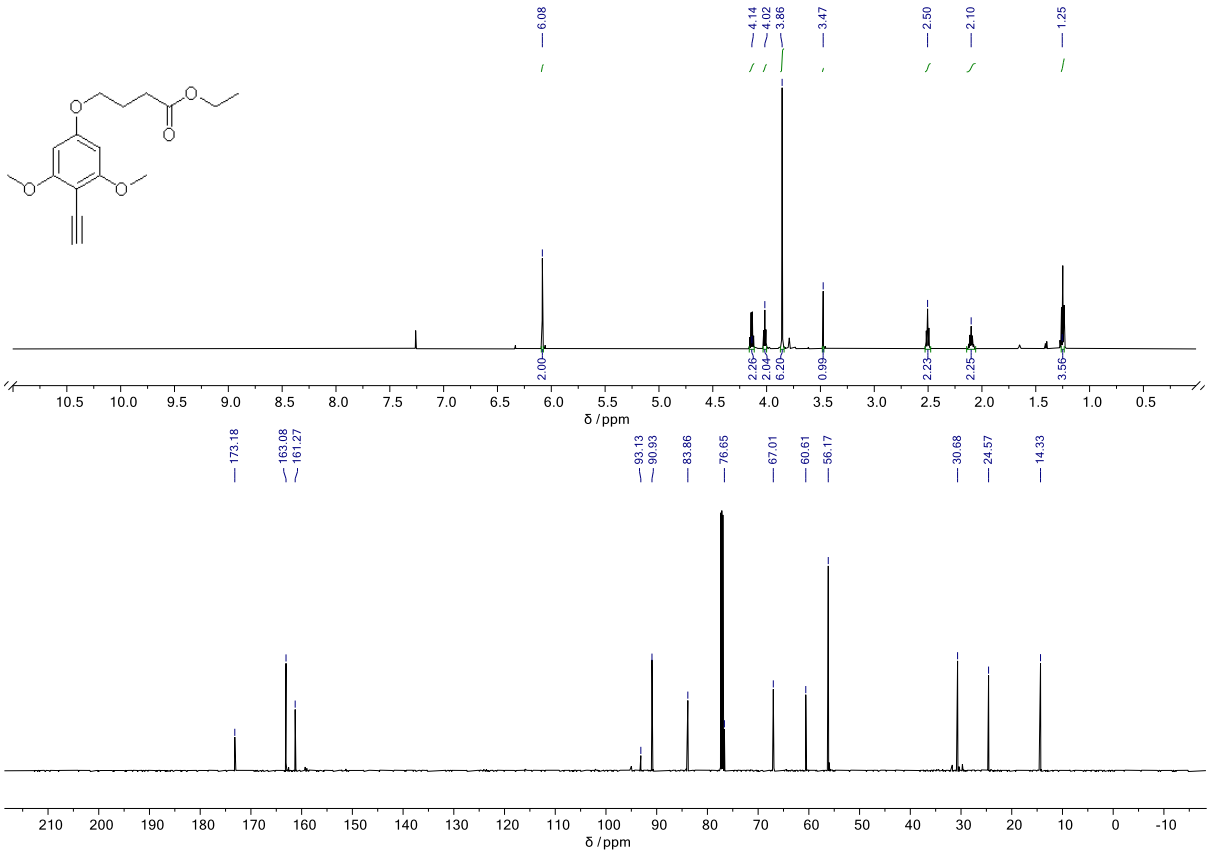

Figure 6.91: ^{1}H NMR (700 MHz, $CDCl_3$) (top) and ^{13}C NMR (151 MHz, $CDCl_3$) (bottom) spectra of **31**.

Ethyl 4-((4-(4-ethoxy-4-oxobutoxy)-2,6-dimethoxyphenyl)ethynyl)-6-(hydroxymethyl)picolinate, **36**

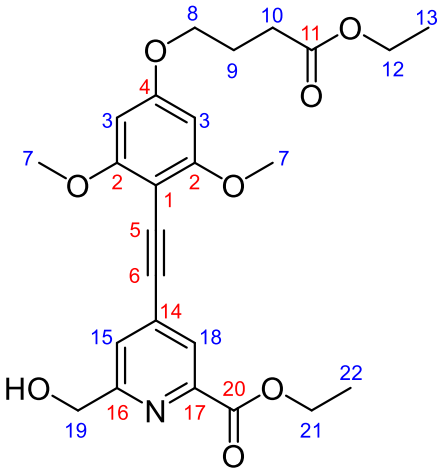

Ethyl 4-(4-ethynyl-3,5-dimethoxyphenoxy)butanoate, **35** (58 mg, 0.12 mmol, 1 eq.), diethyl 4-bromopyridine-2,6-dicarboxylate (98 mg, 0.14 mmol, 1.1 eq.) and $[Pd(allyl)Cl]_2$ (8.0 mg, 0.022 mmol, 0.2 eq.) were dissolved in anhydrous acetonitrile (10 ml) and degassed (freeze-pump-thaw × 3). After that, TEA (1.00 ml, 7.22 mmol, 60 eq.) and piperidine (0.25 ml, 2.6 mmol, 22 eq.) were added, and the resulting solution was stirred at 40°C for 20 hours under argon. After that, all volatile materials were removed under reduced pressure, and the crude was purified by reverse-phase HPLC (Method D, retention time = 10.3 min) to give pale-yellow solid (20 mg, 0.042 mmol, 35%).

HRMS (ESI$^+$) *m/z* 472.1962 $[M+H]^+$ ($C_{25}H_{30}NO_8$ requires 472.1971).

^{1}H NMR (400 MHz, $CDCl_3$) δ 8.11 (1H, s, H19), 7.57 (1H, s, H15), 6.12 (2H, s, H3), 4.82 (2H, s, H19), 4.47 (2H, q, $^3J_{H\text{-}H}$ 7.1, H21) 4.17 (2H, q, $^3J_{H\text{-}H}$ 7.2, H^{12}), 4.06 (2H, t, $^3J_{H\text{-}H}$ 6.3, H^8), 3.90 (6H, s, H^7), 2.53 (2H, t, $^3J_{H\text{-}H}$ 7.2, H^{10}), 2.13 (2H, m, H^9), 1.44 (3H, t, $^3J_{H\text{-}H}$ 7.2, H^{22}) 1.25 (3H, t, $^3J_{H\text{-}H}$ 7.2, H^{13})

^{13}C NMR (151 MHz, $CDCl_3$) δ 173.18 (C^{11}), 163.08 (C^2), 161.27 (C^4), 93.13 (C^5), 90.93 (C^3), 83.86 (C^6), 76.65 (C^1) 67.01 (C^8), 60.61 (C^{12}), 56.17 (C^7), 30.68 (C^{10}), 24.57 (C^9), 14.33 (C^{13}).

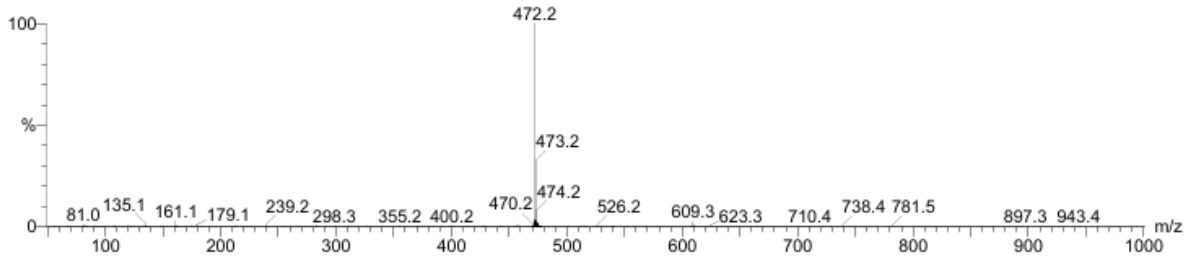

Figure 6.92: Accurate MS (ESI$^+$) of **36**.

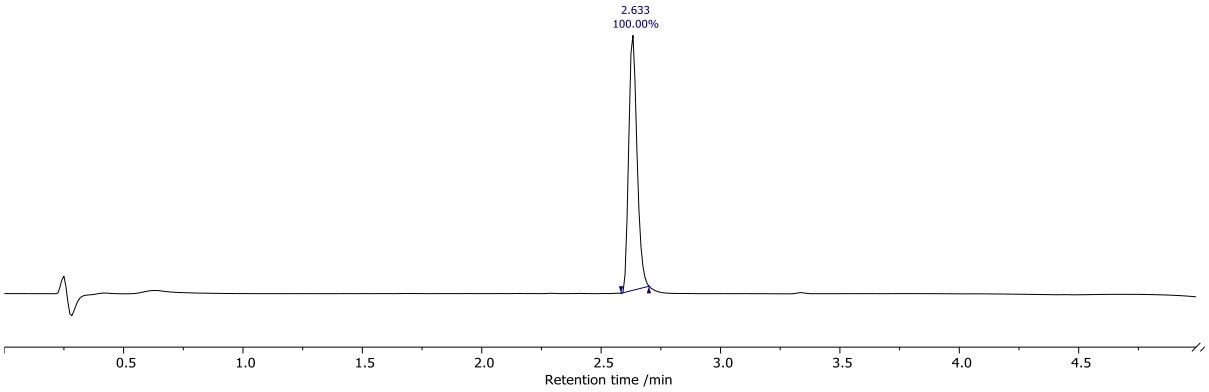

Figure 6.93: LCMS (Method E) of **36** AC (210-400 nm).

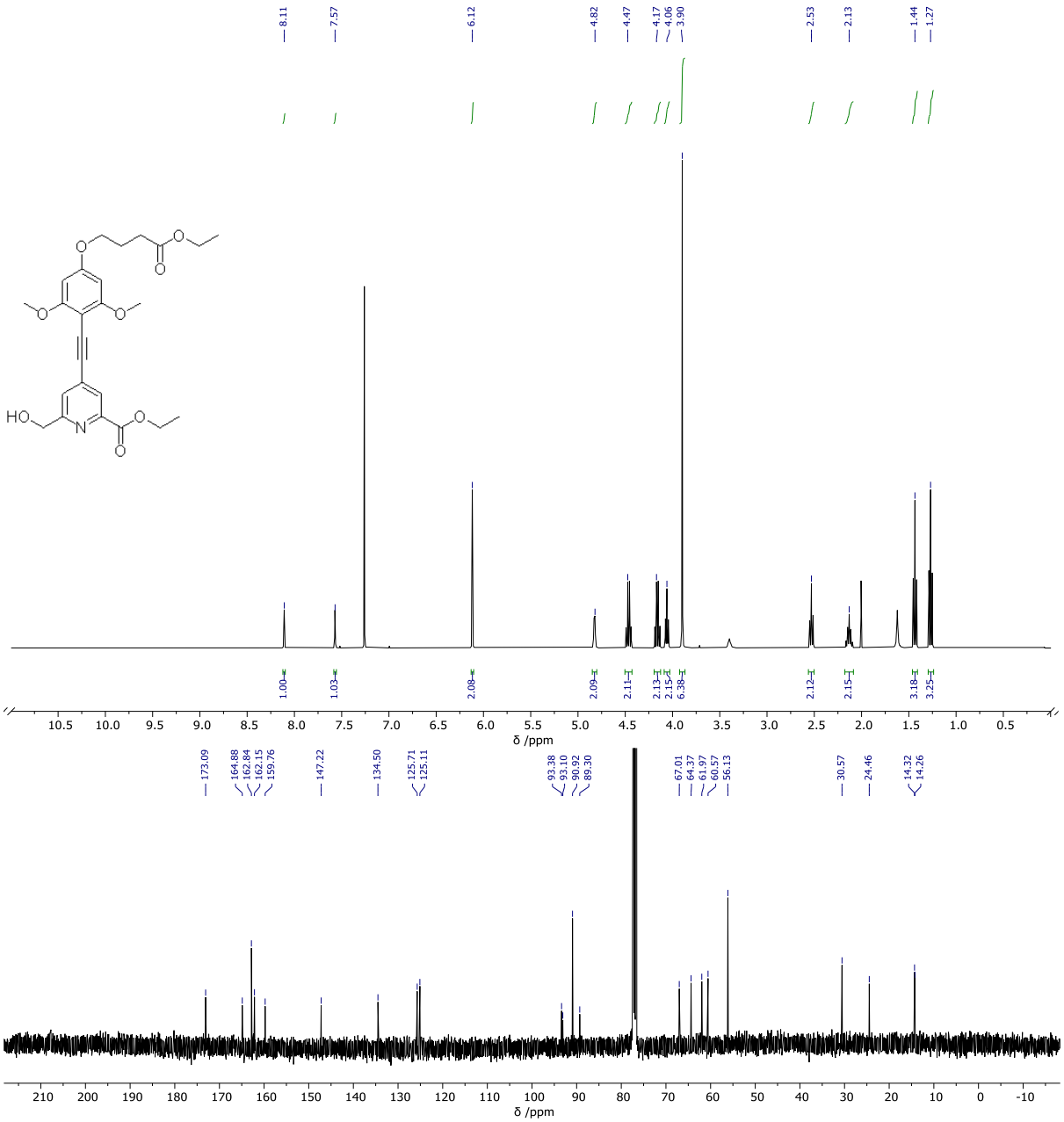

Figure 6.94: ^{1}H NMR (700 MHz, $CDCl_3$) (top) and ^{13}C NMR (151 MHz, $CDCl_3$) (bottom) spectra of **36**.

Ethyl 4-((4-(4-ethoxy-4-oxobutoxy)-2,6-dimethoxyphenyl)ethynyl)-6-(((methylsulfonyl)oxy)methyl)picolinate, **37**

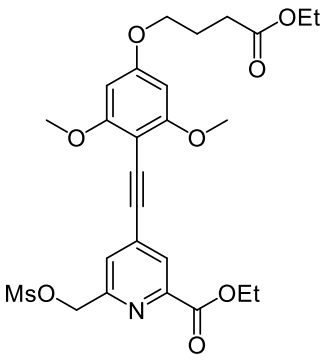

ethyl 4-((4-(4-ethoxy-4-oxobutoxy)-2,6-dimethoxyphenyl)ethynyl)-6(hydroxymethyl)picolinate, **36** (20 mg, 0.042 mmol, 1 eq.) and methanesulfonic anhydride (27 mg, 0.155 mmol, 3.7 eq.) were dissolved in anhydrous THF (4 ml) and DIPEA (22 µl, 0.126 mmol, 3 eq.) was added. The resulting solution was stirred at rt for 1 hour under argon. After that, volatile organic materials were evaporated under reduced pressure, and the obtained yellow solid was redissolved in DCM (10 ml). The resulting solution was washed with water (10 ml × 3), and the combined aqueous phases were extracted with DCM (5 ml × 3). The combined organic layers were dried over $MgSO_4$, filtered, and DCM was evaporated under reduced pressure to yield pale yellow solid that was used in the next step without further purification.

HRMS(ESI$^+$) *m/z* 550.1744 $[M+H]^+$ ($C_{26}H_{32}NO_{10}S$ requires 550.1747)

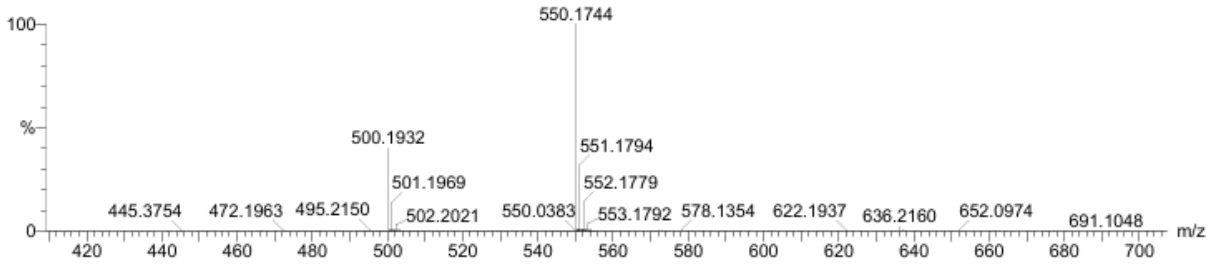

Figure 6.95: Accurate MS (ESI$^+$) of **37**.

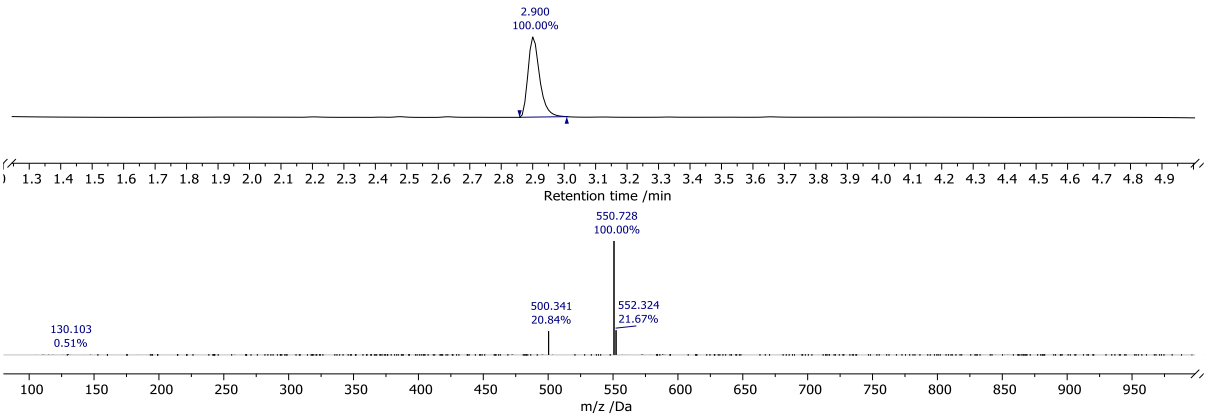

Figure 6.96: LCMS (Method E) of **37** AC (210-400 nm) (top) and the MS (ESI$^+$) at 2.900 minutes (bottom).

38

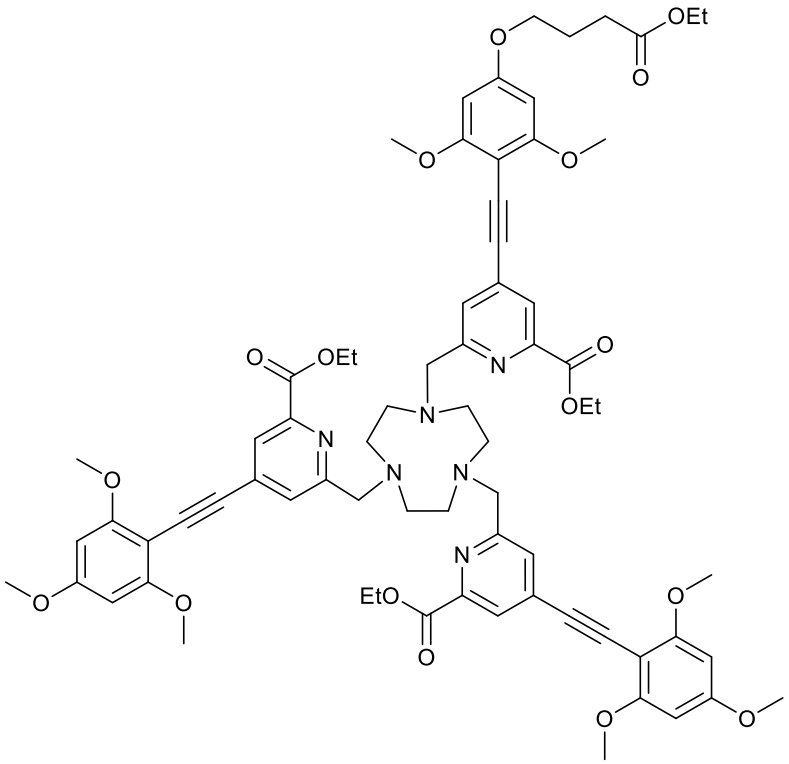

Potassium carbonate (38 mg, 0.275 mmol, 7 eq.), ethyl 4-((4-(4-ethoxy-4-oxobutoxy)-2,6-dimethoxyphenyl)ethynyl)-6-(((methylsulfonyl)oxy)methyl)picolinate, **37** (*0.042 mmol,* 1.1 eq.) and TACN•3HCl (9.2 mg, 0.039 mmol, 1 eq.) were dissolved in MeCN (5 ml) and stirred at 60°C for 20 hours under argon. After that ethyl 6-(((methylsulfonyl)oxy)methyl)-4-((2,4,6-trimethoxyphenyl)ethynyl)picolinate, **15** (0.085 mmol, 2.2 eq., prepared by mesylation of 31.6 mg of **14**) was dissolved in MeCN (5 ml) and added to the reaction mixture. After that, the mixture was stirred at 60°C for additional 20 hours under argon. After that, MeCN was removed under reduced pressure, and the crude mixture of products was redissolved in MeOH (5 ml) and used in the next step without further purification.

LCMS (ESI$^+$) *m/z* 1289.739 [M+H]$^+$

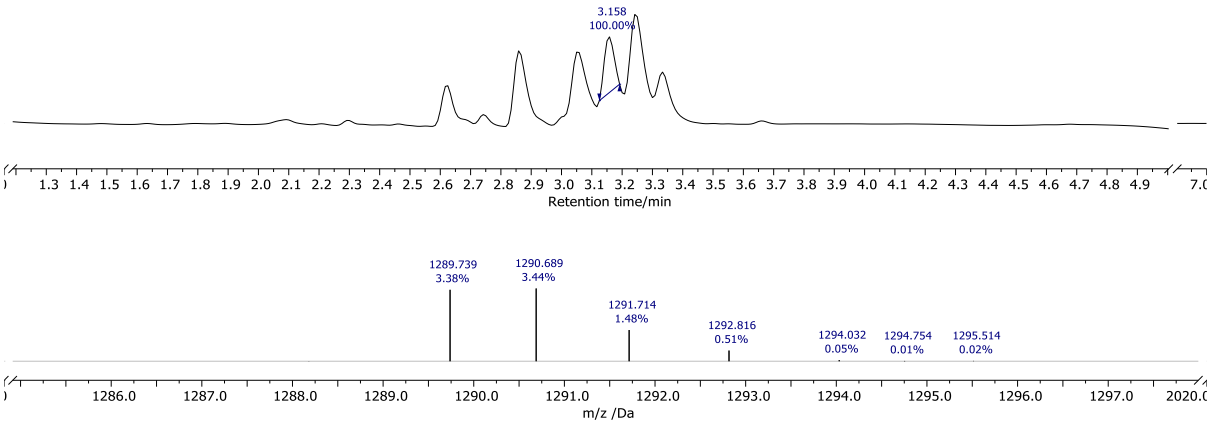

Figure 6.97: LCMS (Method E) of **38** AC (210-400 nm) (top) and the MS (ESI$^+$) at 3.158 minutes (bottom).

EuL⁴

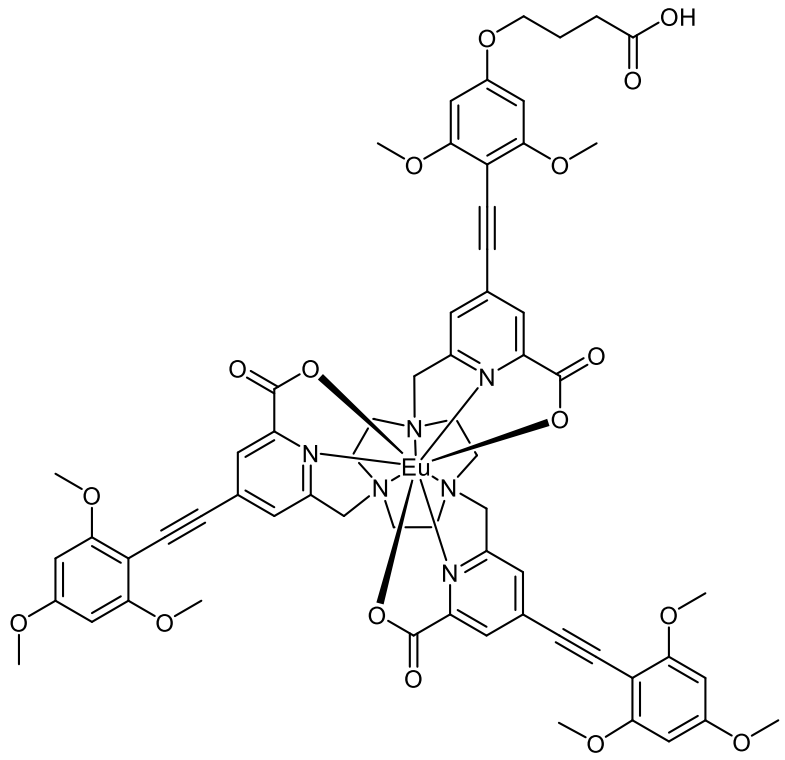

To a solution of **38** (*0.039 mmol*) in MeOH (5 ml) was dropwise added water until white precipitate remained. pH of the resulting solution was adjusted to 12.5 using 1M NaOH. The solution was stirred at 60 °C for 3 hours while its pH was periodically adjusted to 12.5 until hydrolysis completion was confirmed by LCMS. After that, the solution pH was readjusted to 6.5 using 1 M HCl. $EuCl_3.6HCl$ was then added (15 mg, 0.041 mmol, 1 eq.) and the resulting solution was stirred at rt for 20 hours. After that, the solvent was removed under pressure to yield yellow solid which was purified by reverse-phase HPLC (C_{18}, Method C, retention time = 20.7 min) to yield yellow solid (3.1 mg, 0.0023 mmol, 6% over two steps).

HRMS (ESI$^+$) 1325.3356 [M+H$^+$] ($C_{63}H_{61}{}^{151}EuN_6O_{17}$ requires 1325.3370)

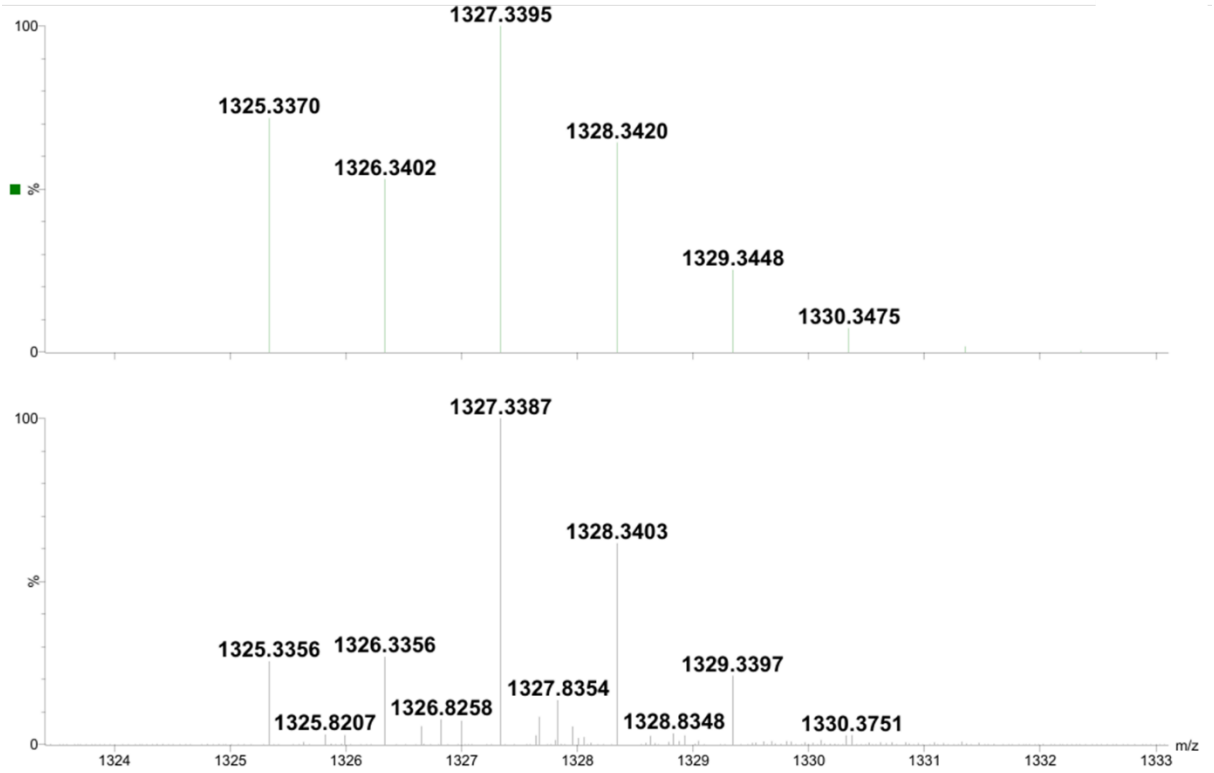

Figure 6.98: Simulated (top) and recorded (bottom) accurate MS (ESI⁺) of **EuL⁴**.

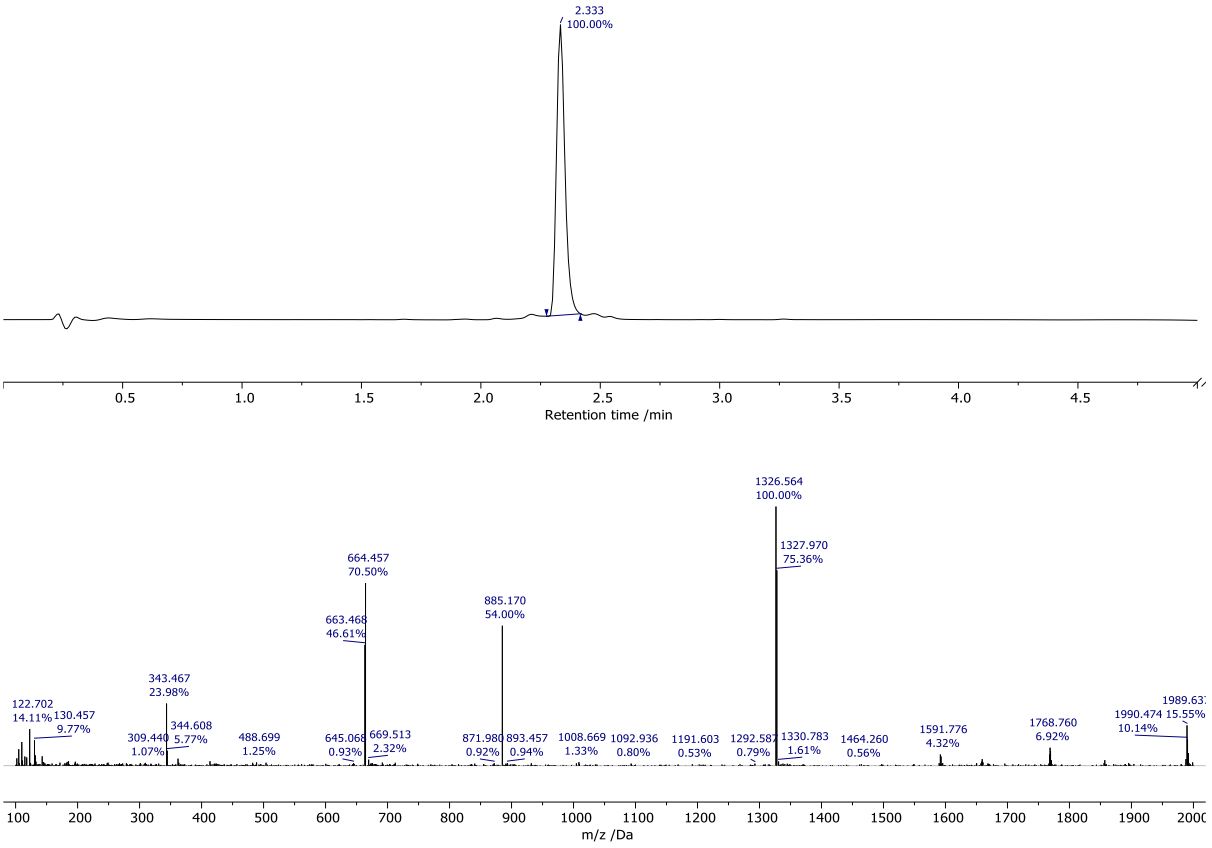

Figure 6.99: LCMS (Method E) of **EuL⁴** AC (210-400 nm) (top) and the MS (ESI⁺) at 2.900 minutes (bottom).

References

1 M. Kasha, *Discuss. Faraday Soc.*, 1950, **9**, 14.
2 A. Jablonski, *Nature*, 1933, **131**, 839–840.
3 K. Binnemans, *Coordination Chemistry Reviews*, 2015, **295**, 1–45.
4 C. Görller-Walrand, L. Fluyt, A. Ceulemans and W. T. Carnall, *The Journal of Chemical Physics*, 1991, **95**, 3099–3106.
5 J.-C. G. Bünzli and S. V. Eliseeva, *Chem. Sci.*, 2013, **4**, 1939.
6 A. J. Freeman and R. E. Watson, *Phys. Rev.*, 1962, **127**, 2058–2075.
7 S. Cotton, *Lanthanide and Actinide Chemistry*, 2006.
8 D. Parker, J. D. Fradgley and K.-L. Wong, *Chem. Soc. Rev.*, 2021, **50**, 8193–8213.
9 S. Pandya, J. Yu and D. Parker, *Dalton Trans.*, 2006, 2757.
10 O. L. Malta, *Journal of Non-Crystalline Solids*, 2008, **354**, 4770–4776.
11 J.-C. G. Bünzli, *Coordination Chemistry Reviews*, 2015, **293–294**, 19–47.
12 D. Parker, P. K. Senanayake and J. A. Gareth Williams, *J. Chem. Soc., Perkin Trans. 2*, 1998, 2129–2140.
13 S. Blair, R. Kataky and D. Parker, *New J. Chem.*, 2002, **26**, 530–535.
14 J. Yu, L. Sun, H. Peng and M. I. J. Stich, *J. Mater. Chem.*, 2010, **20**, 6975.
15 G.-L. Law, R. Pal, L. O. Palsson, D. Parker and K.-L. Wong, *Chem. Commun.*, 2009, 7321.
16 J. A. Sobrinho, G. A. Brito Júnior, I. O. Mazali and F. A. Sigoli, *New J. Chem.*, 2020, **44**, 8068–8075.
17 R. Hueting, M. Tropiano and S. Faulkner, *RSC Adv.*, 2014, **4**, 44162–44165.
18 S. J. Butler, L. Lamarque, R. Pal and D. Parker, *Chem. Sci.*, 2014, **5**, 1750.
19 S. J. Butler, M. Delbianco, L. Lamarque, B. K. McMahon, E. R. Neil, R. Pal, D. Parker, J. W. Walton and J. M. Zwier, *Dalton Trans.*, 2015, **44**, 4791–4803.
20 P. Stachelek, L. MacKenzie, D. Parker and R. Pal, *Nat Commun*, 2022, **13**, 553.
21 A. T. Frawley, R. Pal and D. Parker, *Chem. Commun.*, 2016, **52**, 13349–13352.
22 L. E. MacKenzie and R. Pal, *Nat Rev Chem*, 2020, **5**, 109–124.
23 A. D'Aléo, A. Picot, A. Beeby, J. A. Gareth Williams, B. Le Guennic, C. Andraud and O. Maury, *Inorg. Chem.*, 2008, **47**, 10258–10268.
24 D. Parker, *Coordination Chemistry Reviews*, 2000, **205**, 109–130.
25 A. Beeby, S. W. Botchway, I. M. Clarkson, S. Faulkner, A. W. Parker, D. Parker and J. A. G. Williams, *Journal of Photochemistry and Photobiology B: Biology*, 2000, **57**, 83–89.
26 E. Mathieu, A. Sipos, E. Demeyere, D. Phipps, D. Sakaveli and K. E. Borbas, *Chem. Commun.*, 2018, **54**, 10021–10035.
27 Y. Bretonniere, M. J. Cann, D. Parker and R. Slater, *Org. Biomol. Chem.*, 2004, **2**, 1624.
28 G. Bobba, J. C. Frias and D. Parker, *Chem. Commun.*, 2002, 890–891.
29 S. Petoud, G. Muller, E. G. Moore, J. Xu, J. Sokolnicki, J. P. Riehl, U. N. Le, S. M. Cohen and K. N. Raymond, *J. Am. Chem. Soc.*, 2007, **129**, 77–83.
30 Y. Zhou, H. Li, T. Zhu, T. Gao and P. Yan, *J. Am. Chem. Soc.*, 2019, **141**, 19634–19643.
31 C. V. Raman and S. Bhagavantam, *Nature*, 1932, **129**, 22–23.
32 R. A. Beth, *Phys. Rev.*, 1936, **50**, 115–125.
33 J. G. Foss, *J. Chem. Educ.*, 1970, **47**, 778.
34 J. L. Greenfield, J. Wade, J. R. Brandt, X. Shi, T. J. Penfold and M. J. Fuchter, *Chem. Sci.*, 2021, **12**, 8589–8602.
35 K. Mawatari, S. Kubota and T. Kitamori, *Anal Bioanal Chem*, 2008, **391**, 2521–2526.
36 T. Narushima and H. Okamoto, *Sci Rep*, 2016, **6**, 35731.
37 H. Tsumatori, T. Harada, J. Yuasa, Y. Hasegawa and T. Kawai, *Appl. Phys. Express*, 2011, **4**, 011601.
38 N. Berova, P. L. Polavarapu, K. Nakanishi and R. W. Woody, Eds, in *Comprehensive Chiroptical Spectroscopy*, John Wiley & Sons, Inc., Hoboken, NJ, USA, 2012, pp. i–xiii.
39 L. Arrico, L. Di Bari and F. Zinna, *Chem. Eur. J.*, 2021, **27**, 2920–2934.
40 J. L. Lunkley, D. Shirotani, K. Yamanari, S. Kaizaki and G. Muller, *J. Am. Chem. Soc.*, 2008, **130**, 13814–13815.

41 J. Kumar, B. Marydasan, T. Nakashima, T. Kawai and J. Yuasa, *Chem. Commun.*, 2016, **52**, 9885–9888.
42 L. Arrico, L. Di Bari and F. Zinna, *Chem. Eur. J.*, 2021, **27**, 2920–2934.
43 J. Andres, R. D. Hersch, J. Moser and A. Chauvin, *Adv. Funct. Mater.*, 2014, **24**, 5029–5036.
44 M. R. Carro-Temboury, R. Arppe, T. Vosch and T. J. Sørensen, *Sci. Adv.*, 2018, **4**, e1701384.
45 R. Carr, R. Puckrin, B. K. McMahon, R. Pal, D. Parker and L.-O. Pålsson, *Methods Appl. Fluoresc.*, 2014, **2**, 024007.
46 L. E. MacKenzie, L.-O. Pålsson, D. Parker, A. Beeby and R. Pal, *Nat Commun*, 2020, **11**, 1676.
47 D. F. De Rosa, P. Stachelek, D. J. Black and R. Pal, *Nat Commun*, 2023, **14**, 1537.
48 D. F. Caffrey, T. Gorai, B. Rawson, M. Martínez-Calvo, J. A. Kitchen, N. S. Murray, O. Kotova, S. Comby, R. D. Peacock, P. Stachelek, R. Pal and T. Gunnlaugsson, *Advanced Science*, 2024, **11**, 2307448.
49 D. Hartmann, S. E. Penty, A. Krimovs, R. Pal, T. Gianga, G. Siligardi and T. A. Barendt, *Angew Chem Int Ed*, 2026, **65**, e20567.
50 P. Lowe, *Journal of Financial Crime*, 2006, **13**, 255–257.
51 B. Hardwick, W. Jackson, G. Wilson and A. W. H. Mau, *Adv. Mater.*, 2001, **13**, 980–984.
52 Countries around the world using Guardian™ polymer bank notes, https://cclsecure.com/where-is-guardian-used/.
53 B. Mennucci, *Int. J. Quantum Chem.*, 2015, **115**, 1202–1208.
54 M. Soulié, F. Latzko, E. Bourrier, V. Placide, S. J. Butler, R. Pal, J. W. Walton, P. L. Baldeck, B. Le Guennic, C. Andraud, J. M. Zwier, L. Lamarque, D. Parker and O. Maury, *Chem. Eur. J.*, 2014, **20**, 8636–8646.
55 S. D. Belair, C. L. Maupin, M. W. Logue and J. P. Riehl, *Journal of Luminescence*, 2000, **86**, 61–66.
56 A. T. Frawley, Doctoral Thesis, Durham University, 2017.
57 S. J. Butler, M. Delbianco, N. H. Evans, A. T. Frawley, R. Pal, D. Parker, R. S. Puckrin and D. S. Yufit, *Dalton Trans.*, 2014, **43**, 5721–5730.
58 E. R. Neil, A. M. Funk, D. S. Yufit and D. Parker, *Dalton Trans.*, 2014, **43**, 5490–5504.
59 N. H. Evans, R. Carr, M. Delbianco, R. Pal, D. S. Yufit and D. Parker, *Dalton Trans.*, 2013, **42**, 15610.
60 J. W. Walton, A. Bourdolle, S. J. Butler, M. Soulie, M. Delbianco, B. K. McMahon, R. Pal, H. Puschmann, J. M. Zwier, L. Lamarque, O. Maury, C. Andraud and D. Parker, *Chem. Commun.*, 2013, **49**, 1600.
61 H. Xu, Q. Wang, Z. Qi, X. Li, Y. Lei, H. An, H. Tian and D. Qu, *Angew Chem Int Ed*, 2025, **64**, e202420707.
62 J. D. Fradgley, Doctoral Thesis, Durham University, 2021.
63 H. McErlain, L. M. Riley and A. Sutherland, *J. Org. Chem.*, 2021, **86**, 17036–17049.
64 V. Boekelheide and W. J. Linn, *J. Am. Chem. Soc.*, 1954, **76**, 1286–1291.
65 E. J. Corey and P. L. Fuchs, 1972, 3769–3772.
66 R. Chinchilla and C. Nájera, *Chem. Rev.*, 2007, **107**, 874–922.
67 C. Glaser, *Ber. Dtsch. Chem. Ges.*, 1869, **2**, 422–424.
68 K. Sonogashira, Y. Tohda and N. Hagihara, 1975, 4467–4470.
69 A. Soheili, J. Albaneze-Walker, J. A. Murry, P. G. Dormer and D. L. Hughes, *Org. Lett.*, 2003, **5**, 4191–4194.
70 M. Gazvoda, M. Virant, B. Pinter and J. Košmrlj, *Nat Commun*, 2018, **9**, 4814.
71 M. Starck, J. D. Fradgley, R. Pal, J. M. Zwier, L. Lamarque and D. Parker, *Chem. Eur. J.*, 2021, **27**, 766–777.
72 K. Rurack and M. Spieles, *Anal. Chem.*, 2011, **83**, 1232–1242.
73 S. J. Butler, L. Lamarque, R. Pal and D. Parker, *Chem. Sci.*, 2014, **5**, 1750.
74 R. A. Poole, G. Bobba, M. J. Cann, J.-C. Frias, D. Parker and R. D. Peacock, *Org. Biomol. Chem.*, 2005, **3**, 1013–1024.
75 D. Liu, V. García-López, R. S. Gunasekera, L. Greer Nilewski, L. B. Alemany, A. Aliyan, T. Jin, G. Wang, J. M. Tour and R. Pal, *ACS Nano*, 2019, **13**, 6813–6823.
76 L.-O. Pålsson, R. Pal, B. S. Murray, D. Parker and A. Beeby, *Dalton Trans.*, 2007, 5726.
77 N. S. Makarov, M. Drobizhev and A. Rebane, *Opt. Express*, 2008, **16**, 4029.

78 J. W. Walton, R. Carr, N. H. Evans, A. M. Funk, A. M. Kenwright, D. Parker, D. S. Yufit, M. Botta, S. De Pinto and K.-L. Wong, *Inorg. Chem.*, 2012, **51**, 8042–8056.
79 D. Parker, J. D. Fradgley and K.-L. Wong, *Chem. Soc. Rev.*, 2021, **50**, 8193–8213.
80 A. T. Frawley, R. Pal and D. Parker, *Chem. Commun.*, 2016, **52**, 13349–13352.
81 M. Delbianco, L. Lamarque and D. Parker, *Org. Biomol. Chem.*, 2014, **12**, 8061–8071.
82 D. F. De Rosa, M. Starck, D. Parker and R. Pal, *Chemistry A European J*, 2024, **30**, e202303227.
83 M. Starck, L. E. MacKenzie, A. S. Batsanov, D. Parker and R. Pal, *Chem. Commun.*, 2019, **55**, 14115–14118.
84 D. Thakur and S. Vaidyanathan, *J. Mater. Chem. C*, 2025, **13**, 9410–9452.
85 J. W. Walton, L. D. Bari, D. Parker, G. Pescitelli, H. Puschmann and D. S. Yufit, *Chem. Commun.*, 2011, **47**, 12289.
86 G. da S. Padilha, V. M. Giacon and J. R. Bartoli, *Polímeros*, 2017, **27**, 195–200.
87 M. S. Hamdy, S. AlFaify, A. Al-Hajry and I. S. Yahia, *Optik*, 2016, **127**, 4959–4963.
88 M. O'Kane, Solution Coating Methods: A Comparison, https://www.ossila.com/pages/solution-processing-techniques-comparison, (accessed 5 June 2023).
89 N. G. Semaltianos, *Microelectronics Journal*, 2007, **38**, 754–761.
90 J. Kámán, Doctoral Thesis, Budapest University of Technology and Economics, 2022.
91 J. Schindelin, I. Arganda-Carreras, E. Frise, V. Kaynig, M. Longair, T. Pietzsch, S. Preibisch, C. Rueden, S. Saalfeld, B. Schmid, J.-Y. Tinevez, D. J. White, V. Hartenstein, K. Eliceiri, P. Tomancak and A. Cardona, *Nature Methods*, 2012, **9**, 676–682.
92 M. Starck, J. D. Fradgley, S. Di Vita, J. A. Mosely, R. Pal and D. Parker, *Bioconjugate Chem.*, 2020, **31**, 229–240.
93 Y. Hasegawa, Y. Miura, Y. Kitagawa, S. Wada, T. Nakanishi, K. Fushimi, T. Seki, H. Ito, T. Iwasa, T. Taketsugu, M. Gon, K. Tanaka, Y. Chujo, S. Hattori, M. Karasawa and K. Ishii, *Chem. Commun.*, 2018, **54**, 10695–10697.
94 S. Ma, J. Jiang, Z. Liu, Y. Jiang, Z. Wu and M. Liu, *Nanoscale*, 2020, **12**, 7895–7901.
95 T. Goto, Y. Okazaki, M. Ueki, Y. Kuwahara, M. Takafuji, R. Oda and H. Ihara, *Angew Chem Int Ed*, 2017, **56**, 2989–2993.
96 F. D. Bellamy and K. Ou, *Tetrahedron Letters*, 1985, **26**, 1362.
97 F. D. Bellamy and K. Ou, *Tetrahedron Letters*, 1984, **25**, 839–842.
98 K. Barral, A. D. Moorhouse and J. E. Moses, *Org. Lett.*, 2007, **9**, 1809–1811.
99 Sadtler research laboratories, Ed., *The Interpretation of vapor-phase infrared spectra*, Sadtler, Philadelphia (Pa.), 1984.
100 D. Lin-Vien, N. B. Colthup, W. G. Fateley and J. G. Grasselli, in *The Handbook of Infrared and Raman Characteristic Frequencies of Organic Molecules*, Elsevier, 1991, pp. 179–189.
101 W. M. Haynes, Ed., *CRC handbook of chemistry and physics: a ready-reference book of chemical and physical data*, CRC Press, Boca Raton London New York, 97th edition., 2017.
102 P. Sobczak, T. Sierański, M. Świątkowski, A. Trzęsowska-Kruszyńska and J. Kolińska, *RSC Adv.*, 2025, **15**, 1514–1526.
103 T. Javorskis and E. Orentas, *J. Org. Chem.*, 2017, **82**, 13423–13439.
104 P. Spieß, A. Sirvent, I. Tiefenbrunner, J. Sargueil, A. J. Fernandes, A. Arroyo-Bondía, R. Meyrelles, D. Just, A. Prado-Roller, S. Shaaban, D. Kaiser and N. Maulide, *Chemistry A European J*, 2023, **29**, e202301312.
105 T. Kan and T. Fukuyama, *Chem. Commun.*, 2004, 353.
106 U. C. Dyer, D. A. Henderson, M. B. Mitchell and P. D. Tiffin, *Org. Process Res. Dev.*, 2002, **6**, 311–316.
107 I. S. Kritchenkov, J. R. Shakirova and S. P. Tunik, *RSC Adv.*, 2019, **9**, 15531–15535.
108 N. R. M. Reintjens, E. Tondini, C. Vis, T. McGlinn, N. J. Meeuwenoord, T. P. Hogervorst, H. S. Overkleeft, D. V. Filippov, G. A. Van Der Marel, F. Ossendorp and J. D. C. Codée, *ChemBioChem*, 2021, **22**, 434–440.
109 R. Daly, G. Vaz, A. M. Davies, M. O. Senge and E. M. Scanlan, *Chemistry A European J*, 2012, **18**, 14671–14679.
110 N. George, S. Ofori, S. Parkin and S. G. Awuah, *RSC Adv.*, 2020, **10**, 24017–24026.
111 C. Xu and W. W. Webb, *J. Opt. Soc. Am. B*, 1996, **13**, 481.

112 R. Lengacher, K. E. Martin, D. Śmiłowicz, H. Esseln, P. Lotlikar, A. Grichine, O. Maury and E. Boros, *J. Am. Chem. Soc.*, 2023, **145**, 24358–24366.
113 A. Krimovs, D. J. Black, A. Congreve and R. Pal, *Chem. Sci.*, 2026, **17**, 4649–4658.
114 D. J. Black, A. Krimovs and R. Pal, 2026, preprint, DOI: 10.26434/chemrxiv.10001935/v1.

Appendix 1

Krimovs et. al, 2026[113]

Chemical Science

ROYAL SOCIETY OF CHEMISTRY

EDGE ARTICLE

View Article Online
View Journal | View Issue

Cite this: *Chem. Sci.*, 2026, **17**, 4649

All publication charges for this article have been paid for by the Royal Society of Chemistry

Complete stereochemical control to unlock monosign circularly polarised luminescence with superior circularly polarised brightness for chameleon security inks

Artemijs Krimovs, Dominic J. Black, Aileen Congreve and Robert Pal *

A novel arylalkynylpyridine-sensitised nine coordinate quasi-C_3 symmetric all carboxylate donor europium(III) complex (EuL) possessing exceptionally high circularly polarised brightness in both $\Delta J = 1$ and $\Delta J = 2$ transitions was prepared and tested in spin-coated solid-state PMMA thin films. The authentication of the circularly polarised luminescence (CPL) layer was successfully performed using CPL photography (CPLP) and enantioselective differential chiral contrast (EDCC) imaging for both transitions simultaneously using appropriate band pass filters. The effect of reflective properties of different thin film substrate materials on the recorded chiral contrast was quantified using the newly introduced CPLP dissymmetry factor (g_{CPLP}) which compared to the average dissymmetry factor values obtained using a photo elastic modulator (PEM) based CPL spectrometer. Circularly polarised brightness (CPB) of $\Delta J = 2$ (590 mol^{-1} dm^3 cm^{-1} at 607 nm) was the highest ever reported and that of $\Delta J = 1$ (307 mol^{-1} dm^3 cm^{-1} at 596 nm) was third best across other CPL-active materials with reported CPB. This makes EuL the best candidate for next-generation CPL-active multi-tier 'chameleon security inks'.

Received 16th July 2025
Accepted 2nd January 2026

DOI: 10.1039/d5sc05303j

rsc.li/chemical-science

Introduction

Light emitting materials that possess circularly polarised luminescence (CPL) have been increasingly developed for security applications.[1–4] CPL-based security layer could improve the existing anti-counterfeiting technologies for the use in passports, driving-licenses and banknotes.[5–16] The strength of CPL is characterised by luminescence dissymmetry factor (g_{lum}):

$$g_{lum} = \frac{2(I_{CPL\text{-}L} - I_{CPL\text{-}R})}{(I_{CPL\text{-}L} + I_{CPL\text{-}R})} \quad (1)$$

where I_L and I_R are intensities of left-handed and right-handed components of CPL. The values of g_{lum} range between $g_{lum} = 2$ (100% left-handed polarisation) and $g_{lum} = -2$ (100% right-handed polarisation), where $g_{lum} = 0$ indicates no net circular polarisation (CP). Practically useful CPL-active dyes must not only have high g_{lum} but also luminescence brightness (B) which is a product of molar absorption coefficient (ε) and photoluminescence quantum yield (φ). The product of the two is known as CPL brightness (CPB):[17]

$$CPB = B\frac{g_{lum}}{2} = \varepsilon\Phi\frac{g_{lum}}{2} \quad (2)$$

CPB can also be used as a reference parameter to compare the performance of different CPL-active materials, where the maximal observed value of the g_{lum} is used. CPB can also be calculated for individual transition (CPB_i) using branching factor (β_i) which is the ratio between the intensities of the emission band of interest (I_i) and total emission:[17]

$$CPB_i = \beta_i \times CPB \quad (3)$$

It is particularly useful for applications where the wavelength of the detected light can be selected, for instance, by a band pass filter (BPF).[18] In that case, the average g_{lum} for the selected wavelength region is used to calculate CPB_i. Therefore, the emission manifold with single CPL sign is desired to maximise CPB_i by avoiding cancellation of CP. Therefore, materials with high CPB_i can be used in security tags suitable for rapid CPL verification.

CPL-active materials with the highest known CPB values are organometallic lanthanide complexes.[17] Here we explore arylalkynylpyridine-sensitised nine-coordinate quasi-C_3 symmetric 9N3 europium(III) complexes.[19–27] These already found applications in bioimaging due to their advantageous photophysical properties such as millisecond long emission lifetime, narrow fingerprint like lanthanide-centred f–f emission bands, large *pseudo*-Stokes' shift and tunability of sensitisation *via* the ligand structure optimisation of absorption maxima and targeted cell localisation.[22,23]

Department of Chemistry, Durham University, South Road, Durham, DH1 3LE, UK. E-mail: robert.pal@durham.ac.uk

Eu(III) complexes have been explored as candidates for CPL-active security inks, that can be authenticated by both enantioselective differential chiral contrast (EDCC) imaging using CPL microscopy and circularly polarised luminescence photography (CPLP) using a novel handheld CPLP camera (SI Section 2.3).[18,28] The latter exploits a narrow 10 nm BPF for isolation of individual transitions, for example, 594 ± 5 nm BPF (BPF594/10) and 610 ± 5 nm BPF (BPF610/10) to select $^5D_0 \rightarrow {}^7F_1$ ($\Delta J = 1$) and $^5D_0 \rightarrow {}^7F_2$ ($\Delta J = 2$) respectively. Commonly, only magnetic-dipole (MD) allowed $\Delta J = 1$ transition has been used for CPL-imaging due to its strong CPL activity and single CPL sign conservation. The use of $\Delta J = 1$ transition is not optimal since it makes up only around 5% of total EuL emission. The use of the brightest $\Delta J = 2$ ($\beta_i = \sim 35\%$) is more desirable since it would require around 7 times less material to produce the same emission intensity and therefore CPB_i. On the other hand, due to its MD forbidden nature, $\Delta J = 2$ usually shows low g_{lum}. In addition to that, the environmentally hypersensitive $\Delta J = 2$ manifold often shows complex variation in CPL sign that result in overall cancellation of the detected CPL signal.[29] Both factors significantly reduce CPB_i of $\Delta J = 2$, making it unsuitable for CPLP.

This leads to the main requirement for a CPL-active security ink: conservation of the CPL sign across the emission manifold to maximise the average g_{lum} within the selected wavelength region. Therefore, it is important to consider the symmetry at the Eu(III) emitting centre that affects the multiplicity of the electronic states involved in a transition. For Eu(III), the emissive $^5D_0$ state has a multiplicity of 1 ($J = 0$) in all symmetries unlike the multiplicities of the $^7F_1$ and $^7F_2$ which depend on the point group. As a result, a lower symmetry at Eu(III) increases the multiplicity of the two states which then leads to multiple CPL emission bands within $\Delta J = 1$ and $\Delta J = 2$ with potentially opposing helicity.

The symmetry at Eu(III) site in the complexes of interest is attributed to the C_3 point group, which suggests the multiplicity of 2 and 3 for the $^7F_1$ and $^7F_2$ states respectively. This multiplicity is the same across other high symmetry classes such as hexagonal and octagonal but can increase when the symmetry is lowered.

Parent Eu(III) complex structures that were the most widely explored for their CPL activity contained phosphinate donor groups.[2,20,28,30] The use of pentavalent phosphorus allows for additional structural modifications. For example, bulky phenyl groups on phosphorus are believed to limit complex racemisation since it requires simultaneous inversion of the chiral phosphorus centre as well as inversion of the 1,4,7-triazacyclononane (TACN) ring and rotation of the sensitising chromophores.[2] This is important since enantiopure complexes must not racemise during short-term exposure to high temperature (up to 150 °C) during lamination. On the contrary, phosphinate donor complexes normally possess multiple low intensity CPL bands in the $\Delta J = 2$ manifold which often demonstrate CPL sign fluctuation. A recent exception to this was a mixed-donor complex containing two phosphinate and one carboxylate donor groups.[4] Although it produced a single-sign CPL $\Delta J = 2$ manifold, it only contained two sensitising chromophores (out of 3 possible) reducing ε and therefore inherently reducing CPB. Although a direct relationship between the complex structure and its observed CPL spectrum is not fully understood, it was proposed that substitution of chiral phosphinate donors with achiral centrosymmetric bidentate carboxylate donors would reduce the magnetic dipole moment induced (total angular momentum driven). This would greatly affect the overall rotatory strength of the molecule and the variation on CPL sign within the $\Delta J = 1$ and $\Delta J = 2$ manifold. In contrast to the pseudo-tetrahedral geometry of the phosphinate donor, trigonal planar geometry of the carboxylate donor does not allow the oxygen atom to approach the luminescent Eu^{3+} centre as closely. This leads to a weaker crystal field experienced by Eu^{3+} which reduces the crystal field splitting of the individual ^7F_J electronic states (especially relevant for the 'hypersensitive' $\Delta J = 2$ transition). As a result, the transition multiplet is simplified on both the total emission spectrum and the CPL spectrum. This increases the probability of the CPL sign conservation within a transition by decreasing the total number of individual bands that can produce sequentially opposite sign of CPL.

In this work, the design of the novel EuL complex was aimed on conservation of the CPL sign within both $\Delta J = 1$ and $\Delta J = 2$ transition manifolds. This will make the EuL the best known candidate for the recently proposed Chameleon Security Inks (CSI) concept comprising of a blend of achiral short-lived (ns) luminescent dyes and chiral (or achiral) long-lived (ms) europium(III) emitters.[18] Strong dissymmetry of the $\Delta J = 2$ would generate an additional CPL security layer to the existing five-tier multi-coloured, multi-spectral, opposing helicity security, combined with high spatial and temporal resolution. In addition, the ability to use the brightest $\Delta J = 2$ transition for CPL based security authentication would reduce the required amount of the material and therefore the resulting cost of the security tag, bringing it another step closer towards widespread commercial application.

Results and discussion

Synthesis of EuL

The synthetic design of EuL was based on the examples of the previously reported modular approach for isostructural materials with details provided in the supplementary information (SI Section 6).[19,20,22,24,27] The 'top' aryl-alkynyl (Fig. 1 – red) and the 'bottom' pyridyl (Fig. 1 – blue) components of the sensitising chromophore are synthesised separately (SI Fig. 5 and 6) before they are coupled in a Sonogashira reaction. This provides a functionalisation flexibility to achieve the desired photophysical properties. The chromophore is then mesylated and attached to the 1,4,7-triazacyclononane (TACN) to form a macrocycle containing three chromophores. This if followed by a base-catalysed hydrolysis and complexation to a europium(III) chloride hexahydrate to produce EuL as a racemic mixture. The two enantiomers of EuL were then separated using chiral HPLC (SI Section 3).

General photophysical properties

Similarly to other sensitised lanthanide complexes, a large pseudo-Stokes shift of around 257 nm was observed for EuL

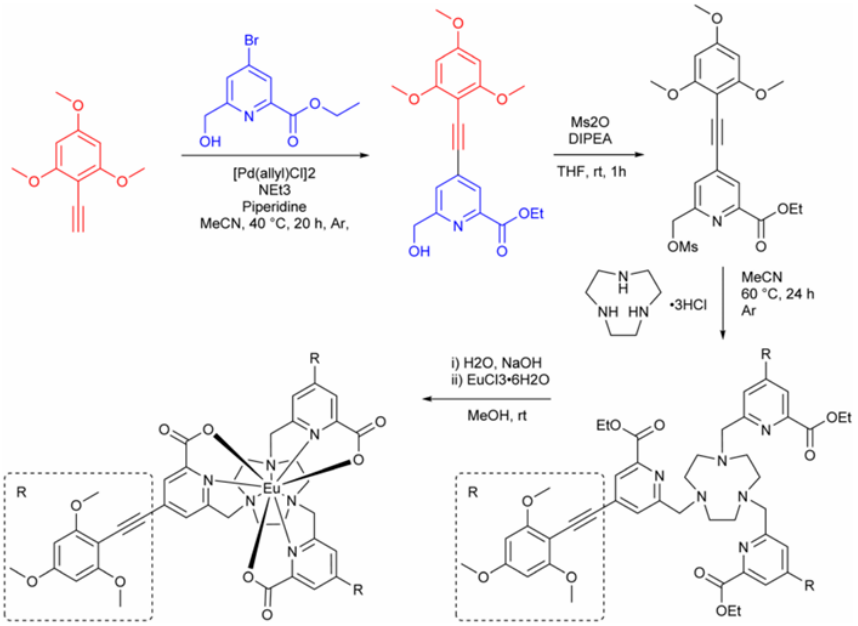

Fig. 1 Reaction scheme for the synthesis of EuL from the arylalkynyl (red) and bromo pyridyl (blue) components of the chromophore.

(Fig. 2A). The band shape match between the absorption and excitation spectra of EuL in MeCN confirmed the sensitised nature of the Eu(III) emission. Importantly, the emission profile was independent of the solvent, which is advantageous for wide security application, where different host material can be used. The quantum yield (Φ) of EuL was measured as 45% in acetonitrile (MeCN) using the absolute method (SI Section 2). The molar extinction coefficient (ε) of EuL was determined as 77 000 $\pm$ 1000 M^{-1} cm^{-1} in MeCN (Fig. 2B). In order to confirm the accuracy, the ε of a single chromophore was measured as 27 000 $\pm$ 200 M^{-1} cm^{-1} in MeCN which was approximately one third of that measured for EuL containing three chromophores.

EuL is sensitised by arylalkynyl pyridyl containing chromophores that are known to possess a photoinduced internal charge transfer (ICT) excited state.[31] This is provided by an electron rich aryl and electron poor pyridyl groups conjugated by the alkyne linker. It was previously reported that the highest occupied molecular orbital (HOMO) of such chromophore is localised on the electron-rich aryl.[21] Therefore, substitution of the aryl with electron-donating groups results in a bathochromic shift of the absorption maximum (λ_{max}) mediated by an increased HOMO energy.[19] This is beneficial for the application in security inks where longer excitation wavelengths such as that of commercially available 365 nm light emitting diodes (LEDs). As a result, λ_{max} of EuL in MeCN was recorded at 358 nm (Fig. 2C), with still 94% of maximal absorbance at 365 nm. A bathochromic shift of λ_{max} with increasing solvent polarity was also observed, which was in agreement with the ICT nature of the transition.[32]

No strong correlation between the emission lifetime (τ) and solvent polarity was observed for the chosen group of solvents with τ values ranging between 1.0 and 0.9 ms at room temperature (Fig. 2D). A significantly lower τ of 0.6 ms was recorded in methanol (MeOH). The experiment was repeated in deuterated methanol (MeOD) to produce a higher τ of 0.9 ms. Since τ obtained in MeOD was similar to the rest of the other alcohols, emission quenching was not attributed to vibrational relaxation of the chromophore excited state *via* O–H oscillators. Instead, the difference in τ was attributed to hydrogen bonding ability of the solvent, where the carboxylate donor group of the chromophore can act as a hydrogen bond acceptor. This decreases the energy of the ICT excited state resulting in a higher rate of the thermally activated back energy transfer (BET) from the excited $^5D_0$ state of Eu(III). This increases the lifetime of the ICT excited state and therefore the probability of nonradiative relaxation processes.

Circularly polarised luminescence spectroscopy and circularly polarised brightness

The two enantiomers of EuL produced mirrored CPL spectra of opposite signs. The enantiomers were assigned as Δ and Λ based on the CPL sign of the $\Delta J = 1$ transition, which was in accordance with the previously reported X-ray crystallographic study of isostructural materials.[33] The racemisation study of

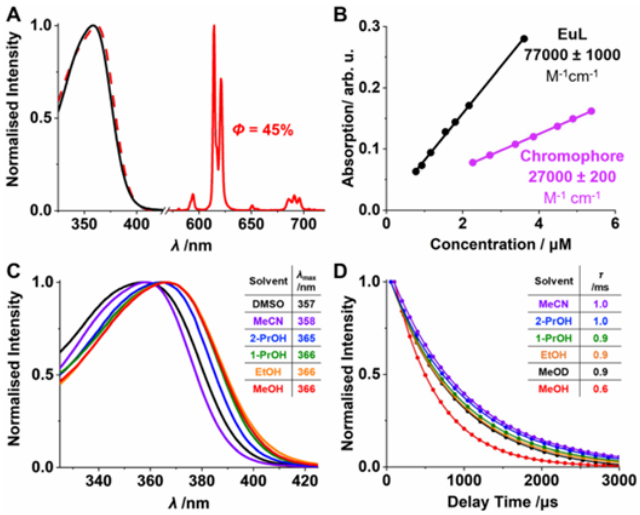

Fig. 2 (A): Normalised absorption (black), excitation (dashed red, $\lambda_{em} = 615$ nm) and emission (red, $\lambda_{exc} = 360$ nm) spectra and Φ of EuL in MeCN. (B): Absorption against concentration of EuL and its chromophore in MeCN. (C): Normalised absorption spectra of EuL in solvents of increasing polarity. (D): Normalised fluorescence emission lifetime of EuL in solvents of increasing polarity [EuL] = 1 μM.

EuL in different solvents at 60 °C determined racemisation half-life of 190 ± 20 hours (SI Section 3, SI Fig. 3), while no racemisation was observed at room temperature. This suggests that EuL would be suitable for security applications with long-term conservation of CPL dissymmetry at ambient conditions and short-term stability towards racemisation during document lamination (150 °C, 1 s cm^{-1}).[18] In addition, CPL profile was independent on solvent (SI Fig. 7) suggesting suitability for a wide-spread application in different host materials with conservation of CPL properties. In contrast to the previously reported CPL spectra of various phosphinate donor complexes,[4,18,20,29] the $\Delta J = 2$ band was highly CPL active with significant sign retention (Fig. 3). This resulted in the peak CPL intensity of the $\Delta J = 2$ (at 615 nm) around 2.5 times higher than that of $\Delta J = 1$ (at 594 nm). The only example with such strongly CPL-active monosign $\Delta J = 2$ band is Eu:BPEPC, a commonly known CPL-standard.[34] The whole $\Delta J = 1$ manifold (588–605 nm) of EuL was single-sign, producing the average g_{lum} of 0.21 and the highest g_{lum} values of +0.30 (at 597 nm) and +0.29 (at 601 nm) for Δ-EuL and −0.29 (at 597 nm) and −0.29 (at 601 nm) for Λ-EuL (Fig. 3). Such outstanding g_{lum} values of EuL are higher than those of most other reported Eu(III) complexes

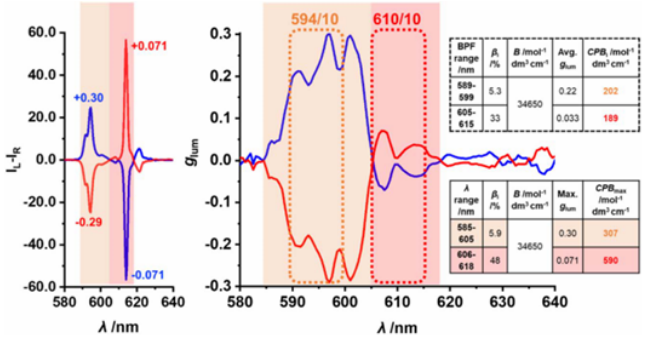

Fig. 3 CPL spectra with maximal g_{lum} values for $\Delta J = 1$ and $\Delta J = 2$ shown (left) and the corresponding g_{lum} plots (right) of Δ-EuL (blue) and Λ-EuL (red) in MeCN ($\lambda_{ex} = 360$ nm, 5 averages) and their maximal with the λ ranges used for CPB calculations shown and the relevant values summarised in the inset tables.

Although there are few examples that report Eu(III) complexes with higher than 0.30 g_{lum} values for the $\Delta J = 1$ transition, they often have lower values of Φ and ε, resulting in lower CPB_i which limits their security application.[17,35] For example, one material demonstrated the g_{lum} values of ± 0.33 (at 600 nm) but a relatively low Φ of 11%.[36] Another example reported similar g_{lum} values of +0.298 and −0.294 but much lower ε (23 000 mol^{-1} dm3 cm^{-1}) and Φ (11%).[37] The material (Cs[Eu(+)-(hfbc)$_4$]) with the highest ever reported g_{lum} of 1.38 (at 595 nm) also has significantly lower ε (35 000 mol^{-1} dm^3 cm^{-1}) and Φ (3%).[38] This highlights the superiority of CPB_i over glum to assess the performance of the CPL emitters for practical applications.

The average g_{lum} of the single-sign region within the $\Delta J = 2$ manifold (606–618 nm) was 0.031 with the highest values of −0.071 (at 607.5 nm) for Δ-EuL and +0.071 (at 607 nm) for Λ-EuL. This puts EuL the third best in terms of previously reported g_{lum} for $\Delta J = 2$ after previously mentioned Cs[Eu(+)-(hfbc)$_4$] producing g_{lum} of 0.25 (at 614 nm) and another material with 0.11 at (616 nm).[34,38] The latter also has lower values of ε (55 000 mol^{-1} dm^3 cm^{-1}) and Φ (11%) which reduces the CPB_i.

In order to assess the applicability of EuL for the use in security tags authenticated by CPLP, CPB_i for the single-sign regions of $\Delta J = 1$ and $\Delta J = 2$ CPL bands were estimated. To account for the variation of the CPL intensity and g_{lum} within the selected (by BPFs) wavelength regions, the average g_{lum} value for each region was used to calculate CPB_i (Fig. 3, top table). As a result, the calculated CPB_i for $\Delta J = 1$ and $\Delta J = 2$ transitions were similar (202 and 189 mol^{-1} dm^3 cm^{-1}), suggesting both transitions can be used for CPLP. Since previously reported CPB values for other materials were calculated using the maximal g_{lum} for each transition, they were also calculated as CPB_{max} (Fig. 3, bottom table) for comparative study. As a result, the maximal CPB_i for $\Delta J = 1$ and $\Delta J = 2$ were calculated as 307 (at 596 nm) and 590 (at 607 nm) mol^{-1} dm^3 cm^{-1} respectively. This puts CPB_i of EuL above the average for both $\Delta J = 1$ and $\Delta J = 2$ (286.6 and 69.4 mol^{-1} dm^3 cm^{-1} respectively) in previously reported CPL-active Eu^{3+} complexes.[17] EuL is the third best in terms of the CPB_i for $\Delta J = 1$ after the recently reported tetrahedral $Eu_4L_4(L')_4$ cages with CPB_i of 3240 and 1122 mol^{-1} dm^3 cm^{-1}.[39] On the other hand, CPB_i for the $\Delta J = 2$ transition in these materials was not reported. The unprecedented CPB_i of 590 mol^{-1} dm^3 cm^{-1} (at 607 nm) produced by the $\Delta J = 2$ of EuL is the highest ever reported to the knowledge of the author with the second best producing almost three times lower value of 213 mol^{-1} dm^3 cm^{-1}.[34]

Circularly polarised luminescence photography

The proposed security tags containing enantiopure EuL would be authenticated with the recently developed CPL photography (CPLP) camera (SI Section 2.3).[18] Its working principle is based on precise alignment of a quarter waveplate (QWP) with 4 different orientations (0°, 45°, 90° and −45°) linear polarisers covering an array of photodiodes. QWP converts CPL into a linearly polarised (LP) light with polarisation plane at 45° (right-hand CPL (RCPL)) and −45° (left-hand CPL (LCPL)) with respect to the fast axis. This LP light then passes through the polarisers before sensitising the underlying photodiodes. This generates sensitivity of the camera towards the CPL sign where 4 simultaneously taken images contain different information on chirality of the light emitted by the probe. For example, if the QWP is aligned with the 45° polarisers, then 0° and 90° channels will be more sensitive towards LCPL (L image) and RCPL (R image) respectively while 45° and −45° will each contain half of the total emitted light intensity. Since chiral probes still emit both LCPL and RCPL, image subtraction is required to generate a 'true' CPL image, which was previously reported as enantioselective differential chiral contrast (EDCC).[28] For example, to obtain a CPL image of a LCPL-active probe, the intensity of the R image can be subtracted from the intensity of the L image (L − R). Since the Fiji (version 1.53q) software[40] doesn't allow for negative intensity, the R − L image of such probe will be zero rather than negative (practically near zero due to solarisation dependent pixel displacement and directional light guided reflection). Therefore, for RCPL-active probes the R − L image will be relevant. The total intensity can be calculated by L + R and used to obtain the CPLP specific dissymmetry factor (g_{CPLP}):

$$g_{CPLP} = 2 \times \frac{(L - R)}{(L + R)} \quad (4)$$

Importantly, when R − L image was used in calculation, the g_{CPLP} value must be multiplied by −1 to account for the negative CPL sign of RCPL:

$$g_{CPLP} = -2 \times \frac{(R - L)}{(L + R)} \quad (5)$$

The choice of the correct formula is based on relative intensity of the L − R and R − L images, where the brightest image is used.

In theory, g_{CPLP} must correlate with g_{lum} due to a similar light polarisation information acquisition principle between the CPLP camera and photo elastic modulator (PEM) based CPL spectrometer. In the CPLP camera blueprint the QWP is fixed and orientations of the linear polariser clusters are used to distinguish the L- and R-CPL, whilst the conventional CPL spectrometer exploits a PEM that serves as a QWP with a variable angular orientation in combination with a fixed linear polariser.

As a result, not only the observed CPL sign but also g_{CPLP} numerical values could be used to authenticate a CPL-active security ink. To test the CPL security performance of EuL, polymethyl methacrylate (PMMA) thin films (200 nm) containing the two enantiomers (labelled as Δ and Λ) were spin coated on glass (SI Section 4) and subjected to CPLP followed by EDCC (Fig. 4). Due to the similarity between the obtained CPB_i values of 202 and 189 mol^{-1} dm^3 cm^{-1} for the wavelength regions of BPF594/10 and BPF610/10, both $\Delta J = 1$ and $\Delta J = 2$ transitions were imaged. The L + R, L − R and R − L calculated images were then used for g_{CPLP} calculations. In contrast to measuring the intensity of the whole image, a specific region of interest was chosen to avoid the error associated with rough edges of the glass substrate which is a source of undesired reflections of the emitted light.

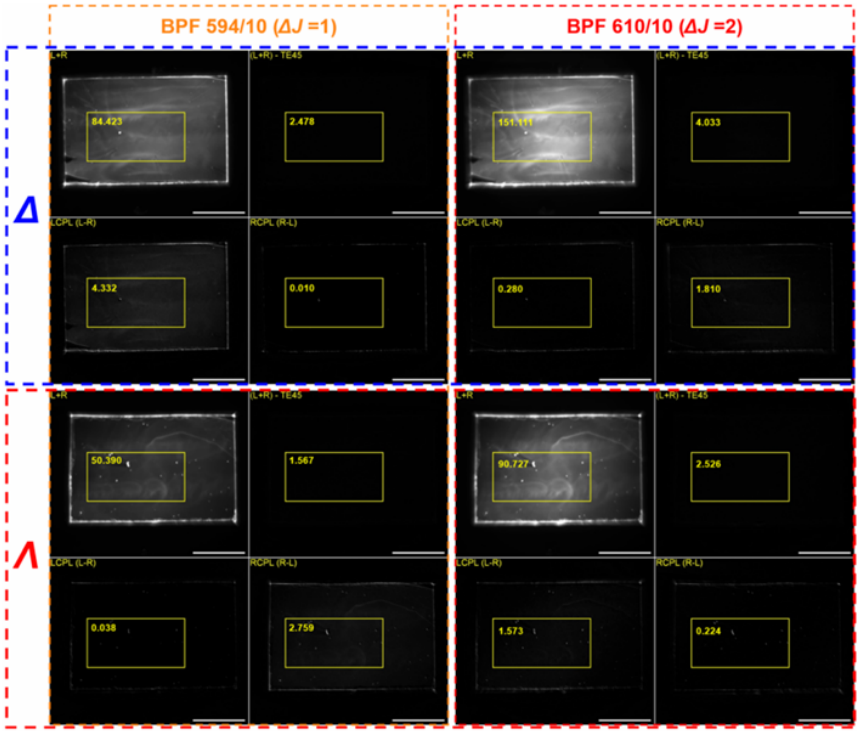

Fig. 4 CPLP calculated images (L + R, (L + R)-TE45*, L − R and R − L) of the spin coated PMMA films under 365 nm excitation containing Δ (top two rows) and Λ (bottom two rows) enantiomers of EuL_1 using BPF594/10 (two left columns) and BPF610/10 (two right columns) with regions of interest for g_{CPLP} calculations and their average intensities shown in yellow. Scale bar = 5 mm. R − L and L − R images are 6 times contrast enhanced for display.*TE45 image is a sum of the two images generated from 45° and −45° channels that have no CPL sign preference (QWP aligned with 45° polarisers) and record half of the total intensity each; subtraction of TE45 from (L + R) should theoretically produce an image with zero intensity, which is practically nonzero due to experimental error.

As expected, each enantiomer produced intensity in either L − R or R − L depending on the BPF used. This correlated with the CPL sign of each enantiomer within the selected wavelength regions of the $\Delta J = 1$ and $\Delta J = 2$ manifolds. For example, the CPL spectrum of *Δ*-EuL has a positive sign in 589–599 nm region (BPF594/10, $\Delta J = 1$) and a negative sign in 605–615 nm region (BPF610/10, $\Delta J = 2$), which correlated with L − R and R − L images when using BPF594/10 and BPF = 610/10 respectively. The g_{CPLP} values were then calculated from the L − R and R − L images as +0.10 and −0.0024 respectively. When compared to the average g_{lum} values recorded using a PEM-CPL spectrometer for the equivalent wavelength regions (+0.21 for 589–599 nm and −0.033 for 605–615 nm and), it was evident that the magnitude of dissymmetry factor produced by the *Δ*-EuL containing film in $\Delta J = 1$ and $\Delta J = 2$ decreased by ∼50% and ∼30%. Similar results were obtained for the film containing *Λ*-EuL, where the g_{CPLP} value of −0.11 decreased by ∼50% compared to g_{lum} of −0.22 for $\Delta J = 1$; however, remained essentially the same for the $\Delta J = 2$ where $g_{CPLP} = +0.035$ and $g_{lum} = +0.033$.

To confirm that the reduction in g_{CPLP} is not a product of a random error, the calculation was repeated for multiple films that were sequentially spin coated using the same method as for the original film (SI Fig. 10 and 11). This could also determine whether the structural imperfections of the spin-coated films significantly impact the g_{CPLP}.

As a result, all 4 films consistently produced nearly identical g_{CPLP} values when using the same BPF, resulting in 50% and 30% g_{CPLP} reduction for the $\Delta J = 1$ (BPF594/10) and $\Delta J = 2$ (BPF610/10) respectively compared that of the *Δ*-EuL solution (Table 1). It was hypothesised that such reduction in g_{CPLP} resulted from reflection of CPL from the glass substrate that led to the sign inversion. The stronger effect observed in the 589–599 nm region could be attributed to shorter wavelength light being more susceptible to scattering compared to that of longer wavelength.

Table 1 Comparison of the g_{CPLP} of spin-coated Δ-EuL PMMA films on glass with Δ-EuL in MeCN over the applied band-pass filter (BPF) range

	Glass substrate g_{CPLP}					
BP filter	1	2	3	4	Solution state g_{CPLP}	% g_{CPLP} reduction
BPF594/10	+0.10	+0.10	+0.11	+0.11	+0.21	50%
BPF610/10	−0.024	−0.024	−0.024	−0.024	−0.031	30%

Table 2 Comparison of g_{CPLP} for 6 sequentially spin-coated Δ-EuL PMMA films on glass and Δ-EuL in MeCN over the applied band-pass filter (BPF) range

	Black tape substrate g_{CPLP}							
BP filter	1	2	3	4	5	6	Solution state g_{CPLP}	% g_{CPLP} reduction
BPF594/10	0.17	0.17	0.16	0.17	0.17	0.16	0.21	20%
BPF610/10	−0.038	−0.039	−0.037	−0.041	−0.037	−0.038	−0.031	—

To test this proposal, the glass substrate was covered with black matt tape, which is non-reflective in the wavelength of interest, non-emissive under 365 nm irradiation (SI Fig. 9) and not soluble in DCM. The same solution of Δ-EuL was then used to prepare 6 spin-coated PMMA films for CPLP (SI Fig. S12).

Similarly to the films spin-coated on glass, the obtained g_{CPLP} values (Table 2) were consistent across the 6 films using both BPFs which suggested high reproducibility of the method. The change of substrate increased the g_{CPLP} for the $\Delta J = 1$ (BPF594/10); however, they are slightly lower (20%) compared to the solution. Similarly to that, the g_{CPLP} for the $\Delta J = 2$ increased (BPF610/10) to become essentially equal to its g_{lum} equivalent.

In order to confirm the substrate dependence of the g_{CPLP}, the experiment was repeated with solution state EuL. Black non-reflective in the wavelength region of interest non-emissive plastic caps (SI Fig. S9) were filled with Δ-EuL, Λ-EuL and racemic EuL solutions in acetonitrile of equal concentration and placed within a single frame for CPLP and EDCC (Fig. 5). The relevant areas of the calculated images were then used to calculate g_{CPLP} values of 0.21 and −0.17 for Δ-EuL and Λ-EuL respectively when using the BPF594/10 and ± 0.031 for the BPF610/10. This correlated with the g_{lum} values within the experimental error for dissymmetry factor of around ± 0.02 (~11%) for the $\Delta J = 1$ possessing brightest CPL and around ± 0.003 (~9%) for $\Delta J = 2$ when reflection is minimal. The racemate did not produce a significant intensity in either L − R or R − L images as expected.

The experimental error associated with CPLP could arise from the photoexcitation of the stage not being perfectly homogenous leading to unequal spatial excitation of the sample. As a result, certain pixels of the camera module might get oversaturated, serving as a source of error in image calculation. Moreover, the pixels within the module are not identical and might have slightly different sensitivity. The same applies

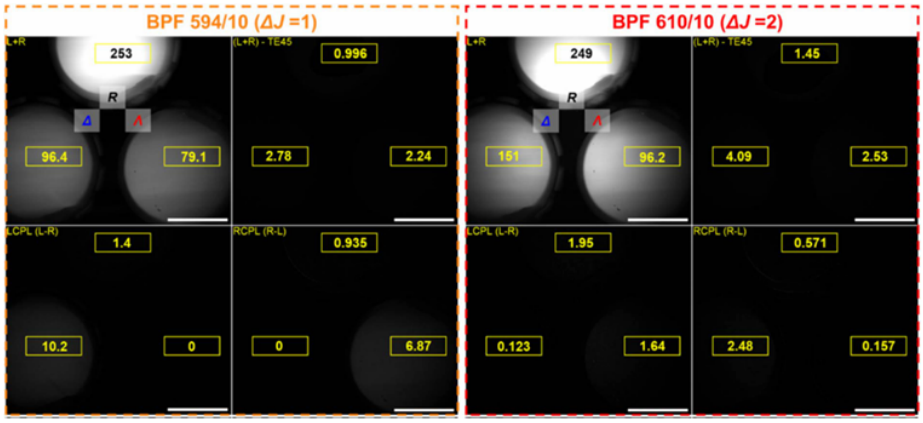

Fig. 5 2 sets (using BPF594/10 and BPF610/10) of 4 CPLP images: (L + R, (L + R)-TE45, L − R, R − L) of the Δ (bottom left), Λ (bottom right) and racemic (R) (centre top) samples of EuL under 365 nm excitation with the regions of interest for g_{CPLP} and their average intensities shown in yellow. Scale bar = 5 mm.

to the imperfect alignment of the linear polarisers at each pixel. If distribution of such pixels is not random, the error is generated when a specific area of an image is selected for the average intensity measurement. Another source of error could be associated with inelastic scattering of the excitation light by the sample, making it fall into the detection wavelength range. Such light would likely be linearly polarised, and therefore L and R channels would be subjected to linear dichroism.

Since each enantiomer of EuL produces $\Delta J = 1$ and $\Delta J = 2$ of mutually opposite CPL sign, a single enantiomer results in detectable intensity in either (L − R) or (R − L) images depending on the BPF used. This makes EuL a unique security ink that simultaneously incorporates two CPL security layers. In contrast to this, most other reported CPL-active Eu^{3+} complexes could only produce detectable intensity in the wavelength region of the $\Delta J = 1$ band.

As a proof of concept, two films spin coated on the matt black tape containing one enantiomer each were imaged together. For example, an authentic tag would contain Δ-EuL on the left-hand side and Λ-EuL on the right-hand side (right and left can be replaced with different parts of the security tag pattern). The left-hand side would then appear on the L − R image when using BPF594/10 ($\Delta J = 1$) and R − L image when using BPF610/10 ($\Delta J = 2$). Simultaneously, the right-hand side will show on the R − L image with the BPF610/10 and L − R image with the BPF594/10 (Fig. 6). Since sequentially produced films resulted in consistent g_{CPLP} values in both BPF594/10 and BPF610/10, the tag can be further secured by cross-checking the g_{CPLP} numerical values for each spatial region with the expected threshold. The whole sequence can be then automated and combined with other security layers as chromatic (colour), spectral (emission profile) and temporal (time-gating to cut off nanosecond scale emission of organic dyes present, lifetime of the both Δ- and Λ-EuL in PMMA films were measured as 0.8 ± 0.1 ms – see SI Fig. 14) that are already present in banknotes and identification documents.[1]

During prolonged experiments using CW excitation in excess of 1 hour, using our commercially available 365 nm UV LED irradiation source (1 W total power, collimated and focused to a $d = 1$ cm circle) we have not recorded any photodegradation and loss of CPL intensity of the studied films. These observations of photostability are based on camera exposure time and CPB being constant and unaltered throughout the studies.

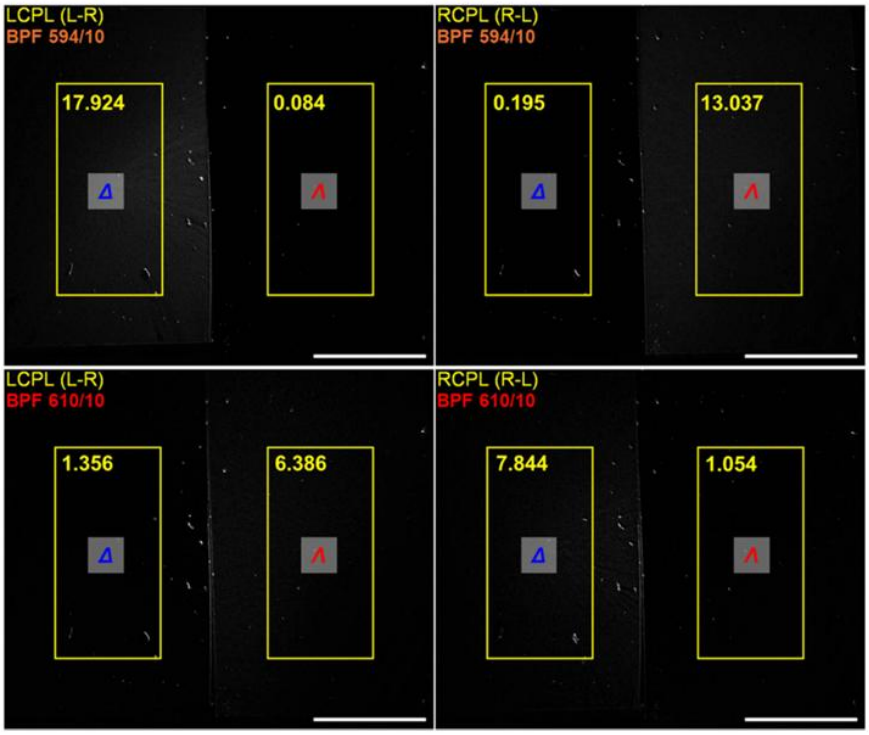

Fig. 6 CPLP calculated images used for authentication of the proof-of-concept security tag containing Δ-EuL_1 (left of each image) and Λ-EuL_1 (right of each image) under 365 nm excitation with average intensities of the regions of interest shown in yellow scale bar = 5 mm.

Conclusion

A novel bright CPL-active quasi-C_3 symmetric EuL complex containing all carboxylate donor groups was prepared, chirally separated and photophysically characterised. EuL was exceptionally bright due to high values of the quantum yield (45%) and molar extinction coefficient (77 000 M^{-1} cm^{-1}) while its near 365 nm maximal absorbance suggested optimal excitation by commercially available 365 nm UV LEDs. Invisible to the unaided naked eye, their large *pseudo*-Stokes' shift allowed for absorption in the UV and emission in the visible regions. Emission lifetime on the millisecond time scale allows for temporal separation by time gating out nanosecond time-scale emission of applied organic dyes. Both $\Delta J = 1$ and $\Delta J = 2$ transitions demonstrated strong monosign CPL with CPB_{max} values of 307 mol^{-1} cm^{-1} at 596 nm and 590 mol^{-1} cm^{-1} at 607 nm respectively, rendering it to be best known candidate up to date for CPL security ink so far. The CPB_i was also calculated for the 594 ± 5 nm and 610 ± 5 nm single sign regions selected by BPFs to confirm the suitability of both transitions for authentication by CPLP. EuL was embedded into solid-state PMMA spin-coated thin films for a Proof of Concept (POC) security tag. Both enantiomers were successfully authenticated *via* CPLP and EDCC where dissymmetry of both $\Delta J = 1$ and $\Delta J = 2$ transitions was rapidly detected. The recorded dissymmetry was also quantified using the newly introduced term g_{CPLP} and the results compared to the average g_{lum} values recorded by the PEM-CPL spectrometer in the same wavelength regions. The g_{CPLP} values calculated from the EDCC images of solutions of EuL enantiomers were in good agreement with the g_{lum} values; however, the g_{CPLP} was significantly reduced in PMMA films on a glass substrate. The proposed hypothesis of dissymmetry reduction *via* reflection induced CPL sign cancellation from substrate was confirmed by replacing glass with black non-reflective tape that recovered the magnitude of g_{CPLP}. The g_{CPLP} values remained consistent across multiple sequentially spin-coated films, suggesting high repeatability and consistent CPL security feature.

Spurred on from the reliability of g_{CPLP} as a performance indicator for CPL active chiral emitters when measured using our polarisation sensitive CPLP camera,[18] as a future direction we propose to use blends of enantiopure Ln(III)-complexes utilising CPL-fingerprint engineering resulting in the 2nd generation of more sophisticated CPL-CSIs (Chameleon Security Inks). The sign, and importantly the recorded numerical dissymmetry factor (g_{CPLP} *via* CPLP) of these blended dyes, can be compared to an expected value during authentication. This will take security to another level, as the same exact blend of enantiopure (Δ and Λ) Ln(III) complexes and their precise enantiomeric ratios would need to be replicated to counterfeit such security inks.

Statistics and reproducibility

Where instruments incorporating a scanning monochromator have been used (absorption, emission, and excitation spectra) each sample has been recorded and averaged as triplicate measurements. Spectra, where CCD detectors have been employed, have been measured as an average of one hundred to a thousand spectra on triplicate samples according to the protocol detailed in the SI Section.

Author contributions

AK: synthesised EuL complex, performed all photophysical measurements, assisted in chiral HPLC separation, contributed to the concept of CPLP and LED carousel design drafted and edited the manuscript. DJB: performed all 2-photon and quantum yield studies and edited the manuscript. AC: performed chiral HPLC analysis and separation. RP: secured project funding, conceptualised CPLP and associated detection methodology, designed the LED carousel, performed independent validation experiments, drafted and edited the manuscript.

Conflicts of interest

R. P. is inventor on patent WO2016174395A1: light detecting apparatus for simultaneously detecting left-and right-handed circularly polarised light. R. P., D. J. B. and A. K. are inventors on patent application P408669.GB.01: Apparatus and method for detecting circularly polarised light. There are no other competing interests.

Data availability

All data generated and analysed during this study including spectra and drawings are available from the corresponding author upon request.

Code availability: custom codes written and developed and used during this study are available from the corresponding author upon request on a collaboration basis.

Supplementary information (SI) is available. See DOI: https://doi.org/10.1039/d5sc05303j.

Acknowledgements

R. P. and D. J. B thank the BBSRC (BB/S017615/1 and BB/X001172/1), and the EPSRC (EP/X040259/1) for funding. A. K. and R. P thanks EPSRC DTP (DU) for the PhD support. All authors thank Dr Davide De Rosa for help with chromophore arm precursor synthesis strategy, Dr Franco Pilar and Daicel for their invaluable help with chiral HPLC separation, Kelvin Appleby for the construction of the USB powered signal generator box, LED carousel and control box, Josephine Binks and Marcos Perez-Pucheta for their help with AFM studies and Dr Patrycja Brook for the assitance with photoluminescence quantum yield measurements.

References

1 L. E. MacKenzie and R. Pal, *Nat. Rev. Chem.*, 2020, **5**, 109–124.
2 A. T. Frawley, R. Pal and D. Parker, *Chem. Commun.*, 2016, **52**, 13349–13352.

3 Y. Kitagawa, S. Wada, M. D. J. Islam, K. Saita, M. Gon, K. Fushimi, K. Tanaka, S. Maeda and Y. Hasegawa, *Commun. Chem.*, 2020, **3**, 119.
4 D. F. De Rosa, M. Starck, D. Parker and R. Pal, *Chem.–Eur. J.*, 2024, **30**, e202303227.
5 B. Hardwick, W. Jackson, G. Wilson and A. W. H. Mau, *Adv. Mater.*, 2001, **13**, 980–984.
6 M. R. Carro-Temboury, R. Arppe, T. Vosch and T. J. Sørensen, *Sci. Adv.*, 2018, **4**, e1701384.
7 E. L. Prime and D. H. Solomon, *Angew. Chem., Int. Ed.*, 2010, **49**, 3726–3736.
8 S. Baek, E. Choi, Y. Baek and C. Lee, *Digital Signal Process.*, 2018, **78**, 294–304.
9 A. K. Singh, S. Singh and B. K. Gupta, *ACS Appl. Mater. Interfaces*, 2018, **10**, 44570–44575.
10 P. Kumar, J. Dwivedi and B. K. Gupta, *J. Mater. Chem. C*, 2014, **2**, 10468–10475.
11 E. Sonnex, M. J. Almond, J. V. Baum and J. W. Bond, *Spectrochim. Acta, Part A*, 2014, **118**, 1158–1163.
12 R. Arppe and T. J. Sørensen, *Nat. Rev. Chem.*, 2017, **1**, 0031.
13 E. Imperio, E. Calò, L. Valli and G. Giancane, *Vib. Spectrosc.*, 2015, **79**, 52–58.
14 M. Gariup and J. Piskorski, *Int. J. Crit. Infrastruct. Prot.*, 2019, **24**, 100–110.
15 I. M. Lancaster and A. Mitchell, in *Optical Document Security*, ed. R. L. Van Renesse, Artech House, Norwood, San Jose, CA, 3rd edn, 2004, p. 34.
16 F. Zinna, C. Resta, S. Abbate, E. Castiglioni, G. Longhi, P. Mineo and L. Di Bari, *Chem. Commun.*, 2015, **51**, 11903–11906.
17 L. Arrico, L. Di Bari and F. Zinna, *Chem.–Eur. J.*, 2021, **27**, 2920–2934.
18 D. F. De Rosa, P. Stachelek, D. J. Black and R. Pal, *Nat. Commun.*, 2023, **14**, 1537.
19 M. Soulié, F. Latzko, E. Bourrier, V. Placide, S. J. Butler, R. Pal, J. W. Walton, P. L. Baldeck, B. Le Guennic, C. Andraud, J. M. Zwier, L. Lamarque, D. Parker and O. Maury, *Chem. -Eur. J.*, 2014, **20**, 8636–8646.
20 N. H. Evans, R. Carr, M. Delbianco, R. Pal, D. S. Yufit and D. Parker, *Dalton Trans.*, 2013, **42**, 15610–15616.
21 A. D'Aléo, A. Picot, A. Beeby, J. A. Gareth Williams, B. Le Guennic, C. Andraud and O. Maury, *Inorg. Chem.*, 2008, **47**, 10258–10268.
22 S. J. Butler, L. Lamarque, R. Pal and D. Parker, *Chem. Sci.*, 2014, **5**, 1750–1756.
23 S. J. Butler, M. Delbianco, L. Lamarque, B. K. McMahon, E. R. Neil, R. Pal, D. Parker, J. W. Walton and J. M. Zwier, *Dalton Trans.*, 2015, **44**, 4791–4803.
24 E. R. Neil, A. M. Funk, D. S. Yufit and D. Parker, *Dalton Trans.*, 2014, **43**, 5490–5504.
25 S. J. Butler, M. Delbianco, N. H. Evans, A. T. Frawley, R. Pal, D. Parker, R. S. Puckrin and D. S. Yufit, *Dalton Trans.*, 2014, **43**, 5721–5730.
26 M. Starck, J. D. Fradgley, D. F. De Rosa, A. S. Batsanov, M. Papa, M. J. Taylor, J. E. Lovett, J. C. Lutter, M. J. Allen and D. Parker, *Chem.–Eur. J.*, 2021, **27**, 17921–17927.
27 J. W. Walton, A. Bourdolle, S. J. Butler, M. Soulie, M. Delbianco, B. K. McMahon, R. Pal, H. Puschmann, J. M. Zwier, L. Lamarque, O. Maury, C. Andraud and D. Parker, *Chem. Commun.*, 2013, **49**, 1600–1602.
28 P. Stachelek, L. MacKenzie, D. Parker and R. Pal, *Nat. Commun.*, 2022, **13**, 553.
29 A. T. Frawley, *Highly emissive chiral lanthanide(III) complexes for labelling and imaging*, Doctoral thesis, Durham University, 2017.
30 M. Delbianco, L. Lamarque and D. Parker, *Org. Biomol. Chem.*, 2014, **12**, 8061–8071.
31 M. Latvaa, H. Takalob, V.-M. Mukkala, J. C. Rodriguez-Ubisd and J. Kankarea, *J. Lumin.*, 1997, **75**(2), 149–169.
32 J. R. Lakowicz and B. R. Masters, *Principles of Fluorescence Spectroscopy*, 3rd edn, 2008, vol. 13.
33 J. W. Walton, R. Carr, N. H. Evans, A. M. Funk, A. M. Kenwright, D. Parker, D. S. Yufit, M. Botta, S. De Pinto and K.-L. Wong, *Inorg. Chem.*, 2012, **51**, 8042–8056.
34 M. Starck, L. E. MacKenzie, A. S. Batsanov, D. Parker and R. Pal, *Chem. Commun.*, 2019, **55**, 14115–14118.
35 D. Thakur and S. Vaidyanathan, *J. Mater. Chem. C*, 2025, **13**, 9410–9452.
36 J. W. Walton, L. D. Bari, D. Parker, G. Pescitelli, H. Puschmann and D. S. Yufit, *Chem. Commun.*, 2011, **47**, 12289–12291.
37 S. Petoud, G. Muller, E. G. Moore, J. Xu, J. Sokolnicki, J. P. Riehl, U. N. Le, S. M. Cohen and K. N. Raymond, *J. Am. Chem. Soc.*, 2007, **129**, 77–83.
38 J. Kumar, B. Marydasan, T. Nakashima, T. Kawai and J. Yuasa, *Chem. Commun.*, 2016, **52**, 9885–9888.
39 Y. Zhou, H. Li, T. Zhu, T. Gao and P. Yan, *J. Am. Chem. Soc.*, 2019, **141**, 19634–19643.
40 J. Schindelin, I. Arganda-Carreras, E. Frise, V. Kaynig, M. Longair, T. Pietzsch, S. Preibisch, C. Rueden, S. Saalfeld, B. Schmid, J.-Y. Tinevez, D. J. White, V. Hartenstein, K. Eliceiri, P. Tomancak and A. Cardona, *Nat. Methods*, 2012, **9**, 676–682.

Complete Stereochemical Control to Unlock Monosign Circularly Polarised Luminescence with Superior Circularly Polarised Brightness for Chameleon Security Inks

Artemijs Krimovs,[1] Dominic J. Black[1], Aileen Congreve[1] and Robert Pal[1]*

[1]Department of Chemistry, Durham University, South Road, Durham, DH1 3LE, UK

*robert.pal@durham.ac.uk

Supplementary Information

Table of Contents

1. General procedures

All starting materials are commercially available and distributed by Merck. Analytical and HPLC grade solvents were used and degassed using freeze-pump-thaw or cycling where appropriate.

Silica gel plates on aluminium support (0.2 mm thick, 60 F254, Merck) were used in thin layer chromatography (TLC) and resolved under UV radiation source at 254 or 365 nm. Flash column chromatography was manually prepared using silica gel (60 (230-400 mesh, Flourochem).

Preparative reverse-phase HPLC was performed using a Shimadzu module comprising of a Vacuum Degasser (DGU-20AR5), a Prominence Liquid Chromatography pump (LC-20AP), a Prominence UV-Vis Detector (SPD-20A) and a Communications Bus Module (CBM-20A). Sample separation was performed using a preparative XBridge C_{18} OBD column (19 × 100 mm, 5 µm, flow rate = 17 cm^3 min^{-1}) with fractions collected manually. The solvent system was a mixture of H_2O and MeCN, where the proportion of the two solvents was varied in time(Table 1).

Table 1: proportion of H_2O and MeCN or MeOH solvents in time-dependent gradient elution.

Step	Time/ mins	H_2O fraction	MeCN fraction
0	0	0.9	0.1
1	4	0.9	0.1
2	14	0	1
3	19	0	1
4	22	0.9	0.1

^1H and ^{13}C NMR was performed on A Bruker Advance-400 (^1H at 400.06 MHz and^{13}C at 100.61 MHz), a Mercury 400 (^1H at 399.95 MHz), a Varian VNMRS-600 (^1H at 599.67 MHz and ^{13}C at 150.79 MHz) or a Varian VNMRS-700 (^1H at 699.73 MHz and ^{13}C at 175.95 MHz) using deuterated chloroform (Merck). Chemical shifts and J-couplings were reported in ppm and Hz respectively.

Electrospray ionisation mass spectrometry was performed on a TQD mass spectrometer containing an Aquity UPLC system and an electrospray ionisation source. Accurate mass determination was performed on an LCT Premier XE mass spectrometer or a QToF Premier Mass spectrometer. All mass spectrometers were equipped with an Aquity photodiode array detector (Waters Ltd., UK).

2. Photophysical measurements

2.1. Absorption, emission and lifetime measurements

All solution state optical analyses were carried out in quartz cuvettes with a path length of 1.0000 cm. Solid state (PMMA) samples were recorded using a custom-built holder. UV-Vis absorption was measured on an ATI Unicam UV-Vis spectrometer (Model UV2) using Vision software (version 3.33). Emission experiments were performed on an ISA Jobin-Yvon Spex Fluorolog-3 luminescence spectrometer using DataMax software (version 2.2.10). Lifetime was measured with a Perkin Elmer LS55 spectrometer using FL Winlab software either in solution state (using a range of solvents (Main text Figure 2D) or neat PMMA films (Figure S14). All emission experiments were performed at 1 μM solution concentration. Absolute photoluminescent quantum yields were determined using a Horiba FluoroMax Plus fitted with a QuantaPhi-2 integrating sphere in solution state (MeCN). All samples were recorded at 1 μM in a 1 cm by 1 cm path length quartz cuvette with four clear sides. Excitation and emission slits were fixed at 2 nm with neutral density filters (ThorLabs, NEK01S) used at the excitation aperture to maintain a signal of approximately 10^6 cps at the excitation wavelength.

2.2.CPL spectroscopy

CPL was measured with a home-built (modular) spectrometer.[1] The excitation source was a broad band (200 – 1000 nm) laser- driven light source EQ 99 (Elliot Scientific). The excitation wavelength was selected by feeding the broadband light into an Acton SP-2155 monochromator (Princeton Instruments); the collimated light was focused into the sample cell (1 cm quartz cuvette). Sample PL emission was collected perpendicular to the excitation direction with a lens (f = 150 mm). The emission was fed through a photoelastic modulator (PEM) (Hinds Series II/FS42AA) and through a linear sheet polariser (Comar). The light was then focused into a second scanning monochromator (Acton SP2155) and subsequently on to a photomultiplier tube (PMT) (Hamamatsu H10723 series). The detection of the CPL signal was achieved using the field modulation lock-in technique. The electronic signal from the PMT was fed into a lock-in amplifier (Hinds Instruments SignaLoc Model 2100). The reference signal for the lock-in detection was provided by the PEM control unit. The monochromators, PEM control unit and lock-in amplifier were interfaced to a desktop PC and controlled by a custom-written LabVIEW graphic user interface. The lock-in amplifier provided two signals, an AC signal corresponding to (IL- IR) and a DC signal corresponding to (IL+ IR) after background subtraction. The emission dissymmetry factor was therefore readily obtained from the experimental data, as 2 AC/DC. Spectral calibration of the scanning monochromator was performed using a Hg-Ar calibration lamp (Ocean Optics, HG-2). A correction factor for the

wavelength dependence of the detection system was constructed using a calibrated lamp (Ocean Optics, HL-2000). The measured raw data was subsequently corrected using this correction factor. The validation of the CPL detection systems was achieved using light emitting diodes (LEDs) at various emission wavelengths. The LED was mounted in the sample holder and the light from the LED was fed through a broad band polarising filter and $\lambda/4$ plate (ThorLabs, LPVISE100-A and AQWP05M-600) to generate circularly polarised light. The emission spectra were recorded with 0.5 nm step size and the slits of the detection monochromator were set to a slit width corresponding to a spectral resolution of 0.25 nm. CPL spectra (as well as total emission spectra) were obtained through an averaging procedure of several scans.; all calculations were carried out using raw spectral data. Prior to all measurements, the $\lambda/4$ plate and a LED were used to set the phase of the lock-in amplifier correctly.

2.3. Circularly polarised luminescence photography (CPLP) and enantioselective differential chiral contrast (EDCC)

The CPLP handheld instrument for EDCC comprises of an externally triggered Kiralux® polarisation 5.0 Megapixel CMOS USB camera (CS505MUP1, Thorlabs). It is synchronised to a 365 nm LED (Nichia, 5.2V, 500mW) flash illuminator driven by an internal custom built signal generator module operating at master frequencies of 0.1, 1 or 10 Hz. This device has been constructed to be able to provide both a variable illumination (1 ms - 1 s) and image acquisition (0.027 ms – 14 s) sequence with a constant 20 µs time delay between the two pulses to allow discrimination of short lived organic (ns- µs) and long-lived lanthanide pseudo phosphorescence (ms). The chiroptical separator of the apparatus comprises of the built in pixel decoded wire grid polariser array complemented by a precisely aligned broad wavelengths (λ = 400 – 800 nm) quarter waveplate (QWP, Thorlabs AQWP05M-600), a machine vision (Navitar f = 25mm/F1.4) objective lens (interchangeable to a LWD f-50 mm/F2.8 lens and 0.63x video relay lens (Edmund Optics) for epifluorescence microscopy) and a selectable filter wheel containing high precision narrow band pass filters (such as Edmund optics BP546/10, BP589/10, BP594/10, and BP610/10) to achieve chromatic discrimination.

Camera control and image acquisition were performed with ThorLab's commercial camera software ThorCam™ or an adapted custom LabView code to facilitate time-resolved detection and controlled external camera triggering.[43] The camera was operated in quad view (Figure SI 20) where the 16-bit overlayed total image has been split up into four individual 8-bit images decoding each wire grid polariser state orientation (0, 90, 45 and -45 degree) captured image as a 2 x 2 array in one captured frame. These images were generated by area defined crop and paste individual image generation without pixel position reassignment. Such as the

previously reported EDCC using our recently developed CPL-LSCM, this one step resolution preserving (lossless compression) image processing is achieved using a custom written script (macro) in ImageJ (v1.53).[2] EDCC imaging was also built into our custom written macro 2.0 or can be post processed using ImageJ's built-in image calculator add-on software by subtracting one CPL channel from the other, and vice versa. The convention used herein is: left-handed enantioselective contrast = left CPL – right CPL; right-handed enantioselective contrast = right CPL – left CPL. Images were recorded with the camera's native 2448 x 2048 pixel field of view (FOV) without image cropping with total accumulated integration time varied from 20 ms to 1 s with 5 – 32 frame averaged sequences. The total integration time has been determined case by case by careful monitoring of maximum 8-bit pixel values to eliminate pixel saturation and achieve maximum overall image brightness for EDCC calculation.

The all-important 8-bit average pixel chiroptical contrast value calculations were facilitated by selecting and averaging equal size and shape arbitrary area portions of the sample. Due to the 2448 x 2024 pixel size of each recorded image total field of view (FOV), this arbitrary area has been kept at a constant size of 300 x 600 pixels region of interest (ROI). The average maximum 8-bit greyscale pixel intensity values were determined using ImageJ Analyse-Measure macro with mean ROI intensity value mode that employs a maximum average value ROI histogram methodology that is based on a standard Gaussian distribution profiling of the average intensity values. Due to the employed methodology and the averaging nature of image acquisition and ROI calculation, the limit of detection (error associated with) 8-bit greyscale contrast value is below 1% (< 3 average greyscale value/pixel on a 0 – 255 pixel intensity scale). This is determined using the total europium emission image and the selected arbitrary ROI area selection is then kept identical throughout the imaging sequence resulting in high precision chiroptical contrast calculations.

2.4. Two photon cross section determination

The cross-section (σ^2) is calculated according to established procedures:[3]

$$\sigma^2 = \frac{F_S}{\phi_S C_S} \times \frac{\phi_R C_R \sigma_R^2}{F_R} \#[1]$$

where *S* is sample, *R* is reference, ϕ is the total emission quantum yield of the EuL (ϕ_S), *C* is the concentration, *n* is the refractive 7 index and F_S (λ) and F_R (λ) are the integrated PL spectrum for the sample and reference, respectively. Additionally, the two-photon nature of the excitation process was proven by recording an excitation power dependence; the resulting line has a slope of two on a logarithmic scale.[4] The cross sections were calculated with reference to Rhodamine B in methanol.

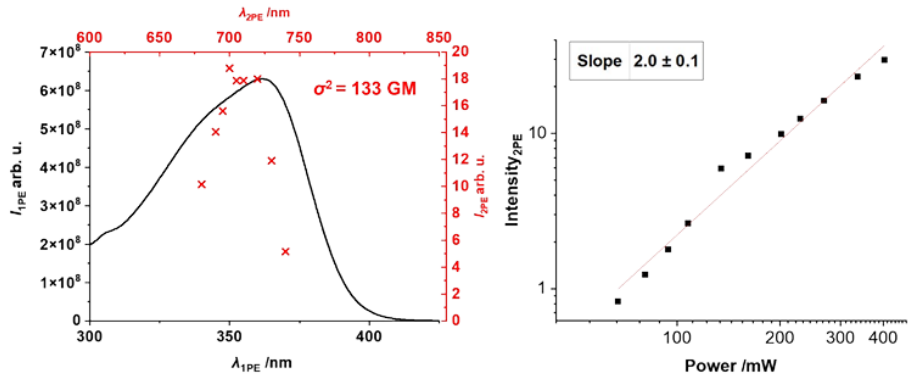

Figure S1: 1PE (black) and 2PE (red) spectra (λ_{em} = 615 nm) of EuL in MeCN (left) and integrated emission intensity plot against the laser excitation power (λ_{2PE} = 700 nm) on a logarithmic scale (right); GM = 10^{-50} cm^4 s $photon^{-1}$.

Two photon spectroscopy was performed using a tuneable femtosecond pulsed laser (680 – 1300 nm, Coherent Discovery TPC, 100 fs, 80 MHz) perpendicularly mounted to an Ocean Optics HR2000Pro (2048- pixel linear CCD Sony ILX5 chip, 200 µm slit, H3 grating, 350 – 850 nm spectral region) spectrometer.[5] The laser beam was focused onto the centre of the 1 cm path sample holder (Thor labs CVH100) by a dedicated ultrafast laser lens (Edmund Optics 11711, 50 mm focal length). The spectrometer has also been equipped with a perpendicularly mounted 365 nm LED (nichia, 1W) and been operated using a modified version of the above-mentioned custom time resolved detection and accumulation algorithm written in Labview2013 program. In order to eliminate unwanted artefacts associated with stray light from MP excitation the spectrometer have been equipped with a rotating filter wheel (Thor Labs, CFW6) housing an LP420 (Comar Optics, for 365 nm UVLED excitation) and SP650 and SP700 (Edmund Optics, 8472 and 8474 for MP excitation) filters.

3. Chiral HPLC and Racemisation Studies.

Chiral HPLC was performed using a Perkin Elmer Series 200 module consisting of a Perkin Elmer Series 200 pump, autosampler, UV-Vis detector and either CHIRALPAK-IE or IB N-5 columns (4.6 × 250 mm, flow rate = 2 ml min^{-1} at 40 °C). The solvent system consisted of EtOH/MeOH/TEA/TFA at 50/50/0.5/0.3 ratio; injection volume: 50 µL; sample concentration: 0.5 mg/ml in acetonitrile.

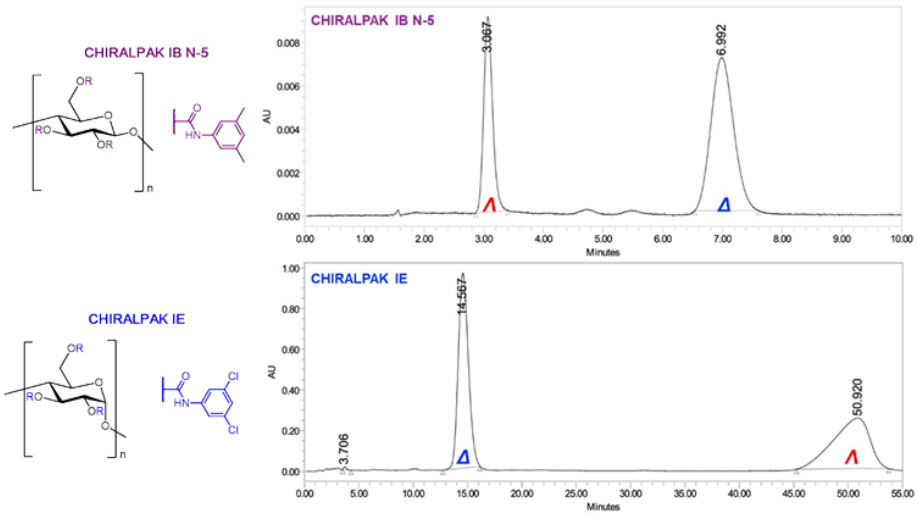

Figure S2: chiral high performance liquid chromatography (CHPLC) chromatogram (360 nm) for the chiral separation of the enantiomers of EuL using the CHIRALPAK IE and IB N-5 columns (stationary phase structures shown).

Solutions of *Δ*-EuL with ~0.5 aborbance at 360 nm were prepared in MeCN, MeOH, MeOD and 2-PrOH and then heated and stirred at 60 °C. 20 µL fractions of each solution was taken after every 25 hours and frozen for chiral HPLC analysis. The same was repeated for another solution of *Δ*-EuL in MeCN but without heating. The resulting solutions were analysed using CHIRALPAK IE column using the method above. The absorbance chromatograms recorded at 360 nm was then used to express the concentration of the enantiomers by integrating the area under the peaks. When racemisation of the enantiopure sample with 100 % enantiomeric excess of the *Λ* enantiomer is considered, an equilibrium is established:

$$\Lambda \underset{k_{-1}}{\overset{k_1}{\rightleftharpoons}} \Delta \qquad [2]$$

where the rates of interconversion for each enantiomer is assumed to be equal $k_1 = k_{-1} = k$. Therefore, the rate expression for racemisation can be written as

$$\frac{-d[\Lambda]}{dt} = k[\Lambda] - k[\Delta] = k([\Lambda] - [\Delta]) \#[3]$$

$$\frac{1}{[\Lambda]-[\Delta]}d[\Lambda] = -kdt\#[4]$$

Since $[\Delta] = [\Lambda]_0 - [\Lambda]$, integration of the rate equation gives

$$\int_{[\Lambda]_0}^{[\Lambda]} \frac{1}{2[\Lambda]-[\Lambda]_0} d[\Lambda] = \int_{t_0}^{t} -k\,dt\#[5]$$

$$\frac{ln(2[\Lambda]-[\Lambda]_0) - ln(2[\Lambda]_0-[\Lambda]_0)}{2} = -kt\#[6]$$

$$ln\left(\frac{[\Lambda]_0}{2[\Lambda]-[\Lambda]_0}\right) = 2kt\#[7]$$

which allows for determination of 2*k* by taking gradient of the plot of $ln\left(\frac{[\Lambda]_0}{2[\Lambda]-[\Lambda]_0}\right)$ against *t*.

The half-life for racemisation ($\tau_{1/2}$) is a time during which the enantiomeric excess of 50% is reached, which can be interpreted as a mixture containing 75% of the starting enantiomer and 25% of the other enantiomer which was formed by interconversion. Substitution of 1 and 0.75 into $[\Lambda]_0$ and $[\Lambda]$ respectively gives equation for the relationship between the experimentally obtained 2*k* and $\tau_{1/2}$.

$$2k\tau_{1/2} = ln\left(\frac{1}{2\times 0.75 - 1}\right) = ln2\#[8]$$

$$\tau_{1/2} = \frac{ln2}{2k}\#[9]$$

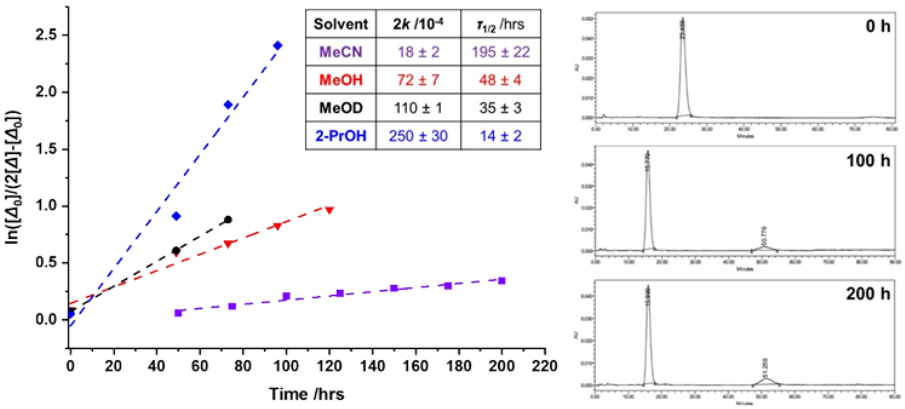

Figure S3: ln([Δ_0]/(2[Δ]-[Δ_0]) against heating time at 60 °C in MeCN (purple), MeOH (red), MeOD (black) and 2-PrOH (blue) with obtained gradients (2*k*) and calculated racemisation half-life ($\tau_{1/2}$) where [Λ] and [Λ_0] are factual and initial concentrations of Λ-EuL respectively (left); three examples of 360 nm absorbance chromatograms for Δ-EuL heated in MeCN at 60 °C (right).

4. Spin coating and atomic force microscopy

Spin coating solutions contained 22 mg PMMA (average M_w ~15000 by gel permeation chromatography, density 1.18 g cm^{-3}) and ~17 µg of EuL (obtained by preparing 5 ml of 0.22 max absorbance solution and then evaporating the solvent) dissolved in 0.500 ml of DCM. This resulted in PMMA concentration of 44 mg ml^{-1} in DCM and 650 µM EuL concentration in PMMA. The solutions were spin coated on 1*1.5 cm cut glass microscope slides. To prepare films on the black electrical tape substrate, the tape was attached to the glass substrates and cut to size. Each film was prepared by casting 15 µl of the solution on the substrate spinning at 8000 rpm.

Atomic force microscopy was performed on an SPM SmartSPM™-1000 (AIST-NT) which consisted of the base and scanning head, both operated by an SPM controller. The base contained the sample metal holder that allowed for magnetic attachment of the SPM Specimen discs (15 mm, Agar Scientific) containing a sample (polymer film spin-coated on a microscope glass slide (manually cut to 1.5 × 1.0 cm) which was attached to the specimen discs using carbon tabs (9mm, Agar Scientific). The metal holder was attached to a digitally controlled (SmartSPM software) motorised positioning system allowing for translation of the sample holder vertically (18 mm range) and horizontally (5 × 5 mm). The scanning head comprised of a cantilever probe holder, laser and a four-sectional photodiode. The probe was a silicon tip with the 10 nm diameter and force constant of 0.02 - 0.77 N/m designed for contact-mode (NANOSENSORS™).

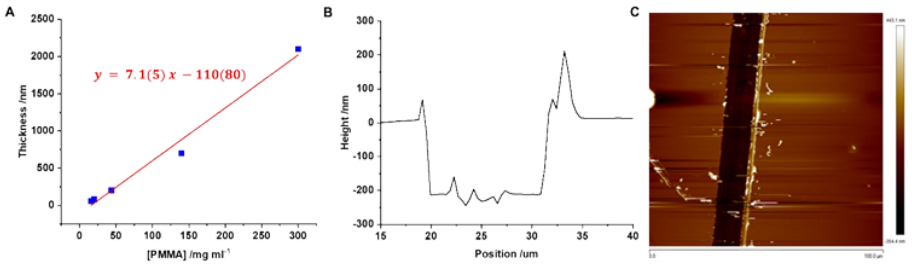

Figure S4: The established dependence of the PMMA concentration ([PMMA]) on the resulting film thickness spin-coated at 8000 rpm (A); the example of depth profile (B) and the corresponding AFM image (C) of an incision on a spin-coated PMMA film using 44 mg ml^{-1} [PMMA].

5. Other Supplementary Figures

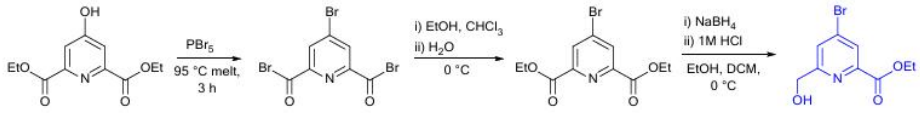

Figure S5: Synthesis of the 'bottom' of the sensitising chromophore.

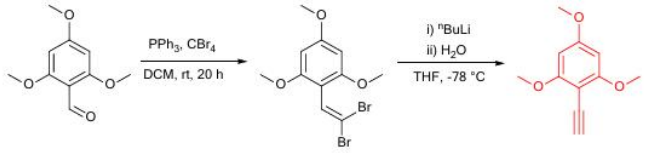

Figure S6: Synthesis of the 'top' of the sensitising chromophore.

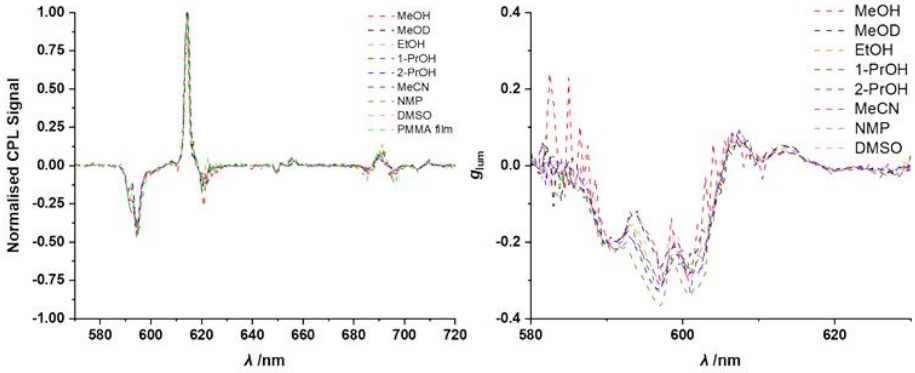

Figure S7: Normalised (0 to 1) CPL spectra of *Λ*-EuL in different solvents demonstrating the CPL profile independence on solvent (left) and the corresponding g_{lum} plots for the $\Delta J = 1$ and $\Delta J = 2$ transitions.

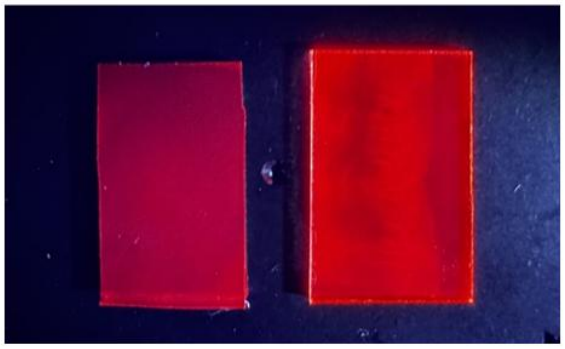

Figure S8: photograph of the *Δ*-EuL_1 containing PMMA films spin-coated on black electrical tape (left) and glass (right) under 365 nm UV irradiation.

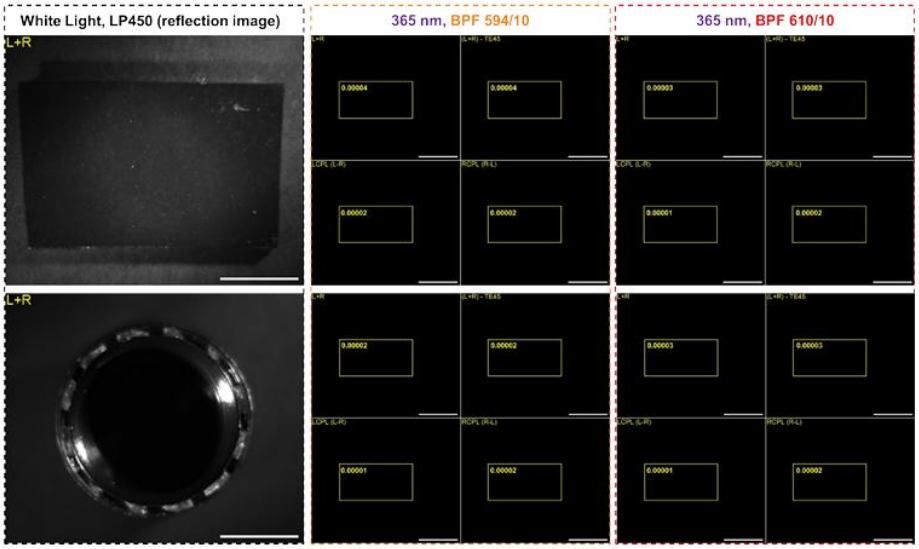

Figure S9: CPLP of black tape substrate (top) and black plastic cap (bottom) using BPF594/10 and BPF610/10 under 365 nm excitation with the regions of interest and their average intensities shown in yellow. The relevant L+R images under white light using 450 nm long pass filter (LP450); Scale bar = 5 mm.

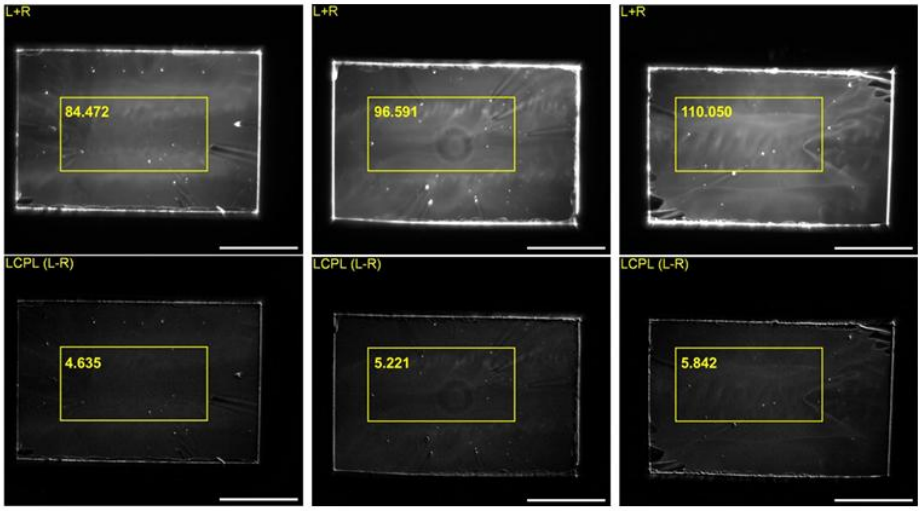

Figure S10: CPLP of three sequentially spin coated PMMA films containing *Δ*-EuL using BPF594/10 where L+R (top row) and L-R (bottom row) with the regions of interest for g_{CPLP} calculations and their average intensities shown in yellow. Scale bar = 5 mm. R-L and L-R images are 6 times contrast enhanced for display.

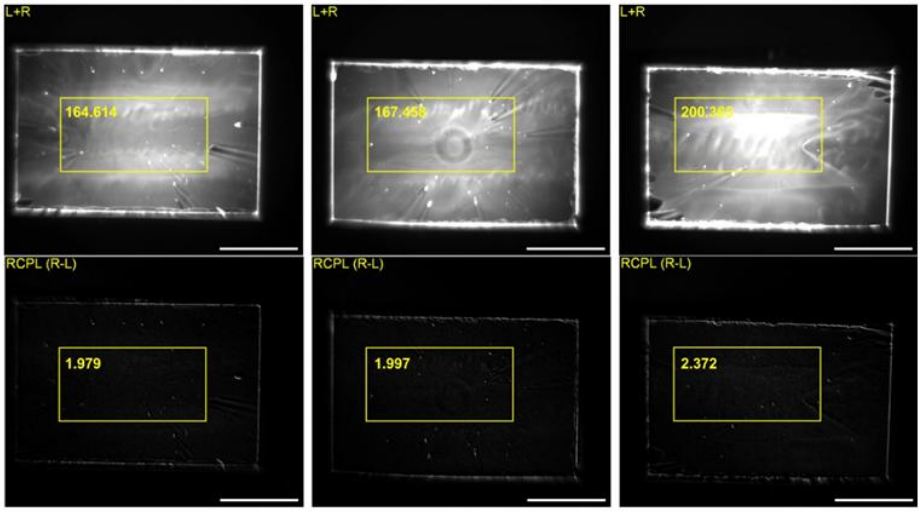

Figure S11: CPLP of three sequentially spin coated PMMA films containing *Δ*-EuL using BPF610/10 where L+R (top row) and R-L (bottom row) with the regions of interest for g_{CPLP} calculations and their average intensities shown in yellow. Scale bar = 5 mm. R-L and L-R images are 6 times contrast enhanced for display.

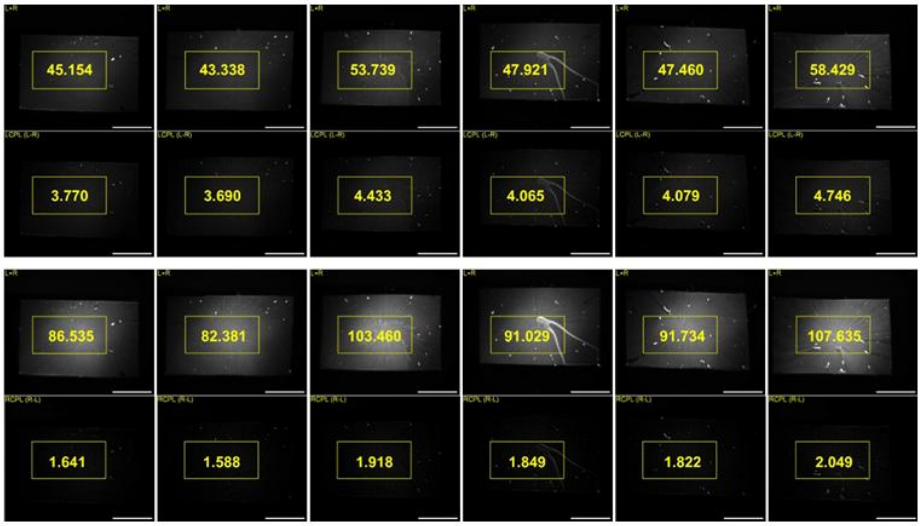

Figure S12: CPLP of six sequentially spin coated PMMA films containing *Δ*-EuL using BPF594/10 (top two rows) and BPF610/10 (bottom two rows) where L+R (1st and 3rd rowas) and L-R (2nd and 4th rows) with regions of interest for g_{CPLP} calculations and their average intensities shown in yellow. Scale bar = 5 mm. R-L and L-R images are 6 times contrast enhanced for display.

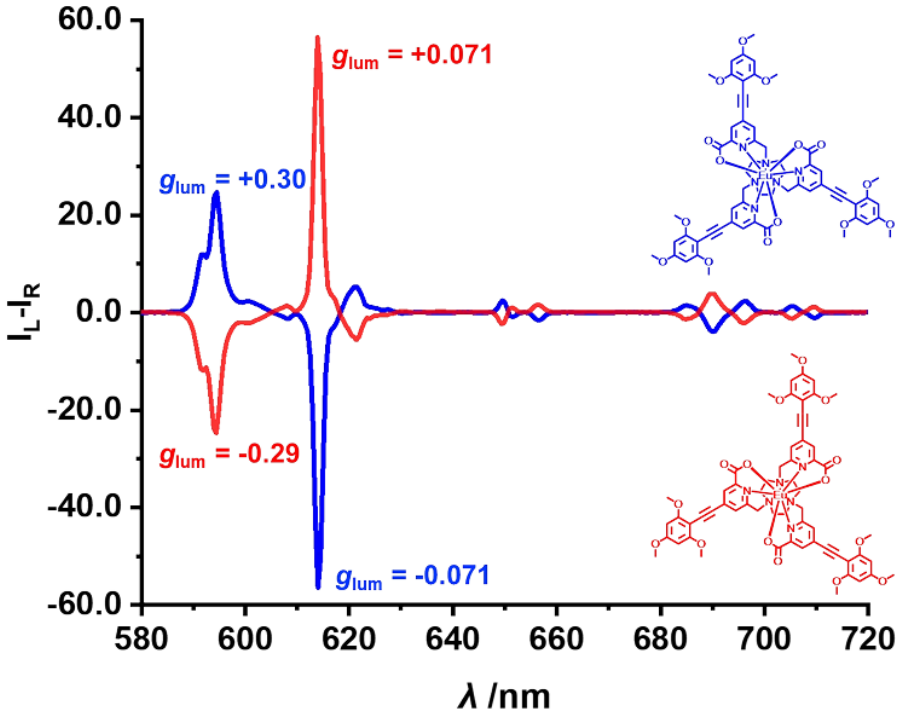

Figure S13: CPL spectra of *Δ*-EuL (blue) and *Λ*-EuL (red) (and their colour-coded structures) in acetonitrile, λ_{ex} = 360 nm, 5 averages.

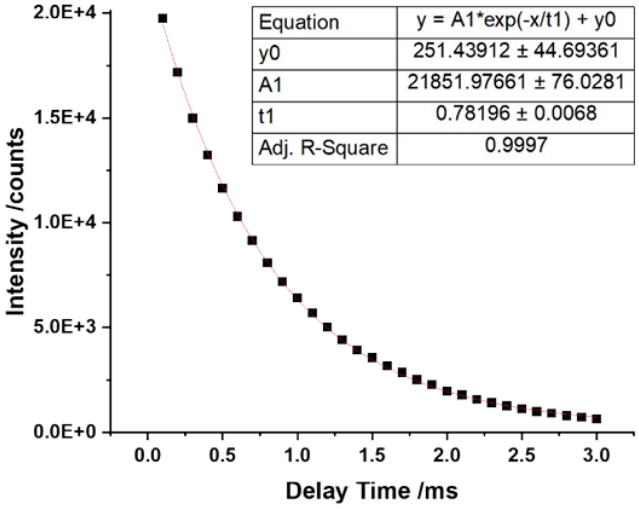

Equation	y = A1*exp(-x/t1) + y0
y0	251.43912 ± 44.69361
A1	21851.97661 ± 76.0281
t1	0.78196 ± 0.0068
Adj. R-Square	0.9997

Figure S14: Exponential decay fitted to a plot of lifetime data (0.1 ms steps) for a ~200 nm thick PMMA film spin-coated on a glass substrate containing EuL.

6. Synthetic Procedures

diethyl 4-bromopyridine-2,6-dicarboxylate

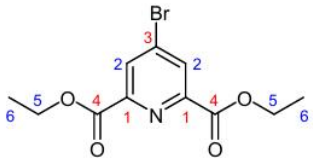

A solid mixture of chelidamic acid (1.64 g, 8.97 mmol, 1 eq.) and phosphorus pentabromide (11.6 g, 26.9 mmol, 3 eq.) was melted and heated (95 °C, 3 h). After that anhydrous chloroform (30 ml) was added, and the resulting hot mixture was filtered and cooled in an ice bath. Cold ethanol was then added drop-wise (20 ml), and the resulting solution was stirred (rt, 15 min). After that, the solvent was evaporated under the reduced pressure to yield brown oil. It was then dissolved in ice-cold water and stirred (0 °C, 1 h) to allow for precipitation of the crude. The resulting brown solid was dried and recrystallised from hexane to yield light-brown solid (1.23 g, 4.07 mmol, 45%);

^{1}H NMR (400 MHz, $CDCl_3$) δ 8.42 (2 H, s, H^2), 4.50 (4 H, q, $^{3}J_{H\text{-}H}$ 7.1, H^5), 1.46 (6 H, t, $^{3}J_{H\text{-}H}$ 7.4, H^6);

HRMS (ESI$^+$) *m/z* 302.0023 ($C_{11}H_{13}NO_4Br$ requires 302.0028).

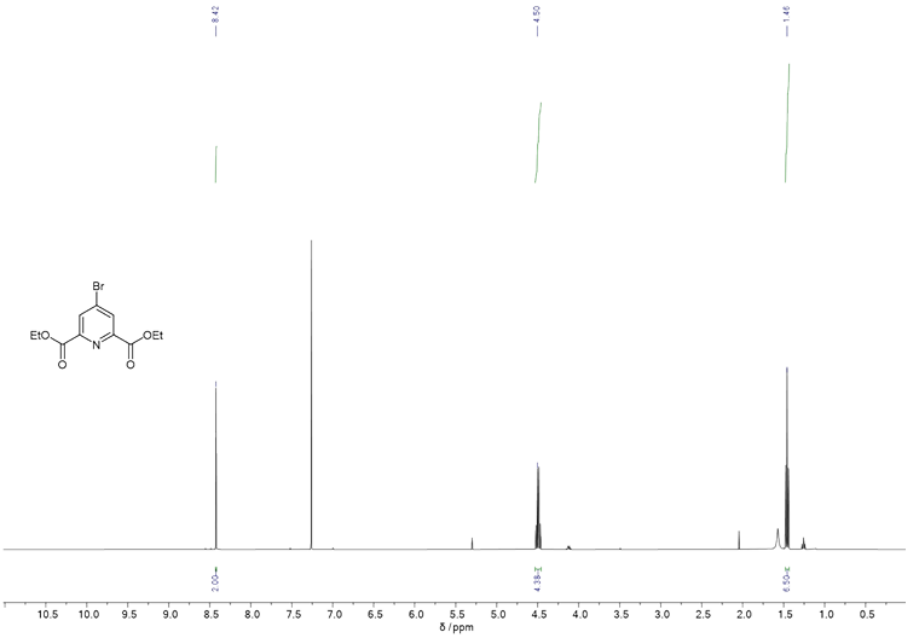

Figure S15: ^{1}H NMR (400 MHz, $CDCl_3$) spectrum of diethyl 4-bromopyridine-2,6-dicarboxylate.

Single Mass Analysis
Tolerance = 3.0 mDa / DBE: min = -1.5, max = 50.0
Element prediction: Off
Number of isotope peaks used for i-FIT = 5

Monoisotopic Mass, Even Electron Ions
976 formula(e) evaluated with 8 results within limits (up to 200 closest results for each mass)
Elements Used:
C: 0-100 H: 0-100 N: 0-20 O: 0-20 Br: 0-2

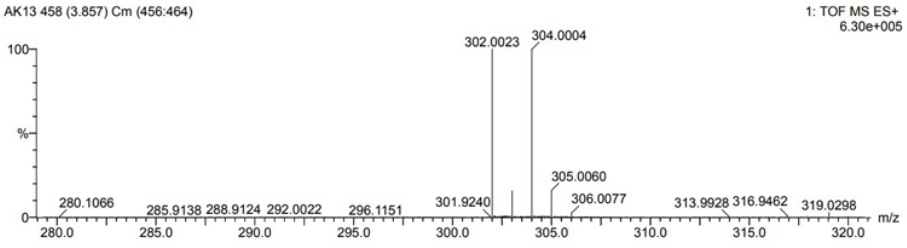

Minimum:				-1.5			
Maximum:		3.0	5.0	50.0			
Mass	Calc. Mass	mDa	PPM	DBE	i-FIT	i-FIT (Norm)	Formula
302.0023	302.0022	0.1	0.3	13.5	1447.5	21.2	C8 N9 O5
	302.0028	-0.5	-1.7	5.5	1427.2	0.9	C11 H13 N O4 Br

Figure S16: HRMS data for diethyl 4-bromopyridine-2,6-dicarboxylate.

ethyl 4-bromo-6-(hydroxymethyl)picolinate

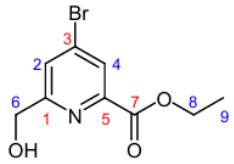

Diethyl 4-bromopyridine-2,6-dicarboxylate (1.23 g, 4.07 mmol, 1 eq.) was dissolved in a solution of dichloromethane (7 ml) and ethanol (9 ml) and cooled in an ice bath. After that, solid sodium borohydride (0.23 g, 6.11 mmol, 1.5 eq.) was slowly added and the resulting solution was stirred (0 °C, 4 h), while monitoring the reaction using TLC (silica, 3% methanol in dichloromethane). After that, a solution of 1 M hydrochloric acid (6 ml) was added, followed by water (25 ml) and dichloromethane (20 ml). The resulting aqueous layer was separated and washed with dichloromethane (10 ml × 3). After that, the combined organic layers were washed with water (10 ml × 3), dried over magnesium sulphate, filtered and concentrated under reduced pressure. The crude solution was then purified by column chromatography (silica, dichloromethane to 2.5% methanol in dichloromethane) to yield white solid (0.675 g, 2.60 mmol, 64%);

^{1}H NMR (400 MHz, $CDCl_3$) δ 8.17 (1 H, d, $^{4}J_{H\text{-}H}$ 1.83, H^{4}), 7.73 (1 H, d, $^{4}J_{H\text{-}H}$ 1.83, H^{2}), 4.84 (2 H, s, H^{6}), 4.46 (2 H, q, $^{3}J_{H\text{-}H}$ 6.9, H^{8}), 1.43 (6 H, t, $^{3}J_{H\text{-}H}$ 7.1, H^{9});

LCMS (ESI^{+}) *m/z* 261 $[M+H]^{+}$.

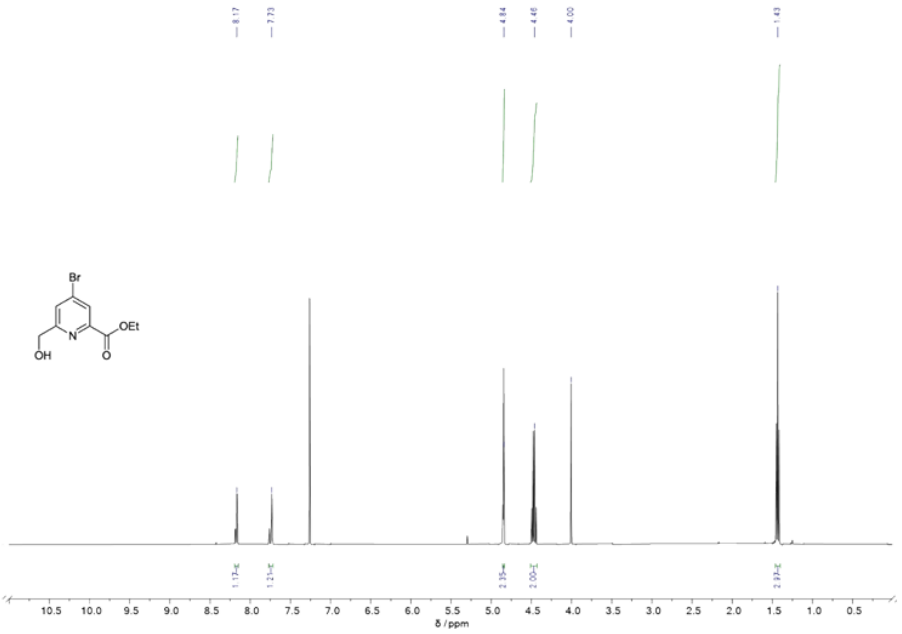

Figure S17: ^{1}H NMR (400 MHz, $CDCl_3$) spectrum of ethyl 4-bromo-6-(hydroxymethyl)picolinate.

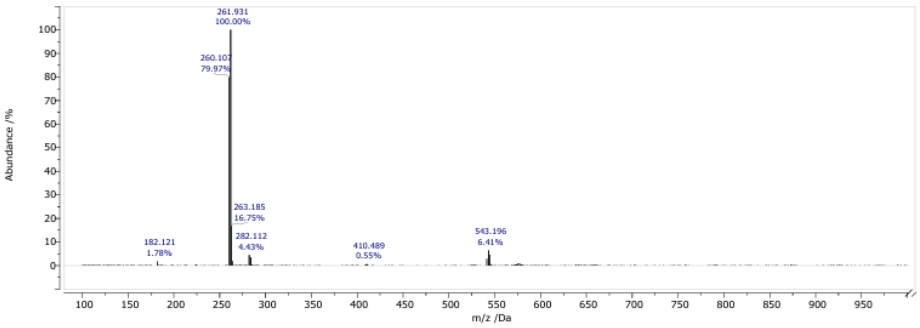

Figure S18: ES+ MS data for ethyl 4-bromo-6-(hydroxymethyl)picolinate.

2-(2,2-dibromovinyl)-1,3,5-trimethoxybenzene

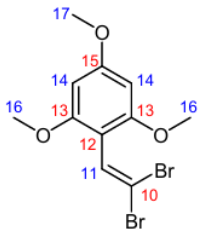

A solution of CBr_4 (1.69 g, 5.10 mmol) in anhydrous dichloromethane (3 cm^3) was dropwise added to a cooled (ice bath) solution of 2,4,6-trimethoxybenzaldehyde **7** (0.5 g, 2.5 mmol) and PPh_3 (5.36 g, 20.5 mmol) in anhydrous dichloromethane (3 cm^3), and the resulting solution was stirred (rt, 20 h, argon). After that, the solution was washed with deionised water (10 cm^3 × 5) followed by extraction of combined aqueous layers with dichloromethane (10 cm^3 × 3). The combined organic layers were dried over Na_2SO_4, filtered and concentrated. The crude product was purified by column chromatography (silica, 30 to 50 % dichloromethane in hexane) to yield white solid (321 mg, 0.912 mmol, 36%);

^{1}H NMR (400 MHz, $CDCl_3$) δ 7.19 (1 H, s, H^{11}), 6.11 (2 H, s, H^{14}), 3.83 (3 H, s, H^{17}), 3.81 (6 H, s, H^{16});

LCMS (ESI^+) *m/z* 351 $[M+H]^+$.

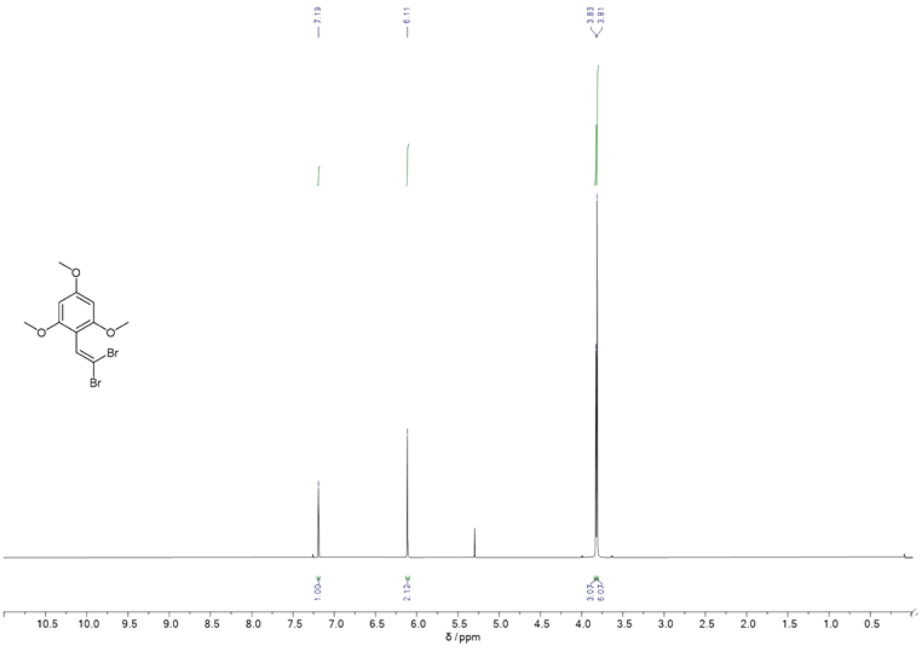

Figure S19: ^{1}H NMR (400 MHz, $CDCl_3$) spectrum of 2-(2,2-dibromovinyl)-1,3,5-trimethoxybenzene.

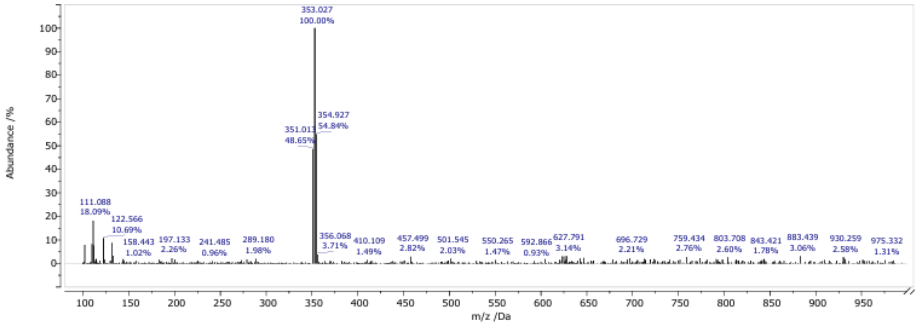

Figure S20: ES+ MS data for 2-(2,2-dibromovinyl)-1,3,5-trimethoxybenzene.

2-ethynyl-1,3,5-trimethoxybenzene

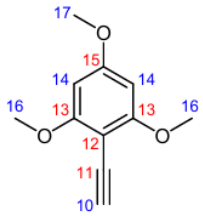

2-(2,2-dibromovinyl)-1,3,5-trimethoxybenzene **8** (321 mg, 0.912 mmol) was dissolved in anhydrous tetrahydrofuran and cooled to -78 °C (acetone, dry ice). 1.6 M solution of n-butyllithium in hexane (1.5 cm^3, 2.4 mmol) was then added dropwise, and the resulting orange solution was stirred (20 min). Deionised water (4 cm^3) was then added dropwise, and the resulting green solution was stirred (rt, 30 min). After that, the organic solvents were removed under reduced pressure, and the resulting aqueous solution was extracted with ethyl acetate (20 $cm^3 \times 3$). The combined organic layers were washed with brine, dried over Na_2SO_4, filtered and dried in vacuo to yield green solid that was used without further purification (0.171 g, 0.890 mmol, 98 %);

^{1}H NMR (400 MHz, $CDCl_3$) δ 6.10 (2 H, s, H^{14}), 3.88 (6 H, s, H^{16}), 3.83 (3 H, s, H^{17}), 3.50 (1 H, s, H^{10}).

LCMS (ESI^+) *m/z* 192 $[M+H]^+$.

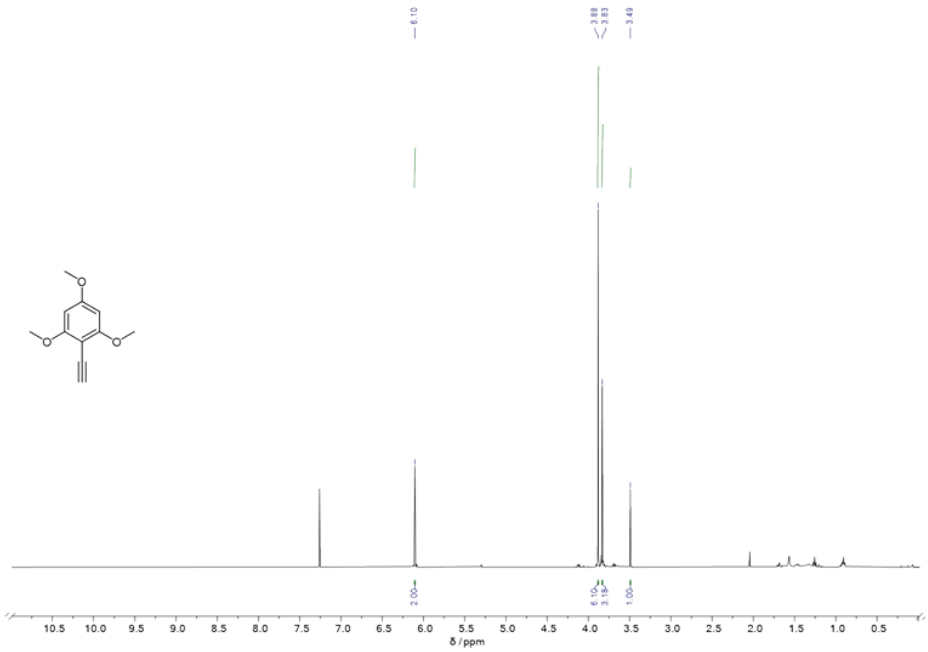

Figure S21: ^{1}H NMR (400 MHz, $CDCl_3$) spectrum of 2-ethynyl-1,3,5-trimethoxybenzene.

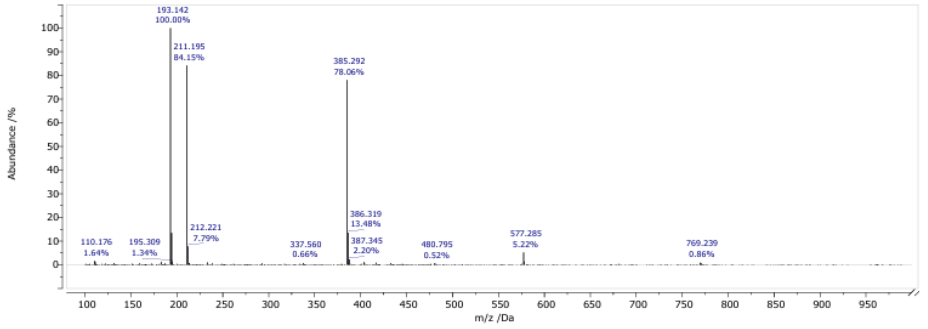

Figure S22: ES+ MS data for 2-ethynyl-1,3,5-trimethoxybenzene.

ethyl 6-(hydroxymethyl)-4-((2,4,6-trimethoxyphenyl)ethynyl)picolinate

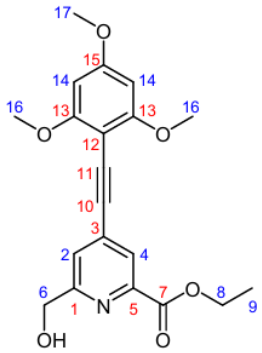

2-ethynyl-1,3,5-trimethoxybenzene (300 mg, 1.56 mmol, 1 eq.), diethyl 4-bromopyridine-2,6-dicarboxylate (446 mg, 1.72 mmol, 1.1 eq.) and $[Pd(allyl)Cl]_2$ (60 mg, 0.164 mmol, ~10 mol%) were dissolved in anhydrous acetonitrile (2 ml) and degassed. After that, triethylamine (2.16 ml, 15.6 mmol, 10 eq.) and piperidine (0.6 ml, 6.24 mmol, 4 eq.) were added, and the resulting solution was stirred (40°C, 12 h, argon). Organic solvents were then removed under reduced pressure, and the residue was dissolved in dichloromethane (10 ml). The resulting solution was washed with deionised water (5 ml × 3), and the combined aqueous phases were extracted with dichloromethane (5 ml × 3). The combined organic layers were dried over magnesium sulphate, filtered and isolated from the solvent under reduced pressure. The resulting yellow oil was purified by column chromatography (silica, 4% methanol in dichloromethane) to yield yellow solid (204 mg, 0.550 mmol, 35%).

^{1}H NMR (700 MHz, $CDCl_3$) δ 8.10 (1 H, d, $^{4}J_{H\text{-}H}$ 1.4, H^{4}), 7.58 (1 H, d, $^{4}J_{H\text{-}H}$ 1.4, H^{2}), 6.11 (2 H, s, H^{14}), 4.82 (2 H, s, H^{6}), 4.47-4.43 (2H, m, H^{8}), 3.90 (6 H, s, H^{16}), 3.85 (3 H, s, H^{17}), 1.42 (3 H, t, $^{3}J_{H\text{-}H}$ 7.1, H^{9});

^{13}C NMR (700 MHz, $CDCl_3$) δ 164.86 (C^{7}), 162.87 (C^{15}), 162.82 (C^{13}), 159.92 (C^{1}), 147.14 (C^{5}), 134.48 (C^{3}), 125.61(C^{4}), 125.14 (C^{2}), 93.35 (C^{10}), 93.07 (C^{11}), 90.44 (C^{14}), 89.26 (C^{12}), 64.38 (C^{6}), 61.94 (C^{8}), 56.07 (C^{16}), 55.48 (C^{17}), 14.27 (C^{9});

HRMS (ESI^{+}) *m/z* 372.1443 ($C_{20}H_{22}NO_6$ requires 372.1447).

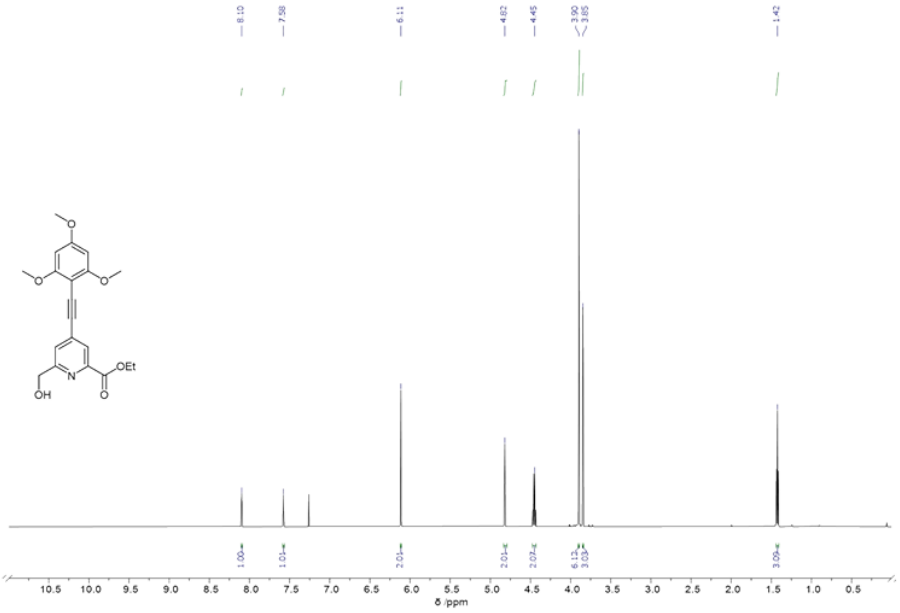

Figure S23: ^{1}H NMR (600 MHz, $CDCl_3$) spectrum of ethyl 6-(hydroxymethyl)-4-((2,4,6-trimethoxyphenyl)ethynyl)picolinate.

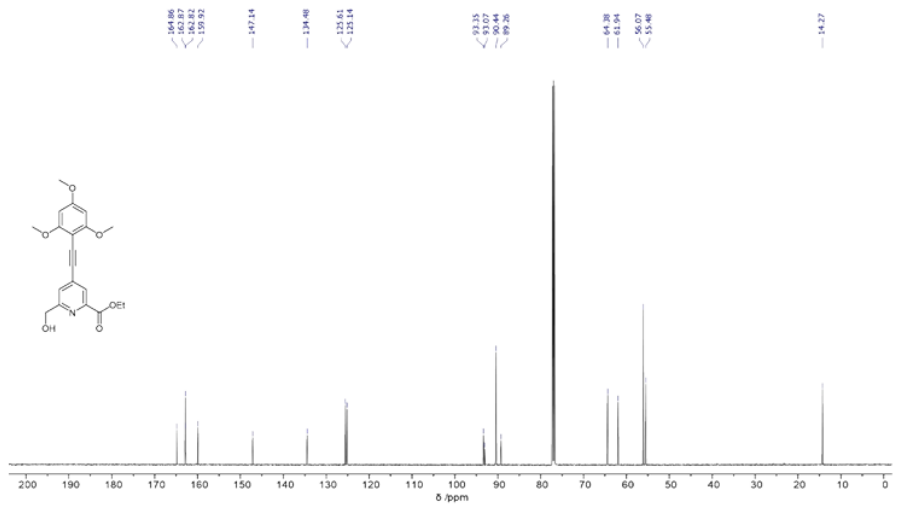

Figure S24: ^{13}C NMR (151 MHz, $CDCl_3$) spectrum of ethyl 6-(hydroxymethyl)-4-((2,4,6-trimethoxyphenyl)ethynyl)picolinate.

Single Mass Analysis
Tolerance = 3.0 mDa / DBE: min = -1.5, max = 50.0
Element prediction: Off
Number of isotope peaks used for i-FIT = 5

Monoisotopic Mass, Even Electron Ions
1158 formula(e) evaluated with 5 results within limits (up to 200 closest results for each mass)
Elements Used:
C: 0-40 H: 0-60 N: 0-6 O: 0-10 P: 0-3

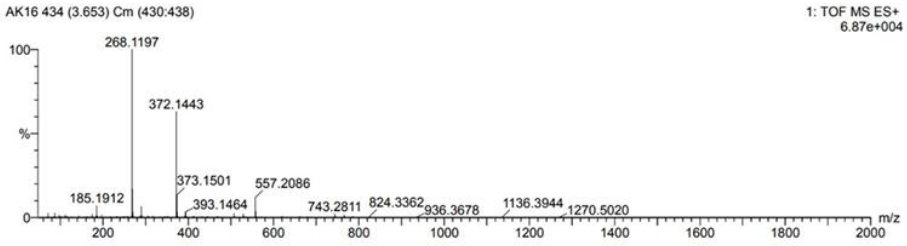

Minimum:		3.0	5.0	-1.5			
Maximum:				50.0			
Mass	Calc. Mass	mDa	PPM	DBE	i-FIT	i-FIT (Norm)	Formula
372.1443	372.1447	-0.4	-1.1	10.5	755.9	0.1	C20 H22 N O6

Figure S25: HRMS data for ethyl 6-(hydroxymethyl)-4-((2,4,6-trimethoxyphenyl)ethynyl)picolinate.

ethyl 6-(((methylsulfonyl)oxy)methyl)-4-((2,4,6-trimethoxyphenyl)ethynyl)picolinate

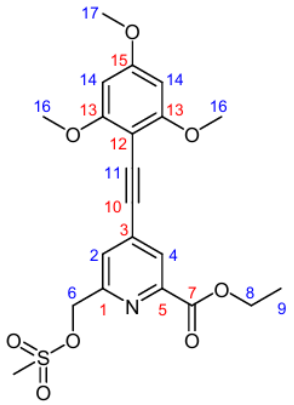

Ethyl 6-(hydroxymethyl)-4-((2,4,6-trimethoxyphenyl)ethynyl)picolinate (119 mg, 0.320 mmol, 1eq.) was dissolved in anhydrous tetrahydrofuran (3.5 ml). *N*,*N*-Diisopropylethylamine (0.17 ml, 0.960, 3 eq.) and methanesulfonic anhydride (0.223 g, 1.280 mmol, 4 eq.) were added, and the resulting solution was stirred (rt, 4h, argon) and monitored by TLC (silica, 5% methanol in dichloromethane). Organic solvents were then evaporated under reduced pressure, and the residue dissolved in dichloromethane (10 ml). The resulting solution was washed with deionised water (10 ml × 3), and the combined aqueous phases were extracted with dichloromethane (5 ml × 3). The combined organic layers were dried over magnesium sulphate, filtered and isolated from the solvent under reduced pressure to yield pale yellow solid that was used in the next step without further purification.

^{1}H NMR (400 MHz, $CDCl_3$) ^{1}H NMR (400 MHz, $CDCl_3$) δ 8.17 (1 H, s, H^4), 7.72 (1 H, s, H^2), 6.12 (2 H, s, H^{14}), 5.44 (2 H, s, H^6), 4.58-4.47 (2H, m, H^8), 3.91 (6 H, s, H^{16}), 3.86 (3 H, s, H^{17}), 1.44 (3 H, t, $^{3}J_{H\text{-}H}$ 7.5, H^9).

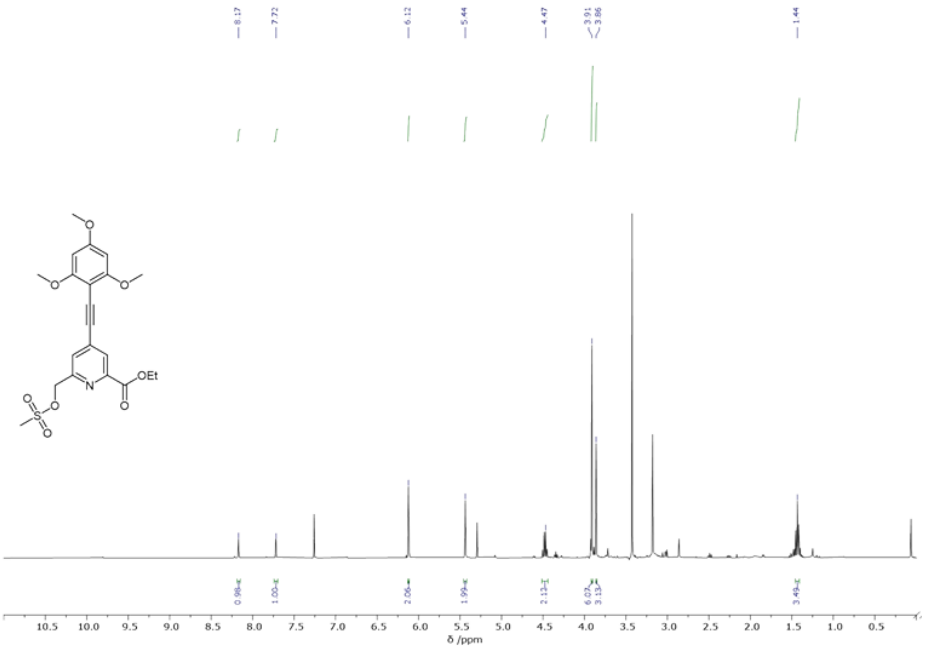

Figure S26: ^{1}H NMR (400 MHz, $CDCl_3$) spectrum of ethyl 6-(((methylsulfonyl)oxy)methyl)-4-((2,4,6-trimethoxyphenyl)ethynyl)picolinate.

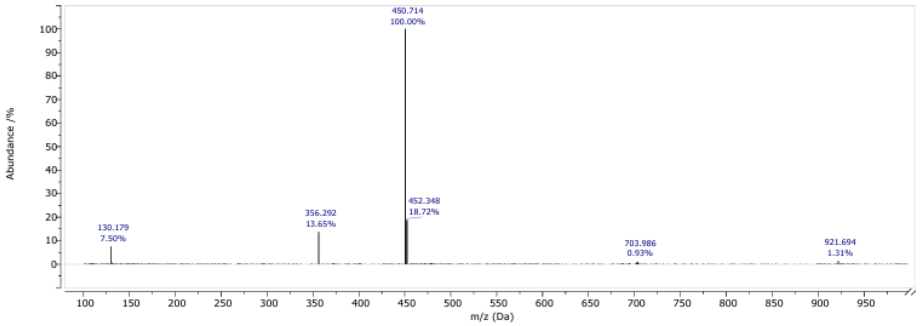

Figure S27: HRMS data for ethyl 6-(((methylsulfonyl)oxy)methyl)-4-((2,4,6-trimethoxyphenyl)ethynyl)picolinate.

triethyl 6,6',6''-((1,4,7-triazonane-1,4,7-triyl)tris(methylene))tris(4-((2,4,6-trimethoxyphenyl)ethynyl)picolinate)

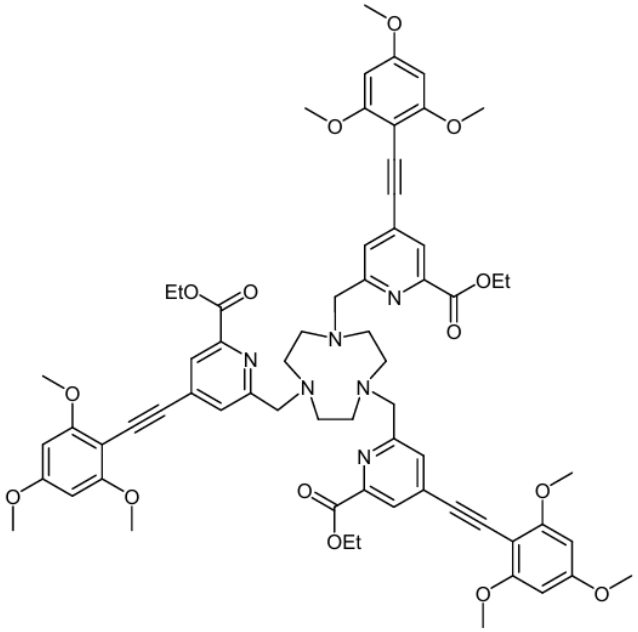

Ethyl 6-(((methylsulfonyl)oxy)methyl)-4-((2,4,6-trimethoxyphenyl)ethynyl)picolinate (*0.144 g, 0.320 mmol,* 3.5 eq.), TACN•3HCl (22 mg, 0.0914 mmol, 1 eq.) and potassium carbonate (88 mg, 0.6398 mmol, 7 eq.) were dissolved in anhydrous acetonitrile (5 ml) and stirred (60°C, 12 h, argon). The crude was isolated from the solvent under reduced pressure and dissolved in dichloromethane. It was then washed with deionised water (5 ml × 3), and the combined aqueous phases were extracted with dichloromethane (5 ml × 3). The combined organic layers were dried over magnesium sulphate, filtered and isolated from the solvent under reduced pressure to yield pale yield yellow solid (*0.0914 mmol*) that was used in the next step without further purification.

HRMS (ESI$^+$) *m/z* 1189.5195 $[M+H]^+$ ($C_{66}H_{72}N_6O_{15}$ requires 1189.5134).

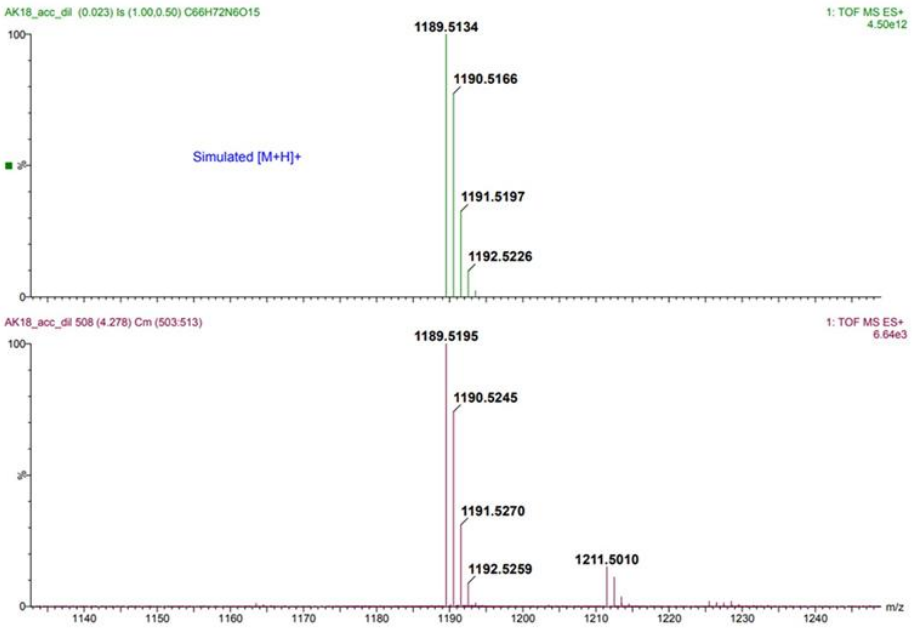

Figure S28: HRMS data for triethyl 6,6',6''-((1,4,7-triazonane-1,4,7-triyl)tris(methylene))tris(4-((2,4,6-trimethoxyphenyl)ethynyl)picolinate).

EuL

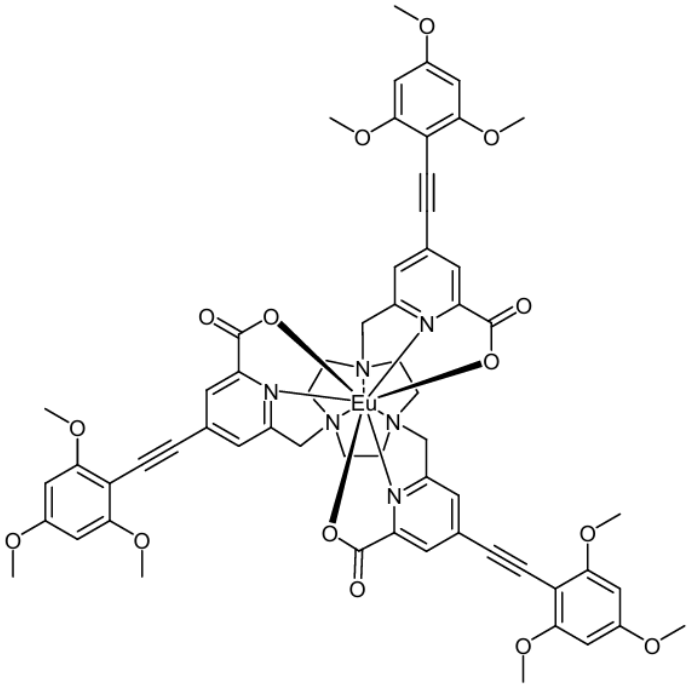

Triethyl 6,6',6''-((1,4,7-triazonane-1,4,7-triyl)tris(methylene))tris(4-((2,4,6-trimethoxy phenyl)ethynyl)picolinate) (*0.0914 mmol*) was dissolved in methanol (5 ml) and deionised water until white precipitate remained undissolved. pH of the resulting solution was adjusted to 12.5 using solution of sodium hydroxide in methanol. The solution was stirred (rt, 72 h), while its pH was monitored and periodically adjusted to 12.5 until hydrolysis completion was confirmed by LCMS. After that, the solution pH was readjusted to 6.5 using 1 M solution of hydrochloric acid. $EuCl_3 \bullet 6H_2O$ was then added (37 mg, 0.101 mmol, 1.1 eq.) and the resulting solution was stirred (rt, 18 h). Solvent was then removed under reduced pressure to yield pale yellow solid which was redissolved in dichloromethane (10 ml). The resulting solution was washed with deionised water (5 ml × 3), and the combined aqueous phases were extracted with dichloromethane (5 ml × 3). The combined organic layers were dried over magnesium sulphate, filtered and isolated from the solvent under reduced pressure to yield pale yield yellow solid that was purified using was purified using reverse-phase HPLC (10 to 100% acetonitrile in water, retention time = 11.4 mins) to yield yellow solid (67 mg, 58% over 3 steps); HRMS (ESI+) *m/z* 1253.3190 $[M+H]^+$ ($C_{60}H_{57}EuN_6O_{15}$ requires 1253.3159).

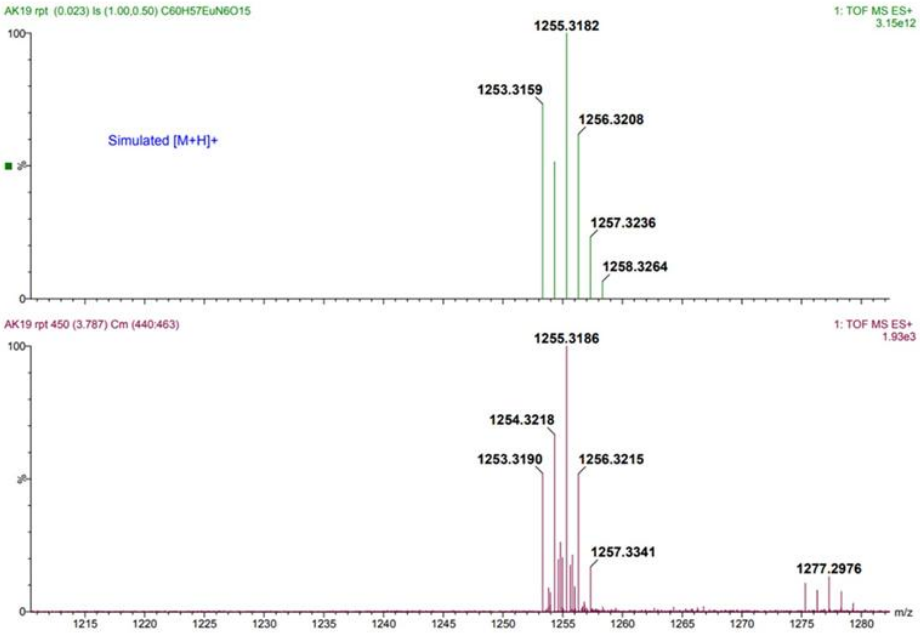

Figure S29: HRMS data for EuL.

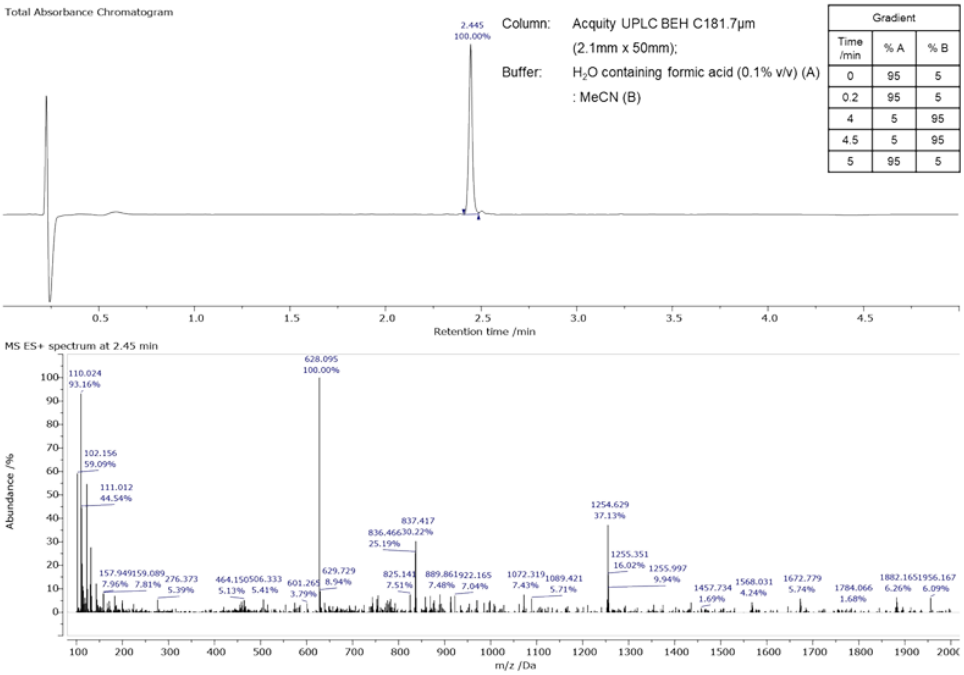

Figure S30: Total absorbance chromatogram (top) and the ES+ MS spectrum at 2.445 min (bottom) for the sample of EuL.

Supplementary References

1 R. Carr, R. Puckrin, B. K. McMahon, R. Pal, D. Parker and L.-O. Pålsson, Induced circularly polarized luminescence arising from anion or protein binding to racemic emissive lanthanide complexes, *Methods Appl. Fluoresc.*, 2014, **2**, 024007.

2 J. D. Fradgley, A. T. Frawley, R. Pal and D. Parker, Striking solvent dependence of total emission and circularly polarised luminescence in coordinatively saturated chiral europium complexes: solvation significantly perturbs the ligand field, *Physical Chemistry Chemical Physics*, 2021, **23**, 11479–11487.

3 C. Xu and W. W. Webb, Measurement of two-photon excitation cross sections of molecular fluorophores with data from 690 to 1050 nm, *J. Opt. Soc. Am. B*, 1996, **13**, 481.

4 L.-O. Pålsson, R. Pal, B. S. Murray, D. Parker and A. Beeby, Two-photon absorption and photoluminescence of europium based emissive probes for bioactive systems, *Dalton Trans.*, 2007, 5726.

5 P. Stachelek, L. MacKenzie, D. Parker and R. Pal, Circularly polarised luminescence laser scanning confocal microscopy to study live cell chiral molecular interactions, *Nat Commun*, 2022, **13**, 553.

Appendix 2

Black *et al.*, 2026[114]

4 February 2026

Paving the Way Towards a Compact Complete Chiroptical Toolbox

Dominic J Black[1], Artemijs Krimovs[1], Robert Pal[1]

1. Department of Chemistry Durham University

Abstract

Circularly polarised luminescence (CPL) spectroscopy is a technique with applications in materials chemistry, bioimaging, probing fundamental chirality, but conventional photo-elastic modulator CPL instruments remain bulky, expensive and slow. We report a compact single-channel CPL (SC-CPL) spectrometer that alternates left-and righthanded emission through a piezo-actuated pair of orthogonally aligned achromatic quarter-wave plates using a rapid CCD detector. This design minimises moving optics and eliminates the need for detector matching and pre-calibration. It can operate in various acquisition modes such as time gated acquisition mode for long-lived CPL emission and a quasi-continuous mode for short-lived CPL emission. Validation against a benchmark PEM-CPL system using a range of CPL emitters reproduced fine CPL resolution with high sensitivity, orders of magnitude faster. This blueprint SC-CPL reported herein paves the way towards the world's first complete compact chiroptical toolbox. This could lead to significant advancements with pivotal scientific and societal impact.

Keywords

CPL, Circularly Polarised Light, Polarisation

Paving the Way Towards a Compact Complete Chiroptical Toolbox

Dominic J. Black,[1] Artemijs Krimovs[1] and Robert Pal[1]*

[1]Department of Chemistry, Durham University, South Road, Durham, DH1 3LE, UK

*robert.pal@durham.ac.uk

Abstract

Circularly polarised luminescence (CPL) spectroscopy is a technique with applications in materials chemistry, bioimaging, probing fundamental chirality, but conventional photo-elastic modulator CPL instruments remain bulky, expensive and slow. We report a compact single-channel CPL (SC-CPL) spectrometer that alternates left- and right-handed emission through a piezo-actuated pair of orthogonally aligned achromatic quarter-wave plates using a rapid CCD detector. This design minimises moving optics and eliminates the need for detector matching and pre-calibration. It can operate in various acquisition modes such as time gated acquisition mode for long-lived CPL emission and a quasi-continuous mode for short-lived CPL emission. Validation against a benchmark PEM-CPL system using a range of CPL emitters reproduced fine CPL resolution with high sensitivity, orders of magnitude faster. This blueprint SC-CPL reported herein paves the way towards the world's first complete compact chiroptical toolbox. This could lead to significant advancements with pivotal scientific and societal impact.

Introduction

Circularly polarised luminescence (CPL) is the emission analogue of circular dichroism (CD), describing the differential emission of left- and right-handed circularly polarised light from chiral luminescent systems. Light which is left- and right- circularly polarised has a spin angular momentum of $+\hbar$ and $-\hbar$ respectively.[1–3] Unlike CD, which probes differences in absorption of circularly polarised light, CPL offers a direct insight into the excited-state electronic structure and stereochemistry of emissive chiral molecules.[4] The intrinsic ability of a compound or system to emit left- or right-handed CPL is quantified by the luminescence dissymmetry factor (g_{lum}):

$$g_{\mathrm{lum}} = 2\frac{I_{\mathrm{left-CPL}} - I_{\mathrm{right-CPL}}}{I_{\mathrm{left}} - CPL + I_{\mathrm{right-CPL}}} \qquad \text{Equation 1}$$

Where I_{left} is the intensity of left-handed circularly polarised light and I_{right} is the intensity of right-handed circularly polarised light; g_{lum} ranges from −2 to +2, corresponding to purely right- or left-handed circularly polarised emission, respectively. The intensity of circularly polarised luminescence can be quantified by circularly polarised brightness (CPB, $M^{-1}\,cm^{-1}$):

$$\mathrm{CPB} = \varepsilon\phi\frac{g_{\mathrm{lum}}}{2} \qquad \text{Equation 2}$$

Where ε is the molar absorption coefficient and ϕ is the luminescence quantum yield. This parameter combines the dissymmetry factor and brightness (the product of ε and ϕ) of a compound and high values indicate the compound is capable of emitting large quantities of one handed circularly polarised photons.[5] Although relatively high CPBs have been reported for some organic materials – such as cyclophanes, BODIPYs, helicenes, pyrenes and some transition metal complexes – the highest CPB compounds are typically observed in lanthanide(III) coordination complexes, particularly those of europium(III) with their CPBs being an order of magnitude higher than the next brightest class of compounds. [6–25] This is due to their favourable photophysical characteristics: magnetic dipole-allowed transitions, long-lived excited states, and narrow emission bands that arise from minimal perturbation of the emitting states by the surrounding environment.[26,27] These features make lanthanide complexes uniquely suited for applications where high CPL contrast and long-lasting emission are desirable. The emergence of circularly polarised emission as a means of encoding chiral molecular fingerprints adds a new dimension to both molecular diagnostics and device engineering. CPL-active materials have demonstrated utility across a growing number of fields, including live-cell chiral imaging,[28–30] enantioselective sensing,[31] circularly polarised organic light-emitting devices (CP-OLEDs), [32–38] and bright, high CPB security inks.[39]

Despite its powerful capabilities, the adoption of CPL spectroscopy has been hindered by instrumental limitations. Conventional CPL spectrometers, often based on a 60 year old design comprising PEM (photoelastic modulator), lock-in-amplifier (LIA) and scanning monochromator (SM) architectures are bulky, expensive, and slow, typically requiring tens of minutes to acquire a single spectrum for lanthanide(III) coordination complexes (100 nm spectral window, 0.5 nm/sec step size) and even longer, hours, for purely organic CPL emitters which have inherently lower g_{lum} ($<10^{-4}$).[40] This renders them ill-suited for dynamic measurements or high-throughput screening of compounds and applications. Furthermore, the reliance on high-energy excitation sources exacerbates issues such as photobleaching and phototoxicity in biological samples.

Recent advances in instrumentation, particularly the development of all-solid-state (SS) CPL spectrometers and dual-channel optical layouts, have addressed many of these limitations.[41–43] These new-generation systems offer rapid total spectral acquisition (on the order of milliseconds/spectrum), compact design, and compatibility with multiphoton and time-gated detection methods.[44] As a result, CPL spectroscopy has transitioned from a niche technique into a powerful tool that can be deployed in portable, real-time imaging platforms – ranging from handheld CPL photocameras[45,46] to live cell laser scanning confocal microscopes[44] – greatly expanding its accessibility and utility across disciplines. These developments are now driving a renaissance in CPL research

and application, unlocking new possibilities in life sciences, advanced materials, and beyond.

Novel SS-CPL spectrometers have used one of two approaches to overcome the limitations of conventional PEM-based CPL spectrometers. Both approaches involve spatially separating left- and right-handed circularly polarised light using a combination of achromatic, broad spectral range, quarter waveplates (Fresnel rhombs or a pair of precisely aligned half-waveplates) and a linear polariser. The difference comes in how these are measured. In the first approach the two channels are measured individually by two separate but matched detectors (two 1D (linear) CCDs);[42] in the second approach the two channels are both fed into the same detector (2D (full frame) CCD) which can differentiate between both feeds.[41] Both methods have their advantages and disadvantages: in the first approach the setup is simpler but requires careful matching and calibration of the detectors to ensure both handedness's are measured equally; in the second approach only one detector is used so no matching is required but the instrument needs to be carefully aligned so the 2D CCD can detect each handedness equally. The other experimental hurdle with this 2D CCD approach is the need of expensive multi core optical fibres that often surpass the offered simplicity and the cost of a dual 1D CCD setup. In this work a combined approach is explored, using only one 1D CCD to detect both left- and right-handed CPL by sequentially discriminating between them. This method eliminates the need for detector matching, in-depth spectral post corrections and simplifies optical alignment, offering a compact, versatile solution for both accurate and precise CPL measurements, which could be adopted and adapted into existing spectrometers.

Results

The Single Channel CPL Spectrometer (SC-CPL) was designed around a one detection channel principle, where polarisation states are modulated via a simple and elegant, method of alternating QWPs (Figure 1). The wavelength of the excitation light/LED[42,45,49-50] is fully customisable. A custom-built array of depolarised pulsed LEDs with various common wavelengths (365 – 760 nm, Supplementary Note 3) was used as the excitation source due to its stability, ease of time modulation and ability to excite a broad range of compounds. The LED excitation light was diffused and focused onto the sample and the collection arm was fixed at a 90° angle to the excitation resulting in a 3 mm beam waist at the centre of a 1 cm pathlength cuvette. The switchable polarisation of the arm comes from a piezoelectric controlled linear stage that consists of two orthogonally aligned achromatic broad spectrum quarter wave plates (QWPs). After the piezoelectric stage a linear polariser (LP) with its axis aligned perfectly to a 1D CCD was introduced. Aligning the LP with respect to the CCD results in complete elimination of any inherent birefringence of the applied CCD chip. Subsequently, the QWP fast axis were aligned at +45° and -45° with respect to the axis of the LP. Conversely, alternating orthogonally

aligned LPs with respect to a stationary QWP would introduce significant error in measuring L- and R-CPL precisely due to incident angle dependent detector birefringence. It is crucial to emphasize that rotation of one QWP instead of the alternation of the pair of two orthogonally aligned QWPs, even the best rotation mounts on the market are only precise to 0.5 degree of rotation[42] that would introduce levels of noise close to S/N=1 with organic, weak CPL emitting (g_{lum},10^{-4}) molecules. Instead, the stage can rapidly (~200 ms, 5 Hz) switch between both QWP orientations that, importantly, is faster than a full rotation cycle of a rotational mount (~2 sec/full rotation). One of the two QWPs converts CPL into linearly polarised light that is aligned with the axis of the linear polariser when the incident light is left-CPL, and orthogonal to it for right-CPL which allows for only left-CPL to be collected. When the stage switches the other orthogonally aligned QWP allows for only right-CPL to be collected since it is aligned to the linear polariser while left-CPL is excluded.

The well know advantage of using a linear CCD for spectroscopy is that it captures the whole spectral range of interest with often as high as 0.05 nm spectral resolution (2000-pixel CCD with 100 nm spectral window) in a single cycle eliminating the need for scanning monochromators and the classical PEM-LIA-SM combination. This contributes to a significantly faster acquisition time (400 ms vs 10 minutes per spectrum) and a significantly more compact instrument design. The only moving part is the piezoelectric stage which has two set points that will not drift out of alignment over time, avoiding the problem associated with rotating components. This reduces the need for recalibration every time the instrument is used, or for an internal reference being required to compensate for any drift in axis alignment.

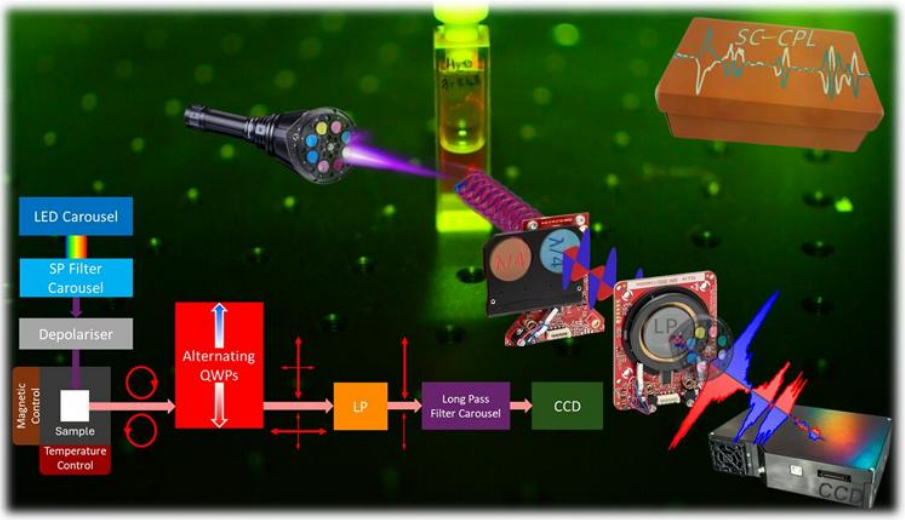

Figure 1: Schematic of the SC-CPL spectrometer. *A custom-built LED carousel is used to excite the sample (with various wavelengths available with corresponding short pass (SP) filters) which emits left- and right-handed circularly polarised light. The light passes through a quarter wave plate (QWP) housed on a piezoelectric controlled stage. This stage alternates between two orthogonally aligned QWPs between each spectral acquisition converting left- and right-handed circularly polarised light to linearly polarised light of mutually orthogonal orientation. The linearly polarised light passes through a static linear polarised (LP), through a long pass filter and to a CCD detector to acquire the full spectrum in one measurement cycle. The sample holder is equipped with attachment points for variable temperature or magnetic field regulation during measurements.*

In order to confirm the two QWPs were orthogonally aligned to one another the achiral fluorophore Rhodamine 6G was used. In solution Rhodamine 6G exhibits no discernible circularly polarised luminescence or fluorescence anisotropy, emitting equally across all polarisation angles and modes. This leads to a net zero CPL spectrum and a g_{lum} value of 0. The use of Rhodamine 6G served as a reliable control to confirm that any detected CPL was not an artifact of misalignment or instrumental asymmetry. In this case, the spectrometer was operated with constant illumination from the LED to ensure maximum emission detection from the short-lived (ns) excited state. The output from the SC-CPL spectrometer are two spectra, one corresponding to left-CPL and the other to right-CPL. The spectra were corrected for background and spectrometer sensitivity (red-correction using an Ocean Optics HL-2000 standard lamp calibration protocol).[42] Once corrected, these spectra can be combined to give the total emission and the CPL spectrum (Figure 2). The CCD (Ocean Optics MayaPro, 2000 pixel, H3 grating, 200 µm slit, 74-DA collimator lens), by default design, recorded the spectral range of 400-800 nm but only the relevant area is shown in the spectra. Each spectrum consists of 100 averages with an integration time of 6 ms per spectrum for each. The recorded CPL spectrum (Figure 2D) showed a flat baseline with no measurable deviation as anticipated for a perfectly achiral system. This result indicates that the optical alignment, including the QWPs, is properly configured, and that the system does not introduce polarisation bias. Furthermore, the effectively zero-value g_{lum} measurement confirms that the spectrometer is capable of resolving small CPL signals and accurately reports the absence thereof when expected.

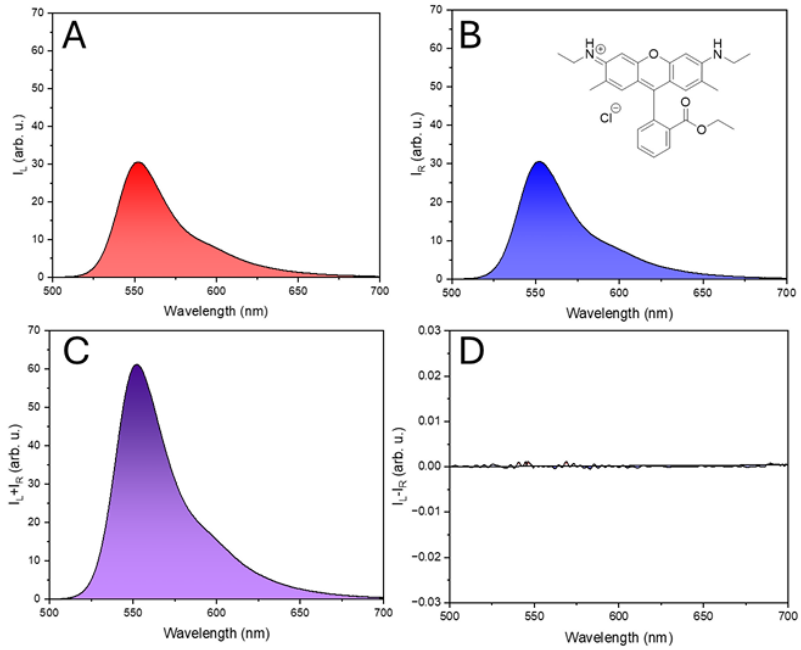

Figure 2: CW-SC-CPL spectra of achiral fluorophore Rhodamine 6G to demonstrate null-measurement. *(A): I_L; (B): I_R; (C): $I_L + I_R$; (D): $I_L - I_R$ spectrum of Rhodamine 6G. A and B consist of 100 average scans ($t_{acq.}$ = 2.5 seconds, λ_{ex} = 365 nm, 400-800nm fixed spectral range, EtOH, [C] = 0.8 μM) each with an integration time of 6 ms/spectrum. Inset: structure of Rhodamine 6G. (For spectral resolution and S/N comparison of 100 vs. 10000 scans averaged for Rhodamine 6G please refer to SI Figure 11.)*

To test the capability of the instrument for measuring CPL spectra the delta (Δ) enantiomer of complex EuL^1 was selected (see structure in Figure 3B) which has been used to previously validate our fast dual channel rapid CPL spectrometer in 2020 (structure shown in Figure 3).[42,44] EuL^1 exhibits a strong CPL signal and sharp fingerprint CPL motifs which allow for rigorous validation of the capabilities of the spectrometer (resolution, time-domain, and sensitivity). The compound was tested under the exact same experimental parameters as were used for collecting the spectra for Rhodamine 6G with correction for background and spectrometer sensitivity and then combined to give total and CPL spectra (Figure 3D).

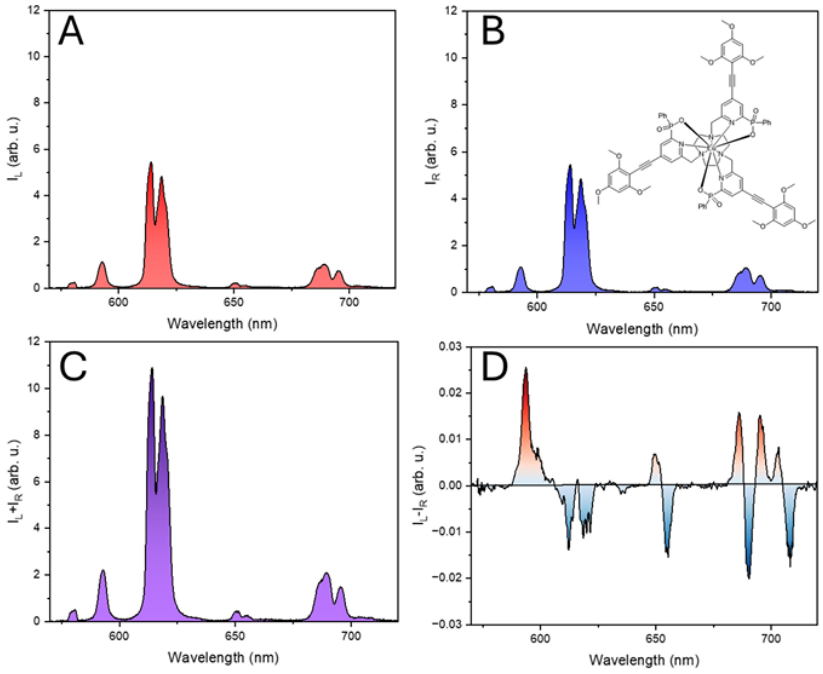

Figure 3: TG-SC-CPL spectra of EuL¹. *(A): I_L; (B): I_R; (C): $I_L + I_R$; (D): $I_L - I_R$ spectrum of Δ-EuL¹. (A) and (B) consist of 100 average scans each with an integration time of 6 ms/spectrum ($t_{acq.}$ = 50 seconds, λ_{ex} = 365 nm, 400-800nm fixed spectral range, MeCN, [C] = 1.5 μM)). Inset: Structure of EuL¹.*

To further enhance the capabilities of the design, the SC-CPL spectrometer can employ three different timing sequence coordinated with the QWP orientation which allows for measurement of the CPL of various emitters (SI Figure 5). A time gated (TG) acquisition mode can be used for compounds with a long lifetime (on the order of microseconds and above such as Ln(III) complexes), a quasi-continuous wave (CW) acquisition mode can be used for shorter lived emitters (e.g. organic compounds) and continuous acquisition can be used for shorter lived emitters that are photostable (SI Materials and Methods section and Supplementary Note 1).[47]

To validate the accuracy of the SC-CPL spectrometer, the recorded data were directly compared, as previously,[42] with those from a standard PEM-CPL spectrometer (Figure 5). This facilitated two key comparisons where the sensitivity of the instrument was tested in both resolving fine detail in CPL spectra and small g_{lum} values. Δ-EuL¹ was used to compare resolution of fine detail, while a previously reported chirally locked bis-perylene diimide macrocycle (PP-PDI¹) was used to compare small g_{lum} values (Figure 4).[23]

The top spectra in Figure 4 C and D shows the total emission spectrum ($I_L + I_R$) from the SC-CPL (red line) overlaid with that from the PEM-CPL spectrometer (blue line). The two produced an excellent overlap where shapes (fingerprint), positions and relative intensities of the Eu(III) emission bands were the same, confirming that the SC-CPL spectrometer correctly captures identical emission spectra of EuL[1].

The middle spectra of Figure 4E and 4F compare the CPL difference spectra (I_L - I_R) obtained by the two methods. Again, there is an excellent agreement, the SC-CPL spectrometer data (red line) coincides with that of the PEM-CPL spectrometer (blue line) within the noise level across the spectrum with perfect CPL recovery. Both spectrometers identify the same sign and relative intensity of CPL across the whole emission profile of Eu(III). This includes inversion points of the CPL spectrum matching to within 0.5 nm (spectral resolution of PEM-CPL spectrometer) of one another between both spectrometers. It should be noted that small differences in spectral form can attributed to differences in the spectral resolution of each spectrometer and are not due to polarisation sensitive optics. Namely, the SC-CPL has a spectral resolution of 0.2 nm whilst the PEM-CM CPL has a set emission resolution of 1.5 nm when measuring EuL[1] and 7 nm when measuring PDI[1]. This is especially evident in the $\Delta J = 2$ transition of EuL[1] where finer resolution results in a small change in the recorded spectral form (narrower and more intense bands). The difference in shape and spectral broadening of the recorded emission between PEM-CPL and SC-CPL also bears a contribution from the difference in excitation light bandwidth (excitation slit).

The full width half maxima (FWHM) of the LEDs used with SC-CPL are 10 nm, whilst the adjustable excitation slit using the PEM-CPL are set to result in 1 nm when measuring EuL[1] and 9 nm when measuring PDI[1]. It is important to note that matching the PEM-CPLs the resolution of 0.2 nm emission and 10 nm excitation of the SC-CPL is not possible due to the applied monochromators limitations (Acton SP2155, adjustable range 1 – 9 nm). However, due to the modular design of the SC-CPL excitation FWHM can be controlled and tuned by the employment of laser lines (~1 nm), pulsed white light sources (LDLS) paired to appropriate narrow bandpass (BP) filters (SI Supplementary Note 3). Emission spectral resolution can be modulated by tuning the width of the spectral range of interest of the CCD via gratings, emission slits or/and by the number of pixels of the linear CCD.

As demonstrated in Figure 4 G and H the derived g_{lum} spectra from each spectrometer are in excellent agreement. For Δ-EuL[1] (both total emission and CPL spectra of Δ and Λ enantiomers shown in SI Figure 8) , the SC-CPL spectrometer yields a peak g_{lum} of 0.18 *vs.* 0.17 at 600 nm from the PEM-CPL spectrometer (corresponding to the $^5D_0 \rightarrow {}^7F_1$ Eu (III) transition) and 0.22 *vs.* 0.21 at 655 nm from PEM-CPL spectrometer (corresponding to the $^5D_0 \rightarrow {}^7F_3$ Eu (III) transition), within a ±0.01 of each other. Given experimental conditions can vary, these differences are not significant, indicating that no systematic bias is introduced by the SC-CPL spectrometers detection scheme. Comparing the

measured g_{lum} averaged across the two transitions also shows negligible variation. For the $^5D_0 \rightarrow {}^7F_1$ transition (575 – 600 nm) the difference is 1.03% and for the $^5D_0 \rightarrow {}^7F_3$ transition (640 – 660 nm) the difference is 0.77%. This level of agreement is excellent, on the same order as the signal to noise ratio of both spectrometers, showing that the new instrument can quantitatively reproduce CPL metrics from a trusted reference instrument, despite their above detailed different spectral resolution. The greater difference between the spectra that is evident towards the red end of the wavelength range can be explained by a reduced sensitivity of the PEM-CPL (that is present even after red correction avoiding electronically over boosting S/N) in the lower energy region of the spectrum. For PP-PDI[1], the recorded g_{lum} values are in excellent agreement where the PEM-CPL produced a g_{lum} of $1.3*10^{-2}$ at the peak wavelength of 665 nm and the SC-CPL measuring $1.2*10^{-2}$ at the same peak wavelength.

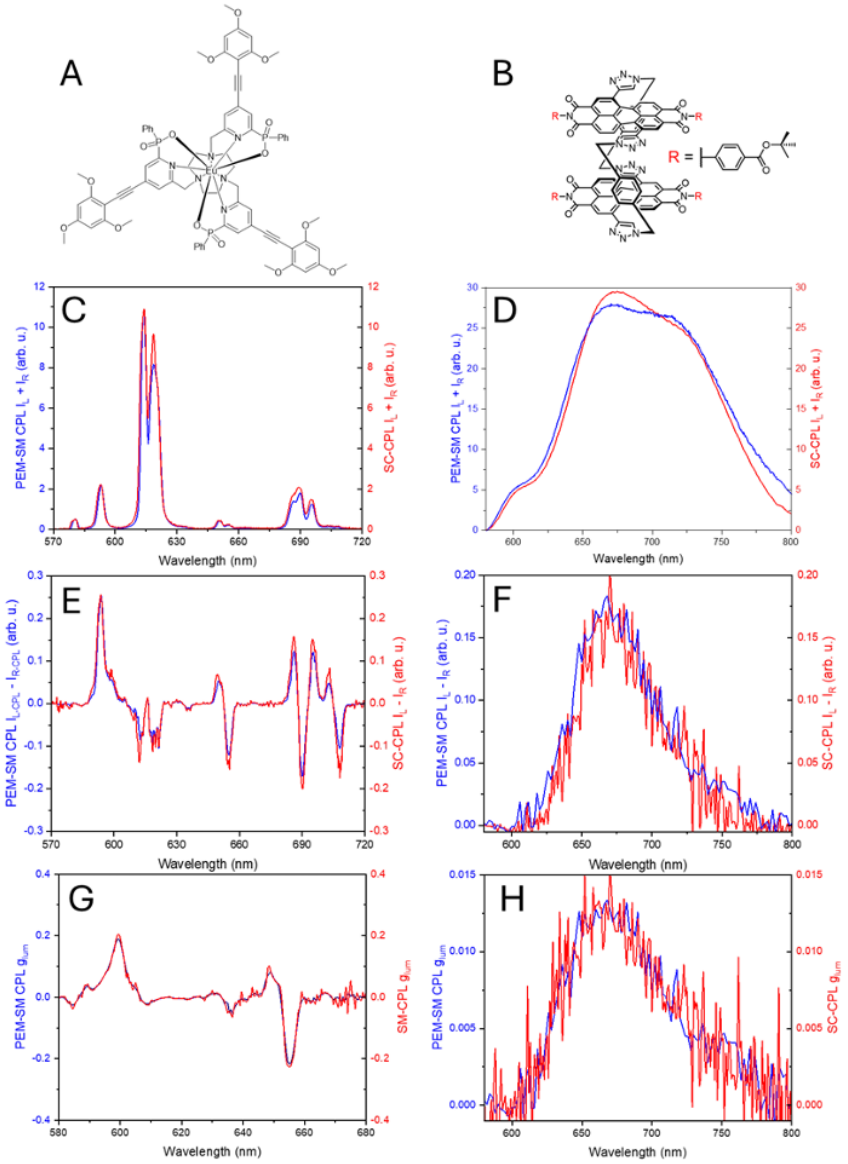

Figure 4: Comparison of SC-CPL and PEM-CPL spectra of Δ-EuL¹ and PP-PDI¹. *Structures of both (A): Δ-EuL¹ and (B): PP-PDI¹; (C + D): $I_L + I_R$; (E + F): $I_L - I_R$; (G + H): g_{lum} of ΔJ = 1 and ΔJ = 2 transitions of Δ-EuL¹ and full spectrum PP-PDI¹ respectively. Blue traces are for the spectra recorded on a PEM-CPL and red traces are for the SC-CPL. λ_{ex} = 365 nm and 525 nm for [Δ-EuL¹] = 1.5 μM and [PP-PDI¹] = 1.5 μM respectively. The mode of SC-CPL acquisition of spectra is TG for of Δ-EuL¹ and CW for PP-PDI¹(100 avg. spectra, total $t_{acq..}$ = 50 and 2.5 seconds respectively, PEM-CPL: 20 avg. spectra. total $t_{acq..}$ = 4 h). (For spectral resolution and S/N comparison of 100 vs. 10000 scans averaged for PP-PDI¹ please refer to SI Figure 13.)*

Finally, to validate the limitations of the sensitivity of the SC-CPL using the organic emitter (*R*)-BOD-3 (Figure 5) we have demonstrated that the SC-CPL instrument is capable to record very small g_{lum} ($1.1*10^{-3}$) values for organic compounds in very short experiments with total CPL and g_{lum} recovery. [29] This measurement was recorded in CW mode 60 times faster by recording 500 times more spectra, whilst demonstrating no unwanted photobleaching or sample degradation as compared to the gold standard PEM-CPL. To conclude our observations using (R)-BOD-3 we believe that the SC-CPL instrument in its current form is capable of recording CPL spectra from robust organic emitters possessing g_{lum} values as low as $5*10^{-5}$ and still outperform PEM-CPL in terms of spectral range and tunability, speed and number of acquisitions.

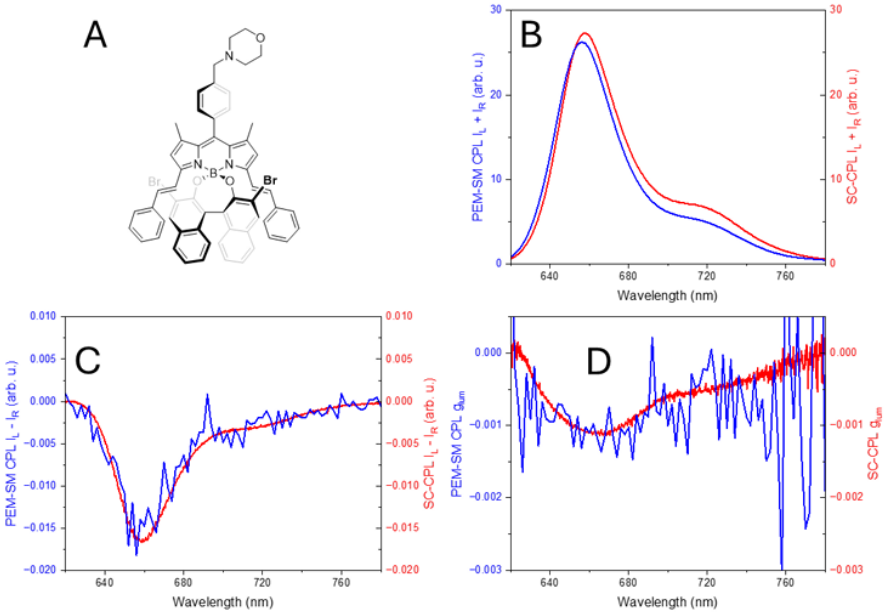

Figure 5: Validation of the sensitivity and limitations of SC-CPL (red line) against the benchmark PEM-CPL using low g_{lum} BOD-3. *(A): Structure of (R)-BOD-3; (B): $I_L + I_R$; (C): $I_L - I_R$; (D): g_{lum}. Blue traces are for the spectra recorded on a PEM-CPL and red traces are for the SC-CPL. The mode of SC-CPL acquisition of spectra is CW (λ_{ex} = 470 nm, 10000 avg. spectra, total $t_{acq..}$ = 250 seconds, PEM-CPL: 20 avg. spectra. total $t_{acq..}$ = 4 h). The SC-CPL has a spectral resolution of 0.2 nm whilst the PEM-CM CPL has a set excitation and emission resolution of 9 nm respectively. [R-BOD-3] = 1.5 μM*

From our library of CPL active compounds, the one possessing the smallest g_{lum} ($2*10^{-4}$), BOD-2,[29] was also measured with complete CPL spectral fingerprint and intensity recovery when compared with PEM-CPL at fraction of the time, crucially with no observed photobleaching (SI Figure 10).

Discussion

This work demonstrates a new approach to designing faster, more compact and more versatile CPL spectrometers that takes the advantages of both methods used to date with none of their associated drawbacks. It must also be emphasised that the SC-CPL spectrometer data were obtained in a fraction of the time a full scanned spectrum would normally take – effectively the entire 570–720 nm range (for Eu (III) emission) is acquired in one shot per polarisation, rather than stepwise. Moreover, the agreement holds across the spectral range, demonstrating that the linear optical elements (QWP, linear polariser) in the SC-CPL spectrometer measures the relative intensities of L-CPL *vs* R-CPL with perfect spectral recovery. Any residual linear polarization artifacts (e.g. circular and linear dichroism in optical components) appear to cancel out upon alternating and averaging, as the difference spectrum baseline was essentially flat. This set up eliminates the artefacts that would be introduced by rotating a single QWP with respect to the optical axis of the LP whilst also counteracts the inherent birefringence of the applied CCD detector by alternating orthogonally aligned QWPs instead of LPs. We validated this and the elimination of any potential linear anisotropy/dichroism induced stray polarised light reaching the CCD detector by performing a series of variable viscosity CPL measurement of our standard non-CPL emitter Rhodamine 6G (SI Figure 12). The instrument is further enhanced by a method of removing short lived emission of organic emitters from longer lived emission in one acquisition mode. In addition, a quasi-continuous mode allows recording of CPL spectra from shorter lived organic emitters. We have demonstrated that the instrument is capable of resolving fine detail in Eu(III) complexes while still being able to record very small g_{lum} ($>5*10^{-5}$) values for organic compounds in very short experiments. Accurate detection of such low g_{lum} value renders the SC-CPL instrument detailed here being able to detect CPB values of compounds possessing high quantum yields (ϕ) and molar extinction coefficient (ε) as low as >2 M^{-1} cm^{-1} subject to sufficient number of averaging and S/N ratio achieved. As a future direction of SC-CPL, a simple adaptation where the excitation light is modulated by a fast-alternating QWP-LP architecture to facilitate pure CP excitation control phase matched to the detection QWP-LP architecture orientations could open new horizons in CPL spectroscopy (SI Figure 9). This will pave the way towards the world's first complete compact chiroptical toolbox (C2PL), a tandem SC-CD/CPL CCD spectrometer that could play a pivotal role in gaining deeper understanding of CPL light generation, modulation and amplification of both CPL active and 'silent' (achiral or racemic mix) molecules. Furthermore, it could help us draw mathematical correlations between observed g_{abs} (CD) and g_{lum} (CPL) values. The main design criteria of our blueprint SC-CPL were versatility, adaptability, simplicity and economy. With more sophisticated detectors and light sources all performance aspects, such as speed of acquisition, spectral and time resolution and sensitivity can be enhanced but it would also come at the price of complexity, cost and restrictions to niche specialist segments of CPL spectroscopy. To conclude, we foresee that the widespread

adaptation of the blueprint SC-CPL spectrometer will establish and democratize CPL spectroscopy as a widely available and routine analytical technique that can lead to significant advancements in the wider scientific community such as the fields of security inks, chiral screening, enantiopurity testing, CP-OLED development and chiral imaging.

Methods

The optical layout of the spectrometer is shown in Figure 1 (image of the spectrometer is shown in SI Figure 1). The compound is excited by an LED capable of being pulsed which is depolarised by a ground glass diffuser. The LEDs are mounted onto a custom-built low-profile compact carousel (see SI Figure 1 and SI Figure 7) allowing for multiple excitation wavelengths to be used (365, 470, 525, 660 and 760 nm), the excitation light passes through a clean-up short pass filter carousel (ThorLabs, FW102C) appropriately paired to the pre-selected LED excitation source (OD4.0 400, 500, 550 and 700 and 780 nm respectively). The emitted light is collected at 90 degrees to the incident light. Two quarter wave plates (Thorlabs, AQWP05M-600) with their fast axes orthogonally aligned were mounted to a piezoelectric switchable stage (Thorlabs, ELL6K). The emission passes through either of these quarter wave plates and then through a static linear polariser (Edmund Optics, 47216). The emission light passes through a long pass filter carousel (ThorLabs, FW102C) appropriately paired to the pre-selected LED excitation source (OD4.0 400, 475, 525 and 675 and 775 nm respectively). The CCD used for spectral collection is an Ocean Optics MayaPro equipped with a 200µm slit and H3 grating optimized for the visible spectrum, providing a resolution of 0.2 nm/pixel in the range of 400–800 nm. Spectral validation of the applied MayaPro CCD was performed using a Hg-Ar calibration lamp (Ocean Optics, HG-2). A correction factor for the wavelength dependence of the detection system was constructed using a calibrated lamp (Ocean Optics, HL-2000). The measured raw data is automatically corrected using this correction factor. The static linear polariser was initially aligned using a precision rotation mount (ThorLabs, ELL14K) and subsequently fixed to the inherent birefringence of the CCD (SI Figure 2 and SI Figure 3) and each quarter wave plate fast axis aligned at -45 degrees and +45 degrees to the polarisation axis of the linear polariser. All electronic components (LEDs, SP/LP filter wheels, switchable linear stage and MayaPro CCD with HR4-break out box for triggering) were controlled by a custom script in LabView 2023. The script allowed for data collection in a continuous illumination mode, a quasi-continuous mode and a pulsed mode where the CCD and LED were synchronised to reduce the amount of exposure the sample received from the excitation source. The validation of the SS-CPL detection systems, with respect to L- and R- CPL was achieved using light emitting diodes (LEDs) at various emission wavelengths covering the entire spectral range. The LED was mounted in the sample holder and the light from the LED was fed through a broad band LP (polarising filter, ThorLabs, LPVISE100-A) and QWP ($\lambda/4$ plate, ThorLabs AQWP05M-600) to generate circularly polarised light'. For details on gold standard PEM-CPL method and full list of components used for SC-CPL please see SI

(Supplementary Note 2 and 3 respectively). All measurements were carried out at a controlled and regulated T = 20.0˚C (enclosure temperature stabilisation and the integrated temperature-controlled sample holder) in order to avoid any previously observed temperature dependant changes in CPL spectra and the emission dissymmetry factor especially with low glum (<10-2) emitters.[48]

Statistics and Reproducibility

Where instruments incorporating a scanning monochromator have been used (absorption, emission, and excitation spectra) each sample has been recorded and averaged as triplicate measurements. Spectra, where CCD detectors have been employed, have been measured as an average of one hundred to a thousand spectra on triplicate samples according to the protocol detailed in the Supplementary Information (SI) section. All measurements were carried out at a controlled and regulated T = 20.0˚C (enclosure temperature stabilisation and the integrated temperature-controlled sample holder) in order to avoid any previously observed temperature dependant changes in CPL spectra and the emission dissymmetry factor especially with low g_{lum} ($<10^{-2}$) emitters.[48]

Data availability

All data generated and analysed during this study including spectra and drawings are available from the corresponding author upon request.

Code availability

Custom codes written and developed and used during this study are available from the corresponding author upon request on a collaboration basis.

Author Contribution:

DJB: Designed and constructed the SC-CPL spectrometer, wrote SC-CPL LabVIEW code, performed all spectroscopy experiments, drafted and edited the manuscript.

AK: Synthesised and provided EuL^1 complex, contributed to the concept of the SC-CPL spectrometer and LED carousel and edited the manuscript.

RP: Secured project funding, designed the SC-CPL spectrometer and associated detection methodology, designed the LED carousel, performed independent validation experiments, drafted and edited the manuscript.

Acknowledgements:

R.P. and D.J.B thank the BBSRC (BB/S017615/1 and BB/X001172/1), and the EPSRC (EP/X040259/1) for funding. A.K. and R.P thanks EPSRC DTP (DU) for the PhD support. All

authors thank Dr. Timonthy A. Barendt and Dr. Samuel E. Penty for the provision of PDI[1] and Santiago de la Moya for BOD-2 and 3 compound for verification, Dr Andrew Frawley for the original synthesis of EuL[1] complex used herein (subsequently re-synthesized by A.K.), Kelvin Appleby for the construction of the USB powered signal generator box and LED carousel and control box. We also express our gratitude to Dr Lewis E. MacKenzie and Professor Andrew Beeby for their work on the prototype rapid dual channel CPL spectrometer, and for their ongoing interest in our CPL research.

Ethics declarations

R.P. is inventor on patent WO2016174395A1: Light detecting apparatus for simultaneously detecting left-and right-handed circularly polarised light. R.P., D.J.B. and A.K. are inventors on patent application P408669.GB.01: Apparatus and method for detecting circularly polarised light. There are no other competing interests.

References

1. Raman, C. V & Bhagavantam, S. Experimental proof of the spin of the photon. *Nature* **129**, (1932).

2. Beth, R. A. Mechanical detection and measurement of the angular momentum of light. *Phys. Rev.* **50**, (1936).

3. Foss, J. G. Photonic angular momentum and selection rules for rotational transitions. *J. Chem. Educ.* **47**, (1970).

4. Schellman, J. A. Circular dichroism and optical rotation. *Chem Rev* **75**, 323–331 (1975).

5. Arrico, L., Bari, L. & Zinna, F. Quantifying the overall efficiency of circularly polarized emitters. *Chem. – A Eur. J.* **27**, (2021).

6. Gon, M., Morisaki, Y. & Chujo, Y. Optically active cyclic compounds based on planar chiral [2.2]paracyclophane: extension of the conjugated systems and chiroptical properties. *J Mater Chem C Mater* **3**, 521–529 (2015).

7. Morisaki, Y., Inoshita, K. & Chujo, Y. Planar-Chiral Through-Space Conjugated Oligomers: Synthesis and Characterization of Chiroptical Properties. *Chemistry – A European Journal* **20**, 8386–8390 (2014).

8. Saikawa, M., Nakamura, T., Uchida, J., Yamamura, M. & Nabeshima, T. Synthesis of figure-of-eight helical bisBODIPY macrocycles and their chiroptical properties. *Chemical Communications* **52**, 10727–10730 (2016).

9. Zinna, F. *et al.* Circularly Polarized Luminescence from Axially Chiral BODIPY DYEmers: An Experimental and Computational Study. *Chemistry – A European Journal* **22**, 16089–16098 (2016).

10. Schaack, C. *et al.* Helicene Monomers and Dimers: Chiral Chromophores Featuring Strong Circularly Polarized Luminescence. *Chemistry – A European Journal* **25**, 8003–8007 (2019).

11. Ushiyama, A., Hiroto, S., Yuasa, J., Kawai, T. & Shinokubo, H. Synthesis of a figure-eight azahelicene dimer with high emission and CPL properties. *Organic Chemistry Frontiers* **4**, 664–667 (2017).

12. Dhbaibi, K. *et al.* Modulation of circularly polarized luminescence through excited-state symmetry breaking and interbranched exciton coupling in helical push–pull organic systems. *Chem Sci* **11**, 567–576 (2020).

13. Homberg, A. *et al.* Combined reversible switching of ECD and quenching of CPL with chiral fluorescent macrocycles. *Chem Sci* **9**, 7043–7052 (2018).

14. Takaishi, K., Takehana, R. & Ema, T. Intense excimer CPL of pyrenes linked to a quaternaphthyl. *Chemical Communications* **54**, 1449–1452 (2018).

15. Jiménez, J.-R. *et al.* Chiral Molecular Ruby [Cr(dqp)2]3+ with Long-Lived Circularly Polarized Luminescence. *J Am Chem Soc* **141**, 13244–13252 (2019).

16. Dee, C. *et al.* Strong circularly polarized luminescence of an octahedral chromium(iii) complex. *Chemical Communications* **55**, 13078–13081 (2019).

17. Petoud, S. *et al.* Brilliant Sm, Eu, Tb, and Dy Chiral Lanthanide Complexes with Strong Circularly Polarized Luminescence. *J Am Chem Soc* **129**, 77–83 (2007).

18. Lama, M. *et al.* Lanthanide Class of a Trinuclear Enantiopure Helical Architecture Containing Chiral Ligands: Synthesis, Structure, and Properties. *Chemistry – A European Journal* **13**, 7358–7373 (2007).

19. Seitz, M., Moore, E. G., Ingram, A. J., Muller, G. & Raymond, K. N. Enantiopure, Octadentate Ligands as Sensitizers for Europium and Terbium Circularly Polarized Luminescence in Aqueous Solution. *J Am Chem Soc* **129**, 15468–15470 (2007).

20. Butler, S. J. Utility of tris(4-bromopyridyl) europium complexes as versatile intermediates in the divergent synthesis of emissive chiral probes. *Dalt. Trans.* **43**, (2014).

21. Frawley, A. T., Pal, R. & Parker, D. Very bright, enantiopure europium(III) complexes allow time-gated chiral contrast imaging. *Chem. Commun.* **52**, (2016).

22. Zhou, Y., Li, H., Zhu, T., Gao, T. & Yan, P. A highly luminescent chiral tetrahedral Eu4L4(L')4 cage: Chirality induction, chirality memory, and circularly polarized luminescence. *J. Am. Chem. Soc.* **141**, (2019).

23. Penty, S. E. *et al.* A Chirally Locked Bis-perylene Diimide Macrocycle: Consequences for Chiral Self-Assembly and Circularly Polarized Luminescence. *J Am Chem Soc* **146**, 5470–5479 (2024).

24. Pålsson, L.-. O., Pal, R., Murray, B. S., Parker, D. & Beeby, A. Two-photon absorption and photoluminescence of europium based emissive probes for bioactive systems. *Dalt. Trans.* **48**, (2007).

25. Shuvaev, S., Pal, R. & Parker, D. Selectively switching on europium emission in drug site one of human serum albumin. *Chem. Commun.* **53**, (2017).

26. Kitagawa, Y., Tsurui, M. & Hasegawa, Y. Steric and Electronic Control of Chiral Eu(III) Complexes for Effective Circularly Polarized Luminescence. *ACS Omega* **5**, 3786–3791 (2020).

27. Niu, X. *et al.* Chiral europium halides with high-performance magnetic field tunable red circularly polarized luminescence at room temperature. *Nat Commun* **16**, 2525 (2025).

28. Butler, S. J., Lamarque, L., Pal, R. & Parker, D. EuroTracker dyes: Highly emissive europium complexes as alternative organelle stains for live cell imaging. *Chem. Sci.* **5**, (2014).

29. Stachelek, P., Serrano-Buitrago, S., Maroto, B. L., Pal, R. & de la Moya, S. Circularly Polarized Luminescence Bioimaging Using Chiral BODIPYs: A Model Scaffold for Advancing Unprecedented CPL Microscopy Using Small Full-Organic Probes. *ACS Appl Mater Interfaces* **16**, 67246–67254 (2024).

30. Fabri, B. *et al.* Two-photon Excitation of Bright Diaza[4]Helicenes for Isotropic and Circularly Polarized Emission. *Chemistry – A European Journal* **31**, e202501212 (2025).

31. Chen, P. *et al.* Supramolecular chiroptical sensing of chiral species based on circularly polarized luminescence. *Soft Matter* **20**, 8937–8946 (2024).

32. Wan, L. *et al.* Highly Efficient Inverted Circularly Polarized Organic Light-Emitting Diodes. *ACS Appl Mater Interfaces* **12**, 39471–39478 (2020).

33. Poulard, L. *et al.* Circularly polarized-thermally activated delayed fluorescent materials based on chiral bicarbazole donors. *Chemical Communications* **58**, 6554–6557 (2022).

34. Wang, J. *et al.* Helically chiral multiresonant thermally activated delayed fluorescent emitters and their use in hyperfluorescent organic light-emitting diodes. *Chem Sci* **15**, 16917–16927 (2024).

35. Chen, L. *et al.* Hyperfluorescence circularly polarized OLEDs consisting of chiral TADF sensitizers and achiral multi-resonance emitters. *Nat Commun* **16**, 1656 (2025).

36. Jia, J. *et al.* Circularly polarized electroluminescence from a single-crystal organic microcavity light-emitting diode based on photonic spin-orbit interactions. *Nat Commun* **14**, 31 (2023).

37. Li, M. & Chen, C.-F. Advances in circularly polarized electroluminescence based on chiral TADF-active materials. *Organic Chemistry Frontiers* **9**, 6441–6452 (2022).

38. Wan, L., Wade, J., Wang, X., Campbell, A. J. & Fuchter, M. J. Engineering the sign of circularly polarized emission in achiral polymer – chiral small molecule blends as a function of blend ratio. *J Mater Chem C Mater* **10**, 5168–5172 (2022).

39. MacKenzie, L. E. & Pal, R. Circularly polarized lanthanide luminescence for advanced security inks. *Nat Rev Chem* **5**, 109–124 (2021).

40. Carr, R. *et al.* Induced circularly polarized luminescence arising from anion or protein binding to racemic emissive lanthanide complexes. *Methods Appl Fluoresc* **2**, 024007 (2014).

41. Baguenard, B. *et al.* Theoretical and experimental analysis of circularly polarized luminescence spectrophotometers for artifact-free measurements using a single CCD camera. *Nat Commun* **14**, 1065 (2023).

42. MacKenzie, L. E., Pålsson, L. O., Parker, D., Beeby, A. & Pal, R. Rapid time-resolved Circular Polarization Luminescence (CPL) emission spectroscopy. *Nat Commun* **11**, 1–9 (2020).

43. Reponen, A.-P. M. *et al.* Broadband transient full-Stokes luminescence spectroscopy. *Nature,* **643**, 675-682 (2025).

44. Stachelek, P., MacKenzie, L., Parker, D. & Pal, R. Circularly polarised luminescence laser scanning confocal microscopy to study live cell chiral molecular interactions. *Nat Commun* **13**, 1–8 (2022).

45. De Rosa, D. F., Stachelek, P., Black, D. J. & Pal, R. Rapid handheld time-resolved circularly polarised luminescence photography camera for life and material sciences. *Nat Commun* **14**, 1537 (2023).

46. Kitagawa, Y. *et al.* Chiral lanthanide lumino-glass for a circularly polarized light security device. *Commun Chem* **3**, 119 (2020).

47. Pal, R. & Beeby, A. Simple and versatile modifications allowing time gated spectral acquisition, imaging and lifetime profiling on conventional wide-field microscopes. *Methods Appl. Fluoresc.* **2**, (2014).

48. Kondo, Y. *et al.* Temperature-Dependent Circularly Polarized Luminescence Measurement Using KBr Pellet Method. *Front Chem* **8-,** (2020).

49 Cei, M. *et al.* CPL photoscopy: circularly polarized luminescence detected by chromaticity differences. *Chem Sci, ,***16**, 15347-15354 (2025).

50. Castiglioni, E. *et al.* Revisiting with Updated Hardware an Old Spectroscopic Technique: Circularly Polarized Luminescence. *Appl Spectrosc*, **64**, 1416 (2010)

Paving the Way Towards a Compact Complete Chiroptical Toolbox

A Rapid and Versatile Single Channel Time Resolved Circularly Polarised Luminescence Spectrometer

Supplementary Information

Dominic J. Black,[1] Artemijs Krimovs[1] and Robert Pal[1]*

[1]Department of Chemistry, Durham University, South Road, Durham, DH1 3LE, UK

*robert.pal@durham.ac.uk

Materials and Methods

The optical layout of the spectrometer is shown in Figure 1 (image of the spectrometer is shown in SI Figure 1). The compound is excited by an LED capable of being pulsed which is depolarised by a ground glass diffuser. The LEDs are mounted onto a custom-built low-profile compact carousel (see SI Figure 1 and SI Figure 7) allowing for multiple excitation wavelengths to be used (365, 470, 525, 660 and 760 nm), the excitation light passes through a clean-up short pass filter carousel (ThorLabs, FW102C) appropriately paired to the pre-selected LED excitation source (OD4.0 400, 500, 550 and 700 and 780 nm respectively). The emitted light is collected at 90 degrees to the incident light. Two quarter wave plates (Thorlabs, AQWP05M-600) with their fast axes orthogonally aligned were mounted to a piezoelectric switchable stage (Thorlabs, ELL6K). The emission passes through either of these quarter wave plates and then through a static linear polariser (Edmund Optics, 47216). The emission light passes through a long pass filter carousel (ThorLabs, FW102C) appropriately paired to the pre-selected LED excitation source (OD4.0 400, 475, 525 and 675 and 775 nm respectively). The CCD used for spectral collection is an Ocean Optics MayaPro equipped with a 200µm slit and H3 grating optimized for the visible spectrum, providing a resolution of 0.2 nm/pixel in the range of 400–800 nm. The static linear polariser was initially aligned using a precision rotation mount (ThorLabs, ELL14K) and subsequently fixed to the inherent birefringence of the CCD (SI Figure 2 and SI Figure 3) and each quarter wave plate fast axis aligned at -45 degrees and +45 degrees to the polarisation axis of the linear polariser. All electronic components (LEDs, SP/LP filter wheels, switchable linear stage and MayaPro CCD with HR4-break out box for triggering) were controlled by a custom script in LabView 2023. The script allowed for data collection in a continuous illumination mode, a quasi-continuous mode and a pulsed mode where the CCD and LED were synchronised to reduce the amount of exposure the sample received from the excitation source. For details on gold standard PEM-CPL method and full list of components used for SC-CPL please see SI (Supplementary Note 2 and 3 respectively). All measurements were carried out at a controlled and regulated T = 20.0˚C (enclosure temperature stabilisation and the

integrated temperature-controlled sample holder) in order to avoid any previously observed temperature dependant changes in CPL spectra and the emission dissymmetry factor especially with low glum (<10-2) emitters.[1]

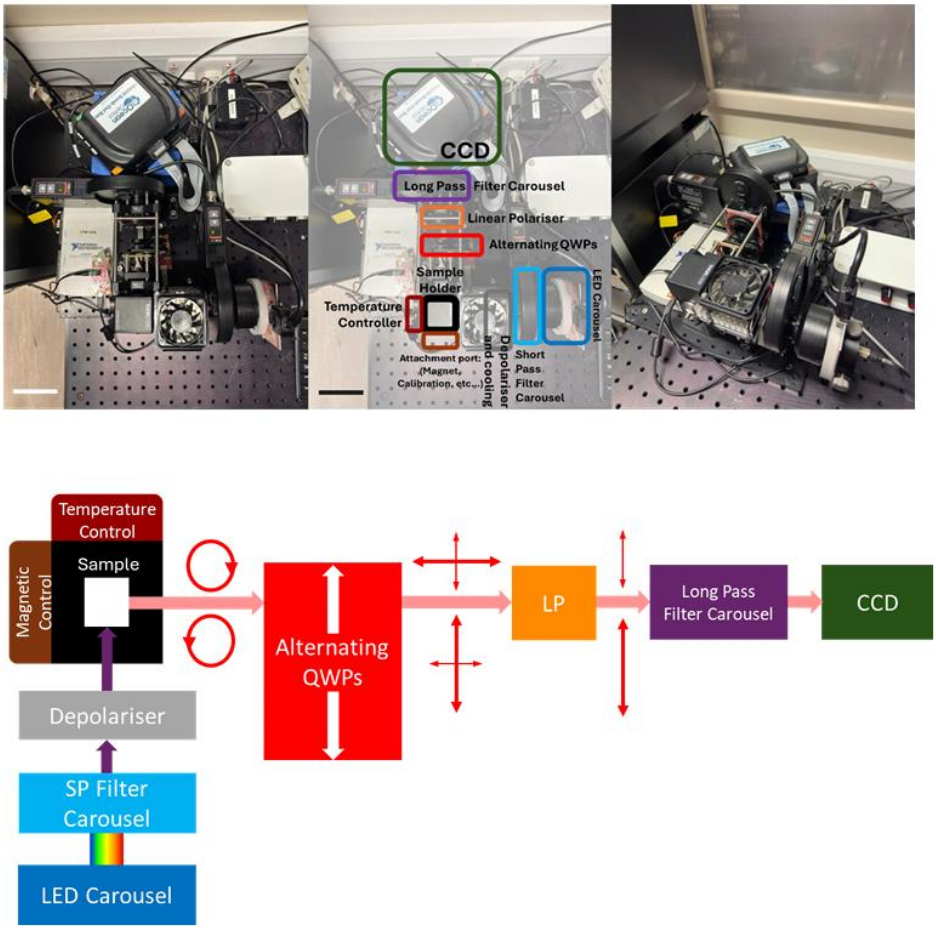

Supplementary Figure 1: Photograph (top) and Schematics (Bottom) of SC-CPL Instrument. All components assigned and colour-coded according to main text Figure1. Scale bar 10 cm.

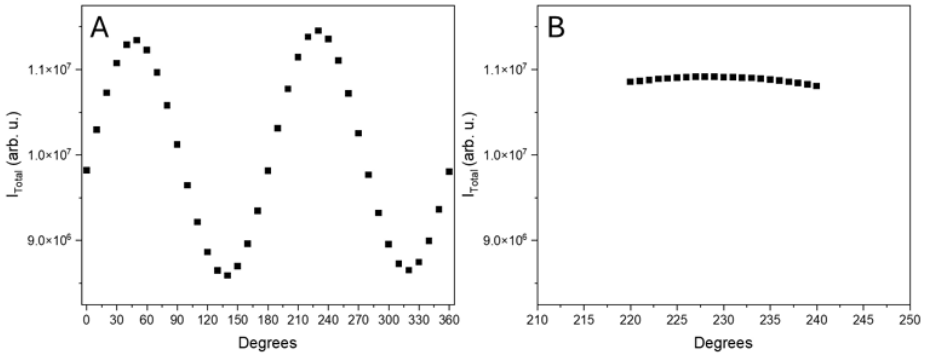

Supplementary Figure 2: Angular position vs. intensity dependence of the CCD with respect to linear polariser (LP) alignment. This method was used to establish and fix the LP at its optimal position that guided the final alignment of the two orthogonally fixed QWPs.

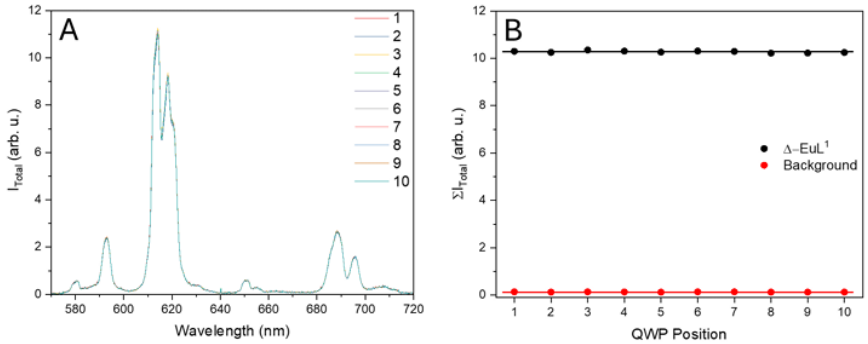

Supplementary Figure 3: Dependence of transmission and polarisation on QWP position. (A) 100 spectra of Δ-EuL[1] were recorded across the aperture of one aligned QWP using TG acquisition mode, 365 nm excitation, 6 ms/spectrum integration time, 100 averaged spectra. At each position the sample was removed and the experiment repeated to yield two measurements, a background and an emission. (B) Integrated total intensity plot of background corrected spectra (570-720 nm) of each position. The lack of deviation away form a perfect straight line ($m_{TotalIntesity}$ and $m_{Background}$ = 0, $r^2_{TotalIntesity}$= 0.932 and $r^2_{Background}$ = 0.956 respectively) verify that there is no dependence on position of the QWP for true transmission both in intensity and polarisation). Each point corresponds to a 1 mm shift across the 10 mm optical aperture of the QWP.

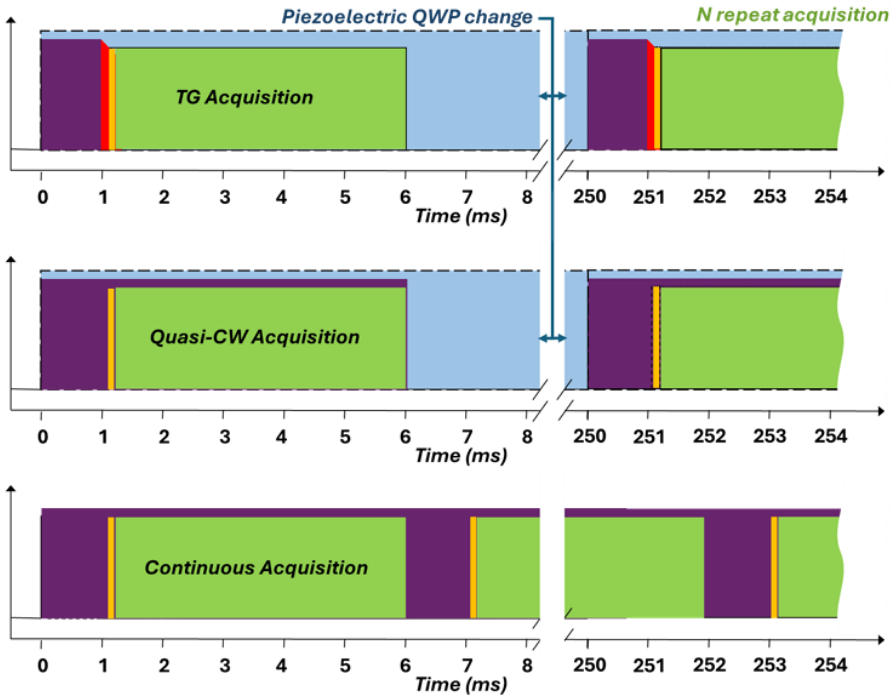

Supplementary Figure 4: Schematic representation of three available time sequence modes. Purple: pulse for UV-LED illumination; Orange: 100 µs pulse to activate the CCD detector – in TG mode this is delayed by 20 µs (t_{delay}) to account for the 11 µs fall time of the LED (red); Green: 6 ms acquisition time ($t_{acq.}$); Blue: waveplate alternation. In TG acquisition mode the QWPs start to switch and the LED is pulsed for 1 ms ($t_{exc.}$), a 100 µs pulse activates the CCD which records for t_{acq} = 6 ms. The sequence runs at 4 Hz. In Quasi-CW acquisition mode the LED remains on for the whole time the CCD records then is disabled to reduce photobleaching while the QWP switches. In Continuous acquisition mode the LED remains on constantly and the CCD collects all spectra for one QWP orientation then the opposite QWP orientation.

Supplementary Note 1: Detailed description of the timing sequences coordinated with QWP orientation.

In TG acquisition mode a periodic pulse sequence (4 Hz cycle frequency) is used to alternate the QWP and trigger the LED and CCD to allow variable delay time resolved CPL detection. The QWP is shifted to one orientation for a fixed dwell time before switching to the other orientation for the next cycle to collect one spectrum for each of left- and right-CPL. This enables observation of changing CPL signals vs time that can allow monitoring of dynamic reactions and processes. During each 250 ms interval, a brief LED pulse ($t_{exc.}$

= 1 ms duration) is used to excite the sample. Pulsed excitation is an important attribute as it allows minimisation of excitation light exposure to avoid photobleaching that is often a mitigating factor in collecting spectra over longer time periods. After a short delay (t_{delay} = 0.02 ms) allowing for the fall time of the LED (0.011ms),[2] the CCD detector is electronically gated on and integrates the luminescence for a $t_{acq.}$ = 6 ms acquisition window. This set 6 ms integration time represents the manufacturers default minimum exposure time of the employed CCD (Ocean Optics MayaPro). At the end of the 6 ms window, the CCD is read out, yielding one full emission spectrum corresponding to the QWP orientation (i.e. essentially a left-CPL or right-CPL spectrum). The QWP then switches to the alternate orientation and the sequence (LED pulse → CCD gate) repeats, producing the next spectrum for the opposite circular polarisation. The switching of the QWPs using the piezoelectric stage takes ~200 ms, however, an additional rest time (50 ms) is added to ensure the QWP has settled in the correct position and all emission has decayed before the alternate spectrum is obtained. The QWP can start moving once the LED begins its pulse because the precise alignment results in the same transmission intensity and polarisation across the whole window and the CCD exposure is complete before the QWP has shifted out of the emission beam (SI Figure 3). Recording one left-CPL spectrum then one right-CPL spectrum has the advantage that any degradation of the compound happens at an equal rate as opposed to recording all left-CPL spectra then all right-CPL spectra. The use of such time gating mechanism removes any shorter-lived emission from organic luminophores compared to longer-lived emission from, for example, Eu(III) complexes (SI Figure 5 and 6). To allow for recording of CPL spectra of compounds with shorter lifetimes, the timing sequence has to be altered so that the excitation is on during the whole acquisition exposure of the CCD. This would increase the risk of photobleaching which would decrease the emission intensity over the whole spectral measurement time, however, there is no need for the LED to remain on during the shift of QWPs, only while the individual exposure is taken. Switching the LED off while there is no emission collection results in a quasi-CW acquisition mode. This greatly reduces sample degradation allowing for a larger number of spectra averages to be recorded to reduce signal to noise ratio. This is particularly useful for organic samples with considerably lower g_{lum} values. For measurements where the sample is resistant towards photobleaching and faster acquisition times are desirable, the instrument can be operated in continuous mode where the excitation LED remains on for the whole measurement. In this mode, the experiment times can be significantly reduced by first recording all of the set number of left-CPL spectra to be, followed by the switch to the alternative QWP orientation to record all of the right-CPL spectra.

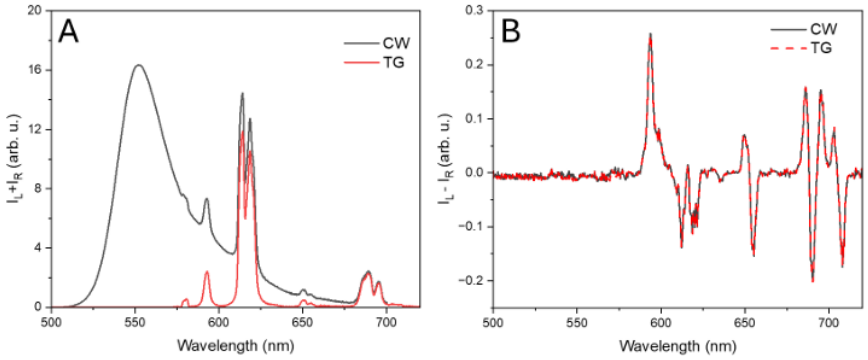

Supplementary Figure 5: Removal of short-lived emission (ns) using TG acquisition mode. (A) Total emission spectra of a blend of Rhodamine 6G and Δ-EuL^1 ([C] = 1 μM respectively (B) Comparison of the corresponding CPL spectrum. λ_{ex} = 365 nm, 6 ms/spectrum integration time and 100 average spectra). (Black) Spectrum recorded using quasi-CW acquisition mode, whilst (Red) spectrum recorded using TG acquisition mode (as detailed in SI Figure 4 using a 20 μs delay between excitation pulse and emission detection window). Total $t_{acq..}$ = 50 and 2.5 seconds respectively.

Name	Structure	λ_{max} (nm)	ε ($M^{-1}cm^{-1}$)	φ	g_{lum}	β_i (λ- range in nm)	CPB_i (M^{-1} cm^{-1})
Rhodamine 6G	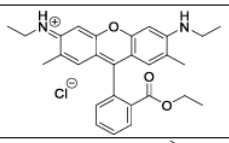	530	116000	0.95	0	1 (500 – 700 nm)	0 *(/200 nm)*
Δ-EuL^1	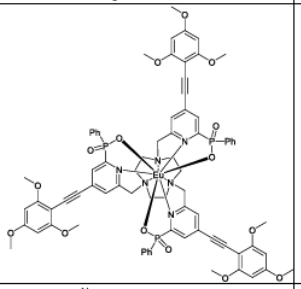	356	65000	0.50	0.18 (ΔJ_1) 0.001 (ΔJ_2)	0.053 (585 – 605 nm) 0.33 (605 – 625 nm)	155 *(/ 20 nm)* 10.7 *(/ 20 nm)*
PP-PDI^1	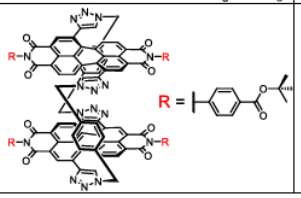	522	61700	0.35	1.2* 10^{-2}	1 (600 – 800 nm)	129.6 */200 nm*

(R)-BOD-3	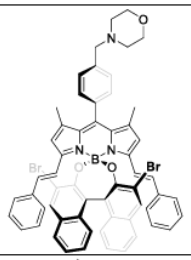	635	64000	0.77	$1.4^{*}10^{-3}$	1 (620 – 780 nm)	34.5 (/ 160 nm)
(S)-BOD-2	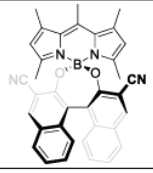	503	50800	0.87	$2.0^{*}10^{-4}$	1 (580 – 800 nm)	4.4 *(/ 220 nm)*

Supplementary Figure 6: Structure and photophysical parameters of test compounds. ***CPB*** $= \varepsilon * \phi * (g_{lum}/2)$; $CPB_i = CPB * \beta_i$.

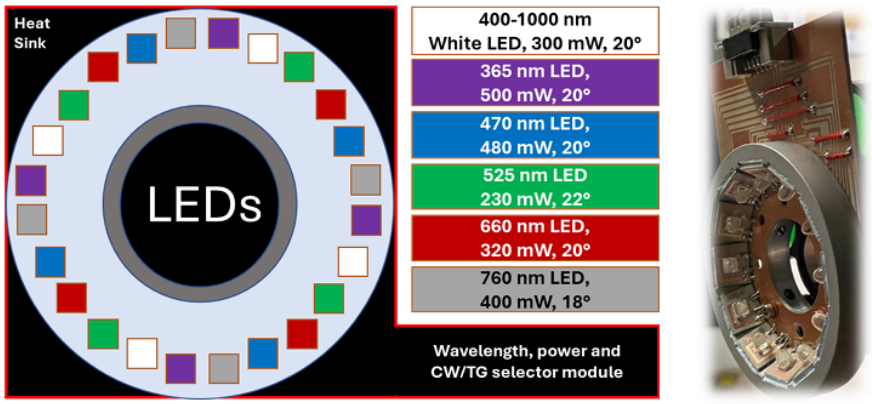

Supplementary Figure 7: (Left) Blueprint (Right) actual image of the custom-built LED carousel excitation source incorporating an array of LEDs with different wavelength ranges (Supplementary Note 3).

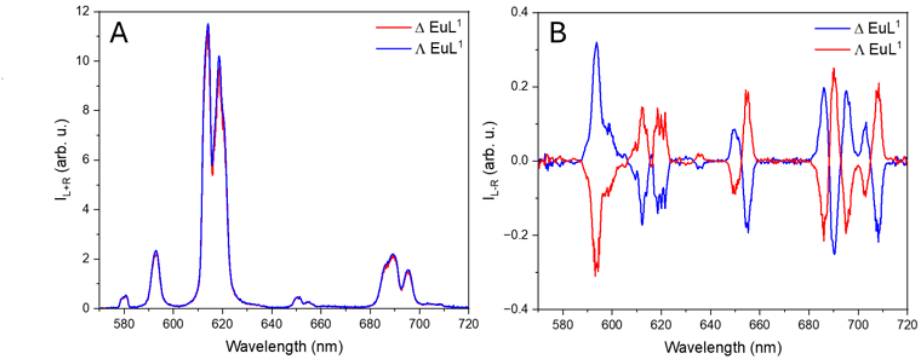

Supplementary Figure 8: TG SC- CPL of Δ and Λ EuL¹. (A) Total emission spectra (B) CPL spectra. [C] = 1 μM respectively, λ_{ex} =365 nm, 6 ms/spectrum integration time and 100 average spectra. Spectra recorded using TG acquisition mode (total $t_{acq..}$ = 50 seconds).

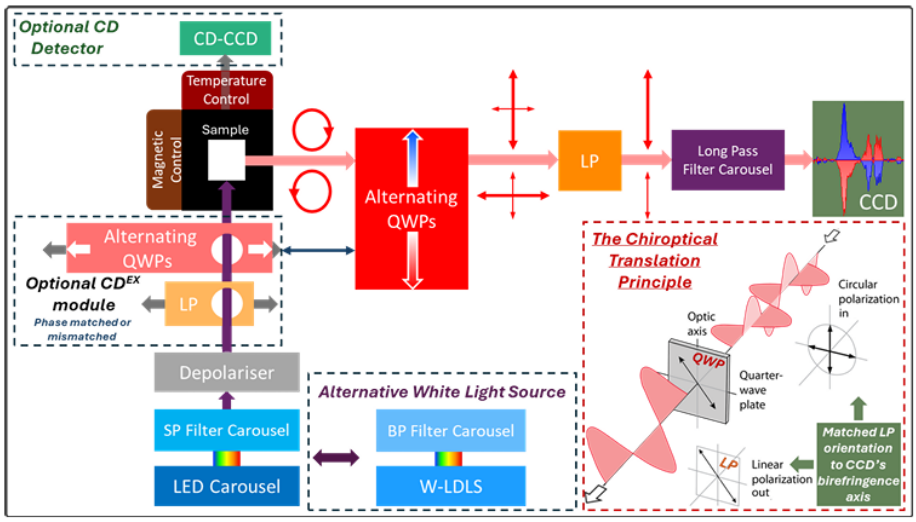

Supplementary Figure 9: Concept of SC/CD-C2PL – a Complete Compact Chiroptical Toolbox. The original design of SC-CPL has been extended with an add-in alternating (phase matched or mismatched) CPL excitation module. To maximise versatility a second CCD dedicated to true CD measurements can also be incorporated. *(This is necessary as beam routing the CD spectroscopy arm classically measured at a 180-degree orientation (absorbance: parallel vs. emission: perpendicular detection) to a 90-degree detection orientation using mirrors would detrimentally alter and change the CD measurements due to reflection induced CPL inversion. Calibration and correction of this would add complexity that is outweighed by the simplicity and cost of adding a*

secondary dedicated CD CCD detector. Employing a secondary CCD will also introduce the added benefit of CD wavelength range and resolution tuning via grating and slits.) An alternative pulsed White Laser Driven Light Source (W-LDLS) and Band Pass filter-based wavelength selector can also be employed to fine tune and extend the excitation light range (Supplementary Note 3).

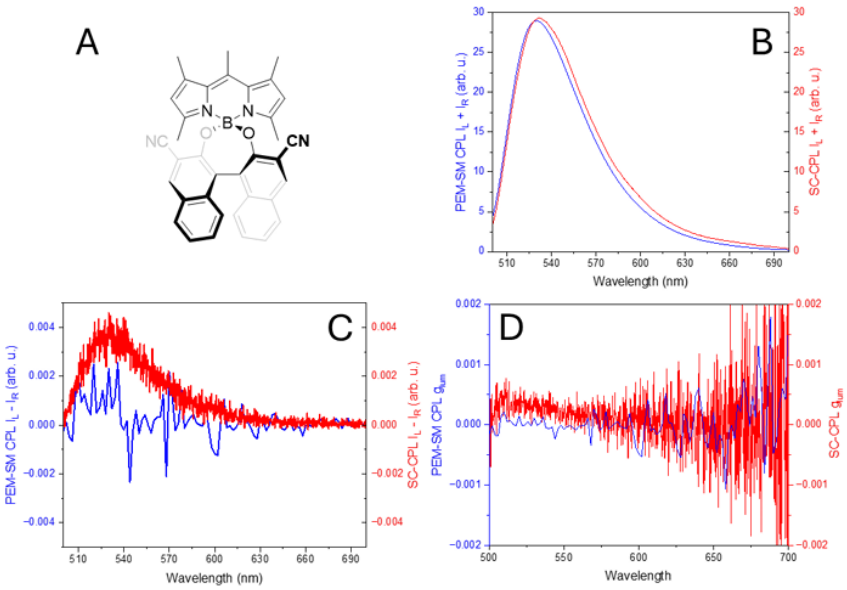

Supplementary Figure 10: Validation of the sensitivity and limitations of SC-CPL (red line) against the benchmark PEM-CPL using low g_{lum} BOD-2. *Structure of (A) (S)-BOD-2; (B): $I_L + I_R$; (C): $I_L - I_R$; (D): g_{lum}. Blue traces are for the spectra recorded on a PEM-CPL and red traces are for the SC-CPL. The mode of SC-CPL acquisition of spectra is TG (λ_{ex} = 470 nm, 1000 avg. spectra, total $t_{acq..}$ = 25 seconds, PEM-CPL: 20 avg. spectra. total $t_{acq..}$ = 4 h). The SC-CPL has a spectral resolution of 0.2 nm whilst the PEM-CM CPL has a set excitation and emission resolution of 9 nm respectively. [S-BOD-2] = 1.5 μM*

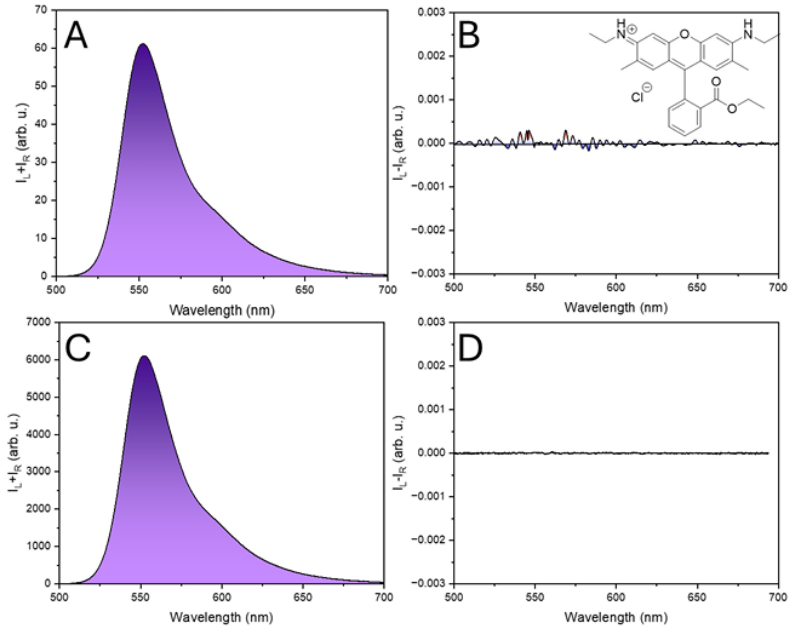

Supplementary Figure 11: CW-SC-CPL spectral comparison of achiral fluorophore Rhodamine 6G to demonstrate null-measurement and improved S/N ratio 100 vs. 10000 averaged scans. *(A + C): $I_L + I_R$; (B+ D): $I_L - I_R$ spectrum of Rhodamine 6G. A + B and B consist of 100 average scans ($t_{acq..}$ = 2.5 seconds) and C + D 10000 average scans ($t_{acq..}$ = 250 seconds) respectively (λ_{ex} = 365 nm, 400-800nm fixed spectral range, EtOH, [C] = 0.8 µM) each with an integration time of 6 ms/spectrum. Inset: structure of Rhodamine 6G.*

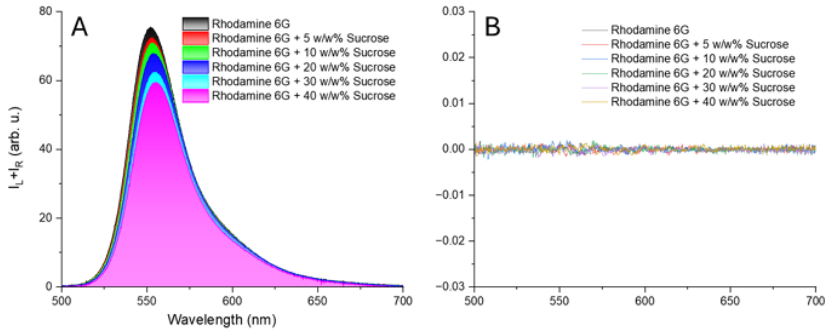

Supplementary Figure 12: CW-SC-CPL spectra of achiral fluorophore Rhodamine 6G for validation of the elimination of stray linear polarised light reaching the detector in the SC-CPL layout. *(A): $I_L + I_R$; (B): $I_L - I_R$ spectrum with incremental addition of sucrose in water (0 – 40 w/w%), [C] = 0.8 µM). Eash spectra consist of 100 average scans ($t_{acq..}$ = 2.5 seconds, λ_{ex} = 365 nm, 400-800nm fixed spectral range, EtOH each with an integration time of 6 ms/spectrum.*

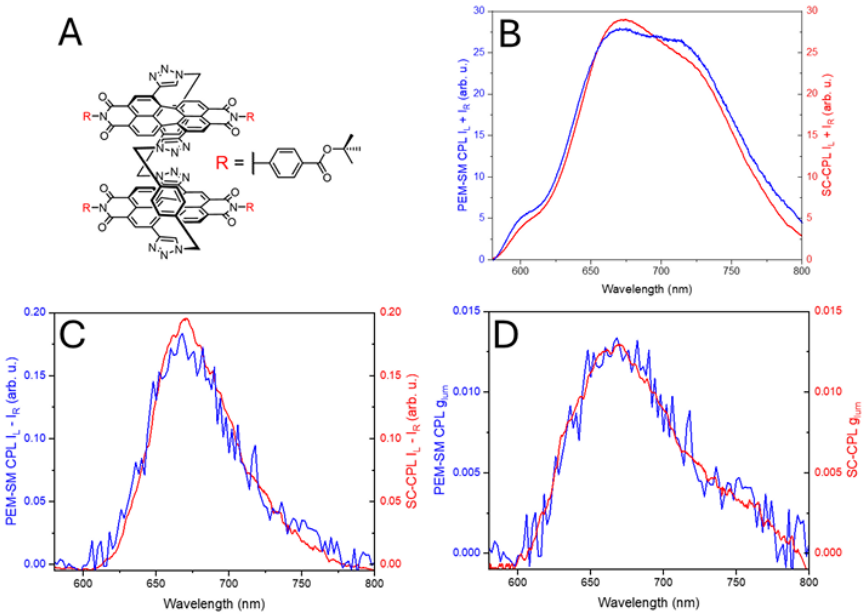

Supplementary Figure 13: Comparison of SC-CPL and PEM-CPL spectra of Δ-EuL[1] and PP-PDI[1]. *(A) Structure of PP-PDI[1]; (B): $I_L + I_R$; (C): $I_L - I_R$; (D): g_{lum} full spectrum PP-PDI[1] ([C] = 1.5 μM) λ_{ex} 525 nm. Blue traces are for the spectra recorded on a PEM-CPL and red traces are for the SC-CPL. The mode of SC-CPL acquisition of spectra is quasi-CW (10000 avg. spectra, total $t_{acq..}$ = 33.5 minutes, PEM-CPL: 20 avg. spectra. total $t_{acq..}$ = 4 h). No observed photobleaching of PP-PDI[1] was observed with SC-CPL, using PEM-CPL 5% total intensity and CPL signal loss was observed with constant g_{lum} calculated for each averaged spectrum.*

Supplementary Note 2: PEM-SM CPL Operating Principle.[3]

CPL was measured with a home-built (modular) spectrometer. The excitation source was a broad band (170 nm – 2500 nm) laser- driven light source EQ 99 (Elliot Scientific, 0.75W). The excitation wavelength was selected by feeding the broadband light into an Acton SP-2155 monochromator (Princeton Instruments); the collimated light was focused into the sample cell (1 cm quartz cuvette). Sample PL emission was collected perpendicular to the excitation direction with a lens (f = 150 mm). The emission was fed through a photoelastic modulator (PEM) (Hinds Series II/FS42AA) and through a linear sheet polariser (Edmund Optics, 47216). The light was then focused into a second scanning monochromator (Acton SP2155) and subsequently on to a photomultiplier tube (PMT) (Hamamatsu H10723 series). The detection of the CPL signal was achieved using the field modulation lock-in technique. The electronic signal from the PMT was fed into a lock-in amplifier (Hinds Instruments Signaloc Model 2100). The reference signal for the

lock-in detection was provided by the PEM control unit. The monochromators, PEM control unit and lock-in amplifier were interfaced to a desktop PC and controlled by a custom-written LabVIEW graphic user interface. The lock-in amplifier provided two signals, an AC signal corresponding to (I_L- I_R) and a DC signal corresponding to (I_L+ I_R) after background subtraction. The emission dissymmetry factor was therefore readily obtained from the experimental data, as 2 AC/DC. Spectral calibration of the scanning monochromator was performed using a Hg-Ar calibration lamp (Ocean Optics, HG-2). A correction factor for the wavelength dependence of the detection system was constructed using a calibrated lamp (Ocean Optics, HL-2000). The measured raw data was subsequently corrected using this correction factor. The validation of the CPL detection systems was achieved using light emitting diodes (LEDs) at various emission wavelengths. The LED was mounted in the sample holder and the light from the LED was fed through a broad band polarising filter and λ/4 plate (ThorLabs, LPVISE100-A and AQWP05M-600) to generate circularly polarised light. Prior to all measurements, the λ/4 plate and a LED were used to set the phase of the lock-in amplifier correctly. The emission spectra were recorded with 0.5 nm step size and the slits of the detection monochromator were set to a slit width corresponding to a spectral resolution of 0.25 nm. CPL spectra (as well as total emission spectra) were obtained through an averaging procedure of several scans.; all calculations were carried out using raw spectral data.

Supplementary Note 3: Components Used

Component	**Manufacturer**	**Model**	**Price** *(GBP)*
400-1000 nm white LED (300 mW)	Roithner LaserTechnik	SMB1N-BB450-02	£16.10
365 nm LED (640 mW)	Roithner LaserTechnik	SMB1N-365V-02	£14.50
470 nm LED (470 mW)	Roithner LaserTechnik	SMB1N-D470-02	£8.50
525 nm LED (230 mW)	Roithner LaserTechnik	SMB1N-525V-02	£8.50
660 nm LED (320 mW)	Roithner LaserTechnik	SMB1N-D660N-02	£8.00
760 nm LED (400 mW)	Roithner LaserTechnik	SMB1N-760D-02	£9.10
LED collimator lens	Comar Optics	10 TS 25	£241.10
400 nm short pass filter	Edmund Optics	15466	£93.70
500 nm short pass filter	Edmund Optics	15257	£93.70
550 nm short pass filter	Edmund Optics	15258	£93.70
700 nm short pass filter	Edmund Optics	15261	£93.70
800 nm short pass filter	Edmund Optics	15263	£93.70
Filter wheel (x2)	Thor Labs	FW102C	£1242
Ground glass filter	Thor Labs	DGUV10-220	£28.20
400 nm long pass filter	Edmund Optics	62981	£223.30

475 nm long pass filter	Edmund Optics	84743	£223.30
525 nm long pass filter	Edmund Optics	84744	£223.30
675 nm long pass filter	Edmund Optics	84747	£223.30
775 nm long pass filter	Edmund Optics	86069	£223.30
Cuvette holder	ThorLabs	CVH100/M	£524.70
Piezoelectric stage	ThorLabs	ELL6K	£198.30
Piezoelectric rotational mount	ThorLabs	ELL14K	£513.40
Achromatic quarter wave plate 400-800 nm (x2)	ThorLabs	AQWP05M-600	£815.20
Linear polariser (10000 :1)	Edmund Optics	47216	£172.50
CCD	Ocean Optics	Maya2000Pro	£6800
CCD collimating lens	Ocean Optics	74-DA	£138
DAQ device	National Instruments	USB-6210	£825
Calibration lamp	Ocean Optics	HL-2000	£2400

To demonstrate versatility even further, a broad wavelength pulsed laser driven light source (LDLS) coupled to a controlled rotational carousel with appropriately selected bandpass (BP) filters was also used as an alternative excitation source. In our case we have equipped and tested our SC-CPL spectrometer with a Edmund Optics white light source kit LS-WL1(23881, £2750), equipped with LS-fiber-1000 (28743, £315) and LightPath 354260 0.16NA collimator lens(47227)) with a ThorLabs FW212C (12 position, ½" optic) filter wheel containing the following BP filters (Edmund optics, OD 4.0, £153.40 each): 365/10 (65069), 400/10 (65071), 420/10 (65075), 440/10 (88567), 480/10 (65084), 500/10 (65088), 535/10 (65095), 568/10 (65099), 600/10 (65102), 636/10 (65106), 660/10 (86086) and 700/25 (87888) nm. Additionally available interchangable ½" filters to facilitate maximised photon flux and wider UV excitation range are Edmund Optics 355/10 (34490), 375/25 (12077) and 375/50 (12091) nm. Both light source and filter wheel were integrated and automated by the SC-CPL's dedicated LabVIEW automation and readout software. The CW, quasi-CW and TG sequences are identical for both LED and LDLS excitation. Results shown throughout the manuscript were conducted using the dedicated LED carousel due to ease of use and prior availability. The total final build cost of the SC-CPL instrument (built as per main text Figure 1) presented herein is £15k.

Supplementary Note 4: Sample Preparation

EuL[1] was prepared according to established procedures.[4]

PDI[1] was prepared according to established procedures.[5]

BOD-2 and 3 was prepared according to established procedures.[6]

Rhodamine 6G perchlorate (99%) was purchased from Sigma Aldrich.

All samples were prepared to be optically dilute with an absorbance of 0.1 at the excitation wavelength used. EuL^1 was prepared in MeCN, [C] = 1.5 μM, PDI^1 was prepared in DCM, BOD-2 and BOD-3 [C] = 1.5 μM was prepared in $CHCl_3$ and Rhodamine 6G was prepared in EtOH, [C] = 0.8 μM.

References

1. Kondo, Y. *et al*. Temperature-Dependent Circularly Polarized Luminescence Measurement Using KBr Pellet Method. *Front Chem* **Volume 8-**, (2020).
2. Pal, R. & Beeby, A. Simple and versatile modifications allowing time gated spectral acquisition, imaging and lifetime profiling on conventional wide-field microscopes. *Methods Appl. Fluoresc.* **2**, (2014).
3. Carr, R. *et al*. Induced circularly polarized luminescence arising from anion or protein binding to racemic emissive lanthanide complexes. *Methods Appl Fluoresc* **2**, 024007 (2014).
4. Frawley, A. T., Pal, R. & Parker, D. Very bright, enantiopure europium(III) complexes allow time-gated chiral contrast imaging. *Chem. Commun.* **52**, (2016).
5. Penty, S. E. *et al*. A Chirally Locked Bis-perylene Diimide Macrocycle: Consequences for Chiral Self-Assembly and Circularly Polarized Luminescence. *J Am Chem Soc* **146**, 5470–5479 (2024).
6. Stachelek, P., Serrano-Buitrago, S., Maroto, B. L., Pal, R. & de la Moya, S. Circularly Polarized Luminescence Bioimaging Using Chiral BODIPYs: A Model Scaffold for Advancing Unprecedented CPL Microscopy Using Small Full-Organic Probes. *ACS Appl Mater Interfaces* **16**, 67246–67254 (2024).